The Landau-Pomeranchuk-Migdal effect within a partonic transport approach

Dissertation
zur Erlangung des Doktorgrades
der Naturwissenschaften

vorgelegt beim Fachbereich Physik
der Johann Wolfgang Goethe-Universität
in Frankfurt am Main

von

Florian Senzel

aus Frankfurt am Main

Frankfurt am Main 2020
(D 30)

Vom Fachbereich Physik der Johann Wolfgang Goethe-Universität
als Dissertation angenommen.

Dekan: Prof. Dr. Michael Lang

Gutachter/-in: Prof. Dr. Carsten Greiner, Prof. Dr. Hannah Elfner

Datum der Disputation: 14. August 2020

Für Carina,

Sophia und Katharina

Contents

List of Figures

List of Tables

Deutschsprachige Zusammenfassung

Tomographie des Quark-Gluon-Plasmas im Labor

Angesiedelt in der Schnittmenge zwischen Kern- und Teilchenphysik, bietet die moderne Schwerionenphysik einen viel versprechenden Ansatz zur Beantwortung fundamentalster Fragen nach der Entstehung des Universums. Werden die Kerne schwerer Atome, sogenannte Schwerionen, auf nahezu Lichtgeschwindigkeit beschleunigt und anschließend kontrolliert zur Kollision gebracht, so werden in den entstehenden Kollisionszonen ungeheure Mengen Energie deponiert, was zur Folge hat, dass sich die vorliegende Materie in einem sehr heißen und dichten Zustand befindet, wie er auch kurz nach dem Urknall vorgelegen haben könnte. Durch die enormen Temperaturen in diesem Zustand sind die relevanten Freiheitsgrade der Materie nicht länger nuklearer Natur, sondern sind überwiegend von subnuklearen Teilchen, den Quarks und Gluonen, bestimmt, was dazu führt, dass dieser Zustand auch als Quark-Gluon-Plasma (QGP) bezeichnet wird. Diese Partonen wechselwirken miteinander mithilfe der starken Kernkraft, die beschrieben wird durch die Quantenchromodynamik (QCD) und die, neben der elektromagnetischen, der schwachen und der Gravitationskraft, eine der vier fundamentalen Wechselwirkungen des Standardmodells der Teilchenphysik ist.

Zu den wichtigsten Eigenschaften der Quantenchromodynamik gehören das sogenannte *confinement* und die *asymptotische Freiheit*. Während Ersteres besagt, dass die Kopplung zwischen Partonen stärker ist je weiter beide Partonen voneinander entfernt werden, so beschreibt Letzteres den Effekt, dass Partonen bei kleiner Distanz oder hohen Impulsskalen als quasi-frei angesehen werden können. Diese asymptotische Freiheit der QCD erlaubt die Anwendung von perturbativen Methoden (perturbative QCD, pQCD) bei hohen Teilchenenergien oder hohen Temperaturen der zu untersuchenden Materie. Ultrarelativistische Schwerionenkollisionen bieten nun einen aussichtsreichen Zugang zu einem besseren Verständnis dieser Eigenschaften der Quantenchromodynamik unter extremen Bedingungen.

Beginnend mit Studien am SPS[1]-Beschleuniger des europäischen Kernforschungszentrums CERN in der Nähe von Genf/Schweiz, konnten in verschiedenen Experimenten am RHIC[2] des BNL[3] auf Long Island/USA und am LHC[4]-Beschleunigers am CERN interessante Eigenschaften dieser heißen und dichten Materie festgestellt werden. Eine der phänomenalsten Entdeckungen in diesen Studien am RHIC- und LHC-Beschleuniger war, dass der neu entstandene Materiezustand als ein nahezu *ideales* Fluid mit einem geringen Scherviskositäts-über-Entropiedichte-Verhältnis beschrieben werden kann. Da jedoch die partonischen Freiheitsgrade des QGP aufgrund des *confinement* unter Raumbedingungen in Hadronen eingeschlossen und damit nicht direkt messbar sind, kann der Nachweis der Eigenschaften der entstandenen Materie nur indirekt erfolgen. Dazu werden Observablen definiert, von denen man eine Sensitivität auf die zu untersuchenden Eigenschaften erwartet

---

[1] Super Proton Synchrotron

[2] Relativistic Heavy-Ion Collider

[3] Brookhaven National Laboratory

[4] Large Hadron Collider

und für die theoretische Modelle formuliert werden können. Nur das Zusammenspiel der experimentellen Messung und diesen theoretischen Modellen ermöglicht anschließend eine verlässliche Charakterisierung der entstandenen Materie.

Eine der prominentesten Observablen zur Untersuchung heißer und dichter Materie in ultrarelativistischen Schwerionenkollisionen ist das sogenannte „Jet Quenching“. Jets sind hochenergetische Partonen, die paarweise durch seltene Parton-Parton-Interaktionen mit hohem Impulsübertrag in z.B. Proton-Proton-Kollisionen oder den anfänglichen Nukleon-Nukleon-Streuungen einer Schwerionenkollision entstehen. Während Jets in Proton-Proton-Experimenten aufgrund ihrer hohen Virtualität weitere Partonen abstrahlen und somit Schauerstrukturen ausbilden, wechselwirken Jets, die in der Anfangsphase von Schwerionenkollisionen produziert werden, zusätzlich mit dem weicheren Hintergrundmedium der Schwerionenkollision bevor sie schließlich als Hadronen in den Detektoren nachgewiesen werden können. Abhängig von den Eigenschaften des durchquerten Mediums, wie z.B. Temperatur, Dichte oder Länge, verlieren Jets durch diese Interaktionen Energie und Impuls, sodass die anschließende Untersuchung ihres Energieverlusts sie zu einer tomographischen Sonde des entstandenen heißen und dichten Mediums macht.

Ein besonderer Vorteil ist dabei die hohe Energie der Jets, führt sie doch zum Einen zu einer kurzen Formationszeit, sodass Jets bereits früh mit dem Hintergrundmedium interagieren und damit auch an der frühen Phase der Schwerionenkollision teilnehmen können. Zum Anderen kann durch die hohen relevanten Impulsskalen die Produktion der Jets mithilfe von perturbativer QCD beschrieben werden. Ausgehend von einer Faktorisierung zwischen der Anfangsverteilung von Partonen in Nukleonen, dem eigentlichen harten Parton-Parton-Streuprozess und der anschließenden Fragmentation der Partonen zu Hadronen, lässt sich die eigentliche Mediumsmodifikation von Jets durch einen Vergleich von Jet-Ereignissen in Schwerionenkollisionen mit entsprechenden Ereignissen in Proton-Proton-Kollisionen charakterisieren. Somit konnte der Energieverlust von Jets experimentell auf verschiedene Arten nachgewiesen werden: Während der nukleare Modifikationsfaktor R_{AA} das Verhältnis der Transversalimpuls-Spektren in Schwerionenkollisionen mit entsprechend skalierten Spektren in Proton-Proton-Kollisionen vergleicht, wurden durch die gesteigerten Kollisionsenergien am LHC-Beschleuniger und damit einhergehend höheren Produktionswahrscheinlichkeiten sehr hochenergetischer Jets auch Untersuchungen möglich, in denen Jets basierend auf ihren Teilchenschauer rekonstruiert und dann sowohl deren Spektren als auch Jet-Korrelationen pro Ereignis verglichen werden konnten. In beiden Arten von Studien konnte ein signifikanter Energieverlust bzw. eine starke Unterdrückung hochenergetischer Jets bestätigt werden, was als weitere Evidenz für die Entstehung eines Quark-Gluon-Plasmas in diesen Schwerionen-Experimenten gilt.

Verschiedene theoretische Modelle basierend auf perturbativer Quantenchromodynamik erklären den enormen Jet-Energieverlust durch sowohl partonische Streuungen der Jets innerhalb des heißen Hintergrundmediums als auch durch gluonische Abstrahlprozesse, die durch Streuungen der Jets mit dem Medium induziert werden. Ein wichtiger quantenmechanischer Effekt, der bei Bremsstrahlungsprozessen hochenergetischer Teilchen innerhalb eines Mediums berücksichtigt werden muss, ist der Landau-Pomeranchuk-Migdal-Effekt (LPM-Effekt). Dieser Effekt, der zunächst für photonische Bremsstrahlungsprozesse hochenergetischer Elektronen innerhalb der Quantenelektrodynmik durch Landau, Pomeranchuk und Migdal entdeckt wurde, sagt eine kohärente Unterdrückung von aufeinanderfolgenden Bremsstrahlungsprozessen voraus, die durch die endliche Formationszeit der abgestrahlten Teilchen hervorgerufen wird. Ist diese Formationszeit länger als die mittlere, freie Weglänge zwischen den Streuungen, so kann nicht mehr länger von unabhängigen, radiative Prozessen gesprochen werden, die durch die Bethe-Heitler-Gleichung beschrieben werden und z.B. zu einer linearen Weglängenabhänigkeit des radiativen Energieverlusts führt. Im Falle von gluonischen Abstrahlprozessen innerhalb der Quantenchromodynamik wird dieser Effekt noch verstärkt, da die abgestrahlten Gluonen selber mit den Mediumskomponenten wechselwirken können. Dies führt zu einer charakteristischen, nicht-linearen Abhängigkeiten des resultierenden, radiativen Jet-Energieverlusts in dünnen QCD-Medien.

Verwendetes Modell für den Energieverlust von Jets im Quark-Gluon-Plasma

In dieser Arbeit werden die Auswirkungen des nicht-Abelschen Landau-Pomeranchuk-Migdal-Effekts auf den Energieverlust hochenergetischer Jets innerhalb ultrarelativistischer Schwerionenkollisionen untersucht. Dazu wird das heiße und dichte Hintergrundmedium der Schwerionenkollisionen als expandierendes Quark-Gluon-Plasma beschrieben und mithilfe des semi-klassischen Transportmodells BAMPS[5] simuliert, welches die 3+1-dimensionale, relativistische Boltzmann-Gleichung durch einen stochastischen Testteilchen-Ansatz löst und bereits in zahlreichen vorherigen Studien seine Anwendbarkeit in der Beschreibung von Schwerionenkollisionen am RHIC- und LHC-Beschleuniger unter Beweis gestellt hat. Innerhalb von BAMPS stellen quasi-freie Gluonen und leichte Quarks die Freiheitsgrade des Mediums dar, sodass die mikroskopischen Prozessen innerhalb dieses partonischen Mediums mithilfe von Wirkungsquerschnitten aus perturbativer Quantenchromodynamik berechnet werden können. Dabei dürfen die Partonen untereinander sowohl mittels elastischer $2 \rightarrow 2$-Streuungen, welche die Teilchenzahl erhalten, als auch inelastischer $2 \leftrightarrow 3$ Prozesse, welche durch Gluonemission bzw. -annihilation die Teilchenzahl verändern, miteinander wechselwirken. Während $2 \rightarrow 2$-Interaktionen durch pQCD-Prozesse in führender Ordnung („leading-order pQCD"), wie z.B. $gg \rightarrow gg$ oder $gq \rightarrow gq$, beschrieben werden, wird für die inelastischen $2 \leftrightarrow 3$-Prozesse, wie z.B. $gg \rightarrow ggg$ oder $ggg \rightarrow gg$, eine verbesserte Gunion-Bertsch-Näherung für Bremsstrahlungsprozesse verwendet, für die eine verbesserte Übereinstimmung mit dem exakten pQCD-Matrixelement bei Vorwärts- bzw. Rückwärtsrapidität der Gluonemissionen in früheren Studien nachgewiesen werden konnte. Die daraus resultierenden Eigenschaften der mikroskopischen Prozesse werden in Kapitel 3 dieser Arbeit eingeführt. In den verschiedenen pQCD-Wirkungsquerschnitten auftretende Divergenzen, die durch die begrenzte Anwendbarkeit von pQCD bei soften Impulsskalen entstehen, werden durch effektive Debye-Massen abgeschirmt, die durch die Präsenz anderer Partonen innerhalb des heißen und dichten Mediums hervorgerufen werden. Weitere Details des verwendeten Ansatzes zur Modellierung des Quark-Gluon-Plasmas werden in Kapitel 4 diskutiert.

Im Gegensatz zu anderen theoretischen Modellen, die die Jet-Medium-Interaktionen mithilfe von pQCD-Wechselwirkungen und die Evolution des Mediums durch relativistische Hydrodynamik beschreiben, hat die Anwendung eines partonischen Transportmodells für die Untersuchung des Jet-Energieverlusts den Vorteil, dass sowohl für die Jet-Medium-Interaktionen als auch die Interaktionen zwischen den partonischen Mediumskomponenten die gleiche Art der Wechselwirkung verwendet wird. Auf der anderen Seite erschwert speziell die Betrachtung der Partonen als semi-klassische, mikroskopische Teilchen und nicht als quantenmechanische Objekte eine rigorose Implementation des quantenfeldtheoretischen LPM-Effekts in ein partonisches Transportmodell. Während die Beschreibung

---

[5] Boltzmann Approach for Multi-Parton Scattering

der Interaktionen durch die Boltzmann-Gleichung eine Lokalität der Interaktionen voraussetzt, führt die endliche Formationszeit von Gluonemissionen unter Berücksichtigung des LPM-Effekts zu einer räumlichen Ausdehnung der Wechselwirkungen. Daher wird in der vorliegenden Arbeit ein besonderer Fokus auf die Untersuchung verschiedener Ansätze für die Implementierung des nicht-abelschen LPM-Effekt in ein semi-klassisches Transportmodell gelegt, um damit die Auswirkungen des LPM-Effekts auf die Eigenschaften des resultierenden, radiativen Jet-Energieverlusts zu zeigen.

Numerische Implementierungen des LPM-Effekts

Den wegweisenden, analytischen Arbeiten von Baier u. a. (BDMPS) [Bai+95; Bai+97a; Bai+98b] bezüglich des LPM-Effekts in der Quantenchromodynamik folgend, erwartet man für den radiativen Energieverlust eines hochenergetischen, partonischen Projektils mit Energie E, das ein thermisches Medium mit Temperatur T und Länge L durchquert und dabei medium-induziert Gluonen der Energie ω und Transversalimpuls $k_\perp$ abstrahlt, im eikonalen Limit $E \gg \omega \gg k_\perp$ folgende charakteristische Abhängigkeiten:

- Durch die endliche Formationszeit, $\tau_f \sim \omega/k_\perp^2$, werden hochenergetischere Gluonemissionen unterdrückt, da sie bei gegebenem Transversalimpuls eine längere Formationszeit besitzen. Dies führt dazu, dass die differentielle Emissionsrate eines Projektils im LPM-Limit wie $\mathrm{d}\Gamma/\mathrm{d}\omega \sim \omega^{-3/2}$ von der Gluonenergie ω abhängt.
- Gleichzeitig führt die Berücksichtigung der endlichen Formationszeit der Gluonemissionen zu einer charakteristischen Längenabhängigkeit des radiativen Energieverlusts des Projektils, sodass sich für den radiativen differentiellen Energieverlust $\mathrm{d}E/\mathrm{d}x \sim L$ in dünnen Medien und $\mathrm{d}E/\mathrm{d}x \sim \mathrm{const.}$ in dicken Medien ergibt.

Im Rahmen dieser Arbeit werden drei verschiedene Ansätze zur Beschreibung des LPM-Effekts in BAMPS implementiert und deren Auswirkungen auf den resultierenden numerischen Energieverlust der Jets zunächst in5 durch Vergleich mit den erwarteten analytischen Abhängigkeiten im eikonalen Limit verglichen:

θ-LPM Die bisherige Implementation des LPM-Effekts in BAMPS basiert auf einer effektiven Unterdrückung der radiativen $2 \leftrightarrow 3$-Matrixelemente mithilfe der Thetafunktion $\theta(\tau_f - \lambda)$, wobei τ_f die Formationszeit des abgestrahlten Gluons und λ die mittlere freie Weglänge des abstrahlenden Partons innerhalb des Mediums ist. Durch diesen „θ-LPM“-Ansatz werden longitudinale Gluonabstrahlungen, deren längere Formationszeit zu einem Überlapp zwischen aufeinanderfolgenden Streuprozessen führen würde, unterdrückt und damit sichergestellt, dass nur inkohärente (unabhängige) Gluonemissionen stattfinden können. Mithilfe des „θ-LPM“-Ansatzes kann für die differentielle Gluonemissionsrate $\mathrm{d}\Gamma/\mathrm{d}\omega$ die charakteristische $\omega^{-3/2}$-Abhängigkeit des nicht-Abelschen LPM-Effekts innerhalb von BAMPS nachgewiesen werden.

Obwohl die endliche Formationszeit der Gluonemissionen zwar im Matrixelement berücksichtigt wird, findet jedoch die eigentliche Abstrahlung instantan und damit an der räumlichen Position des $2 \to 3$-Prozesses statt. Dadurch zeigt der „θ-LPM“-Ansatz zwar die für den LPM-Effekt charakteristische Abhängigkeit des Gluon-Spektrums, vernachlässigt aber die $\mathrm{d}E/\mathrm{d}x \sim L$-Abhängigkeit des radiativen Energieverlusts in dünnen Medien und zeigt nur die für dicke Medien gültige Beziehung $\mathrm{d}E/\mathrm{d}x \sim \mathrm{const.}$.

Um auch kohärente Abstrahlprozesse im „θ-LPM“-Ansatz effektiv berücksichtigen zu können, wird der Parameter X_{LPM} eingeführt, der über $\theta\big(\tau_f - X_{\mathrm{LPM}}\lambda\big)$ parametrisch auch softere Gluonabstrahlungen erlaubt. Die erhöhte Emissionsrate bei kleinen Transversalimpulsen $k_\perp$ führt dabei zu einer logarithmischen Sensitivität des radiativen Energieverlusts auf den Parameter X_{LPM}.

Stochastischer LPM Durch einen Vergleich mit den analytischen Ergebnissen von BDMPS, konnte Zapp, Wiedemann und Stachel [ZSW09; ZSW11] einen numerischen Algorithmus entwickeln, der den LPM-Effekt durch eine stochastische Unterdrückung der Gluonen während ihrer Formationszeit modelliert. Dazu werden die durch einen $2 \to 3$-Bremsstrahlungsprozess abgestrahlten Gluonen zunächst als Test-Gluonen behandelt, die während ihrer Formationszeit elastisch wechselwirken und somit ihre Formationszeit selbstkonsistent modifizieren können. Nach Beendigung dieser endlichen Formationszeit wird stochastisch ermittelt, ob die jeweilige Emission tatsächlich stattgefunden hat oder ob sie nachträglich unterdrückt wird. Durch diesen Algorithmus sind die Gluonabstrahlprozesse nicht mehr lokal, sondern über eine endliche Zeit ausgedehnt, was zur Folge hat, dass die korrekte Längenabhängigkeit des radiativen Jet-Energieverlusts sowohl in dünnen als auch in dicken Medien reproduziert werden kann.

In Rahmen der vorliegenden Dissertation wird diese „stochastische LPM“-Methode in BAMPS implementiert und ihr Zusammenspiel mit den bisherigen Modellannahmen innerhalb von BAMPS untersucht. Dazu wird zunächst ein vereinfachtes Modell mit konstanten Wirkungsquerschnitten für die elastischen Interaktionen der abgestrahlten Gluonen und der radiativen Prozesse der abstrahlenden Projektile definiert, für das sich die charakteristischen Abhängigkeiten des LPM-Effekts analytisch herleiten lassen. Unter diesen kontrollierten Bedingungen kann erfolgreich die numerische Anwendbarkeit des „stochastischen LPM“-Algorithmus innerhalb von BAMPS für verschiedene Projektilenergien E und Mediumslängen L demonstriert werden.

Im weiteren Verlauf der Arbeit werden die vereinfachten Interaktionen schrittweise durch die bekannten $\sqrt{\hat{s}}$-abhängigen $2 \to 2$- und $2 \to 3$-pQCD-Prozesse von BAMPS ersetzt und die Auswirkungen dieser Ersetzungen auf den resultierenden Jet-Energieverlust präsentiert. Dabei kann erfolgreich nachgewiesen werden, dass die endliche Formationszeit innerhalb der „stochastischen LPM“-Methode auch unter Verwendung der pQCD-Wirkungsquerschnitte zu einer L^2-Abhängigkeit des Energieverlusts ΔE in dünnen Medien und einer L-Abhängigkeit in dicken Medien führt.

Obwohl die differentielle Emissionsrate $\mathrm{d}\Gamma/\mathrm{d}\omega$ des „stochastischen LPM“-Algorithmus bei mittleren Gluonenergien $T < \omega < E$ wie erwartet eine $\omega^{-3/2}$-Abhängigkeit zeigt, führen sowohl Effekte der $2 \to 2$- als auch der initialen $2 \to 3$-Prozesse in BAMPS zu Abweichungen bei niedrigen Gluonenergien $\omega < T$. Dabei stellt sich durch Vergleich mit differentiellen Streuraten aus „Hard Themal Loop“-Rechnungen (HTL) heraus, dass insbesondere die konkrete Wahl der effektiven Debye-Abschirmung in den $2 \to 2$-Prozessen innerhalb von BAMPS eine signifikante Unterdrückung von soften Impulsüberträgen ($q_\perp^2 \lessapprox T^2$) bewirkt. Gleichzeitig führt die $\sqrt{\hat{s}}$-Divergenz im Vier-Gluonen-Kanal des Prozesses $\mathrm{gg} \to \mathrm{gg}$, der in anderen analytischen Rechnungen oft vernachlässigt wird, zu einer divergierenden Streurate bei kleinen Gluonenergien. Beide Resultate zusammen ergeben Abweichungen zwischen BAMPS und anderen Modellen bei kleinen Gluonenergien $\omega < T$ für die Energie-Abhängigkeit des Transportparameters $\hat{q}$, welcher das Vermögen der Gluonen quantifiziert während ihrer Formationszeit Transversalimpuls zu akkumulieren. Diese Akkumulation wiederum bestimmt maßgeblich die resultierende Unterdrückung durch den nicht-Abelschen LPM-Effekt innerhalb des „stochastischen LPM“-Ansatzes. Des Weiteren wird bereits die Emissionsrate des anfänglichen Bremsstrahlungsprozesses bei kleinen Gluonenergien durch die softe $k_\perp$-Divergenz in Gunion-Bertsch-Näherung bestimmt, welche im „stochastischen LPM“-Ansatz nicht mehr durch eine Thetafunktion unterdrückt, sondern durch den Parameter ξ_{LPM} kontrolliert wird, der ein minimales Limit $k_{\perp;\,\text{min}} = \xi_{\text{LPM}}\sqrt{\hat{s}}$ vorgibt. Es kann gezeigt werden, dass wie bereits im „θ-LPM“-Ansatz auch, der resultierende Jet-Energieverlust logarithmisch von der Wahl des Parameters ξ_{LPM} abhängt.

AMY Während die beiden effektiven LPM-Methoden, „θ-LPM“ und „stochastischer LPM“, durch die Verwendung des Gunion-Bertsch-Matrixelements von Parametern für die Abschirmung softer Gluonemissionen abhängen, verhindern andere pQCD-Modelle diese soften Divergenzen durch eine Resummierung unendlich vieler Leiterdiagramme. Gleichzeitig wird durch die Resummierung der verschiedenen Leiterdiagramme der nicht-Abelsche LPM-Effekt implizit berücksichtigt. Eines dieser Modelle ist der AMY[6]-Formalismus [AMY02b], welcher die makroskopische Gluonemissionsrate basierend auf thermischer Feldtheorie berechnet. Unter Annahme einer Skalenseparation $T \gg g_s T \gg g_s^2 T$ und eines unendlich langen, thermischen Mediums, lassen sich damit differentielle Emissionsraten $\mathrm{d}\Gamma/\mathrm{d}\omega$ formulieren, deren numerische Berechnung innerhalb dieser Arbeit durchgeführt und anschließend mithilfe effektiver „$1 \leftrightarrow 2$“-Prozesse in BAMPS implementiert wird. Während die resultierende Gluonemissionsrate der „AMY“-Methode innerhalb von BAMPS die erwartete $\omega^{-3/2}$-Abhängigkeit zeigt, führt die Annahme eines unendlich langen Mediums zu der bereits diskutierten Längenunabhängigkeit des radiativen differentiellen Energieverlusts $\mathrm{d}E/\mathrm{d}x$. Durch den erfolgreichen Vergleich des Jet-Energieverlusts der „AMY“-Methode in BAMPS mit entsprechenden Rechnungen des MARTINI-Modells, welches die AMY-Raten in ein hydrodynamisches Medium einbettet, wird die numerische Implementation innerhalb von BAMPS validiert.

Nachdem die numerischen Realisierungen des LPM-Effekts innerhalb von BAMPS diskutiert wurden, werden im weiteren Verlauf die verschiedenen Ansätze quantitativ miteinander verglichen. Da es keine physikalischen Argumente für eine bestimmte Wahl der Parameter X_{LPM} und ξ_{LPM} in den beiden effektiven LPM-Ansätzen „θ-LPM“ und „stochastischer LPM“ gibt, werden deren Werte zunächst durch einen Vergleich mit dem Energieverlust in dicken Medien innerhalb der „AMY“-Methode bestimmt. Während innerhalb der „θ-LPM“-Methode die beste Übereinstimmung mit dem AMY-Energieverlust für $X_{\text{LPM}}^{\text{AMY}} = 0.05$ gefunden wird, werden die Parameter im „stochastischen LPM“-Ansatz zu $\xi_{\text{LPM}}^{\text{AMY; g}} = 0.015$ für eikonale Gluon-Projektile und zu $\xi_{\text{LPM}}^{\text{AMY; q}} = 0.01$ für eikonale Quark-Projektile bestimmt. Obwohl die drei Methoden nun einen ähnlichen differentiellen Energieverlust zeigen, unterscheiden sich die zugrundeliegenden differentiellen Emissionsraten $\mathrm{d}\Gamma/\mathrm{d}\omega$ und $\mathrm{d}\Gamma/\mathrm{d}k_\perp$ signifikant. Während der AMY-Formalismus eine divergierende Emissionsrate sowohl bei $\omega \to 0$ als auch $\omega \to E$ zeigt, führen die verschiedenen Annahmen in den beiden effektiven LPM-Ansätzen, wie z.B. die zugrundeliegenden, elastischen Interaktionen der Gluonen während der Formationszeit (Debye-abgeschirmte $2 \to 2$-Prozesse vs. elastische Streuungen aus HTL) oder das Abschirmen softer und kollinearer Gluonemissionen (Minimales $k_\perp$ vs. Resummierung der Leiterdiagramme), zu einer endlichen bzw. verschwindenden Rate bei kleinen und großen Gluonenergien. Auf der anderen Seite unterscheidet sich der „stochastische LPM“-Ansatz von den beiden anderen Methoden durch die explizite Berücksichtigung der endlichen Formationszeit und

---

[6] Arnold, Moore, Yaffe

der damit korrekten Längenabhängigkeit des Energieverlusts in dünnen Medien. Des Weiteren führt die einsetzende Thermalisierung der Gluonen während ihrer Formationszeit im „stochastischen LPM“-Ansatz zu einem transversaleren Emissionsspektrum im Vergleich zur „θ-LPM“-Methode. Damit der resultierende Energieverlust dennoch vergleichbar ist, wird dieses softere Emissionsspektrum im „θ-LPM“-Ansatz durch eine höhere totale Emissionsrate kompensiert.

Jets in einem statischen, thermischen Medium

Während die vorherigen Ergebnisse unter Annahme eines eikonalen Projektils erhalten wurden, wird Kapitel 6 der radiative Energieverlust in den verschiedenen LPM-Ansätzen für den Fall eines nicht-eikonalen Projektils diskutiert. Für solch ein Projektil gilt nicht länger $\omega \ll E$, sodass der Jet bei Durchquerung des Mediums seine Energie verändert und somit der zeitliche Verlauf der Projektilenergie $E(t)$ bei Durchquerung eines thermischen Medium untersucht werden kann. Zunächst wird als Referenz der Energieverlust eines Jets simuliert, der nur durch elastische $2 \rightarrow 2$-Wechselwirkungen Energie an das Medium abgibt. Wie erwartet, kann gezeigt werden, dass der Anteil des elastischen Energieverlusts im Vergleich zum radiativen Energieverlust vernachlässigbar ist. Mit den zuvor bestimmten Parametern X_{LPM} und ξ_{LPM} kann für das nicht-eikonale Szenario festgestellt werden, dass Projektile durch die Prozesse der „θ-LPM“-Methode am schnellsten Energie verlieren, wohingegen die zeitlichen Energieverläufe des „stochastischen LPM“-Ansatzes und von AMY einen langsameren Energieverlust zeigen. Gründe für diesen langsameren Energieverlust sind zum Einen die Divergenzen in AMY, die zu einem „Alles-oder-Nichts“-Energieverlust führen, und zum anderen die endliche Formationszeit im „stochastischen LPM“-Ansatz, die den Energieverlust von Jets durch hochenergetische bzw. kollineare Gluonemissionen verlangsamt.

Um die Verteilung der abgestrahlten Gluonen in den verschiedenen LPM-Methoden charakterisieren zu können, wird darüber hinaus die Modifikation rekonstruierter Jets bei Durchquerung eines thermischen Mediums untersucht. Dazu werden mithilfe des Anti-$k_\perp$-Algorithmus und einer Auflösung von $R = 0.3$ Jets basierend auf Partonenschauern rekonstruiert, die aus einem führenden partonischen Projektil und seiner softeren Partonenwolke bestehen und die durch den Ereignisgenerator PYTHIA erzeugt wurden, bevor sie das thermische Medium durchquert haben. Die eigentliche Mediumsmodifikation der Partonenschauer durch die verschiedenen LPM-Wechselwirkungen wird anschließend durch entweder den zeitlichen Verlauf der rekonstruierten Jet-Energie oder die Modifizierung der Energie-Verteilung um den Jet herum, den eigens definierten „shower shapes $\hat{\rho}(r)$“, quantifiziert. Im Vergleich zum Energieverlust einzelner Projektile ist die Modifizierung der Partonenschauer durch das Medium ein Multiteilchen-Effekt, der auf verschiedenen Mechanismen basiert:

- Zum Einen verlieren die einzelnen Schauerpartonen Energie durch elastische Streuungen innerhalb des Mediums oder durch medium-induzierte Bremsstrahlung. Abhängig von der konkreten LPM-Modellierung werden die abgestrahlten Gluonen dadurch entweder transversal und damit aus dem rekonstruierten Jet abgestrahlt, was zu einer Erhöhung des rekonstruierten Jet-Energieverlusts führt, („θ-LPM“ und „stochastischer LPM“) oder aber sie verbleiben durch kollineare Abstrahlungen nahe der eigentlichen Jet-Achse und verändern damit die rekonstruierte Jet-Energie nicht (AMY).

- Zum Anderen kann sowohl die ursprüngliche Vakuumsstrahlung aus PYTHIA als auch die medium-induzierte Strahlung durch elastische Wechselwirkung der Gluonen zu größeren Winkeln transportiert werden und damit den rekonstruierten Jet-Energieverlusts erhöhen.
- Gleichzeitig können aber auch die durch elastische $2 \rightarrow 2$-Wechselwirkungen gestreuten Mediumskomponenten innerhalb der Jets verbleiben und damit den rekonstruierten Jet-Energieverlust wieder abschwächen.

Es wird gezeigt, dass die Unterschiede im radiativen Energieverlust der einzelnen Schauerpartonen in den verschiedenen LPM-Ansätzen zu unterschiedlichen zeitlichen Verläufen der rekonstruierten Jet-Energien führen. Der endliche Transversalimpuls $k_\perp$ der Emissionen in den beiden effektiven LPM-Ansätzen führt zu einem Jet-Energieverlust mit voranschreitender Zeit, wobei erneut im „θ-LPM“-Ansatz aufgrund der verschwindenden Formationszeit der schnellere Energieverlust auftritt. Im Gegensatz zu den effektiven LPM-Methoden zeigen die kollinearen Emissionen innerhalb der „AMY“-Methode einen nahezu verschwindenden Energieverlust der rekonstruierten Jets. Erst wenn der Transport von abgestrahlten Gluonen durch weitere elastische Streuungen erlaubt wird, führen auch die Emissionen durch den AMY-Formalismus zu einem rekonstruierten Jet-Energieverlust, der den anderen beiden Ansätzen ähnelt. Diese Ähnlichkeit wird durch die zusätzliche Betrachtung von gestreuten Mediumskomponenten zusätzlich verstärkt, sodass sich sowohl die rekonstruierten Jet-Energien als auch die zugrundeliegenden $\hat{\rho}(r)$-Verteilungen stark ähneln.

Jets im expandierenden Medium einer Schwerionenkollision

Aufgrund der extrem kurzen Lebenszeit des Mediums innerhalb einer Schwerionenkollision sind Experimente zur Bestimmung der Eigenschaften des entstandenen heißen und dichten Materiezustands auf Vergleiche mit theoretischen Simulationen angewiesen. Daher werden Kapitel 7 der vorliegenden Arbeit zunächst makroskopische Größen wie z.B. die Dichte oder Temperatur des expandierenden Schwerionen-Mediums innerhalb von BAMPS bestimmt, bevor anschließend die numerischen Simulationen für den Energieverlust von Jets unter Berücksichtigung der verschiedenen LPM-Ansätze mit experimentellen Resultaten des LHC-Beschleunigers für „Jet Quenching“-Observablen in Blei-Blei-Kollisionen mit $\sqrt{s_{\mathrm{NN}}} = 2.76\,\mathrm{TeV}$ verglichen werden. Diese makroskopischen Größen werden durch Mittelung der mikroskopischen Verteilungen innerhalb des Mediums bestimmt, die wiederum durch eine Überlagerung vielzähliger Nukleon-Nukleon-Interaktionen aus PYTHIA initialisiert und anschließend durch sowohl $2 \rightarrow 2$- als auch $2 \leftrightarrow 3$-Prozesse („θ-LPM“-Ansatz mit $X_{\mathrm{LPM}} = 0.3$) innerhalb von BAMPS evolviert werden. Es wird gezeigt, dass die anfänglich hohe Teilchenzahldichte ($n \sim \mathcal{O}(10^2\,\mathrm{fm}^{-3})$) und Energiedichte ($\epsilon \sim \mathcal{O}(10^2\,\mathrm{GeV fm}^{-3})$) aufgrund der starken Expansion des Mediums rapide abnimmt. Da eine Definition der Temperatur im Prinzip nur in äquilibrierten Systemen gerechtfertigt ist und besonders die frühe Phase einer Schwerionenkollision weit weg von einer Äquilibrierung ist, werden verschiedene Möglichkeiten für die Definition einer effektiven Temperatur diskutiert, da die Temperatur als Parameter für die anschließende Untersuchung des Jet-Energieverlusts mithilfe der AMY-Emissionsraten essentiell ist. Dabei bestätigt sich die Annahme einer hohen anfänglichen Temperatur $T \sim \mathcal{O}(1\,\mathrm{GeV})$ im Zentrum der Kollisionszone.

Des Weiteren wird präsentiert, dass die mikroskopischen pQCD-Interaktionen innerhalb von BAMPS zu einer starken Kollektivität im partonischen Medium führen. Dazu wird der integrierte elliptische Fluss v_2 für verschiedene Zentralitäten berechnet und mit experimentellen Ergebnissen des LHC-Beschleunigers für Blei-Blei-Kollisionen bei einer Schwerpunktsenergie von $\sqrt{s_{\mathrm{NN}}} = 2.76\,\mathrm{TeV}$ verglichen. Sowohl elastische $2 \rightarrow 2$-Interaktionen, deren Wirkungsquerschnitt mithilfe eines effektiven Faktors $K = 3.5$ skaliert wurde, als auch elastische und radiative Prozesse innerhalb von BAMPS führen zu einem signifikanten elliptischen Fluss während der partonischen Phase der Schwerionenkollision, der vergleichbar mit den gemessenen Werten für das hadronische v_2 ist.

Nachdem die verschiedenen LPM-Ansätze unter kontrollierten Bedingungen innerhalb eines statischen Mediums diskutiert wurden, wird ihr Einfluss auf den Energieverlust von Jets unter realistischen Bedingungen in sowohl zentralen als auch peripheren Blei-Blei-Kollisionen bei einer Schwerpunktsenergie von $\sqrt{s_{\mathrm{NN}}} = 2.76\,\mathrm{TeV}$ untersucht. Im Gegensatz zu soften Observablen, wie z.B. dem elliptischen Fluss v_2, können hadronische Spektren bei hohem Transversalimpuls $p_\perp$ durch eine Faltung der partonischen Spektren mit Fragmentationsfunktionen bestimmt werden, die in elementareren Teilchenreaktionen gemessen wurden. Dies erlaubt einen Vergleich der Unterdrückung partonischer Spektren aus BAMPS, die entweder auf skalierten, elastischen Wechselwirkungen ($K = 3.5$) oder den radiativen Prozessen der verschiedenen LPM-Implementierungen basieren, mit dem nuklearen Modifikationsfaktor R_{AA} geladener Hadronen, der in zentralen oder peripheren Kollisionen am LHC gemessen wurde. Dadurch kann interessanterweise gezeigt werden, dass bereits die skalierten, elastischen Wechselwirkungen zu einer realistischen Unterdrückung der Hadron-Spektren sowohl in zentralen als auch peripheren Ereignissen führen. Die radiativen Prozesse hingegen zeigen für alle drei vorgestellten LPM-Ansätze (mit den an AMY angepassten Parametern) einen hohen Jet-Energieverlust und damit eine zu starke Unterdrückung der hadronischen Spektren. Dieses Ergebnis eines zu großen Energieverlusts ist konsistent mit anderen Modellen, die R_{AA} basierend auf den Emissionen des AMY-Formalismus innerhalb hydrodynamischer Simulationen berechnet haben. Erst nachdem die Parameter der effektiven LPM-Ansätze auf $X_{\mathrm{LPM}} = 0.3$ und $\xi_{\mathrm{LPM}} = 0.05$ verringert werden und die laufende QCD-Kopplung berücksichtigt wird, können sowohl der „θ-LPM“- als auch der „stochastische LPM“-Ansatz die gemessene Unterdrückung von Hadronen in zentralen Kollisionen beschreiben. Darüber hinaus führt die endliche Formationszeit innerhalb des „stochastischen LPM“-Algorithmus zu einer leicht verbesserten Übereinstimmung mit dem gemessenen R_{AA} in peripheren Kollisionen. Jedoch kann keines der untersuchten LPM-Modelle den signifikanten, elliptischen Fluss bei hohen Transversalimpulsen erklären.

Die Studien von Jets innerhalb des thermischen Mediums fortführend wird die Mediumsmodifizierung rekonstruierter Jets innerhalb von Blei-Blei-Kollisionen mit Schwerpunktsenergie $\sqrt{s_{\mathrm{NN}}} = 2.76\,\mathrm{TeV}$ mithilfe des nuklearen Modifikationsfaktor $R_{\mathrm{AA}}^{\mathrm{jet}}$ rekonstruierter Jets und der Verteilung der Impulse um die Jet-Achsen, den „jet shapes $\rho(r)$“, berechnet. Dazu werden die anfänglichen Partonenschauer mithilfe von PYTHIA generiert und anschließend innerhalb des expandierenden BAMPS-Medium mittels der verschiedenen LPM-Ansätze unter Berücksichtigung der neu festgelegten Parameter X_{LPM} und ξ_{LPM} evolviert. In Übereinstimmung mit anderen theoretischen Modellen wird demonstriert, dass für eine realistische Unterdrückung der rekonstruierten Jets in allen untersuchten LPM-Ansätzen die zusätzliche Berücksichtigung von Effekten gestreuter Mediumsteilchen eine essentielle Rolle spielt. Obwohl beide effektive LPM-Ansätze die Unterdrückung inklusiver Hadronen beschreiben kann, ist die Übereinstimmung der Simulation mittels des „stochastischen LPM“-Ansatzes bei den untersuchten Rekonstruktionsparametern $R = 0.2$ und $R = 0.4$ leicht besser. Auch die puren elastischen Wechselwirkungen, skaliert mit $K = 3.5$, zeigen eine realistischen Unterdrückung rekonstruierter Jets, was darauf hindeutet, dass eher die Streurate als die Kinematik der Prozesse den resultierenden Jet-Energieverlust bestimmt. Erneut zeigt die Simulation mittels des AMY-Formalismus einen zu starken rekonstruierten Jet-Energieverlust. Durch Berechnung der Impulsverteilung um die rekonstruierten Jet-Achse kann nachgewiesen werden, dass der Energieverlust der rekonstruierten Jets hauptsächlich durch eine Modifizierung der äußeren Jet-Regionen hervorgerufen wird. Bei diesen größeren Winkeln kann eine Erhöhung der Impulse festgestellt werden, wohingegen der innere Teil der rekonstruierten Jets nahezu unverändert ist. Während dieser unmodifizierte innere Teil der Jets auch in den experimentellen Daten gefunden werden kann, überschätzen die verschiedenen LPM-Ansätze innerhalb von BAMPS die Erhöhung der Impulse bei großen Winkeln.

Ausblick

Basierend auf den in dieser Arbeit durchgeführten Studien und deren Resultaten werden in Kapitel 8 abschließend Vorschläge unterbreitet, wie die Untersuchungen dieser Arbeit in Zukunft weitergeführt werden könnten:

- Im Zuge dieser Arbeit wurde herausgefunden, dass einige der untersuchten Observablen allein durch skalierte, elastische Wechselwirkungen beschrieben werden können. Des Weiteren zeigte die Untersuchung der elastischen Wechselwirkungen von Gluonen während ihrer Formationszeit signifikante Unterschiede zu feldtheoretischen Rechnungen in HTL-Näherung. Ein ähnliches Ergebnis wurde bereits in anderen Studien innerhalb von BAMPS beim Vergleich der elastischen Wechselwirkungen schwerer Quarks mit entsprechenden HTL-Rechnungen festgestellt. In diesen Studien wurde der Energieverlust schwerer Quarks durch Einführung eines effektiven Faktors für die Debye-Masse an die HTL-Rechnung kalibriert. Solch eine Studie könnte im Prinzip auch für leichte Quarks durchgeführt und somit die Abweichungen zwischen BAMPS und den HTL-Rechnungen quantifiziert werden. Eine andere Möglichkeit die elastischen Wechselwirkungen in BAMPS zu verbessern, wäre eine Aufteilung der $2 \to 2$-Prozesse nach ihrem zugrundeliegenden Impulsübertrag. Ähnlich zu anderen theoretischen Modellen könnten Streuungen mit hohem Impulsübertrag ($\hat{t} \gtrapprox m_D^2$) weiter durch pQCD beschrieben werden, wohingegen Prozesse mit niedrigem Impulsübertrag durch Diffusionsprozesse innerhalb eines Langevin-Ansatzes simuliert werden. Ein erster Ansatz für eine solche Studie könnte die Implementierung der elastischen Streurate aus HTL innerhalb von BAMPS sein. Allerdings wäre solch eine Streurate, ähnlich wie die Emissionsrate aus AMY, im Prinzip nur für thermische Systeme gültig.

- Aktuell werden Partonenschauer durch $1 \to 2$-Splittings der führenden Partonen innerhalb des Ereignisgenerators PYTHIA generiert. Dabei kommt es aufgrund der Masselosigkeit der Partonen innerhalb von BAMPS zu einer Trennung zwischen den Vakuumsemissionen in PYTHIA und den Bremsstrahlungsprozessen in BAMPS. Jedoch könnte man das Konzept der Virtualität effektiv in BAMPS implementieren und dadurch eine stochastische Entwicklung dieser Virtualität mithilfe von $1 \to 2$-Splittings ähnlich zu PYTHIA realisieren. Die Wahrscheinlichkeit bei welcher Virtualität solch ein Splitting auftritt und wie die Impulse der ausgehenden

Partonen aussehen, könnte mithilfe der etablierten Sudakov-Faktoren modelliert werden. Bei diesem Vorgehen wird eine detaillierte Studie von Kohärenzeffekten zwischen Vakuums- und medium-induzierter Strahlung essentiell sein. Dennoch bleibt es fraglich, ob solch eine Modellierung von Partonen mit einer Virtualität im Kontext der Boltzmann-Gleichung gerechtfertigt ist oder ob man nicht viel mehr die Kadanoff-Baym-Gleichung für „off-shell“-Transport verwenden sollte, für die aktuell aber noch keine analytische Lösung gefunden wurde.

- Einer der aktuell größten Nachteile von BAMPS ist die allgemein fehlende mikroskopische Beschreibung des QCD-Phasenübergangs zwischen partonischen und hadronischen Freiheitsgraden: Bei hohen Partonenergien existiert mit den Fragmentationsfunktionen zwar eine verlässliche Möglichkeit zumindest partonische Spektren in hadronische Spektren zu überführen, allerdings kann dies nicht für Studien rekonstruierter Jets verwendet werden, da diese nur mithilfe individueller Ereignisse und nicht basierend auf Spektren-Ebene rekonstruiert werden können. Ein möglicher Ausweg ist die Modellierung der Fragmentationsprozesse mithilfe von Monte-Carlo-Methoden. Basierend auf den Fragmentationswahrscheinlichkeiten $D_i^h\left(z, Q^2\right)$ könnte man entsprechende Prozesse modellieren, für die allerdings die Erhaltung von Energie und Impuls bei jedem Splitting eine entscheidende Rolle spielen wird. Um diese Monte-Carlo-Fragmentation anschließend zu validieren, könnte der Vergleich mit Spektren nützlich sein, die aus der üblichen Faltung mit Fragmentationsfunktionen berechnet werden können. Für softe Partonenergien ist jedoch die Anwendung von Fragmentationsfunktionen aufgrund der hohen QCD-Kopplung bei diesen Energien nicht erlaubt. Es gibt dennoch bereits erste Versuche innerhalb von BAMPS diese soften Partonen basierend auf ihrer Entfernung im Konfigurations- und Impulsraum zu gruppieren und anschließend effektiv zu hadronisieren. Es wird sich zeigen, welchen Einfluss eine solche Hadronisierung für die in dieser Arbeit vorgestellten Resultate von Observablen des Hintergrundmediums haben werden.

- Vor kurzem wurde der „run II“ des LHC-Programms erfolgreich abgeschlossen, in dem die Schwerpunktsenergie auf $\sqrt{s_{\mathrm{NN}}} = 5.02\,\mathrm{TeV}$ nahezu verdoppelt wurde. Obwohl man von theoretischer Seite nur kleinere, eher quantitative Änderungen in den Eigenschaften des Hintergrundmediums erwarten könnte, führt die erhöhte Kollisionsenergie zu einer erhöhten Produktionswahrscheinlichkeit sehr hochenergetischer Jets und damit einhergehend zu der Möglichkeit „Jet Quenching“-Observablen noch differentieller zu untersuchen. Zu diesen Observablen, die prinzipiell auch durch die vorgestellten Methodiken durch BAMPS berechnet werden können, gehören sowohl Interjet-Observablen, wie z.B. die Modifikation der Fragmentationsfunktionen rekonstruierter Jets, als auch Intrajet-Observablen, wie z.B. die Korrelationen von Jets mit energetischen Photonen oder Bosonen, dem sogenannten „goldenen Kanal des Jet Quenchings“. Darüber hinaus kann man vermuten, dass auch in Zukunft weitere Studien zum Energieverlust von Jets in Schwerionenexperimenten bei verschiedenen Kollisionsenergien geplant sind, sodass eine erneute Überprüfung der in dieser Arbeit vorgestellten Modellannahmen unter den geänderten Bedingungen zu empfehlen ist.

1 Introduction

Among the most intriguing, open questions of humanity are the questions of our origin. Where are we from? Why are we here? Why is the universe how it is? While religions give their very own answers, with modern science we are able to at least aim for more rational answers. One field that is especially promising for finding answers to several of above questions is high energy physics, and in particular the field of ultra-relativistic heavy-ion collisions. When heavy nuclei at velocities close to the speed of light collide, they deposit an enormous amount of energy within a small region of space. Consequently, the energy density within these regions exceeds the density of usual nuclear densities by far, potentially forming a new state of matter. In this state of matter the relevant degrees of freedom are sub-nucleonic (partonic) particles, namely quarks and gluons, coining its name *quark-gluon plasma* (QGP). In the QGP, quarks and gluons interact with each other via the strong nuclear force, which can be described theoretically by the fundamental theory of quantum chromodynamics (QCD), which is an essential part of the standard model of particle physics. Although the study of the QGP and thereby QCD under extreme conditions is interesting in its own, these extreme conditions of matter are also expected to be present shortly after the *Big Bang*. Therefore its study may additionally reveal essential information about the early phase of the universe and thereby give further evidence for the big bang theory.

In recent years, experiments both at the *Relativistic Heavy-Ion Collider* (RHIC) at BNL[1] and the *Large Hadron Collider* (LHC) at CERN[2] made huge efforts in experimentally proving the existence of the quark-gluon plasma. To this end, heavy-ions like gold (^{197}Au) or lead (^{208}Pb) nuclei are accelerated to almost the speed of light and subsequently collided in dedicated collision zones, which are surrounded by a variety of different detector systems. Unfortunately, due to the short lifetime of the hot and dense matter and the confinement of partons into colorless hadrons, a direct measurement of a heavy-ion collision is not possible. Rather each detector component aims for a different aspect by measuring different remnants of the actual heavy-ion collision. However, it is only the interplay between these experimental observations and appropriate theoretical calculations that enables us to draw reliable conclusions about the properties of the created matter and thereby the existence of the quark-gluon plasma.

One of the most prominent observables for studying the quark-gluon plasma created in ultra-relativistic heavy-ion collisions at RHIC and LHC is *jet quenching*. When jets—highly energetic partons produced in hard processes of the initial nucleon-nucleon interactions within the colliding nuclei—travel through the hot and dense environment of the heavy-ion collision, they interact with medium components and thereby lose energy and momentum. These mainly partonic interactions are dominated by binary scattering and radiative Bremsstrahlung processes, which can be both described by perturbative quantum chromodynamics due to the small QCD coupling at these large parton energies. Assuming a factorization between the jet production process and the subsequent medium modification,

---

[1] Brookhaven National Laboratory

[2] European Organization for Nuclear Research

the original jets are indifferent from jets that are produced in more elementary collisions as $\mathrm{p+p}$ collisions, where no formation of a background medium is expected. Consequently, the comparison of the measurement of quenched jets in a heavy-ion collision and unquenched jets in $\mathrm{p+p}$ collision represents a promising opportunity for probing the properties of QCD matter under extreme conditions.

Especially when considering radiative processes of energetic partons, coherence effects play an essential role. Due to the finite formation time of emitted gluons, subsequent Bremsstrahlung processes may act coherently to each other and thereby lead to a suppression of gluon emissions wrt. the incoherent Bethe-Heitler regime. While first discovered in the 1950s in Bremsstrahlung processes of photons within quantum electrodynamics, this *Landau-Pomeranchuk-Migdal* (LPM) suppression leads in the case of a non-Abelian theory as QCD to a remarkable energy and path-length dependence of the partonic energy loss.

The main purpose of this thesis is the study of jet quenching in ultra-relativistic heavy-ion collisions at LHC and especially its dependence on coherence effects as the non-Abelian LPM effect. To this end, we employ the partonic transport approach BAMPS (Boltzmann Approach for Multi-Parton Scattering) and revise its current description for the LPM effect. BAMPS simulates the quark-gluon plasma by solving the 3+1-dimensional[3] Boltzmann equation for massless partons while employing matrix elements calculated in leading-order perturbative quantum chromodynamics (pQCD). The partons within BAMPS, which fulfill the *on-shell* condition $E^2 = \vec{\mathbf{p}}^2 + m^2$, may scatter elastically via binary $2 \rightarrow 2$ process as well as radiate gluons via $2 \leftrightarrow 3$ Bremsstrahlung and annihilation processes described by an improved version of the Gunion-Bertsch approximation. By applying the same Debye-screened pQCD matrix elements to both the jet-medium interactions and medium-medium interactions, BAMPS is one of the few approaches describing jets and the underlying bulk medium evolution within the same framework.

However, due to the local nature of interactions underlying the Boltzmann equation, a formal description of quantum-mechanical processes as the coherent suppression of gluon emissions due to the LPM effect is highly demanding. Previously the LPM effect was modeled within BAMPS by an effective suppression factor in the radiative $2 \leftrightarrow 3$ matrix elements. In the course of this work, we will revise this implementation and its dependencies and confront it with two other approaches for coherent gluon emissions, namely the gluon emission rate from thermal field theory and a stochastic description based on a formal pQCD calculation for gluon radiation. By studying the different LPM approaches both in the more academic setup of a static brick of quark-gluon plasma and afterwards in the expanding medium of a heavy-ion collision, this comparison will then allow us to understand and point out the different ingredients of radiative, partonic energy loss and how it can be identified in the experimental observations at LHC.

Structure of the work

The present thesis is structured as follows: the next Chapter 2 gives a comprehensive overview of the physics of quantum chromodynamics and ultra-relativistic heavy-ion collisions in general and thereby aims for bringing the present thesis into a broader scientific context. After introducing in Chapter 3 the different microscopic interactions of partons within the quark-gluon plasma by discussing both elastic and radiative processes from perturbative quantum chromodynamics, we review in Chapter 4 the partonic transport

---

[3] In this context, “3+1-dimensional” corresponds to three space and one time dimensions.

approach BAMPS and its underlying assumptions. A heuristic derivation of the non-Abelian Landau-Pomeranchuk-Migdal and its dependencies is given in the beginning of Chapter 5, where we then introduce the different methods for describing the LPM effect, which were studied in this work. To this end, we discuss our assumptions about the different LPM approaches and study their characteristics in a simplified scenario of a static brick of QCD matter. While the energy loss studied in Chapter 5 considers an *eikonal* projectile, we study in Chapter 6 the more realistic case of a *non-eikonal* projectile that modifies its energy while traversing the quark-gluon plasma. Finally, in Chapter 7 we simulate the medium modification of jets from the different LPM approaches in the expanding bulk medium of a heavy-ion collision and confront it with results from the experiments at the LHC.

Natural units

Although the standard unit system in physics is the SI[4] unit system, one often chooses an unit system that is more appropriate for the specific problem at hand. Therefore we will employ throughout this work the *Natural unit* system popular in high-energy physics and cosmology. In this unit system, one defines for the physical constants

$$\hbar = c = k_B = 1\,,$$

where $\hbar$ is the Planck constant, k_B is the Boltzmann constant and c is the speed of light. This choice significantly simplifies calculations at high energy and small length scales, since both space and time are defined in the same units as well as energy and momentum, respectively. While the former are mainly given in *femtometer* (“Fermi”, fm), the latter are written in magnitudes of *electronvolt* (eV), in our case mostly in *giga-electronvolt* (GeV). Furthermore, one can show that in Natural units

$$1 = \hbar c = 0.197\,\mathrm{fm}\,\mathrm{GeV} \tag{1.1}$$

holds and therefore space/time coordinates can be translated to energy/mass units.

---

[4] International System of Units, abbreviated from the French Système international (d’unités)

2 Smashing nuclei: the quark-gluon plasma in the laboratory

The following chapter summarizes the state-of-the-art of our theoretical and experimental knowledge about nuclear matter under extreme conditions. Among the extraordinary properties of this hot and dense state of matter are energy and number densities vastly exceeding the values of usual matter. Consequently, the relevant degrees of freedom are partons, quarks and gluons, obeying the laws of quantum chromodynamics (QCD), which leads to the label "quark-gluon plasma" (QGP) for this state of matter. QCD is the theory of the strong interactions between quarks and gluons and thereby an important part of the standard model of particle physics, the most fundamental physics theory at the moment. In Section 2.1 we briefly revise the main characteristics of QCD, before we discuss in Section 2.2 our current understanding of the phase diagram of strongly interacting matter. One of the most promising ways to study the properties of hot and dense nuclear matter experimentally are collisions of heavy-ions at enormous energies. In Section 2.3 we recapitulate recent experimental results measured at the Relativistic Heavy-Ion Collider (RHIC) at Brookhaven National Laboratory and the Large Hadron Collider (LHC) at CERN. Since the main topic of this work are the tomographic capabilities of hard probes we will focus the discussion mainly on the phenomena of *jet quenching*, the modification of energetic partons due to the transition through the expanding medium of a heavy-ion collisions.

The overview given in this chapter is supposed to bring the present work into the broader context of the research field of quark-gluon plasmas in ultra-relativistic heavy-ion collisions. Obviously such an introduction has to be written selectively by focusing on the main concepts important for the following studies of this work. For a more detailed discussion of other properties of the quark-gluon plasma in heavy-ion collisions we refer to the given literature.

2.1 Basics of QCD and the standard model

The most successful theory to date for describing the physics of elementary particles is the *standard model of particle physics*. Developed in the second half of the 19^{th} century, the standard model categorizes elementary particles based on their quantum properties and describes the fundamental interactions— strong, electromagnetic and weak interaction—[1] between these particles. In the standard model one differs between particles with spin $s \in \{0; 1\}$, so called *bosons*, and particles with half-integer spin $s = 1/2$ called *fermions*. The Pauli principle forbids two fermions to exist in the same quantum state, whereas

---

[1] At the moment there is no successful approach for renormalization in general relativity, the theory describing gravitation, so that it cannot be incorporated into the canon of the other gauge theories of the standard model. Hence, gravitation is commonly not considered as part of the standard model. Furthermore, although gravitation can be crucial at macroscopic scales from a bouncing ball to the density in neutron stars, its influence on the dynamics of quarks and gluons is negligible due to the small coupling between their masses in comparison to the strong coupling in QCD. Therefore we neglect gravitation for the results within this work.

the same does not hold for bosons for which an arbitrary number of bosons in the same quantum state are allowed. While fermions are massive[2] particles that can be components of heavier subatomic particles as protons or neutrons, bosons are either massless (in the case of the strong and electromagnetic interaction) or massive (in the case of the weak interaction) particles that mediate the fundamental interactions between fermions.

The category of fermions itself is subdivided into *leptons*, which only interact via the electromagnetic and weak interactions, and *quarks*, which have color charge and thereby additionally interact via the strong interactions. The quarks and leptons are further categorized in different families based on their particles masses: While the leptons are divided into electrons e^-, muons μ^- and tauons τ^-, the quarks are split into three families with each two quark flavors, namely up (u) and down (d), strange (s) and charm (c), bottom (b) and top (t). Furthermore, each quark and each lepton has an anti-particle with the same mass but opposite quantum numbers.

The three fundamental forces within the standard model are $\cdots$

- $\cdots$ the *electromagnetic interaction* mediated by massless *photons* (bosons with spin $s = 0$), e.g., responsible for the bounding within atoms of negatively charged electrons to positively charged nuclei.
- $\cdots$ the *weak interaction* mediated by the massive $\mathrm{W}^{\pm}$ and Z bosons, which is responsible for decays of subatomic particles as, e.g., the β-decay $\mathrm{n} \rightarrow \mathrm{e}^- + \mathrm{p} + \overline{\nu}_{\mathrm{e}}$.
- $\cdots$ the *strong interaction* mediated by massless *gluons* (bosons with spin $s = 0$), which acts on small length scales between the components of nucleons in atom nuclei.

In a seminal work for which they were awarded the 1979 Nobel Prize in Physics, both Glashow, Salam and Ward and Weinberg demonstrated that the electromagnetic and weak force are two aspects of the same interaction and can therefore be unified within one *electroweak* theory [Gla59; SW59; Wei67].

One similarity of the three fundamental interactions of the standard model is that they can be described by quantum field theories with underlying renormalizable, gauge symmetries. Since our main research interest in this work is the interaction of partons with color charge, we focus in this work on the quantum field theory called quantum chromodynamics (QCD) which describes the strong interaction between sub-nucleonic particles. For more details about quantum field theories related to the other fundamental interactions, we refer to the literature [PS95; Wei95; Wei96; Mag05; Zee10; MS10].

Quantum chromodynamics is a non-Abelian quantum field theory with an underlying SU(3) gauge symmetry. Hence, the Lie algebra of this theory, $[T_a, T_b] = i f_{abc} T_c$, is based on eight generators T_a with structure constants f_{abc}, where $a, b, c \ldots$ may have $N_c^2 - 1$ values and N_c is the number of *colors*—the quantum number attributed to QCD. The generators are related to the gluon fields A_μ^a, whereas the quark fields with flavor k are described, due to their fermionic spins, by spinors ψ_k and $\overline{\psi}_k = \psi_k^\dagger \gamma^0$ for the respective anti-quark. By combining the different fields, one can formulate the Lagrangian density of QCD,

$$\mathcal{L}_{QCD} = \sum_k \overline{\psi}_k \left(i\gamma^\mu D_\mu - m_k \right) \psi_k - \frac{1}{4} F_{\mu\nu}^a F^{\mu\nu,a} \,, \tag{2.1}$$

---

[2] Recent measurements provide hints to a very small, but finite neutrino mass ($m_\nu < 2\,\mathrm{eV}$) [Tan+18].

where the covariant derivative $D^\mu = \partial^\mu - igT_a A_a^\mu$ describes both the quark dynamics and the coupling of the quark fields to the gluon fields. The mass of quarks is given in the second term of the sum $m_k \overline{\psi}_k \psi_k$, where m_k is the mass of a free quark and should not be confused with the so called *constituent mass* of partons within nucleons. The constituent mass gets additional contributions from virtual sea quarks leading to significantly larger quark masses.

Especially, the non-Abelian symmetry of QCD complicates solutions of Eq. (2.1) for problems with even few particles. Consequently the QCD Lagrangian is at the moment only solvable under certain circumstances:

- One common way for solving quantum field theories is the perturbative expansion of the Lagrangian Eq. (2.1) via an appropriate order parameter. In perturbative QCD (pQCD), the order parameter is the QCD color charge g as defined in the covariant derivative of Eq. (2.1) representing the coupling of quark to gluon fields. Correspondingly to quantum electrodynamics, where for the electric charge e and the QED coupling constant $\alpha = e^2/(4\pi)$ holds, one can define the QCD coupling as $\alpha_s = g^2/(4\pi)$. As we will see in the next section, due to the non-Abelian nature of QCD, α_s is not a constant but depends on the momentum scale of the respective physics problem at hand. However, this complicates a perturbative expansion that relies on a small order parameter $g \ll 1$ or $\alpha_s \ll 1$ in order to truncate higher orders in the expansion. The actual perturbative expansion is then accomplished by the concept of Feynman diagrams. Within this work we mainly focus on solving QCD by leading-order perturbation theory (cf. Chapter 3). For more details about the perturbative expansion of QCD we refer to the excellent textbook by Peskin and Schroeder [PS95].

- In contrast, lattice QCD (lQCD) solves QCD based on a discretization of the QCD action in space and time. This prevents divergences at small length scales and thereby allows to numerically calculate quark and gluon interactions at arbitrary coupling strengths g. However, lQCD suffers from the necessity of calculating the action in imaginary time which prevents calculations of dynamic problems as, e.g., the scattering of partons. Nevertheless, lattice QCD is extremely successful in calculating static phenomena at soft momentum scales as, e.g., quark masses or the critical temperature of nuclear matter (cf. Section 2.2). For more details about lattice QCD, especially at high temperatures and densities, we refer to Refs. [Boy+96; Pet12; Phi13].

As we will see in the course of this work, the presented picture for solving Eq. (2.1) gets further complicated when considering the dynamics of QCD for macroscopic systems consisting of dozens of quarks and gluons, where one cannot avoid further phenomenological approximations and model assumptions. In the following sections, we briefly revise two main characteristics regarding QCD, the parton model underlying QCD and the asymptotic freedom of partons at large momentum scales.

2.1.1 Parton model

Historically, quantum chromodynamics was formulated inspired by the *parton model* primarily developed by Gell-Mann, Zweig and Feynman. In order to sort the enormous number of newly discovered “elementary particles” by particle physics experiments in the 1960s, Gell-Mann [Gel64] and Zweig [Zwe64] proposed sub-nucleonic particles, which they coined *quarks*. These quarks form compound particles named *hadrons*, which were categorized depending on their mass and their quark content: the heavier hadrons consisting of three quarks or anti-quarks were named *baryons*, whereas hadrons consisting of a quark and an anti-quark were called *mesons*. This scheme allowed to categorize all discovered particles at that time. The idea that hadrons as protons, p, or pions, π, are built from more fundamental particles was supported by Feynman [Fey69], who called these components *partons*. These partons were then identified with the quarks and gluons within nucleons whose existence was confirmed by deep inelastic scattering of electrons on nucleons.

However, both parton models struggled with the description of the Δ^{++} resonance: in the parton model the Δ^{++} contains three u quarks, which is forbidden for fermions obeying Fermi-Dirac statistics derived from the Pauli principle. Consequently, a new quantum number called *color* with values *red*, *green* and *blue* was introduced to the parton model. Each quark possesses one of these colors, whereas gluons have both a color and an anti-color. As we will see in the next section, due to the so called confinement, individual colored partons cannot be observed in nature. Quarks and gluons are bound within colorless hadrons. The theoretical concept of quark and gluon colors was experimentally confirmed by measurements of the hadron production in $\mathrm{e}^+ + \mathrm{e}^-$ collisions that could only be described by a finite number of colors, $N_c = 3$ [Pov+06].

2.1.2 Asymptotic freedom and confinement

We discussed earlier that the QCD coupling g or $\alpha_s = g^2/(4\pi)$ serves as the order parameter for solving QCD via a perturbative expansion. Therefore perturbative QCD, as it is applied in this work, relies on the smallness of the coupling in order to be able to truncate higher orders of the expansion. However, different measurements of the QCD coupling in high-energy particle collisions observed that the QCD coupling α_s is not constant but depends on the respective momentum scale Q^2 underlying the specific problem at hand. Figure 2.1 shows the current status of the measured Q^2 dependence of $\alpha_s\left(Q^2\right)$ from various experimental studies aiming for different phenomena within QCD. Apparently, the QCD coupling diverges for small momentum scales Q^2 and logarithmically vanishes for larger momentum scales. One parametrization for this "running" of the QCD coupling is given by leading-order pQCD as

$$\alpha_s(Q^2) = \frac{12\pi}{(11N_c - 2N_f)\ln\left(Q^2/\Lambda^2_{QCD}\right)}\,, \tag{2.2}$$

where $N_c = 3$ is the number of different colors, N_f the number of active quark flavors and Λ_{QCD} the only free parameter of QCD representing the typical energy scale of QCD. It depends on N_f and is fitted based on experimental studies [Bet07] to

$$\Lambda_{QCD}(N_f = 3) = 346\,\mathrm{MeV} \quad \Lambda_{QCD}(N_f = 4) = 305\,\mathrm{MeV} \quad \Lambda_{QCD}(N_f = 5) = 220\,\mathrm{MeV}\,. \tag{2.3}$$

The reason for the high Q^2 behavior of α_s is the non-Abelian nature of QCD. While photons do not couple directly to an other photon in quantum electrodynamics (QED), gluons significantly interact with other gluons in QCD. This "self-coupling" in QCD then implies the phenomenon of *asymptotic freedom*, the vanishing coupling at high momentum scales. At these high momentum scales, quarks and gluons can hence be described as quasi-

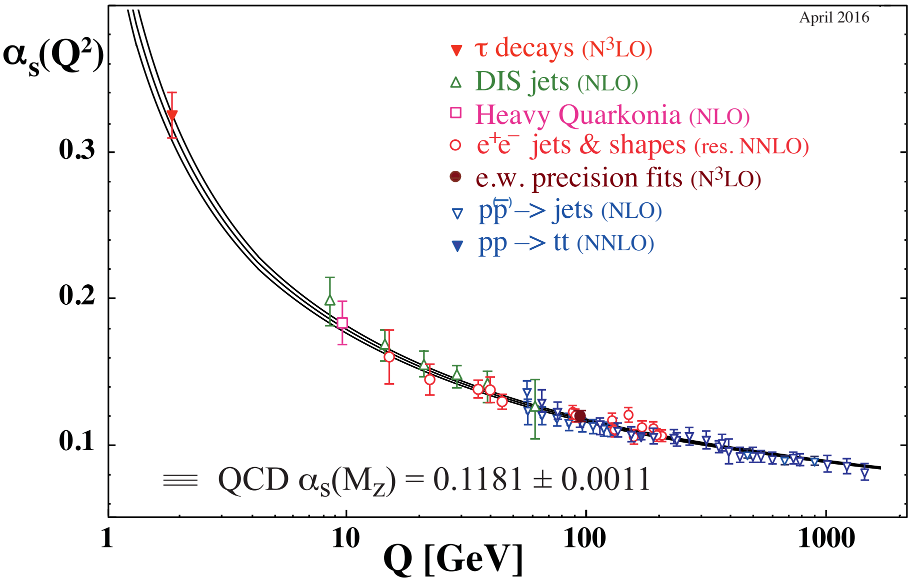

Figure 2.1: Compilation of measurements of the QCD coupling α_s as a function of the momentum scale Q^2 taken from Ref.[Tan+18].

free particles. For the derivation of asymptotic freedom from first-principles QCD, GROSS, WILCZEK and POLITZER were awarded with the 2004 Nobel Prize in Physics [GW73b; GW73a; Pol73; GW74; Dav74]. Contrary to asymptotic freedom, calculations at small Q^2 are not possible within perturbative QCD due to the diverging QCD coupling. This divergence corresponds to an infinite QCD potential at small momentum or large length scales that leads to the *confinement* of partons within hadrons and the fact that there is no possibility to directly measure free, colored partons. Due to this large QCD coupling, phenomena at soft momentum scales as, e.g., the hadronization of partons, cannot be calculated within perturbative QCD. Although there are effective models for the QCD potential at these small momentum or large length scales, respectively, at the moment there is no formal approach for deriving confinement directly from QCD. This problem is of such outstanding importance for both mathematics and theoretical physics, that it is one of the Millennium Prize Problems stated by the Clay Mathematics Institute[3].

2.2 The phase diagram of strongly interacting matter

Due to the strength of the strong interaction at small length scales, the behavior of ordinary matter at subatomic scales is dominated by QCD. As we have seen in the previous section, partons are confined within hadrons due to the diverging QCD coupling at soft momentum scales. Consequently, unbound partons cannot be observed at standard conditions ($T \approx 300\,\mathrm{K} \approx 0\,\mathrm{MeV}$) in nature. However, several theoretical models predict that when nuclear matter is either significantly heated or compressed, the relevant microscopic degrees of freedom of matter change from hadrons to quarks and gluons and thereby a phase transition

---

[3] `http://www.ams.org/notices/200606/fea-jaffe.pdf`

may occur. In this section we briefly revise the current theoretical understanding of these different phases of nuclear matter, which can be derived from the specific characteristics of QCD, and discuss where and how phase transitions change the medium parameters of QCD matter.

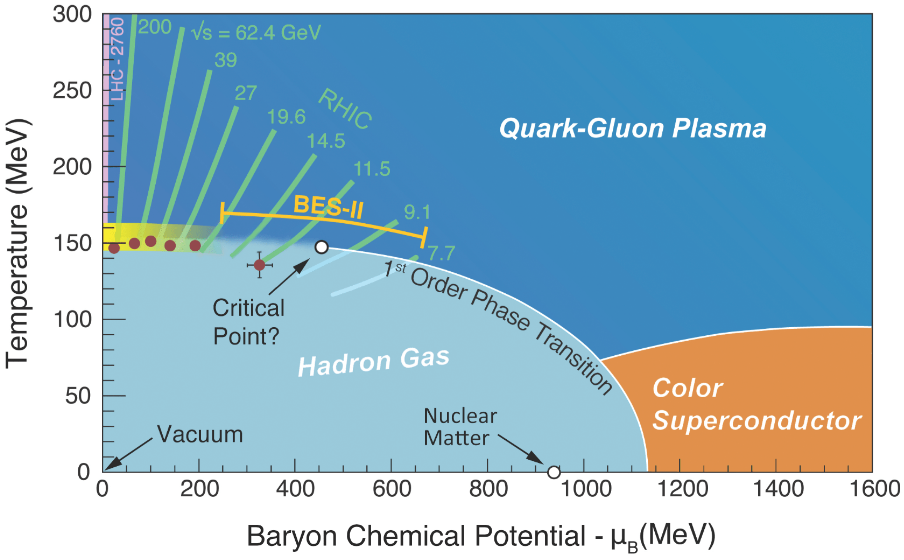

Figure 2.2: Phase diagram of strongly interacting matter as a function of baryon chemical potential μ_B and temperature T predicted by theoretical considerations together with trajectories taken by different heavy-ion experiments. Figure taken from Ref. [Muk16].

Correspondingly to water and other systems, one can define a phase diagram of QCD matter. In this phase diagram, different phases of strongly interacting matter are given as regions in the plane spanned by the temperature T and the baryon chemical potential μ_B measuring the excess of baryons over anti-baryons, which is related to the density of baryons[4]. Figure 2.2 shows current expectations for the different phases of strongly interacting matter. Nuclear matter under standard conditions is located at $(\mu_B; T) \approx (924; 0)$MeV in the phase diagram [Ris04]. For investigating the phase diagram one has in principle two possibilities: either heating up (increasing T) or compressing (increasing μ_B) the matter under study.

By heating matter with vanishing net baryon density, one moves on a vertical line close to $\mu_B \approx 0$ MeV in Fig. 2.2. This region of small μ_B and high T is of special interest, since one assumes that it was also realized in nature shortly after the *Big Bang*, when the early universe cooled down along a trajectory in this μ_B-region. Phase transitions at small baryon chemical potential can be calculated by lattice QCD calculations, which predict that at this baryon chemical potential a *crossover* transition occurs [Aok+06]. This crossover transition corresponds to a gradual change of medium parameters and thereby mixtures of partonic and hadronic degrees of freedom can be found. Above temperatures $T \approx$ 160–190 MeV the QCD coupling is then small enough that the matter is dominated by quasi-free quarks and gluons and therefore the formation of a quark-gluon plasma is expected [KLP00; Kar01; FK01; FK04; Bor+11].

On the contrary, an additional compression of matter, which can be represented by horizontal lines in Fig. 2.2, leads to a prediction of smaller transition temperatures at higher μ_B, where the application of contemporary lattice QCD is demanding. Reason for

---

[4] The corresponding quark chemical potential μ_q can be approximated by the valence quarks giving $\mu_q = 1/3\mu_B$.

this complication is the so-called sign problem which emerges from the transformation to Euclidean space [FP02; FP03; For10]. Consequently, phenomenological models for QCD [MK89; Hal+98; Sca+00; AK02] are often applied that expect a *first-order* phase transition at these higher μ_B. First-order phase transitions are characterized by a rapid change of the medium parameters leading to a discontinuity in the first derivative of, e.g., the energy density ϵ or the number density n.

At even higher μ_B, matter is then compressed strong enough so that partons from different hadrons begin to overlap and thereby form a phase of quasi-free quarks and gluons even at low temperatures. Such a phase is expected in neutron stars, where the enormous density of neutrons leads to quarks and gluons traveling within multiple neutrons. At these densities, partons are also expected to build pairs similar to Cooper pairs in electric superconductors. Consequently, this proposed state of matter is often called "color superconductor" [Rue+05; Ris04].

In principle, our previous knowledge about the phase diagram was mostly limited to the region around nuclear matter at standard conditions, to which we are used to in our everyday life. However, modern heavy-ion experiments allow us to investigate further regions of the phase diagram in order to extend our knowledge about QCD and its application to macroscopic systems. In Fig. 2.2 we show the expected trajectories in the phase diagram taken by matter produced in various modern heavy-ion experiments probing QCD matter. These experiments and their various results are covered in the next section.

2.3 Experimental signatures of the quark-gluon plasma

As mentioned in the previous section, modern heavy-ion experiments are an excellent tool for investigating matter under extreme conditions and thereby study the properties of the quark-gluon plasma. To this end, heavy ions—the nuclei of heavy atoms like lead ^{208}Pb or gold ^{197}Au—are accelerated to ultra-relativistic velocities in particle accelerators, as, e.g., the Relativistic Heavy-Ion Collider (RHIC) at Brookhaven National Laboratory (BNL) or the Large Hadron Collider (LHC) at CERN. Two of these energetic beams of heavy-ions are subsequently collided with center-of-momentum (CoM) energies $\sqrt{s_{\mathrm{NN}}} \sim \mathcal{O}(100\text{–}1000\,\mathrm{GeV})$ per nucleon-nucleon scattering in dedicated collision zones, which are covered by detector experiments measuring the emerging reaction products.

The different stages of such an ultra-relativistic heavy-ion collision are sketched in Fig. 2.3, where we denote the direction of the beam axis of the heavy ions as z and the time as t, and can be outlined as follows:

- During the initial heavy-ion collision, the nucleons of both heavy-ions interact with each other. One model for describing these nucleon interactions is the *Glauber model* as introduced in Section 7.1.1 and further discussed in Appendix D. Depending on the impact parameter—the distance between the center of the colliding nuclei in the transverse plane wrt. the beam axis—of the specific collision, one distinguishes in the Glauber model between *participant* nucleons—nucleons that have interacted with nucleons from the other heavy-ion—and *spectator* nucleons—nucleons that have not interacted with other nucleons but travel undeflected through the collision zone. As we will discuss later, the individual nucleon-nucleon interactions or rather the partonic processes underlying these collisions can be further categorized depending on their individual momentum transfer. For example, hard and therefore rare nucleon-nucleon scatterings may produce partons with high transverse momentum $p_\perp$, so called jets. Due to their high energy and thus short formation time, these jets are

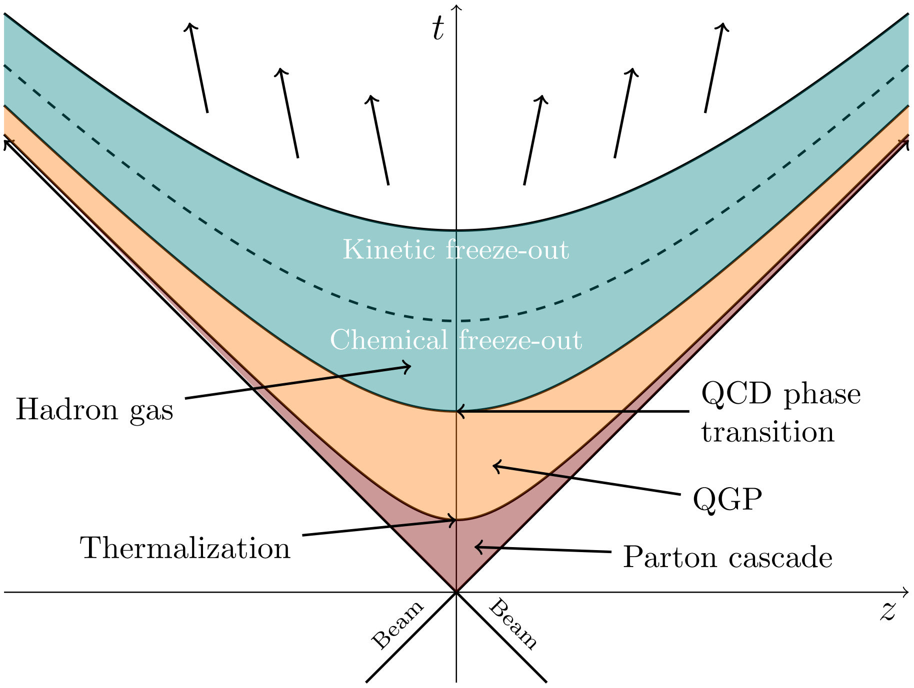

Figure 2.3: Sketch of the different stages of an ultra-relativistic heavy-ion collision. Figure based on Ref. [Shi10].

formed early and therefore exhibit most of the following phases of the heavy-ion collision, which makes them a prominent probe for studying the quark-gluon plasma

- By the collision of multiple nucleons of both nuclei, an enormous amount of energy is deposited in a small volume, leading to a collective medium with energy densities (and effective temperatures) vastly exceeding values of usual nuclear matter. Therefore the relevant degrees of freedom of this matter are assumed to be quarks and gluons which form an expanding quark-gluon plasma. Due to the initial nucleon-nucleon interactions, this system is supposed to be far from equilibrium at these early phases. This non-equilibrium phase can then be described, e.g., by partonic transport approaches as the partonic cascade model BAMPS[5] [Xu04] (cf. Chapter 4) employed in this work (cf. Section 7.1). After some thermalization time τ_0 the strong partonic interactions within the created medium lead to a thermalization of momenta, which allows to apply also hydrodynamical calculations only valid in thermal systems. Several hydrodynamical models [Huo+01; KH03; RR07; SJG11; Nie+11; Nie+13; NEP16; HS13; STV12a; GJS13; STV12c], including both ideal and viscous hydrodynamics, are successful in describing these early, thermalized phases of heavy-ion collisions. However, in these models often an early thermalization time $\tau_0 \lessapprox 1\,\text{fm}$ [Hei04] is assumed. As we will see later in this work, the transport approach BAMPS was one of the first approaches giving microscopic evidence for such a fast thermalization time by including not only binary but also number changing partonic pQCD processes.
- With progressing time, the partonic system expands and cools down. As described in the previous section, this cooling leads to a phase transition, which can be described macroscopically via various equation of states calculated, e.g., from lattice

---

[5] Boltzmann Approach to Multiple Parton Scatterings

QCD [Phi13]. After this phase transition, the microscopic degrees of freedom of the expanding medium are hadrons which form a hadron gas. Consequently, an appropriate choice for simulating the further medium evolution could be hadronic transport approaches as, e.g., URQMD [Bas+98; Ble+99] and SMASH [Wei+16]. Within these models, hadronic scattering processes as well as hadron resonance decays are implemented based on either measured or calculated hadronic cross sections. At the moment, the actual hadronization of the partonic medium cannot be described from first-principles on the microscopic level (cf. Section 2.1.2). However, there are phenomenological descriptions for the hadronization reaching from fragmenting strings [Lin+04] to recombination models [Fri+03]. Another way for considering a hadronization is the combination of hydrodynamics, including an appropriate equation of state, and a *particulization* scheme, commonly realized via the Cooper-Frye method [CF74]. The so obtained hadrons can then be further simulated within hadronic transport approaches leading to so-called *hybrid models* [Pet+08; HP12]. Unfortunately, applying such a hadronization procedure leads to the loss of microscopic information during the hadronization process.

- The hadronic medium further expands and cools down until it first chemically and later kinetically freezes out. After the chemical freeze-out the interactions between hadrons do not further modify the chemical composition of the medium, whereas at kinetic freeze-out the hadronic interactions terminate at all. Finally, the hadrons reach the detectors where their energy and momentum as well as their species is determined within the detectors.

Besides the presented ultra-relativistic heavy-ion collisions, which aim to produce the quark-gluon plasma via an increase in temperature, there are also experimental attempts to create a quark-gluon plasma via the compression of nuclear matter. Such low-energy and high-baryon-density interactions are, e.g., planned at the upcoming FAIR[6] facility at GSI[7] in Darmstadt. Since we focus in this work on the investigation of matter produced in ultra-relativistic heavy-ion collisions at LHC, we refer to Ref. [Fri+11] for more information about high density heavy-ion collisions.

However, in all possible approaches for creating a quark-gluon plasma in experiment, the experimental detectors are only capable to measure the confined hadrons emerging from the initial heavy-ion collisions. Therefore, one has to infer properties of the QGP based on the final-state hadrons measured in the detectors. Since the initial heavy-ions posses only longitudinal momentum wrt. the beam axis before the collision, one focuses in these measurements mainly on the transverse momenta wrt. the beam axis since these momentum components must have been produced predominantly by final state interactions.

In the following sections we review different hadronic observables proposed for studying the characteristics of the partonic medium created in ultra-relativistic heavy-ion collisions. Due to the complexity of a heavy-ion collision, each observable on its own has only limited significance. It is rather the interplay of various observables considering different aspects of the bulk medium evolution that allow reliable conclusions about the hot and dense matter. In this work we mainly focus on the energy loss of energetic, light partons and the elliptic flow within the bulk medium as measured in the *run I* of the LHC program. For other observables as, e.g., the energy loss of heavy quarks, the melting of charmonia or the

---

[6] Facility for Antiproton and Ion Research

[7] Gesellschaft für SchwerIonenforschung

bulk medium emission of photons, or the recent *run II* of the LHC program[8] we refer to the literature.

2.3.1 Collective flow of the bulk medium

The general character of a single heavy-ion collision is mainly determined by the impact parameter of the colliding heavy-ions. If two heavy-ions collide head-on with vanishing impact parameter, a larger number of reaction products and higher energy densities are expected in the created medium than in collisions with larger impact parameter. Experimentally, the centrality of a collision is determined by detectors positioned at larger distances along the beam axis which measure the remnants of the heavy-ion collision. While head-on collisions are called *central* collisions, heavy-ion events with larger impact parameter are called *peripheral* collisions. This centrality can be related via the Glauber model introduced in Appendix D to the number of participating nucleons N_{part} and the number of binary nucleon-nucleon interactions N_{coll}.

Due to the relativistic velocities of the nuclei, the initial shape of the heavy ions can be approximated by thin, circular discs in the (x, y)-plane transverse to the beam axis, which point along the z-direction. Since in peripheral collisions most of the spectator nucleons leave the collision zone unmodified, the collision zone of peripheral events is therefore given by the intersection of two circles in the (x, y) plane. A sketch of this *almond*-shaped distribution of the initial nucleon-nucleon interaction is given in Fig. 2.4. Due to the collectivity of the created medium and thereby the generated pressure gradients, this initial eccentricity in configuration space is translated to an asymmetry in the transverse momentum of the individual partons and hadrons during the medium expansion. This relation between spatial eccentricity and momentum anisotropy is stronger for more effective microscopic interactions, which lead to a stronger flow within the medium.

In order to quantify the momentum anisotropy one decomposes the measured hadronic spectra $\mathrm{d}N/\mathrm{d}\phi$ depending on the azimuthal angle ϕ into Fourier harmonics v_n. The angle ϕ is defined as the azimuthal angle relative to the reaction plane spanned by the beam axis and the impact parameter vector $\vec{\mathrm{b}}$. The Fourier decomposition is then given by [VZ96; PV98]

$$\begin{aligned} E\,\frac{\mathrm{d}^3N}{\mathrm{d}^3p} &= \frac{\mathrm{d}^3N}{p_\perp\,\mathrm{d}p_\perp\,\mathrm{d}y\,\mathrm{d}\phi} \\ &= \frac{1}{2\pi}\frac{\mathrm{d}^2N}{p_\perp\,\mathrm{d}p_\perp\,\mathrm{d}y}\left(1+\sum_{n=1}^{\infty}2v_n\cos\left(n(\phi-\Psi_r)\right)\right), \end{aligned} \tag{2.4}$$

where $\left(E, p_x, p_y, p_z\right)$ is the four-momentum of a particle, $p_\perp = \sqrt{p_x^2 + p_y^2}$ its transverse momentum and $y = \log\left((E+p_z)/(E+p_z)\right)$ its momentum space rapidity, which is similar to a velocity generalized to relativistic kinematics. As sketched in Fig. 2.4 the reaction plane angle is denoted by Ψ_r and considers the orientation of the specific event at hand. The different Fourier coefficients v_n have different physical meanings: while the *directed flow* v_1 measures the radial expansion of the medium, the *elliptic flow* v_2 considers the momentum anisotropy of particles in the transverse direction (s. below).

---

[8] Although most of the observables measured in the *run I* of the LHC program were recently repeated during *run II* at the higher CoM energy $\sqrt{s_{\text{NN}}} = 5.02\,\text{TeV}$, in this work we focus on results from *run I* only. This is mainly reasoned by the additional, significant effort necessary for recalculating the numerical simulations within this work, while at the same time we expect only modest quantitative differences for the results presented.

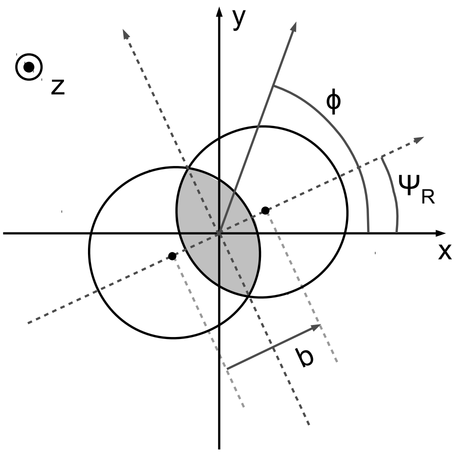

Figure 2.4: Sketch for the almond-shaped collision zone of a peripheral heavy-ion collision. The circles represent the colliding heavy-ions flying in the z direction. The different given quantities are defined for the calculation of $\mathrm{d}N/\mathrm{d}\phi$ (for more details see text). Figure taken from Ref. [CMS13a].

Higher-order Fourier coefficients with $n \geq 3$ are sensitive to fluctuations in the initial nucleon distributions of the colliding heavy-ions that are translated to the final state hadron distribution.

For the experimental measurement of the Fourier coefficients v_n a precise determination of the reaction plane of a given event, the so called *event plane*, is necessary in order to correctly define the azimuthal angles ϕ and Ψ_r. This determination is challenging in experiments, so that recent experiments use *cumulants*—momentum correlations between different measured particles—to appropriately calculate the different Fourier coefficients [Sne11; Bil+11]. For example, $v_2\{4\}$ denotes the four-particles cumulant of the elliptic flow v_2. In contrast, for studies of elliptic flow within theoretical simulations (cf. Section 7.1.3) one can arbitrarily define the orientation of the event plane and therefore choose $\Psi_r = 0$. One can show that the elliptic flow coefficient v_2 of a particle can then be derived to [VZ96]

$$v_2 = \left\langle \frac{p_x^2 - p_y^2}{p_\perp^2} \right\rangle . \tag{2.5}$$

In ideal hydrodynamics, the measured elliptic v_2 is directly proportional to the initial spatial eccentricity of the heavy-ion collision. However, the inclusion of viscous effects may reduce the resulting v_2, which makes a measurement of v_2 to an observable sensitive to the shear viscosity-over-entropy ratio η/s of the produced matter. By studying v_2 in peripheral Au + Au collisions at $\sqrt{s_{\mathrm{NN}}} = 200\,\mathrm{GeV}$, experiments at RHIC first discovered matter that could be described by a significant small value for η/s, which was interpreted by the creation of a nearly “perfect fluid”. Figure 2.5 shows results for different flow coefficients v_n obtained in peripheral to central $\sqrt{s_{\mathrm{NN}}} = 2.76\,\mathrm{TeV}$ Pb + Pb collisions at LHC together with hydrodynamical calculations based on Glauber initial conditions and employing different values for η/s. In these comparisons, the experimental results for v_n in peripheral collisions at LHC agree with the assumption of a small η/s close

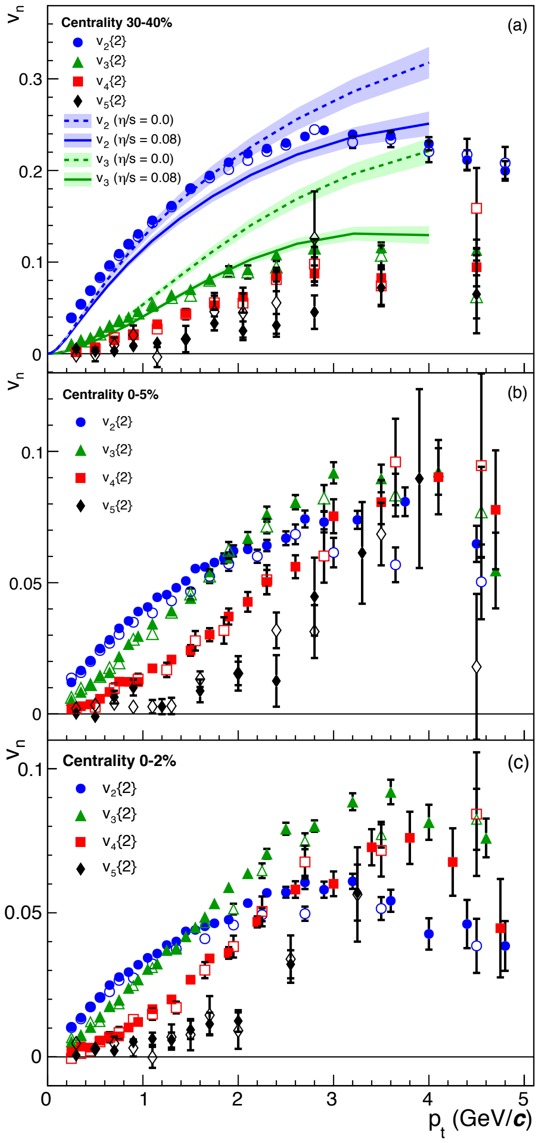

Figure 2.5: Comparison of the flow harmonics v_n of charged particles depending on their transverse momentum $p_\perp$ measured by the ALICE collaboration [ALI11] for different centralities 30–40 % (top panel), 0–5 % (middle panel) and 0–2 % (bottom panel). Additionally, hydrodynamical predictions [SJG11] for v_2 and v_3 calculated with Glauber initial conditions and different shear viscosity-over-entropy ratios η/s are given. Figure taken from Ref. [ALI11].

to the limit $\eta/s = 1/(4\pi)$ predicted by ADS/CFT[9] [KSS04]. On the other hand, the finite v_2 in central collisions and the significant triangular flow additionally point to the importance of fluctuations in the initial state. Recent studies within viscous hydrodynamics are successful in describing higher-order Fourier coefficients $v_{n\geq 3}$ by considering both a finite η/s and fluctuating distributions of the initial nucleon-nucleon collisions [SJG11; STV12c; STV12a]. These fluctuations then may lead to triangular structures giving rise to triangular eccentricities that are translated by collective effects to a triangular flow of hadrons. Furthermore, if one compares the measured v_2 of different hadron species by their respective valence quark content, one finds that the elliptic flow scales with the number of valence quarks. These findings point to the assumption that the elliptic flow is mainly caused during the early partonic phase of a heavy-ion collision (for more details, see Ref. [JZ06]). Therefore we present in Section 7.1.3 numerical results for the elliptic flow v_2 in $\sqrt{s_{\mathrm{NN}}} = 2.76\,\mathrm{TeV}$ Pb + Pb collisions obtained by the partonic transport approach BAMPS.

2.3.2 Jet quenching

Besides the presented collectivity of hadrons, one of the most prominent observables for studying the partonic stages of ultra-relativistic heavy-ion collisions is *jet quenching*. Jets are partons with high transverse momentum $p_\perp$ that are produced in hard processes—processes with a high momentum transfer Q^2—in elementary $\mathrm{e}^+ + \mathrm{e}^-$ as well as hadronic collisions as, e.g., $\mathrm{p}+\mathrm{p}$ collisions. Within $\mathrm{p}+\mathrm{p}$ collisions, these hard processes arise from scatterings between the partons of the incoming protons. Due to the necessary significant momentum transfer between partons, the probability for the production of a jet is drastically smaller than for softer interactions. However, the high momentum transfers of these processes and thereby small QCD coupling α_s (cf. Section 2.1.2) also allow the calculation of these partonic production processes within perturbative QCD. In order to conserve energy and momentum, jets are produced (at leading-order pQCD) as *back-to-back*[10] pairs. Assuming the factorization theorem of hard processes in pQCD [CSS89], the differential production cross section of these di-jet pairs in, e.g., $\mathrm{p}+\mathrm{p}$ collisions is given by the convolution [Wie09]

$$\mathrm{d}\sigma^{p+p\to h+X} = \sum_{f}\sum_{i,j,k\cdots} f_i\left(x_1, Q^2\right) \otimes f_j\left(x_2, Q^2\right) \otimes \hat{\sigma}_{ij\to f+k\cdots} \otimes D_{f\to h}\left(z, \mu_F^2\right) \, . \tag{2.6}$$

While $f_{i,j}$ denotes the parton distribution functions of parton species i and j in the incoming protons, $\hat{\sigma}_{i\,j\to f\,k}$ is the elementary cross section for the characterizing partonic process $i\,j \to f\,k$ calculated within pQCD. Finally, the hadronization of the outgoing partons is obtained by fragmentation functions $D_{f\to h}\left(z, \mu_F^2\right)$, which are determined empirically in elementary $\mathrm{e}^+ + \mathrm{e}^-$ collisions and which give the probability for a parton of species f and momentum $p_\perp^{\mathrm{p}}$ to fragment into a hadron h with momentum $p_\perp^{\mathrm{h}} = z p_\perp^{\mathrm{p}}$. μ_F denotes the factorization scale distinguishing between hard and soft processes. Different to the pQCD cross section, the parton distribution functions as well as the fragmentations functions

---

[9] Anti-de-Sitter/conformal field theory. In this conjecture, a conformal field theory similar to QCD is related to an Anti-de-Sitter space obeying the laws of general relativity. For example, the high energetic partons studied in this work are described by strings falling on the horizon of a black hole.

[10] "Back-to-back" means in this context that the di-jet pair is produced with an angle $\Delta\phi = \pi$ in the azimuthal plane wrt. the beam axis due to transverse momentum conservation. At higher orders, there is the finite probability for additional particle production so that there are deviations to $\Delta\phi = \pi$.

can, at the moment, only be determined experimentally. In Section 7.3.1 we will further discuss the role of fragmentation functions for obtaining hadronic spectra from the partonic transport approach BAMPS.

Besides more elementary $\mathrm{p+p}$ collisions, jets are also produced in hard nucleon-nucleon interactions of the colliding nuclei in a heavy-ion collision. In contrast to $\mathrm{p+p}$ collisions, these jets have to traverse the bulk medium created by soft interactions of other nucleon-nucleon scatterings before reaching the detectors. On their way through the medium, the jet partons interact with the partonic background medium, lose energy and momentum and thereby probe different phases of the hot matter. Already in the 1980s Bjorken [Bjo82] anticipated the tomographic capabilities and proposed *jet quenching* as an observable for obtaining information about the medium properties of the partonic matter created in heavy-ion collisions. Jet quenching was then first experimentally observed in $\sqrt{s_{\mathrm{NN}}} = 200\,\mathrm{GeV}$ Au + Au collisions at RHIC, where an attenuation of the away-side[11] peak in the angular correlation distribution of energetic hadrons was found [STA03; STA05].

The number and the spatial position of the hard nucleon-nucleon interactions and thereby the production points of jets can be calculated by the *Glauber model* discussed in Appendix D and applied in Section 7.1.1.

Among the advantages of jet studies in heavy-ion collisions are the short formation time $\tau_f \sim 1/p_\perp$ of jets due to its large transverse momentum. Hence, jets are formed already at the beginning of the heavy-ion collision and may therefore probe also the early stages of a heavy-ion collision. Furthermore, the possibility to calculate the initial jet production within pQCD and the assumed universality of the jet production allows a direct comparison of the hadronic spectra at high $p_\perp$ measured in heavy-ion collisions with corresponding spectra obtained in $\mathrm{p+p}$ collisions. Any difference between both spectra can then be attributed to final-state effects originating from jet quenching within the heavy-ion medium.

However, the above outlined picture of jets and jet quenching is ill-defined. The outgoing partons of the initial hard scattering may have obtained a significant virtuality, $m^2 > E^2 - \vec{\mathrm{p}}^2$, both in $\mathrm{p+p}$ and nucleon-nucleon interactions of heavy-ion collisions. Consequently, the partons aim to reduce their virtuality by emitting additional gluons via $1 \to 2$ process leading to an evolution in virtuality that can be described by DGLAP[12] evolution equations [AP77; Dok77; GL72]. Moreover, the emitted gluons themselves may further emit other gluons or split into quark-antiquark pairs and thereby form entire *parton showers* which consist of one (or few) hard parton(s), the leading parton, together with its surrounding cloud of softer emitted partons. In heavy-ion collisions, the parton showers then evolve within the partonic medium and thereby modify their distribution around the respective leading parton. By reconstructing jets based on these parton showers one may characterize the medium modification of jets more differentially than based on only the leading partons.

Therefore, depending on the specific physics question at hand, one may categorize jet quenching studies in two major categories:

Suppression of leading hadron spectra

By studying jet quenching, one is interested in the medium modification of jets due to their transition through the hot matter created in heavy-ion collisions. These medium

---

[11] While the *near-side* defines the hemisphere around a distinguished particle as, e.g., a jet, the *away-side* defines the opposite hemisphere.

[12] Dokshitzer-Gribov-Lipatov and Altarelli-Parisi

modifications may then serve as a probe for the medium properties as, e.g., the density of the underlying background medium. In order to quantify this medium modification one defines the nuclear modification factor R_{AA}, which compares the spectra at high transverse momentum $p_\perp$ from $\mathrm{p}+\mathrm{p}$ collisions with the corresponding spectra within heavy-ion collisions. It is given by

$$R_{\mathrm{AA}} = \frac{\mathrm{d}^2 N_{\mathrm{AA}} \big/ \mathrm{d}p_\perp\,\mathrm{d}y}{N_{\mathrm{coll}}\,\mathrm{d}^2 N_{\mathrm{pp}} \big/ \mathrm{d}p_\perp\,\mathrm{d}y}\,, \tag{2.7}$$

where $\mathrm{d}^2 N_{\mathrm{AA}} \,/\, \mathrm{d}p_\perp\,\mathrm{d}y$ denotes the differential spectrum from heavy-ion collisions and $N_{\mathrm{coll}}\,\mathrm{d}^2 N_{\mathrm{pp}} \,/\, \mathrm{d}p_\perp\,\mathrm{d}y$ is the corresponding spectrum from $\mathrm{p}+\mathrm{p}$ collisions scaled by the number of binary nucleon-nucleon interactions N_{coll}. Hence, a value of $R_{\mathrm{AA}} = 1$ corresponds to no modification of the spectra within heavy-ion collision, whereas any deviation from this value, especially at high $p_\perp$, may hint to final-state effects as, e.g., jet quenching.

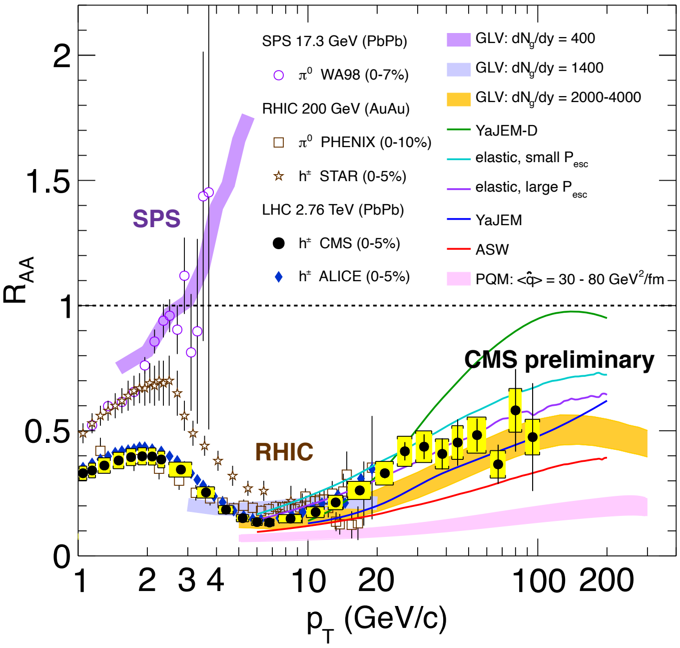

Figure 2.6: Comparison of the nuclear modification factor R_{AA} within central heavy-ion collisions measured by different experiments at SPS, RHIC and LHC together with theoretical calculations. Figure taken from Ref. [CMS12e].

In Fig. 2.6 we show the $p_\perp$ dependence of the nuclear modification factor R_{AA} measured in Au + Au and Pb + Pb collisions with different CoM energies $\sqrt{s_{\mathrm{NN}}} = \{17.3\,\mathrm{GeV}; 200\,\mathrm{GeV}; 2760\,\mathrm{GeV}\}$ together with theoretical calculations from perturbative QCD. And indeed, the more energetic heavy-ion collisions at RHIC and LHC show a significant attenuation of hadrons over the entire $p_\perp$ range, whereas at lower SPS energies this suppression is absent (for more details, see Ref. [DEn04]). This finding strongly supported the proposed jet quenching as a signal for the formation of the quark-gluon plasma at RHIC and LHC energies. The suppression of charged hadrons at LHC is strongest around $p_\perp \approx 6$–$8\,\mathrm{GeV}$ and rises at higher $p_\perp$. Theoretical models including radiative pQCD energy loss of jets are successful in describing the measured suppression. We extend these models in Chapter 7 by calculating the nuclear modification factor R_{AA} within BAMPS simulations for jets traversing an expanding heavy-ion media.

Modification of parton showers and reconstructed jets

While the previously introduced R_{AA} of charged hadrons measures the suppression of individual, high $p_\perp$ particles and thereby the energy/momentum loss of only the leading parton/hadron, modern experiments are capable to also determine the medium modification of entire parton showers, namely the leading parton together with its associated vacuum and medium-induced radiation. For this, partons or hadrons are clustered into objects called *reconstructed jets* by well-defined jet reconstruction algorithms. Developed in more elementary $\mathrm{e}^+ + \mathrm{e}^-$ and $\mathrm{p}+\mathrm{p}$ collisions, these algorithms aim to appropriately group the different partons in order to obtain information about the initial hard-scattered parton initiating the parton shower. In other words, jet reconstruction algorithms in elementary particle collisions reenact the different QCD splittings of the virtual parton to reconstruct the initial parton. When applying the concept of reconstructed jets to heavy-ion collisions, this allows for more differential studies of the medium modification of jets by not only considering the energy loss of the leading parton but, e.g., also a potential widening or narrowing of the parton shower around the leading parton. In the following we briefly revise the concept of reconstructed jets and its application in heavy-ion physics. For more information about the actual concept of jet reconstruction in general we refer to the excellent review in Ref. [Sal10].

A poor man's version for a jet reconstruction algorithm defining which particles belong to the same jet could be *fixed cones* around the leading parton. Consequently, the reconstructed jets could then be found by associating every parton within an angular distance $r_i = \sqrt{\Delta\phi_i^2 + \Delta y_i^2} < R$ to the same reconstructed jet, where $\Delta\phi_i$ and Δy_i are the distances of parton i to the leading parton in the azimuthal angle ϕ and the momentum space rapidity y, respectively. The resolution parameter or jet cone radius R then defines the maximum distance in the ϕ-y plane for a parton to be reconstructed in the same jet. The final momenta of the reconstructed jets are obtained by summing the four-momentum of each parton within the same reconstructed jets. However, this fixed cone approach assumes that the leading parton is the most reasonable choice for the center of the reconstructed jets. In contrast, *iterative cone* algorithms, as they are employed in modern hadron collider studies, choose a (random) *seed* particle to which the particle momenta with $r < R$ are added. After each added momentum the newly obtained jet axis is then the seed for the next iteration step. This iteration procedure is completed, when the reconstructed jets are stable.

However, the presented iterative cone algorithms suffer from the characteristics of QCD: there is always a finite probability for a very soft and/or very collinear additional gluon emission. Since the reconstructed jets from the iterative cone algorithm depend on the specific choice of seed, any other choice of seed resulting from one additional QCD splitting could lead to an other result for the reconstructed jets. In order to avoid these issues, one defines requirements for modern jet algorithms called *infrared safety* and *collinear safety*. While infrared safety ensures that the resulting reconstructed jets are robust against any additional *soft* gluon splitting, the collinear safety is defined so that results do not change if another *collinear* gluon emission occurs. Both requirements lead to the assumption that reconstructed jets are insensitive to hadronization processes at a soft momentum scale. Therefore we assume within this work, that jets being reconstructed from partons are comparable to jets being reconstructed from the corresponding hadrons after the hadronization.

Another approach for reconstructing jets are *sequential recombination* or *clustering* jet algorithms that attempt to recapitulate the original QCD branchings. These clustering algorithms are both infrared and collinear safety since they calculate at each step combinations of all particles and therefore the concrete choice of a seed is dispensable. The algorithm for such a recombination algorithm with resolution parameter or “cone radius” R can be written as [Sal10]:

Algorithm 1: Jet clustering algorithm

```
do
    foreach particle pair i, j do
        Calculate distance $d_{ij} = \min\left(p_{\perp;\,\mathrm{i}}^{2p}, p_{\perp;\,\mathrm{j}}^{2p}\right) \frac{(\phi_i-\phi_j)^2+(y_i-y_j)^2}{R^2}$
    foreach particle $i$ do
        Determine $d_{iB} = p_{\perp;\,\mathrm{i}}^{2p}$
    if $\min\left(d_{ij}, d_{iB}\right) = \min\left(d_{ij}\right)$ then particle $i$ and $j$ belong to same jet
        Combine particle $i$ and $j$ to new particle $k$
        Remove particle $i$ and $j$ from particle list
    else if $\min\left(d_{ij}, d_{iB}\right) = \min\left(d_{ij}\right)$ then no other particle close enough to particle $i$
        Define particle $i$ as final jet
        Remove particle $i$ from particle list
while number of particles $N \neq 0$;
```

Please note that all employed quantities in the reconstruction algorithm are Lorentz invariant, a crucial requirement for the ultra-relativistic collisions at RHIC and LHC. As for the cone algorithms, the particles are combined by summing their respective four-momenta. Depending on the specific choice of parameter p one distinguishes between different clustering algorithms:

- The choice $p = 1$ represents the *$k_\perp$ algorithm* [ES93] preferring clusterings around soft particles.
- The *Cambridge/Aachen algorithm* [WW99; Wob00] neglects any particle momentum dependence by setting $p = 0$ and thereby reconstruct jets by only considering angular distances.
- Opposite to the $k_\perp$ algorithm and most often used in the heavy-ion context, the *anti-$k_\perp$ algorithm* [CSS08] with $p = -1$ reconstructs jets around hard cores reaching to softer outer partons.

We show in Fig. 2.7 typical clustering results from the different recombination algorithms together with a modern choice of cone algorithm [SS07]. One drawback of clustering algorithms are their significant numerical costs: depending on the employed algorithm it takes $\sim N^3$ steps to cluster N particles. By applying techniques based on Voronai diagrams, modern clustering algorithms as published in the FASTJET package achieve speeds $\sim N \log N$ [CSS12; CS05].

These performance improvements together with the increased production probability of jets at LHC enabled experiments to not only measure jets in $\mathrm{p}+\mathrm{p}$ collisions but also in heavy-ion collisions. The first evidence of the medium modification of reconstructed jets was the momentum asymmetry between the two leading reconstructed jets in a heavy-ion event [ATL10; CMS11b; CMS12b]. Already in $\mathrm{p}+\mathrm{p}$ collisions, the stochastic nature of the shower evolution together with the finite resolution parameter R leads to an imbalance between the jets reconstructed from the partons showers initiated by the initially back-to-back partons. This momentum imbalance is further enhanced by the medium modification

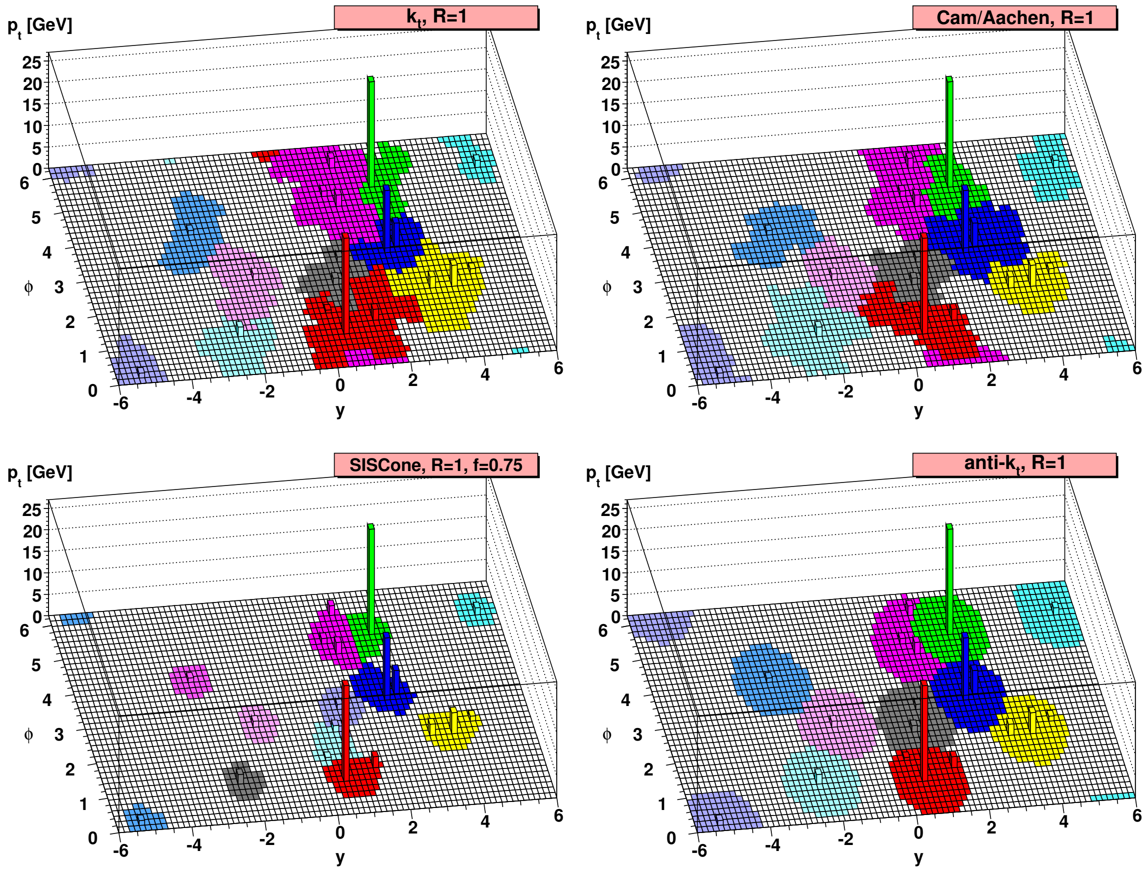

Figure 2.7: Comparison of the results of different jet reconstruction algorithms applied to a parton-level event by the event generator HERWIG [Mar+92; Cor+01]. In order to visualize the "area" of the reconstructed jets soft and random particles, so called *ghosts* were added to the events. While the anti-$k_\perp$ and SIS-CONE algorithms lead to rather circular jet areas, the found jets by the $k_\perp$ and Cambridge/Aachen algorithms are more fuzzy. Figure taken from Ref. [Sal10].

of the parton showers, which may be different for the two partons showers depending on their traveled path-lengths within the expanding medium. For example, if the initial production point of the hard scattering is on the edge of the heavy-ion collision, one parton shower may leave the collision almost unmodified while the other parton shower has to traverse a significant amount of hot and dense matter before reaching the detectors. The momentum imbalance is quantified by

$$A_\mathrm{J} = \frac{p_{\perp;\,\mathrm{Leading}} - p_{\perp;\,\mathrm{Subleading}}}{p_{\perp;\,\mathrm{Leading}} + p_{\perp;\,\mathrm{Subleading}}}\,, \tag{2.8}$$

where $p_{\perp;\,\mathrm{Leading}}$ ($p_{\perp;\,\mathrm{Subleading}}$) is the transverse momentum of the leading (subleading) reconstructed jet. Consequently, $A_\mathrm{J} = 0$ corresponds to the case of equal transverse momentum of the reconstructed jets, whereas $A_\mathrm{J} = 1$ would represent the case where the subleading jet completely vanishes. Figure 2.8 shows the first measurement of A_J in central Pb + Pb collisions with $\sqrt{s_\mathrm{NN}} = 2.76\,\mathrm{TeV}$ by the ATLAS collaboration. And indeed the distribution of momentum imbalance measured in $\mathrm{p}+\mathrm{p}$ collision significantly differs from the distribution measured in heavy-ion collisions, where an enhancement of events with larger momentum asymmetry can be found. In contrast to other models [QM10; You+11a; Col+12], we found in Ref. [Sen+15] that the momentum imbalance is mainly determined by the asymmetry already present in the initial state of the collision and not by the different path lengths within the medium. We revise in Section 7.4.2 these results and present current calculations within the BAMPS framework.

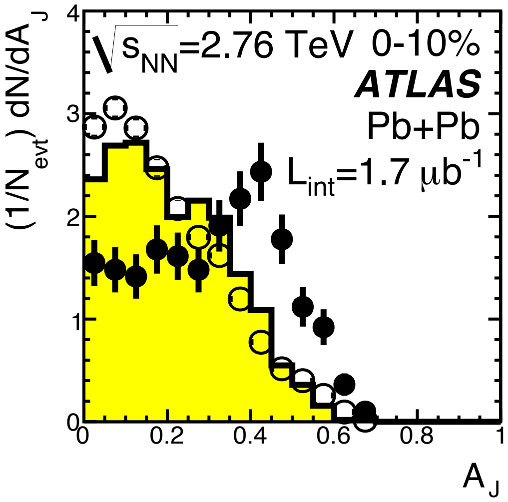

Figure 2.8: Momentum asymmetry A_J between the two leading reconstructed jets measured by the ATLAS experiment [ATL10] within central (0–10 %) $\sqrt{s_{NN}} = 2.76\,\mathrm{TeV}$ Pb + Pb (solid points) and corresponding p + p (open points) collisions. In addition the yellow histogram shows the theoretically expected A_J distribution from unquenched jets superimposed into an heavy-ion background. Figure taken from Ref. [ATL10].

Furthermore, similar to the nuclear modification factor R_{AA} of charged hadrons, one can define a jet R_{AA} comparing the $p_\perp$ spectra of reconstructed jets in p + p collisions with the corresponding spectra in heavy-ion collisions

$$R_{\mathrm{AA}}^{\mathrm{jet}} = \frac{\mathrm{d}^2 N_{\mathrm{AA}}^{\mathrm{jet}} \big/ \mathrm{d}p_\perp\, \mathrm{d}y}{N_{\mathrm{coll}}\, \mathrm{d}^2 N_{\mathrm{pp}}^{\mathrm{jet}} \big/ \mathrm{d}p_\perp\, \mathrm{d}y} \,. \tag{2.9}$$

Different to the R_{AA} of individual particles, the jet R_{AA}^{jet} is due to the finite resolution R of jet reconstruction additionally sensitive to a potential medium-induced broadening of the parton shower. Figure 2.9 shows the jet R_{AA}^{jet} measured by the ALICE and ATLAS experiments. Interestingly, the suppression of reconstructed jets is comparable to the suppression of single hadrons as presented in the previous section. Furthermore, the difference between the R_{AA}^{jet} with $R = 0.2$ and $R = 0.4$ seems to be negligible, which hints to a medium modification of jets at larger angles to the reconstructed jet axis.

Among the further inter-jet observables studied in *run I* of the LHC program are the suppression of heavy-flavor tagged jets and the correlation of jets with energetic photons. The heavy-flavor tagged jets aim to characterize the different energy loss mechanisms of (approximately) massless quarks and massive quarks by, e.g., tagging a reconstructed jet with a bottom quark nearby a b-tagged jet and comparing it to the inclusive jet results [CMS14a]. On the other hand, γ+jet correlation studies consider a medium-modified reconstructed jet that was produced initially in, e.g., an initial hard $q + \mathrm{g} \to \gamma + q$ interaction [CMS12d]. While the jet interacts with the medium and thereby loses energy and momentum, the photon traverses the medium almost undisturbed. Since both were produced back-to-back at leading-order, this allows a reliable definition of the energy loss of the jet, which coined the term “golden channel” for such kind of processes.

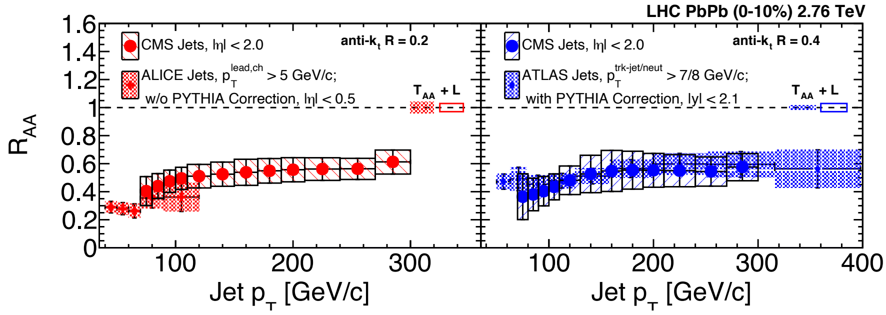

Figure 2.9: Comparison of the nuclear modification factor R_{AA} of reconstructed jets measured by different experiments in central $\sqrt{s_{\mathrm{NN}}}$s=2.76 TeV Pb + Pb collisions. While the left panel shows the R_{AA} of reconstructed jets with $R = 0.2$ measured by the CMS and ALICE collaborations, the right panel presents the corresponding results with $R = 0.4$ measured by the CMS and ATLAS collaborations. Figure taken from Ref. [CMS16].

While the above presented inter-jet observables dealt with the medium modification of a reconstructed jet as a whole, there are also intra-jet studies relating individual particles to the reconstructed jets in order to obtain information about the modification of particles around and within the reconstructed jets. For example, the jet shape observable $\rho(r)$ measures the transverse momentum distribution around the jet axis [CMS13b]. As we will further discuss in Section 7.4.3, one quantifies the medium modification of jet shapes by comparing their distribution in central Pb + Pb collisions with the corresponding distribution in $\mathrm{p}+\mathrm{p}$ collisions. Different intra-jet observables [CMS12c; CMS14b] showed that the energy and momentum loss of reconstructed jets is mainly caused by soft particles transported to large angles wrt. the jet axis and a collimation of the inner, hard jet core. We will further discuss these findings in Section 7.4.3, where we present the jet shapes as calculated in the partonic transport approach BAMPS.

3 Microscopic processes of partons in the quark-gluon plasma

We learned in the previous chapter that there is evidence that partons, quarks and gluons, are the relevant degrees of freedom in the early phases of ultra-relativistic heavy-ion collisions. We discussed in Section 2.1 that the fundamental theory for these partons is quantum chromodynamics (QCD), which can be solved by a perturbative expansion (pQCD) of the Lagrangian Eq. (2.1) on page 6 in orders of the QCD coupling α_s. Within the partonic transport approach employed in this work for simulating the quark-gluon plasma, these pQCD interactions are used when numerically solving the 3+1D Boltzmann equation (cf. Chapter 4). In this chapter we present the different microscopic processes from pQCD that are considered within the present work: While Section 3.1 introduces the binary $2 \rightarrow 2$ matrix elements from leading-order pQCD, Section 3.2 briefly revises the Gunion-Bertsch approximation of $2 \rightarrow 3$ Bremsstrahlung processes valid for the kinematical region of hard parton interactions. The processes presented in Sections 3.1 and 3.2 are calculated in vacuum pQCD, which may suffer from infrared divergences originating from massless internal propagators. We will discuss how these divergences can be screened in the hot and dense environment of a quark-gluon plasma by attaching effective masses to the internal propagators, which are inspired by more formal thermal field theory calculations, namely from the Hard-Thermal-Loop approximation (HTL). Furthermore, we explain how the scale-dependence of the QCD coupling $\alpha_s(Q^2)$ discussed in the previous section can be considered in the context of microscopic interactions in a partonic medium.

One key concept in any kind of particle scatterings is the cross section σ measuring the probability for a specific final state emerging from a given initial state of particles. For example, if two bunches of particles A and B with lengths l_A, l_B and densities ρ_A, ρ_B scatter with each other, the cross section is defined by [PS95]

$$\sigma := \frac{\text{No. of scattering events}}{\rho_A \, l_A \, \rho_B \, l_B \, \mathcal{A}} \tag{3.1}$$

where $\mathcal{A}$ is the transverse area of each bunch. In quantum theory, the quantity measuring the transition from initial to final states is the invariant matrix element $\mathcal{M}$. The cross section for a $2 \rightarrow N$ process of two particles A and B is then given by [PS95]

$$\sigma_{2\rightarrow N} = \frac{1}{2\hat{s}} \frac{1}{\nu_{AB}} \left(\prod_{i=1}^{N} \int \frac{d^3 p_i}{(2\pi)^3 2E_i} \right) (2\pi)^4 \delta^{(4)}(p_A + p_B - \sum_{i=1}^{N} p_i) \left|\overline{\mathcal{M}}_{2\rightarrow N}\right|^2 , \tag{3.2}$$

where $\hat{s} = (p_A + p_B)^2$ is the Mandelstam variable representing the available center-of-momentum energy, $|\mathcal{M}_{2\rightarrow N}|^2$ is the matrix element of the respective scattering process averaged over all initial and summed over all final quantum states and ν_{AB} considers whether the initial state particles A and B are distinguishable. The integration over the phase space of final state particle momenta preserves energy and momentum conservation between the initial and final state via the $\delta^{(4)}$-function. This section reviews these total cross sections calculated for both elastic $2 \to 2$ and inelastic $2 \leftrightarrow 3$ processes within perturbative QCD.

Please note that the partonic processes introduced in this section are calculated under the assumption that the parton masses are negligible at energy scales $\sim \mathcal{O}(\mathrm{GeV})$ characteristic for high-energy physics. While this assumption seems legit for gluons and the lighter quark flavors, *up* ($m_\mathrm{u} \approx 2.2\,\mathrm{MeV}$), *down* ($m_\mathrm{d} \approx 4.7\,\mathrm{MeV}$) and *strange* ($m_\mathrm{s} \approx 95\,\mathrm{MeV}$), same arguments do not hold for charm ($m_\mathrm{c} \approx 1.275\,\mathrm{GeV}$) and bottom ($m_\mathrm{b} \approx 4.18\,\mathrm{GeV}$) flavored quarks[1]. Hence, the presented framework was previously also extended to massive pQCD matrix elements in order to simulate the transport properties of heavy quarks. Since we constrain ourselves in this work to jet quenching in the light flavor sector, we set $m_q = m_g = 0$ for the rest of this work and refer to Refs. [Uph+10; Uph+11; Uph+12; Uph13; Uph+14; Sen+17] for more details about heavy flavor results within the BAMPS approach.

3.1 Elastic $2 \to 2$ pQCD processes

In a binary $2 \to 2$ scattering, two incoming partons, A and B, with four-momenta $p_A = (E_A, \vec{\mathbf{p_A}})$ and $p_B = (E_B, \vec{\mathbf{p_B}})$ scatter with each other with the result that two outgoing partons, 1 and 2, with momenta p_1 and p_2 leave the scattering. Please note that we orient us in the present work on the standard nomenclature in the BAMPS framework and denote binary $2 \to 2$ interactions often as *elastic* interactions since no additional particle is produced in these interactions. This is in contrast to *inelastic* $2 \leftrightarrow 3$ processes discussed in the next section, where an additional parton is either emitted or absorbed.

As we have seen in the previous section, the cross section of a scattering depends via Eq. (3.2) on the Mandelstam variable $\hat{s}$ determining the available center-of-momentum energy $\sqrt{\hat{s}}$ of the collision. The Mandelstam variables,

$$\begin{aligned} \hat{s} &= (p_A + p_B)^2 = (p_1 + p_2)^2 \\ \hat{t} &= (p_A - p_1)^2 = (p_B - p_2)^2 \\ \hat{u} &= (p_A - p_2)^2 = (p_B - p_1)^2 \,, \end{aligned} \tag{3.3}$$

are Lorentz invariant quantities which characterize the kinematics of a scattering. One can show that the different Mandelstam variables are not independent from each other but the relation $\hat{s} + \hat{t} + \hat{u} = \sum_i m_i^2$ holds, where the sum runs over all particle masses m_i contributing to the specific process. Consequently, for massless partons $\hat{u} = -\hat{s} - \hat{t}$ follows.

At a given scale $\hat{s}$, the outgoing parton momenta p_1 and p_2 are mainly determined by the momentum transfer q^2, or equivalent the Mandelstam variable $\hat{t}$, of the interaction. Moreover, the momentum transfer $\hat{t}$ directly relates to the scattering angle $\theta\angle(\vec{\mathbf{p}}_A, \vec{\mathbf{p}}_1)$ in the center-of-momentum (CoM) system. By projecting out $\hat{t}$ in Eq. (3.2) on the previous page one derives the differential cross section $\mathrm{d}\sigma \,/\, \mathrm{d}\hat{t}$ for a given interaction to [Uph13]

$$\frac{\mathrm{d}\sigma}{\mathrm{d}\hat{t}} = \frac{1}{16\pi\hat{s}^2} \left|\overline{\mathcal{M}}\right|^2_{A,B\to 1,2} \,, \tag{3.4}$$

which describes the distribution of different momentum transfers $\hat{t}$ at a given $\hat{s}$. Obviously,

---

[1] The numerical values for the different quark masses were taken from the 2018 edition of the *Review of Particle Physics* [Tan+18].

the integrated total cross section can also be obtained from the differential cross section via

$$\sigma = \int\limits_{\hat{t}_{\text{min}}}^{\hat{t}_{\text{max}}} \frac{\mathrm{d}\sigma}{\mathrm{d}\hat{t}}\,\mathrm{d}\hat{t}\ . \tag{3.5}$$

By employing the relation $\hat{t} = -\hat{s}/2(1 - \cos\theta)$ between $\hat{t}$ and the scattering angle θ, one derives the integration limits $\hat{t}_{\text{min}} = -s$ and $\hat{t}_{\text{max}} = 0$ from $\theta = [0;\pi]$. Therefore the Mandelstam variable $\hat{t}$ (and also $\hat{u}$) is negative and the corresponding momentum transfers are defined as $q^2 = -\hat{t}$.

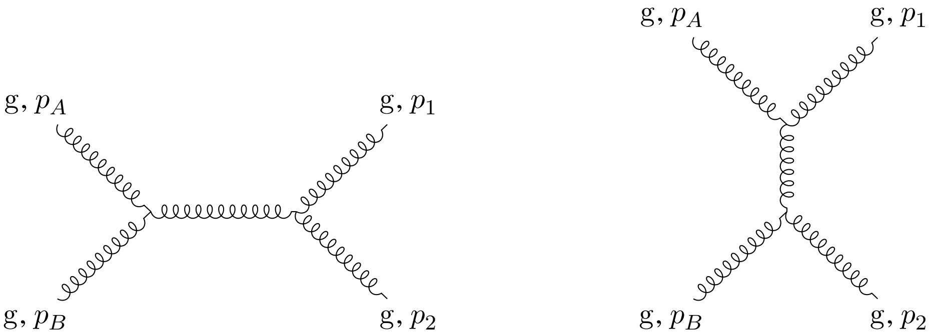

(a) s-channel **(b)** t-channel

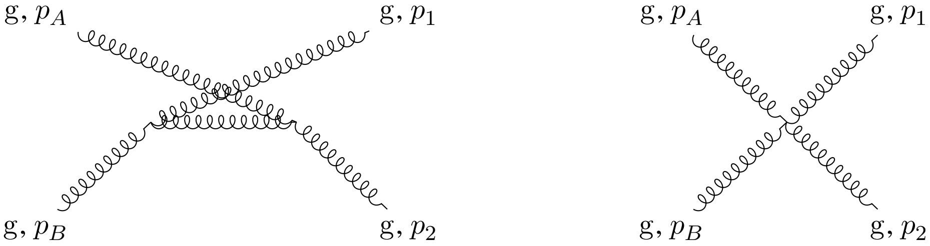

(c) u-channel **(d)** four-gluon vertex

Figure 3.1: Different channels of the process $\mathrm{gg} \rightarrow \mathrm{gg}$ calculated in leading-order pQCD. The respective channel is determined by the characteristic momentum scale given by the momentum of the internal gluon propagator. For more details see Ref. [PS95].

Both the differential and the integrated cross sections rely on the averaged matrix elements $\left|\overline{\mathcal{M}}\right|^2$ of the specific partonic process. These matrix elements can be directly calculated within perturbative QCD with the help of Feynman diagrams, a tool schematically representing the perturbative expansion of Eq. (2.1) on page 6. For example, due to the abundance of gluons and their larger QCD color factor (we will discuss the QCD color factors of quarks and gluons later in this section) the processes $\mathrm{gg} \rightarrow \mathrm{gg}$ and $\mathrm{g}q \rightarrow \mathrm{g}q$ are the dominant processes of partons within the quark-gluon plasma during the initial stages of an ultra-relativistic heavy-ion collision. The differential cross section for the process $\mathrm{gg} \rightarrow \mathrm{gg}$ calculated in perturbative QCD at leading-order in the QCD coupling α_s reads [PS95]

$$\frac{\mathrm{d}\sigma_{\mathrm{gg}\rightarrow\mathrm{gg}}}{\mathrm{d}\hat{t}} = \frac{9\pi\alpha_s^2}{2\hat{s}^2}\left[3 - \frac{\hat{t}\hat{u}}{\hat{s}^2} - \frac{\hat{s}\hat{u}}{\hat{t}^2} - \frac{\hat{s}\hat{t}}{\hat{u}^2}\right]\,. \tag{3.6}$$

The corresponding matrix elements of the active channels contributing to the process

$\mathrm{gg} \rightarrow \mathrm{gg}$ are shown as Feynman diagrams in Fig. 3.1. At large $\hat{s}$, which could be realized, e.g., in a scattering of an energetic parton with a thermal parton, the process $\mathrm{gg} \rightarrow \mathrm{gg}$ is dominated by the t-channel processes $\left|\overline{\mathcal{M}}\right|^2 \sim 1/\hat{t}^2$. This dominance of the t-channel at large CoM energies is a characteristic feature of perturbative QCD and can be found also in other partonic processes at leading order. Therefore, the differential cross sections of quarks and gluons at high $\hat{s}$ scale by the QCD color factors, which are $C_{\mathrm{F}} = (N_c^2 - 1)/(2N_c) = 9/4$ for quarks and $C_{\mathrm{A}} = N_c = 3$ for gluons and which originate from the group Casimir factors of SU(3). Please note that, in contrast to other approaches, we explicitly consider also the four-gluon vertex in the process $\mathrm{gg} \rightarrow \mathrm{gg}$, which follows from the self-interactions of gluons due to the non-Abelian symmetry of QCD. While this channel can be neglected at higher $\sqrt{\hat{s}}$ ($\left|\overline{\mathcal{M}}\right|^2_{4-gluon} \sim 1/\hat{s}^2$), it significantly contributes to the interactions of softer gluons as they are, e.g., considered in Section 5.3.3, where we discuss the momentum broadening of emitted gluons from inelastic Bremsstrahlung processes.

gluons	$\mathrm{gg} \rightarrow \mathrm{gg}$ $\mathrm{g}q \rightarrow \mathrm{g}q$ $\mathrm{g}\bar{q} \rightarrow \mathrm{g}\bar{q}$	$\mathrm{gg} \rightarrow q\bar{q}$	
quarks	$qq \rightarrow qq$ $q\bar{q} \rightarrow q\bar{q}$ $qq' \rightarrow qq'$ $q\mathrm{g} \rightarrow q\mathrm{g}$	$\bar{q}\bar{q} \rightarrow \bar{q}\bar{q}$ $q\bar{q} \rightarrow \mathrm{gg}$ $q\bar{q}' \rightarrow q\bar{q}'$ $\bar{q}\mathrm{g} \rightarrow \bar{q}\mathrm{g}$	$q\bar{q} \rightarrow q'\bar{q}'$

Table 3.1: The different elastic parton processes considered in the present work.

Similar to $\mathrm{gg} \rightarrow \mathrm{gg}$, one can also calculate the matrix elements for other parton processes within pQCD. Table 3.1 shows the elastic processes of different parton flavors—quarks q, gluons g and anti-quarks $\bar{q}$—considered within this work. For an overview of the corresponding matrix elements and their Feynman diagrams we refer to Appendix A.

The previously discussed matrix elements show divergences at soft momentum scales. For example, the t-channel contribution to the $\mathrm{gg} \rightarrow \mathrm{gg}$ matrix element diverges for $\hat{t} \rightarrow 0$ at a fixed $\hat{s}$. These divergences originate from the massless internal quark and gluon propagators of the different channels contributing to the respective process. They can be formally cured by calculating the above cross sections within thermal field theory valid for the hot and dense environment of a quark-gluon plasma. One method which is commonly applied for such calculations is the *Hard-Thermal-Loop* (HTL) approximation [Pis89; BP90]. Within this work, we effectively cure the divergences by introducing a Debye screening mass for the diverging propagators. In other words, due to the screening within the medium, the internal propagators become effectively massive and thereby cure the divergences. The Debye masses of quark and gluons depend on the number of quark flavors N_f and colors N_c, and can be written as [Won96]

$$m_D^2 := m_g^2 = 16\pi\alpha_s \int \frac{\mathrm{d}^3 p}{(2\pi)^3} \frac{1}{p} (N_c f_g + N_f f_q) \tag{3.7}$$

$$m_q^2 = 4\pi\alpha_s \frac{N_c^2 - 1}{2N_c} \int \frac{\mathrm{d}^3 p}{(2\pi)^3} \frac{1}{p} (f_g + f_q)\,, \tag{3.8}$$

where f_i is the phase space distribution of quarks and gluons, respectively. For example,

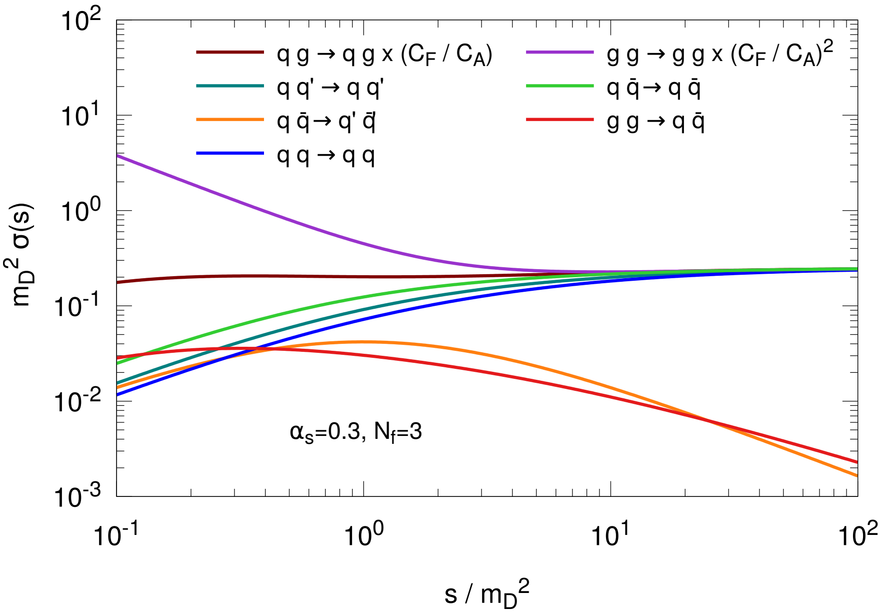

Figure 3.2: Integrated elastic cross section σ depending on the CoM energy $\hat{s}$ of the scattering partons for the different partonic $2 \to 2$ processes considered in this work. The QCD coupling is chosen as $\alpha_s = 0.3$ and the cross section is scaled by the Debye mass m_D^2.

within a thermal medium with temperature T the Debye masses can be evaluated to

$$m_D^2 = \frac{8\alpha_s}{\pi}(N_c + N_f)T^2 \tag{3.9}$$

$$m_q^2 = \frac{2\alpha_s}{\pi}\frac{N_c^2 - 1}{N_c}T^2 \,. \tag{3.10}$$

After introducing the effective Debye screening mass, the differential cross section of the process $\mathrm{gg} \to \mathrm{gg}$ reads

$$\frac{\mathrm{d}\sigma_{\mathrm{gg}\to\mathrm{gg}}}{\mathrm{d}\hat{t}} = \frac{9\pi\alpha_s^2}{2\hat{s}^2}\left[3 - \frac{\hat{t}\hat{u}}{\hat{s}^2} - \frac{\hat{s}\hat{u}}{\left(\hat{t} - m_D^2\right)^2} - \frac{\hat{s}\hat{t}}{\left(\hat{u} - m_D^2\right)^2}\right]. \tag{3.11}$$

Figure 3.2 shows the integrated cross sections σ depending on $\hat{s}$ for the different elastic $2 \to 2$ processes considered in this work. The divergences in the leading-order matrix elements are cured by the described Debye screening. As already discussed, the parton processes which include a t-channel contribution scale with the QCD color factors at high $\hat{s}$. The contribution of the other processes $\mathrm{gg} \to q\bar{q}$ and $q\bar{q} \to q'\bar{q}'$ which include only an active s-channel is negligible at high CoM energies, whereas at softer momentum scales their contribution can be significant.

As we have seen in Section 2.1.2, the scale dependence of the QCD coupling $\alpha_s(Q^2)$ is a crucial property of QCD leading to the confinement of partons within hadrons at soft momentum scales and the asymptotic freedom of partons at large momentum scales. In the previous discussion of the elastic matrix elements we neglected this scale dependence but assumed that the QCD coupling is constant. Although this is a legit approach when investigating phenomena at a fixed scale, the energy loss of jets within a medium studied within this work may obtain contributions from different momentum scales: While the interactions within the heavy-ion medium occur on softer momentum scales and thereby stronger QCD coupling, jet-medium interactions exhibit harder momentum transfers leading to a softer QCD coupling. In order to evaluate this "running" of the QCD coupling microscopically, we choose the value of the QCD coupling $\alpha_s\left(Q^2\right)$ based on Eq. (2.2) on page 8, where the momentum scale Q^2 is chosen by the Mandelstam variable $\hat{s}$, $\hat{t}$ or $\hat{u}$ of the respective channel under consideration. For example, the t-channel contribution in Eq. (3.11) is replaced by

$$\frac{\alpha_s^2}{\left(\hat{t}-m_D^2\right)^2} \rightarrow \frac{\alpha_s^2(\hat{t})}{\left(\hat{t}-m_D^2\left(\alpha_s(\hat{t})\right)\right)^2} . \tag{3.12}$$

Consequently, the running of the QCD coupling is considered both in the vertices of the underlying $2 \rightarrow 2$ process and the screening of the internal propagators. For more details about the microscopic implementation of the running QCD coupling we refer to Refs. [Uph13; Uph+14; Uph+15].

Finally, before introducing inelastic $2 \leftrightarrow 3$ process in the next section, we would like to comment on the *small-angle approximation* for the pQCD matrix elements applied in previous studies within BAMPS [FXG09; Foc11]. In this approximation one exploits the dominance of small momentum transfers, $\hat{t} \rightarrow 0$, at larger $\hat{s}$ and approximates the matrix elements by only considering the t-channel contribution of the respective process. Consequently, any contribution of, e.g., the four-gluon vertex is neglected in the small-angle approximation. Furthermore, for small scattering angles $\theta \rightarrow 0$, the momentum transfer can be estimated as $q^2 = -\hat{t} \approx q_\perp^2$, where $q_\perp^2$ is the momentum component transverse to the initial ingoing parton directions. For example, the differential cross section of the process $\mathrm{gg} \rightarrow \mathrm{gg}$ in the small-angle approximation is then given by

$$\left.\frac{\mathrm{d}\sigma_{\mathrm{gg}\rightarrow\mathrm{gg}}}{\mathrm{d}q_\perp^2}\right|_{\theta\rightarrow 0} = \frac{9\pi\alpha_s^2}{\left(q_\perp^2+m_D^2\right)^2} . \tag{3.13}$$

As we will see in Chapter 5 and also when discussing our results for the medium created in heavy-ion collisions in Chapter 7, the loosening of the small-angle approximation and thereby the consideration of other channels than the t-channel leads to a significant increase of the scattering rate at small parton momenta.

3.2 Inelastic $2 \leftrightarrow 3$ processes

One of the advantages of the partonic transport approach BAMPS is the consistent implementation of elastic scatterings *and* inelastic Bremsstrahlung/annihilation processes. These inelastic interactions represent processes from the next order in the perturbative expansion of Eq. (2.1) on page 6. Furthermore, the inclusion of both gluon emission and annihilation processes ensures the crucial concept of *detailed balance*, which is essential for the statistical treatment of parton interactions. However, the exact calculation of the $2 \leftrightarrow 3$ matrix element from pQCD is ambitious since the necessary screening of divergences emerging in the higher order terms is not ad-hoc clear. Therefore we employ within this work an approximation for the inelastic $2 \leftrightarrow 3$ matrix elements first developed by Gunion and Bertsch [GB82] and recently revised in the context of the partonic transport approach BAMPS by Fochler et al. [Foc+13]. In this section we briefly recapitulate the improved Gunion-Bertsch (GB) approximation of Ref. [Foc+13] and introduce how the differential and integrated cross sections of the $2 \leftrightarrow 3$ processes are calculated. For more details about the actual derivation and a comparison to exact pQCD matrix elements we refer to Refs. [Foc+13; Uph13].

3.2.1 Gluon radiation via $2 \rightarrow 3$ Bremsstrahlung processes

The Gunion-Bertsch approximation was first formulated by Gunion and Bertsch [GB82] for mid-rapidity gluon emissions off hard partonic components within high energy hadron-hadron collisions. Assuming a quark q with momentum p_A from one hadron scatters with another quark q' with momentum p_B from the other hadron, the conceivable processes including an additional gluon emission with momentum $k = \left(k_\perp \cosh y, \vec{\mathbf{k}}_\perp, k_\perp \sinh y\right)$ are depicted in Fig. 3.3, where y and $k_\perp$ are the momentum-space rapidity and transverse momentum, respectively, of the emitted gluon within the CoM frame of the scattering.

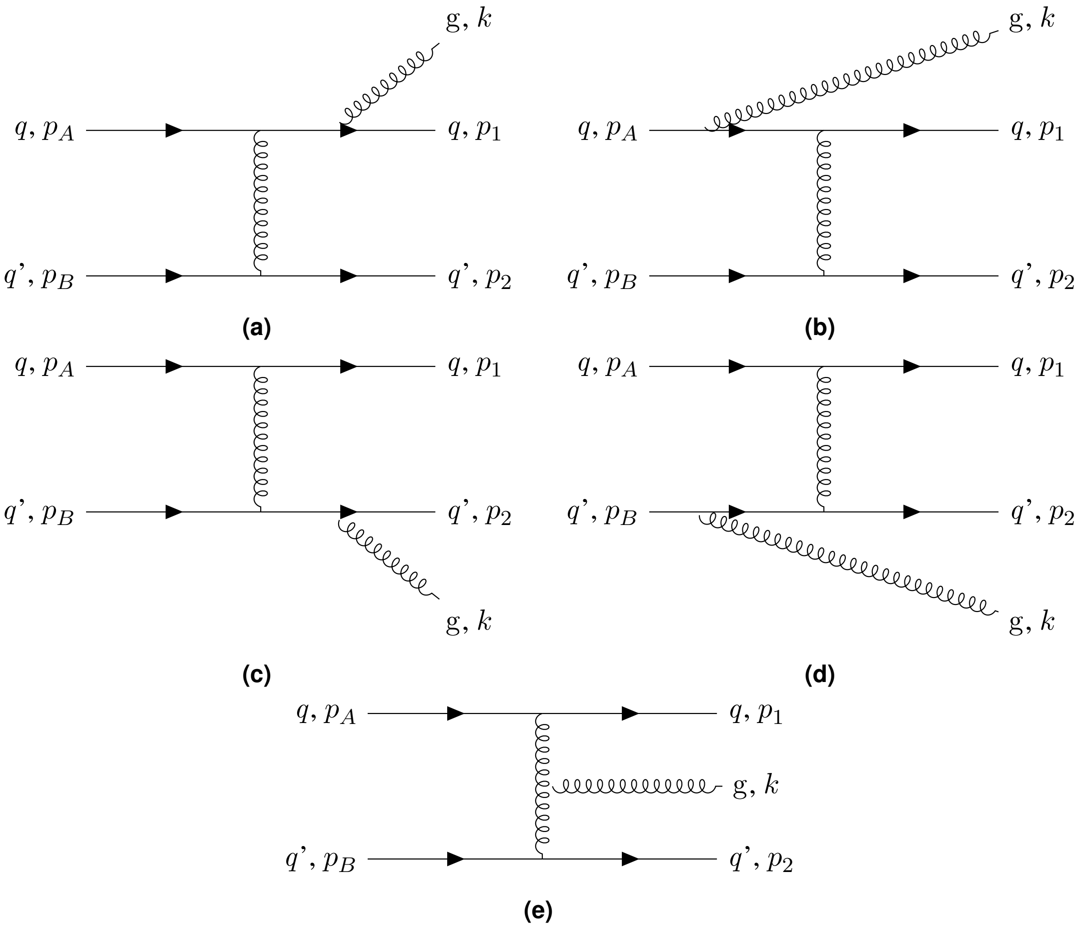

Figure 3.3: The scattering channels of the process $qq' \rightarrow qq'g$ as considered in the Gunion-Bertsch approximation. Depending on the chosen gauge either the first or second row can be neglected within the calculation.

Due to the high energy of the incoming quarks, the original approximation of Gunion and Bertsch was formulated in the limits,

$$k_\perp \ll \sqrt{\hat{s}} \qquad\qquad q_\perp \ll \sqrt{\hat{s}}\,, \tag{3.14}$$

assuming both soft gluon emissions $k_\perp^2$ and soft momentum transfers $q_\perp^2$ between the incoming quarks. Furthermore, after introducing the Lorentz-invariant quantity [Foc+13]

$$x = \frac{k_\perp}{\sqrt{\hat{s}}} e^y \,, \tag{3.15}$$

representing the fraction of light-cone momentum transported away by the radiated gluon, Gunion and Bertsch also stated the third condition

$$x q_\perp \ll k_\perp \,. \tag{3.16}$$

However, the original Gunion-Bertsch approximation is strictly only valid at mid-rapidity and therefore it demands $x \to 0$. Since the scattering probability within a partonic transport approach as BAMPS is based on the total cross section of the respective $2 \to 3$ process, also contributions of gluon emissions at larger forward- and backward-rapidity have to be considered. In order to obtain an improved GB approximation also valid at $x > 0$, Fochler et al. introduced two corrections to the original GB approximation [Foc+13; Uph13]:

1. Within the limit $x \to 0$, a factor $(1-x)^2$ could be omitted during the derivation of Gunion and Bertsch. When considering $x \neq 0$ and thereby finite gluon rapidities, this factor has to be explicitly considered in the final results.

2. The derivation by Fochler et al. demanded for an additional constraint $x^2 s \gg k_\perp^2$, which is equivalent to $y \gg 0$. Consequently, this approximation would be in principle only valid for gluon emissions at mid- and forward rapidities. In order to arrive at an expression also valid at backward rapidity, Fochler et al. compared the results in the $A^+ = 0$ gauge, where the gluon is predominantly emitted from the upper quark line, with the corresponding $A^- = 0$ gauge, where the gluons is mostly radiated from the lower quark line. Combining both results, they could show that a simple expression for the resulting matrix elements can be obtained by substituting

$$x \to \overline{x} := \frac{k_\perp}{\sqrt{\hat{s}}} e^{|y|} \,. \tag{3.17}$$

Combining both corrections, the final result for the $2 \to 3$ matrix element for the process $qq' \to qq'\mathrm{g}$ in the improved Gunion-Bertsch approximation reads [Foc+13; Uph13]

$$|\mathcal{M}|^2_{qq' \to qq'\mathrm{g}} = 48\pi\alpha_s |\mathcal{M}|^2_{qq' \to qq'} (1-\overline{x})^2 \left[\frac{\vec{\mathbf{k}}_\perp}{k_\perp^2} + \frac{\vec{\mathbf{q}}_\perp - \vec{\mathbf{k}}_\perp}{\left(\vec{\mathbf{q}}_\perp - \vec{\mathbf{k}}_\perp\right)^2 + m_D^2} \right]^2 \,, \tag{3.18}$$

where $|\mathcal{M}|^2_{qq' \to qq'}$ is the matrix element of the elastic process $qq' \to qq'$ in the small-angle approximation as discussed in the previous section. Please note that the diverging propagators of the internal gluon lines in Eq. (3.18) are screened with a Debye mass corresponding to the effective screening procedure introduced in Section 3.1.

One of the characteristic features of the high energy limit underlying the Gunion-Bertsch approximation is the splitting of the $2 \to 3$ matrix element into an elastic $2 \to 2$ contribution and a probability for emitting a gluon $P_g = 48\pi\alpha_s (1-\overline{x})^2 \left[\frac{\vec{\mathbf{k}}_\perp}{k_\perp^2} + \frac{\vec{\mathbf{q}}_\perp - \vec{\mathbf{k}}_\perp}{\left(\vec{\mathbf{q}}_\perp - \vec{\mathbf{k}}_\perp\right)^2 + m_D^2} \right]^2$,

$$|\mathcal{M}|^2_{XY \to X'Y'\mathrm{g}} = |\mathcal{M}|^2_{XY \to X'Y'} \, P_g \,. \tag{3.19}$$

This splitting allows to generalize the previous derivation for the process $qq' \rightarrow qq'\mathrm{g}$ also to Bremsstrahlung processes involving other parton flavors by applying the corresponding elastic matrix elements. For example, from the elastic matrix elements in small angle approximation one can infer [Foc+13]

$$|\mathcal{M}|^2_{qq' \rightarrow qq'\mathrm{g}} = \left(\frac{C_\mathrm{F}}{C_\mathrm{A}}\right) |\mathcal{M}|^2_{q\mathrm{g} \rightarrow q\mathrm{gg}} = \left(\frac{C_\mathrm{F}}{C_\mathrm{A}}\right)^2 |\mathcal{M}|^2_{\mathrm{gg} \rightarrow \mathrm{ggg}} , \tag{3.20}$$

where $C_\mathrm{F} = 4/3$ and $C_\mathrm{A} = 3$ are again the QCD color factors of a quark and gluon, respectively.

Based on the Gunion-Bertsch matrix element one can calculate both the differential and the integrated cross section for a radiative process. However, the total integrated cross section defined in Eq. (3.2) on page 25 depends on the Cartesian four-momenta p_i of the outgoing partons leading to a nine-dimensional integration in the case of a $2 \rightarrow 3$ process. In contrast, the discussed Gunion-Bertsch matrix element depends on the squared momentum transfer $q_\perp^2$, the transverse momentum $k_\perp^2$ and rapidity y of the emitted gluon, and the angle ϕ between $\vec{\mathbf{k}}_\perp$ and $\vec{\mathbf{q}}_\perp$. After an appropriate variable transformation (for more details see Refs. [Foc11; Uph13]), one obtains for the total cross section of a radiative $2 \rightarrow 3$ process between two particles A and B [Uph13]

$$\sigma_{2\rightarrow 3} = \frac{1}{256\pi^4} \frac{1}{\nu_{AB}} \frac{1}{\hat{s}} \int\limits_0^{\hat{s}/4} \mathrm{d}q_\perp^2 \int\limits_{k_{\perp;\,\mathrm{min}}}^{\hat{s}/4} \mathrm{d}k_\perp^2 \int\limits_{y_{min}}^{y_{max}} \mathrm{d}y \int\limits_0^{\pi} \mathrm{d}\phi \, |\overline{\mathcal{M}}_{2\rightarrow 3}|^2 \sum \left(\left. \frac{\mathrm{d}F}{\mathrm{d}y_1} \right|_{F=0} \right)^{-1} , \tag{3.21}$$

where y_1 is the rapidity of the outgoing particle with momentum p_1 and the function $F = \hat{s} - 2\sqrt{\hat{s}}(q_\perp \cosh y_1 + k_\perp \cosh y) + 2q_\perp k_\perp \cos\phi + 2q_\perp k_\perp (\cosh y \cosh y_1 - \sinh y \sinh y_1)$ denotes the argument of the delta function of Eq. (3.2) on page 25 written in Gunion-Bertsch variables.

Similar to the previous case of elastic $2 \rightarrow 2$ interactions the running of the QCD coupling can be considered by evaluating $\alpha_s(Q^2)$ at a characteristic momentum scale given by either $Q^2 = q_\perp^2$ or $Q^2 = k_\perp^2$ [Uph13].

As we will discuss in detail in Chapter 5, one has to carefully consider coherence effects when dealing with radiative partonic processes in a hot and dense partonic medium. The Landau-Pomeranchuk-Migdal (LPM) [LP53b; Mig56] effect describes the coherence of gluon emissions if the formation time becomes comparable to the mean free path between subsequent inelastic scatterings and individual gluon emissions begin to overlap, what may lead to a suppression of radiative processes. Consequently, the specific modeling of the LPM effect introduced in Chapter 5 constrains the kinematic limits for the gluon rapidity y_{min} and y_{max}, and the minimum transverse momentum $k_{\perp;\,\mathrm{min}}$ when calculating the total cross section via Eq. (3.21) [Foc11; Uph13].

3.2.2 Gluon annihilation via $3 \rightarrow 2$ processes

When considering microscopic processes in a medium, one key concept for achieving and later preserving thermalization via these processes is *detailed balance*. It demands that for each processes, e.g. $a + b \rightarrow c + d$, a corresponding back-reaction $c + d \rightarrow a + b$

exists, whose matrix element agrees with the matrix element of the forward reaction[2]. The fundamental reason for this behavior is the invariance of quantum chromodynamics under time reversal operations [Uph13]. Consequently, in order to achieve thermalization within a medium considering the previous $2 \to 3$ processes, also the corresponding $3 \to 2$ gluon annihilation processes have to be considered. In this section we briefly sketch these gluon annihilation process based on the improved Gunion-Bertsch approximation from the previous section and discuss their relevance for high energy partons.

Similar to the cross section of a $2 \to n$ process given in Eq. (3.2) on page 25 one can define an object [Foc11]

$$I_{3\to 2} = \frac{1}{\nu_{ABC}} \int \frac{d^3p_1}{(2\pi)^3 2E_1} \int \frac{d^3p_2}{(2\pi)^3 2E_2} (2\pi)^4 \delta^{(4)}(p_A + p_B + p_C - p_1 - p_2) \left|\overline{\mathcal{M}}_{3\to 2}\right|^2 , \tag{3.22}$$

which represents the strength of a $3 \to 2$ annihilation process between partons A, B and C. This formulation for the $3 \to 2$ interactions allows a straight-forward implementation of detailed balance by choosing for $\left|\overline{\mathcal{M}}_{3\to 2}\right|^2$ the corresponding $2 \to 3$ matrix element in GB approximation as given in Eq. (3.18) on page 32 (while considering the different degeneracy factors of partons). For example, the gluon annihilation matrix element for the process $\mathrm{ggg} \to \mathrm{gg}$ then reads [Foc11]

$$\left|\overline{\mathcal{M}}_{\mathrm{ggg}\to \mathrm{gg}}\right|^2 = \frac{1}{\nu_g} \left|\overline{\mathcal{M}}_{\mathrm{gg}\to \mathrm{ggg}}\right|^2 , \tag{3.23}$$

where $\nu_g = \nu_{\text{polarization}} \left(N_c^2 - 1\right) = 16$ is the degeneracy factor of gluons. Furthermore, as in the radiative case coherence effects can be consistently incorporated into gluon annihilation process by appropriately choosing the integration limits of Eq. (3.22). For more details about the specific implementation of annihilation process within the transport approach BAMPS we refer to Refs. [XG05; XG07; Foc11].

In this work we are mainly focused on the energy loss of energetic partons ($E \gg T$), so called jets. Due to the enormous energies, the available phase space for gluon annihilation processes of jets is limited. As a first outlook to our results presented in Chapters 5 to 7, Fig. 3.4 compares the differential energy loss $\mathrm{d}E/\mathrm{d}x$ of quarks and gluons resulting from annihilating $3 \to 2$ interactions with the energy loss from elastic $2 \to 2$ and radiative $2 \to 3$ processes. For more information about the calculation of the differential energy loss $\mathrm{d}E/\mathrm{d}x$ and the underlying model assumptions, especially the treatment of coherence effects, we refer to the later Chapters 4 and 5. Apparently, the contribution of $3 \to 2$ process to the energy loss of partons with $E > T$ is negligible both for quarks and gluons. Please note that the same argument does not hold for $E \lessapprox T$, where especially the interplay between gluon radiation and annihilation leads to a thermalization of the partonic medium. Based on this result we neglect throughout this work the annihilating $3 \to 2$ processes of jets and only consider $3 \to 2$ processes for the simulation of the background medium evolution of heavy-ion collisions as presented in Chapter 7.

---

[2] Only potentially different degeneracy factors of the different particle species have to be considered when calculating the cross section.

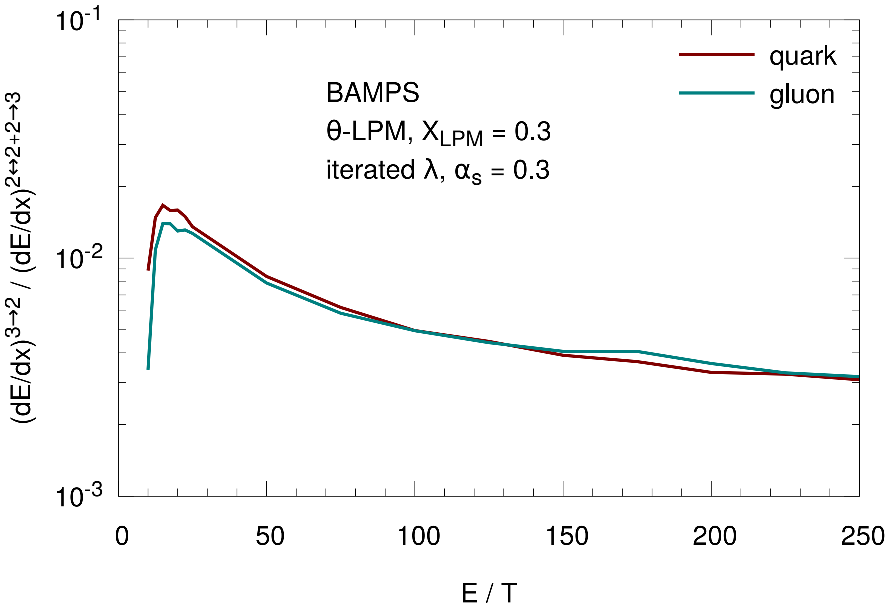

Figure 3.4: Comparison of the differential energy loss $\mathrm{d}E/\mathrm{d}x$ of a quark (red) or a gluon (green) with energy E in a medium with temperature T resulting from either only $3 \to 2$ annihilation processes or from $2 \to 2$ and $2 \to 3$ processes. The Landau-Pomeranchuk-Migdal effect underlying the radiative and annihilation processes was modeled by the θ-LPM approach (cf. Chapter 5). The QCD coupling was chosen as $\alpha_s = 0.3$.

4 Transport of partons within the QGP

In the previous section we discussed how individual partons scatter with each other via Debye-screened perturbative quantum chromodynamics. Multiple of these microscopic scatterings then lead to macroscopic dynamics of the medium that is built up from these individual partons. One possibility to calculate this evolution is kinetic theory or transport theory. Within this section we introduce the 3+1-dimensional (3+1D) transport approach BAMPS (Boltzmann Approach for Multi-Parton Scattering) and review the major building blocks within BAMPS that were employed within this work for describing the dynamics of the quark-gluon plasma. For a comprehensive review of the BAMPS framework and details about its implementation we refer to Refs. [XG05; XG07].

4.1 Partonic transport approach BAMPS

One possible method for describing the evolution of the medium created in ultra-relativistic heavy-ion collisions is relativistic ideal or viscous hydrodynamics. By solving the underlying differential equations, hydrodynamics simulates the macroscopic dynamics of the quark-gluon plasma. However, one major drawback of these models is the limited capability of describing systems far from equilibrium. Such situations are supposed to occur especially during the early phases of heavy-ion collisions.

Among the promising alternatives to hydrodynamical simulations are models based on kinetic theory. In kinetic theory, the phase space distribution of partons, which is the 6-dimensional distribution in configuration space $\vec{\mathbf{x}}$ and momentum space $\vec{\mathbf{p}}$, is evolved based on microscopic interactions between individual particles. The kinetic equation describing, e.g., the evolution of massless partons in the quark-gluon plasma is the relativistic Boltzmann equation [De 80; Rei09]

$$p_i^\mu \partial_\mu f_i(\vec{\mathbf{x}}, \vec{\mathbf{p}}, t) = \left(E_i \frac{\partial}{\partial t} + \vec{\mathbf{p}}_i \cdot \frac{\partial}{\partial \vec{\mathbf{r}}} \right) f_i(\vec{\mathbf{x}}, \vec{\mathbf{p}}, t) = \mathcal{C}_i^{2\to 2} + \mathcal{C}_i^{2\leftrightarrow 3} + \dots \,. \tag{4.1}$$

$f_i(\vec{\mathbf{x}}, \vec{\mathbf{p}})$ denotes the one-particle distribution function of parton species i (quarks or gluons) normalized so that $f_i(\vec{\mathbf{x}}, \vec{\mathbf{p}})\, \mathrm{d}^3x\, \mathrm{d}^3x$ represents the number of particles from species i in a given phase space volume (d^3x,d^3p). The terms $\mathcal{C}_i$ are called collision terms and describe the microscopic interactions of partons leading to changes in the distribution functions. Hence, they are directly related to the rate of particle interactions and may include arbitrary orders of processes ($m \to n$). If all collision terms vanish, $\mathcal{C}_i = 0$, one obtains the evolution equation of the non-interacting, ideal Boltzmann gas. Since, in general, not all collision terms vanish, the Boltzmann equation is an integro-differential equation, which is, without any further assumptions, not analytical solvable at the moment.

One possibility for nevertheless solving the Boltzmann equation from first-principles is the application of numerical techniques. Within this work, we therefore employ the partonic transport approach BAMPS that solves the full 3+1D evolution of the microscopic phase space of massless partons, which fulfill the relativistic energy-momentum relation[1] $E^2 = \vec{\mathbf{p}}^2 + m^2$. The partons scatter within BAMPS both elastically via $2 \rightarrow 2$ and inelastically via $2 \leftrightarrow 3$ processes as presented in Chapter 3. These scatterings are then described by collisions terms, or in other words collision rates, $\mathcal{C}_i^{2\rightarrow 2}$ and $\mathcal{C}_i^{2\leftrightarrow 3}$, which can be related to the matrix elements of the underlying scatterings by integrating the phase space distribution over the other scattering partners' and the outgoing partons' momenta. For example, the collision term $\mathcal{C}_i^{2\rightarrow 2}$ for a $2 \rightarrow 2$ scattering of particles $i\,j \leftrightarrow k\,l$ can be obtained from [Xu04; Uph+12]

$$\begin{aligned}\mathcal{C}_i^{2\rightarrow 2} = \frac{1}{2E_i} \sum_{j,k,l} \int \frac{\mathrm{d}^3 p_j}{(2\pi)^3 2E_j} \int \frac{\mathrm{d}^3 p_k}{(2\pi)^3 2E_k} \int \frac{\mathrm{d}^3 p_l}{(2\pi)^3 2E_l} \times \\ \times \Bigg(\frac{1}{\nu_{ij}} f_k f_l \left|\overline{\mathcal{M}}_{kl\rightarrow ij}\right|^2 (2\pi)^4 \delta^{(4)}(p_k + p_l - p_i - p_j) \\ - \frac{1}{\nu_{kl}} f_i f_j \left|\overline{\mathcal{M}}_{ij\rightarrow kl}\right|^2 (2\pi)^4 \delta^{(4)}(p_i + p_j - p_k - p_l) \Bigg) \,, \end{aligned} \tag{4.2}$$

where $\nu_{ij} = 2$ if the particles i and j are indistinguishable and $\nu_{ij} = 1$ otherwise. The second term in the brackets denotes the process $i\,j \rightarrow k\,l$ (*loss term*), whereas the first term describes the back reaction $k\,l \rightarrow i\,j$ (*gain term*) of the scattering. The delta functions preserve energy and momentum of the incoming and outgoing partons when integrating over the phase space.

The Boltzmann equation and its collision terms are generic and can be applied to arbitrary particle interactions, which enter the collision term via the matrix elements $\left|\overline{\mathcal{M}}_{ij\rightarrow kl}\right|^2$. Within the present work we employ the partonic processes from perturbative QCD as introduced in the previous Chapter 3. Contributions to the collision rate from the different partonic processes are considered in Eq. (4.2) by the sum $\sum_{j,k,l}$ over all possible parton species contributing to the respective process. Similar to the presented $2 \rightarrow 2$ collision term, also a collision term for the inelastic scatterings can be formulated by integrating additionally over the phase space of the third outgoing parton (cf. eq. (2.14) of Ref. [Xu04]). Within BAMPS, the matrix elements for these inelastic $2 \rightarrow 3$ Bremsstrahlung and $3 \rightarrow 2$ annihilation processes are mostly chosen by the radiative partonic processes calculated in the Gunion-Bertsch approximation derived in Section 3.2.1. Later in this work we extend these interactions by effective $1 \leftrightarrow 2$ processes calculated from thermal field theory (cf. Section 5.4).

In order to numerically solve the Boltzmann equation one has to decide how to relate the previously discussed collision terms with microscopic scattering probabilities for partons. One possible approach employed in other transport models as, e.g., URQMD [Bas+98; Ble+99] is the so called *geometrical method*. In this method one decides whether two particles scatter with each other based on their geometrical distance. If two partons are closer than $\sqrt{\sigma/\pi}$, where σ denotes the cross section for the microscopic process, both partons scatter with each other. One major obstacle for applying the geometrical method within BAMPS is that there is no ad-hoc definition for the distance of three ingoing particles from the $3 \rightarrow 2$ processes presented in the previous chapter. Therefore only the dilute outer regions of a heavy-ion collision are simulated within BAMPS based on the geometrical method.

---

[1] If the relation $E^2 = \vec{\mathbf{p}}^2 + m^2$ holds for the energy and momentum of a parton, it is often called a parton *on the mass shell*.

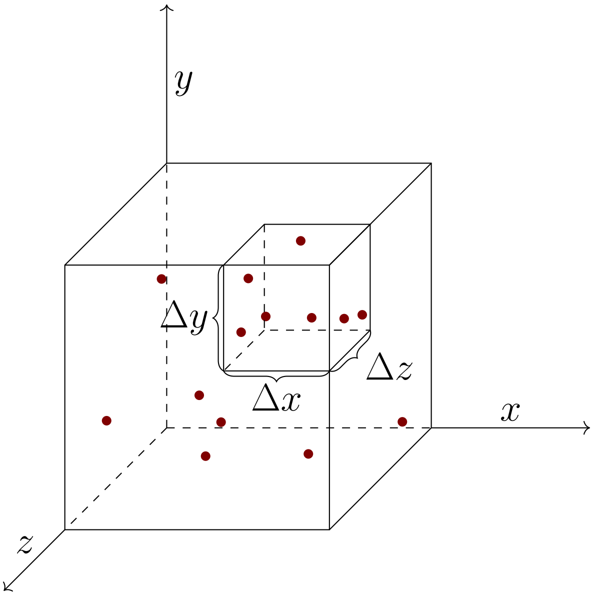

Figure 4.1: Sketch of the 3-dimensional cell grid employed for the discretization of phase space in the stochastic method within BAMPS. As an example, a grid in Cartesian space is chosen in which the cell volume is given by $\Delta^3 x = \Delta x \Delta y \Delta z$. Each point denotes a particle distributed in configuration space.

In all other regions, we apply the so called *stochastic method* for solving numerically the Boltzmann equation within the BAMPS framework [Xu04]. In this method individual parton scatterings are described by probabilities obtained from a discretization of the microscopic phase space distribution $f_i(\vec{\mathbf{x}}, \vec{\mathbf{p}})$. In order to preserve locality of the solution, individual particles are distributed based on their position $\vec{\mathbf{x}}$ in configuration space within an auxiliary cell grid with cell volumes $\Delta^3 x$ as sketched in Fig. 4.1. Depending on the specific physics problem, an appropriate geometry of the cell grid can be chosen. For example, the cell grid shown in Fig. 4.1 would be the natural choice for the calculation of a static brick of quark-gluon plasma, whereas for simulating the expanding bulk medium of a heavy-ion collision relativistic coordinates as the space-time rapidity $\eta_{\text{s}} = \log\left((t+z)/(t-z)\right)$ may be helpful. Furthermore, also the evolution time of the system is discretized into time steps Δt. During each time step, all partons from the same cell volume $\Delta^3 x$ may interact with each other. The probability for these interactions can be derived from a discretization of the collision terms $\mathcal{C}_i$ to [Xu04; XG05]

$$P_{2\to N} = v_{\text{rel}} \sigma_{2\to N} \frac{\Delta t}{\Delta^3 x} \tag{4.3}$$

for a 2 → 2 or 2 → 3 process, where $v_{\text{rel}} = s/2E_1E_2$ for massless partons and $\sigma_{2\to N}$ is the cross section of the microscopic process. Furthermore, this stochastic description of parton interactions within BAMPS can be applied straight-forwardly also to interactions of arbitrary many incoming partons. Hence, the probability for a $3 \to 2$ annihilation process can be derived to [XG05]

$$P_{3\to 2} = \frac{1}{8E_1E_2E_3} I_{32} \frac{\Delta t}{\left(\Delta^3 x\right)^2}\,, \tag{4.4}$$

where E_i is the energy of parton i and I_{32} is given by the phase space integral over the $3 \to 2$ matrix element as presented in Section 3.2.1.

At each time step and for each cell, the probabilities for every combination of partons within this cell are calculated and it is decided by Monte-Carlo techniques whether a particular scattering is realized[2]. If one samples that a scattering occurs, the outgoing parton momenta are determined based on the differential cross sections given in Chapter 3. To this end, the momentum transfer $\hat{t}$ of a $2 \to 2$ process or the momenta $k_\perp^2$ and $q_\perp^2$ of a $2 \to 3$ process are sampled via either a rejection or a metropolis sampling [Has70]. The specific time of the interaction is randomly distributed within Δt, whereas any newly produced parton from a $2 \to 3$ process is added with a random position within the given cell. The above outlined procedure for numerically solving the Boltzmann equation within BAMPS is summarized in Algorithm 2.

Algorithm 2: Schematic view of the BAMPS framework for solving the Boltzmann equation. Modified version based on Ref. [Foc11].

```
At time $t = 0$, initialize partons from distribution in configuration and momentum space
while $t < t_{final}$ do
    foreach cell $\Delta^3 x$ do
        foreach particle pair (triplet) in the given cell do
            Calculate cross section $\sigma$ and probability $P$
            Generate random number $r \in [0, 1)$
            if $r < P$ then
                Sample new momenta of outgoing partons from differential cross section
                Assign new momenta to outgoing partons
    $t = t + \Delta t$ ;
    Propagate particles to time $t$
```

Since one discretizes the phase space distribution for numerically solving Eq. (4.1) on page 37, sufficient statistics is crucial for reliably representing $f_i(\vec{\mathrm{x}}, \vec{\mathrm{p}}, t)$ in each cell. To this end, we artificially increase the number of physical particles $n \to n\, N_{\text{test}}$ by a constant scaling factor N_{test}. This method for enhancing the statistics in the stochastic method is commonly called *test-particles Ansatz* and the corresponding particles are then denoted as *test particles*. Test particles are indistinguishable from "physical" particles and hence are sampled from the same initial distribution for the specific problem at hand. Since an increased number of particles would also lead to an increased collision rate, the probability for a single scattering of test particles has to be decreased by $P_{2\to N} \to 1/N_{\text{test}} P_{2\to N}$ for $2 \to N$ interactions and by $P_{3\to 2} \to 1/{N_{\text{test}}}^2 P_{3\to 2}$ for $3 \to 2$ interactions [XG05]. This scaling of probabilities then ensures that the physical collision rate or mean free path is preserved while enhancing the statistics. Furthermore, it should be noted that the scaling factor N_{test} has to be appropriately considered for any observable measuring the absolute number of particles.

The presented BAMPS framework for solving the Boltzmann equation can be applied to different physical problems. To this end, the initial condition for solving the Boltzmann equation, or in other words the initial distribution of partons in configuration and momentum space, has to be chosen accordingly to the specific characteristics of the problem. For example, the simulations of jets traversing a static, partonic medium in Chapters 5 and 6

---

[2] Technically, one samples a random number $r \in [0; 1]$ and compares it with the probability P_i. If $r < P_i$ the scattering is realized.

are initialized by an energetic parton scattering with thermal partons by the introduced probabilities. The cell grid underlying the stochastic method is then chosen as a Cartesian brick. In contrast, for the simulation of the partonic phase of a heavy-ion collision at LHC presented in Chapter 7 the auxiliary cells are adapted to the collision geometry and are based on the space-time rapidity η_s in the longitudinal direction wrt. the beam axis (cf. Section 7.1.1). The momentum distribution of partons in the bulk medium of these collisions is obtained by the event generator PYTHIA. For a comprehensive overview about previous studies within the BAMPS framework we refer to the following section.

4.2 Selected results from the BAMPS framework

Within the present work, we apply the partonic transport approach BAMPS for simulating jet quenching both in a static brick of quark-gluon plasma and the expanding bulk medium of ultra-relativistic heavy-ion collisions at LHC. Besides these studies, BAMPS was and is applied also to other phenomena regarding the microscopic transport of partons:

- Historically, the BAMPS framework was first employed for studies regarding the thermalization and isotropization of gluonic matter. It could be shown in Refs. [XG05; XG07] that especially the parton number changing $2 \to 3$ and $3 \to 2$ processes within BAMPS lead to a fast equilibration of partons during the partonic phase of heavy-ion collisions at the Relativistic Heavy-Ion Collider (RHIC). These findings gave first evidence that microscopic interactions from perturbative chromodynamics are effective enough for achieving early equilibration times necessary for the applicability of hydrodynamics to the early phases of the medium evolution.

- Furthermore, comparisons between the measurements of the elliptic flow v_2 at RHIC (cf. Section 2.3.1) and ideal hydrodynamics suggested a small shear viscosity over entropy ratio η/s for the matter produced in $\sqrt{s_{\mathrm{NN}}} = 200\,\mathrm{GeV}$ Au + Au collisions at RHIC. In Ref. [XG08; XGS08] and later in [Wes+11; Uph+15] it was found that the pQCD processes within BAMPS also lead to a rather small η/s close to the lower limit $1/(4\pi)$ found in AdS/CFT (Anti-de Sitter/conformal field theory), which gave the first explanation for this medium property from purely microscopic interactions. The shear viscosity over entropy ratio in Ref. [Wes+11] was calculated based on the Green-Kubo formalism, which measures the shear viscosity by time correlations of the shear stress tensor in the long wave limit.

- Besides η/s also other medium properties of a quark-gluon plasma were studied within BAMPS. In Ref. [Gre+13] the heat conductivity of the partonic matter was calculated, whereas the electric conductivity due to the electric charge of quarks was determined in Ref. [Gre+14]. Both studies showed numerical values that agree with other calculations from, e.g., lattice QCD.

- Due to the possibility to simulate the expanding bulk medium within BAMPS, one of the major results within BAMPS was a significant built-up of elliptic flow v_2 during the partonic phase of ultra-relativistic heavy-ion collisions. Starting with calculations of v_2 for gluon matter [XGS08; XG09] at RHIC, flow observables were studied also for matter consisting of both quarks and gluons [FXG09; XG10] and within $\sqrt{s_{\mathrm{NN}}} = 2.76\,\mathrm{TeV}$ Pb + Pb collisions at the Large Hadron Collider (LHC) [Uph+15]. Both at RHIC and LHC large contributions to the finite elliptic flow measured by experiments originate from the microscopic interactions of partons. We further elaborate on these findings in Section 7.1.3, where we discuss the properties of the medium for the jet quenching studies of this work.

- One of the main assumptions within BAMPS is the applicability of perturbative quantum chromodynamics not only for the interactions of high energy partons but also for the interactions between partons within the bulk medium of heavy-ion collisions. Different to other models, this assumption allows to study jet quenching and flow phenomena based on the same microscopic framework. In Ref. [FXG09] first attempts were made in simultaneously describing the nuclear modification factor R_{AA} of charged hadrons at RHIC and LHC within BAMPS. By applying the small angle approximation for the $2 \to 2$ processes and the original Gunion-Bertsch approximation [GB82] for the inelastic $2 \leftrightarrow 3$ matrix elements, a too strong energy loss and thereby suppression of charged hadrons was found. In contrast, the improved Gunion-Bertsch matrix element [Foc+13] leads to a realistic suppression of charged hadrons at RHIC and LHC while still a significant built-up of v_2 during the partonic phase can be found [Uph+15]. For further results of the suppression of hadrons at LHC we refer to Section 7.3.

- One of the open questions concerning the medium modification of heavy quarks, charm and bottom quarks, within heavy-ion collisions is the role of elastic vs. radiative energy loss. Due to the finite mass of heavy quarks collinear gluon emissions off massive quarks are suppressed, which is commonly called the *dead cone effect*. After extending the previous elastic light parton interactions within BAMPS by massive matrix elements from pQCD, the production of charm and bottom quarks in heavy-ion collisions was studied in Ref. [Uph+10]. By applying the same framework as previously for the light flavor, a suppression and flow of heavy-flavor electrons decaying from heavy flavor quarks was observed at RHIC and LHC [Uph+11]. Due to the higher precision of the experiments at LHC, also observables regarding open heavy flavor mesons as, e.g., $\mathrm{D}^{\pm}$ or D^{0} became measurable. The suppression and flow of these mesons from (scaled) elastic interactions within BAMPS was studied in Refs. [Uph13]. The improved Gunion-Bertsch approximation could also be extended to the heavy flavor section, which allowed to study the influence of radiative processes on the heavy quarks [Uph+14]. Due to the interplay between the employed effective description of the Landau-Pomeranchuk-Migdal effect and the dead cone effect, the suppression of heavy flavor mesons was found to be similar to light hadrons. This finding explained the similar R_{AA} of inclusive charged hadrons and D-mesons at LHC. However, the flow of heavy quarks within BAMPS is significantly lower than the data and could not be explained by the microscopic pQCD interactions.

- Correspondingly to the processes from Chapter 3 also processes from quantum electrodynamics (QED) can be implemented into the BAMPS framework. Although the role of QED for energy loss phenomena of jets is negligible due to the small coupling strength α_{EM} in QED, this implementation allowed the study of photon production within the partonic phase of a heavy-ion collision [Gre+17b; Gre18]. By considering photon production processes from both binary $2 \to 2$ (Compton and annihilation processes) and Bremsstrahlung $2 \to 3$ interactions, a smaller yield of direct photons could be found from the non-equilibrium dynamics within BAMPS in comparison with other hydrodynamical models. Reason for this difference is the chemical under-saturation of quarks in the beginning of the heavy-ion collision.

- Finally, this work presents a comparison between different descriptions of the Landau-Pomeranchuk-Migdal effect for jet quenching of single inclusive hadrons and reconstructed jets. There were also previous studies of the medium modification of reconstructed jets within the BAMPS approach. The influence of multiple further scatterings of recoiled medium particles on the momentum asymmetry A_J of the leading jets was investigated in Ref. [Sen12; Sen+15]. It was found that after an appropriate background subtraction, mandatory in experimental studies, the momentum asymmetry is insensitive to the recoil of medium partons. In Ref. [Sen+17] the different energy loss behavior of light and heavy flavor partons was studied by the suppression and jet shapes of inclusive and b-tagged jets at LHC. B-tagged jets are jets that have a bottom quark or meson close to the reconstructed jet axis. Both scaled elastic as well as elastic with radiative heavy flavor interactions showed a realistic suppression of b-tagged jets at LHC. Furthermore, we proposed in Ref. [Sen+17] the jet shapes of b-tagged jets as a measure for discriminating different energy loss mechanisms of light and heavy flavor partons. For more details about the suppression of reconstructed jets and its underlying modification in terms of jet shapes we refer to Section 7.4.

This list should be understood as a condensed overview over the efforts from the last 15 years taken within the BAMPS framework to understand nuclear matter under extreme conditions. For more details about other topics including the formation of shock waves [Bou+10; Bou+12; Bou+14], the built-up of a magnetic field in the early phases of a heavy-ion collision [GGX17], initial state effects in $\mathrm{p} + \mathrm{A}$ collisions from partonic transport [Gre+17a], the momentum imbalance of D mesons [Uph+13], or the hadronization of partons via clustering algorithms[3], we refer to the given references. The possibilities offered by the microscopic interactions in transport approaches as BAMPS are enormous. Therefore we expect also for the future further studies of phenomena from non-equilibrium physics in the context of heavy-ion collisions.

---

[3] Paper to be published.

5 Landau-Pomeranchuk-Migdal effect in a transport approach

One of the main questions of this thesis is whether and how in-medium coherence effects of gluon emissions, especially the non-Abelian Landau-Pomeranchuk-Migdal (LPM) effect, can be faithfully described within a dynamical transport approach. To answer this question we have in this chapter a closer look on the LPM effect and investigate how to implement it into the BAMPS framework. After revising common state-of-the-art models for radiative energy loss and discussing the general dependencies of the LPM effect, we introduce three different approaches for modeling the LPM effect in a partonic transport approach and study their implications for the radiative energy loss within a brick of partonic matter. To this end we will calculate observables as the differential emission rates $\mathrm{d}\Gamma/\mathrm{d}\omega$ or the length-differential energy loss $\mathrm{d}E/\mathrm{d}x$ and discuss their energy and path-length dependence. Conclusively, we compare the three different approaches against each other and estimate possible consequences of the coherence effects for measurable observables in heavy-ion collisions.

5.1 What is the Landau-Pomeranchuk-Migdal effect?

5.1.1 A brief history of the radiative energy loss from pQCD

Recent theoretical and experimental studies point to the dominance of radiative processes for the energy loss of energetic, light partons in comparison to the energy loss originating from elastic $2 \to 2$ scatterings (see, e.g., Ref. [MV11]). While in an elastic scattering the high energy projectile can lose only a small amount of its energy to medium components, the emission of a single hard or many soft particles can contribute significantly to the energy loss of the parent parton. Therefore we revisit in this section the basic concepts of radiative energy loss in perturbative QCD. To this end we give a brief overview over the historic development of different state-of-the-art models for radiative energy loss and discuss their commonalities and differences. For further reading and a detailed access to the topic of radiative energy loss of partons we recommend some excellent review articles that were published recently [BSZ00; Gyu+03; Bas+09; Wie09; DEn09; MV11; Arm+12; MMT13; BM15; QW15].

We discussed in Section 3.2.1 how the gluon emission induced by a single scattering in a $2 \to 3$ process can be calculated from perturbative QCD via an improved version of the Gunion-Bertsch matrix element. Although the divergences were cured by introducing thermal masses for the internal propagator, the actual matrix elements within the Gunion-Bertsch approximation are formulated and derived within vacuum pQCD. However, if the emissions occur in the hot and dense environment of a quark-gluon plasma further effects have to be considered.

Due to the uncertainty principle quanta with discrete energy can only be localized over a finite region in space. Consequently, emission processes should not be treated as spontaneous but as extended over time. The time needed by the emitted photon (in QED)

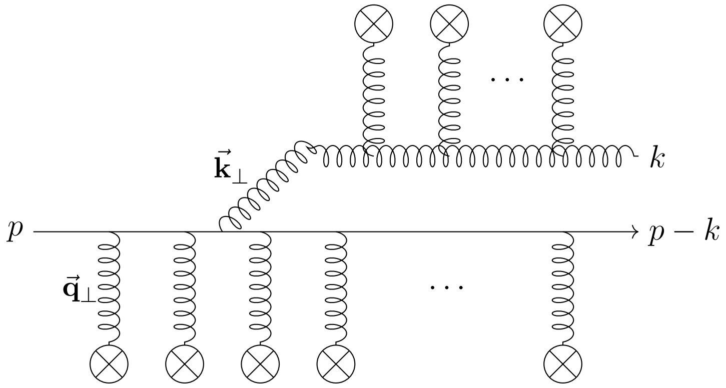

Figure 5.1: Typical diagram for a Bremsstrahlung process in a colored QCD medium. Crosses denote interactions with the surrounding partonic medium that have to be resummed via pQCD.

or gluon (in QCD) to decohere from the parent parton and form as an independent particle is called formation time and can be estimated by

$$\tau_f \sim \frac{\omega}{k_\perp^2} \tag{5.1}$$

where ω is the energy of the emitted particle and $k_\perp$ the transverse momentum wrt. the parent parton. The formation time of emissions can be significant, especially of energetic and collinear emissions. If the formation time of an emission becomes longer than the mean free path of scatterings by the parent-daughter system within the medium, the scatterings must not be described incoherently but the elastic scatterings contribute coherently to the initial emission process. Already in the 1950s Landau, Pomeranchuk and Migdal [LP53a; LP53b; Mig56] discovered this coherence effect and studied its consequences for Bremsstrahlung emissions of photons from energetic electrons traversing matter. Therefore this coherence effect, which was experimentally confirmed in measurements of the photon production rate from electrons traversing thin gold and carbon foils at SLAC[1] [Ant+95; Kle+94], is commonly coined "Landau-Pomeranchuk-Migdal" (LPM) effect or LPM suppression. It is called suppression because the overlapping elastic scatterings centers during the formation time may not act as a source for further 2 → 3 process since they interfere destructively with each other. Consequently, the probability for additional emission processes during the formation time is suppressed in contrast to the case without a medium.

Coherence effects are implicitly considered when calculating the Bremsstrahlung process in a pQCD environment via deriving the corresponding matrix elements from quantum field theory. To this end, all matrix elements leading to exactly one additional gluon in the final state have to be resummed. A diagram for such a calculation is schematically shown in Fig. 5.1. One of the first attempts undertaken to calculate the Bremsstrahlung process while considering the LPM effect in the context of perturbative QCD was in the 1990s by Baier et al. and independently Zakharov (BDMPS-Z) [Bai+95; Bai+96; Bai+97a; Bai+97b; Bai+98b; Zak96a; Zak96b; Zak97].

Due to the non Abelian nature of QCD the emitted gluons themselves may interact with the medium, which complicates a rigorous analytical calculation and different approximations needed to be introduced to solve the problem. Baier et al. [Bai+95] (and most of the models derived later) calculated the differential gluon emission spectrum off a high-energy

---

[1] <u>S</u>tanford <u>L</u>inear <u>A</u>ccelerator <u>C</u>enter

quark traversing a thermal medium in the limit

$$E \gg \omega \gg k_\perp, q_\perp \gg \Lambda_{\text{QCD}}\,, \tag{5.2}$$

where E is the energy of the emitting projectile, ω and $k_\perp$ the energy and transverse momentum of the emitted gluon wrt. the projectile and $q_\perp$ the momentum transfers from the medium to the parent-daughter pair. In this *eikonal* limit the projectile flies on straight lines, which means that both the energy and momentum of the emitting particle is approximately not modified. Furthermore, the scattering centers within the medium were treated as static [GW94] in this model and so they transfer only transverse momentum to the partons, $q^2 = q_\perp^2 + q_\parallel^2 \approx q_\perp^2$. This assumption neglects any collisional energy loss of the projectile. In Refs. [Bai+98a; Wie00a] it could be shown that the approach by Baier et al. coincides with an approach by Zakharov [Zak96a; Zak96b; Zak97], who formulated an independent, elegant approach for resumming the matrix elements based on a path-integral formulation. The resummation in this limit leads to the general formula for the emission spectrum induced by the medium [Arn09b; Arm+12][2]

$$\omega\frac{\mathrm{d}I}{\mathrm{d}\omega} = \frac{\alpha_s x P_{s\to g}(x)}{\left(x(1-x)E\right)^2}\times$$
$$\times\,\text{Re}\int_0^\infty \mathrm{d}t_1 \int_{t_1}^\infty \mathrm{d}t_2 \left[\nabla_{\vec{\mathbf{b}}_1}\cdot\nabla_{\vec{\mathbf{b}}_2}\left(G\left(\vec{\mathbf{b}}_2,t_2;\vec{\mathbf{b}}_1,t_1\right)\right)\right]\Big|_{\vec{\mathbf{b}}_1=\vec{\mathbf{b}}_2=0}\,, \tag{5.3}$$

where $\mathrm{d}I/\mathrm{d}\omega$ is the probability density for emitting a gluon with energy ω from a projectile with energy E, α_s is the QCD coupling and $x = \omega/E$ is the energy fraction of the gluon relative to the projectile. $P_{s\to g}(x)$ is the vacuum splitting function for a parton with flavor s to emit a gluon as derived in the DGLAP formalism [AP77; Dok77; GL72]. The internal variables t_1 and t_2 represent the longitudinal emission points in the amplitude and complex conjugate amplitude, whereas $\vec{\mathbf{b}}_1$ and $\vec{\mathbf{b}}_2$ denote transverse positions of projectile components in the amplitude and complex conjugate amplitude [Arn09b; ZKW13]. The Green's function $G\left(\vec{\mathbf{b}}_2,t_2;\vec{\mathbf{b}}_1,t_1\right)$ solves the time-dependent Hamiltonian of a two-dimensional Schrödinger equation [Arn09b; Arm+12]

$$H\left(\vec{\mathbf{p}}_b,\vec{\mathbf{b}},t\right) = \delta E(\vec{\mathbf{p}}_b,t) - i\Gamma_3\left(\vec{\mathbf{b}},t\right), \tag{5.4}$$

with initial condition $G\left(\vec{\mathbf{b}},t_1;\vec{\mathbf{b}}_1;t_1\right) = \delta^{(2)}\left(\vec{\mathbf{b}}-\vec{\mathbf{b}}_1\right)$. $\delta E(\vec{\mathbf{p}}_b,t)$ is the energy difference between the initial and final state and

$$\Gamma_3\left(\vec{\mathbf{b}},t\right) = \frac{1}{2}C_{\text{A}}\bar{\Gamma}_2\left(\vec{\mathbf{b}},t\right) + \left(C_s - \frac{1}{2}C_{\text{A}}\right)\bar{\Gamma}_2\left(x\vec{\mathbf{b}},t\right) + \frac{1}{2}C_{\text{A}}\bar{\Gamma}_2\left((1-x)\vec{\mathbf{b}},t\right) \tag{5.5}$$

denotes the three-body interaction rate [Arm+12] of the projectile-gluon system[3]. The

---

[2] Eq. (5.3) and the following equations are given in the notation of [Arn09b] that is slightly different to the original formulation of Zakharov. However, this formulation closely relates to the AMY formalism discussed later in Section 5.4. For the differences between both definitions we refer to Ref. [Arn09b], where also a detailed derivation of the presented formalism is given.

[3] C_s are again the QCD color factors, $C_{\text{F}} = \left(N_c^2-1\right)/(2N_c) = 4/3$ for a quark and $C_{\text{A}} = N_c = 3$ for a gluon [Arn09b].

individual scatterings are given by the Fourier transform of the elastic scattering rate

$$\bar{\Gamma}_2\left(\vec{\mathbf{b}},t\right) = \int \mathrm{d}^2 q_\perp \, \frac{\mathrm{d}\bar{\Gamma}_{\mathrm{el}}}{\mathrm{d}^2 q_\perp} \left(1 - \exp^{i\vec{\mathbf{b}}\cdot\vec{\mathbf{q}}}\right) . \tag{5.6}$$

For more details about the derivation of the formalism underlying Eqs. (5.3) to (5.6) we refer to Refs. [Arn09a; Arn09b; CS07].

In order to solve Eq. (5.3), further assumptions about the medium and its interactions with the projectile are necessary and need to be applied to $\bar{\Gamma}_2\left(\vec{\mathbf{b}},t\right)$. One of the possible assumptions were introduced in the original BDMPS-Z derivation by assuming that the interactions of the partonic system are numerous and soft during the formation time. This so called *multiple soft-scattering approximation* leads to

$$\bar{\Gamma}_2\left(\vec{\mathbf{b}},t\right) \approx \frac{1}{4}\bar{\hat{q}} b^2 \, , \tag{5.7}$$

where

$$\hat{q} = C_R \bar{\hat{q}} = C_R \int \mathrm{d}^2 q_\perp \, \frac{\mathrm{d}\bar{\Gamma}_{\mathrm{el}}}{\mathrm{d}^2 q_\perp} q_\perp^2 \tag{5.8}$$

is the transport parameter measuring the average transverse momentum transfer per unit path length from the medium to the projectile. In this approximation, Eq. (5.4) becomes the Hamiltonian of a harmonic oscillator that can be solved analytically. The resulting gluon emission spectrum in the BDMPS-Z formalism then simplifies to [Arn09b]

$$\omega \frac{\mathrm{d}I_{\mathrm{BDMPS}}}{\mathrm{d}\omega} = \alpha_s x P_{s\to g}(x) \log\left|\cos\left(\omega_0 L\right)\right| , \tag{5.9}$$

where L is the path-length of the projectile and ω_0 is a complex number given by [Arn09b]

$$\omega_0^2 = -i \frac{\left((1-x)C_{\mathrm{A}} + x^2 C_s\right)\hat{q}}{2x(1-x)E} \, . \tag{5.10}$$

Please note that in order to arrive at this result the $k_\perp$ distribution of gluon emissions was integrated up to infinity allowing arbitrary large emission angles [Cas+11].

As we discuss in the next section by heuristically deriving the signatures of the non-Abelian LPM effect, the BDMPS-Z emission spectrum results in a $\Delta E \sim \sqrt{E}$ [Bai+95] behavior and the famous non-linear path-length dependence of the radiative energy loss $\Delta E \sim L^2$ [Bai+97b] in pQCD.

Wiedemann [Wie00a; Wie01] extended the path-integral formulation by including vacuum and medium interference and thereby finite in-medium path length effects that result in an infrared cutoff in the emissions spectra [Wie09]. Furthermore, this calculation accounted for rescattering effects in the $k_\perp$-differential emission spectrum and introduced a finite $k_\perp$ integration [Wie09; Wie00b]. Later these findings were further analyzed for massless [SW03] and massive partons [ASW04] and ended up in the ASW formalism [SW02; SW03; ASW04] for gluon emissions [Wie09]. The multiple-soft scattering approximation as realized in ASW is denoted by “ASW-MS” [Arm+12] throughout this work and coincides with BDMPS-Z for an infinite medium length.

Another common limit for the medium interactions of Eq. (5.3) on the previous page is the *opacity expansion*, first studied by Gyulassy, Levai and Vitev (GLV) [GLV00b;

GLV00a; GLV01; Gyu+03] and later also by Wiedemann in the context of the ASW path-integral formalism [Wie00a; SW02; SW03; ASW04]. In this limit the elastic scattering rate, Eq. (5.6) on the facing page, is expanded order-by-order in the number of scatterings (opacity) $n_0\, L$, where n_0 is the density of scattering centers along the projectile path and L is the medium length. Most phenomenological models employing the opacity expansion cut off the expansion at the leading-order term in the expansion owing to a single hard scattering during the formation time [QW15]. This single hard scattering limit was also studied in the context of ASW [SW03] what we will denote as "ASW-SH" [Arm+12] throughout this work.

The previously introduced models for radiative energy loss all rely on the approximation of static scattering centers. The temperature of the thermal bath is only necessary for determining the mean free paths of the partons [Tur+05]. The first formulation of radiative energy loss while considering the medium components as dynamic, thermal scattering centers were developed by Arnold, Moore, and Yaffe (AMY) in the context of thermal field theory. We refer to Section 5.4 for a detailed discussion of the AMY formalism and how to use it in the context of a partonic transport approach.

Another independent approach for calculating the radiative energy loss a projectile suffers in the QGP is the *Higher-Twist* (HT) formalism first developed by Guo and Wang [GW00; WG01] and later extended by Majumder [Maj12; QM15]. In the HT formalism the medium is described by 4-point "higher twist" matrix elements considering vacuum and medium interference effects [Wie09]. For more details about the HT model we refer to Refs. [GW00; WG01; Maj12].

All previously introduced formulations for the radiative processes in QCD neglect interference effects of multiple, subsequent gluon emissions. Rather the emission spectrum of a high-energy projectile is obtained by independently repeating a single gluon emission. Therefore phenomenological studies related to ASW, GLV and BDMPS-Z mostly employ a Poissonian Ansatz for the emission of multiple gluons. The resulting energy loss of the projectile can then be characterized by *quenching weights* [Bai+01; SW03; QW15],

$$P(\Delta E) = \sum_{n=0}^{\infty} \frac{\exp^{-\langle N_g \rangle}}{n!} \left[\prod_{i=1}^{n} \int \mathrm{d}\omega_i \, \frac{\mathrm{d}N_g(\omega_i)}{\mathrm{d}\omega} \right] \delta\!\left(\Delta E - \sum_{i=1}^{n} \omega_i \right) , \tag{5.11}$$

where $\mathrm{d}N_g(\omega)/\mathrm{d}\omega$ is the single emission spectrum and $\langle N_g \rangle = \int_0^\infty \mathrm{d}\omega\, \mathrm{d}N_g(\omega)/\mathrm{d}\omega$ is the average number of gluons expected to be radiated. The quenching weights $P(\Delta E)$ give the probability for a parton with energy E to lose energy ΔE. We use these quenching weights in Section 5.5.3 for a comparison of the different LPM approaches that we will implement into the BAMPS framework. The other two models for radiative energy loss treat multiple gluon emissions differently: while the AMY rates are mostly used in the context of rate equations for evolving distribution functions, which we elaborate further in Section 5.4, phenomenological studies in the HT formalism modify the vacuum DGLAP evolution by considering vacuum radiation together with additional medium-induced radiation [GW00; WG01].

The validity of the assumption that subsequent gluon emissions are independent from each other and thereby do not interfere with each other is at least questionable. However, our knowledge about the coherence of different gluon emissions and its consequences for measurable observables is still limited and topic of ongoing research by the community. Most promising for investigating the interference and (de-)coherence of multiple gluon emissions is the so called *antenna problem* [MST11; CI11; MST12c; MST12b; MST12a;

MT13]. In the antenna problem the coherence or decoherence of gluon emissions is investigated in the context of a dipole that emits gluons. For more information about this approach we refer to Ref. [MMT13].

We have mentioned that, in order to find analytical formulations, different kinematic approximations are necessary in the presented various models of radiative energy loss. For example, the degradation of the energy of the projectile is neglected in the eikonal limit since one assumes by $\omega \ll E$ (cf. Eq. (5.2) on page 47) that the energy of a single gluon emission is much smaller than the energy of the projectile. This strongly simplifies the analytical derivation. However, strictly speaking this also violates energy and momentum conservation. A promising way to circumvent such limitations is the application of Monte-Carlo methods in the context of radiative energy loss. Such event generators simulate gluon emissions numerically both in configuration and momentum space. By calibrating the probability of a single gluon emission to the limit of the respective energy loss model, such Monte-Carlo models are clean representations of the analytical calculations. Among their benefits are the straight-forward consideration of energy and momentum conservation at every gluon emission. Moreover, they are not limited to calculations of leading parton or hadron energy loss but they can be formulated in a way that all partons are treated equally. This allows the simulation of the energy loss of a whole parton shower consisting of the leading parton together with its emitted gluons from both vacuum and medium-induced radiation forming a shower of partons. These parton showers, or hadron showers after hadronization, are measurable by modern heavy-ion experiments. Consequently, phenomenological studies of both the parton energy loss and the in-medium modification of their surrounding showers by means of pQCD energy loss become reachable.

Different approaches aim to simulate microscopically the radiative energy loss by Monte-Carlo methods:

- The model JEWEL [ZSW11; ZKW13; FZ14; Zap14; EZ16b; EZ16a; Ela17; MZ16] is based on the vacuum event generator PYTHIA [SMS06], but extends it by elastic scatterings with medium components as well as medium-induced gluon radiation. By analyzing different orders in the opacity expansion of Eq. (5.3) on page 47 and determining the crucial interference factors between coherent and incoherent gluon emissions, JEWEL was the first model that considered a stochastic implementation of the LPM effect by dynamically suppressing gluon emissions. It could be shown in Refs. [ZSW09; ZSW11; ZW12] that this approach indeed reproduces the parametric dependencies of the multiple soft scattering limit of BDMPS-Z. We will further discuss this method in Section 5.3 where we implement a stochastic treatment of LPM suppression for the radiative processes into the BAMPS framework. By employing a medium evolution from hydrodynamics, JEWEL is also able to simulate the jet evolution within heavy-ion collisions. The suppression and fragmentation of jets was, e.g., studied in Ref. [Lee16].

- The model Q-PYTHIA [ACS09] is also based on the event generator PYTHIA. However, medium-induced radiation is considered by effectively increasing the default probability for a vacuum splitting within PYTHIA by adding a contribution that is proportional to the emission spectrum calculated in the multiple soft-scattering approximation of BDMPS-Z and ASW.

- Another approach for modeling jet energy loss within PYTHIA is taken by YAJEM [Ren08; Ren09a; Ren09b] where the medium-induced radiation is considered literally by effectively increasing the virtuality of the partons due to a momentum broadening in the medium via $\hat{q}$.

- The Monte-Carlo approach MARTINI [JM05; Tur+05; SGJ09; SGQ09; You+11b; You+11a; You+12; You+13; Par15; Par+16; PJG18] numerically simulates the AMY rate equation given in Section 5.4 for single gluon emissions. This closely reproduces the emission spectrum and energy loss as given in the AMY formalism and can be applied to the hydrodynamically evolving background of a heavy-ion collision [SJG10b; SJG10a; STV12b; SJG12; Gal+13]. For more information and a comparison of the AMY formalism within BAMPS to the MARTINI model we refer to Section 5.4.
- Two Monte-Carlo models that employ the Higher-Twist formalism for gluon radiation are MATTER [Maj13] and LBT (*Linearized Boltzmann-Transport*) [Li+11; WZ13; He+15]. While MATTER simulates jet events by a Sudakov factor similar to the previous event generators, the LBT model solves a linearized Boltzmann equation by HTL-inspired elastic scatterings together with HT radiative processes.
- The model LIDO [KXB18a; KXB18b] combines a Langevin treatment of soft momentum transfers with the linearized Boltzmann equation of LBT for the large angle scatterings. Recently radiative processes were implemented into LIDO by gluon radiation calculated in the improved GB approximation (s. Section 3.2.1) together with a stochastic treatment of LPM suppression. This approach is similar to our efforts presented in the following sections. However, our approach has the advantage that we can employ a microscopic description for the expanding medium of an ultra-relativistic heavy-ion collision, while LIDO is at the moment limited to a hydrodynamical background. However, the consideration of soft momentum transfers from HTL-type equations may represent a crucial advantage of LIDO. As we have seen previously in Chapter 3 and we will see in the following the elastic interactions within BAMPS are Debye-screened to circumvent the divergence at soft momentum transfers. Consequently, at large momentum transfers the descriptions may coincides while at smaller momentum transfers significant difference will occur.
- Finally, a combined effort between different models was formed recently by the JETSCAPE collaboration [JET+17]. This collaboration aims to apply different models in their respective limits to the problem of radiative energy loss and build thereby a multistage model of jet modification. While MATTER is used for the high virtuality DGLAP evolution, MARTINI and LBT model describe partons closely on the mass shell and thereby are applied for the low virtuality evolution. Furthermore, MARTINI relies on the assumption of AMY that one can define a hierarchy in scales and is therefore only applicable for momenta well above T. This assumption is not present in LBT which can therefore also be applied to the soft momentum scale of the jet evolution.

All of these models have their different advantages and limits of applicability. For a complete overview and further details of the models we refer to Refs. [QW15; Apo+18; JET+17].

In this work we extend the presented set of models capable for simulating jet energy loss closely related to analytical models for the radiative energy loss from pQCD by the partonic transport approach BAMPS. After heuristically deriving the non-Abelian LPM effect in the next section, we will implement different models for the LPM effect and the radiative processes from QCD into BAMPS. This will allows us to investigate potential differences of the different approaches and see what are the consequences for the jet energy loss within heavy-ion collision that we will study subsequently in Chapter 7.

5.1.2 Heuristic derivation of the LPM effect

Following the discussion of the previous subsection we derive in this section heuristically the most important characteristics of the non-Abelian LPM effect. To this end, we revise in the following the argumentation of Refs. [Bai+97b; BSZ00]. This argumentation is supposed to depict the formal arguments derived in the BDMPS-Z framework while neglecting factors of $\mathcal{O}(1)$ but keeping the relevant characteristics of the coherent emissions pattern [BSZ00].

Let us assume a projectile parton with high energy E that traverses a medium with length L. While traversing the medium, the projectile may scatter with medium components with a rate Γ or mean free path $\lambda \sim \Gamma^{-1}$, respectively. Assuming static scattering centers, these scatterings transfer a mean transverse momentum $q_\perp$ from the medium to the projectile while the energy of the projectile is unchanged. Due to the momentum transfers the projectile increases its virtuality and thereby may induce gluon radiation as, e.g., via the Bremsstrahlung processes as discussed in Section 3.2.1. Consequently the projectile emits a gluon with energy ω and transverse momentum $k_\perp$ with respect to the projectile direction. Since we assume $E \gg \omega, k_\perp$, the resulting energy and momentum change of the projectile can be neglected and we consider the projectile as eikonal, meaning that the projectile flies unmodified after a gluon emission.

One of the fundamental findings of quantum mechanics is that two canonically conjugate variables, as, e.g., position and momentum or energy and time, can only be measured simultaneously with a finite precision. When considering a Bremsstrahlung process it follows that the momentum of the emitted parton can only be precisely determined if the emission is not considered instantaneously but if it is extended over a finite time. This time is called coherence time oder formation time τ_f. In other words, during the coherence time the gluon and its emitting parton cannot be distinguished yet but have to be considered as the same particle. Formally this coherence effect stems from phase factors that are implicitly included in the path-integral formalism mentioned in Section 5.1.1.

Following the uncertainty relation the formation time (or coherence time) of the emitted gluon is

$$\tau_f = \frac{1}{k_\perp^{\text{rest}}} = \frac{\omega}{k_\perp^2} \,, \tag{5.12}$$

where $k_\perp^{\text{rest}}$ is the transverse momentum of the gluon with respect to the initial direction of the mother parton in the gluon rest frame and ω and $k_\perp$ are the gluon energy and transverse momentum boosted with $\gamma \sim \omega/k_\perp$ to the lab frame. At fixed gluon energy ω the more initial transverse momentum is given to the gluon, the quicker the gluon decoheres from the mother parton and thereby the smaller the formation time. On the other hand, more collinear gluons may stay in coherence with their parent partons for a formation time longer than the mean free path between two scatterings. This effect is the actual Landau-Pomeranchuk-Migdal (LPM) [LP53b; Mig56] effect and leads to the necessity to not only deal with incoherent and thereby independent emissions but also consider the coherence between different scattering centers for the resulting emission pattern.

The LPM effect in QED and QCD differs mainly by the emitted quanta and its possibilities to interact with the surrounding medium. An emitted photon of a QED Bremsstrahlung process has a negligible cross section with the surrounding medium. Therefore its formation time is mainly determined by the initial emission process. In contrast, the emitted gluon in the non-Abelian QCD case may interact with the medium. Consequently its transverse momentum is not fixed by the initial emission process but can be modified by scatterings with the medium during the formation time. These scatterings result in a random walk of the emitted gluon undergoing a Brownian motion in the transverse space. Therefore the mean transverse momentum of the gluon after N_{scatt} scatterings or traveling a distance $l = N_{\text{scatt}}\lambda$ within the medium can be determined as

$$\langle k_\perp^2 \rangle \sim q_\perp^2 N_{\text{scatt}} \sim \frac{q_\perp^2}{\lambda} l \sim \hat{q}\, l \,, \tag{5.13}$$

where we defined the transport coefficient $\hat{q}$ that quantifies the transverse momentum broadening per unit path length (cf. Eq. (5.8) on page 48). As a remark, although the definition of $\hat{q}$ is straight-forward in this heuristic derivation, a similar ad-hoc definition in the case of momentum transfers with a high-$q_\perp$ tail is more demanding.

The mean transverse momentum a gluon may gain due to the scatterings during its formation time is

$$\langle k_\perp^2 \rangle \big|_{\tau_f} \sim \frac{q_\perp^2}{\lambda} \tau_f \sim \hat{q}\, \tau_f \,. \tag{5.14}$$

This modified transverse momentum should be also taken into account when calculating the formation time. Consequently the formation time of the gluon is now determined self-consistently and reads

$$\tau_f \sim \frac{\omega}{\langle k_\perp^2 \rangle} \sim \frac{\omega}{\hat{q}\tau_f} \quad \rightarrow \quad \tau_f \sim \sqrt{\frac{\omega}{\hat{q}}} \,. \tag{5.15}$$

Since $q_\perp^2$ and λ as well as $\hat{q}$ are properties of the surrounding medium, any difference in the formation time of different gluon emissions is determined solely by the energy of the gluon. Gluons with higher energy ω need more time to decohere from the parent projectile than gluons with smaller energies. This is a first hint that the LPM effect is an effect mainly affecting gluon emissions with larger energies.

Before discussing the coherence and incoherence of gluon emissions we should discuss the basic building block of gluon radiation: the single gluon emission without any coherence effect. The actual single gluon emission can be described by the already discussed $2 \rightarrow 3$ Bremsstrahlung process in the Gunion-Bertsch approximation (s. Section 3.2.1). As a reminder, in this approximation the Bremsstrahlung process consists of a gluon emission that is induced by an elastic scattering within the medium. If we assume $E \gg \omega$ (*soft ω-limit*) [BSZ00] and use the original approximation of Gunion and Bertsch [GB82] it can be shown that the gluon energy spectrum of a single medium-induced gluon radiation goes like

$$\left.\frac{\mathrm{d}I}{\mathrm{d}\omega}\right|_{\text{GB}} \sim \frac{1}{\omega} \,. \tag{5.16}$$

$\mathrm{d}I/\mathrm{d}\omega$ should be understood as the probability distribution for the gluon energy ω in a single emission.

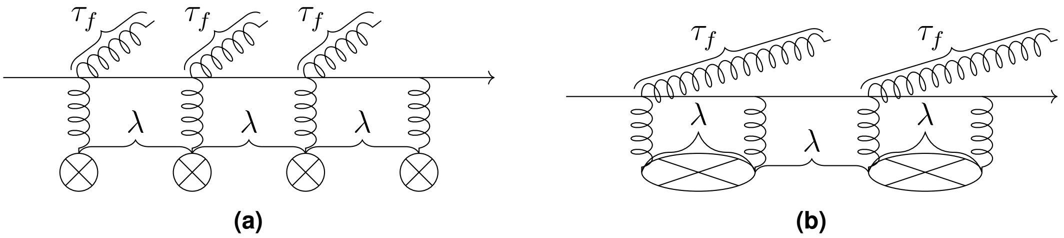

Figure 5.2: Sketch of (a) incoherent and (b) coherent gluon emissions. In the incoherent case, the formation time τ_f is shorter than the mean free path λ between successive scattering centers and the emissions are formed before the next scattering centers. In the coherent case, τ_f is longer than λ and the elastic scattering centers contribute coherently to the gluon production.

Since single gluon emissions are induced by a scattering with the medium, the maximum rate or minimum mean free path for a radiative process is given by λ. For incoherent gluon emissions, meaning gluon emissions resulting from independent scattering centers, the formation time τ_f has to be smaller than the mean free path λ between successive scatterings as depicted in Fig. 5.2a. With Eq. (5.15) it follows that this demands

$$\tau_f \sim \sqrt{\frac{\omega}{\hat{q}}} < \lambda \,, \tag{5.17}$$

which is equivalent to

$$\omega < \omega_{\mathrm{BH}} := q_\perp^2 \lambda = \hat{q}\lambda^2 \,. \tag{5.18}$$

Gluon emissions with energy smaller than the energy scale ω_{BH} are incoherently produced since they decohere from their parent parton before the next scattering center can be reached. The regime of independent gluon emissions is commonly called *Bethe-Heitler* [BH34] limit of gluon emissions. For the differential emission rate in the Bethe-Heitler limit for gluons with $\omega < \omega_{\mathrm{BH}}$ in a medium with length L it follows [BSZ00]

$$\left.\frac{\mathrm{d}\Gamma}{\mathrm{d}\omega}\right|_{\mathrm{BH}} \sim \frac{1}{L}\left.\frac{\mathrm{d}N}{\mathrm{d}\omega}\right|_{L} \sim \frac{1}{L}\frac{L}{\lambda}\left.\frac{\mathrm{d}I}{\mathrm{d}\omega}\right|_{\mathrm{GB}} \sim \frac{1}{\lambda}\frac{1}{\omega} \,, \tag{5.19}$$

where we used that $N_{\mathrm{incoh}} = L/\lambda$ gluons are emitted.

On the contrary, if the formation time of the gluon is larger than the mean free path to the next scattering center, coherence effects have to be taken into account as shown in Fig. 5.2b. For gluon energies $\omega > \omega_{\mathrm{BH}}$, the length scale determining the rate of gluon radiation is no longer the mean free path λ, but the formation time τ_f. All scattering centers during one formation time act coherently with each other and thereby suppress additional gluon emissions. Therefore it follows that exactly one gluon is formed during one formation time. This limit is called *LPM limit* of gluon emissions. For emissions in the LPM limit $\omega > \omega_{\mathrm{BH}}$ it follows

$$\left.\frac{\mathrm{d}\Gamma}{\mathrm{d}\omega}\right|_{\mathrm{LPM}} \sim \frac{1}{L}\left.\frac{\mathrm{d}N}{\mathrm{d}\omega}\right|_{L} \sim \frac{1}{L}\frac{L}{\tau_f}\left.\frac{\mathrm{d}I}{\mathrm{d}\omega}\right|_{\mathrm{GB}} \sim \sqrt{\frac{q_\perp^2}{\lambda\omega}}\frac{1}{\omega} \sim \frac{1}{\lambda}\sqrt{\frac{\omega_{\mathrm{BH}}}{\omega^3}} \,. \tag{5.20}$$

Since $\omega > \omega_{\mathrm{BH}}$, gluon emissions in the LPM limit are suppressed by $\sim 1/\sqrt{\omega}$ due to the coherence between subsequent scatterings.

What happens if the emission is so collinear that the medium interactions are insufficient for the gluon to decohere the gluon from its parent? This holds if the formation time is longer than the medium length L and the corresponding limit is called *factorization limit*. It is realized for gluon energies $\omega > \omega_{\text{fact}}$, where ω_{fact} is defined via

$$\tau_f > L \qquad \leftrightarrow \qquad \omega > \omega_{\text{fact}} := \frac{q_\perp^2}{\lambda} L^2 = \hat{q} L^2 \,. \tag{5.21}$$

These emissions can only be realized if the whole medium act as a single coherent scattering center. It follows that at maximum one gluon is emitted and the emission rate then reads

$$\left.\frac{\mathrm{d}\Gamma}{\mathrm{d}\omega}\right|_{\text{fact}} \sim \frac{1}{L} \left.\frac{\mathrm{d}N}{\mathrm{d}\omega}\right|_{L} \sim \frac{1}{L} \left.\frac{\mathrm{d}I}{\mathrm{d}\omega}\right|_{\text{GB}} \sim \frac{1}{L}\frac{1}{\omega} \,. \tag{5.22}$$

After discussing the differences between a coherent and an incoherent emission pattern we will discuss in the following the consequences of these differences for the resulting radiative energy loss. The differential radiative energy loss per unit path length is the first moment of the differential gluon emission rate and can be written as

$$\begin{aligned} \frac{\mathrm{d}E}{\mathrm{d}x} &= \int \mathrm{d}\omega\, \omega \frac{\mathrm{d}\Gamma}{\mathrm{d}\omega} \\ &\sim \int_0^{\omega_{\text{BH}}} \mathrm{d}\omega\, \omega \left.\frac{\mathrm{d}\Gamma}{\mathrm{d}\omega}\right|_{\text{BH}} + \int_{\omega_{\text{BH}}}^{\omega_{\text{fact}}} \mathrm{d}\omega\, \omega \left.\frac{\mathrm{d}\Gamma}{\mathrm{d}\omega}\right|_{\text{LPM}} + \int_{\omega_{\text{fact}}}^{E} \mathrm{d}\omega\, \omega \left.\frac{\mathrm{d}\Gamma}{\mathrm{d}\omega}\right|_{\text{fact}} , \end{aligned} \tag{5.23}$$

where we built the total differential emission rate from the different limits discussed above.

Before discussing the resulting radiative energy loss, one has to differ between different regions of medium lengths L. If the medium length L is large and the medium is thick, there will be no factorization region in which the whole medium can act as a single scattering center. This holds if $\omega_{\text{fact}} > E$, which is equivalent to

$$L > L_c := \sqrt{\frac{E}{\hat{q}}} \,. \tag{5.24}$$

Therefore, for media with length $L > L_c$ the resulting differential energy loss reads

$$\left.\frac{\mathrm{d}E}{\mathrm{d}x}\right|_{L>L_c} \sim \int_0^{\omega_{\text{BH}}} \mathrm{d}\omega\, \omega \left.\frac{\mathrm{d}\Gamma}{\mathrm{d}\omega}\right|_{\text{BH}} + \int_{\omega_{\text{BH}}}^{E} \mathrm{d}\omega\, \omega \left.\frac{\mathrm{d}\Gamma}{\mathrm{d}\omega}\right|_{\text{LPM}} \tag{5.25}$$

$$\sim \int_0^{\omega_{\text{BH}}} \mathrm{d}\omega\, \frac{1}{\lambda} + \int_{\omega_{\text{BH}}}^{E} \mathrm{d}\omega\, \frac{1}{\lambda}\frac{\omega_{\text{BH}}}{\omega} \tag{5.26}$$

$$\sim \frac{\omega_{\text{BH}}}{\lambda} + 2\frac{\sqrt{\omega_{\text{BH}}}}{\lambda}\left(\sqrt{E} - \sqrt{\omega_{\text{BH}}}\right) \tag{5.27}$$

$$\sim \sqrt{\hat{q}E} \,. \tag{5.28}$$

This $\sim \sqrt{E}$ behavior of the radiative energy loss was one of the first surprising results concerning the non-Abelian LPM effect [Bai+95]. Furthermore, the differential radiative energy loss in thick media $L > L_c$ does not depend on the medium length and thereby the total radiative energy loss goes like $\Delta E \sim L$.

If the medium is thin enough that $L < L_c$, there is a region in which the medium acts totally coherently. Therefore for the radiative energy loss follows

$$\left.\frac{\mathrm{d}E}{\mathrm{d}x}\right|_{L<L_c} \sim \int\limits_0^{\omega_{\mathrm{BH}}} \mathrm{d}\omega\, \omega \left.\frac{\mathrm{d}\Gamma}{\mathrm{d}\omega}\right|_{\mathrm{BH}} + \int\limits_{\omega_{\mathrm{BH}}}^{\omega_{\mathrm{fact}}} \mathrm{d}\omega\, \omega \left.\frac{\mathrm{d}\Gamma}{\mathrm{d}\omega}\right|_{\mathrm{LPM}} + \int\limits_{\omega_{\mathrm{fact}}}^{E} \mathrm{d}\omega\, \omega \left.\frac{\mathrm{d}\Gamma}{\mathrm{d}\omega}\right|_{\mathrm{fact}} \tag{5.29}$$

$$\approx \frac{\omega_{\mathrm{BH}}}{\lambda} + \int\limits_{\omega_{\mathrm{BH}}}^{\omega_{\mathrm{fact}}} \mathrm{d}\omega\, \frac{1}{\lambda} \frac{\omega_{\mathrm{BH}}}{\omega}\,, \tag{5.30}$$

where we neglected the constant factorization contribution $\int_{\omega_{\mathrm{fact}}}^{E} \mathrm{d}\omega\, \omega\ \mathrm{d}\Gamma/\mathrm{d}\omega|_{\mathrm{fact}}$ of the radiative energy loss. The remaining integration then evaluates to

$$\left.\frac{\mathrm{d}E}{\mathrm{d}x}\right|_{L<L_c} \sim \frac{\omega_{\mathrm{BH}}}{\lambda} + 2\frac{\sqrt{\omega_{\mathrm{BH}}}}{\lambda} \left(\sqrt{\omega_{\mathrm{fact}}} - \sqrt{\omega_{\mathrm{BH}}}\right) \tag{5.31}$$

$$\sim \hat{q}\, L\,. \tag{5.32}$$

Different to the case of a thick medium, the radiative energy loss in a thin medium does not explicitly depend on the energy of the parent parton. Furthermore, due to the finite formation time of gluon emissions, the differential radiative energy loss in a thin medium now depends on the medium length. Consequently, the total radiative energy loss in a medium with length L scales like $\Delta E \sim L^2$.

In this section we derived heuristically the main signatures of the non-Abelian LPM effect. Due to finite formation time effects large gluon energies are suppressed in comparison to smaller gluon energies that are realized in the incoherent case. This suppression leads to a radiative energy loss that is quadratical in thin media, while in thicker media the energy loss is linear since several coherent scattering systems now interact incoherently for themselves [ZKW13]. In the following we present three different approaches to model the LPM effect in partonic transport and investigate how reliable the approaches reproduce the presented parametric dependencies of the LPM effect.

5.2 Parametric LPM suppression (θ-LPM)

As we have seen in the previous section the Landau-Pomeranchuk-Migdal effect is an effect that originates from the non-local nature of gluon emissions. Due to the finite formation time, gluon emissions can extend over several mean free paths within the medium. However, this non-local gluon emissions complicate a treatment within transport theory, where interactions like scatterings are assumed to be local [KXB18b]. Therefore the way the LPM effect was considered previously within the partonic transport approach BAMPS was to parametrically suppress coherent gluon emissions via a suppression factor in the radiative matrix elements. We will call this approach the θ-LPM method throughout this work. In this section we revise this approach and investigate possible signatures of this parametric Ansatz for the LPM effect. To this end we first revise the previous implementation as presented in Refs. [FXG10; Foc11; Uph+12] by investigating the gluon emission pattern and the corresponding radiative energy loss. After that we aim to reintroduce more “coherence” into the gluon emissions by introducing the fudge factor X_{LPM}. This will effectively allow more collinear gluon emissions that contribute to the energy loss.

5.2.1 Modeling the incoherent limit of the LPM effect

The first attempt to implement the LPM effect into the BAMPS approach was to forbid gluon emissions that are potentially coherent and thereby only allow incoherent gluon emissions. This is most easily achieved by ensuring that the formation time τ_f of a gluon emission is smaller than the mean free path (MFP) λ of the projectile parton. To this end we introduce a Heaviside theta function in the $2 \to 3$ matrix elements that we derived in Section 3.2.1:

$$\left|\mathcal{M}_{23}\right|^2 \to \left|\mathcal{M}_{23}\right|^2 \Theta\left(\lambda - \tau_f\right) \ . \tag{5.33}$$

Choosing the mean free path of the projectile instead of the mean free path of the emitted gluon corresponds in principle rather to the QED case of the LPM effect and not the QCD case where the gluon may interact for itself [Uph13; Gre18]. When we discuss a stochastic approach to the LPM effect in Section 5.3 we will see how the choice of the mean free path of the gluon, which is additionally evaluated dynamically, alters the emission pattern.

The modified radiative matrix element is then employed for calculating both the differential cross section and the total cross section. Therefore the calculation of the cross sections depends via the theta function on the mean free path. At the same time the cross section also determines the mean free path of the projectile parton. Hence an iterative procedure has to be applied for the calculation of the mean free path [Uph13],

$$\lambda = \lim_{i\to\infty} \lambda_i = \lim_{i\to\infty} \frac{1}{R_{22} + R_{23}\left(\lambda_{i-1}\right) + R_{32}\left(\lambda_{i-1}\right)} \ . \tag{5.34}$$

R_n are the rates for the different possible processes within BAMPS, elastic $2 \to 2$ scatterings and inelastic $2 \to 3$ radiative and $3 \to 2$ annihilation processes. Since the contribution of annihilation processes to the rate of high-energy jets is minor and at the same time the computational effort for these processes is significant, we neglect the annihilation rate for iteratively calculating the mean free path throughout this work (cf. Section 3.2).

Another important point to discuss for the implementation of θ-LPM is the choice of reference frames [Foc11; Uph13]. The mean free path λ is defined in the local rest frame Σ_{cell} of the cell in which the scattering is evaluated, whereas the actual inelastic scattering has to be considered in the center-of-momentum (CoM) frame Σ_{CoM} of the scattering. Moreover, the formation time of the gluon is defined in the frame Σ_{trans}, where the gluon momentum is completely transverse to the direction of the projectile parton. Therefore the mean free path has to be first boosted from Σ_{cell} to Σ_{CoM} to Σ_{trans} before it can be compared to the formation time of the gluon. With the rules for adding Lorentz boosts the total boost for the mean free path then reads[Foc11; Uph13]

$$\gamma = \gamma_{\text{CoM}}\gamma_{\text{trans}}\left(1 + \vec{\beta}_{\text{CoM}} \cdot \vec{\beta}_{\text{trans}}\right) = \frac{\cosh y}{\sqrt{1-\beta_{\text{CoM}}^2}}\left(1 + \beta_{\text{CoM}} \cos\theta \left|\tanh y\right|\right) \ , \tag{5.35}$$

where we used the definition of $\gamma = 1/\sqrt{1-\beta^2}$. The boost from Σ_{CMS} to Σ_{trans} is along the z-axis in the center-of-momentum frame and can therefore be related to the gluon rapidity y in the CoM frame, $\gamma_{\mathrm{trans}} = \cosh y$ and $\beta_{\mathrm{trans}} = |\tanh y|$. The angle between the boost velocities $\vec{\beta}_{\mathrm{CoM}}$ and $\vec{\beta}_{\mathrm{trans}}$ is denoted as θ.

Consequently, the argument of the theta function can be written as

$$\begin{aligned}\theta\left(\lambda - \tau_f\right) &= \theta\left(\frac{\lambda}{\gamma} - \tau_f\right) \\ &= \theta\left(k_\perp - \frac{\cosh y}{\lambda\sqrt{1-\beta_{\mathrm{CoM}}^2}}\left(1 + \beta_{\mathrm{CoM}}\cos\theta\,|\tanh y|\right)\right) ,\end{aligned} \tag{5.36}$$

where we used ${\tau_f}^{\mathrm{trans}} = 1/k_\perp$ in the frame where the gluon is transverse.

Before we present numerical results concerning the θ-LPM method we would like to point out one of the major drawbacks of this approach. Although the theta function in the radiative matrix elements modifies both the differential and total rate of the $2 \leftrightarrow 3$ processes, it does not consider any additional path-length dependence. The gluon emissions are independent from each other and the finite formation time is only considered in determining the rate and the energy of the gluon emissions. Every gluon emission is still considered as localized at one time step. Consequently, the resulting radiative energy loss will be linear and thereby represents strictly only the case of a thick medium $L > L_c$ as discussed in Section 5.1.2. Without explicitly considering the finite formation time of the gluon the reproduction of the thin medium case will not be possible.

This modified matrix element consisting of the improved Gunion-Bertsch matrix element together with the θ function is the previous default way for implementing the LPM effect within BAMPS. In the following we will discuss the constraints that follow from the introduced theta function for the phase space of gluon emissions.

Kinematical limits for gluon emissions from the incoherent θ-LPM approach

As we discussed when evaluating the total cross section in Section 3.2.1 the phase space for a radiative $2 \to 3$ process is firstly constrained by kinematics. Since the energy of the gluon is limited by the CoM energy $\sqrt{\hat{s}}/2$ available in the individual collision, the maximum transverse momentum $k_\perp$ of the gluon is

$$k_\perp < k_\perp^{\mathrm{max}} := \frac{\sqrt{\hat{s}}}{2\cosh y} . \tag{5.37}$$

On the other hand, the theta function of Eq. (5.36) additionally constrains the phase space. Due to the requirement of independent gluon emissions, there is a minimum $k_\perp$ under which gluon emissions are rejected. This effectively cures the divergence of $k_\perp$ in the Gunion-Bertsch matrix element. Defining $A = \beta_{\mathrm{CoM}}\cos\theta$ and $B = \lambda\sqrt{1-\beta_{\mathrm{CoM}}^2}$, the theta function leads to the condition

$$k_\perp > k_\perp^{\mathrm{min}} := \frac{\cosh y + A\sinh y}{B} \tag{5.38}$$

for the transverse momentum in the CoM frame. Combining both constraints leads to the available phase space for gluon emissions [FXG10; Uph+12]. Apparently, the allowed

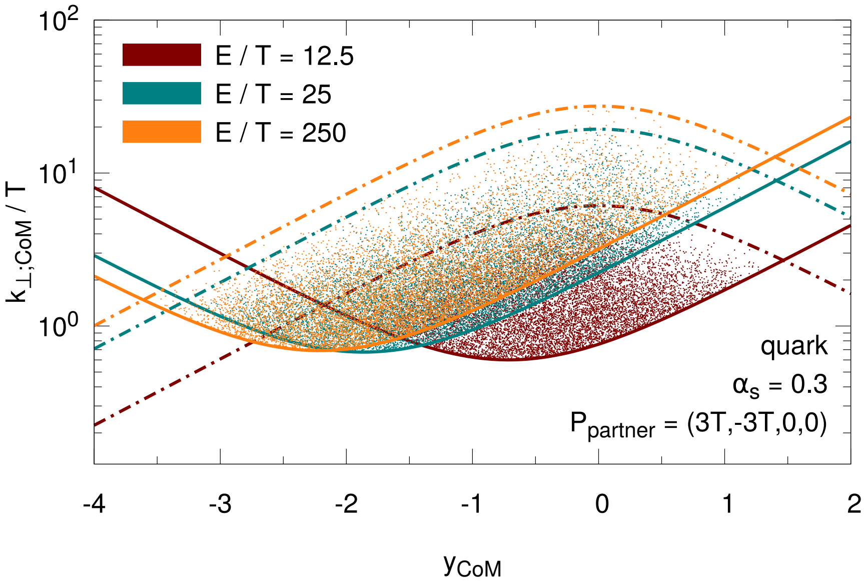

Figure 5.3: Phase space distribution of gluon emissions in the y_{CoM}-$k_{\perp;\text{CoM}}$ plane from the θ-LPM approach for a quark projectile with different energies $E = \{12.5\,\text{T}; 25\,\text{T}; 250\,\text{T}\}$ scattering with parton with fixed “thermal” momentum $p_{\text{partner}} = (3\,\text{T}, -3\,\text{T}, 0, 0)$ and a fixed QCD coupling $\alpha_s = 0.3$. Each dot represents a single gluon emission. While the solid lines depicts the limit imposed by the θ-LPM method, the dash-dotted lines show the kinematical limit for the different projectile energies.

phase space is enclosed by the two functions

$$f_{\max}(y) = \frac{\sqrt{\hat{s}}}{2\cosh y} \quad \text{and} \quad f_{\min}(y) = \frac{\cosh y + A \sinh y}{B} \,. \tag{5.39}$$

The overall maximum allowed rapidity range independent from $k_\perp$ can be obtained by the intersection points of the two functions and is given by [Foc11; Uph13]

$$y_{\text{left/right}} = \frac{1}{2} \ln \frac{b \mp \sqrt{\Delta}}{2a} \tag{5.40}$$

with $a = 1 + A$, $b = 2 - 2B$, $c = 1 - A$, and $\Delta = b^2 - 4ac$. For emissions where the argument of the square root Δ is negative, no phase space is available and no solution exists. On the other hand, if $b \mp \sqrt{\Delta}/2a$ is negative the rapidity range is not limited and $y_{\text{left/right}} = \mp\infty$.

Figure 5.3 shows the y-$k_\perp$-phase space of gluon emissions induced by $2 \rightarrow 3$ processes in the improved Gunion-Bertsch approximation of a quark flying in x-direction with energies $E = \{12.5\,\text{T}; 25\,\text{T}; 250\,\text{T}\}$ and a thermal particle within a medium with temperature T. The QCD coupling is fixed to $\alpha_s = 0.3$ as it is done throughout the whole section. To simplify things, the momentum of the thermal scattering partner is fixed by $p_{\text{partner}} = (3\,\text{T}, -3\,\text{T}, 0, 0)$. Both the rapidity y_{CoM} and the transverse momentum of the gluons $k_{\perp;\text{CoM}}$ are evaluated in the center-of-momentum frame of the respective inelastic scattering. Each dot represents a single gluon emission. The dashed-dotted lines depict the kinematical limit for the phase space as given in Eq. (5.37) on the facing page. Obviously with higher projectile energy also the phase space for gluon emissions opens up and higher transverse momenta are reachable. Furthermore, the solid line shows the LPM limit for the phase space as given in Eq. (5.38) on page 58. The mean free paths underlying this limit were calculated iteratively. While the kinematical limit is symmetric in forward- and backward rapidity, with increasing projectile energies the LPM limit prefers emissions into the backward rapidity region. Reason for these preferred backward emissions is the phase space that opens up due to the enormous Lorentz boost of the higher energy projectiles. Due to the term $\sim k_\perp^{-2}$ in the GB approximation the emissions prefer a smaller $k_\perp$ and therefore the density of emissions tend to the smallest allowed $k_\perp$.

Differential emission rates from the incoherent θ-LPM approach

After discussing the consequences of the θ-LPM implementation for quantities in the CoM system, we present in the following the differential emission rates and the corresponding radiative energy loss following the θ-LPM method. To this end, we consider again an eikonal projectile parton with energy E traversing a medium with temperature T, but this time scattering with particles whose momentum is thermally distributed. Again, for all following results the mean free path entering the theta function is iteratively calculated for each choice of E and T.

Figure 5.4 shows the differential emission rate $\mathrm{d}\Gamma/\mathrm{d}k_\perp$ integrated over rapidity y for a quark and gluon projectile with energy $E = 250\,\mathrm{T}$ in media with different temperatures T. As expected from the discussion about the phase space limitation by the θ-LPM, small transverse momenta are indeed suppressed by the θ-LPM at $k_\perp \sim \mathcal{O}(T)$. Due to the thermally distribution of scattering partners this lower limit is however broadened. Large transverse momenta are suppressed by the kinematical limit in agreement with Fig. 5.3. For more collinear gluon emissions the emission rate scales with temperature T. The differences in the emission rate between a quark and a gluon projectile result from the different QCD color factors (cf. Chapter 3): On the one hand, gluons emit more other gluons than quarks at larger $k_\perp$ due to the increased rate of the elastic part of the GB cross section. On the other hand, at soft $k_\perp$ the different mean free paths ($\lambda_g^{\mathrm{iter}} < \lambda_q^{\mathrm{iter}}$) lead to a stronger cut-off via the θ-LPM function for the gluons and thereby, following Eq. (5.38), less available phase space at soft $k_\perp$.

The radiative energy loss of the projectile is caused by the emission of gluons with energy ω. Therefore we discuss in the following the differential emission rate $\mathrm{d}\Gamma/\mathrm{d}\omega$ for different projectile energies E. In Section 5.1.2 we found that one of the characteristic features of the non-Abelian LPM effect is the suppression of high energy gluon emissions leading to $\mathrm{d}\Gamma/\mathrm{d}\omega \sim \omega^{-3/2}$. This effect can also be found when considering the θ-LPM implementation as shown in Fig. 5.5. Shown is the differential emission rate $\mathrm{d}\Gamma/\mathrm{d}\omega$ for the same setup as in Fig. 5.4 but for projectile energies $E = 25\,\mathrm{T}$ and $E = 250\,\mathrm{T}$. The solid line shows a fit $\sim \omega^{-3/2}$ and demonstrates that the differential emission rate shows the expected behavior of the LPM effect from a scale $\omega \sim \mathcal{O}(T)$ up to scales $\omega \sim \mathcal{O}(E)$, where energy conservation rejects more energetic emissions. This is surprising since the theta function for ensuring independent emissions, in principle, only considers the incoherent limit of gluon emissions. Furthermore, similar to the differential rate $\mathrm{d}\Gamma/\mathrm{d}k_\perp$, also $\mathrm{d}\Gamma/\mathrm{d}\omega$ scales approximately with temperature T and the LPM cut-off prevents emissions with $\omega < \omega_{\mathrm{min}} \approx k_{\perp;\,\mathrm{min}} \sim \mathcal{O}(T)$. Consequently, by showing $\mathrm{d}\Gamma/\mathrm{d}\omega$ in units of the projectile energy E we see that the spectrum of a higher energy jet with $E = 250\,\mathrm{T}$ is broader and ranges to softer relative energies than the spectrum of a jet with $E = 25\,\mathrm{T}$. In other words, a gluon with $\omega = T$ takes away already 4 % of the a jet with $E = 25\,\mathrm{T}$ while for the more energetic jet this this is a factor 10 less relative energy. While the spectrum of a quark

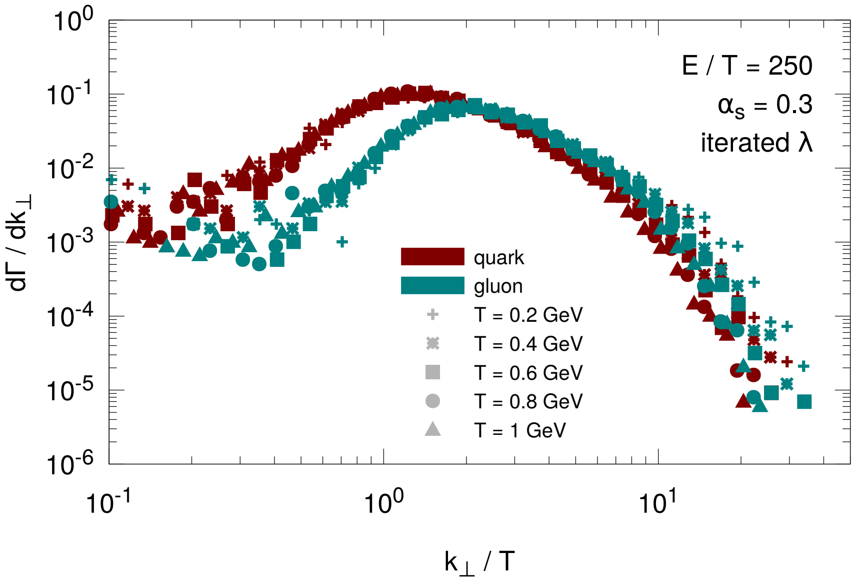

Figure 5.4: Differential emission rate $\mathrm{d}\Gamma/\mathrm{d}k_\perp$ from the θ-LPM approach for a quark (red) and gluon (green) projectile with energy $E = 250\,\mathrm{T}$ scattering in a thermal medium with temperature T and a fixed QCD coupling $\alpha_s = 0.3$. For a numerical check of the scaling with T we show calculation for different temperatures denoted by different point symbols. The mean free path λ entering the θ-LPM approach is iteratively calculated for the different flavors and temperatures.

and gluon projectile is similar at large ω, a deviation at small ω is visible. Reason for this deviation is the different iterated mean free path of a quark and a gluon, $\lambda_\mathrm{g} < \lambda_\mathrm{q}$. As we have discussed previously, this different mean free path lead to different minimum $k_\perp$ with the result that the phase space for collinear gluons is stronger constrained than the phase space of a quark.

The discussed gluon emissions obeying $\mathrm{d}\Gamma/\mathrm{d}k_\perp$ and $\mathrm{d}\Gamma/\mathrm{d}\omega$ lead to a radiative energy loss of the projectile. One can calculate the corresponding differential energy loss per unit path length $\mathrm{d}E/\mathrm{d}x$ by integrating the differential gluon emissions rate $\mathrm{d}\Gamma/\mathrm{d}\omega$ weighted by the gluon energy ω. Therefore it depends not only on the number of gluon emissions but also on their distribution in energy space. Based on this calculation Figure 5.6 shows $\mathrm{d}E/\mathrm{d}x$ scaled with temperature T^2 depending on the projectile energy E, again for quark and gluon projectiles separately. Interestingly, also the expected $\Delta E \sim \sqrt{E}$ behavior discussed in Section 5.1.2 can be reproduced nicely by the θ-LPM approach. Due to the different iterated mean free paths of a quark and gluon projectile the differential energy loss does not scale with $C_\mathrm{F}/C_\mathrm{A}$ between a quark and a gluon. The shorter iterated mean free path of a gluon forbids more gluon emissions and thereby decreases the rate for gluon emissions from a gluon. This counteracts the higher QCD color factor of a gluon with the results that the radiative energy loss of a quark and a gluon projectile is rather comparable in the θ-LPM approach for incoherent gluon emissions.

In conclusion, we showed that the effective theta function in the radiative matrix elements calculated in the Gunion-Bertsch approximation lead to both a $\mathrm{d}\Gamma/\mathrm{d}\omega \sim \omega^{-3/2}$ and $\Delta E \sim \sqrt{E}$ dependence. In the next section we will phenomenologically introduce coherent gluon emissions via the theta function and investigate their influence on the observables.

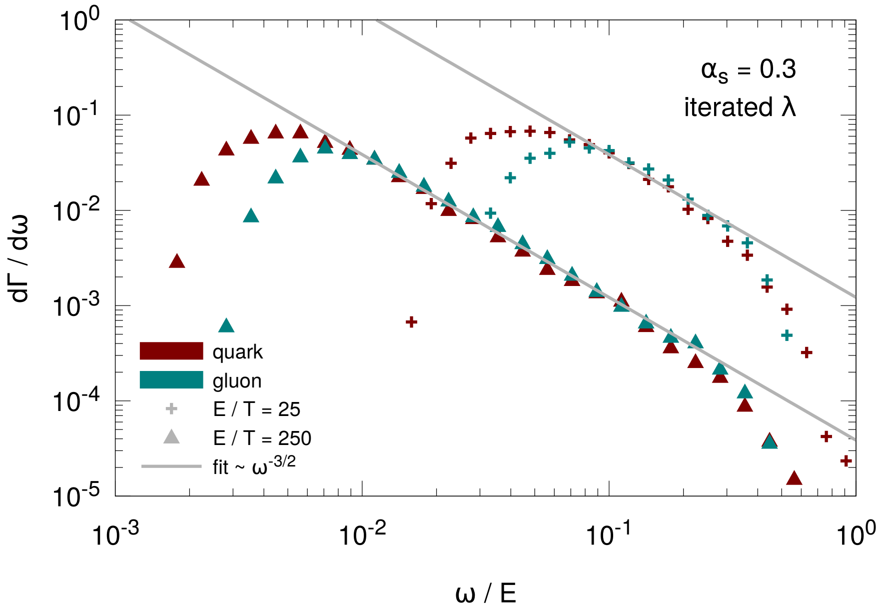

Figure 5.5: Differential emission rate $\mathrm{d}\Gamma/\mathrm{d}\omega$ from the θ-LPM approach for a quark (red) and gluon (green) projectile with energy $E = 25\,\mathrm{T}$ (cross symbol) or $E = 250\,\mathrm{T}$ (triangle symbol) scattering in a thermal medium with temperature T and a fixed QCD coupling $\alpha_s = 0.3$. ω is given in units of E in order to visualize the contribution to the radiative energy loss. The mean free path λ entering the θ-LPM approach is iteratively calculated for the different flavors and temperatures. While the points represent the numerical simulations from BAMPS, the lines show a fit reproducing the expected LPM behavior $\mathrm{d}\Gamma/\mathrm{d}\omega \sim \omega^{-3/2}$.

5.2.2 Effective handling of coherent gluon emissions

Although the implementation of the LPM effect via an effective theta function in the radiative matrix elements seems to be a legit way to consider and ensure only incoherent gluon emissions, one misses any coherence between the scattering centers. Therefore we introduce and investigate in the following a *coherence factor* X_{LPM} in the theta function of Eq. (5.33) on page 57 [FXG09; Foc11; Uph+15; Uph13]

$$\Theta\left(\lambda - \tau_f\right) \rightarrow \Theta\left(\lambda - X_{\mathrm{LPM}}\tau_f\right) . \tag{5.41}$$

X_{LPM} allows to control how much *effective coherence* is introduced into the gluon emissions by rescaling the mean free path (or formation time). Consequently, Eq. (5.36) on page 58 reads then

$$\theta\left(k_\perp - \frac{X_{\mathrm{LPM}}}{\lambda}\frac{\cosh y}{\sqrt{1-\beta_{\mathrm{CoM}}^2}}\left(1+\beta_{\mathrm{CoM}}\cos\theta\,|\tanh y|\right)\right) . \tag{5.42}$$

For $X_{\mathrm{LPM}} \rightarrow 0$, the theta function vanishes what completely switches off the cutoff for $k_\perp$ leading to effectively vacuum-like emissions corresponding to the Bethe-Heitler regime of no LPM effect at all. Furthermore, this also reintroduces the collinear divergence of $k_\perp$ so that the resulting cross section diverges without any further screening. On the other hand, as discussed in the previous section $X_{\mathrm{LPM}} = 1$ allows only incoherent emissions. A value of $0 < X_{\mathrm{LPM}} < 1$ then interpolates between the two cases by effectively allowing gluon emissions that have formation times longer than the mean free path. This means that

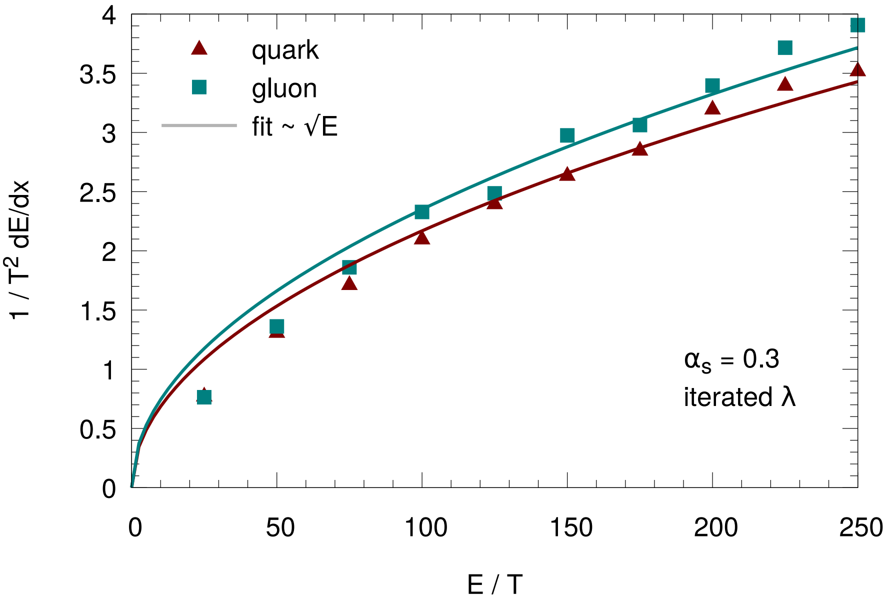

Figure 5.6: Differential radiative energy loss $\mathrm{d}E/\mathrm{d}x$ per unit path length from the θ-LPM approach for a quark (red) and gluon (green) projectile depending on the projectile energy E. The QCD coupling is again fixed at $\alpha_s = 0.3$. While the points represent the numerical results from BAMPS, the lines depict a fit with the expected LPM behavior $\mathrm{d}E/\mathrm{d}x \sim \sqrt{E}$.

by choosing an intermediate value for X_{LPM} additional gluons that could act coherently with the scattering centers are allowed. However, although $X_{\mathrm{LPM}} < 1$ effectively allows "coherent-like" emissions, it is important to note that the actual emission are still produced with a vanishing formation time corresponding to the limit of a thick or even infinite medium. Therefore the case $X_{\mathrm{LPM}} < 1$ should be rather understood as adding more collinear gluon emissions to the incoherent spectrum. This then effectively takes into account "coherent" gluon emissions.

Since there is no physical argument for a specific choice of X_{LPM} we consider for the moment X_{LPM} as a free "coherence" parameter in the calculation of the radiative processes considering θ-LPM suppression. In subsequent sections we will further investigate the choice of parameters by comparing the approach to other theory models (cf. Section 5.5) including a stochastic Ansatz for the LPM effect (cf. Section 5.3) and experimental data (cf. Chapter 7).

Figure 5.7 shows the y-$k_\perp$-phase space in the CoM frame corresponding to Fig. 5.3 but for a fixed projectile energy of $E = 250\,\mathrm{T}$ within a medium with temperature T and different values of X_{LPM}. Again, the scattering partner has a fixed momentum of $p_{\mathrm{partner}} = (3\,\mathrm{T}, -3\,\mathrm{T}, 0, 0)$ and the mean free path underlying the θ-LPM suppression is iteratively determined. While the upper limit of the phase space is constant due to the fixed projectile energy, the lower limit depends on the coherence parameter X_{LPM}. With decreasing X_{LPM} and thereby increasing number of "coherent" gluon emissions the allowed phase space grows, both in $k_\perp$ and rapidity y.

The fact that at fixed energy E and decreasing X_{LPM} the phase space for collinear gluon emissions opens up is also visible in Fig. 5.8 where we show the differential emission rate $\mathrm{d}\Gamma/\mathrm{d}k_\perp$ of a projectile with energy $E = 250\,\mathrm{T}$ in a medium with temperature T for different coherence parameter X_{LPM}. In agreement with Fig. 5.7 a decreasing X_{LPM} allows more collinear gluon emissions, while the rate for more transverse emissions is

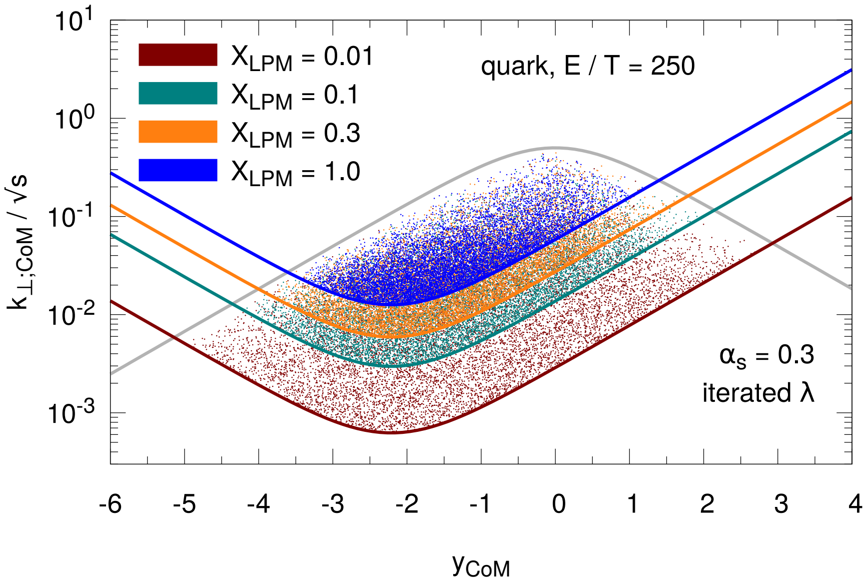

Figure 5.7: Phase space distribution of gluon emissions in the y_{CoM}-$k_{\perp;\mathrm{CoM}}$ plane from the θ-LPM approach with different screening parameters X_{LPM} for a quark projectile with $E = 250\,\mathrm{T}$ scattering with a parton with fixed "thermal" momentum $p_{\mathrm{partner}} = (3\,\mathrm{T}, -3\,\mathrm{T}, 0, 0)$ and a fixed QCD coupling $\alpha_s = 0.3$. Both the transverse momentum (given in units of the CoM energy $\sqrt{\hat{s}}$) and the rapidity are evaluated in the center-of-momentum frame of the respective scattering. While the gray line depicts the limit imposed by kinematics, the colored lines show the LPM limit for the different X_{LPM} parameters.

independent from X_{LPM}. For $X_{\mathrm{LPM}} = 0.01$ even very collinear gluon emissions with $k_\perp \ll T$ are allowed. Interestingly, in this region the spectra become flatter. This behavior originates from the Debye screening $m_D^2 \sim T^2$ in the elastic part of the $2 \to 3$ process and the internal propagator term in the GB matrix element $\sim 1/((\vec{\mathbf{q}}_\perp - \vec{\mathbf{k}}_\perp)^2 + m_D^2)$.

Using the same parameters, Fig. 5.9 shows the differential emissions spectra $\mathrm{d}\Gamma/\mathrm{d}\omega$ for different X_{LPM} values. Different to the distribution of $k_\perp$, decreasing the value of X_{LPM} not only allows softer gluon emissions but also the emission of harder gluons up to $\omega \approx E$. Reason for these enhanced hard gluon emissions is that X_{LPM} limits only the minimum transverse momentum but does not limit the minimum or maximum gluon energy. So a very collinear gluon may have small $k_\perp$ that is allowed by a decreasing X_{LPM} and at the same time have an enormous energy $\omega \sim \mathcal{O}(E)$. Consequently the gluon is emitted very collinearly and adds a contribution to the spectrum at hard ω.

Finally, we discuss the differential radiative energy loss $\mathrm{d}E/\mathrm{d}x$ depending on X_{LPM} as shown in Fig. 5.10. Although the emissions are softer for decreasing X_{LPM}, the increasing rate for gluon emissions efficiently counteracts this and thereby the differential energy loss strongly rises. Furthermore, the difference between quarks and gluons due to their different iterated mean free paths is larger for smaller values of X_{LPM}. Reason for this is the non linearity of the screening (cf. Eq. (5.42) on page 62). Therefore the difference between λ_g and λ_q is additionally enhanced by small X_{LPM} values.

In Fig. 5.11 we further elaborate on this dependence by showing $\mathrm{d}E/\mathrm{d}x$ for two different projectile energies E depending on X_{LPM}. For small values of X_{LPM} we find the dependence $\mathrm{d}E/\mathrm{d}x \sim \log\left(1/X_{\mathrm{LPM}}\right)$ for the differential radiative energy loss. At these small X_{LPM}, the spectrum is dominated by small $k_\perp$ values for which the GB matrix element $\sim 1/k_\perp^2((\vec{\mathbf{q}}_\perp -$

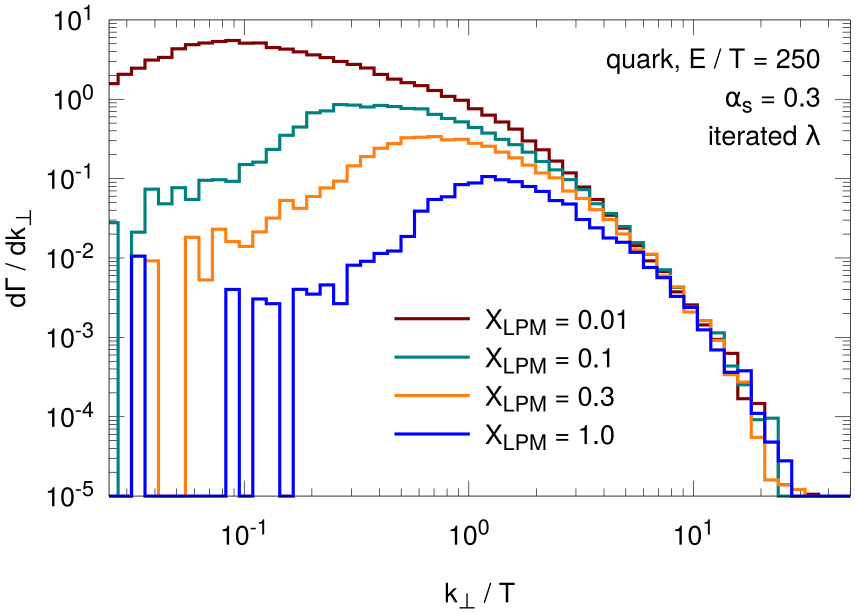

Figure 5.8: Differential emission rate $\mathrm{d}\Gamma/\mathrm{d}k_\perp$ from the θ-LPM approach for different screening parameters X_{LPM} and an eikonal quark projectile with energy $E = 250\,\mathrm{T}$ scattering in a thermal medium with temperature T and a fixed QCD coupling $\alpha_s = 0.3$. The mean free path λ entering the θ-LPM approach is calculated iteratively.

$\vec{\mathbf{k}}_\perp)^2 + m_D^2)$ can be approximated as $\sim 1/k_\perp^2$. Consequently, the integrated rate at small $k_\perp$ scales via the lower integration limit like $\sim \log\left(X_{\mathrm{LPM}}\right)$. Since the differential energy loss is more sensitive to the gluon emission rate than on the collinearity of gluon emissions, it follows that the resulting energy loss also scales like $\mathrm{d}E/\mathrm{d}x \sim \log\left(1/X_{\mathrm{LPM}}\right)$. In contrast, at larger values of $X_{\mathrm{LPM}} \sim \mathcal{O}(1)$ the screening is significantly stronger so that the minimum allowed $k_\perp$ is on the order of the Debye mass. Then the Gunion-Bertsch matrix element cannot be approximated as above and the dependence of $\mathrm{d}E/\mathrm{d}x$ changes to approximately $\mathrm{d}E/\mathrm{d}x \sim 1/\sqrt{X_{\mathrm{LPM}}}$ (not shown).

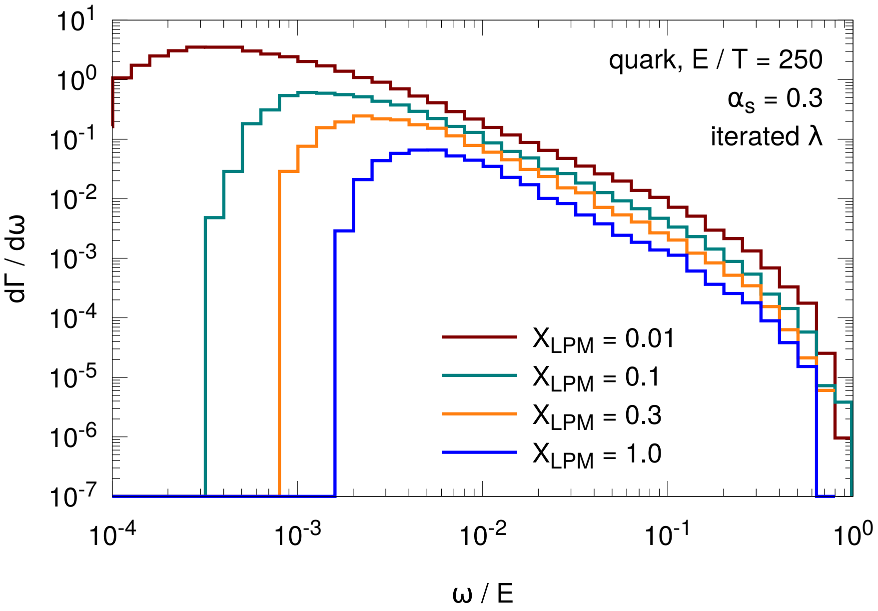

Figure 5.9: Differential emission rate $\mathrm{d}\Gamma/\mathrm{d}\omega$ from the θ-LPM approach for different screening parameters X_{LPM} and an eikonal quark projectile with energy $E = 250\,\mathrm{T}$ scattering in a thermal medium with temperature T and a fixed QCD coupling $\alpha_s = 0.3$. The mean free path λ entering the θ-LPM approach is again calculated iteratively.

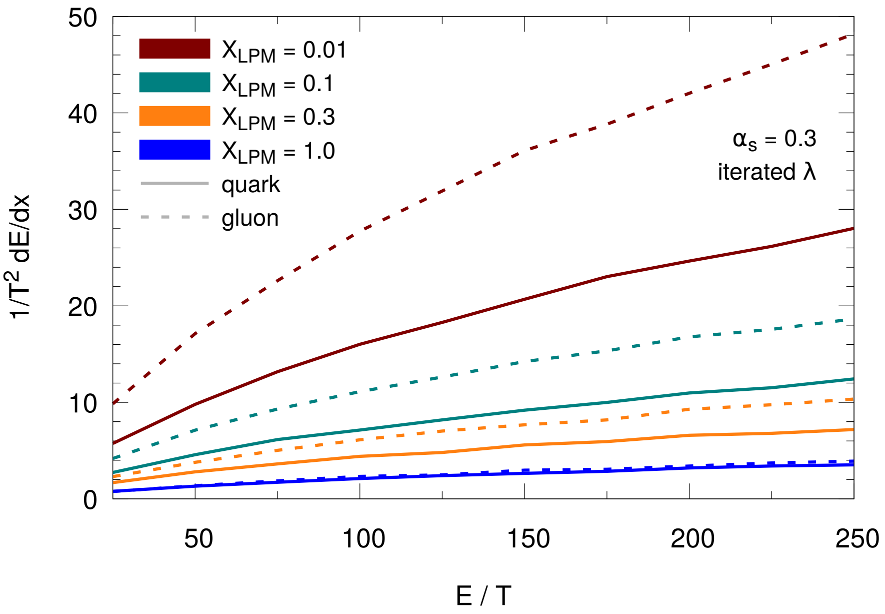

Figure 5.10: Differential radiative energy loss $\mathrm{d}E/\mathrm{d}x$ per unit path length from the θ-LPM approach for different screening parameters X_{LPM} and an eikonal quark (solid lines) and gluon (dashed lines) projectile depending on the projectile energy E. The QCD coupling is again fixed at $\alpha_s = 0.3$ and the MFP is calculated iteratively.

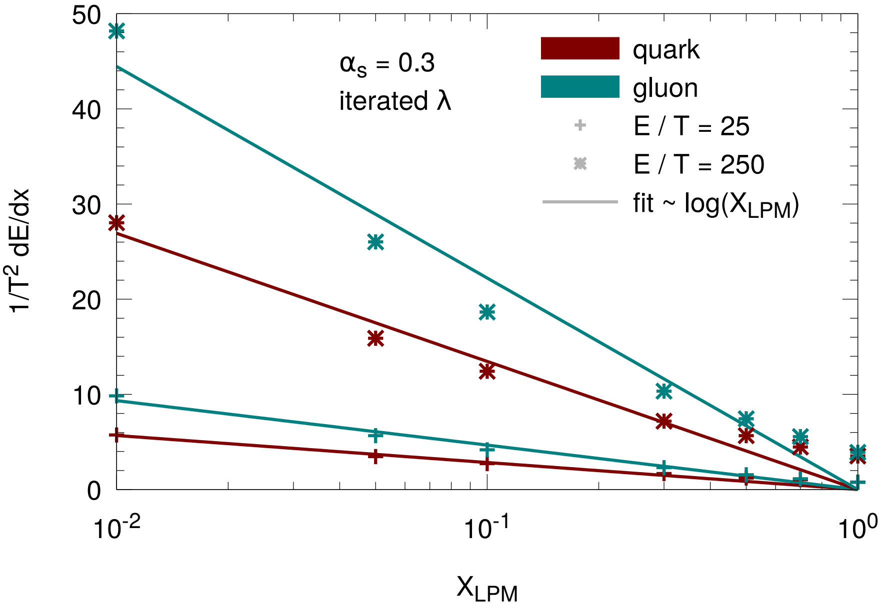

Figure 5.11: Differential radiative energy loss $\mathrm{d}E/\mathrm{d}x$ from the θ-LPM approach depending on the screening parameter X_{LPM} for an eikonal quark (red) or gluon (green) projectile. The different point types denote two different projectile energies $E = \{25\,\mathrm{T}; 250\,\mathrm{T}\}$ and the lines represent fits $\sim \log{(1/X_{\mathrm{LPM}})}$. The QCD coupling is again fixed at $\alpha_s = 0.3$ and the MFP is calculated iteratively.

5.3 Stochastic LPM suppression

One of the findings of Section 5.2 is that the presented θ-LPM method indeed successfully describes the $\sim \omega^{-3/2}$ dependence of the differential emissions rate as expected from the non-Abelian LPM effect. However, a simple suppression of gluon emissions based on a condition for the phase space of the gluon does not take into account the non-local nature of gluon emissions. Furthermore, the consideration of the mean free path entering the cutoff function is approximated by the average, iterated mean free path of the projectile parton. However, as we have shown in Section 5.1.2, also the scatterings of the gluon and thereby the mean free path of the gluon strongly influences the suppression of emissions. Finally, the assumption that the average of the mean free path is sufficient for characterizing the coherence of the process is questionable. Especially calculations in non-equilibrated systems as, e.g., the heavy ion collisions simulated within BAMPS should profit by applying a more microscopic procedure for determining the mean free path and thereby the coherence of the radiative processes.

Consequently, we present in the following an approach for modeling the non-Abelian LPM effect in a partonic transport approach based on a stochastic Ansatz. Instead of approximating the distance to the next scattering center by the mean free path, the next scattering is dynamically determined by evolving the gluon during its formation time as an ordinary parton following the common pQCD interactions within BAMPS. On the one hand, this will allow us to consider the gluon interactions as the significant ones for determining the coherence of the emission process. On the other hand, the crucial distance to the next scattering center is valid not only on averages but on the microscopical level. Both will enables us to reliably reproduce the path length dependence of radiative energy loss in thin and thick media.

Such investigations were done before or are still under active research by several other groups [ZSW09; ZSW11; ZW12; CBS11; KXB18b]. Zapp, Stachel, and Wiedemann [ZSW09] were the first introducing a stochastic method for evaluating the LPM suppression in a dynamic setup. This was done by not only considering the scatterings of the radiated gluon during the formation time but also suppressing the gluon emissions stochastically based on their number of scatterings during the formation time. Although our algorithm for LPM suppression is in the same spirit as the mentioned other approaches, there are minor differences in the final application to the gluon radiation. In contrast to the approach by Zapp, Stachel, and Wiedemann [ZSW09] we approximate the initial gluon radiation by the more realistic Gunion-Bertsch matrix element and thereby consider also a distribution of $k_\perp$ that is not only determined by the momentum transfer $q_\perp$ from the medium but has a divergence in $k_\perp$. Moreover, although we are employing the same improved GB matrix element as Ke, Xu, and Bass the algorithm of Ref. [KXB18b] treats the soft momentum transfers in the initial $2 \rightarrow 3$ process as well as in elastic scatterings of the gluons during the formation time via a Langevin diffusion. This requires a different suppression factor and leads to differences to our approach.

5.3.1 Algorithm for stochastic LPM suppression

This section presents the algorithm underlying the stochastic LPM (sLPM) approach as it was implemented and investigated within BAMPS throughout this work. To this end, we first discuss the algorithm on a more general level. In the following Section 5.3.2 we will then apply the algorithm to fixed interactions and investigate whether the signatures of the QCD LPM effect can be reproduced in a controlled environment. Finally, we investigate in Section 5.3.5 how the sLPM algorithm interplays with the leading-order pQCD cross sections as introduced in Chapter 3.

Based on the algorithm proposed in Ref. [ZSW11] the sLPM method follows the arguments of Section 5.1.2 and extends these ideas by numerically suppressing the gluon emissions. The goal is to formulate an algorithm that is based on Monte-Carlo methods and that interpolates between coherent and incoherent gluon emissions. To this end, gluon emissions are proposed via the usual incoherent way and later the potential coherence of the process is introduced by a reweighting of the emission.

The algorithm for stochastically modeling the non-Abelian LPM effect can be formulated as follows:

1. *Inelastic $2 \to 3$ process takes place at time t_0*

   According to the usual probability for a $2 \to 3$ process in BAMPS (cf. Eq. (4.3) on page 39) it is decided that an inelastic process should take place at time t_0. The cross section underlying the probability is the default incoherent cross section and can either be chosen as fixed (see Section 5.3.2) or calculated via the Gunion-Bertsch matrix element (see Section 5.3.2). By *incoherent* cross section we emphasize that at this stage no coherence of the process is considered yet. In the case of the Gunion-Bertsch matrix element, the screening of $k_\perp$ is not cured by a theta function as in the θ-LPM method (s. Section 5.2) but by other means that we will discuss in the following sections (s. Section 5.3.4).

   In contrast to the usual procedure within BAMPS the Bremsstrahlung process is for now only a proposed gluon emission. After determining the kinematic properties of the trial gluon, the formation time of the process is calculated via $\tau_f = \omega/k_\perp^2$, where ω is the gluon energy and $k_\perp^2$ is the squared initial transverse momentum of the gluon wrt. the projectile, both evaluated in the lab frame. Before the formation time expires, the system of projectile and gluon is indistinguishable. Therefore, at this stage we do not know yet whether the emission is coherent, incoherent or if it is suppressed in the end. This can only be decided after the formation time has expired and the gluon has decohered from the projectile. Since the formation time has to be evaluated with respect to the projectile parton, this trial gluon is associated with the projectile parton. Technically speaking, the trial gluon is added to the projectile's list of trial gluons. During the formation time the projectile's energy and momentum is unmodified. In principle this violates energy and momentum conservation for the length of formation time since the gluon energy and momentum is considered both in the projectile and its associated trial gluon list. However, since we apply the algorithm only in problems that can be solved either in a thermal background or while the background medium is not modified this should not be a major problem. As we will see in a moment, after the formation time is finished, energy and momentum is conserved again.

2. *Propagation of parent parton and trial gluon during formation time*

   In the time step, in which the gluon emissions are proposed and also in each subsequent time step t, it is checked whether the trial gluons are still in their formation time $|t - t_0| < \tau_f$. To this end, the formation time is calculated wrt. the projectile within this time step. If the formation time has not elapsed yet, the projectile and the trial gluon are still in a coherent state. Within this coherent state the trial gluon is only allowed to scatter elastically with the background medium. These scatterings are the coherent scatterings that are resummed, e.g., within the path integral of Eq. (5.3) on page 47. Furthermore, in the previous θ-LPM method the mean free path describes the average of these scatterings. By these scatterings the gluon may accumulate transverse momentum wrt. the projectile and thereby decreases its formation time that will then be checked in the next time step.

The projectile parton is allowed to emit further gluons. At first glance, this contradicts the arguments of Section 5.1.2 where the LPM suppression explicitly means that during a coherence time no other gluons may be emitted. However, one of the main arguments for the algorithm of Ref. [ZSW11] was that in a numerical description of the LPM effect the formation time may not be treated as a dead-time for gluon production. Rather the projectile is allowed to emit multiple gluons which are suppressed after completing the formation time as we will see in the next paragraph. Another argument for this way of considering multiple gluon emissions during the formation time was given in Ref. [KXB18b]: the crucial interactions for the coherence or incoherence of a gluon emission are not the inelastic but the elastic processes of the gluons. If the formation time is a dead time for further gluon emissions, the inelastic mean free path limits the production of gluons. On the other hand, if the proposal of different gluon emissions is independent from each other, the elastic mean free path then represents the crucial scale.

3. *Incorporating coherence effects*

If $|t - t_0| > \tau_f$ the formation time of a trial gluon is elapsed and this gluon is considered as being decohered from the projectile parton. However, since the trial gluon was produced in an incoherent way the gluon emission has to be reweighted. Furthermore, also the emission of multiple gluons during the formation time leads to an increased probability that has to be corrected. By analyzing different orders in an opacity expansion of the path integral shown in Eq. (5.3) on page 47 the authors of Ref. [ZSW11] have demonstrated that the coherent and incoherent limit of gluon emissions differ by a factor of $1/N_{\text{coh}}$, where N_{coh} are the number of coherent elastic scatterings by the gluon during its formation time. Consequently, gluons that were produced incoherently have to be accepted only with a probability [ZSW11]

$$P_{\text{coh}} = \frac{1}{N_{\text{coh}}} \,. \tag{5.43}$$

The elastic part of the initial Bremsstrahlung process that led to the emission process is also counted for N_{coh}. Therefore the minimum limit of N_{coh} is $N_{\text{coh}} = 1$ corresponding to a gluon that has not further scattered elastically with the medium. This is the incoherent or Bethe-Heitler limit where gluon emissions are independent from each other. On the other hand, the more often the gluon has scattered with the medium the less probable is the emission due to the increasing coherence of the process. For $N_{\text{coh}} \to \infty$ the limit of total coherence is reached and the gluons are totally suppressed. Consequently, the suppression by N_{coh} effectively models and interpolates between the incoherent and coherent limit of LPM suppression. Furthermore, due to the consideration of a finite formation time of the whole emission process instead of an instantaneous production of gluons also the path-length dependence of the emission process is considered.

If the emission is accepted by the probability P_{coh} as part of the evolution history one may now subtract the energy and momentum of the gluon as they were at time

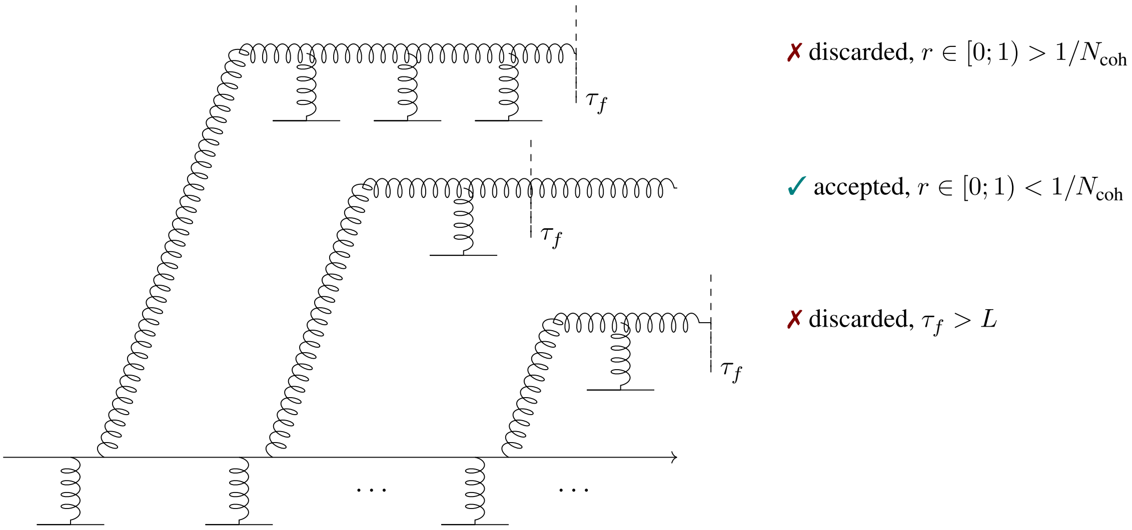

Figure 5.12: Schematic visualization of the stochastic LPM algorithm for a Bremsstrahlung process with subsequent elastic scatterings of trial gluons during the formation time.

t_0 from the projectile and evolve the gluon as an usual parton itself. This further treatment depends obviously on the assumptions about the actual energy loss, eikonal or non-eikonal, and the problem that one wants to solve, energy loss of only the projectile parton or also the surrounding parton shower. If the gluon emission is rejected with probability $1 - P_{\text{coh}}$ the whole gluon emission process is discarded and the projectile stays unmodified.

4. *Discard unformed gluon emissions*

   After completing the simulation time or medium length L all remaining trial gluon emissions that are still in their formation time are discarded. The reason for this rejection can be found in Ref. [ZSW11], where it is argued that for reproducing the path-integral Eq. (5.3) on page 47 only gluons that are formed prior to leaving the medium need to be considered.

The presented algorithm for LPM suppression is schematically shown in Fig. 5.12. It should be understood as rather general since it is formulated independently from a concrete choice for the underlying elastic and Bremsstrahlung processes. Therefore we demonstrate in the next section that for a simplified choice of fixed cross sections the algorithm indeed reproduces the expected analytical dependencies. After that, we apply the algorithm in Section 5.3.5 to more realistic interactions from pQCD that we discuss in Sections 5.3.3 and 5.3.4.

5.3.2 Benchmarking the algorithm for stochastic LPM suppression

In this section we benchmark the algorithm for stochastically suppressing coherent gluon emissions as proposed in Section 5.3.1. To this end, we define a *simplified* model for a projectile parton emitting gluons with constant rates and investigate the characteristics of the resulting radiative energy loss. For this model one can then derive analytically the dependencies of the gluon emission spectra or the radiative energy loss as well as calculate numerically the corresponding quantities based on the stochastic LPM algorithm. This will allow us to demonstrate that the proposed algorithm for LPM suppression of

Section 5.3.1 indeed shows the characteristic dependencies of the non-Abelian LPM effect, especially the $\Delta E \sim L^2$ length dependence for the radiative energy loss. Subsequently we will apply and investigate in Section 5.3.5 the proposed algorithm together with a more realistic treatment of the partonic interactions based on the improved Gunion-Bertsch matrix element together with leading-order pQCD cross sections.

Parametric dependencies of the LPM effect in a simplified model

In the simplified model a projectile parton[4] of energy E traverses a brick of medium with length L and temperature T. Neglecting at the moment any coherence effects, the projectile may emit gluons with energy ω along its trajectory with a constant rate Γ_{inel} and thereby mean free path $\lambda_{\text{inel}} = \Gamma_{\text{inel}}^{-1}$. Assuming a high projectile energy E, the emitting parton remains unmodified by the inelastic process and thereby keeps both its energy and its direction. Furthermore, any elastic processes of the parent parton are neglected at the moment. Although these assumptions are in principle not necessary in our numerical calculation (and will be loosed later in Chapter 6), it allows a robust comparison of the LPM algorithm with the analytical eikonal limit Eq. (5.2) on page 47.

In the incoherent limit of gluon emissions the energy of the emitted gluons ω is approximately distributed by $\mathrm{d}\sigma/\mathrm{d}\omega \sim \omega^{-1}$, that corresponds to the small x limit of the Gunion-Bertsch matrix element [GB82]. While the maximum gluon energy ω_{max} is kinematically limited by the projectile energy E, the minimum energy ω_{min} of the gluon is not physically limited and will be set to $\omega_{\text{min}} \sim \mathcal{O}\left(10^{-2}\,\mathrm{E}\right)$ throughout this section. Therefore the normalized gluon energy distribution underlying a *single* gluon emission within the medium can be written as

$$\omega \frac{\mathrm{d}I}{\mathrm{d}\omega}\bigg|_{\text{single scatt}} \sim \frac{1}{\log\left(E/\omega_{\text{min}}\right)} := \frac{1}{\nu_{\text{norm}}}\,, \tag{5.44}$$

where we defined the normalization factor $\nu_{\text{norm}} := \log\left(E/\omega_{\text{min}}\right)$. Based on this distribution the energies of the trial gluons are sampled before they interact elastically with the medium during their formation time in order to consider the coherence effects. The initial transverse momentum of the emitted gluon is set to the fixed value $k_{\text{t; initial}}$ that will be discussed in a moment. This initial fixed transverse momentum $k_\perp$ serves additionally as a ω_{min} limit for the ω distribution due to kinematics.

According to the algorithm of Section 5.3.1 the emitted trial gluons interact elastically and thereby modify their formation time τ_f self-consistently. In our simplified model, the medium transfers a constant transverse momentum $\vec{\mathbf{q}}_\perp$ to the emitted gluons per mean free path λ_{el}. The direction of $\vec{\mathbf{q}}_\perp$ is transverse to the direction of the projectile but randomly distributed in the corresponding azimuthal angle. Although each scattering transfers $q_\perp$ to the gluon, due to the random angle the gluon undergoes a Brownian motion in transverse space wrt. the projectile. This definition of elastic momentum transfers has the advantage that the transport parameter $\hat{q}$ can be straightforwardly defined as $\hat{q} = q_\perp^2/\lambda_{\text{el}}$ corresponding to the average momentum transfer squared per unit path length. In contrast, the momentum transfers $q_\perp^2$ of the elastic pQCD cross sections presented in Section 5.3.3 may have a broad distribution and a clear definition of $\hat{q}$ is not ad-hoc clear.

As described in Section 5.1.1 the analytic arguments of, e.g., BDMPS-Z are formulated in the kinematical range $\omega \gg q_\perp, k_\perp$. In order to compare the present simplified model

---

[4] In the simplified model the flavors of both the parent and daughter parton as well as the temperature T are arbitrary since the interactions are fully determined by the chosen values for the mean free paths λ_{inel} and λ_{el}.

to these analytical considerations, we assume that the elastic momentum transfers do not modify the gluon energies but only change the transverse momentum of the gluons. The energy of the gluon emission is consequently fixed at the value the gluon obtains by the initial $\sim 1/\omega$ spectrum. Therefore the modification of formation time is only determined by the elastic kicks leading to a change of direction of the emitted gluons. The formation time of the gluons is thus dynamically modified by each scattering and can be written after the i-th scattering as $\tau_i = \omega / \left(\vec{\mathbf{k}}_{\perp;\text{initial}} + \sum_i \vec{\mathbf{q}}_{\perp;\text{i}} \right)^2$, where $\vec{\mathbf{k}}_{\perp;\text{initial}}$ is the initial transverse momentum directly after the emission and $\vec{\mathbf{q}}_{\perp;\text{i}}$ the momentum transfer from the i-th scattering. In Section 6.2 we discuss the consequences of loosening this assumption of constant ω and considering also an evolution in ω by momentum transfers with the medium.

Following the Gunion-Bertsch approximation for a Bremsstrahlung process of a high energy parton, an inelastic process can be factorized into an elastic part and a probability to emit an additional gluon. Based on this factorization we assume in the simplified model that the initial gluon transverse momentum $k^2_{\perp;\text{initial}} \approx q^2_\perp$ and thereby the initial transverse momentum is completely determined by the momentum transfer from the medium. This is in accordance to Ref. [ZSW11], where it is argued that if the final transverse momentum of the gluon is built up by many interactions within the medium, the transverse momentum at the initial emission is unimportant. On the other hand, if there are less interactions the transverse momentum at emission will be dominated by the recoil received by the medium. In Section 5.3.5 we will see how a more realistic distribution of initial $k_\perp$ by the Gunion-Bertsch matrix element results in the emission pattern.

One difference between the heuristic discussion of Section 5.1.2 and the presented simplified model are the definitions of mean free paths. In the analytical derivation the mean free path is the distance between two subsequent scattering centers with which the projectile interacts indifferent from whether this scattering center acts as an elastic scattering center or there is an additional gluon radiation induced. In principle, every scattering center can also induce a gluon emission. In contrast, the simplified model is formulated by explicitly differing between elastic scatterings centers acting on the gluons during formation time and inelastic scattering centers interacting with the projectile. Between two scattering centers that induce an additional gluon emission is λ_inel, while the distance between two scattering centers that only scatter elastically is λ_el. The definition of mean free paths in the simplified model aims already to the discussion of the stochastic LPM approach in the context of the Gunion-Bertsch approximation, in which the $2 \to 3$ and $2 \to 2$ processes, although both calculated in LO pQCD, are different concepts. Therefore we discuss in the following how the different definitions of mean free paths end up in the emission patterns as derived in Section 5.1.2 and label explicitly which mean free path is intended.

The coherence of emission processes is considered by rejecting trial gluons after they finished their formation time as described in Section 5.3.1. The acceptance/rejection criterion $P_\text{coh} = 1/N_\text{coh}$ is determined by the number of scatterings N_coh of the gluon during the formation time τ_f. In terms of the simplified model it follows that

$$N_\text{coh} = \frac{\tau_f}{\lambda_\text{el}} = \sqrt{\frac{\omega}{\hat{q}{\lambda_\text{el}}^2}} = \sqrt{\frac{\omega}{q^2_\perp \lambda_\text{el}}}\,, \tag{5.45}$$

where $\tau_f = \sqrt{\omega/\hat{q}}$ (cf. Eq. (5.15) on page 53) was used. With the suppression factor $\sim P_\text{coh}$ the resulting differential emission rate $\mathrm{d}\Gamma/\mathrm{d}\omega$ of gluons with energy ω per unit time step can then be written as

$$\omega\frac{\mathrm{d}\Gamma}{\mathrm{d}\omega} = \frac{1}{\lambda_{\text{inel}}}\frac{1}{N_{\text{coh}}}\,\omega\frac{\mathrm{d}I}{\mathrm{d}\omega}\bigg|_{\text{single scatt}} \tag{5.46}$$

$$= \frac{1}{\nu_{\text{norm}}}\frac{1}{\lambda_{\text{inel}}}\frac{1}{N_{\text{coh}}}\,. \tag{5.47}$$

Depending on the number of coherent scatterings one can therefore distinguish between two regimes of coherence of the gluon emissions:

- For $N_{\text{coh}} = 1$, which means that there is no additional momentum transfer besides the elastic part of the initial $2 \to 3$ process, subsequent scatterings are independent from each other. The corresponding differential gluon emission rate is therefore only depending on λ_{inel} and reads

  $$\omega\,\frac{\mathrm{d}\Gamma}{\mathrm{d}\omega}\bigg|_{\mathrm{incoherent}} = \frac{1}{\nu_{\text{norm}}}\frac{1}{\lambda_{\text{inel}}}\,. \tag{5.48}$$

  The energy scale under which these incoherent scatterings take place is given by ω_{BH} as defined in Eq. (5.18) on page 54. For the simplified model it follows for ω_{BH}:

  $$\omega_{\text{BH}} = \hat{q}{\lambda_{\text{el}}}^2 = q_\perp^2\lambda_{\text{el}} \tag{5.49}$$

  Therefore although the size of the emission rate is solely determined by the inelastic mean free path the extension of the incoherent limit is constrained by ω_{BH} that is only depending on quantities related to the elastic interactions.

- If the gluon scatters elastically during the formation time, $N_{\text{coh}} > 1$, the differential gluon emission rate reads

  $$\omega\,\frac{\mathrm{d}\Gamma}{\mathrm{d}\omega}\bigg|_{\mathrm{coherent}} = \frac{1}{\nu_{\text{norm}}}\frac{1}{\lambda_{\text{inel}}N_{\text{coh}}} \tag{5.50}$$

  $$= \frac{1}{\nu_{\text{norm}}}\frac{1}{\lambda_{\text{inel}}}\sqrt{\frac{\hat{q}{\lambda_{\text{el}}}^2}{\omega}} = \frac{1}{\nu_{\text{norm}}}\frac{1}{\lambda_{\text{inel}}}\sqrt{\frac{q_\perp^2\lambda_{\text{el}}}{\omega}}\,. \tag{5.51}$$

  These coherent emissions are realized for gluons with energies $\omega > \omega_{\text{BH}}$ up to a scale $\omega_{\text{fact}} = \hat{q}L^2$ (cf. Eq. (5.21) on page 55) and represent the discussed LPM region.

Above $\omega > \omega_{\text{fact}}$ the formation time of gluons is on the same order as the complete medium length L. Therefore in this factorization limit the total medium acts as *one* coherent scattering center. However, this region is hard to consider in the numerical simulations. Since these gluons need at least the whole medium length to decohere from the parent projectile the gluon emission should have been be started directly at the beginning of the medium evolution. This is however due to statistics very rarely the case what leads to the neglection of the factorization region in the following. However, as also argued in Ref. [ZSW11], due to the steeply falling ω spectrum the actual role of large ω for the radiative energy loss should be negligible.

The integrated first moment of the gluon emission rate $\mathrm{d}\Gamma/\mathrm{d}\omega$ gives the differential radiative energy loss

$$\frac{\mathrm{d}E}{\mathrm{d}x} = \int\limits_{\omega_{\text{min}}}^{E} \mathrm{d}\omega\, \omega \frac{\mathrm{d}\Gamma}{\mathrm{d}\omega} \tag{5.52}$$

of the projectile parton for a medium with length L. As discussed in Section 5.1.2 the path-length dependence of the radiative energy loss from the LPM effect differs for thin and thick media. If the medium length L is smaller than the maximum or critical medium length L_c, defined by the maximum formation time ${\tau_f}^{\text{max}}$,

$$L_c = {\tau_f}^{\text{max}} = \sqrt{\frac{\omega^{\text{max}}}{\hat{q}}} = \sqrt{\frac{E}{\hat{q}}}\,, \tag{5.53}$$

again, the whole medium can act as *one* large coherent scattering center. In contrast, if the medium is larger than L_c this is not possible since there is no formation time that is larger than the medium length. Furthermore, different coherent scattering centers then act as if they were single scattering centers that induce incoherent gluon emissions. In other words, for thick media there is no factorization region in the gluon energy spectrum but different coherent scattering centers contribute as incoherent regions to the gluon emission spectrum.

In the simplified model the differential radiative energy loss in a thick medium $L > L_c$ then is derived as

$$\left.\frac{\mathrm{d}E}{\mathrm{d}x}\right|_{L>L_c} = \int\limits_{\omega_{\text{min}}}^{\omega_{\text{BH}}} \mathrm{d}\omega\ \omega \left.\frac{\mathrm{d}\Gamma}{\mathrm{d}\omega}\right|_{\text{BH}} + \int\limits_{\omega_{\text{BH}}}^{E} \mathrm{d}\omega\ \omega \left.\frac{\mathrm{d}\Gamma}{\mathrm{d}\omega}\right|_{\text{LPM}} \tag{5.54}$$

$$= \frac{1}{\nu_{\text{norm}}} \left(2\frac{\lambda_{\text{el}}}{\lambda_{\text{inel}}} \sqrt{\hat{q}E} - \hat{q}\frac{{\lambda_{\text{el}}}^2}{\lambda_{\text{inel}}} - \frac{\omega_{\text{min}}}{\lambda_{\text{inel}}} \right) \tag{5.55}$$

$$= \frac{1}{\nu_{\text{norm}}} \frac{2}{\lambda_{\text{inel}}} \left(\sqrt{\omega_{\text{BH}} E} - \frac{\omega_{\text{BH}} + \omega_{\text{min}}}{2} \right), \tag{5.56}$$

where we used the definition of $\omega_{\text{BH}} = \hat{q}{\lambda_{\text{el}}}^2$. As expected $\left.\frac{\mathrm{d}E}{\mathrm{d}x}\right|_{L>L_c}$ shows the characteristic $\sim \sqrt{E}$ dependence in thick media. Furthermore, the energy loss rate is for $L > L_c$ independent from the medium length L leading to a total radiative energy loss $\Delta E \sim L$ as in the case of the θ-LPM method.

In our specific treatment of curing the divergence of the $1/\omega$-term by specifying a minimum gluon energy ω_{min}, special attention needs to be paid if $\omega_{\text{min}} > \omega_{\text{BH}}$ for a specific choice of parameter. Then the Bethe-Heitler part of the gluon spectrum vanishes (first term in Eq. (5.54)) and the radiative energy loss becomes

$$\left.\frac{\mathrm{d}E}{\mathrm{d}x}\right|_{L>L_c} = \frac{1}{\nu_{\text{norm}}} \frac{2}{\lambda_{\text{inel}}} \left(\sqrt{\omega_{\text{BH}} E} - \sqrt{\omega_{\text{BH}} \omega_{\text{min}}} \right). \tag{5.57}$$

The corresponding calculation for the radiative energy loss in a thin medium ($L < L_c$)

yields

$$\left.\frac{\mathrm{d}E}{\mathrm{d}x}\right|_{L<L_c} = \int\limits_{\omega_{\text{min}}}^{\omega_{\text{BH}}} \mathrm{d}\omega\, \omega \left.\frac{\mathrm{d}\Gamma}{\mathrm{d}\omega}\right|_{\text{BH}} + \int\limits_{\omega_{\text{BH}}}^{\omega_{\text{fact}}} \mathrm{d}\omega\, \omega \left.\frac{\mathrm{d}\Gamma}{\mathrm{d}\omega}\right|_{\text{LPM}} + \int\limits_{\omega_{\text{fact}}}^{E} \mathrm{d}\omega\, \omega \left.\frac{\mathrm{d}\Gamma}{\mathrm{d}\omega}\right|_{\text{fact}} . \tag{5.58}$$

If we neglect the constant contribution of the factorization region $\int_{\omega_{\text{fact}}}^{E} \mathrm{d}\omega\, \omega \frac{\mathrm{d}\Gamma}{\mathrm{d}\omega}\big|_{\text{fact}}$, which will be also neglected in the numerical simulations, it follows

$$\left.\frac{\mathrm{d}E}{\mathrm{d}x}\right|_{L<L_c} \approx \frac{1}{\nu_{\text{norm}}} \left(2\frac{\lambda_{\text{el}}}{\lambda_{\text{inel}}}\hat{q}L - \hat{q}\frac{\lambda_{\text{el}}{}^2}{\lambda_{\text{inel}}} - \frac{\omega_{\text{min}}}{\lambda_{\text{inel}}} \right) \tag{5.59}$$

$$= \frac{1}{\nu_{\text{norm}}} \frac{2}{\lambda_{\text{inel}}} \left(q_\perp^2 L - \frac{\omega_{\text{BH}} + \omega_{\text{min}}}{2} \right) \tag{5.60}$$

This result again reflects the different path-length dependence of the radiative energy loss in thin media. Due to the coherent scattering centers the energy loss rate itself depends linearly on the medium length L. It follows that the total energy loss goes like $\Delta E \sim L^2$. Furthermore, in small media the energy loss is independent from the projectile energy since hard gluons with $\omega > \omega_{\text{fact}}$ and $\omega \sim \mathcal{O}(E)$ are not able to form.

Again, if the minimum energy ω_{min} is larger than the energy scale ω_{BH} the differential energy loss in thin media becomes

$$\left.\frac{\mathrm{d}E}{\mathrm{d}x}\right|_{L<L_c} = \frac{1}{\nu_{\text{norm}}} \frac{2}{\lambda_{\text{inel}}} \left(q_\perp^2 L - \sqrt{\omega_{\text{BH}}\omega_{\text{min}}} \right) . \tag{5.61}$$

In summary, the differential gluon emission rate $\mathrm{d}\Gamma/\mathrm{d}\omega$ and differential radiative energy loss $\mathrm{d}E/\mathrm{d}x$ within the simplified model can be written as

$$\omega \frac{\mathrm{d}\Gamma}{\mathrm{d}\omega} = \begin{cases} \frac{1}{\nu_{\text{norm}}} \frac{1}{\lambda_{\text{inel}}}, & \omega < \omega_{\text{BH}} \\ \frac{1}{\nu_{\text{norm}}} \frac{1}{\lambda_{\text{inel}}} \sqrt{\frac{q_\perp^2 \lambda_{\text{el}}}{\omega}}, & \omega_{\text{BH}} < \omega < \omega_{\text{fact}} \end{cases} \tag{5.62}$$

and

$$\frac{\mathrm{d}E}{\mathrm{d}x} = \begin{cases} \frac{1}{\nu_{\text{norm}}} \frac{2}{\lambda_{\text{inel}}} \left(q_\perp^2 L - \tilde{\omega}_{\text{min}} \right), & L < L_c \\ \frac{1}{\nu_{\text{norm}}} \frac{2}{\lambda_{\text{inel}}} \left(\sqrt{\omega_{\text{BH}} E} - \tilde{\omega}_{\text{min}} \right), & L > L_c \end{cases} , \tag{5.63}$$

where we defined

$$\tilde{\omega}_{\text{min}} := \begin{cases} \frac{\omega_{\text{BH}} + \omega_{\text{min}}}{2}, & \omega_{\text{min}} < \omega_{\text{BH}} \\ \sqrt{\omega_{\text{BH}}\omega_{\text{min}}}, & \omega_{\text{min}} > \omega_{\text{BH}} \end{cases} . \tag{5.64}$$

Eqs. (5.62) and (5.63) are the equations we will test in the following to benchmark whether the proposed Monte-Carlo algorithm can reproduce the expected analytical dependencies. This procedure is similar to Ref. [ZKW13] and will allow a comparison between the analytic expectations and the numerical Monte-Carlo approach in a controlled fashion and thereby provide a deeper understanding for the application of the algorithm to more realistic partonic interactions.

Algorithm 3: Schematic view of the algorithm for testing the stochastic LPM effect in the simplified model.

```
At $t = 0$ initialize projectile with energy $E := \omega_{\text{max}}$ and $t_{\text{last inel.}} = 0$
while $t < L$ do
    if $|(t + \Delta t) - t_{last\ inel.}| > \lambda_{inel}$ then
        Initialize gluon emission with $\omega \in [\omega_{\text{min}}; \omega_{\text{max}}]$ and $k_\perp^2 = q_\perp^2$
        Set $t_{\text{init}} = t_{\text{last el.}} = t$ and $N_{\text{coh}} = 1$ for this emission
        Set $t_{\text{last inel.}} = t$
        Add gluon to list of trial gluon emissions
    foreach trial gluon do
        Calculate formation time $\tau_f = \omega / k_\perp^2$
        if $|(t + \Delta t) - t_{init}| < \tau_f$ then gluon is not formed
            if $|(t + \Delta t) - t_{last\ el.}| > \lambda_{el}$ then
                Transfer constant transverse momentum $q_\perp^2$ to gluon momentum $k_\perp^2$
                Increase $N_{\text{coh}} = N_{\text{coh}} + 1$
        else gluon is formed
            if random number $r \in [0; 1) < 1/N_{coh}$ then gluon is accepted
                Consider gluon for $\mathrm{d}\Gamma/\mathrm{d}\omega$ and $\mathrm{d}E/\mathrm{d}x$ results
            else
                Discard gluon emission
    $t = t + \Delta t$ ;
    Propagate projectile and trial gluons to time $t$
Discard all gluon emissions still in formation time
```

Testing the Monte-Carlo algorithm by the analytical dependencies

After setting the stage for the simplified model in the previous subsection by discussing its analytical dependencies we test in this section whether the stochastic LPM algorithm introduced in Section 5.3.1 numerically reproduces these dependencies. In order to obtain numerical results we have to first choose concrete values for the input parameters of the simplified model. We make this choice by having a high energy projectile in mind that interacts significantly less inelastically with the medium than the emitted gluons interact elastically during their formation time, $\lambda_{\text{el}} \ll \lambda_{\text{inel}}$. These elastic momentum transfers of the gluons during their formation time are supposed to be soft compared to the gluon energy $q_\perp \ll \omega$. Consequently, these selected parameters represent the limit of multiple soft-scatterings of, e.g., the BDMPS-Z approach as discussed in Section 5.1.2. The gluon energies are distributed according to $\sim 1/\omega$ between $\omega_{\text{min}} \sim \mathcal{O}\left(10^{-3}\,\text{E}\right)$ and $\omega_{\text{max}} = E$, whereas its initial transverse momentum $k_{\text{t; initial}} = q_\perp$ is approximated by the momentum transfer $q_\perp$ from the medium. Since in the simplified model the temperature T is not an input parameter, we choose for the following results the jet energy E as the scale of the problem. The numerical parameters are chosen so that, e.g., for a jet with $E = 100\,\text{GeV}$ follows $\lambda_{\text{inel}} \sim \mathcal{O}(1\,\text{fm})$, $\lambda_{\text{el}} \sim \mathcal{O}\left(10^{-1}\,\text{fm}\right)$, $q_\perp^2 \sim \mathcal{O}\left(10^{-1}\,\text{GeV}^2\right)$ and $L \sim \mathcal{O}(10\,\text{fm})$. The momentum broadening parameter results then to $\hat{q} \sim \mathcal{O}\left(1\,\text{GeV}^2/\text{fm}\right)$. While representing the multiple soft-scattering limit, this parameter choice also corresponds to realistic values how they could appear when applying more realistic interactions as we find in Section 5.3.5. The algorithm employed in this section is summarized in Algorithm 3.

Figure 5.13 shows the differential emission rate $\mathrm{d}\Gamma/\mathrm{d}\omega$ of gluons with energy ω emitted

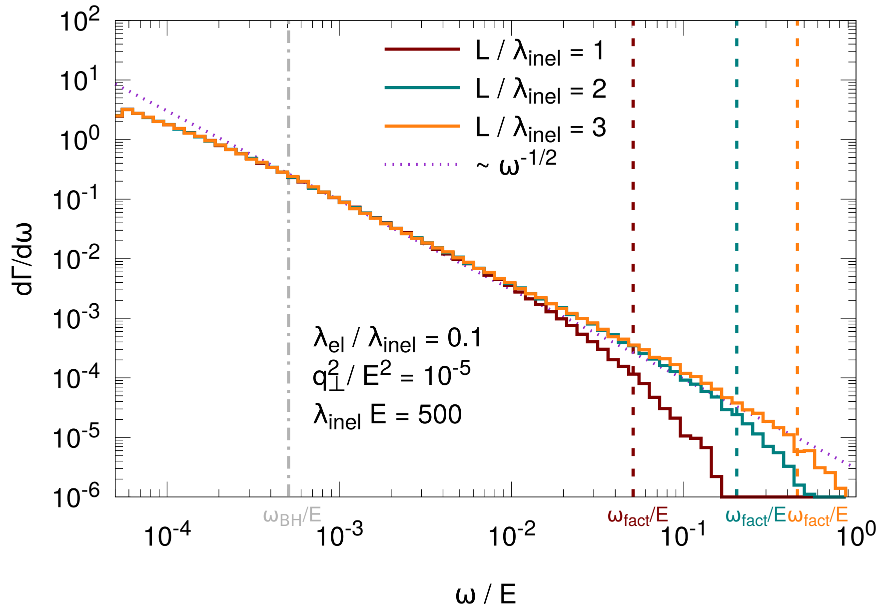

Figure 5.13: Differential rate $\mathrm{d}\Gamma/\mathrm{d}\omega$ of a projectile with energy E for three medium lengths L from the simplified model for the partonic interactions and the stochastic LPM algorithm. While the energy scale ω_{BH}, given in a gray dash-dotted line, depends only on the elastic interactions, the scale ω_{fact} depends on the medium length L and is therefore given as dashed lines in the color corresponding to the respective L. The dotted curve represents a fit with the expected LPM behavior in the range $\omega_{\mathrm{BH}} < \omega < \omega_{\mathrm{fact}}$.

from a projectile with energy E for different medium lengths L. The two characteristic regions of the emission rate originating from coherence effects can be indeed reproduced by the Monte-Carlo algorithm. Soft gluons with energies $\omega \lesssim \omega_{\mathrm{BH}} \sim q_\perp^2 \lambda_{\mathrm{el}}$ (depicted as dashed-dotted line) are produced via incoherent gluon emissions leading to a spectrum that goes with $\mathrm{d}\Gamma/\mathrm{d}\omega \sim 1/\omega$. On the other hand, for harder gluons with energies $\omega \gtrsim \omega_{\mathrm{BH}}$ the formation times τ_f of the single emissions start to overlap. Therefore coherence effects set in and suppress gluon emissions to the steeper $\mathrm{d}\Gamma/\mathrm{d}\omega \sim \omega^{-3/2}$ behavior. For even larger gluon energies $\omega \gtrsim \omega_{\mathrm{fact}} \sim \hat{q}L^2$ the formation time of emissions is larger than the medium length with the result that maximal one gluon can be emitted during L since the whole medium acts effectively as one scattering center. Therefore the emission rate rapidly vanishes for energies larger than ω_{fact}. Since ω_{fact} depends on the medium length L the three different medium lengths result in different energy scales ω_{fact}.

Figure 5.14 shows the total radiative energy loss ΔE resulting from the emission spectrum presented in Fig. 5.13 depending on the medium length L. The crucial length scale for the energy loss is given by $L_c \sim \sqrt{E\lambda_{\mathrm{el}}/q_\perp^2}$. In agreement to the previous considerations the energy loss resulting from the proposed algorithm differs indeed between smaller and larger medium lengths: While traversing the thinner medium with $L < L_c$ leads to a $\Delta E \sim L^2$ behavior, at $\approx L_c$ the energy loss behavior changes. At larger medium lengths $L > L_c$ the energy loss scales like $\Delta E \sim L$. Please note that the rather small values of energy loss are owed to the specific choice of input parameters. We will find later when discussing more realistic values that the radiative energy loss may become significantly larger.

After demonstrating that the proposed Monte-Carlo algorithm indeed reproduces generic

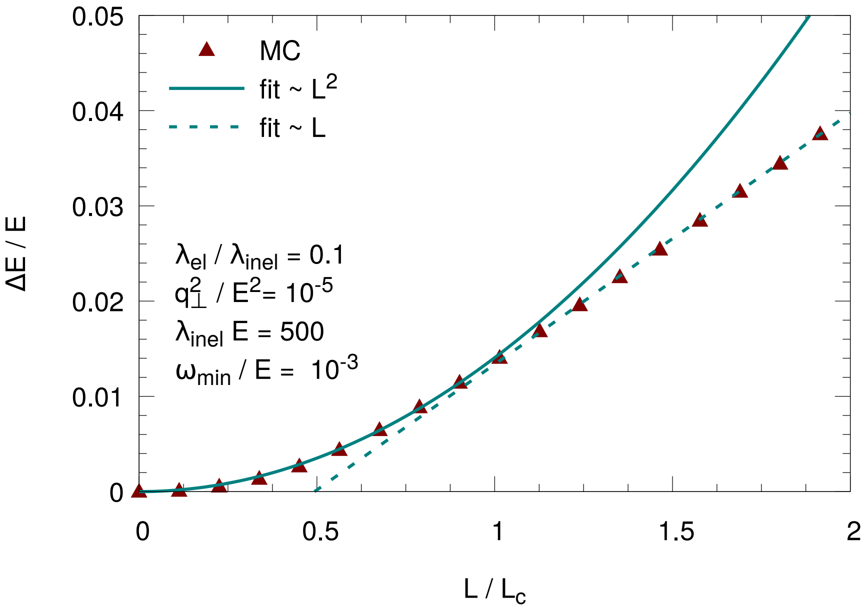

Figure 5.14: Radiative energy loss ΔE of a projectile with energy E depending on the medium length L from the simplified model. The parameters are chosen in correspondence to Fig. 5.13. The critical length scale L_c is given by Eq. (5.24) on page 55. While the points depict the numerical results from the algorithm, the lines represent fits for the thin (solid) and thick (dashed) ΔE behavior from the LPM effect.

features of the non-Abelian LPM effect we have in the following a closer look at the other parameters underlying the simplified model. To this end, we will vary in Figs. 5.15 and 5.16 one of the parameters λ_{inel}, λ_{el} or $q_\perp^2$ while keeping the other parameters fixed at the values discussed previously. This procedure will allow a reliable test for the limits of the proposed algorithm.

Figure 5.15 shows the differential emission rate $\mathrm{d}\Gamma/\mathrm{d}\omega$ for varying elastic mean free path λ_{el} (left) and varying momentum transfer $q_\perp^2$ (right) of a projectile with energy E in a medium with length $L = 10\,\lambda_{\text{inel}}$. And indeed the emission rate shows the characteristic $\sim \omega^{-3/2}$-behavior of the QCD LPM effect. The agreement between Monte-Carlo and analytical expectations is significant. Both energy scales ω_{BH} and ω_{fact} are functions of the input parameters $q_\perp^2$ and λ_{el} in the simplified model. Since the gluon spectrum in the LPM region ($\omega_{\text{BH}} < \omega < \omega_{\text{fact}}$) only depends on $\omega_{\text{BH}} = q_\perp^2 \lambda_{\text{el}}$ (cf. Eq. (5.62) on page 76) one finds similar spectra in the region $\omega > \omega_{\text{BH}}$ for combinations leading to the same ω_{BH} (e.g. $q_\perp^2 = 10^{-5}\,\mathrm{E}^2$, $\lambda_{\text{el}} = \lambda_{\text{inel}}$ and $q_\perp^2 = 10^{-4}\,\mathrm{E}^2$, $\lambda_{\text{el}} = 0.1\,\lambda_{\text{inel}}$). On the other hand, the energy scale $\omega_{\text{fact}} = \left(q_\perp^2/\lambda_{\text{el}}\right) L^2$ depends on the ratio of $q_\perp^2$ and λ_{el}. Therefore the upper limit of the LPM region is different for same values of ω_{BH} and thereby similar slopes. Both effects are visible by a comparison of both plots. The LPM region shrinks for larger elastic mean free paths, since then the chance for the gluon to interact and decrease its formation time decreases. If the elastic mean free path is on the order of the medium length L, corresponding to $\omega_{\text{BH}} = \omega_{\text{fact}}$, the LPM region entirely disappears leading to the situation that either incoherent gluons with $\omega < \omega_{\text{BH}} = \omega_{\text{fact}}$ are produced or gluons that were produced by a totally coherent medium.

The interplay of $q_\perp^2$ and λ_{el} for the gluon emission pattern can further be studied in Fig. 5.16 (left) where we plotted the gluon emissions spectra for constant values of $\hat{q} = q_\perp^2/\lambda_{\text{el}}$ but varying both $q_\perp^2$ and λ_{el}. Although the same value of $\hat{q}$ underlies the

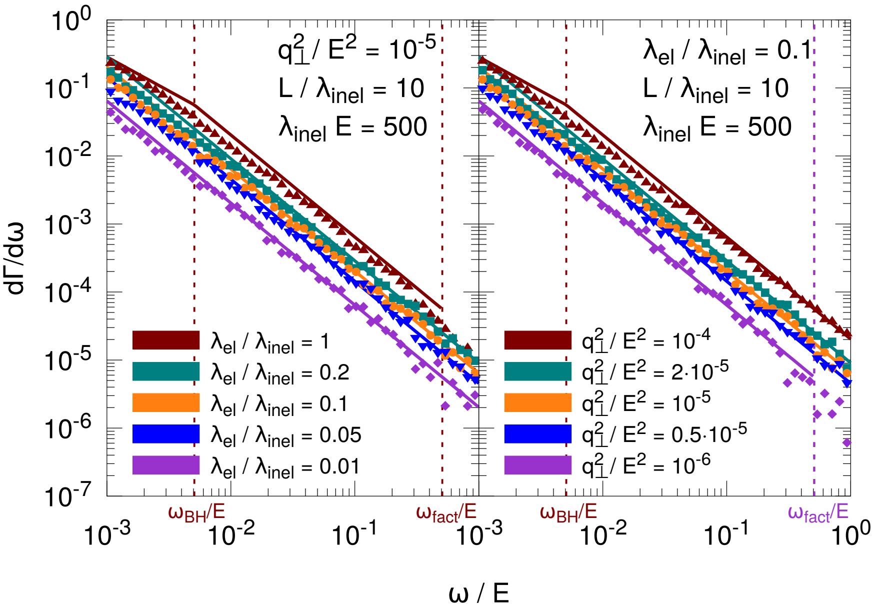

Figure 5.15: Differential emission rate $\mathrm{d}\Gamma/\mathrm{d}\omega$ of a projectile with energy E in a medium with length L from the simplified model for varying elastic mean free path λ_{el} (left) and varying momentum transfer $q_\perp^2$ (right). The respective other parameters are kept fixed. While the points show results from the numerical simulation, the lines represent the analytical dependencies from Eq. (5.62) on page 76. Furthermore, the energy scales ω_{BH} and ω_{fact} are shown for each λ_{el} and $q_\perp^2$ value as dashed lines in the corresponding colors if they lie in the considered ω range.

different calculations the emission spectra differs. This again demonstrates the scaling of $\mathrm{d}\Gamma/\mathrm{d}\omega$ with ω_{BH} instead of $\hat{q}$. For larger values of the momentum transfers and elastic mean free paths the energy scale ω_{BH} increases and thereby the region in which the gluons are produced incoherently.

Since the energy scales ω_{BH} and ω_{fact} are independent from λ_{inel} varying the inelastic mean free path as in Fig. 5.16 (right) does not modify the LPM region in which the $\sim \omega^{-3/2}$-behavior can be reproduced. The shown part of $\mathrm{d}\Gamma/\mathrm{d}\omega$ lies entirely in the LPM region. The smaller the inelastic mean free path and thereby the larger the probability for producing a gluon emission at first hand, the more gluons are also produced after considering the finite formation time. This is in agreement with the dependence as formulated in Eq. (5.62) on page 76.

Finally, after demonstrating that the Monte-Carlo reliably reproduces the $\mathrm{d}\Gamma/\mathrm{d}\omega$ we will discuss the parametric dependencies of the resulting differential energy loss $\mathrm{d}E/\mathrm{d}x$. To this end, we show in Figs. 5.17 and 5.18 results for $\mathrm{d}E/\mathrm{d}x$ depending on the medium length L for fixed projectile energy E with the same parameters used in the previous results for $\mathrm{d}\Gamma/\mathrm{d}\omega$. The scale that is important for the following results are again the length scale $L_c = \sqrt{E/\hat{q}}$ given by the maximum formation time of a gluon. Again, in the $L > L_c$ region the maximum formation time $\tau_f{}^{\mathrm{max}}$ is smaller than the medium length and for $L < L_c$ the maximum formation time can be large enough that the whole medium can be treated as one coherent scattering center and thus the factorization region of the gluon emission rate is active.

In Fig. 5.17 (left) we show the $\mathrm{d}E/\mathrm{d}x$ for varying elastic mean free paths λ_{el} while fixing the other input parameters of the Monte-Carlo algorithm. The numerical simulation

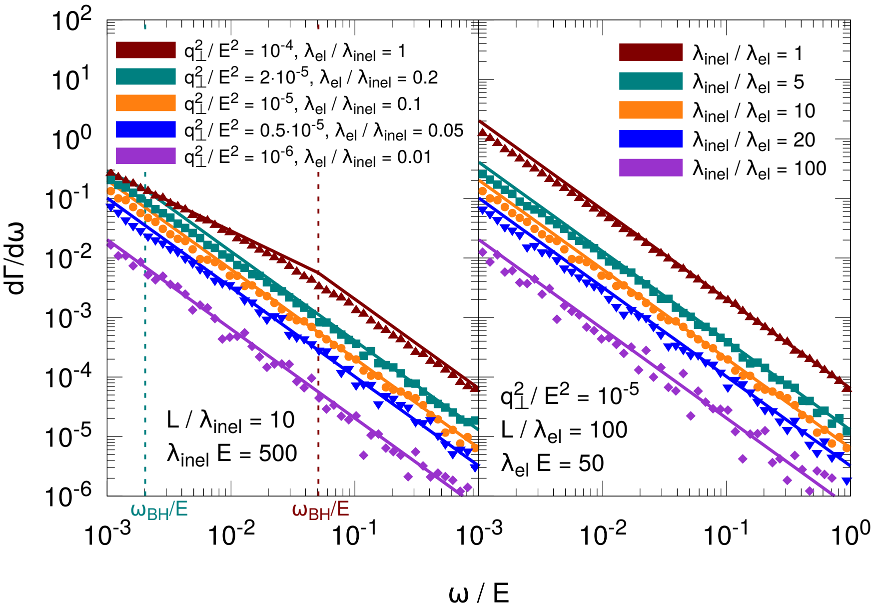

Figure 5.16: Differential emission rate $\mathrm{d}\Gamma/\mathrm{d}\omega$ of a projectile with energy E in a medium with length L from the simplified model for varying elastic mean free path λ_{el} and momentum transfer $q_\perp^2$ but constant momentum broadening $\hat{q} = 5\,\lambda_{\mathrm{inel}}^{-3}$ (left) and for varying inelastic mean free path λ_{inel} (right). The respective other parameters are kept fixed. Again the points show results from the numerical simulation and the lines represent the analytical dependencies from Eq. (5.62) on page 76. The energy scale ω_{BH} is shown as dashed lines in the color corresponding to values of the elastic interaction if they lie in the considered ω range.

agrees again with the analytical expectations. The differential energy loss is the highest for the longest mean free path λ_{el}. We find that with increasing elastic mean free path λ_{el} also the length scale L_c increases. Reason for this is that the formation time of the gluon emissions τ_f goes like $\sim \sqrt{\lambda_{\mathrm{el}}}$ because of the random walk momentum gain per scattering and thereby the contribution of coherent emissions increases with increasing elastic mean free path. On the other hand, for small values of λ_{el} the elastic interactions are so effective that the formation time is negligible and one reaches the incoherent limit of $\mathrm{d}E/\mathrm{d}x \sim \mathrm{const.}$ already for small medium lengths $L \sim \mathcal{O}(2\lambda_{\mathrm{inel}})$.

The radiative energy loss following a variation of the other parameter controlling the elastic interactions, $q_\perp^2$, is shown in Fig. 5.17 (right), again depending on L. Although the behavior seems to be similar to the dependence resulting from the variation of λ_{el} there are subtle differences. Again, varying the elastic momentum transfers $q_\perp^2$ leads to varying values of the critical medium length L_c. However, in Fig. 5.17 (left) the more effective (smaller λ_{el}) the elastic interactions the smaller the resulting differential energy loss $\mathrm{d}E/\mathrm{d}x$. In contrast, we find in Fig. 5.17 (right) that at fixed λ_{el} the differential energy loss increases with more powerful momentum transfers $q_\perp^2$. Reason for this is again the dependence of $\mathrm{d}E/\mathrm{d}x$ on the product ω_{BH} and not $\hat{q}$ as given in Eq. (5.63) on page 76. Moreover, the dependency on $q_\perp^2$ seems to be stronger since not only L_c depends on $q_\perp^2$ but also the energy loss for $L < L_c$ is explicitly depending on $\sim q_\perp^2$.

After varying λ_{el} and $q_\perp^2$ separately, we show in Fig. 5.18 (left) the variation of both while keeping the transport parameter $\hat{q}$ unchanged. Interestingly, although the $\hat{q}$ is the same for all curves, one obtains the strongest energy loss for the more powerful, but rarer

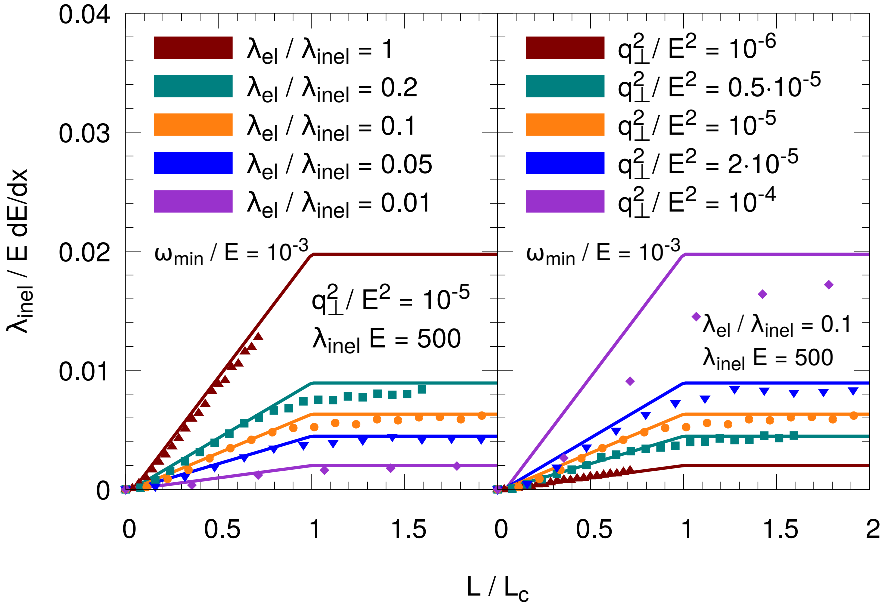

Figure 5.17: Differential radiative energy loss $\mathrm{d}E/\mathrm{d}x$ of a projectile with energy E depending on the medium lengths L from the simplified model for varying elastic mean free path λ_{el} (left) and varying momentum transfer $q_\perp^2$ (right). Same parameters are chosen as in Fig. 5.15. While points represent the numerical results from the simulation, the lines correspond to the analytical derivation from Eq. (5.63) on page 76. The critical length scale L_c is given by Eq. (5.24) on page 55. The minimum gluon energy that contributes to the radiative energy loss is $\omega_{\text{min}} = 10^{-1}$ E.

elastic interactions. Again this represents the dependence of the radiative energy loss on the parameter ω_{BH} that increases for more powerful, rarer gluon interactions.

The last dependence we want to discuss is the $\mathrm{d}E/\mathrm{d}x$ dependence from the inelastic mean free path λ_{inel} shown in Fig. 5.18 (right). As one could expect from our results regarding the differential emission rate also the radiative energy loss scales with $\sim \lambda_{\text{inel}}{}^{-1}$. In other words, the more gluons are initially proposed, the more gluons are available after the algorithm and thereby the more energy is lost from these emissions.

We demonstrated in this section by a simplified approach that the proposed algorithm of Section 5.3.1 indeed reproduces the characteristic features of the non-Abelian LPM effect. These are the findings we further investigate in the following section by applying the algorithm to more realistic interactions, namely Debye-screened leading-order pQCD cross sections for the elastic part and the improved Gunion-Bertsch matrix element for the inelastic interactions.

5.3.3 Momentum broadening of gluons during formation time

One of the major differences between the LPM effect in QED and QCD is the possibility of the emitted gluon to interact with the medium. As we have seen in the simplified model of Section 5.3.2 these interactions modify significantly the formation time of the emitted gluon and thereby the nature of the respective emission. In the simplified algorithm we assumed that a gluon gets constant momentum transfers $q_\perp^2$ in the transverse direction per elastic mean free path λ_{el} during its formation time. However, both the rate for elastic interactions and the corresponding momentum transfer calculated via pQCD are not

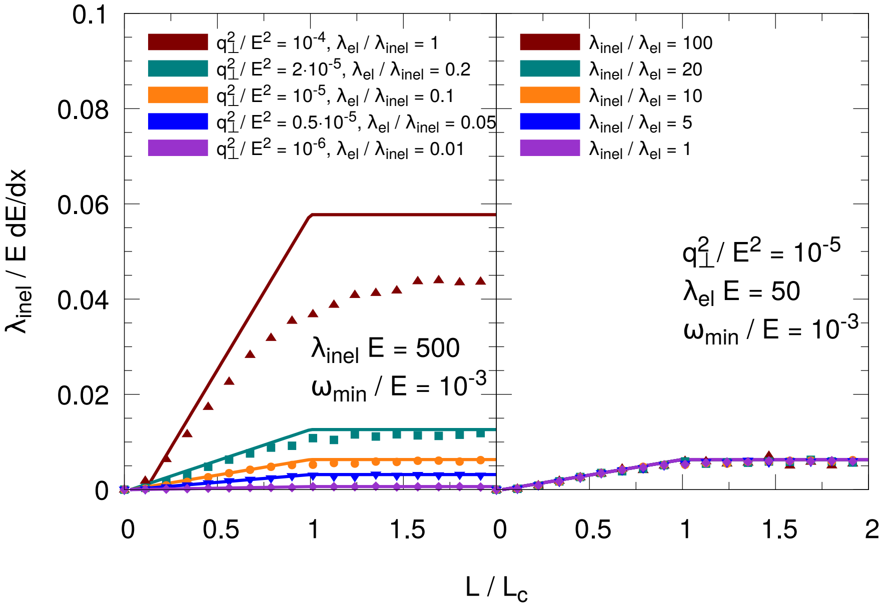

Figure 5.18: Differential radiative energy loss $\mathrm{d}E/\mathrm{d}x$ of a projectile with energy E depending on the medium lengths L from the simplified model for varying elastic mean free path λ_{el} and momentum transfer $q_\perp^2$ but constant momentum broadening $\hat{q} = 5\,\lambda_{\text{inel}}{}^{-3}$ (left) and for varying inelastic mean free path λ_{inel} (right). Same parameters are chosen as in Fig. 5.16. While points represent the numerical results from the simulation, the lines correspond to the analytical derivation from Eq. (5.63) on page 76. The critical length scale L_c is again given by Eq. (5.24) on page 55. The minimum gluon energy that contributes to the radiative energy loss is again $\omega_{\text{min}} = 10^{-1}$ E.

constant but depend on the kinematics of the scatterings, namely the center-of-momentum energy of a scattering and thereby the gluon energy. These dependencies of the elastic gluon scatterings are to be discussed in the following.

Definition of the transverse momentum transfer $q_\perp^2$

Let us assume that a massless parton with momentum $p_1 = (E_1 = \omega, \vec{\mathbf{p_1}})$ scatters with a massless, thermal parton from the medium with $p_2 = (E_2, \vec{\mathbf{p_2}})$ and thereby two partons with momenta $p_3 = (E_3, \vec{\mathbf{p_3}})$ and $p_4 = (E_4, \vec{\mathbf{p_4}})$ are produced. The transverse momentum $q_\perp^2$ that is transfered to $p_{\text{in}} = p_1$ in this scattering follows from geometrical considerations as

$$q_\perp^2 = E_{\text{out}}^2 - \frac{\left(\vec{\mathbf{p}}_{\text{out}} \cdot \vec{\mathbf{p}}_{\text{in}}\right)^2}{E_{\text{in}}^2}\,, \tag{5.65}$$

where p_{out} is the four-momentum of one of the outgoing momenta and p_{in} is, e.g., the four-momentum of the gluon elastically scattering with the background medium during its formation time. Special attention needs to be paid whether $p_{\text{out}} = p_3$ or $p_{\text{out}} = p_4$: If the two outgoing flavors are different from each other, scattering from leading-order pQCD are t-channel ($\hat{t} = (p_1 - p_3)^2$) dominated and therefore $p_{\text{out}} = p_3$. On the other hand, if the outgoing state consists of two partons with the same flavor (e.g. in processes $gg \to gg$ or

$qq \rightarrow qq$), the outgoing partons are interchangeable and one has the freedom to arbitrarily choose either of the outgoing partons[5].

In BAMPS we have access to any information about a single scattering process including, e.g., the Mandelstam variables $\hat{t}$ and $\hat{u}$. In the case of the same outgoing flavor, this information allows us a comprehensible way to correlate ingoing with outgoing partons. If $\hat{t}$ is small, $\left|\hat{t}\right| < \hat{s}/2$, we choose $p_{\mathrm{out}} = p_3$ since then the process will be dominated by the t-channel contributions of the $2 \rightarrow 2$ process. On the other hand, if $\left|\hat{t}\right| > \hat{s}/2$ the u-channel dominates and the outgoing partons switch roles. The most intuitive way is then to choose $p_{\mathrm{out}} = p_4$.

As discussed in Section 3.1, for processes with high CoM energy $\sqrt{\hat{s}}$ or equivalent high gluon energy ω the t-channel $\left|\overline{\mathcal{M}}\right|^2 \sim \hat{t}^{-2}$ underlying the $2 \rightarrow 2$ scatterings dominates. This leads to the commonly used small angle approximation, where it is assumed that for the momentum transfers $q_\perp^2$ of a scattering $\left|\hat{t}\right| = q^2 \approx q_\perp^2$ holds. Although used in previous studies in the BAMPS framework, the small-angle approximation is explicitly not used within this work. Rather all leading-order channels as given in, e.g., Ref. [PS95] and discussed in Chapter 3 are considered for the evaluation of the matrix elements underlying the elastic scatterings.

Differential scattering rate $\mathrm{d}\Gamma/\mathrm{d}q_\perp^2$ from Debye-screened pQCD

In the previous section Section 5.3.2 we used a constant momentum transfer in the elastic gluon scatterings to demonstrate the stochastic LPM algorithm. In contrast, the more realistic interactions from pQCD show a distribution of momentum transfers in each scattering. Figure 5.19 shows the differential scattering rate $\mathrm{d}\Gamma/\mathrm{d}q_\perp^2$ depending on the momentum transfer $q_\perp^2$ of a single elastic scattering of a gluon within a thermal medium with temperature T for different gluon energies $25\,\mathrm{T} < \omega < 250\,\mathrm{T}$. While the scale for the problem at hand is the temperature T, the screening of the divergence is done via a Debye mass $m_D^2 \sim \alpha_s T^2$. Therefore we will present in the following all results scaled either by the temperature T or by the proportional Debye mass m_D^2. Independent from the gluon energy ω, the distribution is dominated by momentum transfers with small $q_\perp^2 \lessapprox m_D^2$. At these small momentum transfers the scattering rate is almost flat, which is a consequence of the Debye screening of the matrix elements prohibiting infinite small values of $q_\perp^2$. On the other hand, the distribution shows a large tail at high $q_\perp^2$ that is constrained kinematically by the energy ω of the gluon. These momentum transfers may transfer a significant amount of transverse momentum to the gluon by one scattering. This is in contrast to the assumptions, e.g., in BDMPS-Z where scatterings of the gluon are multiple but soft.

As we mentioned earlier, scatterings at large parton energies, $\hat{s} \gg m_D^2$, are dominated by t-channel processes. The differential rate of these processes goes like $\mathrm{d}\Gamma/\mathrm{d}q_\perp^2 \sim \left(C_{\mathrm{R}} \alpha_s^2 T^3\right)/(\hat{t} - m_D^2)^2$, where C_{R} is the color factor of the scattering parton and α_s is the QCD coupling constant. This rate leads to increasingly soft momentum transfers that are screened via a Debye mass m_D^2. Furthermore, in the limit $\hat{t} \rightarrow 0$ the longitudinal component of the momentum transfer vanishes so that one may approximate $\hat{t} \approx -q_\perp^2$.

---

[5] An intuitive choice applicable in the case of a high-energy parton scattering with a thermal parton would be to correlate p_{in} with the outgoing parton with the higher energy. This minimizes the energy loss and at the same time forbids that the high energy parton loses a significant amount of its energy while the medium partner has an enormous energy gain. However, if the energy of p_{in} is on the order of the energy of the scattering partner, the same argument does not hold.

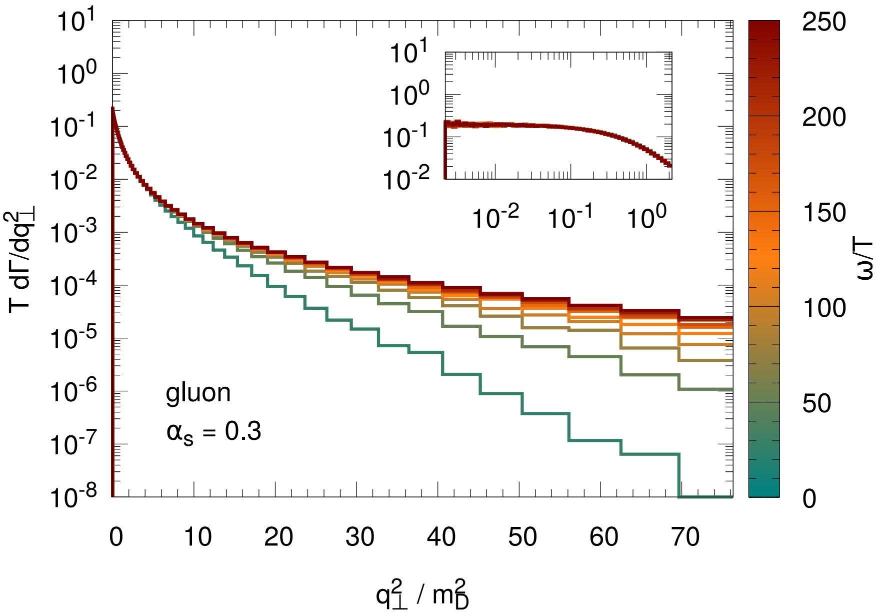

Figure 5.19: Differential scattering rate $\mathrm{d}\Gamma/\mathrm{d}q_\perp^2$ of gluons with different energies ω (shown by different colors) scattering in a thermal medium with temperature T via Debye-screened, leading-order pQCD interactions. $q_\perp^2$ is the squared transverse momentum a gluon obtains in a single elastic interaction as defined in Eq. (5.65) on page 83. The QCD coupling is fixed to $\alpha_s = 0.3$. The inset figure shows a zoom in the small $q_\perp^2 < m_D^2$ region.

The differential scattering rate at larger parton energies then reads

$$\left.\frac{\mathrm{d}\Gamma}{\mathrm{d}q_\perp^2}\right|_{\omega \gg m_D} \approx \frac{C_\mathrm{R}\alpha_s^2 T^3}{(q_\perp^2 + m_D^2)^2}\,. \tag{5.66}$$

And indeed this behavior can be reproduced in the BAMPS simulation as shown in Fig. 5.20, where we plotted the differential scattering rate $\mathrm{d}\Gamma/\mathrm{d}q_\perp^2$ for a quark and a gluon with $E = 250\,\mathrm{T}$ together with corresponding fits.

Furthermore, while our results are calculated via Debye-screened, leading-order pQCD cross sections, the differential elastic scattering rate was also calculated via Hard-Thermal-Loops (HTL) by resumming potential effects from thermal field theory. The elastic scattering rate within HTL reads [AX08; Arn09b; Arm+12]

$$\left.\frac{\mathrm{d}\Gamma}{\mathrm{d}q_\perp^2}\right|_{\mathrm{HTL}} \sim \frac{C_R\alpha_s^2}{\pi}\frac{\mathcal{N}(T)}{q_\perp^2(q_\perp^2 + m_D^2)}\,, \tag{5.67}$$

where $\mathcal{N}(T) = \zeta(3)/\zeta(2)(1 + N_f/4)T^3$ is the weighted number density of the medium with temperature T and C_R the color factor of the scattering parton ($C_\mathrm{F} = \left(N_c^2 - 1\right)/(2N_c) = 4/3$ for a quark and $C_\mathrm{A} = N_c = 3$ for a gluon [Arn09b]). This scattering rate interpolates between the soft and hard momentum transfer region of the HTL calculation [AX08; Arm+12] and corresponds to the collision kernel as used in the AMY formalism that we discuss in Section 5.4. In contrast, the Debye-screened interactions within BAMPS can be understood in the HTL formalism as static scattering centers as they are used, e.g., in the GLV formalism [Arm+12]. In Fig. 5.20 we compare the HTL scattering rate, Eq. (5.67), with the Debye-screened, leading-order interactions. While both

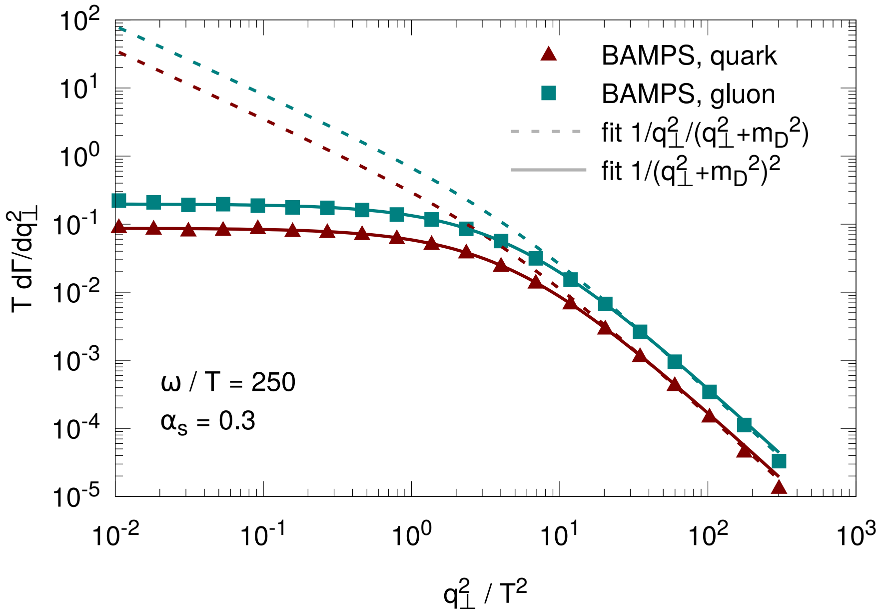

Figure 5.20: Differential scattering rate $\mathrm{d}\Gamma/\mathrm{d}q_\perp^2$ of gluons (red) and quarks (green) with energy $\omega = 250\,\mathrm{T}$ scattering in a thermal medium with temperature T via Debye-screened, leading-order pQCD interactions and QCD coupling $\alpha_s = 0.3$. While points represent the numerical simulations from BAMPS, the solid line represents a fit based on the dependency expected for static scatterings centers [Arm+12]. The dashed line is a fit based on the $\mathrm{d}\Gamma/\mathrm{d}q_\perp^2$ dependence found by the scattering rate calculated in HTL [Arn09b; Arm+12].

approaches agree at large momentum transfers, they show different behaviors for small momentum transfers $q_\perp^2 < m_D^2$. The Debye screening within BAMPS effectively prevents a divergence at small momentum transfers. In contrast this divergence occurs in the HTL case so that arbitrary many, very soft momentum transfers are allowed. Therefore one can conclude that the interactions within BAMPS show the correct large angle behavior but lack the soft momentum transfers in comparison with thermal field theory.

This difference between the interaction in BAMPS and HTL calculation was also found in previous studies within the BAMPS framework [Uph+14]. In these studies the energy loss rate of heavy quark was calculated via the Born term and compared to corresponding HTL calculations. It was found that the Debye mass has to be decreased by an effective factor $\kappa_{22} = 0.2$ in order to find an agreement between the HTL rates and the scattering rate as implemented within BAMPS. Since this study was only valid for heavy quarks and significant differences and difficulties are expected in a corresponding calculation for light partons, we leave such a study for another project but keep in mind the differences between BAMPS and HTL interactions.

Another possibility for improving the elastic scattering rates within BAMPS would be a procedure as in Ref. [KXB18b], where the large angle scattering is described by Debye-screened matrix elements as in BAMPS but the softer interactions are calculated within a Langevin formalism. In this formalism the elastic interactions are not described by single scatterings but as a diffusion process based on the momentum broadening parameter $\hat{q}$, whose values is calculated within HTL. This procedure would bring the BAMPS approach well beyond its current model assumptions and it remains to be seen whether this approach is also applicable in the context of the BAMPS framework.

Total scattering rate Γ_{22} from Debye-screened pQCD

We have seen that the momentum transfers $q_\perp^2$ resulting from interactions calculated in leading-order pQCD follow a distribution that is dominated by small $q_\perp^2$ interactions with a long tail up to high $q_\perp^2$. In order to further characterize the elastic scattering we show in Fig. 5.21 the 2 → 2 scattering rate Γ_{22} (Fig. 5.21a) and the mean momentum transfer $q_\perp^2$ (Fig. 5.21b) that a quark or gluon experiences in a single scattering depending on the parton energy ω for different values of the medium temperature T. We show Γ_{22} of a quark or gluon (scaled by the color factor $\frac{C_\mathrm{F}}{C_\mathrm{A}} = 4/9$) projectile depending on the parton energy ω in units of the Debye mass m_D for different temperatures T. The total scattering rate can be analytically obtained by integrating the differential scattering rate $\mathrm{d}\Gamma/\mathrm{d}q_\perp^2$,

$$\Gamma_{22} = \int\limits_0^{q^2_{\perp;\mathrm{max}}} \mathrm{d}q_\perp^2 \, \frac{\mathrm{d}\Gamma}{\mathrm{d}q_\perp^2} \,, \tag{5.68}$$

where $q^2_{\perp;\mathrm{max}}$ is the maximum momentum transfer in a single elastic scattering. This maximum momentum transfer can be approximated by $q^2_{\perp;\mathrm{max}} \sim \alpha_s \sqrt{\omega T^3}$ [Car09; Arm+12] so that $q^2_{\perp;\mathrm{max}}/m_D^2 \sim \sqrt{\omega/T}$. At large parton energies $\omega > m_D$ the processes are dominated by t-channel processes showing the same ω-independent behavior for both quarks and gluons. This constant dependence can be understood by employing the differential scattering rate at $\omega \gg m_D$ from Eq. (5.66) on page 85,

$$\Gamma_{22}\big|_{\omega \gg m_D} \sim \frac{C_\mathrm{R} \alpha_s^2 T^3 q^2_{\perp;\mathrm{max}}}{m_D^2 \left(q^2_{\perp;\mathrm{max}} + m_D^2\right)} \sim \frac{C_\mathrm{R} \alpha_s T}{1 + \sqrt{\frac{T}{\omega}}} \,. \tag{5.69}$$

The limit $\omega \gg m_D$ also implies $\omega \gg T$, so that the rate at large ω converges to

$$\lim_{\omega \to \infty} \Gamma_{22} \sim C_\mathrm{R} \alpha_s T \,. \tag{5.70}$$

Figure 5.21a shows that the parametrization Eq. (5.69) not only explains the gluon and quark rate at larger ω but also the rate at soft quark energies, so one can infer $\Gamma_{22}^q \approx \Gamma_{22}\big|_{\omega \gg m_D}$.

While the scattering rate of the quark decreases with decreasing energy, the gluon rate diverges for softer energies $\omega \to 0$. Reason for this difference is the four-gluon channel of $\mathrm{gg} \to \mathrm{gg}$ that only exists for gluons and not for quarks. Interactions of a soft parton with thermal partons have a small average CoM energy $\hat{s}$. In these processes the s-channel processes are active but the t- and u-channels are negligible. For gluons the dominant s-channel at these energies is the four-gluon channel $\mathrm{d}\sigma/\mathrm{d}t \sim \alpha_s^2/\hat{s}$ (compare Chapter 3). One can show that the four-gluon vertex, which does not have a dependence on the scattering angle, gives a contribution to the rate of the gluon that goes like $\sim T^2/\omega$ so that the total gluon rate reads

$$\Gamma_{22}^g \sim \frac{C_\mathrm{A} \alpha_s^2 T^3 q^2_{\perp;\mathrm{max}}}{m_D^2 \left(q^2_{\perp;\mathrm{max}} + m_D^2\right)} + \frac{C_\mathrm{A} \alpha_s^2 T^2}{\omega} \sim C_\mathrm{A} \alpha_s T \left(\frac{1}{1 + \sqrt{\frac{T}{\omega}}} + \frac{\alpha_s T}{\omega} \right) , \tag{5.71}$$

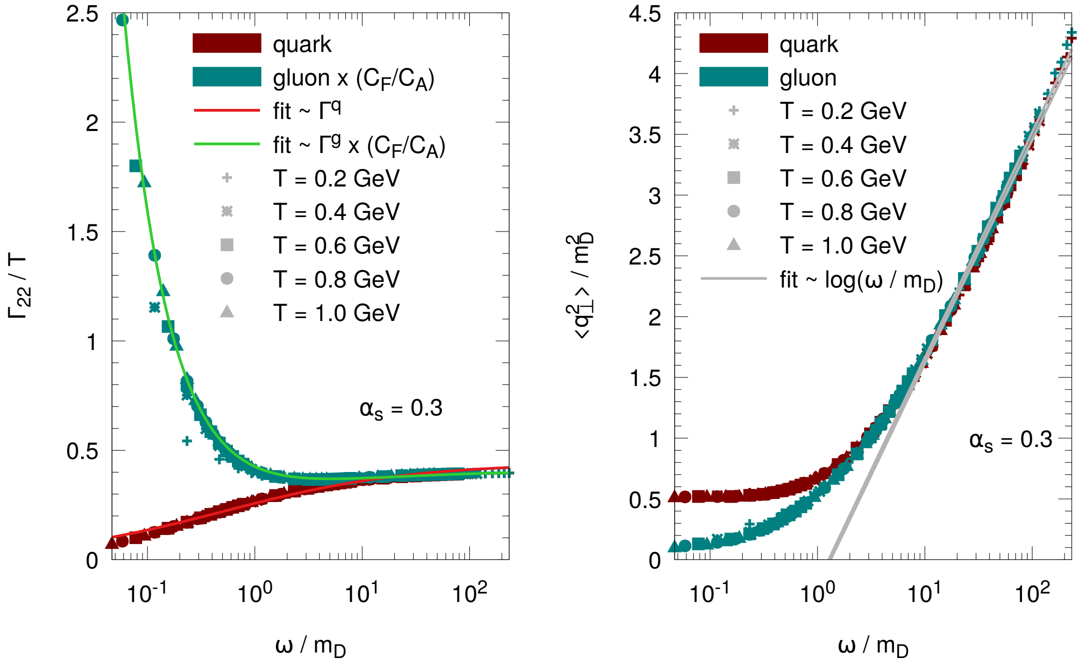

(a) **(b)**

Figure 5.21: Energy ω dependence of the total scattering rate Γ_{22} (Fig. 5.21a) and mean transverse momentum transfer $\langle q_\perp^2 \rangle$ (Fig. 5.21b) of a single elastic scattering via Debye-screened, leading-order pQCD interactions for a quark (red) or a gluon (green, rate scaled by $C_\mathrm{F}/C_\mathrm{A}$). The QCD coupling is fixed to $\alpha_s = 0.3$. While the points shows the numerical results from BAMPS, the solid lines denote the analytical dependencies discussed in the text. Different point types represent different temperatures T in the calculation and serve as an additional confirmation of the expected scaling behavior in the numerical simulation.

which is validated by the fit in Fig. 5.21a. For $\omega \gg m_D$ the four-gluon contribution vanishes and the gluon rate is again dominated by the t-channel.

Mean transverse momentum transfer $\langle q_\perp^2 \rangle$ from Debye-screened pQCD

After discussing how often an elastic scattering occurs we show in Fig. 5.21b the mean momentum transfer in a single scattering. The mean momentum transfer can be obtained via the differential scattering rate $\mathrm{d}\Gamma/\mathrm{d}q_\perp^2$ by

$$\langle q_\perp^2 \rangle = \frac{\int \mathrm{d}q_\perp^2 \, \frac{\mathrm{d}\Gamma}{\mathrm{d}q_\perp^2} q_\perp^2}{\int \mathrm{d}q_\perp^2 \, \frac{\mathrm{d}\Gamma}{\mathrm{d}q_\perp^2}} \tag{5.72}$$

For harder parton energies $\omega \gtrapprox m_D$ the mean momentum transfer obeys a logarithmic ω dependence for both quarks and gluons. This logarithmic dependence is again a typical signature of the t-channel that dominates at high parton energies. If we employ the approximated scattering rate of Eq. (5.66) on page 85 for $\omega \gg m_D$ we obtain

$$\langle q_\perp^2 \rangle\big|_{\omega \gg m_D} \sim \alpha_s T^2 \log\left(\frac{q_{\perp;\mathrm{max}}^2}{m_D^2}\right) \sim \alpha_s T^2 \log\left(\frac{\omega}{T}\right). \tag{5.73}$$

Furthermore, although quark and gluons experience different processes in the medium, the dominance of the t-channel leads to the same mean momentum transfer for quark and gluons with higher energy ω. In contrast, at softer energies $\omega \lessapprox m_D$ the mean momentum transfer of a quark becomes significantly harder than the momentum transfer of a gluon. Reason for this difference is again the four-gluon channel that is not screened by a Debye mass. This allows arbitrary soft momentum transfers of the soft gluon in contrast to a quark where the minimum momentum transfer is limited by the Debye mass. Furthermore, another reason for the flatness of the mean momentum transfer for $\omega < m_D$ is that at these small energies effectively two thermal partons interact with each other. The distribution of the thermal scattering partner then smears the mean momentum transfer and the dependence on ω becomes weaker. The only scale of the scattering is then T.

Momentum broadening parameter $\hat{q}$ from Debye-screened pQCD

The parameter that is commonly used in the jet quenching community for characterizing medium-induced gluon radiation is the already discussed momentum broadening parameter $\hat{q}$. $\hat{q}$ describes how capable the medium distributes transverse momentum per unit path length to a parton. This momentum transfer then may act as a source for inducing gluon radiation. Furthermore, as we have seen earlier, the elastic scatterings that a parton suffers in a QCD medium may be numerous and mainly soft. Therefore other models often treat the interactions not as single scatterings but as a diffusion process, where $\hat{q}$ is the corresponding transport parameter [KXB18b]. While in principle such a treatment, especially of the soft sector, would also be possible within BAMPS, such an approach has difficulties in non-thermal situations, where an ad-hoc way to define a temperature is not trivial. Therefore we stick within this work to the default picture of individual scatterings within BAMPS.

In our approach of individual binary scatterings, $\hat{q}$ can be written as

$$\hat{q} = \int \mathrm{d}q_\perp^2 \, q_\perp^2 \frac{\mathrm{d}\Gamma}{\mathrm{d}q_\perp^2} = \Gamma_{22} \left\langle q_\perp^2 \right\rangle = \frac{\left\langle q_\perp^2 \right\rangle}{\lambda_{22}} \tag{5.74}$$

The resulting $\hat{q}$ of a quark or gluon (again scaled by $C_\mathrm{F}/C_\mathrm{A}$) with energy ω traversing a static medium with temperature T is shown in Fig. 5.22. Due to the almost constant scattering rate at higher parton energies, the increase of $\hat{q}$ for $\omega \gg m_D$ originates from the increasing mean momentum transfer $q_\perp^2$ of an energetic parton. Therefore $\hat{q}$ depends logarithmically on the parton energy ω and scales with the respective color factor C_F or C_A. Using again the differential scattering rate given by Eq. (5.66) on page 85, the $\hat{q}$ parameter at $\omega \gg m_D$ can be estimated to

$$\hat{q}\big|_{\omega \gg m_D} \sim C_\mathrm{R} \alpha_s^2 T^3 \log\left(1 + \frac{q_{\perp;\mathrm{max}}^2}{m_D^2}\right) \overset{q_{\perp;\mathrm{max}}^2 \gg m_D^2}{\approx} C_\mathrm{R} \alpha_s^2 T^3 \log\left(\frac{\omega}{T}\right). \tag{5.75}$$

This dependence on ω is in agreement with other calculations from HTL [Arm+12].

In contrast, at smaller energies $\omega < m_D$ the $\hat{q}$ dependence of quarks and gluons again differs due to the different underlying s-channel processes. The decreasing scattering rate of quarks at soft energies leads also to a decreasing $\hat{q}$ for small ω. On the other hand, the diverging scattering rate of a soft gluon is counteracted by arbitrary small momentum

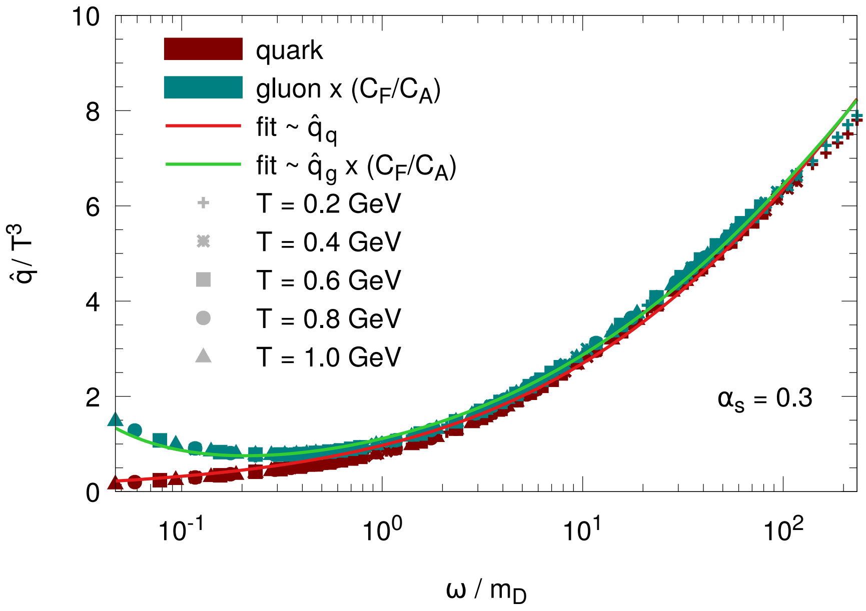

Figure 5.22: Dependence of the momentum broadening parameter $\hat{q}$ from elastic scatterings via Debye-screened, leading-order pQCD interactions for a quark (red) or a gluon (green, scaled by $C_\mathrm{F}/C_\mathrm{A}$) on the parton energy ω. The QCD coupling is fixed to $\alpha_s = 0.3$. While the points show the numerical results from BAMPS, the solid lines denote the analytical dependencies discussed in the text. Different point types represent different temperatures T and serve as an additional confirmation of the expected scaling behavior in the numerical simulation.

transfers. Consequently, the contribution of the four-gluon channel to $\hat{q}$ is

$$\hat{q}_\text{four gluon} \sim \frac{C_\mathrm{A}\alpha_s^2 T^4}{\omega} \,. \tag{5.76}$$

In result, the ω dependence of $\hat{q}$ for a quark or gluon can be summarized by

$$\begin{aligned} \hat{q}_q &\sim C_\mathrm{F}\,\alpha_s^2\,T^3 \log\left(1+\frac{q^2_{\perp;\max}}{m_D^2}\right) \sim C_\mathrm{F}\,\alpha_s^2\,T^3 \log\left(1+\sqrt{\frac{\omega}{T}}\right) \\ \hat{q}_g &\sim C_\mathrm{A}\alpha_s^2 T^3\left(\log\left(1+\frac{q^2_{\perp;\max}}{m_D^2}\right)+\frac{T}{\omega}\right) \\ &\sim C_\mathrm{A}\alpha_s^2 T^3\left(\log\left(1+\sqrt{\frac{\omega}{T}}\right)+\frac{T}{\omega}\right) . \end{aligned} \tag{5.77}$$

Figure 5.22 validates the found analytical dependencies of $\hat{q}$ on the parton energy by comparison to the numerical results.

Momentum broadening parameter $\hat{q}$ via Svetitsky formalism

To further elucidate the dependencies of $\hat{q}$ we confront our calculation with a semi-analytical calculation. This calculation is based on Ref. [Sve88], where diffusion coefficients of charm quarks evolving via pQCD interactions in the QGP were calculated. The charm diffusion coefficient B_0 of Ref. [Sve88] corresponds to the momentum broadening parameter $\hat{q}$ of light partons if the mass of the quark is set to $m = 0$ and the corresponding degeneracy factors are considered. The calculation of $\hat{q}$ is then achieved semi-analytically by folding an integration over the matrix elements with a thermal distribution for the scattering partner, what can be seen as averaging the coefficients over a thermal distribution. However, since the original calculation was done for charm quarks scattering with a medium consisting of gluons and light quarks, the discussed case of same outgoing flavors was not considered in the original calculations. In our notation, for the transport parameter $\hat{q}$ of a massless parton with energy ω in the process $i \to j$ then follows[6]

$$\hat{q}_{i\to j} = \frac{1}{512\pi^4}\frac{1}{\omega}\int\limits_0^\infty \mathrm{d}E_2\, E_2 \hat{f}(E_2) \int\limits_{-1}^{1} \mathrm{d}(\cos\chi) \int\limits_0^{2\pi} \mathrm{d}(\phi_{\text{CoM}}) \times$$
$$\times \left[\int\limits_0^1 \mathrm{d}(\cos\theta_{\text{CoM}})\, \frac{1}{\gamma_c} \sum_{i\to j} |\mathcal{M}|^2_{i\to j}\, q_\perp^2(\vec{\mathbf{p}}_3) + \int\limits_{-1}^{0} \mathrm{d}(\cos\theta_{\text{CoM}})\, \frac{1}{\gamma_c} \sum_{i\to j} |\mathcal{M}|^2_{i\to j}\, q_\perp^2(\vec{\mathbf{p}}_4) \right], \tag{5.78}$$

where χ is the angle between the two incoming partons, ϕ_{CoM} and θ_{CoM} are the azimuthal and polar angle of the outgoing partons in the center-of-momentum frame. $1/\gamma_c \sum |\mathcal{M}|^2$ is the sum over the relevant Debye-screened matrix elements for the process as derived in Section 3.1 and $q_\perp^2(\vec{\mathbf{p}}_{\text{out}})$ is the single transverse momentum transfer as defined in Eq. (5.65) on page 83. The split of the integral $\int \mathrm{d}(\cos\theta_{\text{CoM}})$ reflects the different outgoing flavors that are considered for calculating $q_\perp^2$. The total $\hat{q}$ of a quark or gluon is obtained by a sum of the contribution of the different processes while considering symmetries of the incoming/outgoing partons and the respective degeneracy factors of quarks $\nu_q = \nu_{\text{spin}}\nu_{\text{anti}}N_f N_c = 36$ and gluons $\nu_g = \nu_{\text{polarization}}\left(N_c^2 - 1\right) = 16$,

$$\hat{q}_g = \hat{q}_{\text{gg}\to X} + \nu_q\, \hat{q}_{\text{g}q\to\text{g}q} = \frac{\nu_g}{2}\left(\hat{q}_{\text{gg}\to\text{gg}} + N_f\, \nu_{\text{anti}}\, \hat{q}_{\text{gg}\to q\bar{q}}\right) + \nu_q\, \hat{q}_{\text{g}q\to\text{g}q} \tag{5.79}$$

$$\hat{q}_q = \frac{\nu_{\text{anti}}\, N_f}{2}\hat{q}_{qq\to qq} + \nu_g\, \hat{q}_{\text{g}q\to\text{g}q} + \nu_{\text{spin}}\, \nu_{\text{anti}}\, N_c\, (N_f - 1)\, \hat{q}_{qq'\to qq'} + \nu_{\text{anti}}\, N_f\, \hat{q}_{q\bar{q}\to X}\,, \tag{5.80}$$

where $\hat{q}_{q\bar{q}\to X} = \hat{q}_{q\bar{q}\to q\bar{q}} + \left((N_c - 1)/\left(N_f\right)\right)^2 1/2\, \hat{q}_{\text{gg}\to q\bar{q}} + \nu_{\text{anti}}\, \hat{q}_{q\bar{q}\to q'\bar{q}'}$.

The calculation of $\hat{q}$ via the formalism of Ref. [Sve88] is independent from the numerical calculations within BAMPS and are supposed to provide further confidence in the numerical simulations. And indeed Fig. 5.23 shows that the numerical simulations (shown by points) agree with the semi-analytical calculations (shown by the solid line) both for quarks and gluons. An additional advantage of the procedure by Svetitsky is that one easily can identify the contributions of the different processes by using only the corresponding matrix elements in the semi-analytical calculations. Consequently, we are able to support the assumption that the $\hat{q}$ of gluons is dominated at $\omega < m_D$ by the process $\text{gg} \to \text{gg}$, while at larger energies both processes $\text{gg} \to \text{gg}$ and $\text{g}q \to \text{g}q$ both contribute similarly to $\hat{q}$. In contrast, the process $\text{gg} \to q\bar{q}$ is negligible for $\hat{q}$ over the entire ω range. Furthermore, the main contribution to the momentum broadening of quarks comes also from the process $\text{g}q \to \text{g}q$. The influence of the corresponding process to $\text{gg} \to \text{gg}$, $qq \to qq$, is already significantly suppressed.

---

[6] In the original Ref. [Sve88] an overall factor 2 was missed that we correctly included.

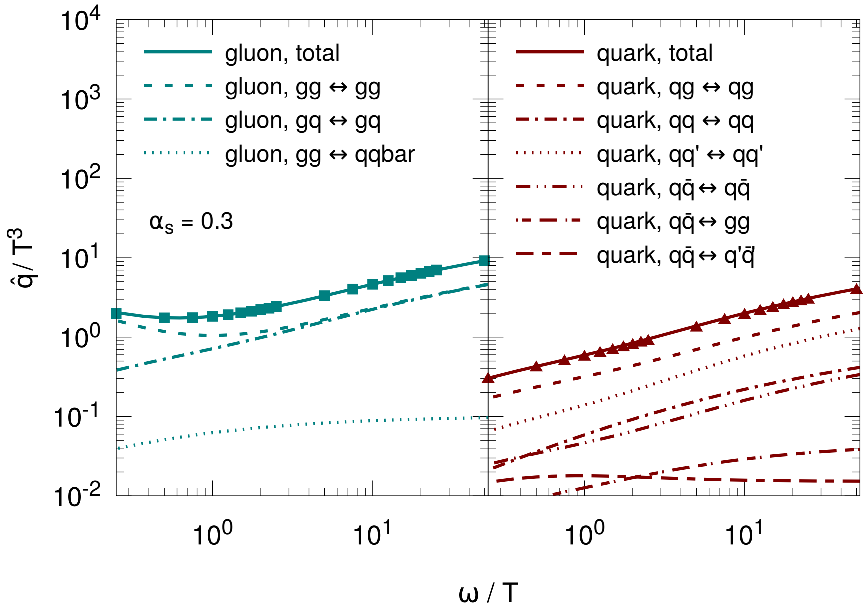

Figure 5.23: Dependence of the momentum broadening parameter $\hat{q}$ from elastic scatterings via Debye-screened, leading-order pQCD interactions for the different processes of a quark (left) or a gluon (right) on the parton energy ω. The QCD coupling is fixed to $\alpha_s = 0.3$. While the points shows the numerical results from BAMPS, the solid lines denote a semi-analytical calculation via the Svetitsky formalism [Sve88]. Different line styles denote the different processes of a quark or gluon in leading-order pQCD.

5.3.4 Screening the $k_\perp$ divergence of the Gunion-Bertsch matrix element

In this section we discuss how the processes as calculated in the (improved) Gunion-Bertsch approximation differ to the simplified inelastic interactions of Section 5.3.2. To this end we investigate the emission rate directly from the $2 \to 3$ process calculated via the GB matrix element without any further LPM suppression. This result may then serve as a reference for a spectrum with no LPM suppression in the following sections, where we discuss the suppression originating from the algorithm introduced in Section 5.3.1.

As mentioned in the course of Section 5.2 one serious issue when dealing with partonic processes calculated in pQCD is the screening of soft and collinear divergences. One of the benefits of the previous θ-LPM method for modeling the LPM effect in BAMPS was that the theta function in the matrix elements cured the $k_\perp$-divergence immanent in the Gunion-Bertsch matrix element. By forbidding very soft and collinear emissions with small $k_\perp$ that lead to large formation times longer than the mean free path any divergence for $k_\perp$ disappears. However, since we are interested in replacing the θ-LPM by the stochastic algorithm proposed in Section 5.3.1 while still employing the matrix elements from the Gunion-Bertsch approximation, special attention needs to be paid to the treatment of these soft, collinear gluon emissions.

One straight-forward way to cure the $k_\perp$ divergence would be to introduce a global, fixed $k_\perp$ cutoff $k_{\perp;\,\mathrm{min}} \sim \mathrm{const.}$. However, such a procedure would neglect any dependence of the screening on both the emitting projectile and the scattering partner from the medium and gives the same screening for any radiative process. Another choice for a potential screening scale would be the temperature T or the Debye mass m_D. Such a choice of screening the $k_\perp$ divergence would be similar to assigning a thermal mass to the emitted gluons. This approach was followed, for example, in Ref. [KXB18b]. However, this choice of scaling neglects on the one hand the energy scale of the emitting parton by setting the scale solely by the scattering partner. On the other hand, since both T and m_D are macroscopic quantities their application in non-thermal situations as, e.g., in the expanding environment is at least questionable. Furthermore, massive gluons would lead to a contradiction in the other assumptions within the BAMPS framework, which is formulated for massless partons on the mass shell. Therefore we choose a more comprehensible way by a $k_\perp$ cutoff that depends on the scale $\sqrt{\hat{s}}$ of each individual inelastic $2 \to 3$ scattering. This treatment considers the energy scale of the emitting parton as well as the scale given by the medium. The minimum $k_\perp$ in the CoM frame of a $2 \to 3$ scattering is then

$$k_{\perp;\,\mathrm{min}}{}^{\mathrm{CoM}} = \xi_{\mathrm{LPM}} \sqrt{\hat{s}}\,, \tag{5.81}$$

where we defined ξ_{LPM} as the proportionality factor between the cutoff and the center-of-momentum energy $\sqrt{\hat{s}}$ of the $2 \to 3$ process. Due to kinematics the maximum value for ξ_{LPM} is $\xi_{\mathrm{LPM}} = 1/2$ (cf. Eq. (5.37) on page 58). In contrast to the screening underlying the θ-LPM effect this screening does not introduce an additional dependence on the rapidity y but is symmetric in the forward- and backward rapidity. Furthermore, the center-of-momentum energy is a Lorentz invariant quantity and can be evaluated in the CoM frame of the respective $2 \to 3$ scattering as well as the lab frame. As a remark, the choice of $k_{\perp;\,\mathrm{min}} \sim \sqrt{\hat{s}}$ for screening the $k_\perp$ divergence should be understood as an arbitrary choice without a profound physical reasoning. However, as we will see in subsequent sections this choice can reproduce other theoretical models and experimental data after adjusting the specific value of ξ_{LPM}. In contrast, we have checked that a screening with, e.g., $k_{\perp;\,\mathrm{min}} \sim m_D$ does not result in a $\sim \sqrt{E}$ dependence of $\mathrm{d}E/\mathrm{d}x$ when applied together with the stochastic LPM algorithm.

The Gunion-Bertsch matrix element is symmetric in the gluon rapidity y (in the CoM frame). However, the cutoff in the θ-LPM method given in Eq. (5.36) on page 58 favored gluon emissions in the backward rapidity region as we demonstrated in Fig. 5.7. The reason for this preference was the Lorentz boost that was needed for comparing the formation time evaluated in the CoM frame and the mean free path determined in the lab frame (cf. Section 5.2). In contrast, the condition from Eq. (5.81) is independent from y and thereby preserves the symmetry of the gluon rapidity. This is verified in Fig. 5.24 where we plot the $y - k_\perp$ phase space in the CoM frame of gluon emissions off a quark with $E = 250\,\mathrm{T}$ scattering with a fixed "thermal" particle with $p_{\mathrm{partner}} = (3T, -3T, 0, 0)$ in a thermal bath with temperature T. These are again typical values expected for a high energy jet traversing the medium produced in ultra-relativistic heavy-ion collisions. As in Fig. 5.7 the solid lines represent the kinematical limits for gluon emissions as given in Eq. (5.37) on page 58. The colored dashed lines are the minimum limits of $k_\perp$ given by three different ξ_{LPM} values. Indeed the resulting gluon emissions are symmetric in y without a preferred emission direction. As expected, lower ξ_{LPM} values allow smaller $k_\perp$ values and due to the $\sim 1/k_\perp^2$ dependence of the GB matrix element, these small $k_\perp$ values are even sampled preferably. Furthermore, since with lower ξ_{LPM} values the transverse component of the gluon momentum may obtain smaller values at same gluon energy there is more phase space available in the longitudinal component of the gluon momentum. Therefore with smaller ξ_{LPM} values, also higher rapidities can be reached. At fixed $k_\perp$ the emissions with large rapidity lead to more energetic gluon emissions in the lab frame via $\omega_{\mathrm{lab}} = k_\perp \cosh\left(y_{\mathrm{CoM}} + \Delta y_{\mathrm{CoM}\to\mathrm{lab}}\right)$ due to the Lorentz boost with $\beta = \tanh\left(\Delta y_{\mathrm{CoM}\to\mathrm{lab}}\right)$.

The softer $k_\perp$ values that are allowed when choosing smaller ξ_{LPM} values are additive to

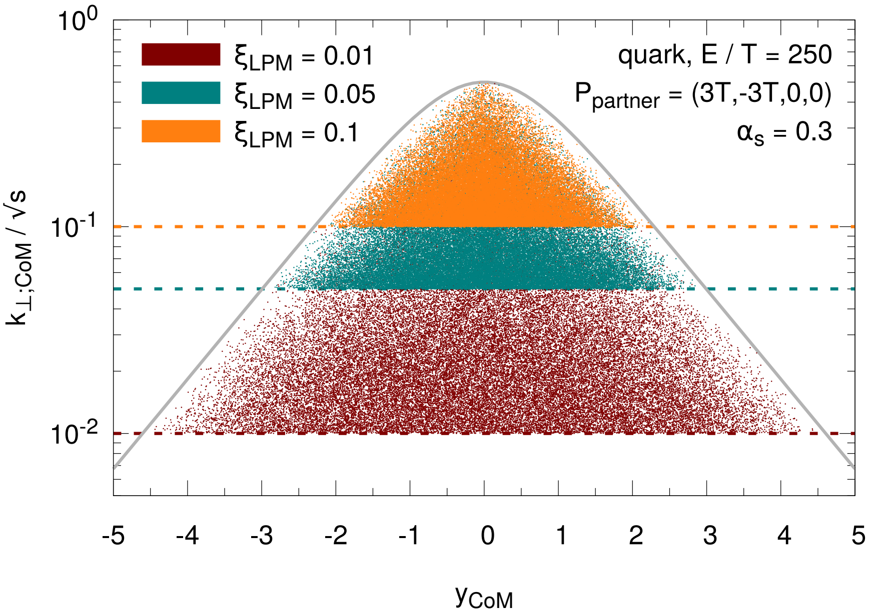

Figure 5.24: Phase space distribution of gluon emissions in the y_{CoM}-$k_{\perp;\text{CoM}}$ plane from the Gunion-Bertsch matrix element without LPM suppression screened via different $\xi_{\text{LPM}} = \{0.01; 0.05; 0.1\}$ for a quark projectile with energy $E = 250\,\text{T}$ scattering with parton with fixed "thermal" momentum $p_{\text{partner}} = (3\,\text{T}, -3\,\text{T}, 0, 0)$ and a fixed QCD coupling $\alpha_s = 0.3$. Each dot represents a single gluon emission. While the solid lines depicts the limit imposed by the θ-LPM method, the dash-dotted lines show the kinematical limit for the different projectile energies.

the differential emission rate $\mathrm{d}\Gamma/\mathrm{d}k_\perp$ and thereby increase the total emission rate. To this end we show in Fig. 5.25 the differential emission rate $\mathrm{d}\Gamma/\mathrm{d}k_\perp$ now evaluated in the lab frame for a quark with energy $E = 25\,\text{T}$ and $E = 250\,\text{T}$ scattering with a thermal parton in a medium with temperature T. Since we consider in this section only the bare Gunion-Bertsch spectrum screened via $\sqrt{\hat{s}}$ the rates are length-independent and therefore follow a Bethe-Heitler emission pattern. As expected, a decreasing ξ_{LPM} value indeed allows more small $k_\perp$ gluon emissions that are added to the differential rate $\mathrm{d}\Gamma/\mathrm{d}k_\perp$ at small $k_\perp$ values while leaving the emissions at high $k_\perp$ unaffected for both projectile energies. Consequently, the available phase space for collinear gluon emissions increases the total emissions rate with decreasing ξ_{LPM}. In contrast to the $k_\perp$ limit underlying Fig. 5.24 the $k_\perp$ cutoff in Fig. 5.25 is broadened due to the thermal distribution of the scattering partner.

Figure 5.26 shows the differential emission rate $\mathrm{d}\Gamma/\mathrm{d}\omega$ of a quark projectile with $E = 25\,\text{T}$ and $E = 250\,\text{T}$. Again the energy of both the gluon and the projectile is evaluated in the lab frame. In order to clearly visualize the ω scaling behavior we weight the rate by ω and show ω in units of the projectile energy E. The minimum gluon energy is limited by $\omega_{\text{min}} \geq k_{\perp;\,\text{min}}$. Consequently, smaller ξ_{LPM} values also allow softer (smaller ω) gluon emissions. In the limit of soft gluon emissions $\omega \ll E$ the Gunion-Bertsch matrix element shows the already employed $\sim 1/\omega$ behavior from the simplified model of Section 5.3.2. While the deviations from $1/\omega$ at small ω again arise from the thermal distribution of the scattering partner, the deviations at high ω originate from the limited phase space in a $2 \to 3$ process to convert the total CoM energy of the Bremsstrahlung process into the energy of the gluon. The total available energy in the $2 \to 3$ process needs to be distributed among the three outgoing partons. Moreover, the variation of ξ_{LPM} leads

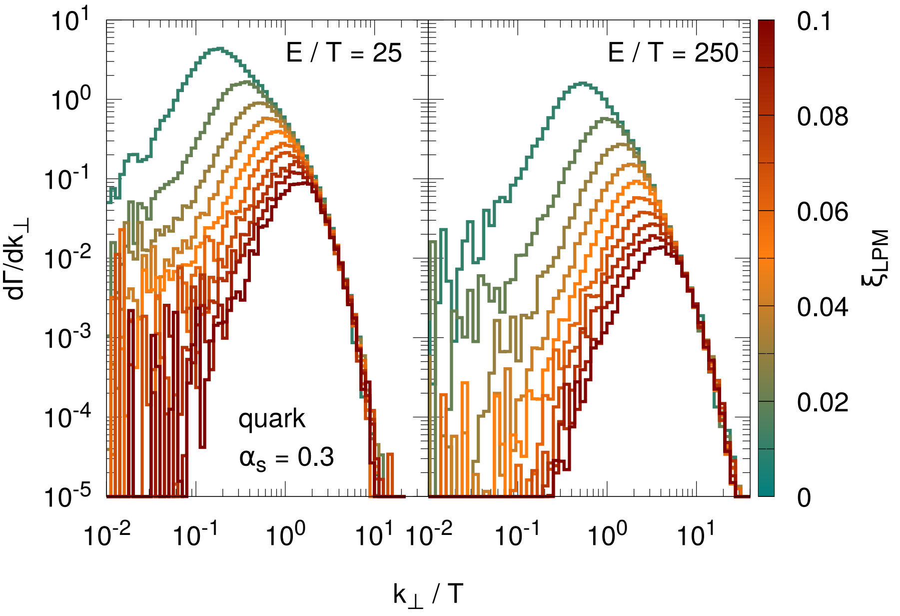

Figure 5.25: Differential emission rate $\mathrm{d}\Gamma/\mathrm{d}k_\perp$ from the Gunion-Bertsch matrix element without LPM suppression screened with varying ξ_{LPM} for a quark projectile with energy $E = \{25\,\mathrm{T}; 250\,\mathrm{T}\}$ scattering in a thermal medium with temperature T and a fixed QCD coupling $\alpha_s = 0.3$. The different values of ξ_{LPM} are given by varying colors from small ξ_{LPM} (green) to larger ξ_{LPM} (red) values.

not only to contributions at soft ω but also at intermediate and high ω values up to $\mathcal{O}(E)$. The increased emission rate is distributed over the whole ω range. In other words, while small ξ_{LPM} values add softer $k_\perp$ emissions, these emissions do not have to be soft (small ω) but can also be energetic in the longitudinal direction. This is in agreement with Fig. 5.24 where we found an increasing phase space at high rapidities with decreasing ξ_{LPM}. This is equivalent with higher-ω gluons in the lab frame.

Apparently not only the range for $k_\perp$ and ω but also the rate Γ_{GB} for producing gluons via the screened Gunion-Bertsch matrix element depends on the screening parameter ξ_{LPM}. Figure 5.27 shows the dependence of the total emission rate Γ_{GB} depending on the projectile energy E for different values of ξ_{LPM}. The radiative matrix element in Gunion-Bertsch approximation factorizes into an elastic part and a probability P_g to emit a gluon (s. Section 3.2.1. Since we neglect at the moment the LPM effect and screen the $k_\perp$ divergence without an iterated mean free path, P_g does not depend on the flavor of the two initial partons initiating the $2 \to 3$ process. In contrast the elastic part of the Gunion-Bertsch matrix element depends on the flavor of the initial scattering partons. This dependence leads to a scaling for the GB emission rate of quarks and gluons with the ratio of QCD color factors $C_{\mathrm{F}}/C_{\mathrm{A}}$. This expectation is confirmed in Fig. 5.27 where lines represent the rate of a quark projectile and the points are the corresponding calculations for a gluon scaled by the color factors. The emission rate for energetic projectiles with $E \gg T$ is almost independent from E. As expected, smaller values of ξ_{LPM} allow more gluon radiations and thereby show an increasing rate Γ_{GB}.

The ξ_{LPM} dependence of the rate can be further studied in Fig. 5.28 where we show Γ_{GB} vs. ξ_{LPM} for a quark projectile and different projectile energies E (shown by different colors). Almost independent from the projectile energy E the best fit for the rate is

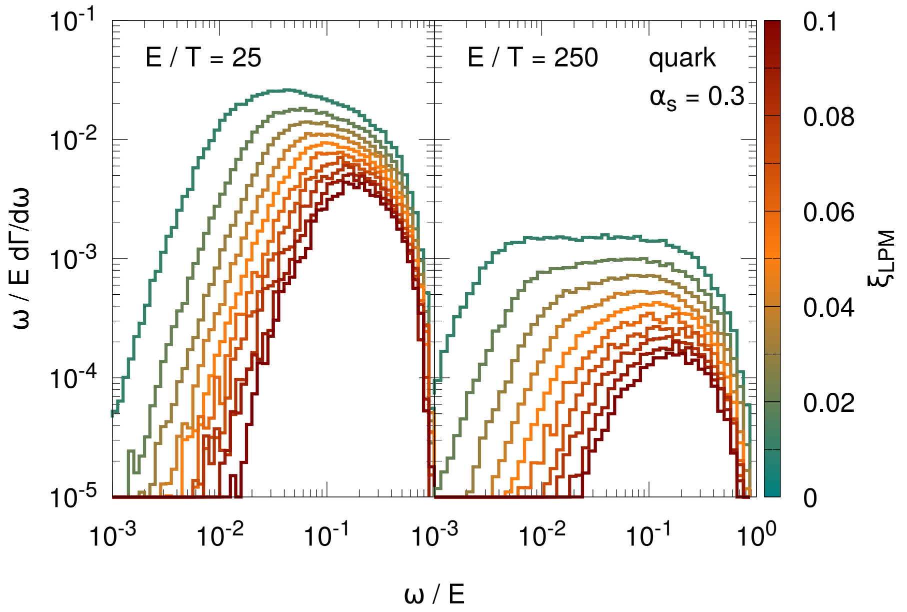

Figure 5.26: Differential emission rate $\mathrm{d}\Gamma/\mathrm{d}\omega$ from the Gunion-Bertsch matrix element without LPM suppression screened with varying ξ_{LPM} for a quark projectile with energy $E = \{25\,\mathrm{T}; 250\,\mathrm{T}\}$ scattering in a thermal medium with temperature T and a fixed QCD coupling $\alpha_s = 0.3$. The different values of ξ_{LPM} are given by varying colors from small ξ_{LPM} (green) to larger ξ_{LPM} (red) values. To better visualize the actual share of radiative energy loss at ω on the total radiative energy loss we scale the rate by ω/E.

$\Gamma \sim \log 1/\xi_{\mathrm{LPM}} + B$, where B is a constant. Consequently, the rate logarithmically diverges for decreasing ξ_{LPM}.

In summary, the differential emission rate $\mathrm{d}\Gamma/\mathrm{d}\omega$ resulting from interactions obeying the improved Gunion-Bertsch matrix element with an effective $k_\perp$ screening $\sim \sqrt{\hat{s}}$ shows indeed a similar characteristic ω^{-1} dependence as assumed in Section 5.3.2. The value of ξ_{LPM} determines both the total emission rate corresponding to the inelastic mean free path λ_{inel} and at the same time the soft scale of the gluon emission ω_{min}. We will see in the subsequent section how this dependence on ξ_{LPM} ends up in the resulting emission rates after applying the sLPM algorithm and discuss how one can fix the value of ξ_{LPM} by comparison to other theoretical approaches.

5.3.5 Stochastic LPM with pQCD cross sections

Although the introduced, simplified model for LPM suppression from Section 5.3.2 gave important first evidence that the proposed algorithm from Section 5.3.1 indeed reproduces signatures of the non-Abelian LPM effect, the assumptions underlying the interactions of the model are rather coarse. Therefore we will study in this section how the algorithm for stochastically describing the coherence from the LPM effect can be applied to more realistic partonic interactions. While the inelastic interactions of the projectile will be described by the Bremsstrahlung $2 \to 3$ processes in the improved Gunion-Bertsch approximations, the elastic interactions of the gluons during the formation time are calculated, as usual in BAMPS, based on Debye-screened, leading-order pQCD cross sections. The previous sections Sections 5.3.3 and 5.3.4 introduced the dependencies following from these microscopic pQCD interactions. In this section we discuss the possible consequences

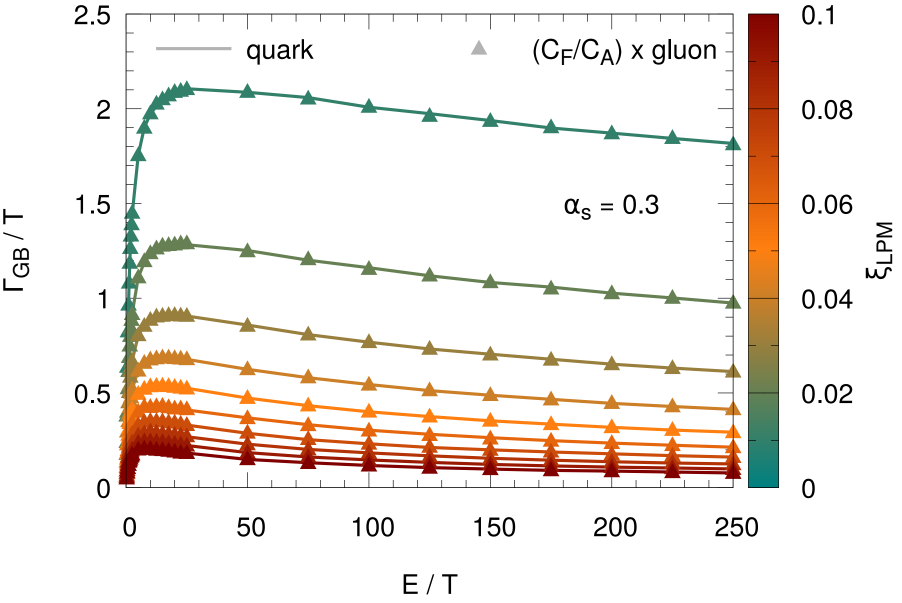

Figure 5.27: Total emission rate Γ_{GB} from the Gunion-Bertsch matrix element without LPM suppression screened with varying ξ_{LPM} for a quark (lines) and gluon (points, scaled by $\frac{C_{\mathrm{F}}}{C_{\mathrm{A}}} = 9/4$) projectile depending on the projectile energy E. The QCD coupling is fixed to $\alpha_s = 0.3$. The different values of ξ_{LPM} are again given by varying colors from small ξ_{LPM} (green) to larger ξ_{LPM} (red) values.

of going from fixed elastic and inelastic interactions to more realistic, energy-dependent pQCD cross sections. To this end, we investigate the dependencies of the scales crucial for the stochastic LPM, namely ω_{BH}, ω_{fact} and L_{c}. Based on these findings we study how the resulting spectra of gluon emissions and thereby the radiative energy loss are modified.

The stochastic LPM algorithm based on pQCD interactions is schematically shown in Algorithm 4. As in the simplified model we approximate both the emitting projectile as well as the emitted gluon as eikonal for the results presented in this section. In other words, the emitting parton does not lose energy or momentum after an emission but keeps flying in the same direction with the same energy as before the emission. Furthermore, although the emitted gluons scatter elastically with the background medium during their formation time and thereby accumulate transverse momentum, we assume that the energy of the gluons stays unmodified at the energy that the gluon had when it was produced initially in the $2 \to 3$ process. This procedure simplifies the investigations of the parametric dependencies significantly. When studying the evolution of partons and their shower in a static medium (s. Chapter 6) or an expanding heavy-ion collision (s. Chapter 7) we will loose this approximation later.

Emission rate from GB matrix element and constant momentum transfers

Before investigating the sLPM method together with ω-dependent elastic interactions we set first the stage by combining the Gunion-Bertsch matrix element screened via ξ_{LPM} with constant momentum transfers of the emitted gluons during their formation time as introduced in Section 5.3.2. Figure 5.29 shows the differential emission rate $\mathrm{d}\Gamma/\mathrm{d}\omega$ for a fixed value $\xi_{\mathrm{LPM}} = 0.01$ and varying constant momentum transfer $q_\perp^2$ or varying elastic mean free path λ_{el}. For comparison, also the distribution without the stochastic LPM

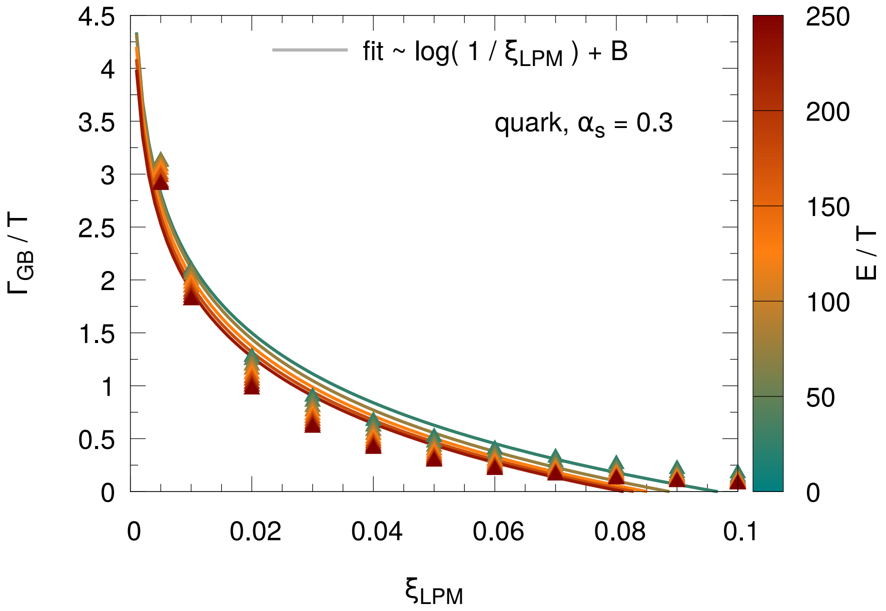

Figure 5.28: Total emission rate Γ_{GB} from the Gunion-Bertsch matrix element without LPM suppression depending on the screening parameter ξ_{LPM} for a quark projectile with different energies E given by varying colors from small E (green) to larger E (red) values. The QCD coupling is fixed to $\alpha_s = 0.3$. While the points show the numerical results, the lines are fits for each energy $\Gamma \sim \log(1/\xi_{\mathrm{LPM}})$, where B is an unitless fit parameter.

algorithm as presented in Section 5.3.4 is depicted in dashed lines. While the distribution shows the expected $\mathrm{d}\Gamma/\mathrm{d}\omega \sim \omega^{-3/2}$ behavior for very soft ($q_\perp^2 \to 0$) but numerous ($\lambda_{\mathrm{el}} \to 0$) elastic scatterings, at harder and rarer scatterings the differential emission rate approaches the $\sim \omega^{-1}$ behavior of the improved Gunion-Bertsch approximation without LPM suppression. This finding gives a first hint that the sLPM algorithm indeed reproduces the expected scaling from the LPM effect for specific values of the elastic interactions.

Energy scales ω_{BH} and ω_{fact} with pQCD interactions

One consequence of using pQCD matrix elements in the sLPM method is that the parameters, that control how gluons are modified during their formation times, are not constant but depend on the gluon energies. Furthermore, instead of a constant momentum transfer, the gluons suffer different $q_\perp^2$ from a distribution that is mainly soft but has a long tail at hard momentum transfers. As discussed in Section 5.1.2, if the formation time is longer than the mean free path of a gluon, $\tau_f > \lambda_{\mathrm{el}}$, its elastic scatterings during the formation time contribute coherently to the emission. By employing the calculations for $q_\perp^2$, Γ_{22} and $\hat{q}$ of Section 5.3.3, we can estimate via $\tau_f = \omega/\hat{q}$ the mean formation time of an emission obeying pQCD interactions. Since these parameters itself now depend on ω the resulting formation time reads with Eq. (5.77) on page 90,

$$\tau_f(\omega) \sim \sqrt{\frac{\omega}{\hat{q}^g(\omega)}} \sim \sqrt{\frac{\omega}{C_{\mathrm{A}} \alpha_s^2 T^3 \left(\log\left(1+\sqrt{\frac{\omega}{T}}\right) + \frac{T}{\omega}\right)}}\,. \tag{5.82}$$

Figure 5.30 compares this formation time $\tau_f(\omega)$ with the elastic mean free path $\lambda_{22}(\omega) = \Gamma_{22}^{-1}(\omega)$ of a gluon with energy ω/T by employing the results from Section 5.3.3. Please

Algorithm 4: Schematic view of the algorithm for the stochastic LPM effect based on pQCD interactions.

```
At $t = 0$ initialize projectile with energy $E$
while $t < L$ do
    Sample medium partons based on thermal distribution
    foreach medium parton do
        Calculate probability $P_{23}$ for Bremsstrahlung process of projectile with medium
          parton
        if $r \in [0;1) < P_{23}$ then initialize trial gluon
            Sample $k_{\mathrm{t;\,initial}}$ and $\omega$ of trial gluon from GB matrix element screened via $\xi_{\mathrm{LPM}}$
            Set $t_{\mathrm{init}} = t$ and $N_{\mathrm{coh}} = 1$ for this emission
            Add gluon to list of trial gluon emissions
    foreach trial gluon do
        Calculate formation time $\tau_f = \omega/k_\perp^2$
        if $|(t + \Delta t) - t_{init}| < \tau_f$ then gluon is not formed yet
            Sample medium partons based on thermal distribution
            foreach medium parton do
                Calculate probability $P_{22}$ for elastic scattering of trial gluon with medium
                  parton
                if $r \in [0;1) < P_{22}$ then initialize scatter gluon
                    Sample $q_\perp^2$ from elastic $2 \to 2$ process
                    Assign new momentum to trial gluon
                    Increase $N_{\mathrm{coh}} = N_{\mathrm{coh}} + 1$
        else gluon is formed
            if random number $r \in [0;1) < 1/N_{coh}$ then gluon is accepted
                Consider gluon for $\mathrm{d}\Gamma/\mathrm{d}\omega$, $\mathrm{d}\Gamma/\mathrm{d}k_\perp$ and $\mathrm{d}E/\mathrm{d}x$ results
            else
                Discard gluon emission
    $t = t + \Delta t$ ;
    Propagate projectile and trial gluons to time $t$
Discard all gluon emissions still in formation time
```

note again that the momentum transfer $\langle q_\perp^2 \rangle$ is again only the mean momentum transfer that is dominated by the soft momentum transfers and considers the hard $q_\perp^2$ tail only to a limited extent.

For hard gluon emissions with energy $\omega > m_D$ we obtain for the mean formation time with the results from Section 5.3.3

$$\tau_f(\omega)\big|_{\omega \gg m_D} \sim \sqrt{\frac{\omega}{C_{\mathrm{A}} \alpha_s^2 T^3 \log\left(\frac{\omega}{T}\right)}} \,. \tag{5.83}$$

On the other hand, we found that the rate Γ_{22} for elastic gluon scattering at $\omega \gg m_D$ is independent from ω and reads $\Gamma_{22}^g \sim C_{\mathrm{A}} \alpha_s T$. Consequently, the condition for a radiative process to be coherent, $\tau_f > \lambda_{\mathrm{el}}$, can be written in terms of the gluon energy

$$\frac{\omega}{T} > \frac{1}{C_{\mathrm{A}}} \log\left(\frac{\omega}{T}\right) . \tag{5.84}$$

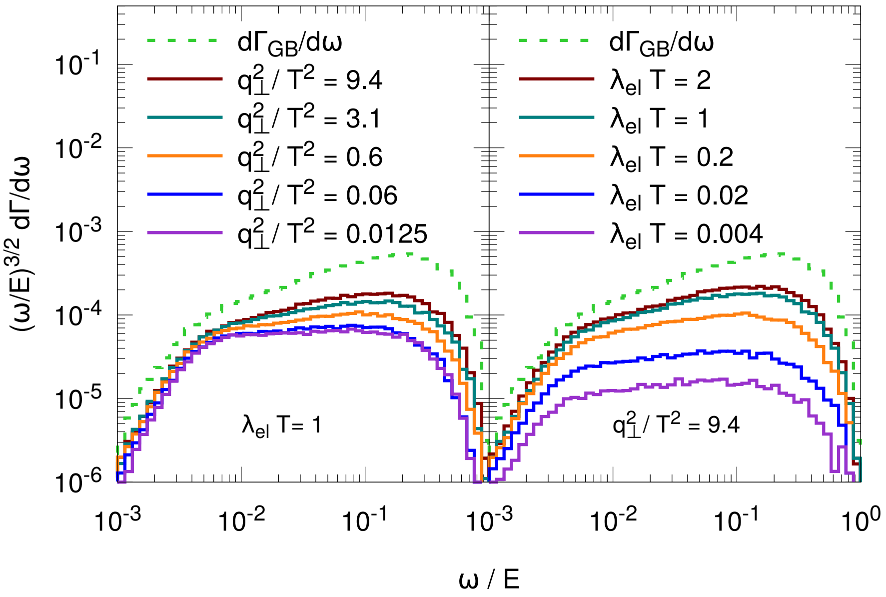

Figure 5.29: Differential emission rate $\mathrm{d}\Gamma/\mathrm{d}\omega$ of a quark projectile with energy $E = 250\,\mathrm{T}$ in a medium with length $L = 20\,\mathrm{T}^{-1}$ from radiative processes calculated by the Gunion-Bertsch matrix element screened via $\xi_{\mathrm{LPM}} = 0.01$ that are suppressed by the sLPM algorithm with fixed elastic interactions of the gluons during τ_f. The QCD coupling is fixed to $\alpha_s = 0.3$. The left plot shows $\mathrm{d}\Gamma/\mathrm{d}\omega$ for different momentum transfers $q_\perp^2$ with constant elastic mean free path λ_{el}. The right plot shows the opposite case: While the elastic mean free path is varied, the momentum transfer is kept fixed. The green dashed line shows the corresponding $\mathrm{d}\Gamma/\mathrm{d}\omega$ behavior if the emissions from the Gunion-Bertsch matrix element are not suppressed by the sLPM algorithm. To better visualize the expected behavior of the non-Abelian LPM effect we scale the differential emission rate by $\omega^{-3/2}$.

One can show that this condition is fulfilled for $\omega > 0$. Hence, when employing the discussed ω-dependent pQCD cross sections energetic gluon emissions are expected to be on average always in the regime of coherent gluon emissions (LPM regime) and at least one elastic scattering occurs during the formation time. This finding is supported by Fig. 5.30, where $\tau_f(\omega) > \lambda_{\mathrm{el}}(\omega)$ for $\omega > m_D$.

Furthermore, at softer gluon energies $\omega < m_D$ the mean formation time can be evaluated with the help of Eq. (5.77) on page 90 to

$$\tau_f(\omega)\big|_{\omega<m_D} \sim \sqrt{\frac{\omega}{\frac{C_{\mathrm{A}}\alpha_s^2T^4}{\omega}}} = \frac{\omega}{\sqrt{C_{\mathrm{A}}}\alpha_s T^2}\,. \tag{5.85}$$

Correspondingly, the mean free path of soft gluons underlying pQCD cross sections goes like

$$\lambda_{\mathrm{el}}\big|_{\omega<m_D} \sim \frac{\omega}{C_{\mathrm{A}}\alpha_s^2 T^2}\,. \tag{5.86}$$

Interestingly both the mean formation time and the mean free path scale linearly with gluon energy ω. So with decreasing gluon energy, both the formation time decreases and the rate of the gluon increases due to the four-gluon vertex. Hence it follows that $\tau_f \approx \lambda_{\mathrm{el}}$ for soft gluon emissions with $\omega < m_D$. This scaling behavior is reproduced by

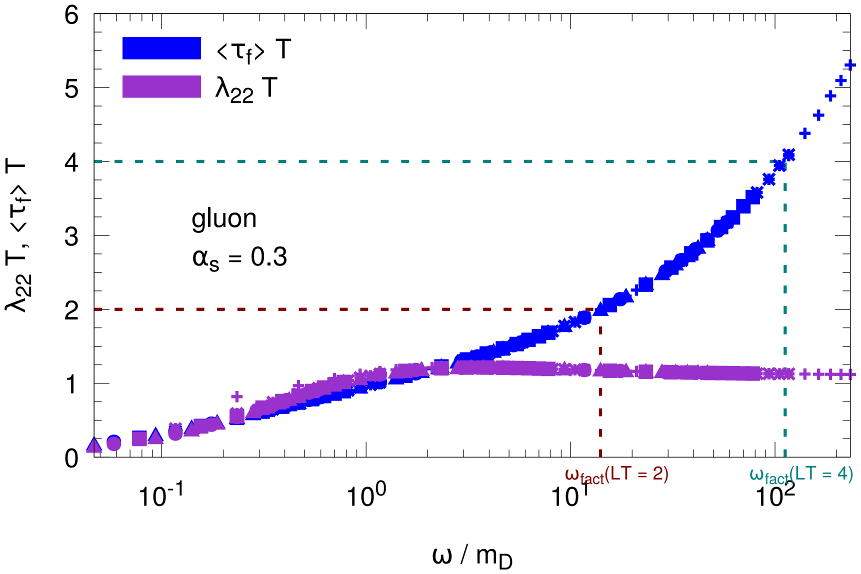

Figure 5.30: Comparison of the mean formation time $\tau_f = \sqrt{\omega\lambda_{22}/q_\perp^2}$ and the elastic mean free path λ_{22} of a gluon with energy ω from leading-order pQCD as discussed in Section 5.3.3. The scales ω_{fact} for $L = \left\{2\,\mathrm{T}^{-1}; 4\,\mathrm{T}^{-1}\right\}$ are highlighted by dashed lines from the condition $\tau_f(\omega) = L$. Different point types represent different temperatures T in the numerical simulation and serve as an additional cross check of the expected scaling behavior.

the numerical calculations shown in Fig. 5.30. Moreover, one can parametrically estimate that an incoherent regime of gluon emissions, $\tau_f < \lambda_{\text{el}}$, is not depending on the gluon energy but only on the QCD coupling

$$\alpha_s \lesssim \frac{1}{\sqrt{C_{\text{A}}}} = \sqrt{\frac{1}{3}}\,. \tag{5.87}$$

In the simplified model of Section 5.3.2 the elastic interactions were determined by fixed values and we could define energy scales $\omega_{\text{BH}} \sim {\lambda_{\text{el}}}^2\hat{q}$ (cf. Eq. (5.18) on page 54) and $\omega_{\text{fact}} \sim \hat{q}L^2$ (cf. Eq. (5.21) on page 55) differing between the Bethe-Heitler, LPM and factorization regime. Obviously the same arguments do not hold in the case of ω-dependent elastic scatterings, since for all ω regions coherent emission processes with $\tau_f \gtrapprox \lambda_{\text{el}}$ may occur and therefore a clean definition of ω_{BH} is not possible. The scale ω_{fact}, at which the mean formation time is longer than the medium length L and gluons cannot be formed, can be derived as

$$\omega_{\text{fact}}(\omega) \sim \hat{q}(\omega)L^2 \sim \hat{q}(w)\big|_{\omega\gg m_D} L^2 \sim C_{\text{A}}\alpha_s^2 T^3 \log\left(\frac{\omega}{T}\right)L^2\,. \tag{5.88}$$

In Fig. 5.30 one can read the numerical results for two different medium lengths, $\omega_{\text{fact}}^{\text{eff}}\left(L = 2\,\mathrm{T}^{-1}\right) \approx 14\,\mathrm{m_D}$ and $\omega_{\text{fact}}^{\text{eff}}\left(L = 4\,\mathrm{T}^{-1}\right) \approx 110\,\mathrm{m_D}$. For $\omega > \omega_{\text{fact}}$ the emission rate is strongly suppressed since gluons can only be formed by stochastically large momentum transfers during the formation time.

In conclusion, the ω-dependence of the elastic scatterings lead to the finding that on average all gluon emissions are produced coherently. At $\omega > m_D$ the formation time increases with increasing energy while the rate is constant. On the other hand, at soft

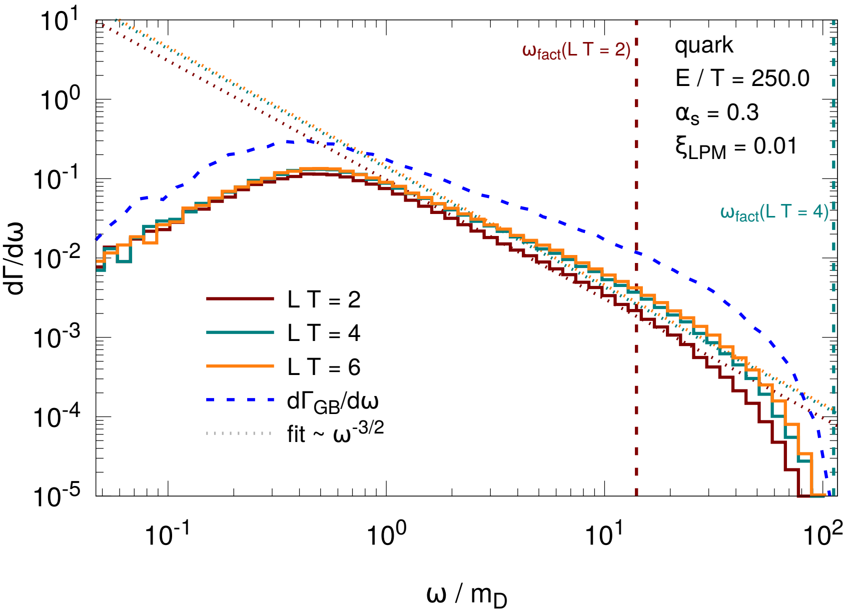

Figure 5.31: Differential emission rate $\mathrm{d}\Gamma/\mathrm{d}\omega$ of a quark with energy $E = 250\,\mathrm{T}$ from the sLPM approach in a medium with temperature T and different lengths $L = \left\{2\,\mathrm{T}^{-1}; 4\,\mathrm{T}^{-1}; 6\,\mathrm{T}^{-1}\right\}$. The QCD coupling is fixed to $\alpha_s = 0.3$. The $k_\perp$ of the initial $2 \to 3$ process is screened via $\xi_{\mathrm{LPM}} = 0.01$ and the corresponding $\mathrm{d}\Gamma/\mathrm{d}\omega$ directly from the Gunion-Bertsch matrix element without LPM suppression can be found by the blue dashed line. The energy scales ω_{fact} found in Fig. 5.30 are denoted by dashed vertical lines depending on L. We fit the expected behavior $\mathrm{d}\Gamma/\mathrm{d}\omega \sim \omega^{-3/2}$ in the intermediate ω region from the non-Abelian LPM effect shown by the dotted lines separately for each L value.

gluon energies $\omega < m_D$ the average formation time is comparable with the elastic mean free path. Therefore, one can infer that there is no gluon energy region where gluons are produced mainly incoherently. However, one feature of the presented algorithm is that it is formulated in a stochastic way: Whether a gluon emission is considered as incoherent or coherent is dynamically evaluated for each emission. Consequently, also a gluon whose mean free path is on the same order as the formation time can be produced incoherently if it is decided stochastically that it does not scatter during its formation time.

Differential emission rate from sLPM with pQCD interactions

After introducing the energy scales underlying the LPM effect in terms of ω-dependent quantities, we show in Fig. 5.31 the differential emission spectra $\mathrm{d}\Gamma/\mathrm{d}\omega$ of an eikonal energetic quark with energy $E = 250\,\mathrm{T}$ (corresponding to $E = 100\,\mathrm{GeV}$ at $T = 0.4\,\mathrm{GeV}$) for different medium lengths L. In Fig. 5.31 and all other results in this section we keep the minimum initial transverse momentum $k_\perp$ of a $2 \to 3$ process at one percent of the CoM energy by fixing the screening parameter to $\xi_{\mathrm{LPM}} = 0.01$[7]. We depict the discussed effective energy scales $\omega_{\mathrm{fact}}^{\mathrm{eff}}$ by dashed vertical lines in the corresponding colors as in Fig. 5.30. The blue dashed curve denotes the differential emissions rate $\mathrm{d}\Gamma_{\mathrm{GB}}/\mathrm{d}\omega$ of the Gunion-Bertsch matrix element without any stochastic LPM suppression as calculated in Section 5.3.4.

---

[7] We study the sensitivity of the stochastic LPM algorithm on ξ_{LPM} later in this section.

As defined in Section 5.3.1 the sLPM algorithm suppresses emissions $\sim 1/N_{\text{coh}}$, where N_{coh} are the number of elastic scatterings during the gluon formation time. The resulting differential emission rate is then

$$\frac{\mathrm{d}\Gamma}{\mathrm{d}\omega} \sim \frac{1}{N_{\text{coh}}} \frac{\mathrm{d}\Gamma_{\text{GB}}}{\mathrm{d}\omega} \tag{5.89}$$

According to the considerations regarding the energy scales we can write the mean suppression factor as

$$\frac{1}{N_{\text{coh}}(\omega)} \sim \frac{\lambda_{\text{el}}(\omega)}{\tau_f(\omega)} \sim \frac{1}{\Gamma_{22}^{g}(\omega)\tau_f(\omega)} \tag{5.90}$$

with $\tau_f(\omega)$ given in Eq. (5.82) on page 98 and $\Gamma_{22}^{g}(\omega)$ from Eq. (5.71) on page 87. Again we are interested in the limits $\omega > m_D$ and $\omega < m_D$. For hard gluons the suppression factor evaluates to

$$\left.\frac{1}{N_{\text{coh}}}\right|_{\omega > m_D} \sim \sqrt{\frac{\log\left(\frac{\omega}{T}\right)}{C_{\text{A}}\frac{\omega}{T}}}\,. \tag{5.91}$$

Different to the discussed estimation in the simplified model, the ω-dependence of the elastic scatterings adds a logarithmic term to the expected $\mathrm{d}\Gamma/\mathrm{d}\omega \sim \omega^{-3/2}$ behavior. This is in agreement with Fig. 5.31 where at higher gluon energies a deviation to the fit $\sim \omega^{-3/2}$ is recognizable. Furthermore, the shape of the spectrum at hard gluon energies is on the one hand limited by the initial production of gluon at these energies via the Gunion-Bertsch matrix element. As we discussed in Section 5.3.4 at these energies $\omega \approx E$ the phase space of a $2 \to 3$ is very limited since the energy has to be distributed among three outgoing partons and is thereby strongly suppressed. On the other hand, the long formation time of hard gluons prohibits a formation time if the medium length L is shorter than the maximum formation time. This additionally suppresses gluon emissions for $\omega > \omega_{\text{fact}}^{\text{eff}}$ as one can see in Fig. 5.31.

Moreover, gluons with softer energy $\omega < m_D$ are suppressed by

$$\left.\frac{1}{N_{\text{coh}}}\right|_{\omega < m_D} \sim \frac{1}{\sqrt{C_{\text{A}}\alpha_s^2}}\,. \tag{5.92}$$

The ω dependence of the elastic scatterings, and especially the mentioned four-gluon vertex, lead to a suppression that does not depend on the gluon energy. This effect is also visible in Fig. 5.31 where the difference between $\mathrm{d}\Gamma/\mathrm{d}\omega$ and $\mathrm{d}\Gamma_{\text{GB}}/\mathrm{d}\omega$ is approximately constant for $\omega \lessapprox m_D$. The suppression of gluon emissions in both $\mathrm{d}\Gamma/\mathrm{d}\omega$ and $\mathrm{d}\Gamma_{\text{GB}}/\mathrm{d}\omega$ at $\omega \lessapprox 0.5 m_D \approx T$ is due to the screening via ξ_{LPM} which introduces a minimum $k_\perp$ as discussed in Section 5.3.4 that is smeared by the thermal distribution of the scattering partner in the initial $2 \to 3$ process.

Number of coherent scatterings during formation time

The previous discussions concerning the mean formation time and $\hat{q}$ always assumed that the broad distribution of $q_\perp^2$ can be approximated by a mean momentum transfer per mean free path. In other words, a gluon suffers multiple rather uniform and soft scatterings during its formation time. In order to investigate the validity of this picture we show in

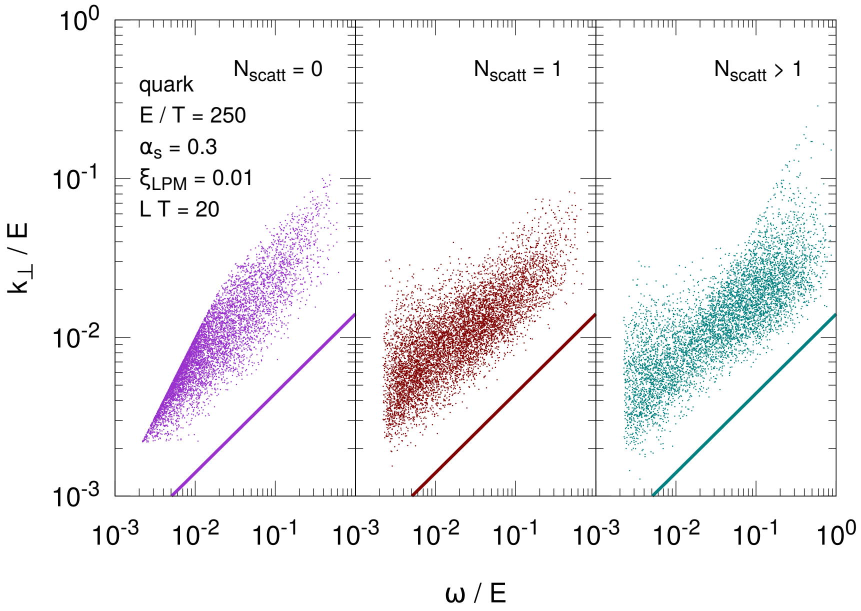

Figure 5.32: Phase space for gluon emissions from the sLPM approach in the ω-$k_\perp$ plane of a quark with $E = 250\,\mathrm{T}$ in a medium with temperature T and length $L = 20\,\mathrm{T}^{-1}$. In the left panel we show only gluon emissions that did not scatter elastically during the formation time τ_f. Furthermore, while the middle panel shows the phase space for emissions with exactly one additional elastic scattering during τ_f, the right panel shows the remaining emissions with $N_{\text{scatt}} > 1$. The gluon energy ω and the transverse momentum $k_\perp$ of the gluons are evaluated in the lab frame. While each point corresponds to a single gluon emission, the lines shows the limit for phase space based on the maximum allowed formation time $\tau_f = \omega/k_\perp^2$. The QCD coupling is fixed to $\alpha_s = 0.3$ and the $k_\perp$ of the initial $2 \to 3$ process is screened via $\xi_{\text{LPM}} = 0.01$.

Fig. 5.32 the single gluon emissions of a quark with $E = 250\,\mathrm{T}$ in the ω-$k_\perp$ plane for a rather long medium length $L = 20\,\mathrm{T}^{-1}$. Each point denotes a single gluon emission and its energy ω and transverse momentum $k_\perp$ at the moment when it reaches its formation time. Different to previous scatter plots, ω and $k_\perp$ are evaluated in the lab frame and not in the CoM frame of the initial $2 \to 3$ process. The lines correspond to the maximum formation time $\tau_f = \omega/k_\perp^2$ in a medium with length $L = 10\,\mathrm{T}^{-1}$. In Fig. 5.32 we differ between three cases: in the left panel we show the emissions for which no additional elastic scattering occurred during the formation time, so $N_{\text{scatt}} = 0$. Please note, while N_{coh} measures the number of scatterings during the formation time including the elastic interaction of the initial $2 \to 3$ process, we define N_{scatt} with the numbers of *additional* elastic scatterings during the formation time. The gluons that can be formed without an additional elastic scattering are mostly either soft (small ω) or have a significant transverse momentum $k_\perp$ already from the initial $2 \to 3$ process. Obviously, the sharp edge at $\omega = k_\perp$ is dictated by the kinematics of the initial $2 \to 3$ process without further interactions. In the central panel we show emissions that experienced exactly one scattering during the formation time, $N_{\text{scatt}} = 1$. By comparing the left and central panel one finds at small ω an enhancement of gluons with $k_\perp > \omega$. This indicates that indeed already a single scattering can transfer sufficient transverse momentum to a soft gluon so that it gets immediately formed. Finally, the right panel of Fig. 5.32 shows all emissions with $N_{\text{scatt}} > 1$. These multiple collision transfer a significant amount of transverse momentum that is especially needed by hard gluons $\omega \sim \mathcal{O}(E)$ for getting formed. From the finding that these hard gluons appear only if they scattered $N_{\text{scatt}} > 1$ times during the formation time one can infer that indeed multiple scatterings are necessary to form the energetic gluon emissions.

Path-length dependence of emission rates in the sLPM approach

One of the major characteristics of the non-Abelian LPM effect is the path-length dependence of the corresponding radiative energy loss. As we discussed in Section 5.1.2 the radiative energy loss is expected to depend quadratically on the medium length. Therefore we will study in the following the path length dependence of both the differential emission rate $\mathrm{d}\Gamma/\mathrm{d}\omega$ and the differential energy loss $\mathrm{d}E/\mathrm{d}x$ depending on the medium length L. We show in Fig. 5.33 again the gluon emissions of a quark with $E = 250\,\mathrm{T}$ in the ω-$k_\perp$ plane, this time depending on the emission time t when the gluon completes its formation time. Please note that the clear cut at soft ω stems from the minimum energy of an emission that is limited by the $k_\perp$ screening via $\xi_{\text{LPM}} = 0.01$ at around one per mill of the projectile energy E. The lines denote the maximum formation time ${\tau_f}^{\max} = \omega/k_\perp^2 = t$ a gluon can have to be formed before time t. This limits the possible minimum $k_\perp$ of a gluon at a given gluon energy ω. Since the formation time increases with increasing gluon energy, hard partons are suppressed at early times unless their transverse momentum wrt. to the emitting parton is large enough to early decohere from the projectile. Therefore at $t = 1\,\mathrm{T}^{-1}$ mainly soft gluons that have a significant transverse momentum are emitted. Gluons that were produced more collinearly or harder are still in their formation time at this stage. At later times also these gluons can be formed and contribute to the emission spectra. Furthermore, also gluons with higher transverse momentum and softer energy and thereby small formation time contribute at later times. These emissions were started late in the evolution so that they complete their short formation time not until $t = 6\,\mathrm{T}^{-1}$.

For a more quantitative analysis we plot in Figs. 5.34 and 5.35 the length dependence of both differential rates $\mathrm{d}\Gamma/\mathrm{d}k_\perp$ and $\mathrm{d}\Gamma/\mathrm{d}\omega$. Again, the calculations were done for an energetic quark with $E = 250\,\mathrm{T}$ and $\xi_{\text{LPM}} = 0.01$. In contrast to the previous scatter plot we show the differential rates for different medium lengths L (denoted by varying colors) that represent the emission rate not *at* a given time but the cumulative sum of emissions up to this time.

Due to the sLPM algorithm the emission rates are indeed path-length dependent in contrast to, e.g., the processes from the θ-LPM approach. In Fig. 5.34 we plot the differential emission rate $\mathrm{d}\Gamma/\mathrm{d}k_\perp$ in units of the temperature T for two projectile energies $E = \{25\,\mathrm{T}; 250\,\mathrm{T}\}$ in comparison with the emission rate $\mathrm{d}\Gamma_{\text{GB}}/\mathrm{d}k_\perp$ from the Gunion-Bertsch matrix element without any LPM suppression. At small medium lengths $L \approx 1\,\mathrm{T}^{-1}$ the emissions are strongly suppressed due to the limited allowed formation, which is in agreement with the findings from Fig. 5.33. By comparing with $\mathrm{d}\Gamma_{\text{GB}}/\mathrm{d}k_\perp$ we infer that only the gluons with the largest transverse momentum $k_\perp > T$ from the initial $2 \to 3$ process are able to form in these thin media. By increasing the medium length L gluons are able to accumulate more transverse momentum. Consequently they begin to thermalize so that the $k_\perp$ distribution shifts from $k_\perp \approx 0.1\,\mathrm{T}$, given by the $k_\perp$ screening via ξ_{LPM} in the initial $2 \to 3$ process, to $k_\perp \sim \mathcal{O}(T)$. So the resulting emission rate in the sLPM approach is much more transverse than the initial $2 \to 3$ processes. The increased transverse momentum leads additionally to decreasing formation times so that more and more gluons are able to complete their formation time during L. This behavior is similar for both projectiles energies $E = 25\,\mathrm{T}$ and $E = 250\,\mathrm{T}$. Above medium lengths $L \approx 3\,\mathrm{T}^{-1}$ the emission rate does not change any more and becomes almost path-length independent. The length at which this maximum emission rate is reached

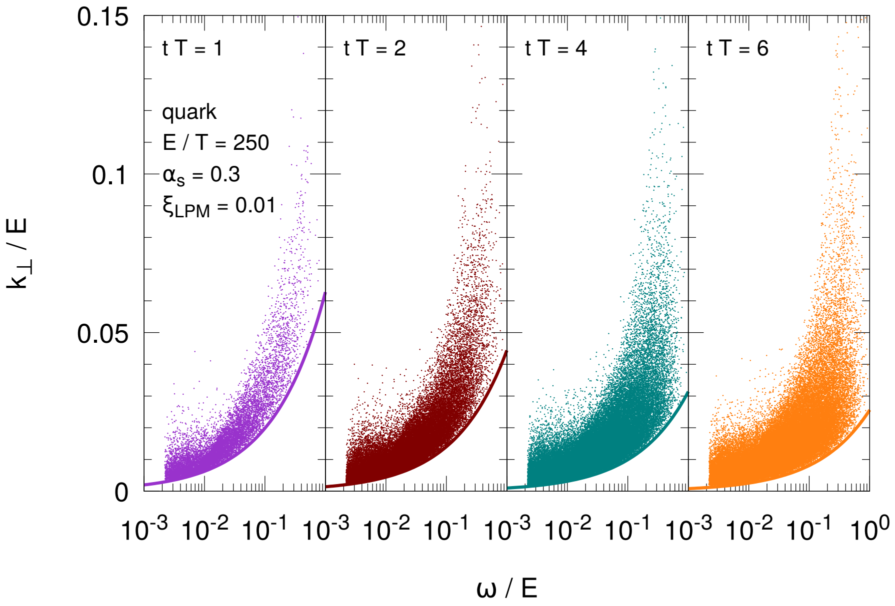

Figure 5.33: Time evolution of the phase space for gluon emissions from the sLPM approach in the ω-$k_\perp$ plane of a quark with $E = 250\,\mathrm{T}$ in a medium with temperature T. In the different panels different evolution times t are depicted. The gluon energy ω and the transverse momentum $k_\perp$ of the gluons are evaluated in the lab frame. While each point corresponds to a single gluon emission, the lines shows the limit for phase space based on the maximum allowed formation time $t = \tau_f = \omega/k_\perp^2$. The QCD coupling is fixed to $\alpha_s = 0.3$ and the $k_\perp$ of the initial $2 \to 3$ process is screened via $\xi_{\mathrm{LPM}} = 0.01$.

is given by the scale $L_c \sim \sqrt{E/\hat{q}(E)}$ of Section 5.1.2 that corresponds to the medium length at which the hardest gluon with $\omega = E$ can still be formed and hence depends on E. With $\hat{q}_g(E = 25\,\mathrm{T}) \approx 7\,\mathrm{T}^3$ and $\hat{q}_g(E = 250\,\mathrm{T}) \approx 15\,\mathrm{T}^3$ from the results discussed in Section 5.3.3, it follows $L_c(E = 25\,\mathrm{T}) \approx 1.9\,\mathrm{T}^{-1}$ and $L_c(E = 250\,\mathrm{T}) \approx 4.1\,\mathrm{T}^{-1}$. Even the interactions within larger medium lengths $L > L_c$ are insufficient to form more collinear gluons and the rate becomes path-length independent.

To complete our picture of emissions in the sLPM algorithm we show in Fig. 5.35 the medium length dependence of $\omega\,\mathrm{d}\Gamma/\mathrm{d}\omega$, of a quark projectile again for two different projectile energies $E = \{25\,\mathrm{T}; 250\,\mathrm{T}\}$ and in comparison with the corresponding rate $\mathrm{d}\Gamma_{\mathrm{GB}}/\mathrm{d}\omega$ from the GB matrix element without LPM suppression. Since we aim to characterize the actual radiative energy loss from the sLPM algorithm, please note that we weight the rate by the gluon energy ω in units of the projectile energy E. This weighted emission rate $\omega\,\mathrm{d}\Gamma/\mathrm{d}\omega$ then directly visualizes how the different ω regions contribute to the radiative energy loss.

At small medium lengths we find again a strong suppression of emission. Since harder gluons have on average a longer formation time, the spectrum at higher gluon energies is stronger suppressed in comparison to more thermal gluon emissions. The main contribution to the energy loss in thin media therefore originates from soft gluon emissions around $\omega \approx 10^{-2}\,\mathrm{E}$ for both projectile energies. With increasing medium lengths again also harder gluons are able to form. At a scale of $L \approx L_c$ the emission rate again becomes independent from the medium length L. Both distributions show even at thick medium lengths $L > L_c$ a suppression in comparison to the initial $\mathrm{d}\Gamma_{\mathrm{GB}}/\mathrm{d}\omega$ distribution. This again demonstrates that the sLPM algorithm additionally screens very collinear and energetic emissions wrt. to

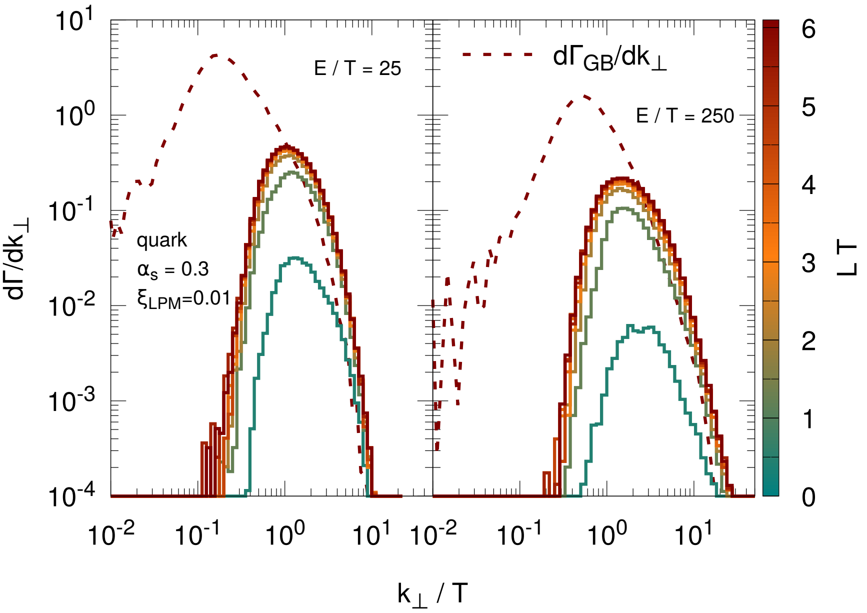

Figure 5.34: Differential emission rate $\mathrm{d}\Gamma/\mathrm{d}k_\perp$ of a quark projectile with energy $E = 25\,\mathrm{T}$ (left) and $E = 250\,\mathrm{T}$ (right) in a medium with temperature T and different medium lengths L from the sLPM approach. The different values of L are given by varying colors from small L (green) to larger L (red) values. The QCD coupling is fixed to $\alpha_s = 0.3$ and the $k_\perp$ of the initial $2 \to 3$ process is screened via $\xi_{\mathrm{LPM}} = 0.01$. The corresponding $\mathrm{d}\Gamma/\mathrm{d}k_\perp$ directly from the Gunion-Bertsch matrix element without LPM suppression can be found by the red dashed line.

the initial GB matrix element. The contribution to the radiative energy loss when assuming no LPM suppression is flat, so all emission between $\omega \approx 10^{-2}$ E and $\omega \approx 10^{-1}$ E contribute equally to the radiative energy loss. On the contrary, as we have already seen in Fig. 5.31, the differential emission rate for an energetic projectile goes for large medium lengths $\sim \omega^{-3/2}$ with a mild maximum around thermal energies $\omega \sim \mathcal{O}(T)$. For less energetic projectiles $E = 25\,\mathrm{T}$ already the distribution from the Gunion-Bertsch matrix element is not flat but shows deviation to the $\sim \omega^{-1}$ behavior. This shape is also slightly recognizable at small medium lengths, when the influence of the initial production distribution is significant. At larger medium lengths the radiative energy loss of a less energetic projectile is again dominated by thermal gluon energies, $\omega \sim \mathcal{O}(T)$. Due to the limited phase space the distribution does not reach as far as in the case of $E = 250\,\mathrm{T}$.

Path-length dependence of the radiative energy loss in the sLPM approach

The emitted gluons take away energy from the projectile and thereby lead to a radiative energy loss. We have seen in the simplified model of Section 5.3.2 that path-length dependent emission rates correspond to a path-length dependent radiative energy loss. Therefore we will study in the following the path length dependence of radiative energy loss in terms of the differential energy loss $\mathrm{d}E/\mathrm{d}x$. Before discussing these modifications, we would like to comment on the concrete definition of the term “energy loss” in the present context. In other models (including the previously discussed, simplified model), the radiative process is similar to a $1 \to 2$ process. The energy loss that the projectile witnesses

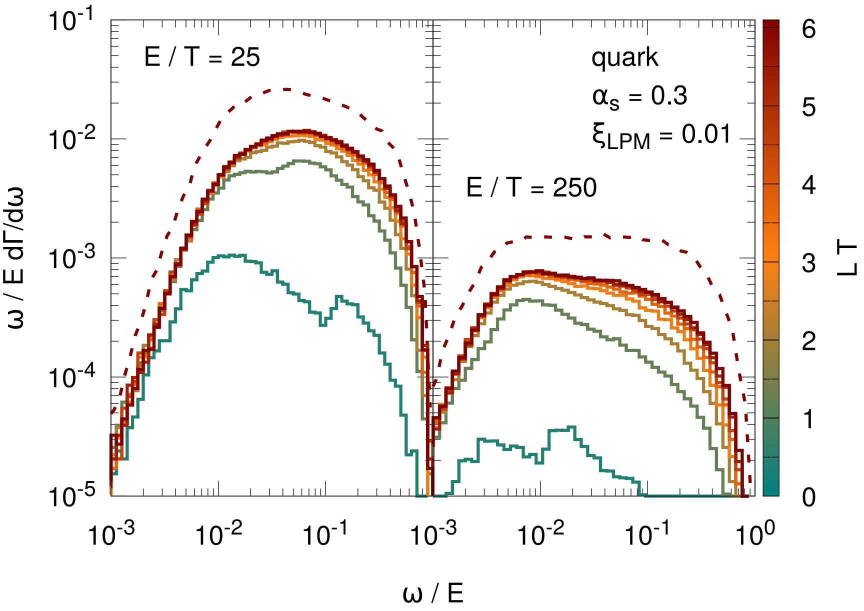

Figure 5.35: Differential emission rate $\mathrm{d}\Gamma/\mathrm{d}\omega$ of a quark projectile with energy $E = 25\,\mathrm{T}$ (left) and $E = 250\,\mathrm{T}$ (right) in a medium with temperature T and different medium lengths L from the sLPM approach. The different values of L are given by varying colors from small L (green) to larger L (red) values. We scale $\mathrm{d}\Gamma/\mathrm{d}\omega$ by ω/E in order to better visualize the contribution of the different ω to the total radiative energy loss. The QCD coupling is fixed to $\alpha_s = 0.3$ and the $k_\perp$ of the initial $2 \to 3$ process is screened via $\xi_{\mathrm{LPM}} = 0.01$. The corresponding $\mathrm{d}\Gamma/\mathrm{d}\omega$ directly from the Gunion-Bertsch matrix element without LPM suppression can be found by the red dashed line.

is completely determined by the energy that the emitted gluon takes away. Therefore we could define $\mathrm{d}E/\mathrm{d}x$ by integrating the gluon spectrum as in Eq. (5.52) on page 75.

In contrast, the radiative processes in this section are $2 \to 3$ Bremsstrahlung processes. Therefore the energy loss that the projectile suffers consists of the energy that the gluon carries away and an additional contribution of the $2 \to 2$ part of the initial $2 \to 3$ process. The energy of the incoming partons is distributed among three final state partons. However, the previously discussed differential emission rates were calculated based on only the gluon energy. Therefore the integration of these gluon rates in order to obtain $\mathrm{d}E/\mathrm{d}x$ as defined in Eq. (5.23) on page 55 will not lead to the total radiative energy loss but neglect the $2 \to 2$ contribution. Since we are interested in the total radiative energy loss of the projectile we show in the following the results including the elastic $2 \to 2$ contribution. Later, Fig. 5.38 will then quantify the difference between the two definitions of energy loss.

Moreover, in contrast to our results, e.g., in Section 5.2 we have seen that the gluon emission rate of the stochastic LPM depends on the medium length L. Therefore we would like to point out that it is necessary to evaluate $\mathrm{d}E/\mathrm{d}x$ as the derivative per time step, $\mathrm{d}E/\mathrm{d}x = \Delta E(\Delta t)/\Delta t$, instead of evaluating it via a ratio of the total energy loss $\mathrm{d}E/\mathrm{d}x = \Delta E(L)/L$ per medium length L. This procedure will give the correct path length dependence also for small medium lengths, where the energy loss rate will be L dependent.

Figure 5.36 shows the length dependence of the differential energy loss $\mathrm{d}E/\mathrm{d}x$ of a quark (denoted as triangles) and a gluon (scaled by $C_{\mathrm{F}}/C_{\mathrm{A}}$ and denoted by squares)

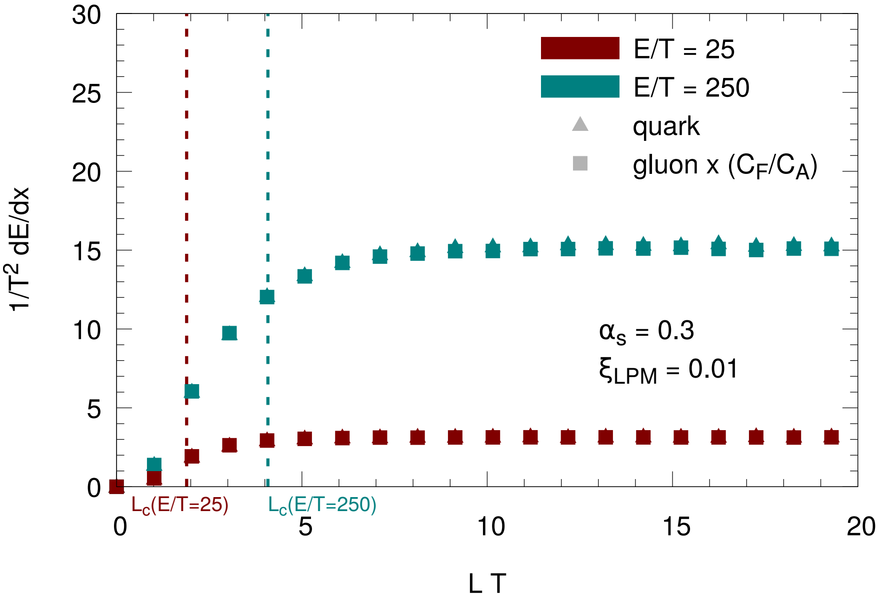

Figure 5.36: Differential radiative energy loss $\mathrm{d}E/\mathrm{d}x$ of a quark (triangles) or gluon (squares, scaled by $C_\mathrm{F}/C_\mathrm{A}$) projectile with energies $E = 25\,\mathrm{T}$ (red) or $E = 250\,\mathrm{T}$ (green) in a medium with temperature T depending on the medium length L. The QCD coupling is fixed to $\alpha_s = 0.3$ and the $k_\perp$ of the initial $2 \to 3$ process is screened via $\xi_\mathrm{LPM} = 0.01$. The critical length scales L_c are given by dashed lines in the color of the corresponding projectile energy.

projectile for two different projectile energies $E = \{25\,\mathrm{T}; 250\,\mathrm{T}\}$. Since both the inelastic $2 \to 3$ processes from the Gunion-Bertsch matrix element and the elastic $2 \to 2$ processes from pQCD scale approximately with $C_\mathrm{F}/C_\mathrm{A}$, also the radiative energy loss from the sLPM method scales with the ratio of QCD color factors. The differential energy loss increases approximately linearly with increasing medium length for both projectile energies before becoming constant at larger medium lengths. This is the expected behavior of the QCD LPM effect as discussed in Section 5.1.2: up to the length scale $L_c = \sqrt{E/\hat{q}(E)}$ (cf. Eq. (5.24) on page 55) the medium may act as a single coherent scattering center before at larger medium length combined coherent scattering centers contribute incoherently to the energy loss. The corresponding values for L_c of the two shown projectile energies, $L_c(E = 25T) \approx 1.9\,\mathrm{T}^{-1}$ and $L_c(E = 250\,\mathrm{T}) \approx 4.1\,\mathrm{T}^{-1}$, are depicted in Fig. 5.36 by dashed lines. Since L_c is the maximum formation of a gluon emitted by a projectile with energy E a further increase of the medium length to $L > L_c$ does not increase the energy loss rate and it becomes almost independent from the medium length L with values $\mathrm{d}E/\mathrm{d}x(E = 25\,\mathrm{T}, L > L_c) \approx 9/4 C_\mathrm{R}\, T^2$ and $\mathrm{d}E/\mathrm{d}x(E = 250\,\mathrm{T}) = 45/4 C_\mathrm{R}\, T^2$, where C_R is the color factor of the projectile. As we have seen previously the main contribution to the radiative energy loss comes from emissions with thermal gluon energies. Therefore the less energetic projectile loses relatively twice as much energy per unit path length than the more energetic projectile $(1/E\,\mathrm{d}E/\mathrm{d}x(E = 25\,\mathrm{T}) = 0.09 C_\mathrm{R}\, T$ vs. $1/E\,\mathrm{d}E/\mathrm{d}x(E = 250\,\mathrm{T}) = 0.045 C_\mathrm{R}\, T)$.

The dependence of the radiative energy loss on the projectile energy leads to the other important signature of the non-Abelian LPM effect: As discussed in Section 5.1.2 the coherence of scattering centers during the formation time leads to a $\sim \sqrt{E}$ dependence of $\mathrm{d}E/\mathrm{d}x$ at high projectile energies (cf. Eq. (5.28) on page 55). Therefore we show in Fig. 5.37 the differential energy loss rate $\mathrm{d}E/\mathrm{d}x$ of a quark and a gluon depending on the

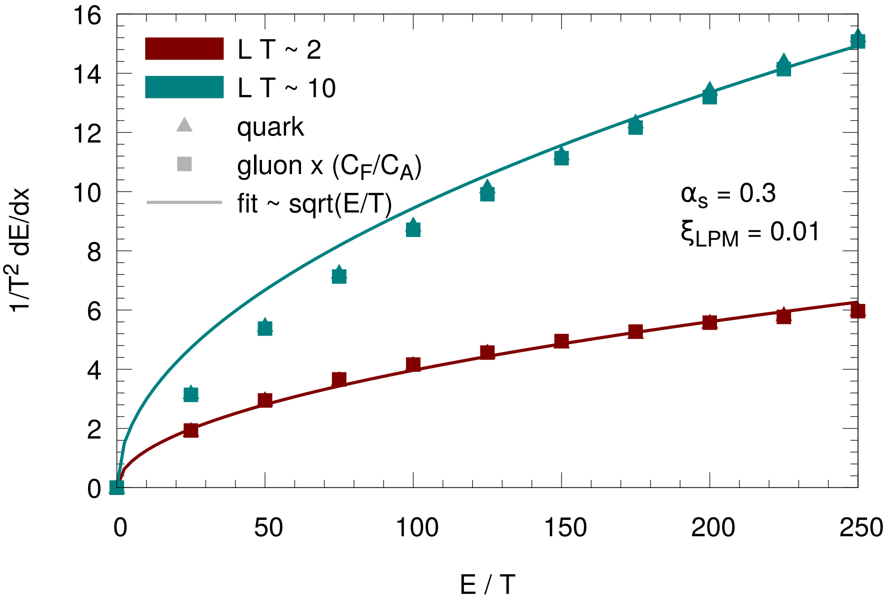

Figure 5.37: Differential radiative energy loss $\mathrm{d}E/\mathrm{d}x$ of a quark (triangles) or gluon (squares, scaled by $C_\mathrm{F}/C_\mathrm{A}$) projectile for medium lengths $L = 2\,\mathrm{T}^{-1}$ (red) or $L = 10\,\mathrm{T}^{-1}$ (green) in a medium with temperature T depending on the projectile energy E. The QCD coupling is fixed to $\alpha_s = 0.3$ and the $k_\perp$ of the initial $2 \to 3$ process is screened via $\xi_\mathrm{LPM} = 0.01$. While the points show the numerical results from BAMPS, the solid lines show a fit with the expected $\mathrm{d}E/\mathrm{d}x \sim \sqrt{E}$ behavior from the non-Abelian LPM effect.

projectile energy E for two different medium lengths $L = 2\,\mathrm{T}^{-1}$ and $L = 10\,\mathrm{T}^{-1}$. And indeed, the radiative energy loss $\mathrm{d}E/\mathrm{d}x$ obtained by the sLPM method depends $\sim \sqrt{E}$ on the projectile energy.

For completeness we show in Fig. 5.38 the integrated energy loss ΔE of a quark for two projectile energies E depending on the medium length L. Up to a scale L_c the energy loss shows the well-known $\sim L^2$ dependence of the non-Abelian LPM effect as first proposed in Ref. [Bai+97b]. Above this scale the linear L dependence of incoherent gluon production is recovered. Following the previous discussion about the definition of "energy loss" we differ in Fig. 5.38 between two different definitions for ΔE: either only the radiated energy due to the gluon emission (ΔE^rad) or both the radiated energy and the energy loss due to the $2 \to 2$ part of the $2 \to 3$ ($\Delta E^{22} + \Delta E^\mathrm{rad}$) contribute to the energy loss. The energy loss due to the elastic part of the $2 \to 3$ process contributes approximately 20–30 % to the total radiative energy loss. The corresponding results for a gluon projectile would be again scaled by $C_\mathrm{F}/C_\mathrm{A}$ (not shown).

Dependence of the sLPM approach on the screening parameter ξ_LPM

Finally, after we demonstrated the main dependencies of the sLPM algorithm in terms of path-length and energy dependence it remains a discussion of the interplay between the LPM suppression and the $k_\perp$ screening underlying the Gunion-Bertsch matrix element of the initial $2 \to 3$ process. As a reminder, the transverse momentum $k_\perp$ of the gluon in the GB approximation diverges in the limit $k_\perp \to 0$. Different to the θ-LPM approach of Section 5.2, where the parametric suppression via the theta function cures the collinear divergence, we introduced in Section 5.3.4 an effective parameter ξ_LPM that limits the

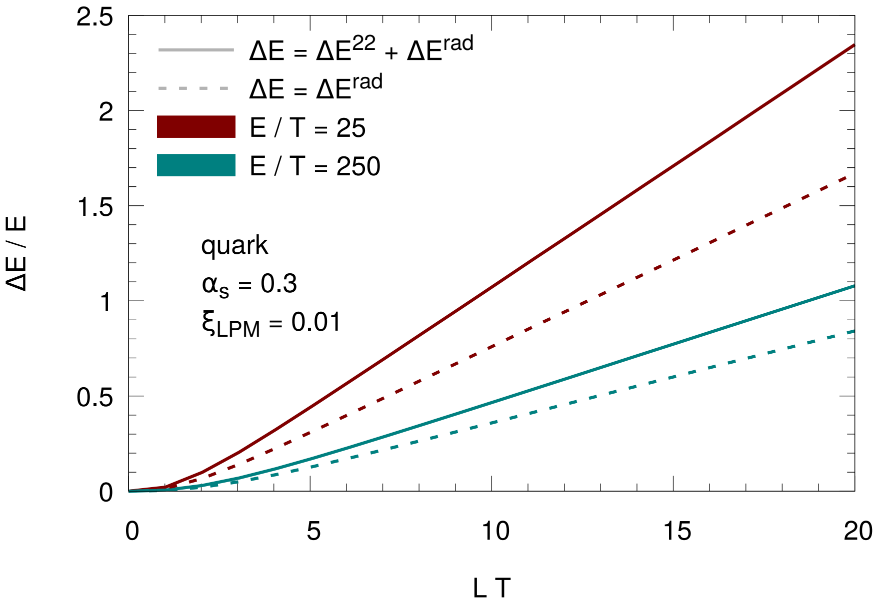

Figure 5.38: Radiative energy loss ΔE of a quark with energy $E = 25\,\mathrm{T}$ (red) or $E = 250\,\mathrm{T}$ (green) in a medium with temperature T depending on the medium length L. The QCD coupling is fixed to $\alpha_s = 0.3$ and the $k_\perp$ of the initial $2 \to 3$ process is screened via $\xi_{\mathrm{LPM}} = 0.01$. The solid lines correspond to the previous results for the energy loss consisting of the energy taken away by the gluon and an elastic contribution from the $2 \to 2$ scattering of initial $2 \to 3$ process. In contrast, the dashed lines show the results for the radiative energy loss neglecting the $2 \to 2$ contribution by only integrating the radiated gluon energies.

minimum $k_\perp$ of a $2 \to 3$ proportionally to the CoM energy $\sqrt{\hat{s}}$. While we study in this section the general dependence of the LPM algorithm on the parameter ξ_{LPM} we will calibrate ξ_{LPM} in Section 5.5 by comparing the algorithm with other LPM models.

We begin this investigation again by studying the LPM algorithm in the scenario of screened $2 \to 3$ processes from the Gunion-Bertsch approximation together with constant, ω-independent elastic interactions of the gluons during their formation time. This corresponds to the studies from Fig. 5.29, where we changed the simplified elastic interactions of gluons while employing the Gunion-Bertsch matrix elements for the radiative part. In Fig. 5.39 we show the differential emission rate $\mathrm{d}\Gamma_{\mathrm{GB}}/\mathrm{d}\omega$, scaled by $\omega^{-3/2}$, for a constant momentum transfer $q_\perp^2 = 0.06\,\mathrm{T}^2$ per mean free path $\lambda_{\mathrm{el}} = 1\,\mathrm{T}^{-1}$ and different values of ξ_{LPM}. As projectile we choose a quark with energy $E = 250\,\mathrm{T}$. In Section 5.3.5 we could show that this specific choice of elastic interactions indeed reproduced the expected $\mathrm{d}\Gamma/\mathrm{d}\omega \sim \omega^{-3/2}$ behavior of the QCD LPM effect for $\xi_{\mathrm{LPM}} = 0.01$. Figure 5.39 shows that this behavior also can be found for larger values of ξ_{LPM}. However, the range over which it is reproduced shrinks with increasing ξ_{LPM}. This in agreement with the study of the emission rate via the initial $2 \to 3$ process in GB approximation that we presented in Fig. 5.26. By increasing ξ_{LPM} and thereby forbidding collinear gluons we found that the ω region where the emission rate goes like $\mathrm{d}\Gamma/\mathrm{d}\omega \sim 1/\omega$ diminished. After applying the LPM algorithm this is reflected by a shrinking $\sim \omega^{-3/2}$ region. On the contrary, the emission rate at higher gluon energies is not affected by the choice of ξ_{LPM}. This is different to the initial Gunion-Bertsch distribution where we found that also collinear gluons allowed by small ξ_{LPM} values may end up at high ω in the distribution. Reason for this is that the

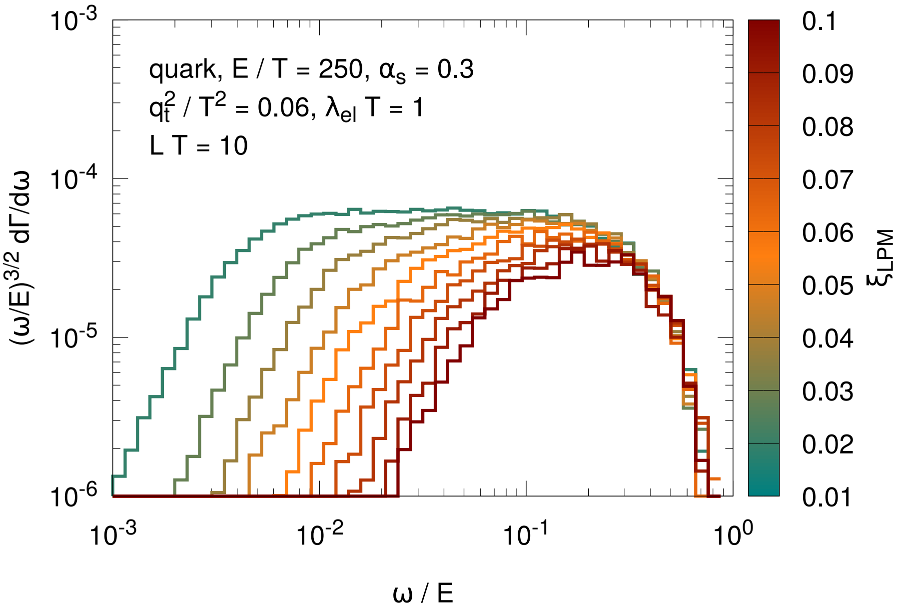

Figure 5.39: Differential emission rate $\mathrm{d}\Gamma/\mathrm{d}\omega$ of a quark projectile with energy $E = 250\,\mathrm{T}$ in a medium with length $L = 10\,\mathrm{T}^{-1}$ from radiative processes calculated by the Gunion-Bertsch matrix element screened with different ξ_{LPM} values (denoted by different colors) and subsequently suppressed by the sLPM algorithm with fixed elastic interactions of the gluons during τ_f. The QCD coupling is fixed to $\alpha_s = 0.3$. To better visualize the expected behavior of the non-Abelian LPM effect we scale the differential emission rate by $\omega^{-3/2}$.

formation time condition of the sLPM algorithm forbids gluons with these small transverse momenta at high gluon energies due to their larger formation time.

In the following we present the results from the LPM algorithm together with the ω dependent pQCD interactions of the gluons during τ_f. Figure 5.40 shows the differential emission rates $\omega\,\mathrm{d}\Gamma/\mathrm{d}\omega$ (left) and $\mathrm{d}\Gamma/\mathrm{d}k_\perp$ (right) of a quark projectile with energy $E = 250\,\mathrm{T}$ and a medium length $L = 10\,\mathrm{T}^{-1}$ for different screening parameter ξ_{LPM}. For both distributions a larger value of ξ_{LPM} forbids collinear gluon emissions and the rate decreases. The $\mathrm{d}\Gamma/\mathrm{d}\omega \sim \omega^{-3/2}$ behavior shifts to an almost Gaussian distribution at high values of $\xi_{\mathrm{LPM}} \approx 0.1$. This decreasing rate not only affects the soft region of the spectrum but also the hard component of the projectile. Same holds for the transverse momentum distribution: we found in the initial distribution from the GB matrix elements (compare Section 5.3.4) that small values of ξ_{LPM} add collinear gluon emissions to the spectrum. In contrast small values of ξ_{LPM} not only increase the rate of collinear gluon emissions but also emissions at larger $k_\perp$. Reason for this is that more collinear gluon emissions in the beginning, also have on average a longer formation time in which they may accumulate transverse momentum. Therefore these emissions appear at transverse momenta $k_\perp \gtrapprox 3\,\mathrm{T}$.

The increased emission rate with decreasing ξ_{LPM} also leads to an increasing radiative energy loss as we can deduce from Fig. 5.41, where we study $\mathrm{d}E/\mathrm{d}x$ for a quark depending on the medium length L (left) and the projectile energy E (right). While varying ξ_{LPM} indeed leads to a varying $\mathrm{d}E/\mathrm{d}x$ the underlying length scale L_c remains constant. This finding will allow us in Section 5.5 and Chapter 7 to calibrate ξ_{LPM} and thereby the $k_\perp$ screening by comparing the algorithm to either other LPM models or experimental data.

Correspondingly to Fig. 5.11, where we have shown the X_{LPM} dependence of $\mathrm{d}E/\mathrm{d}x$ in the θ-LPM approach, Fig. 5.42 shows the ξ_{LPM} dependence of $\mathrm{d}E/\mathrm{d}x$ in the stochastic

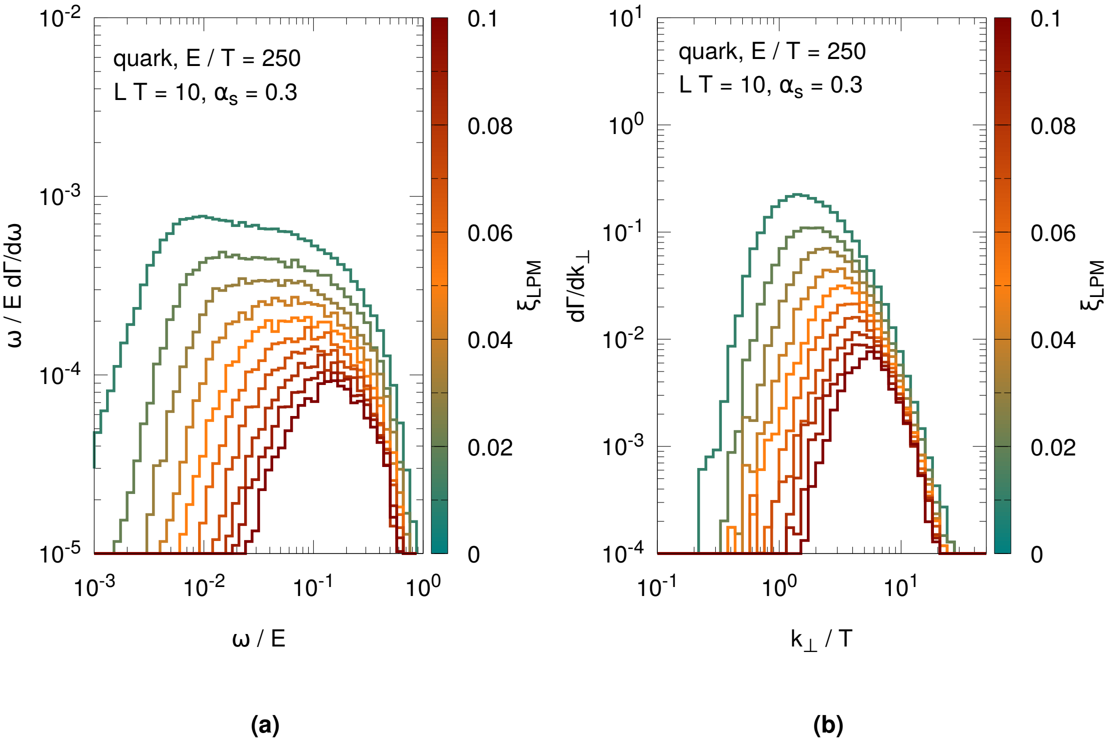

Figure 5.40: Differential emission rate $\mathrm{d}\Gamma/\mathrm{d}\omega$ (Fig. 5.40a) and $\mathrm{d}\Gamma/\mathrm{d}k_\perp$ (Fig. 5.40b) of a quark projectile with energy $E = 250\,\mathrm{T}$ in a medium with temperature T and length $L = 10\,\mathrm{T}^{-1}$ for varying $k_\perp$ screening with ξ_{LPM} in the sLPM approach. The different values of ξ_{LPM} are given by varying colors from small ξ_{LPM} (green) to larger ξ_{LPM} (red) values. The QCD coupling is fixed to $\alpha_s = 0.3$. We scale $\mathrm{d}\Gamma/\mathrm{d}\omega$ by ω/E in order to better visualize the contribution of the different ω to the total radiative energy loss.

LPM approach. In Fig. 5.11 we found that the radiative energy loss in the θ-LPM approach scales like $\sim \log X_{\mathrm{LPM}}$ at small X_{LPM}. Also the emission rate in the stochastic LPM approach shown in Fig. 5.28 leads to a $\mathrm{d}E/\mathrm{d}x \sim \log 1/\xi_{\mathrm{LPM}} + B$ dependence.

In conclusion, we demonstrated and validated the proposed algorithm for stochastically suppressing coherent gluon emissions in this section by discussing the parametric dependencies of both the gluon emission rate and the resulting radiative energy loss. Both the simplified, energy independent interactions and the ω-dependent interactions from LO pQCD reproduced the expected signatures of the non-Abelian LPM effect. After we introduce in the next section another method for considering the suppression from the LPM effect we will use in Section 5.5 the screening parameter ξ_{LPM} to compare the algorithm with other approaches for modeling the coherence effects from the LPM effect within BAMPS.

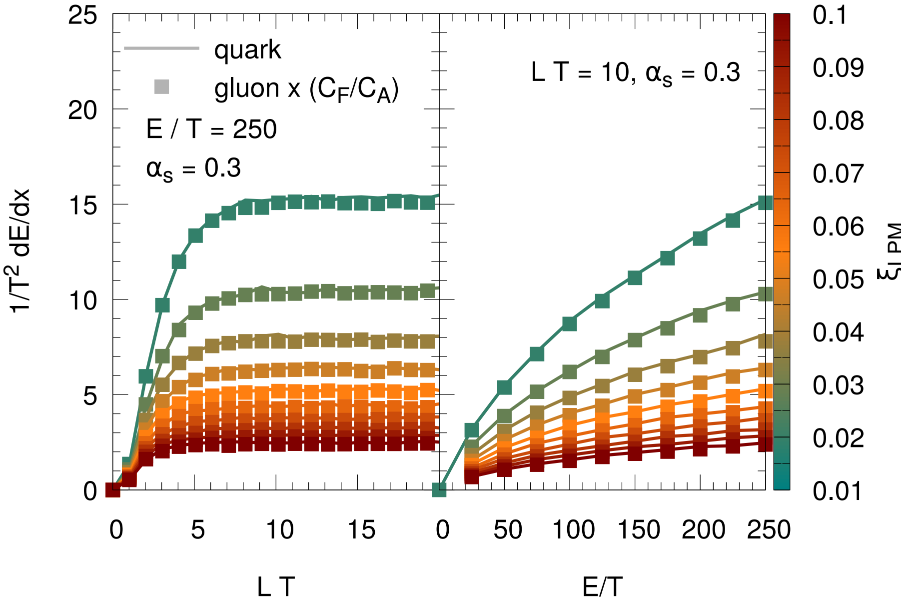

Figure 5.41: Differential radiative energy loss $\mathrm{d}E/\mathrm{d}x$ of a quark (lines) or gluon (squares, scaled by $C_\mathrm{F}/C_\mathrm{A}$) projectile with a $k_\perp$ screening with varying ξ_LPM in the sLPM approach and depending on the medium length L (left) or projectile energy E (right). The different values of ξ_LPM are given by varying colors from small ξ_LPM (green) to larger ξ_LPM (red) values. The QCD coupling is fixed to $\alpha_s = 0.3$.

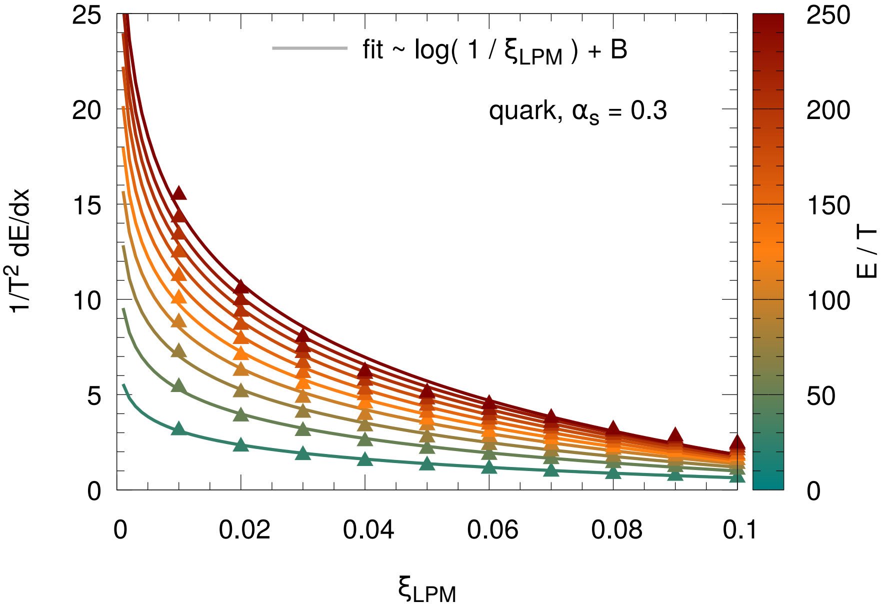

Figure 5.42: Differential radiative energy loss $\mathrm{d}E/\mathrm{d}x$ of a quark projectile depending on ξ_LPM underlying the $k_\perp$ screening in the sLPM approach. The different values of the projectile energy E are given by varying colors from small E (green) to larger E (red) values. The QCD coupling is fixed to $\alpha_s = 0.3$.

5.4 LPM suppression via the AMY formalism

So far we treated the LPM suppression originating from the coherence of gluon emissions via effective approaches, namely either via a parametric suppression function (θ-LPM) or via considering a finite, dynamically evaluated formation time for emitting gluons (sLPM). Among the advantages of these methods was that they were applicable mainly on the microscopic level: Whether emissions are coherent or not is decided based on properties of the respective single scattering, not on macroscopic properties as, e.g., the temperature T. Only the screening of the internal propagator via the Debye mass was evaluated on the macroscopic scale. Furthermore, in the sLPM approach the interactions of the gluons during formation time were explicitly evaluated and thereby in principle also potential effects of these scatterings could be considered. On the other hand, the presented approaches have the drawback that they phenomenologically introduced the suppression of gluon emissions and thereby can only provide guidance to a reliable LPM implementation.

In this section we discuss an implementation for the LPM effect that is closer to a rigorous theoretical QCD calculation by applying rate equations based on the AMY formalism (cf. Section 5.1.1). Starting from the thermal emission rate for photon and gluon emission as calculated by Arnold, Moore, and Yaffe (AMY) [AMY01b; AMY02b; AMY02a] we review how to calculate the differential emission rate $\mathrm{d}\Gamma/\mathrm{d}k$ for a single parton to emit a gluon as it is used, e.g., in the Monte-Carlo model MARTINI [Tur+05; Tur06; JM05; SGJ09; You+11a]. In this approach the coherent scatterings during the formation time are resummed within thermal field theory and by that can be absorbed in an effective "$1 \leftrightarrow 2$" emission/absorption rate. Although $1 \leftrightarrow 2$ splitting processes are, in principle, kinematically forbidden for massless partons, these *effective* $1 \leftrightarrow 2$ emission rates can then be implemented into BAMPS allowing to study the gluon spectrum and radiative energy loss of partons via AMY in BAMPS. By using these effective rates microscopic information about the coherent scatterings during the formation time is lost. Furthermore, this approach has the drawback that due to the application of thermal field theory the medium that the jet traverses has to be thermal. We will further discuss this issue and its consequences for observables later when applying the formalism in non-thermal situations of heavy-ion collisions Chapter 7.

5.4.1 Thermal emission rate for gluons from AMY

Assuming a clear separation of scales $T \gg g_s T \gg g_s^2 T$ in a thermal bath with temperature T and QCD coupling $g_s = \sqrt{4\pi\alpha_s}$, Arnold, Moore, and Yaffe were able to calculate the thermal emission rate of both photons and gluons [AMY01b; AMY02b]. By resumming all possible ladder diagrams and thereby calculating the gluon self-energy via a leading-order hard thermal loop calculation, coherence effects originating from scatterings during the emission process can be explicitly considered. Consequently, the AMY calculation provides an emission rate that is valid both for the Bethe-Heitler and the LPM regime [Tur+05]. The resummed scattering centers have thermal and by that dynamical momenta instead of static scattering centers. This was a major improvement in comparison to other radiative pQCD energy loss calculations. On the other hand, to achieve these dynamic scattering centers the AMY formalism has to be formulated in the thermodynamical limit and thereby in momentum space, which is tantamount to an infinite-sized thermal medium. As we have seen previously, thick media lead to an emission pattern that shows a length independent differential rate $\mathrm{d}\Gamma/\mathrm{d}k$ and thereby $\mathrm{d}E/\mathrm{d}x \sim \text{const.}$. Therefore the resulting radiative energy loss within AMY will be $\Delta E \propto L$. Furthermore, since AMY expects partons to be close to the mass shell the original AMY formulation that we discuss in this section only considers the medium-induced radiation of partons and no interference between vacuum and medium radiation. In Ref. [CG10] the AMY formalism was extended by re-solving the path-integral discussed in Section 5.1.1 and thereby incorporating both finite-size effects and vacuum-medium interference. For more details about the actual derivation of the AMY formalism and the underlying HTL calculation we refer to Refs. [AMY01b; AMY01a; AMY02b; AMY02a], where also the previously developed problem of photon emissions in thermal field theory is covered.

In the AMY formalism, the thermal emission rate for gluons with energy k per unit volume in a thermal bath with temperature T via the processes $q \to q\mathrm{g}$ and $q\bar{q} \to \mathrm{g}$ is [AMY02b; Tur06]

$$\begin{aligned} k\frac{\mathrm{d}R^g}{\mathrm{d}^3\mathbf{k}} = \frac{g_s^2}{16\,(2\pi)^3 k^4}\sum_s N_s\, d_s\, C_s \int\limits_{-\infty}^{+\infty} \frac{\mathrm{d}p_\parallel}{2\pi} f_F(p_\parallel+k)\,[1-f_F(p_\parallel)]\,[1+f_B(k)] \\ \times \frac{p_\parallel^2+(p_\parallel+k)^2}{p_\parallel^2(p_\parallel+k)^2}\int\frac{\mathrm{d}^2\vec{\mathbf{h}}}{(2\pi)^2} 2\vec{\mathbf{h}}\cdot\mathrm{Re}\,\vec{\mathbf{F}}(\vec{\mathbf{h}},p_\parallel+k,p_\parallel,k)\,. \end{aligned} \tag{5.93}$$

$p_\parallel$ is the longitudinal momentum of the emitting (absorbing) quark and is on the order of $p_\parallel \sim T$. Since the emitting quark is on the mass shell and its transverse momentum is $q_\perp \sim gT$, its energy is $p \sim p_\parallel + \mathcal{O}\big(g_s^2 T\big)$. Therefore we identify the longitudinal momentum $p_\parallel$ with the energy p of the quark and use it interchangeably. C_s is the respective color factor (for gluons $C_\mathrm{A} = 3$, for quarks $C_\mathrm{F} = 4/3$), $f_F(p) = 1/(e^p - 1)$ and $f_B(p) = 1/(e^p + 1)$ are the Fermi- and Bose distribution functions, and $\big(p^2 + (p+k)^2\big)/\big(p^2(p+k)^2\big)$ is the common DGLAP splitting function for the process $q \to q\mathrm{g}$ [AP77; Dok77; GL72].

In contrast to the case of photon emissions off a quark [AMY02b], both the emitting quark and the emitted gluon suffer kicks in the transverse direction that have to be resummed. Therefore Eq. (5.93) should include integrations over both transverse momenta $p_\perp$ of the quark and $k_\perp$ of the gluon in order to evaluate this transverse kicks. However, in Ref. [AMY02b] the authors exploited the rotational invariance of the problem and introduced the internal quantity $\vec{\mathbf{h}} = (\mathbf{k} \times \mathbf{p}) \times \mathbf{e}_\parallel$ that points in a direction nearly collinear to $\vec{\mathbf{p}}$, $\vec{\mathbf{k}}$ and $\vec{\mathbf{p}} - \vec{\mathbf{k}}$ and thereby measures the collinearity of the final state [Tur+05]. $\vec{\mathbf{h}}$ is of the order $\mathcal{O}\big(g_s T^2\big)$ and therefore small compared to $\vec{\mathbf{p}} \cdot \vec{\mathbf{k}}$ [SGJ09]. This allows to replace the $\vec{\mathbf{p}}_\perp$ and $\vec{\mathbf{k}}_\perp$ integration by an integration over $\vec{\mathbf{h}}$ in the transverse space in Eq. (5.93).

The vector $\vec{\mathbf{F}}(\vec{\mathbf{h}}, p+k, p, k)$ is the solution of the integral equation [AMY02b; Tur06]

$$\begin{aligned} 2\vec{\mathbf{h}} = i\delta E(\vec{\mathbf{h}},p,k)\vec{\mathbf{F}}(\vec{\mathbf{h}}) + g_s^2\int\frac{\mathrm{d}^2\vec{\mathbf{q}}_\perp}{(2\pi)^2}C(\vec{\mathbf{q}}_\perp)\Big\{(C_s - C_\mathrm{A}/2)[\vec{\mathbf{F}}(\vec{\mathbf{h}}) - \vec{\mathbf{F}}(\vec{\mathbf{h}}-k\,\vec{\mathbf{q}}_\perp)] \\ +(C_\mathrm{A}/2)[\vec{\mathbf{F}}(\vec{\mathbf{h}}) - \vec{\mathbf{F}}(\vec{\mathbf{h}}+(p+k)\,\vec{\mathbf{q}}_\perp)] \\ +(C_\mathrm{A}/2)[\vec{\mathbf{F}}(\vec{\mathbf{h}}) - \vec{\mathbf{F}}(\vec{\mathbf{h}}-p\,\vec{\mathbf{q}}_\perp)]\Big\}\,, \end{aligned} \tag{5.94}$$

that describes how the state $|p+k\rangle\,\langle p,k|$ evolves in time [Tur06]. The energy difference

δE in Eq. (5.94) between the initial and final state

$$\delta E(\vec{\mathbf{h}}, p, k) = \frac{\vec{\mathbf{h}}^2}{2pk(p+k)} + \frac{m_k^2}{2k} + \frac{m_p^2}{2p} - \frac{m_{p+k}^2}{2(p+k)} \tag{5.95}$$

is related to the inverse formation time of the emission process. The masses m_p, m_k, and m_{p+k} are the thermal masses of the external propagators and are either $m_q^2 = 2/9\, m_D^2$ or $m_g^2 = m_D^2/2$ depending on the respective splitting, where the thermal Debye mass is $m_D^2 = 3/2 g_s^2 T^2$. The Debye-screened collision kernel for the elastic interactions during the formation time is

$$C(\vec{\mathbf{q}}_\perp) = \frac{m_D^2}{\vec{\mathbf{q}}_\perp^2 \left(\vec{\mathbf{q}}_\perp^2 + m_D^2\right)} \,. \tag{5.96}$$

Since the collision term in Eq. (5.94) on the preceding page involves only differences in the form of $[\vec{\mathbf{F}}(\vec{\mathbf{h}}) - \vec{\mathbf{F}}(\vec{\mathbf{h}} - p_i\, \vec{\mathbf{q}}_\perp)]$, which vanish for $q_\perp \to 0$, infrared divergences of the collision integral are automatically canceled [AMY02b].

As a remark, the corresponding result for photon emission from a thermal bath in the AMY formalism can be obtained by replacing C_s in Eq. (5.93) on the facing page by the electrical charge q_s^2, setting $C_A = 0$ inside the collision integral of Eq. (5.94) on the preceding page and using the photon thermal mass in Eq. (5.95) [AMY02b]. Therefore the procedure we discuss in this section can be straight-forwardly generalized also to the case of photon emissions, what was done in Refs. [Gre+17b; Gre18].

Since the energy of the quark has values $p = [-\infty; \infty]$ in Eq. (5.93), the spectrum of gluons with energy k gets contributions from different p. The different p regions represent different underlying physical processes: While $p > 0$ corresponds to the contribution of a quark emitting a gluon via Bremsstrahlung ($q \to qg$), the $p < -k$ region describes the same Bremsstrahlung from an antiquark ($\bar{q} \to \bar{q}g$) and the case $-k < p < 0$ is an antiquark annihilating with a quark resulting in a gluon with energy k. It can be shown [Gre18] that the p integration can be written as

$$\int_{-\infty}^{+\infty} \frac{\mathrm{d}p}{2\pi} G(p,k) = 2 \int_{0}^{+\infty} \frac{\mathrm{d}p}{2\pi} G(p-k,k) \left(\Theta(p-k) + \frac{1}{2}\Theta(k-p) \right) , \tag{5.97}$$

where we defined

$$\begin{aligned} G(p,k) = f_F(p+k)\,[1 - f_F(p)]\,[1 + f_B(k)] \times \\ \times \frac{p^2 + (p+k)^2}{p^2 (p+k)^2} \int \frac{\mathrm{d}^2\vec{\mathbf{h}}}{(2\pi)^2} 2\vec{\mathbf{h}} \cdot \mathrm{Re}\, \vec{\mathbf{F}}(\vec{\mathbf{h}}, p+k, p, k) \,. \end{aligned} \tag{5.98}$$

Thus, while prohibiting a double counting in the quark-antiquark annihilation with the term $1/2\Theta(k-p)$, the contribution of quarks and antiquarks to the gluon spectrum is the same and can be considered by a factor 2 together with a shift $G(p,k) \to G(p-k,k)$.

The integral equation Eq. (5.94) on the preceding page describes the actual resummation of ladder diagrams by integrating over the momentum transfers $\vec{\mathbf{q}}_\perp^2$. Due to the complexity of this equation it is solved numerically by Fourier transforming it and applying the *impact parameter* method [AGZ02; Aur+02]. For more details about this procedure and the numerical calculation of the kernel $G(p-k,k)$ we refer to Appendix C.

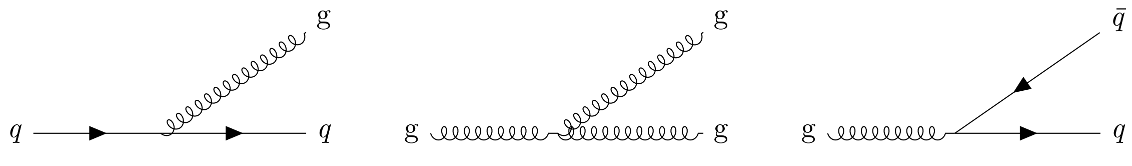

(a) $q \leftrightarrow q\mathrm{g}$ **(b)** $\mathrm{g} \leftrightarrow \mathrm{gg}$ **(c)** $\mathrm{g} \leftrightarrow q\bar{q}$

Figure 5.43: Partonic processes in the AMY formalism.

5.4.2 From thermal rates to transition rates for gluon emissions in AMY

The emission rate $\mathrm{d}R^g/\mathrm{d}^3\vec{\mathbf{k}}$ in Eq. (5.93) on page 116 is the rate for producing gluons with energy k per unit volume and unit time. For reproducing this rate within BAMPS we need to define a transition rate $\mathrm{d}\Gamma/\mathrm{d}k$ that gives the rate for a single parton with energy p to emit (absorb) a gluon/quark with energy k. This is achieved by realizing that the thermal emission rate $k\mathrm{d}R^g/\mathrm{d}^3\vec{\mathbf{k}}$ can also be obtained by folding the number of emitters in the medium per unit volume with the differential emission rate per time $\mathrm{d}\Gamma/\mathrm{d}k$ of a single parton with energy p [Tur06]

$$k\frac{\mathrm{d}R^g}{\mathrm{d}^3\vec{\mathbf{k}}} = \sum_p \frac{\text{Number of quarks with } p}{\text{Volume}}\, k\frac{\mathrm{d}\Gamma}{\mathrm{d}^3\vec{\mathbf{k}}} \tag{5.99}$$

$$= \sum_s N_s\, d_s \int \frac{\mathrm{d}^3\vec{\mathbf{p}}}{(2\pi)^3} f_F(p)\, k\frac{\mathrm{d}\Gamma}{\mathrm{d}^3\vec{\mathbf{k}}} \tag{5.100}$$

$$= \sum_s N_s\, d_s \int_0^\infty \frac{\mathrm{d}p}{(2\pi)^3} f_F(p) \frac{p^2}{k}\frac{\mathrm{d}\Gamma}{\mathrm{d}k}(p,k)\,. \tag{5.101}$$

Comparing Eq. (5.93) on page 116, including the considerations from Eq. (5.97), with Eq. (5.99) one arrives at the rate of an $1 \leftrightarrow 2$ process for a quark with energy p to emit/absorb a thermal parton (gluon or antiquark) with energy k [Tur06; SGJ09]:

$$\frac{\mathrm{d}\Gamma(p,k)}{\mathrm{d}k} = \frac{C_s g_s^2}{16\pi p^7}\frac{1}{1 \pm e^{-k/T}}\frac{1}{1 \pm e^{-(p-k)/T}} \times \left\{ \begin{array}{ll} \frac{1+(1-x)^2}{x^3(1-x)^2}, & q \leftrightarrow q\mathrm{g} \\ N_f\frac{x^2+(1-x)^2}{x^2(1-x)^2}, & \mathrm{g} \leftrightarrow q\bar{q} \\ \frac{1+x^4+(1-x)^4}{x^3(1-x)^3}, & \mathrm{g} \leftrightarrow \mathrm{gg} \end{array} \right\} \times \int \frac{\mathrm{d}^2\vec{\mathbf{h}}}{(2\pi)^2} 2\vec{\mathbf{h}} \cdot \mathrm{Re}\,\vec{\mathbf{F}}(\vec{\mathbf{h}},p,k)\,, \tag{5.102}$$

where we introduced $x = k/p$.

In contrast to photons, gluons itself may scatter with other partons in the medium and by that emit other gluons via medium-induced radiation. The corresponding additional processes of a gluon, $\mathrm{g} \to \mathrm{gg}$ and $\mathrm{g} \to q\bar{q}$, can be obtained with the same procedure as above and are shown in Eq. (5.102) and in Fig. 5.43. For the different processes the corresponding DGLAP splitting kernel (given in the curly braces of Eq. (5.102)) has to be used and the masses m_p, m_k and m_{p-k} in the inverse formation time δE of Eq. (5.94) on page 116 have to be chosen appropriately. Furthermore, for the process $\mathrm{g} \to q\bar{q}$ the color factors in the collision integral have to be switched [Tur06; SGJ09],

$$(C_s - C_{\mathrm{A}}/2)\,[\vec{\mathbf{F}}(\vec{\mathbf{h}}) - \vec{\mathbf{F}}(\vec{\mathbf{h}} - k\,\vec{\mathbf{q}}_\perp)] \to (C_{\mathrm{A}}/2)\,[\vec{\mathbf{F}}(\vec{\mathbf{h}}) - \vec{\mathbf{F}}(\vec{\mathbf{h}} - k\,\vec{\mathbf{q}}_\perp)] \tag{5.103}$$

$$(C_{\mathrm{A}}/2)\,[\vec{\mathbf{F}}(\vec{\mathbf{h}}) - \vec{\mathbf{F}}(\vec{\mathbf{h}} + (p+k)\,\vec{\mathbf{q}}_\perp)] \to (C_s - C_{\mathrm{A}}/2)\,[\vec{\mathbf{F}}(\vec{\mathbf{h}}) - \vec{\mathbf{F}}(\vec{\mathbf{h}} + (p+k)\,\vec{\mathbf{q}}_\perp)]\,. \tag{5.104}$$

While we previously characterized the underlying physical processes in AMY by their p value at fixed k, same can be done for the transition rate $\mathrm{d}\Gamma/\mathrm{d}k$ at fixed p but depending on k:

- Considering the process $q \leftrightarrow q\mathrm{g}$, shown in Fig. 5.44, the range $p > k > 0$ corresponds to the emission of a gluon with energy k from a quark with energy p leading to an energy loss for the outgoing quark of energy $p - k < p$. On the other hand, the region $k < 0$ corresponds to a gluon from the thermal bath that is captured leading to an net energy gain for the quark $p - k > p$. In both cases the incoming quark keeps its flavor. In contrast, the remaining region $k > p > 0$ of the process corresponds to the case where the incoming quark annihilates with an thermal antiquark with energy $p - k < 0$ in order to produce a gluon with energy k. Thereby the incoming quark changes its flavor and becomes a gluon.

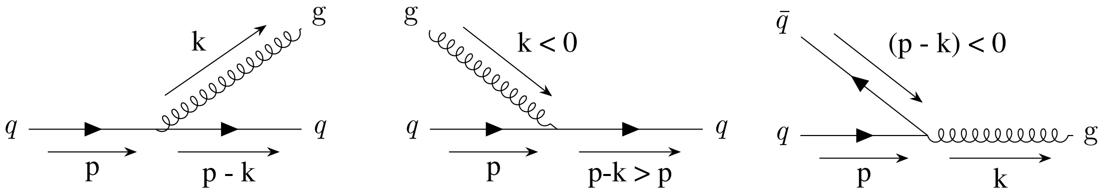

(a) Bremsstrahlung **(b)** Absorption of gluon **(c)** Absorption of antiquark

Figure 5.44: Schematic representation of the different k regions in the process $q \leftrightarrow q\mathrm{g}$.

- Different to $q \leftrightarrow q\mathrm{g}$ the process $\mathrm{g} \leftrightarrow \mathrm{gg}$ (Fig. 5.45) has a symmetric final state. Therefore, in order to avoid a double counting of the final states, the k-range is limited to $k < p/2$. For $k = p/2$ the two outgoing gluons share equally the incoming energy, while for $k > p/2$ the outgoing gluons switch roles. Consequently the region $0 < k < p/2$ corresponds again to the emission of a gluon with energy k from this time a gluon with energy p, which leads to an energy loss of the incoming gluon $(p - k < p)$. On the other hand, the region $k < 0$ corresponds to two gluons fusing to produce a gluon with an increased energy $p - k > p$.

(a) Bremsstrahlung **(b)** Absorption of thermal gluon

Figure 5.45: Schematic representation of the different k regions in the process $\mathrm{g} \leftrightarrow \mathrm{gg}$.

- Finally, the process $\mathrm{g} \leftrightarrow q\bar{q}$ (Fig. 5.46) describes, for the region $p > k > 0$, the production of a quark-antiquark pair, where the quark has energy $p - k$ and the antiquark k. Also the region $k > p > 0$ corresponds to a production of a quark-antiquark pair, yet with switched roles of the outgoing partons, this time the antiquark has energy $p - k$ and the quark energy k. Therefore, again the k-range is limited to $k < p/2$ in order to avoid a double counting of final states. The remaining region of $k < 0$ corresponds to the case where a gluon with energy p fuses with a quark from the thermal bath with energy k to produce a quark with higher energy $p - k > p$. Analogous to the region $k > p > 0$ of the process $q \leftrightarrow qg$, this process converts the incoming gluon into a quark with energy larger energy $p - k > p$.

(a) Quark-antiquark production **(b)** Absorption of quark/antiquark

Figure 5.46: Schematic representation of the different k regions in the process $\mathrm{g} \leftrightarrow q\bar{q}$.

5.4.3 Semi-analytical results for gluon radiation from AMY

In the following we will present results for both the actual AMY rates and their implementation within the BAMPS framework. To this end, we tabulate both the differential rates $\mathrm{d}\Gamma/\mathrm{d}k$ and their corresponding integrated rates $\Gamma(p) = \int \mathrm{d}k\, \mathrm{d}\Gamma/\mathrm{d}k(p,k)$ obtained via the numerical calculation discussed in Appendix C. These tables are then read during the simulation and combinations of p and k that were not tabulated are obtained via two-dimensional interpolation routines from the GSL[Gal+] computing library. For numerical accuracy we split these tables in two p regions, $0.15\,\mathrm{T} < p < 1.5\,\mathrm{T}$ and $p > 1.5\,\mathrm{T}$. Since Eqs. (5.94) and (5.102) on page 116 and on page 118 scale both with temperature T and the QCD coupling g_s^2 the tables are calculated for unitless quantities, so T and g_s^2 are multiplied to the rate during runtime. As one can see, e.g., in the splitting kernel of $q \leftrightarrow qg$, $\left(1 + (1-x)^2\right)/\left(x^3(1-x)^2\right)$, the emission rate within AMY diverges for $x = k = 0$ and $x = 1 \rightarrow k = p$. Therefore, when tabulating the emission rate $\mathrm{d}\Gamma/\mathrm{d}k$, these divergences are omitted in a range $\Delta k = 0.05\,\mathrm{T}$ around $k = 0$ and $k = p$.

In Fig. 5.47 we show our calculation of the differential emission rate $\mathrm{d}\Gamma/\mathrm{d}k$ in the AMY formalism for the process $q \leftrightarrow qg$ for a fixed value $p = 45\,\mathrm{T}$ and a QCD coupling of $\alpha_s = 0.3$. The result is obtained directly from the tabulated values and therefore close to the actual AMY formalism. While the divergence at $k = 0$ is clearly identifiable, the other divergence at $k = p$ is not visible due to numerical accuracy. The three different regions corresponding to the processes $q \rightarrow qg$, $qg \rightarrow q$ and $q\bar{q} \rightarrow \mathrm{g}$ are separated by dashed lines at $k = 0$ and $k = p$. At small $|k| \lessapprox 2T$ the distribution is rather symmetric. This means that the rates of emitting a gluon and absorbing a soft gluon are similar. In contrast, the Bremsstrahlung contribution of $q \rightarrow qg$ is dominated between $k \approx 2\,\mathrm{T}$ and $k = p$ by the LPM effect and therefore scales as expected with $\frac{\mathrm{d}\Gamma}{\mathrm{d}k} \sim k^{-3/2}$ (s. Section 5.1.2). For $k > p$ the rate for quark-antiquark annihilation is steeply decreasing with increasing gluon energy.

The p dependence of $\mathrm{d}\Gamma/\mathrm{d}k$ is shown in Fig. 5.48 where we plot $\mathrm{d}\Gamma/\mathrm{d}k$ of the three different processes $q \leftrightarrow qg$, $\mathrm{g} \leftrightarrow \mathrm{gg}$ and $\mathrm{g} \leftrightarrow q\bar{q}$ for different values of p, again for a constant QCD coupling $\alpha_s = 0.3$. As discussed previously the distribution of $\mathrm{g} \leftrightarrow \mathrm{gg}$

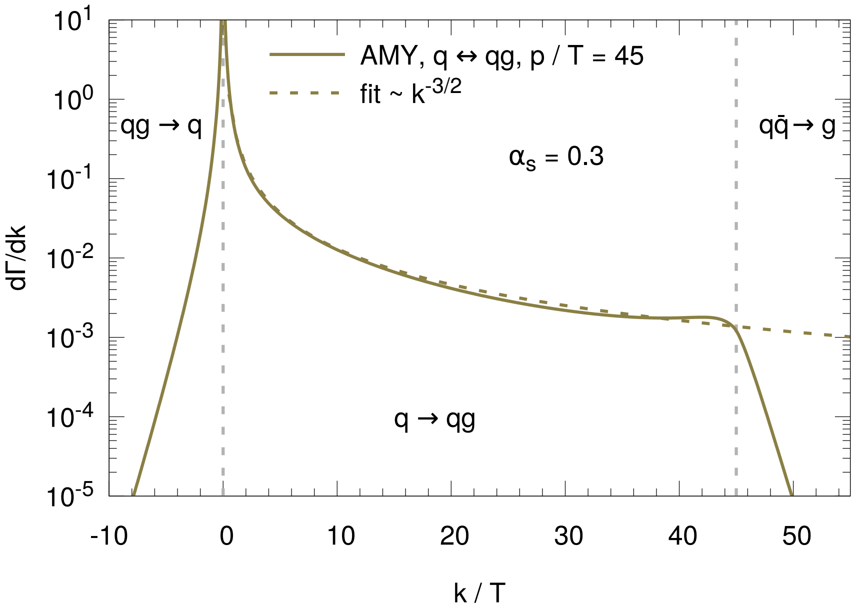

Figure 5.47: Differential emission rate $\mathrm{d}\Gamma/\mathrm{d}k$ from the $q \to qg$ process of the AMY formalism for a projectile with energy $p = 45\,\mathrm{T}$ emitting partons with energy k in a medium with temperature T and a fixed QCD coupling $\alpha_s = 0.3$. The different k regions from different underlying physical process are separated by dashed lines. While the divergence at $k = 0$ is clearly visible, the divergence at $k = p$ is due to numerical accuracy only mildly recognizable. The dashed gray line shows a fit with the expected $\mathrm{d}\Gamma/\mathrm{d}k \sim k^{-3/2}$ behavior.

and $\mathrm{g} \leftrightarrow q\bar{q}$ are limited by $k = p/2$ since then the process can be obtained by switching the final state partons. The distribution of the processes $q \leftrightarrow q\mathrm{g}$ and $\mathrm{g} \leftrightarrow \mathrm{gg}$ are almost independent from p at small k values. So soft gluons are emitted and absorbed independently from the energy of the projectile. The different p values mainly constrain the maximum allowed emitted gluon/quark energy and thereby the limit of the distribution. On the other hand, the distribution of the process $\mathrm{g} \leftrightarrow q\bar{q}$ strongly depends on the energy of the gluon. Soft gluons will hence more likely split into a quark-antiquark pair than a gluon with larger energy p.

Due to the different color factors C_F and C_A, a hard gluon will radiate more than a hard quark. In Fig. 5.49 we show the integrated rate $\Gamma(p) = \int \mathrm{d}k\, \mathrm{d}\Gamma/\mathrm{d}k(p,k)$ for the different processes $q \leftrightarrow q\mathrm{g}$, $\mathrm{g} \leftrightarrow \mathrm{gg}$ and $\mathrm{g} \leftrightarrow q\bar{q}$. Indeed, at large energies p the difference between quark and gluon Bremsstrahlung is exactly $C_\mathrm{F}/C_\mathrm{A}$. The rate of $\mathrm{g} \leftrightarrow \mathrm{gg}$ at softer energies then increases stronger than the rate of $q \leftrightarrow q\mathrm{g}$. As already identified in the differential rate, the rate for $\mathrm{g} \to q\bar{q}$ strongly depends on the energy p of the gluon. While the rate at thermal energies $p \lessapprox T$ comparable to the rate of $q \leftrightarrow q\mathrm{g}$, its contribution at higher energies is negligible in comparison with the more dominant process $\mathrm{g} \to \mathrm{gg}$.

5.4.4 Implementing the effective $1 \leftrightarrow 2$ processes into BAMPS

After discussing the semi-analytical results for the AMY emission rate we introduce the evaluation of the effective $1 \leftrightarrow 2$ processes within the BAMPS framework. One already existing approach that uses the discussed transition rates in a numerical simulation is the Monte-Carlo model MARTINI [JM05; Tur06; SGJ09; SGQ09]. By combining the transition rate with Fokker-Planck type equations MARTINI compute the evolution of the

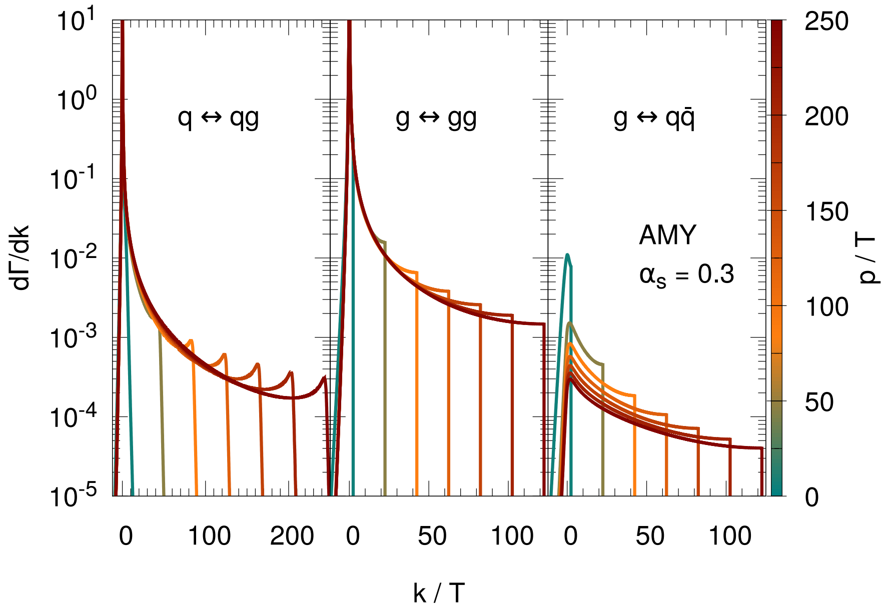

Figure 5.48: Differential emission rate $\mathrm{d}\Gamma/\mathrm{d}k$ for different projectile energies p and processes from the AMY formalism. The different values of p are given by varying colors from small energies (green) to larger energies (red). We show in the left panel the rate of the process $q \leftrightarrow qg$, in the middle panel the rate of the process $\mathrm{g} \leftrightarrow \mathrm{gg}$ and in the right panel the rate of the process $\mathrm{g} \leftrightarrow q\bar{q}$. The QCD coupling is fixed to $\alpha_s = 0.3$.

jet-momentum distribution in a hydrodynamic background [SGJ09]. The evolution of the hard quark/antiquark and gluon distributions then reads [JM05],

$$\begin{aligned}
\frac{\mathrm{d}P_{q\bar{q}}(p)}{\mathrm{d}t} &= \int_k P_{q\bar{q}}(p{+}k)\frac{\mathrm{d}\Gamma^q_{qg}(p{+}k,k)}{\mathrm{d}k} + 2P_g(p{+}k)\frac{\mathrm{d}\Gamma^g_{q\bar{q}}(p{+}k,k)}{\mathrm{d}k} - P_{q\bar{q}}(p)\frac{\mathrm{d}\Gamma^q_{qg}(p,k)}{\mathrm{d}k}\,, \\
\frac{\mathrm{d}P_g(p)}{\mathrm{d}t} &= \int_k P_{q\bar{q}}(p{+}k)\frac{\mathrm{d}\Gamma^q_{qg}(p{+}k,p)}{\mathrm{d}k} + P_g(p{+}k)\frac{\mathrm{d}\Gamma^g_{gg}(p{+}k,k)}{\mathrm{d}k} \\
&\quad - P_g(p)\left(\frac{\mathrm{d}\Gamma^g_{q\bar{q}}(p,k)}{\mathrm{d}k} + \frac{\mathrm{d}\Gamma^g_{gg}(p,k)}{\mathrm{d}k}\Theta(2k{-}p)\right)\,,
\end{aligned} \tag{5.105}$$

where $P_{q\bar{q}}$ is the distribution of both quarks and antiquarks, P_g is the distribution of gluons, and the superscript of $\mathrm{d}\Gamma/\mathrm{d}k$ represents the initial state, whereas the subscript denotes the final state flavors, respectively. Positive contributions are gain terms and negative contributions represent loss terms for partons with energy p.

The probability for a microscopic scattering within BAMPS is proportional to the cross section of this process (cf. Chapter 4). For an $1 \leftrightarrow 2$ splitting/absorption process the probability to occur is then correspondingly given by

$$P_{1\leftrightarrow 2} = \Delta t\, \Gamma_{1\leftrightarrow 2}(p) = \Delta t \int \mathrm{d}k\, \frac{\mathrm{d}\Gamma}{\mathrm{d}k}(p,k)\,, \tag{5.106}$$

where Δt is the time step in the simulation and $\Gamma_{1\leftrightarrow 2}$ the integrated rate for a parton with energy p. In contrast to the other scattering probabilities within BAMPS the probability for the $1 \leftrightarrow 2$ process does not depend on the discretization in coordinate space, namely the

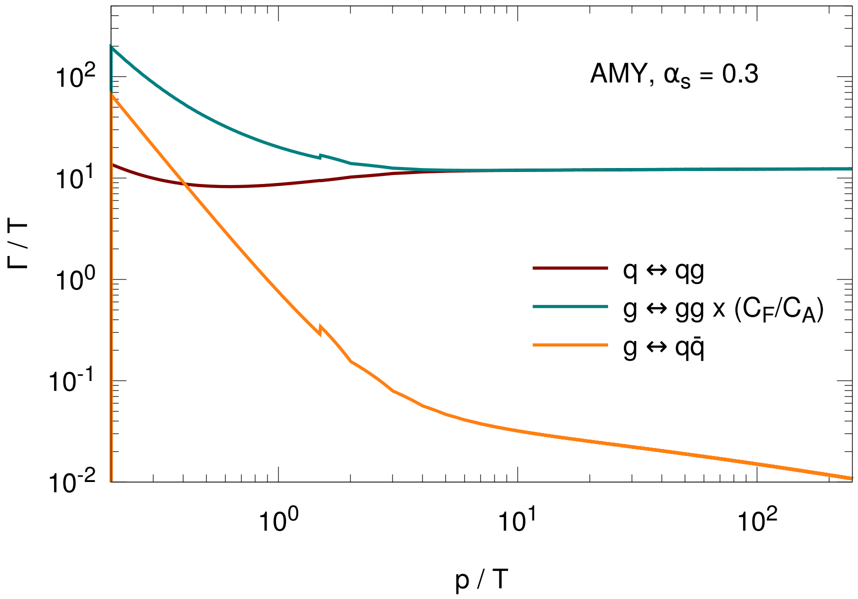

Figure 5.49: Total emission rate Γ depending on the projectile energy p for the different processes from the AMY formalism. In order to demonstrate the scaling of $q \leftrightarrow qg$ and $\mathrm{g} \leftrightarrow gg$ at high projectile energies we scale the process $\mathrm{g} \leftrightarrow gg$ by $C_\mathrm{F}/C_\mathrm{A}$. The QCD coupling is fixed to $\alpha_s = 0.3$. The numerical artifact at $p = 1.5T$ originates from using two different tables for $p < 1.5T$ and $p > 1.5T$.

cell volume, but only on the time step. However, since the AMY rate is calculated for a thermal bath, the quantities in AMY as, e.g., the projectile energy p or the temperature T have to be evaluated in the local rest frame of the cell. While this is trivial for the static, thermal medium in this chapter, the boost to the local rest frame has to be considered when applied in the expanding medium of a heavy-ion collision (s. Chapter 7). Furthermore, in the expanding scenario also the definition of the temperature in the AMY formalism needs further consideration.

If it is decided that a parton undergoes a $1 \leftrightarrow 2$ process, both the actual process and the corresponding k is sampled based on the differential emission rate $\mathrm{d}\Gamma/\mathrm{d}k$. For example, if for an emitting quark a negative value for k is sampled, the quark absorbs a thermal antiquark from the medium and thereby gains energy to $p + |k|$. On the other hand, if a value of $0 < k < p$ is sampled, a gluon is generated that takes away an energy k from the quark. We have seen that the transverse momentum of both the emitter and the emitted parton are $\mathcal{O}(g_s T)$. Therefore we neglect any transverse momentum of the emitting or emitted parton: all outgoing partons fly in the same direction as the ingoing partons while shifting the energies between the partons. In the case of $\mathrm{g} \to q\bar{q}$ the flavor of the outgoing quarks is randomly determined.

It is important to note, that although the coherent scatterings of the gluon and quark during the formation time were explicitly considered in the derivation of the AMY formalism, they are not explicitly simulated in contrast to the previous sLPM approach. Rather the emitting parton undergoes an effective $1 \leftrightarrow 2$ process (or in the case $q\bar{q} \to \mathrm{g}$ a “$1 \to 1$” process) within the surrounding thermal medium for which the scatterings were resummed into the effective rate. Also the absorbed thermal antiquark in a $q\bar{q} \to \mathrm{g}$ process is assumed to come from a thermal distribution. This procedure obviously neglects the microscopic nature of the single scattering processes and consequently any back reaction of

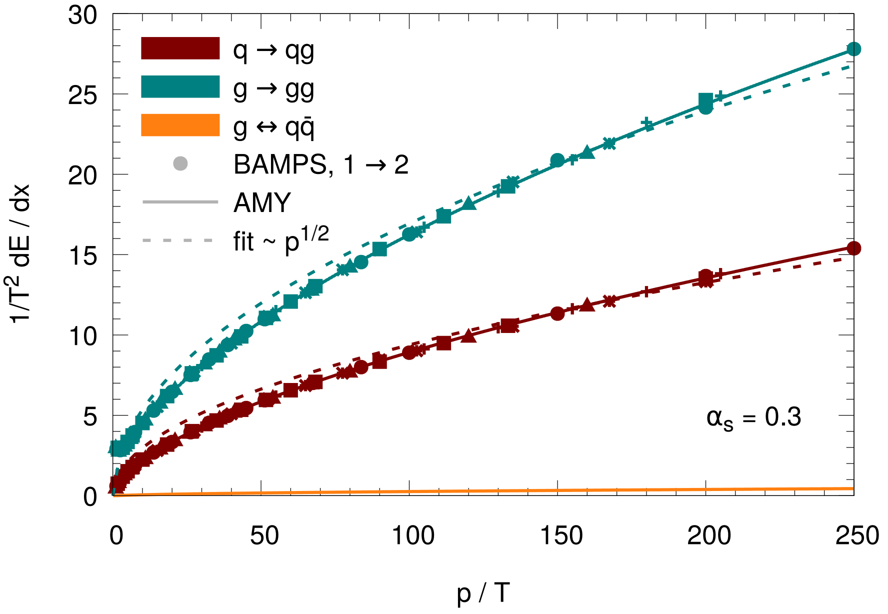

Figure 5.50: Differential energy loss $\mathrm{d}E/\mathrm{d}x$ depending on the projectile energy p for the different processes $q \to qg$, $\mathrm{g} \to \mathrm{gg}$ and $\mathrm{g} \to q\bar{q}$ from the AMY formalism. The QCD coupling is fixed to $\alpha_s = 0.3$. While the points show the numerical results from BAMPS simulations, the solid lines are obtained by directly integrating the AMY emission spectra. The additional dashed lines show the expected $\mathrm{d}E/\mathrm{d}x \sim \sqrt{p}$ behavior of the non-Abelian LPM effect.

these scatterings to the medium. This is a valid assumption in the case of a high energy jet traversing a static thermal medium but can have limitations if applied to situations where either the emitting parton is rather thermal $p \sim \mathcal{O}(T)$ or in a non-thermal background.

5.4.5 Validating the numerical implementation of AMY

In order to validate the discussed implementation we compare in Fig. 5.50 the differential energy loss rate $\mathrm{d}E/\mathrm{d}x$ of a parton with energy E in the AMY formalism, obtained via (a) a semi-analytic calculation,

$$\frac{\mathrm{d}E}{\mathrm{d}x}(p) = \int_0^{\{p;p/2\}} \mathrm{d}k\, k\, \frac{\mathrm{d}\Gamma}{\mathrm{d}k}(p,k) \tag{5.107}$$

and (b) the numerical simulation of the $1 \to 2$ processes within the BAMPS framework. The results for $q \to qg$ and $\mathrm{g} \to \mathrm{gg}$ only consider the respective Bremsstrahlung process, which is tantamount to $0 < k < \{p; p/2\}$. Concerning the potential double counting in the process $\mathrm{g} \to \mathrm{gg}$, in the BAMPS simulation the softer gluon is identified with the momentum k in order to be consistent with the $k = p/2$ limit in the AMY formalism. The semi-analytical calculation and the simulation agree nicely proving the validity of the discussed numerical implementation of the AMY formalism within BAMPS. Furthermore, as expected by the considerations of Section 5.1.2 the $\mathrm{d}E/\mathrm{d}x$ within the AMY formalism shows the $\mathrm{d}E/\mathrm{d}x \sim \sqrt{E}$ signature of the non-Abelian LPM effect.

To further check the numerical procedure implementing the AMY rates within BAMPS we also show in Fig. 5.51 a comparison of our numerical simulation of AMY within

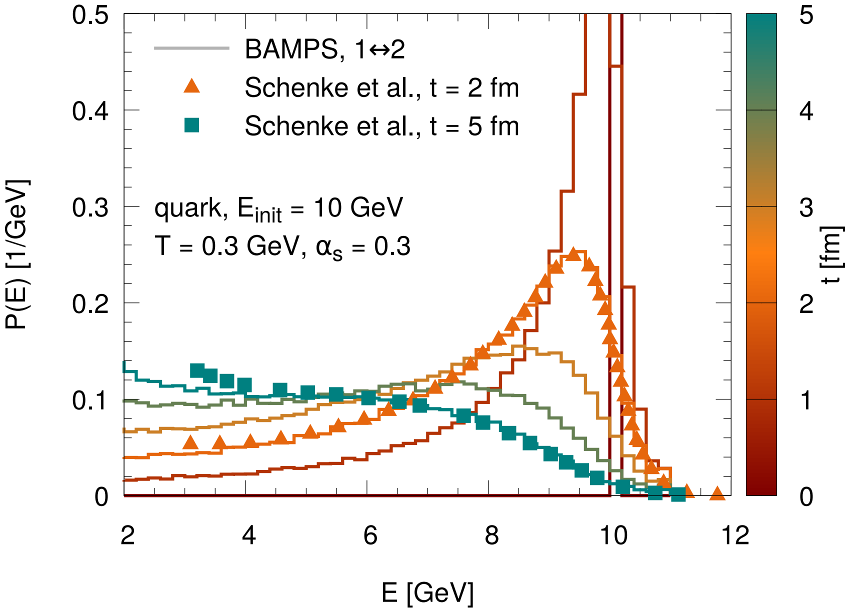

Figure 5.51: Time evolution of the energy distribution of an initial quark jet with $E_{\text{init}} = 10\,\text{GeV}$ from Bamps with Amy interactions (shown by lines) in comparison with the corresponding results of Martini taken from Ref. [SGQ09] (shown by points). The jet traverses a medium with temperature $T = 0.3\,\text{GeV}$ and the QCD coupling is fixed to $\alpha_s = 0.3$. The color of the distribution depicts different evolution times t of the jet in the medium.

Bamps to the previously mentioned Martini model [SGQ09]. Shown is the evolution of the energy distribution of a quark with initial energy $E = 10\,\text{GeV}$ that traverses a thermal medium with temperature $T = 0.3\,\text{GeV}$ and constant QCD coupling $\alpha_s = 0.3$. Different to the other calculations in this chapter the quark is not assumed to be eikonal, so every emission/absorption process indeed changes the energy of the emitting quark. The agreement between Bamps and Amy at both $t = 2\,\text{fm}$ and $t = 5\,\text{fm}$ is compelling.

This section concludes the discussion about how to implement the LPM effect into the partonic transport approach Bamps as it was done in the present work. We defined three different ways how to model the coherence of gluon emissions either parametrically or dynamically, either microscopically or from a more macroscopic picture. In the next section we will compare these approaches among each other and confront it with other models for the radiative energy loss in pQCD.

5.5 Comparison of different LPM approaches

In the previous sections we discussed three different approaches for investigating the LPM effect in a partonic transport model: an effective parametrization via a theta function in the radiative matrix elements, a stochastic suppression by explicit elastic scatterings of the emitted gluons during their finite formation time and an Ansatz incorporating the radiative rates calculated via hard thermal loops, namely the Amy formalism. The different model assumptions are summarized in Table 5.1. In this section we discuss potential differences and their origins between the presented models. First, we will study in the next subsection the differences between the microscopic formulations, θ-LPM and stochastic LPM, and the Amy formalism based on macroscopic quantities. In doing so we calibrate the microscopic approaches to the AMY formalism and compare them against each other to see how their emission patterns differ. Finally, we will confront the three approaches with different other calculations of radiative energy loss in pQCD and find potential similarities and differences.

	θ-LPM	stochastic LPM	AMY
characteristics	microscopic scattering	microscopic scattering	thermal rate
underlying processes	$2 \to 3$	$2 \to 3 + 2 \to 2$	"$1 \leftrightarrow 2$"
finite formation time τ_f	✗	✓	✗
scatterings during τ_f	✗	✓ (LO-pQCD)	✓ (HTL)
parametric coherence $\sim \theta(\lambda - \tau_f)$	✓	✗	✗
stochastic coherence $\sim 1/N_{\mathrm{coh}}$	✗	✓	✗

Table 5.1: Comparison of the model assumptions in the different LPM approaches studied in this work.

5.5.1 Effective LPM approaches vs. AMY formalism

Both effective approaches for the LPM effect within BAMPS, the θ-LPM model of Section 5.2 and the stochastic LPM algorithm of Section 5.3, initiate a potential gluon emission by a $2 \to 3$ process calculated in the improved Gunion-Bertsch approximation (cf. Chapter 3). After we presented in the previous sections how both approaches depend on their respective screening parameter, we will compare in this section both approaches to the more formal AMY calculation where such a free parameter does not exist. This will allow us to determine values for the screening parameters that reproduce a more formal LPM suppression.

Model differences between AMY and the effective LPM approaches

In the θ-LPM approach we model the LPM suppression by constraining the allowed phase space with the help of a theta function in the radiative matrix element. This theta function ensures that the formation time of a gluon is smaller than the mean free path of the projectile to the next scattering center. Consequently the emissions are produced incoherently. The contribution of coherent gluon emissions is then added by effectively increasing the phase space by the parameter X_{LPM}. On the contrary, in the sLPM approach the gluon scatterings during the formation time are explicitly simulated. This allows to dynamically decide for each emission how coherent scatterings contribute to the radiative process. After formation, the gluons are suppressed based on their number of coherent scatterings during the formation time. We found that there is no ad-hoc way of screening the $k_\perp$ divergence of the initial $2 \to 3$ matrix element in this approach. Therefore we introduced the parameter ξ_{LPM} that effectively controls the minimum transverse momentum $k_{\perp;\,\mathrm{min}} = \xi_{\mathrm{LPM}}\sqrt{\hat{s}}$.

Both parameters X_{LPM} and ξ_{LPM} logarithmically affect both the radiative energy loss and the underlying emission rates in the effective implementations for the LPM effect. In the AMY formalism the $k_\perp$ divergence of the radiative processes is cured by resumming an arbitrary number of interactions of the gluons within their formation time. The resulting transverse momentum $k_\perp$ of the gluon is expected to be on the order $k_\perp \sim \mathcal{O}(g_s T)$ and thereby negligible. Gluons are produced collinearly wrt. the emitting parton and only

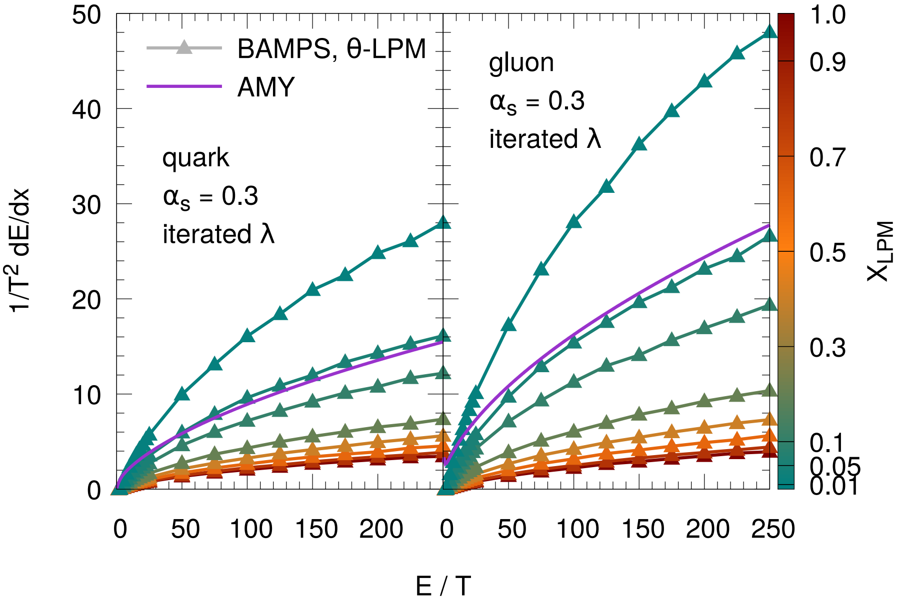

Figure 5.52: Differential radiative energy loss $\mathrm{d}E/\mathrm{d}x$ of a quark (left) or gluon (right) projectile depending on the projectile energy E from the θ-LPM approach with varying X_{LPM} in comparison to AMY. The different values of X_{LPM} are given by varying colors from small X_{LPM} (green) to larger X_{LPM} (red) values. Each given numerical value corresponds to a shown line. The mean free path entering the θ-function is calculated iteratively and the QCD coupling is fixed to $\alpha_s = 0.3$.

transfer energy away from the projectile. Consequently, a comparison of the $k_\perp$ spectra of the effective approaches and AMY are unrewarding in the following.

The energy loss of a projectile in the AMY formalism is exclusively caused by the radiation of gluons. Therefore the energy loss of the projectile can be calculated by integrating the ω-differential emission rate. In contrast, the radiative energy loss of the $2 \to 3$ underlying the θ-LPM and sLPM approaches has an additional $2 \to 2$ component (cf. Section 5.3.5). Therefore we define the energy loss in these approaches as the total energy loss of the projectile including the elastic component. For the comparison of the radiative processes for a gluon, $\mathrm{g} \to \mathrm{gg}$ in the AMY formalism or, e.g., $\mathrm{gg} \to \mathrm{ggg}$ in the other two approaches, one needs to take into account a consistent handling of symmetric outgoing partons. We decide to take the limit of soft gluon emissions and track the outgoing gluon with the higher energy as the outgoing projectile in the different approaches.

Furthermore, the AMY model is calculated in the thermodynamic limit, which is equivalent with a calculation solely in momentum space. The traversed medium is assumed to be infinite and hence the validity of the AMY formalism in thin media is questionable. Also the emissions rates and thereby the differential energy loss of the θ-LPM approach is independent from the medium length L. Consequently, the following comparison between θ-LPM and AMY will be independent from the specific choice of medium length.

Comparison of θ-LPM and AMY

We show in Fig. 5.52 the differential radiative energy loss $\mathrm{d}E/\mathrm{d}x$ of a quark or gluon projectile for the AMY formalism and the θ-LPM approach employing different screening values X_{LPM} (given by different colors). Since the mean free path itself depends on the inelastic radiation rate in the θ-LPM approach we calculated the underlying mean free path again iteratively for each X_{LPM} (cf. Section 5.2). We choose also a constant value of $\alpha_s = 0.3$ for the QCD coupling. As we found previously in Section 5.2 a decreasing value of X_{LPM} allows more collinear gluon emissions and thereby increases the radiative energy loss. The best agreement between the AMY formalism and the θ-LPM approach is given at $X_{\text{LPM}} := X_{\text{LPM}}^{\text{AMY}} = 0.05$ for both quark and gluon projectiles. This rather small value of X_{LPM} could have been expected since the AMY formalism is calculated in the small $k_\perp$ approximation, where the transverse momentum of gluon emissions are $k_\perp \sim \mathcal{O}(g_s T) \to 0$. We have seen in Section 5.2 that the radiative energy loss of quarks and gluon in the θ-LPM approach does not scale with the color factor $C_{\text{F}}/C_{\text{A}}$ due to the iterative calculation of the mean free path underlying the theta function. Interestingly this difference in the radiative energy loss is captured also in the AMY formalism where the elastic interactions of the quark-gluon system are formally resummed.

In the AMY formalism the $k_\perp$ divergence is cured by resumming the elastic scatterings of the gluons during the formation time to arbitrary orders. However, a same argument does not hold for the soft ω divergence from AMY originating from the DGLAP splitting kernel (cf. Section 5.4). The effective $k_\perp$ screening of the θ-LPM effect on the contrary does not only lead to a screening in $k_\perp$ but also a suppression of very soft (small ω) gluon emissions. This difference can be seen in Fig. 5.53 where we show the ω-weighted differential emission rate $\omega\, \mathrm{d}\Gamma/\mathrm{d}\omega$ of a quark (left) and gluon (right) projectile for different energies E (shown by different colors) comparing the AMY calculation with the θ-LPM approach together with the previously fixed value $X_{\text{LPM}}^{\text{AMY}}$. The distribution is again plotted in units of E in order to visualize the contribution of the different projectile components to the energy loss. The different treatment of the soft divergence is visible by the discrepancy of both approaches at very soft components. On the other hand, at hard gluon energies, $\omega \approx \mathcal{O}(E)$ in the quark case and $\omega \approx \mathcal{O}(E/2)$ in the gluon case, again the kinematical differences between a $1 \to 2$ process, where the emitted gluon may take away all the energy, and a $2 \to 3$ process, where the outgoing phase space has to be distributed among three final state partons, is recognizable. The spectrum within the θ-LPM approach is suppressed at high gluon energies, while in the AMY formalism the divergence at $\omega = E$ from the DGLAP splitting kernel is visible.

In order to reproduce nevertheless the energy loss of AMY the emission rate of the θ-LPM approach has to compensate the suppression of soft and high ω gluon emission by a higher rate of gluon emissions at intermediate regions. For a quark projectile with energy $E = 250\,\text{T}$, which corresponds to a quark with $E = 100\,\text{GeV}$ in a medium with temperature $T = 0.4\,\text{GeV}$, this intermediate region reaches from $\omega \approx 2 \cdot 10^{-3}\,\text{E}$ up to $\omega \approx 2 \cdot 10^{-1}\,\text{E}$. Please note that this difference in the intermediate ω region is more pronounced in the quark case than in the gluon case since the divergence at $\omega = E$ does not occur in the gluon case and therefore does not have to be compensated. One can conclude that, although the final radiative energy loss of the AMY formalism is well reproduced by choosing $X_{\text{LPM}}^{\text{AMY}}$ in the θ-LPM model the underlying spectrum shows differences by overestimating the intermediate ω region in the θ-LPM approach.

Comparison of stochastic LPM and AMY

We demonstrated in Section 5.3 that the finite formation time of gluon emissions in the sLPM approach leads to length dependent gluon emissions rates and thereby to a linear L dependence of the radiative energy loss $\mathrm{d}E/\mathrm{d}x$. In contrast the AMY formalism is formulated in the approximation of an infinite, thermal medium. Therefore we compare

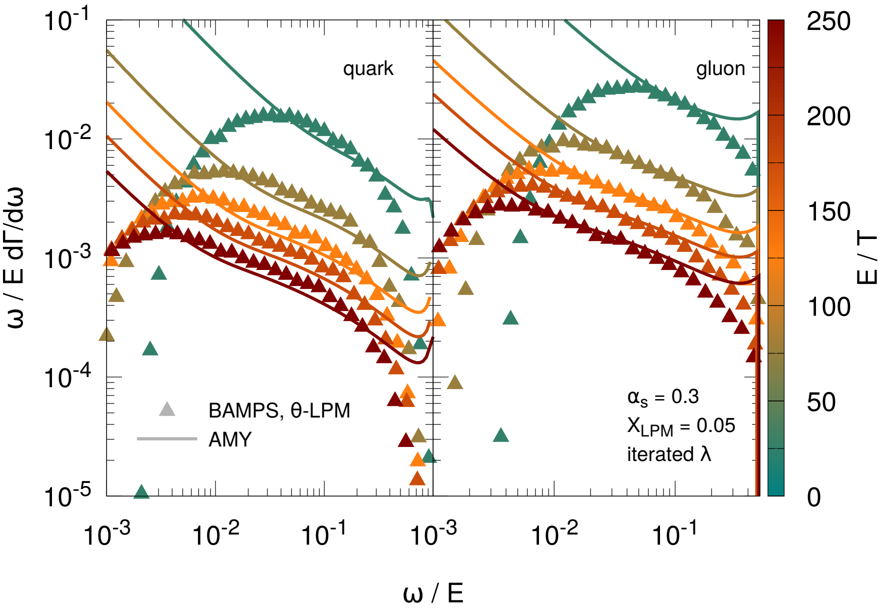

Figure 5.53: Differential emission rate $\mathrm{d}\Gamma/\mathrm{d}\omega$ of a quark (left) or gluon (right) projectile with different energies E from the θ-LPM approach with $X_{\text{LPM}} = 0.05$ in comparison to AMY. The different values of E are given by varying colors from small E (green) to larger E (red) values. The mean free path entering the θ-function is calculated iteratively and the QCD coupling is fixed to $\alpha_s = 0.3$. We scale $\mathrm{d}\Gamma/\mathrm{d}\omega$ by ω/E in order to better visualize the contribution of the different ω to the total radiative energy loss.

in the following the radiative energy loss of AMY with the radiative energy loss in the sLPM algorithm for a large medium length $L = 20\,\mathrm{T}^{-1}$, where also the stochastic LPM shows a path-length independence. This choice of $L = 20\,\mathrm{T}^{-1}$ corresponds, e.g., for a medium temperature $T = 0.4\,\mathrm{GeV}$ to $L = 10\,\mathrm{fm}$ and is longer than the typical critical medium length L_c even for the more energetic projectiles $E = 250\,\mathrm{T}$. Figure 5.54 shows $\mathrm{d}E/\mathrm{d}x$ depending on the projectile energy E for a quark (left) and gluon projectile (right) calculated via the stochastic LPM implementation for different values of ξ_{LPM} together with the results from AMY. This plot corresponds to Fig. 5.52, where we compared the θ-LPM approach with AMY. Again, in order to reproduce the enormous radiative energy loss in AMY a small value of the screening parameter ξ_{LPM} has to be chosen. In the case of a quark, $\xi_{\text{LPM}} := \xi_{\text{LPM}}^{\text{AMY; q}} = 0.01$ gives the best agreement with AMY. This parameter choice corresponds to an average minimum transverse momentum $k_{\perp;\,\text{min}} = \xi_{\text{LPM}}\sqrt{\hat{s}} \approx 0.4\,\mathrm{T}$ for a quark with $E = 250\,\mathrm{T}$, where we used $\langle \hat{s} \rangle = 6\,E\,T$ for the average center-of-momentum energy of a scattering between the jet and a thermal particle. The sLPM approach reproduces the energy dependence from AMY for the radiative energy loss of a quark over a wide E range. In contrast, in the case of a gluon projectile the sLPM approach favors a screening parameter $\xi_{\text{LPM}} := \xi_{\text{LPM}}^{\text{AMY; g}} = 0.015$. This choice then agrees with AMY at hard projectile energies but the different shape of $\mathrm{d}E/\mathrm{d}x$ leads to slight deviations at softer projectile energies. Reason for this different choice of $\xi_{\text{LPM}}^{\text{AMY}}$ for quarks and gluons is the already discussed $C_{\text{F}}/C_{\text{A}}$-scaling of the radiative energy loss $\mathrm{d}E/\mathrm{d}x$ within the sLPM model. In order to nevertheless calibrate the sLPM model to the AMY formalism we take into account the different scaling of the energy loss of quarks and gluons phenomenologically by different values of ξ_{LPM}.

In order to further study the radiative energy loss, Fig. 5.55 shows again the differential

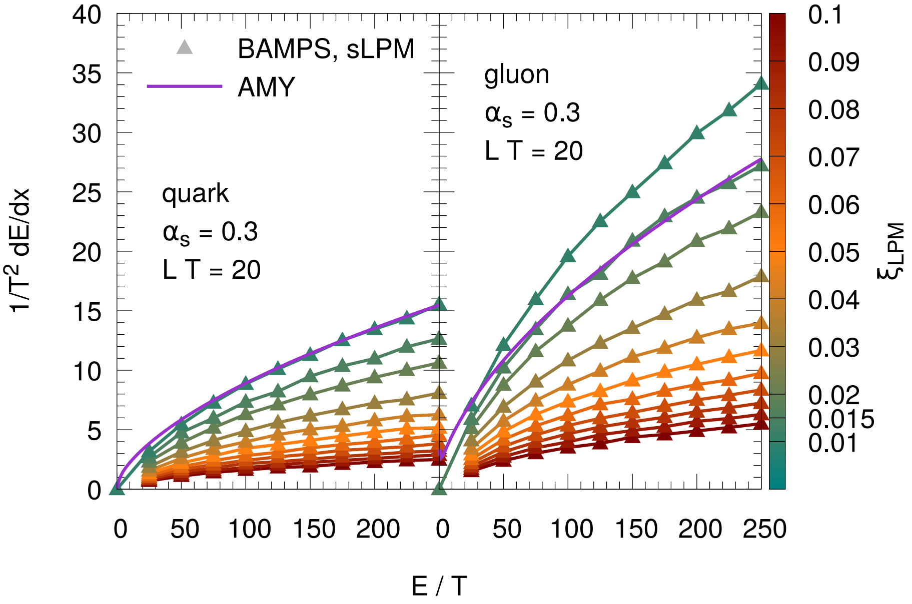

Figure 5.54: Differential radiative energy loss $\mathrm{d}E/\mathrm{d}x$ of a quark (left) or gluon (right) projectile in a medium with temperature T and length $L = 20\,\mathrm{T}^{-1}$ depending on the projectile energy E from the sLPM approach with varying ξ_{LPM} in comparison to AMY. The different values of ξ_{LPM} are given by varying colors from small ξ_{LPM} (green) to larger ξ_{LPM} (red) values. The QCD coupling is fixed to $\alpha_s = 0.3$.

emission rate $\omega\,\mathrm{d}\Gamma/\mathrm{d}\omega$ for both AMY and the stochastic LPM approach employing the just fixed values of $\xi_{\mathrm{LPM}}^{\mathrm{AMY}}$. Similar to the θ-LPM approach the spectra differ from each other both at soft and high gluon energies. Reason for this is again the limited phase space of the $2 \to 3$ process at high ω and the screening of collinear gluons at soft ω. In contrast to the θ-LPM approach, the sLPM algorithm leads to the same $\mathrm{d}\Gamma/\mathrm{d}\omega$ at soft ω for different projectile energies. Reason for this scaling is the dependence of the $k_\perp$ screening on the CoM energy $\sqrt{\hat{s}}$, which itself depends on the projectile energy. The similar suppression at hard and soft gluon energies lead to a similar overestimation of the differential rate at intermediate gluon energies as in the θ-LPM approach.

Comparison to AMY formalism with finite formation time

Caron-Huot and Gale successfully extended in Ref. [CG10] the AMY formalism by introducing finite-size effects. To this end, they started by the path-integral formulation of radiative energy loss from [Zak97] and Fourier transformed the path-integral. By cleverly rearranging the time integrations they arrived at a time-dependent emission rate

$$\frac{\mathrm{d}\Gamma^a_{bc}(t)}{\mathrm{d}\omega} = \frac{P^a_{bc}(x)}{\pi E}\mathrm{Re}\int\limits_0^t \mathrm{d}t_1 \int\limits_{\vec{\mathbf{q}},\vec{\mathbf{p}}} \frac{i\vec{\mathbf{q}}\cdot\vec{\mathbf{p}}}{\delta E\{\vec{\mathbf{q}}\}} C(t)K(t,\vec{\mathbf{q}};t_1,\vec{\mathbf{p}})\,, \tag{5.108}$$

where t_1 is the time of the last scattering during the formation time, $P^a_{bc}(x)$ are the DGLAP splitting kernels, $\delta E\{\vec{\mathbf{q}}\}$ is the inverse formation time and $C(t)K(t,\vec{\mathbf{q}};t_1,\vec{\mathbf{p}})$ the time-dependent emission kernel from the AMY formalism. This equation can then be solved numerically. For more information about the derivation as well as its numerical calculation

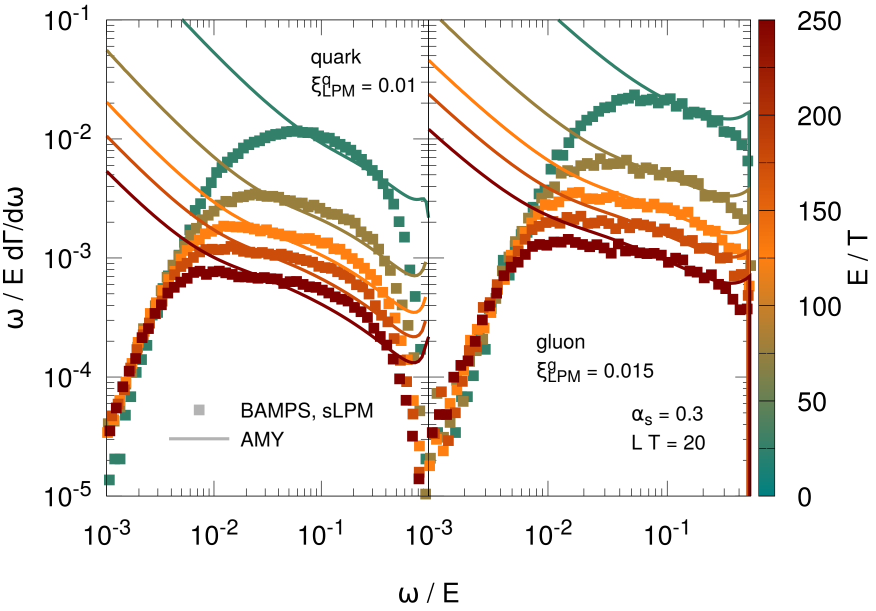

Figure 5.55: Differential emission rate $\mathrm{d}\Gamma/\mathrm{d}\omega$ of a quark (left) or gluon (right) projectile with different energies E from the sLPM approach with $\xi_{\mathrm{LPM}} = 0.01$ for the quark and $\xi_{\mathrm{LPM}} = 0.015$ for the gluon in comparison to AMY. The different values of E are given by varying colors from small E (green) to larger E (red) values. The QCD coupling is fixed to $\alpha_s = 0.3$. Again we scale $\mathrm{d}\Gamma/\mathrm{d}\omega$ by ω/E in order to better visualize the contribution of the different ω to the total radiative energy loss.

we refer to Ref. [CG10], where it was also shown that other models for the radiative energy loss, namely BDMPS-Z and GLV, could be reproduced as specific limits of Eq. (5.108) on the preceding page.

Figure 5.56 shows the time t dependence of the differential emission rate of gluons with $\omega = 7.5\,\mathrm{T}$ and $\omega = 20\,\mathrm{T}$ from a quark with energy $E = 40\,\mathrm{T}$ as calculated in Ref. [CG10] together with the corresponding rate from the sLPM implementation with $\xi_{\mathrm{LPM}} = \xi^{\mathrm{AMY}}_{\mathrm{LPM}}$ and AMY. Indeed the AMY emission rate can be viewed as the large t limit of Eq. (5.108) on the facing page. At small times t the finite-size effects suppress the rate in comparison with AMY. This finding is also seen in the sLPM approach, however, the rate in the sLPM approach builds up slower than the rate from Eq. (5.108) on the preceding page. Furthermore, as in Fig. 5.55 the rate at large t from the sLPM implementation shows slight deviation in comparison to the result by Caron-Huot and Gale. One reason for these discrepancies could be the different elastic interactions calculated either from leading-order pQCD in the sLPM approach or HTL in the AMY formalism.

5.5.2 Parametric vs. stochastic LPM

After we discussed the differences between the effective LPM approaches and AMY within BAMPS and thereby found potential values for the screening parameters $X^{\mathrm{AMY}}_{\mathrm{LPM}} = 0.05$ and $\xi^{\mathrm{AMY;\,q}}_{\mathrm{LPM}} = 0.01$ for quarks and $\xi^{\mathrm{AMY;\,g}}_{\mathrm{LPM}} = 0.015$ for gluons, respectively, we compare in this section both effective LPM implementations, θ-LPM and stochastic LPM, with each other. While the θ-LPM method parametrically suppresses gluon emissions, the gluons from the sLPM algorithm scatter elastically during the formation time and are subsequently suppressed stochastically.

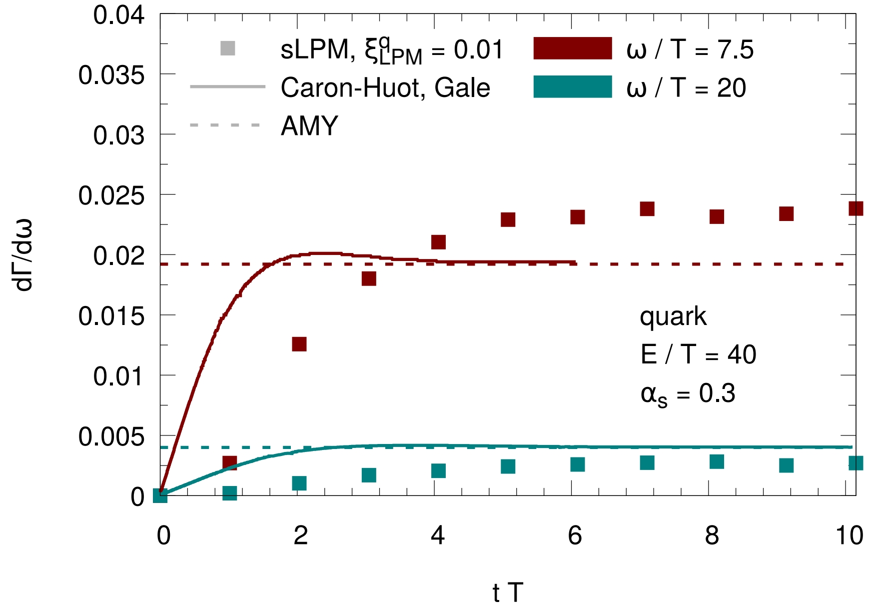

Figure 5.56: Time evolution of the differential emission rate $\mathrm{d}\Gamma/\mathrm{d}\omega$ at $\omega = 7.5\,\mathrm{T}$ (red) or $\omega = 20\,\mathrm{T}$ of a quark projectile with $E = 40\,\mathrm{T}$ traversing a medium with temperature T from the sLPM approach with $\xi_{\mathrm{LPM}} = 0.01$ in comparison with the semi-analytical results from Ref. [CG10]. The results from the BAMPS framework are shown by points and the results from Caron-Huot and Gale are given by solid lines. Additionally, we show in dashed lines the corresponding rate from the AMY formalism representing the infinite L limit of the calculation by Caron-Huot and Gale.

One major consequence from this different treatment is that the sLPM algorithm explicitly considers the finite formation time of the gluon emissions. Therefore the differential emission rates $\mathrm{d}\Gamma/\mathrm{d}\omega$ and $\mathrm{d}\Gamma/\mathrm{d}k_\perp$ in the sLPM method are path-length dependent. On the other hand, the rates from the θ-LPM approach have no path-length dependence. Therefore we choose for the following results as in the previous section $L = 20\,\mathrm{T}^{-1}$, which is in the large $L > L_c$ region, where also the stochastic LPM follows a path-length independent rate. Later we will then present potential differences emerging from the path-length dependence of the sLPM algorithm.

In Fig. 5.57 we show the radiative energy loss $\mathrm{d}E/\mathrm{d}x$ of a quark and gluon projectile from the θ-LPM approach in comparison to the large $L = 20\,\mathrm{T}^{-1}$ radiative energy loss from the sLPM algorithm. Due to the specific choice of screening parameters the radiative energy losses in the θ-LPM and sLPM approach looks unsurprisingly similar: While the energy loss in the θ-LPM is slightly higher for a quark, the gluon energy loss is slightly higher in the sLPM approach.

Figure 5.58 shows the total emission rate underlying the radiative energy loss of the two LPM models. Both LPM methods show a total emission rate that is rather independent for the shown projectile energies $E > 25\,\mathrm{T}$. The total rate of gluon emissions in the sLPM approach is smaller than the corresponding rate in the θ-LPM approach for both quark and gluon projectiles. This difference even slightly increases at higher projectile energies since the sLPM approach has a decreasing rate for increasing projectile energies due to hard ω emissions that are suppressed due to their long formation time. One can conclude that although the radiative energy loss in the θ-LPM and sLPM approach is comparable, the

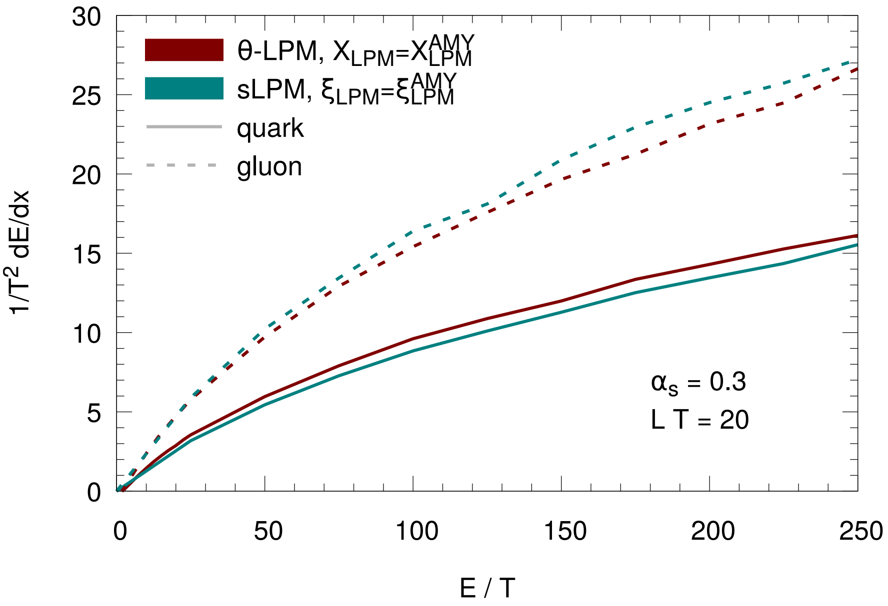

Figure 5.57: Differential radiative energy loss $\mathrm{d}E/\mathrm{d}x$ of a quark (solid lines) or gluon (dashed lines) projectile in a medium with temperature T and length $L = 20\,\mathrm{T}^{-1}$ depending on the projectile energy E from the θ-LPM (red) and the sLPM approach (green). The screening parameters are chosen by $X_{\mathrm{LPM}}^{\mathrm{AMY}} = 0.05$ in the θ-LPM and $\xi_{\mathrm{LPM}}^{\mathrm{AMY;\,q}} = 0.01$ or $\xi_{\mathrm{LPM}}^{\mathrm{AMY;\,g}} = 0.015$ in the stochastic LPM approach in order to reproduce the corresponding differential energy loss from the AMY formalism. The mean free path entering the θ-LPM approach is calculated iteratively and the QCD coupling is fixed to $\alpha_s = 0.3$.

θ-LPM needs more gluon emissions to achieve this energy loss in comparison to the sLPM calculation.

To further investigate the origin of the different emission rates we present in Fig. 5.59 the weighted differential emission rates $\omega\,\mathrm{d}\Gamma/\mathrm{d}\omega$ for both approaches. In the left panel we show $\mathrm{d}\Gamma/\mathrm{d}\omega$ from a quark, while the emission rates from a gluon are depicted in the right panel. For all shown projectile energies, the differential emission rates at gluon energies $\omega \to E$ are higher in the stochastic LPM approach than the corresponding rates from the θ-LPM approach. Reason for these higher rates in the stochastic LPM method is the possibility of energetic gluon emissions to accumulate transverse momentum during their formation time and thereby to finish their formation time. In contrast, these gluon emissions are not allowed in the θ-LPM approach where only the initial $k_\perp$ and ω of the $2 \to 3$ Bremsstrahlung process are considered. Therefore, in order to achieve a similar radiative energy loss wrt. the AMY formalism, this lack of gluons at high ω needs to be compensated in the θ-LPM approach by allowing more gluons at soft energies. This explains the significantly larger emission rate in the θ-LPM approach found in Fig. 5.58 for the specific choice of screening parameters calibrated to the AMY radiative energy loss. Furthermore, the different screening procedures of soft gluon emissions in the θ-LPM approach ($k_{\perp;\,\mathrm{min}} \sim \gamma/\lambda$) and the stochastic LPM approach ($k_{\perp;\,\mathrm{min}} \sim \sqrt{\hat{s}}$) lead to different dependencies of the emission rate at soft ω from the projectile energies. Therefore, the agreement between both approaches is better at smaller projectile energies than at large projectile energies.

The previous result can be further confirmed by showing in Fig. 5.60 the differential emission rate $\mathrm{d}\Gamma/\mathrm{d}k_\perp$ from both effective LPM approaches. Again, while the gluon

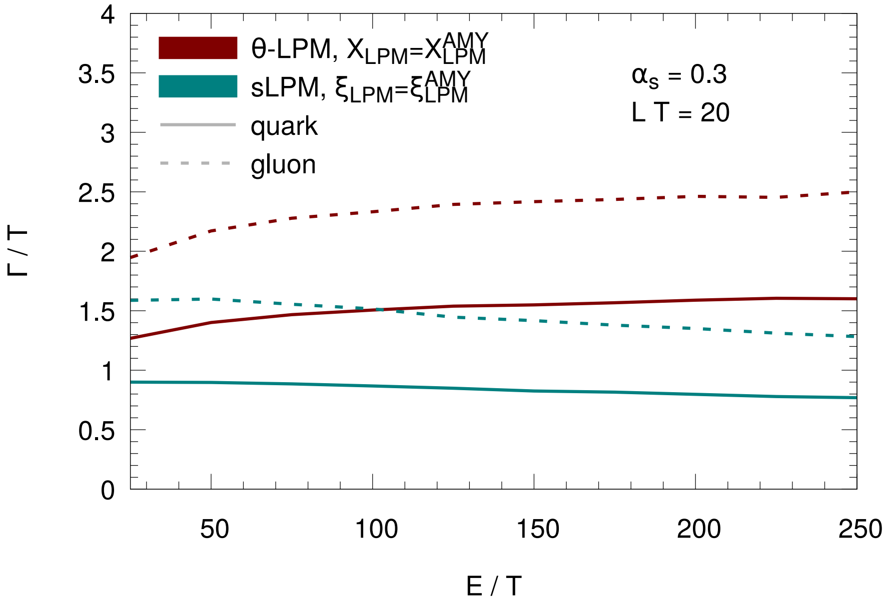

Figure 5.58: Total emission rate Γ of a quark (solid lines) or gluon (dashed lines) projectile in a medium with temperature T and length $L = 20\,\mathrm{T}^{-1}$ depending on the projectile energy E from the θ-LPM (red) and the sLPM approach (green). The screening parameters are chosen by $X^{\mathrm{AMY}}_{\mathrm{LPM}} = 0.05$ in the θ-LPM and $\xi^{\mathrm{AMY;\,q}}_{\mathrm{LPM}} = 0.01$ or $\xi^{\mathrm{AMY;\,g}}_{\mathrm{LPM}} = 0.015$ in the stochastic LPM approach in order to reproduce the corresponding differential energy loss from the AMY formalism. The mean free path entering the θ-LPM approach is calculated iteratively and the QCD coupling is fixed to $\alpha_s = 0.3$.

emissions in the θ-LPM approach are suppressed directly in the $2 \to 3$ matrix element, the gluons in the sLPM approach accumulate transverse momentum $k_\perp$ while they complete their formation time. Therefore, the gluon emissions in the θ-LPM approach show a peak at soft $k_\perp \approx 10^{-1}\,\mathrm{T}$, whereas the gluons from the sLPM approach thermalize during their formation time so that their final distribution peaks at $k_\perp \approx T$. This effect is again further amplified by the different choices of screening procedures in both approaches.

Finally, we show in Fig. 5.61 the radiative energy loss of both approaches for different projectile energies E depending on the medium length L. As mentioned earlier, the sLPM approach incorporates length-dependent emission rates up to the critical path length $L \approx L_c$ due to the finite formation time of gluon emissions. In contrast, the θ-LPM approach has L-independent rates since the suppression of gluons is evaluated by iterating the mean free path. Since the critical path length L_c depends on the projectile energy E, the length dependent radiative energy loss persists up to $L \approx 5\,\mathrm{T}^{-1}$ for a quark with $E = 25\,\mathrm{GeV}$ and up to $L \approx 10\,\mathrm{T}^{-1}$ for a quark with $E = 250\,\mathrm{GeV}$. For thicker media the $\mathrm{d}E/\mathrm{d}x$ of the sLPM approach reaches the L-constant $\mathrm{d}E/\mathrm{d}x$ from the θ-LPM approach that we discussed in Fig. 5.57.

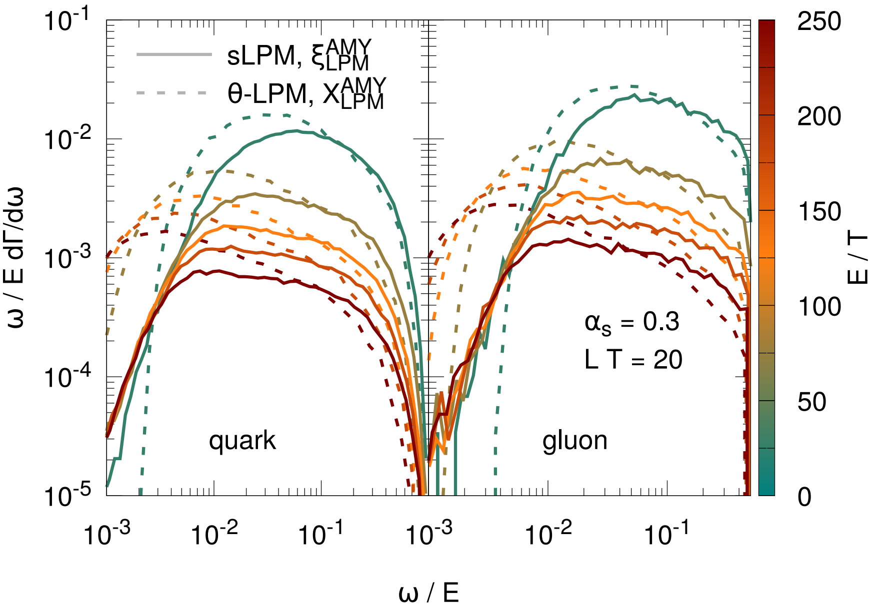

Figure 5.59: Differential emission rate $\mathrm{d}\Gamma/\mathrm{d}\omega$ of a quark (left) or gluon (right) projectile in a medium with temperature T and length $L = 20\,\mathrm{T}^{-1}$ from the θ-LPM (solid lines) and the sLPM approach (dashed lines) for different projectile energies E given by varying colors from small E (green) to larger E (red) values. The screening parameters are chosen by $X_{\mathrm{LPM}}^{\mathrm{AMY}} = 0.05$, $\xi_{\mathrm{LPM}}^{\mathrm{AMY;\,q}} = 0.01$ and $\xi_{\mathrm{LPM}}^{\mathrm{AMY;\,g}} = 0.015$ in order to reproduce the differential energy loss from the AMY formalism. We scale $\mathrm{d}\Gamma/\mathrm{d}\omega$ by ω/E in order to better visualize the contribution of the different ω to the total radiative energy loss. The mean free path entering the θ-LPM approach is calculated iteratively and the QCD coupling is fixed to $\alpha_s = 0.3$.

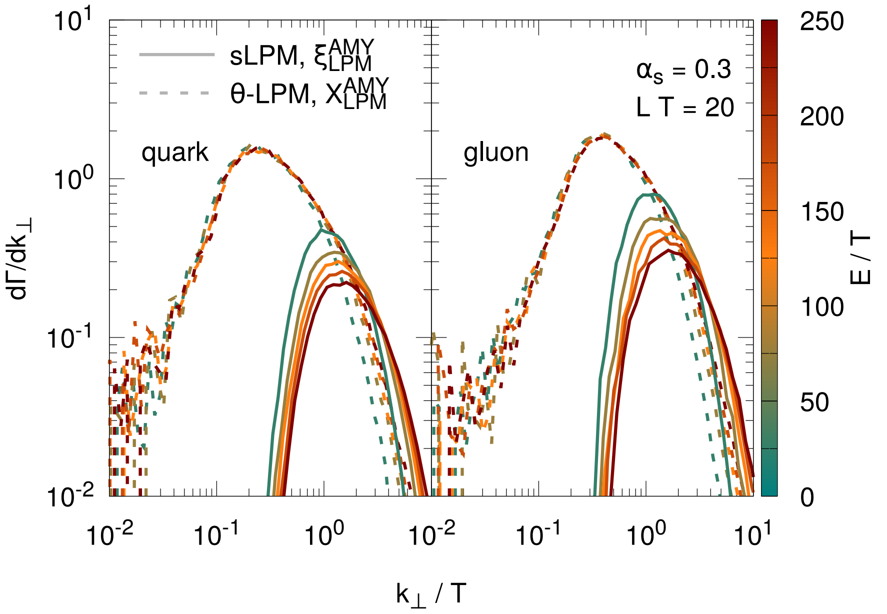

Figure 5.60: Differential emission rate $\mathrm{d}\Gamma/\mathrm{d}k_\perp$ of a quark (left) or gluon (right) projectile in a medium with temperature T and length $L = 20\,\mathrm{T}^{-1}$ from the θ-LPM (solid lines) and the sLPM approach (dashed lines) for different projectile energies E given by varying colors from small E (green) to larger E (red) values. The screening parameters are chosen by $X_{\mathrm{LPM}}^{\mathrm{AMY}} = 0.05$, $\xi_{\mathrm{LPM}}^{\mathrm{AMY;\,q}} = 0.01$ and $\xi_{\mathrm{LPM}}^{\mathrm{AMY;\,g}} = 0.015$ in order to reproduce the differential energy loss from the AMY formalism. The mean free path entering the θ-LPM approach is calculated iteratively and the QCD coupling is fixed to $\alpha_s = 0.3$.

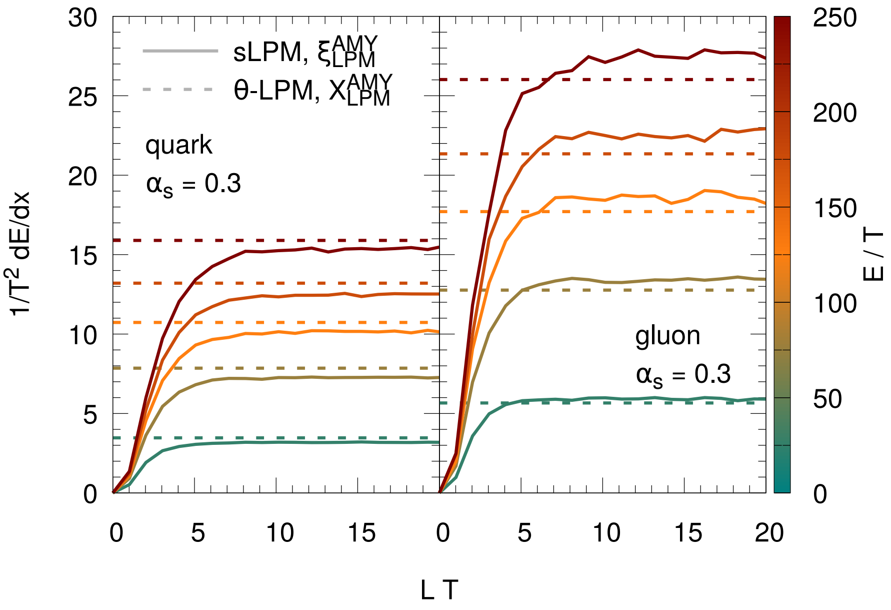

Figure 5.61: Length dependence of the differential radiative energy loss $\mathrm{d}E/\mathrm{d}x$ of a quark (left) or gluon (right) projectile in a medium with temperature T from the θ-LPM (solid lines) and the sLPM approach (dashed lines) for different projectile energies E given by varying colors from small E (green) to larger E (red) values. Same parameters used as in Fig. 5.60.

5.5.3 Comparison to other radiative energy loss calculations

The results from the comparison of the different LPM approaches studied in the previous section are summarized in Table 5.2. In order to further improve our picture of the radiative energy loss emerging from the non-Abelian LPM suppression, we confront in this section our three implementations of the LPM effect with other models for the radiative energy loss.

	θ-LPM	stochastic LPM	AMY
screening parameter	$X_{\text{LPM}}^{\text{AMY}} = 0.05$	$\xi_{\text{LPM}}^{\text{AMY; q}} = 0.01$ $\xi_{\text{LPM}}^{\text{AMY; g}} = 0.015$	-
differential rate $\mathrm{d}\Gamma/\mathrm{d}\omega$			
... at soft ω	$\mathrm{d}\Gamma/\mathrm{d}\omega\|_{\theta\text{-LPM}} > \mathrm{d}\Gamma/\mathrm{d}\omega\|_{\text{sLPM}}$		$\mathrm{d}\Gamma/\mathrm{d}\omega\|_{\text{AMY}} \to \infty$
... at hard ω	$\mathrm{d}\Gamma/\mathrm{d}\omega\|_{\theta\text{-LPM}} < \mathrm{d}\Gamma/\mathrm{d}\omega\|_{\text{sLPM}}$		$\mathrm{d}\Gamma/\mathrm{d}\omega\|_{\text{AMY}} \to \infty$
... at $\omega \to 0$	$\to 0$	$\to 0$	$\to \infty$
... at $\omega \to E$	$\to 0$	$\to 0$	$\to \infty$
... $\mathrm{d}\Gamma/\mathrm{d}\omega \sim \omega^{-3/2}$	(✓)	✓	✓
differential rate $\mathrm{d}\Gamma/\mathrm{d}k_\perp$			
⋯ collinear ($k_\perp = 0$) emissions	✗	✗	✓
⋯ $\mathrm{d}\Gamma/\mathrm{d}k_\perp$ shifted to thermal $k_\perp$	✗	✓	✗
⋯ $\mathrm{d}\Gamma/\mathrm{d}k_\perp$ peaked at $k_{\perp;\,\text{min}}$	✓	✗	✗
energy loss $\mathrm{d}E/\mathrm{d}x$			
... $\mathrm{d}E/\mathrm{d}x \sim \sqrt{E}$	✓	✓	✓
... $\mathrm{d}E/\mathrm{d}x \sim L$ for $L < L_c$	✗	✓	✗
... $\mathrm{d}E/\mathrm{d}x \sim$ const. for $L > L_c$	✓	✓	✓
... scaling with $C_{\text{F}}/C_{\text{A}}$	✗	✓	✗

Table 5.2: Comparison of the characteristics of the different LPM approaches after the effective approaches were calibrated to the AMY formalism.

Comparison to BDMPS-Z

As we have introduced in Section 5.1.1, one of the first investigations of the non-Abelian LPM effect in the context of parton energy loss was undertaken in the BDMPS-Z approach [Bai+95; Bai+97a; Bai+98a]. By assuming the scatterings of the quark-gluon system during its formation time as multiple and soft, Baier et al. predicted a $\sqrt{E}$ dependence of the energy loss [Bai+95] as well as a L^2 dependence of ΔE at thin media [Bai+97b]. In the following we will investigate the differences between BDMPS-Z and the three different LPM approaches in BAMPS.

The probability distribution for emitting gluons in the BDMPS-Z formalism can be written as in Eq. (5.9) on page 48 or in the small $x \to 0$ limit as given in, e.g., Ref. [Cas+11],

$$\omega \frac{\mathrm{d}I_{\text{BDMPS}}}{\mathrm{d}\omega} \sim \frac{2\alpha_s C_{\text{R}}}{\pi} \log\left|\cos\left((1+i)\sqrt{\frac{\omega_{\text{c}}}{\omega}}\right)\right| \tag{5.109}$$

where the critical gluon energy ω_{c} is equivalent to ω_{fact} in our notation. We tested that both formulas Eq. (5.109) and Eq. (5.9) on page 48 indeed agree numerically. As we have discussed in Section 5.1.2 the BDMPS-Z spectrum can be considered in the limiting cases [Cas+11]

$$\omega \frac{\mathrm{d}I_{\text{BDMPS}}}{\mathrm{d}\omega} \sim \frac{2\alpha_s C_{\mathrm{R}}}{\pi} \begin{cases} \sqrt{\frac{\omega_{\mathrm{c}}}{2\omega}} & \text{for} \quad \omega \ll \omega_{\mathrm{c}} \\ \frac{1}{12}\left(\frac{\omega_{\mathrm{c}}}{\omega}\right)^2 & \text{for} \quad \omega \gg \omega_{\mathrm{c}} \end{cases} . \tag{5.110}$$

This again demonstrates the familiar $\sim \omega^{-3/2}$ behavior in the LPM region and the strongly suppressed emissions in the factorization region $\omega > \omega_{\text{fact}}$.

Figure 5.62 shows a comparison of the emission spectrum given by Eq. (5.109) and the θ-LPM approach in BAMPS for a quark or a gluon projectile with energy E in a medium with temperature T and two different lengths L. The crucial parameter in the radiative energy loss from the BDMPS-Z formalism is the momentum broadening parameter $\hat{q}$. We determine this parameter for the presented comparison by calculating it via the leading-order Debye-screened elastic scatterings from pQCD as described in Section 5.3.3.

Furthermore, for comparison we also show the corresponding emission rate from the AMY formalism. As found, e.g., in Refs. [Arn09b; Arn09a; Arm+12] it can be shown that the long path-length limit of the BDMPS-Z approach coincides with the AMY formalism in the limit of multiple soft scatterings. However, since the BDMPS-Z formalism depends on the choice of $\hat{q}$ and our result for $\hat{q}$ is based on the discussed Debye-screened elastic interactions within BAMPS instead of scatterings from HTL, we find differences in the emission spectrum of BDMPS-Z and the AMY formalism. These differences are smaller at large medium lengths and increase by decreasing medium lengths when also finite-size effects in the BDMPS-Z set in that are missing in the AMY formalism.

The screening parameter entering the θ-LPM approach was chosen previously by $X_{\text{LPM}}^{\text{AMY}}$ in order to reproduce the AMY formalism. However, this choice of screening parameter shows too many gluon emissions in comparison to the given BDMPS-Z results of quarks and gluons at all medium lengths. Therefore we additionally show a different parameter choice of $X_{\text{LPM}} = X_{\text{LPM}}^{\text{BDMPS}} := 0.3$ that shows the closest agreement with the BDMPS-Z gluon emission spectrum of a quark projectile at large medium length $L = 10\,\text{fm}$. Interestingly, as we will see later in Chapter 7 this parameter choice also reproduces the suppression of charged hadrons in central heavy-ion collisions. For both parameter choices, at smaller ω again screening effects set in due to the choice of $k_\perp$ screening. While the parameter choice $X_{\text{LPM}}^{\text{BDMPS}}$ reproduces the emission rate of a quark, the θ-LPM approach with this parameter overshoots the BDMPS-Z spectra of a gluon. Reason for this difference is that the BDMPS-Z formalism in the small-x limit scales by the ratio of color factors $C_{\mathrm{F}}/C_{\mathrm{A}}$, whereas the θ-LPM approach does not. Furthermore, the θ-LPM approach lacks the length dependence due to the finite formation time of emissions. Consequently, the spectra at small medium lengths of the θ-LPM approach and BDMPS-Z differ. This difference is stronger at higher gluon energies, since these emissions have on average a longer formation time τ_f and the missing effect of finite formation times becomes more significant.

In contrast to the θ-LPM approach, the stochastic LPM approach introduced in Section 5.3 of this work, considers the finite formation time of gluon emissions and thereby a path-length dependence of the emission rate. Hence we show in Fig. 5.63 our results from the sLPM approach in comparison to BDMPS-Z. We use the same parameters entering the BDMPS-Z formalism as in Fig. 5.62. The screening parameter ξ_{LPM} of the sLPM approach is again either fixed by the values $\xi_{\text{LPM}}^{\text{AMY; q}}$ or $\xi_{\text{LPM}}^{\text{AMY; g}}$ for reproducing the AMY radiative energy loss or, similar to the previous procedure, by $\xi_{\text{LPM}}^{\text{BDMPS}} := 0.05$ in order to reproduce

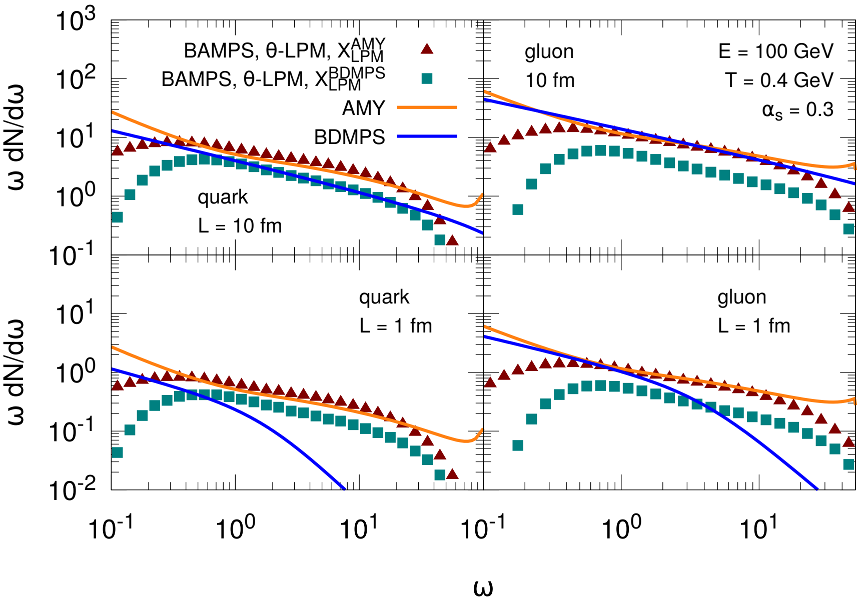

Figure 5.62: Emission spectrum $\mathrm{d}N/\mathrm{d}\omega$ of a quark (left column) or gluon (right column) projectile with energy $E = 100\,\mathrm{GeV}$ in a medium with temperature $T = 0.4\,\mathrm{GeV}$ and length $L = 10\,\mathrm{fm}$ (upper row) and $L = 1\,\mathrm{fm}$ (lower row). While the points show the numerical results from the θ-LPM approach in BAMPS for two different choices of screening parameters, $X_{\mathrm{LPM}}^{\mathrm{AMY}}$ (triangles) or $X_{\mathrm{LPM}}^{\mathrm{BDMPS}}$ (squares), the solid lines show the results from the AMY formalism (yellow) and the BDMPS-Z approach (blue). We scale the emission spectrum by by ω in order to better visualize the contribution of the different ω to the total radiative energy loss. The mean free path entering the θ-LPM approach is calculated iteratively and the QCD coupling is fixed to $\alpha_s = 0.3$. The momentum broadening parameter $\hat{q}$ of a quark ($\hat{q}_q(E = 100\,\mathrm{GeV}, T = 0.4\,\mathrm{GeV}) = 2.12\,\mathrm{GeV}^2/\mathrm{fm}$) or a gluon ($\hat{q}_g(E = 100\,\mathrm{GeV}, T = 0.4\,\mathrm{GeV}) = 4.85\,\mathrm{GeV}^2/\mathrm{fm}$) entering the BDMPS-Z calculation is determined by the elastic BAMPS interactions as described in Section 5.3.3.

the BDMPS-Z emission rate of a quark at large medium length $L = 10\,\mathrm{fm}$. Again we additionally show the corresponding AMY emission rate.

As the θ-LPM approach, the stochastic LPM calibrated to the AMY formalism overestimates the gluon emission rate of a quark at intermediate gluon energies in a medium with length $L = 10\,\mathrm{fm}$. On the other hand, due to the separate screening parameters for a quark or gluon projectile, the agreement between the stochastic LPM with $\xi_{\mathrm{LPM}}^{\mathrm{AMY;\,g}}$ and BDMPS-Z gets better in the case of a gluon projectile at $L = 10\,\mathrm{fm}$. While the other parameter choice $\xi_{\mathrm{LPM}}^{\mathrm{BDMPS}}$ shows an agreement in the intermediate $\omega > 10\,\mathrm{GeV}$ region of $\mathrm{d}N/\mathrm{d}\omega$ for a quark in a medium with $L = 10\,\mathrm{fm}$, this parameter choice underestimates the corresponding emission rate of a gluon projectile. Furthermore, the larger parameter $\xi_{\mathrm{LPM}}^{\mathrm{BDMPS}}$ cuts off stronger the soft gluon energies and hence the deviations of the stochastic LPM from BDMPS-Z at small ω increase.

At smaller medium lengths the spectrum of the sLPM approach is suppressed due to the finite formation time of emissions. Although the magnitude of the spectrum becomes comparable between BDMPS-Z and the sLPM approach at $L = 1\,\mathrm{fm}$, emissions with $\omega \gtrapprox 1\,\mathrm{GeV}$ are suppressed in the BDMPS-Z formalism while the spectrum from the sLPM method get its main contribution from this ω region for both ξ_{LPM} parameter choices. Reason for this differences are again the different elastic scatterings within the BAMPS approach that neglect the soft momentum transfers as they are predicted by HTL

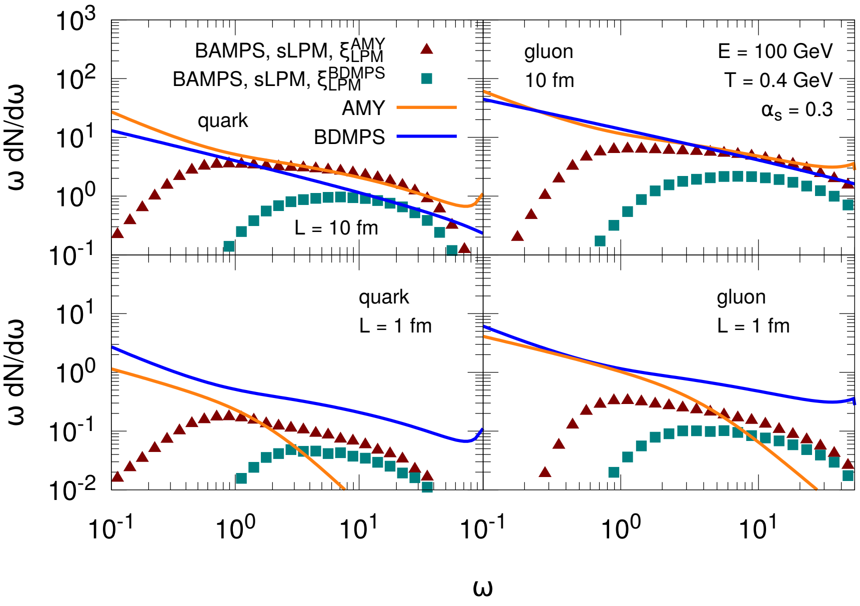

Figure 5.63: Emission spectrum $\mathrm{d}N/\mathrm{d}\omega$ of a quark (left column) or gluon (right column) projectile with energy $E = 100\,\mathrm{GeV}$ in a medium with temperature $T = 0.4\,\mathrm{GeV}$ and length $L = 10\,\mathrm{fm}$ (upper row) and $L = 1\,\mathrm{fm}$ (lower row). While the points show the numerical results from the sLPM approach in BAMPS for the two different choices of screening parameters, $\xi_{\mathrm{LPM}}^{\mathrm{AMY;\,q}}$ or $\xi_{\mathrm{LPM}}^{\mathrm{AMY;\,g}}$ (triangles) or $\xi_{\mathrm{LPM}}^{\mathrm{BDMPS}}$ (squares), the solid lines show the results from the AMY formalism (yellow) and the BDMPS-Z approach (blue). We scale the emission spectrum by by ω in order to better visualize the contribution of the different ω to the total radiative energy loss. The QCD coupling is fixed to $\alpha_s = 0.3$. The momentum broadening parameter $\hat{q}$ of a quark ($\hat{q}_q(E = 100\,\mathrm{GeV}, T = 0.4\,\mathrm{GeV}) = 2.12\,\mathrm{GeV}^2$/fm) or a gluon ($\hat{q}_g(E = 100\,\mathrm{GeV}, T = 0.4\,\mathrm{GeV}) = 4.85\,\mathrm{GeV}^2$/fm) entering the BDMPS-Z calculation is determined by the elastic BAMPS interactions as described in Section 5.3.3.

calculations. While in the θ-LPM approach these interactions enter the suppression by iterating a mean free path, in the sLPM approach the scatterings are explicitly evaluated and the influence of these scatterings becomes significant. It remains to investigate how a more realistic treatment of the elastic scatterings modifies the differences to the BDMPS-Z spectrum.

Comparison to ASW

Another approach for solving the path-integral Eq. (5.3) on page 47 for gluon emissions calculated in pQCD is the ASW formalism by Armesto, Salgado, and Wiedemann. This formalism investigated the gluon radiation in both common limits of multiple soft-scatterings ("ASW-MS") and a single hard scattering ("ASW-SH") during the formation time of an emission. While "ASW-SH" is strongly connected to the GLV formalism discussed in Section 5.1.1, the "ASW-MS" calculation extends the BDMPS-Z formalism by finite-length effects as formation time effects at small L or a finite transverse momentum $k_\perp$ of the emissions [Arm+12]. Consequently a comparison to both limits of the ASW model allows a further investigation of the characteristics of the presented LPM approaches.

A quantity for characterizing the radiative energy loss of a parton that is commonly attributed to ASW are the quenching weights $P(\Delta E/E)$, given in Eq. (5.11) on page 49. Based on a Poissonian Ansatz for multiple gluon emissions [SW02; SW03], the quenching

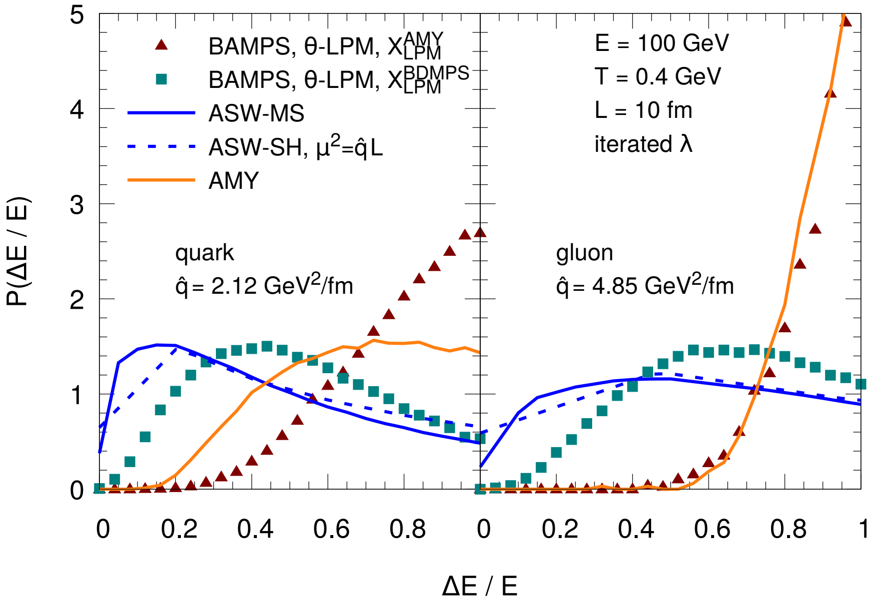

Figure 5.64: Quenching weights $P(\Delta E/E)$ of a quark (left column) or gluon (right column) projectile with energy $E = 100\,\text{GeV}$ in a medium with temperature $T = 0.4\,\text{GeV}$ and length $L = 10\,\text{fm}$. While the points show the numerical results from the θ-LPM approach in BAMPS for the two different choices of screening parameters, $X_{\text{LPM}}^{\text{AMY}}$ (triangles) or $X_{\text{LPM}}^{\text{BDMPS}}$ (squares), the lines show the calculations from the AMY formalism (yellow) and the ASW approach (blue). The ASW results are shown for the multiple-soft scattering limit "ASW-MS" (solid) and the single hard scattering limit "ASW-SH" (dashed). The momentum broadening parameter $\hat{q}$ of a quark or a gluon entering the ASW calculations is determined by the elastic BAMPS interactions as described in Section 5.3.3. The distributions are normalized to unity in the range $0 < \Delta E/E < 1$. The mean free path entering the θ-LPM approach is calculated iteratively and the QCD coupling is fixed to $\alpha_s = 0.3$.

weights give the probability for a parton with energy E to radiatively lose the energy ΔE. This probability can also be calculated in the BAMPS framework employing both the effective LPM approaches, θ-LPM and sLPM, and the AMY formalism, what allows a subsequent comparison to both ASW limits.

Figure 5.64 shows the quenching weights calculated in the θ-LPM approach in comparison with calculations obtained from "ASW-MS" and "ASW-SH". The quenching weights of all different approaches are calculated for a quark (left) or gluon (right) projectile with energy E traversing a medium with temperature T and length L. As for the comparison with BDMPS-Z, the momentum broadening parameter $\hat{q}$ necessary for the ASW calculations is calculated by the Debye-screened elastic interactions in the BAMPS framework as presented in Section 5.3.3. The parameter μ^2 in the "ASW-SH" case represents the mean momentum transfer in the single-hard-scattering limit. We choose its value by $\mu^2 = \hat{q}\,L$, what represents the situation that the transverse momentum a gluon can accumulate in a medium with length L and momentum broadening $\hat{q}$ in the "ASW-MS" limit is transferred in one single hard scattering in the "ASW-SH" limit. Large values of $\Delta E/E \to 1$ correspond to jets that lose almost their complete energy after traversing the medium and thereby are stopped by the medium. On the other hand, small values $\Delta E/E \to 0$ correspond to jets that lose almost no energy radiatively in the medium. Both ASW limits show a broad distribution of quenching weights with a mild peak around $\Delta E \approx 0.2\,\text{E}$, both for a quark and a gluon projectile. As one expects from the QCD color factors,

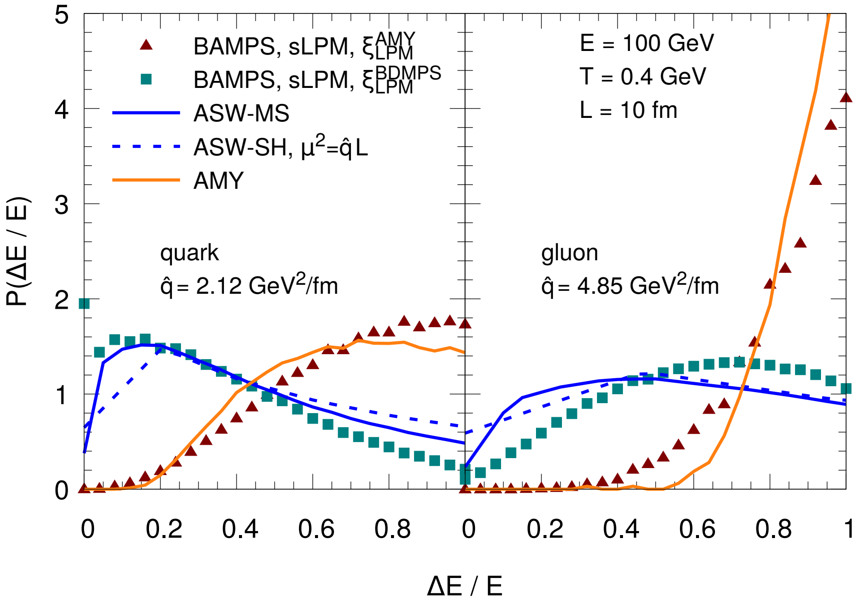

Figure 5.65: Quenching weights $P(\Delta E/E)$ of a quark (left column) or gluon (right column) projectile with energy $E = 100\,\text{GeV}$ in a medium with temperature $T = 0.4\,\text{GeV}$ and length $L = 10\,\text{fm}$. The QCD coupling is fixed to $\alpha_s = 0.3$. While the points show the numerical results from the sLPM approach in BAMPS for the two different choices of screening parameters, $\xi_{\rm LPM}^{\rm AMY;\,q}$ or $\xi_{\rm LPM}^{\rm AMY;\,g}$ (triangles) or $\xi_{\rm LPM}^{\rm BDMPS}$ (squares), the lines show the calculations from the AMY formalism (yellow) and the ASW approach (blue). The ASW results are shown for the multiple-soft scattering limit "ASW-MS" (solid) and the single hard scattering limit "ASW-SH" (dashed). The momentum broadening parameter $\hat{q}$ of a quark ($\hat{q}_q(E = 100\,\text{GeV}, T = 0.4\,\text{GeV}) = 2.12\,\text{GeV}^2/\text{fm}$) or a gluon ($\hat{q}_g(E = 100\,\text{GeV}, T = 0.4\,\text{GeV}) = 4.85\,\text{GeV}^2/\text{fm}$) entering the ASW calculations is determined by the elastic BAMPS interactions as described in Section 5.3.3. The distributions are normalized to unity in the range $0 < \Delta E/E < 1$.

the distribution of a gluon has a higher tail in comparison to the quark. By adjusting the momentum transfer μ^2 based on $\hat{q}$, the quenching weights of the "ASW-MS" and "ASW-SH" limits are comparable with a slightly harder distribution from the single hard scattering limit. The quenching weights from the AMY formalism are shifted significantly to higher ΔE values again demonstrating the enormous radiative energy loss of the AMY formalism without finite-size effects. Not surprisingly, the quenching weights from the θ-LPM method screened with $X_{\rm LPM}^{\rm AMY}$ are close to the results from the AMY formalism. On the other hand, the choice of $X_{\rm LPM}^{\rm BDMPS}$ that we motivated in the previous subsection by fitting to the large L emission spectra from the BDMPS-Z approach shifts the quenching weights from the θ-LPM closer to the results obtained from ASW.

Finally, we show in Fig. 5.65 the results for the quenching weights of a projectile with energy E traversing a medium with temperature T and length L obtained from numerical simulations with the sLPM approach in the BAMPS framework. For the ASW and AMY results we employ the same parameters as in Fig. 5.64. The $k_\perp$ screening within the sLPM approach is controlled again either by $\xi_{\rm LPM}^{\rm AMY;\,q}$ and $\xi_{\rm LPM}^{\rm AMY;\,g}$ or by $\xi_{\rm LPM}^{\rm BDMPS}$. Due to the fit to the AMY emission spectrum the quenching weights obtained by $\xi_{\rm LPM}^{\rm AMY;\,q}$ and $\xi_{\rm LPM}^{\rm AMY;\,g}$ reproduce the strong energy loss distributions of the AMY formalism. Interestingly, the choice of $\xi_{\rm LPM}^{\rm BDMPS}$ that we obtained previously by comparing the sLPM approach to the BDMPS-Z formalism closely reproduces the quenching weights calculated in the ASW formalism.

In summary, we demonstrated in this section that the three different approaches for implementing the LPM effect in the partonic transport model BAMPS are comparable to other, more formal approaches for the radiative energy loss from pQCD. Obviously such a modeling of quantum coherence effects in a transport approach can only be fulfilled by limited accuracy and compromises have to be made. It remains to be seen whether and how these compromises and limitations end up in the final calculation of measurable observables within heavy-ion collisions as we will discuss in Chapter 7.

6 Evolution of jets in a brick of quark-gluon plasma

In the previous chapter we introduced and discussed the different LPM approaches investigated in this work. To this end, we studied the dependencies of both the radiative energy loss and the underlying gluon emission spectra of an energetic parton traversing a static medium by comparing different common models for radiative energy loss.

One of the main assumptions of these models is an eikonal evolution of the partonic projectiles, which is equivalent to resetting the projectile energy and momentum after each scattering within the medium. While this eikonal limit is a justified assumption for energetic partons and simplifies the analytical calculations, its validity becomes questionable if it is applied at softer parton energies where the energy loss of a parton may become comparable to its energy. We therefore extend in this chapter the previous eikonal studies by discussing the non-eikonal evolution of a parton projectile traversing a static, thermal medium with length L and temperature T. By scattering elastically and radiating gluons the projectiles lose energy and modify their momentum after each interaction with medium particles so that their energy and momentum evolves with time t. The previous results from the eikonal limit can then be found as the actual energy loss of the projectile at a specific time (and projectile energy) in the projectile evolution. Different to the case of an energetic parton traversing an expanding heavy-ion collision as discussed in the next Chapter 7, all macroscopic properties of the medium in this section are kept fixed during the simulation, which allows a comprehensible study of the parton evolution and serves as a link between the theoretical results from the previous and the experimental results from the subsequent chapter.

Before discussing in Section 6.2 the evolution of a parton via radiative processes from the three different LPM methods as introduced in Chapter 5, we complete in Section 6.1 our picture for the partonic energy loss by introducing the energy loss from only elastic $2 \to 2$ interactions. We then compare in Section 6.2 the radiative parton evolution and investigate how the different LPM approaches end up in the full evolution of an energetic projectile in a static quark-gluon plasma. As we discussed in Section 2.3.2 partons radiate due to their virtuality also in vacuum and thereby build parton showers. While the previous studies considered the evolution of a single, energetic parton and thereby neglecting these vacuum splittings, Section 6.3 studies the evolution of a parton shower consisting of both the leading, most-energetic parton and its surrounding parton shower. To this end, we investigate the energy and momentum loss of reconstructed jets and find the origin of the energy loss in the modification of the distribution of jet components by studying the jet shapes in comparison to the corresponding vacuum distributions.

6.1 Evolution of partons via elastic interactions

In the previous chapter we assumed that the elastic scatterings of an emitted gluon during its formation time only deflects the gluon and consequently increase its transverse momentum

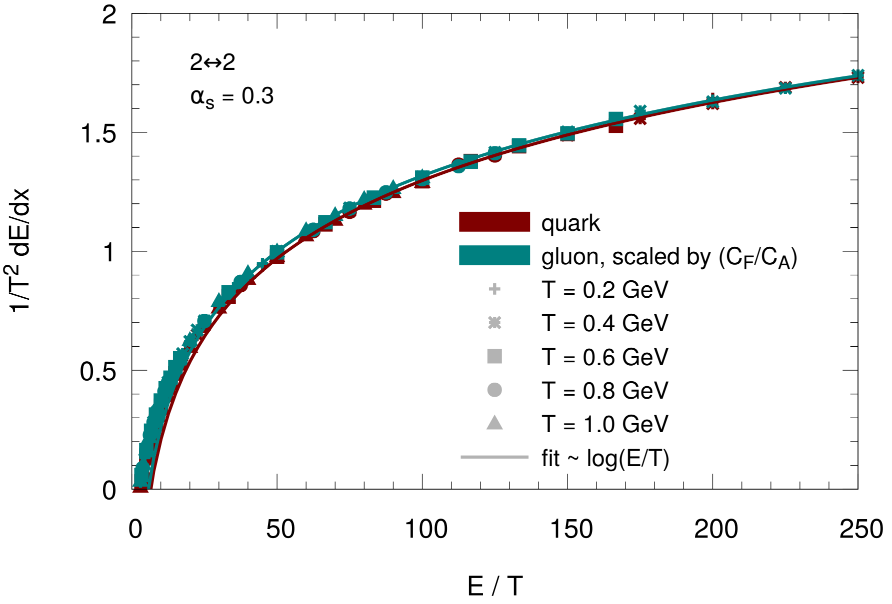

Figure 6.1: Differential radiative energy loss $\mathrm{d}E/\mathrm{d}x$ per unit path length from elastic $2 \to 2$ scatterings for a quark (red) and gluon (green, scaled by $C_\mathrm{F}/C_\mathrm{A}$) projectile depending on the projectile energy E. The QCD coupling is fixed at $\alpha_s = 0.3$. While the points represent the numerical results from BAMPS, the lines depict a logarithmic fit $\mathrm{d}E/\mathrm{d}x \sim \log\left(E/T\right)$. For a numerical check of the scaling with T we show calculations for different temperatures denoted by different point symbols.

wrt. the parent parton. This leads to modifications of the formation time of the gluon in radiative processes obeying the LPM effect. However, elastic interactions of partons do not only deflect the partons but may also lead to an energy transfer between the scattering particles. For example, if we assume a projectile parton with energy $E \gg \mathcal{O}(T)$ traversing an infinite thermal medium with temperature T, even if this parton only scatters elastically, it transfers energy in each scattering to medium components and will eventually thermalize to a projectile energy $E \sim \mathcal{O}(T)$.

Since the elastic interactions described by leading-order pQCD are dominated by soft momentum transfers ($\hat{t} \to 0$) the energy loss is expected to be smaller than the energy loss resulting from radiative processes, where hard or multiple gluon emissions can transfer a significant amount of energy away from the projectile. However, the introduction of a Debye mass in the elastic matrix elements constrains the minimum momentum transfer and thereby the potential minimum energy transfer. Moreover, in former BAMPS simulations the small angle approximation was applied to the $2 \to 2$ interactions simplifying the elastic scatterings by considering only a transverse momentum transfer $q_\perp^2$ in the underlying matrix elements. In contrast, we loose this approximation in the present work and consider the $2 \to 2$ pQCD matrix elements in terms of the Mandelstam variable $\hat{t}$ that explicitly considers also longitudinal momentum transfers. Both effects may enhance the resulting elastic energy loss of the projectile.

Before discussing the non-eikonal evolution of a parton projectile via elastic scatterings, we extend the previous studies of Chapter 5 and show in Fig. 6.1 the differential energy loss $\mathrm{d}E/\mathrm{d}x$ of an *eikonal* quark or gluon with projectile energy E in a medium with temperature T from purely elastic $2 \to 2$ interactions. This corresponds to, e.g., Figs. 5.6, 5.37 and 5.50 for the radiative energy loss. Due to the dominance of the t-channel $\sim 1/\left(\hat{t} - m_D^2\right)^2$ in

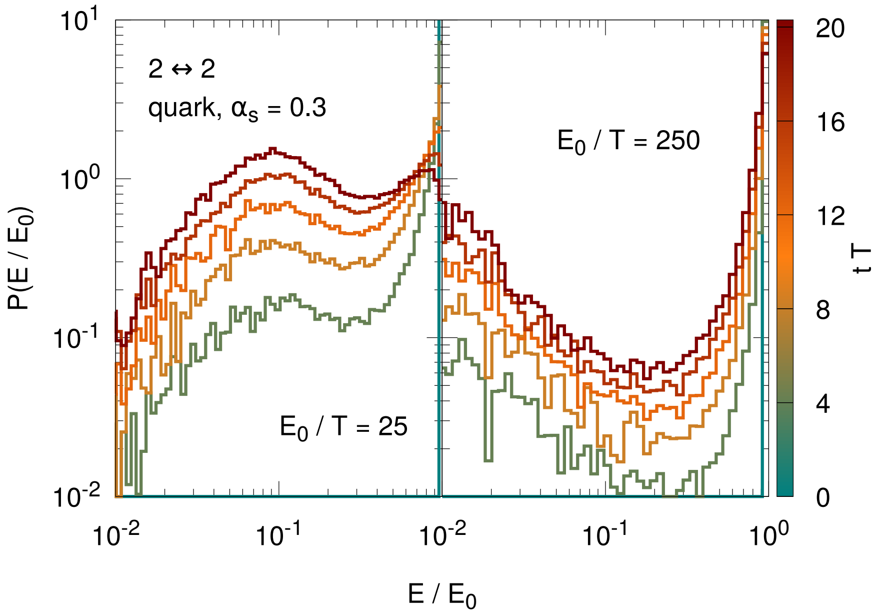

Figure 6.2: Time evolution of the energy distribution $P(E(t))$ of an initial quark projectile with initial energy $E_0 = 25\,\mathrm{T}$ (left) or $E_0 = 250\,\mathrm{T}$ (right) that scatters only elastically in a medium with temperature T. The QCD coupling is fixed to $\alpha_s = 0.3$. The color of the distribution depicts different evolution times t of the projectile in the medium.

the $2 \to 2$ pQCD matrix elements at high CoM energies, the elastic energy loss shows a logarithmic dependence at high projectile energies $E \gg T$. Furthermore, at these energies, the matrix elements between a quark and a gluon only differ by the different QCD color factors C_{R}, $C_{\mathrm{F}} = 4/3$ for a quark and $C_{\mathrm{A}} = 3$ for a gluon projectile. Consequently also the elastic energy loss of a quark or a gluon scales by C_{R}. Comparing the elastic energy loss with our results from Chapter 5 we find that the elastic energy loss is indeed almost a magnitude smaller than the various radiative energy losses (cf. Figs. 5.6, 5.37 and 5.50). However, for softer projectile energies even the elastic interactions may lead to a significant relative energy loss of the projectile.

After introducing the eikonal elastic energy loss, we study in the following the non-eikonal evolution of parton projectiles via elastic $2 \to 2$ scatterings. Each elastic scattering of the projectile may modify its energy and momentum so that the projectile energy evolves with time. Due to the stochastic nature of the individual scatterings within the medium, the evolution of the same initial projectile may show a broad distribution. Figure 6.2 shows the energy distribution $P(E) = 1/N\,\mathrm{d}N/\mathrm{d}E$ depending on the evolution time t of a quark projectile with initial energy E_0 scattering only via elastic $2 \to 2$ processes with medium particles in a medium with temperature T. The quark projectile is initialized with two different energies $E_0 = 25\,\mathrm{T}$ (left) and $E_0 = 250\,\mathrm{T}$ (right), which corresponds to an initial distribution $P(E) = \delta(E - E_0)$. The distributions show a broader maximum at $E \sim \mathcal{O}(T)$, a narrow peak at $E \sim E_0$, and a minimum between both maxima. While the broad maximum at $E \sim \mathcal{O}(T)$ grows with proceeding evolution time t, the narrow peak at $E = E_0$ shrinks and slightly broadens at the same time. This behavior is more pronounced in the case of the "softer" projectile with initial energy $E_0 = 25\,\mathrm{T}$. Reason for these two regions are the different possible elastic channels that are active for a quark. As we have already seen in Section 5.3.3, the dominant elastic process of a quark at higher energies is the process $g\,q \to g\,q$. In this process, both the t-channel and the u-channel are active. The

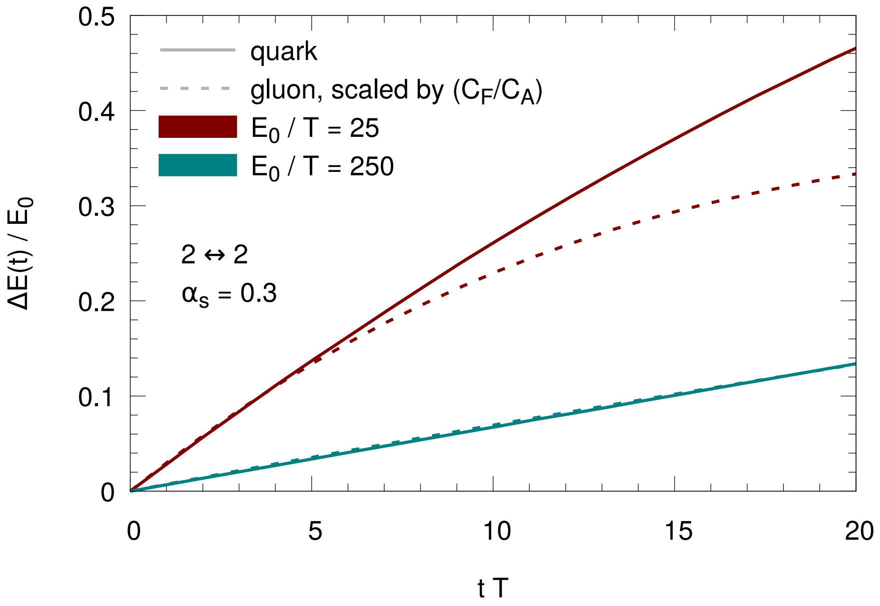

Figure 6.3: Mean energy loss $\Delta E(t) = E_0 - E(t)$ depending on time t for a quark (solid lines) or gluon (dashed lines, scaled by $C_{\mathrm{F}}/C_{\mathrm{A}}$) projectile with initial energy $E_0 = 25\,\mathrm{T}$ (red) or $E_0 = 250\,\mathrm{T}$ (green) scattering via elastic $2 \to 2$ in a thermal medium with temperature T and fixed QCD coupling $\alpha_s = 0.3$. The energy loss is normalized by the initial projectile energy E_0.

t-channel leads to a soft momentum transfer and thereby a smaller energy loss of the quark. Therefore the quark energy is only slightly modified and broadens the peak at $E = E_0$. On the other hand, if the quark interacts via an active u-channel the momentum transfer is large and the scattered, thermal gluon takes away a significant amount of the CoM energy. In contrast the quark leaves the scattering with thermal momenta, which results in a peak in the quark energy distribution at $E \sim \mathcal{O}(T)$. Obviously, at very late evolution times both maxima will end up in the thermal region, since also multiple t-channel processes eventually lead to a thermalization of the projectile.

In order to further characterize the evolution of the projectile energy, we show in Fig. 6.3 the mean elastic energy loss $\Delta E(t) := E_0 - E(t)$ of a quark (solid lines) or gluon (dashed lines) projectile with two different initial energies $E_0 = \{25\,\mathrm{T}; 250\,\mathrm{T}\}$ depending on the evolution time t. We found in Fig. 6.1 that the elastic energy loss depends logarithmically on the projectile energy. Consequently, the relative elastic energy loss $\Delta E(t)/E_0$ is larger for smaller initial projectile energies E_0. Furthermore, at earlier times the difference between a quark and gluon projectile is determined by the different QCD color factors for all different initial projectile energies E_0 and hence the energy loss scales as $\Delta E_q \sim C_{\mathrm{F}}/C_{\mathrm{A}} \Delta E_g$. With increasing evolution time this scaling does not longer hold for smaller initial projectile energies. Due to the higher mean energy loss of a gluon, a gluon projectile degrades its energy faster than a quark projectile and reaches earlier a thermal projectile energy. When a parton has thermalized, it does, on average, not further change its energy after an elastic scattering. This reduces the mean elastic energy loss of a gluon in comparison to a quark projectile whose energy is not thermal yet. In contrast, projectiles with higher initial energies E_0 need a longer evolution time before they thermalize. Therefore the scaling with QCD color factors holds at the higher initial energy up to longer evolution times $t \gtrapprox 20\,\mathrm{T}^{-1}$.

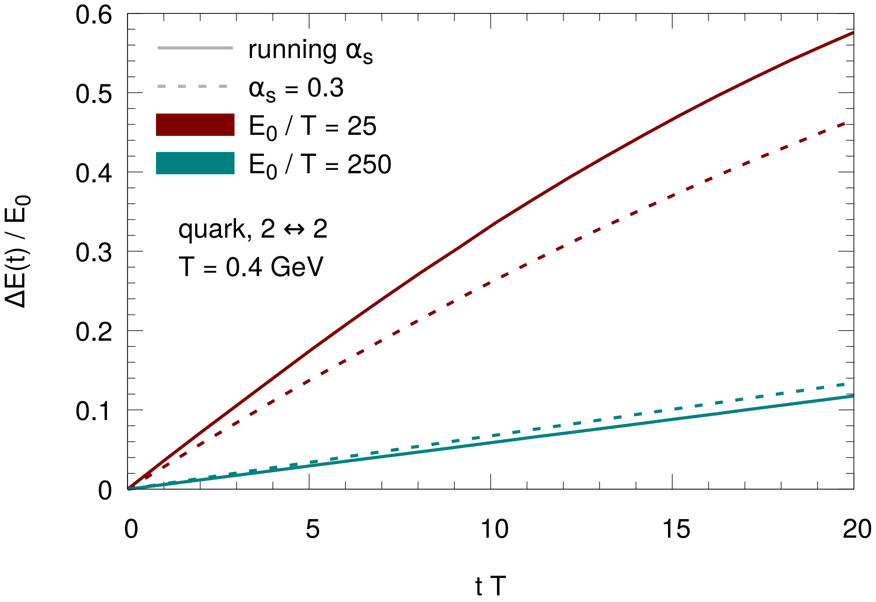

Figure 6.4: Mean energy loss $\Delta E(t) = E_0 - E(t)$ depending on time t for a quark projectile with initial energy $E_0 = 25\,\mathrm{T}$ (red) or $E_0 = 250\,\mathrm{T}$ (green) scattering via elastic $2 \to 2$ in a thermal medium with temperature $T = 0.4\,\mathrm{GeV}$ and either a running QCD coupling (solid lines) or fixed QCD coupling $\alpha_s = 0.3$ (dashed lines). The energy loss is normalized by the initial projectile energy E_0.

In Section 3.1 we introduced how the running of the QCD coupling can be considered in the BAMPS framework. The QCD coupling is then microscopically evaluated by setting the relevant scale at the momentum of the internal propagator in a $2 \to 2$ process (either $\hat{s}$, $\hat{t}$ or $\hat{u} = -\hat{s} - \hat{t}$). Figure 6.4 compares the elastic energy loss employing a fixed QCD coupling with $\alpha_s = 0.3$ and the running QCD coupling by showing the time evolution of ΔE for a quark with different initial projectile energies $E_0 = \{25\,\mathrm{T}; 250\,\mathrm{T}\}$ traversing a medium with temperature T. At an initial projectile energy of $E_0 \approx 250\,\mathrm{T}$, the evolution and the energy loss with a running QCD coupling is comparable to the case of a fixed $\alpha_s = 0.3$. On the other hand, for softer initial projectiles the QCD coupling increases due to the softer momentum scales so that the energy loss is stronger for a projectile with $E_0 = 25\,\mathrm{T}$ with running coupling compared to the fixed coupling case with $\alpha_s = 0.3$. Please note, that due to the specific choice of Debye screening in combination with our implementation of the running coupling based on the microscopic momentum transfer, the energy loss considering the running coupling does not scale with temperature. Therefore we calculated the energy loss for an explicit temperature of $T = 0.4\,\mathrm{GeV}$, which could be a typical temperature in the inner region of an ultra-relativistic heavy-ion collision.

In this section we reviewed the elastic energy loss of an energetic projectile traversing a static and thermal quark-gluon plasma. We find that the differential energy loss from elastic scatterings is indeed significantly smaller than the energy loss from gluon radiation. However, we also find that for “softer” projectiles with $E < 30\,\mathrm{T}$ the accumulated elastic energy loss when traversing the medium leads to a thermalization of these projectiles. We continue this discussion in the next section where we investigate the evolution of the projectile energy following the radiative processes with LPM suppression from Chapter 5.

6.2 Evolution of partons via radiative interactions

The previous section discussed the evolution of an energetic projectile in a static, thermal medium via only elastic interactions. In this section we study the in-medium evolution of a projectile while considering the radiative processes as introduced in Chapter 5. This will extend the previous eikonal considerations by allowing both the projectile (and the emitted gluons in the stochastic LPM approach) to modify its energy and momentum after each interaction and thereby evolve with time. While Section 6.2.1 compares the energy evolution of an energetic projectile in the different LPM approaches, Section 6.2.2 presents the different emission patterns from a non-eikonal parton evolution. Finally, in Section 6.2.3 we discuss how the flavor of the projectile is modified while traversing dynamically the static medium. Throughout this section, the screening parameter employed in the effective LPM approaches are chosen by $X_{\mathrm{LPM}}^{\mathrm{AMY}} = 0.05$ or $\xi_{\mathrm{LPM}}^{\mathrm{AMY;\,q}} = 0.01$ and $\xi_{\mathrm{LPM}}^{\mathrm{AMY;\,g}} = 0.015$, respectively, as we found in Section 5.5.1 when comparing $\mathrm{d}E/\mathrm{d}x$ to the AMY formalism.

6.2.1 Non-eikonal energy evolution

The effective LPM approaches studied in this work, namely the θ-LPM and stochastic LPM approach, rely on the parameters constraining the collinear and soft gluon emissions at small transverse momentum $k_\perp$. In Chapter 5 we determined values for these screening parameters by comparing the differential radiative energy loss $\mathrm{d}E/\mathrm{d}x$ of the θ-LPM and stochastic LPM method to the AMY formalism. However, this comparison assumed an eikonal evolution of both the projectile and, in the case of the stochastic LPM method, the emitted gluons while traversing the static medium. Furthermore, the stochastic LPM algorithm shows a path-length dependence of the differential radiative energy loss $\mathrm{d}E/\mathrm{d}x$. Consequently the screening parameter were determined within a large medium with length $L = 20\,\mathrm{T}^{-1}$, where the differential radiative energy loss is expected to be independent from the medium length. It remains to be studied how the different path-length dependence affects a projectile that evolves non-eikonally and thereby dynamically changes its energy and momentum with time.

Before presenting the results for the non-eikonal evolution via radiative process, we first discuss assumptions necessary in the different LPM approaches if they are applied to a non-eikonal scenario:

- A crucial ingredient for the θ-LPM approach is the mean free path λ entering the theta function in the radiative matrix element (cf. Section 5.2). Since λ depends on both the projectile energy E and the medium temperature T, the mean free path of the projectile has to be determined at each time t since the projectile energy $E(t)$ may change with time. In order to increase the numerical efficiency of the simulations we therefore tabulated the mean free path $\lambda(E, T)$ before the simulations and interpolate these offline values at runtime.

- Different to the θ-LPM approach the emitted gluons from the stochastic LPM method scatter themselves elastically during their formation and thereby modify their formation time. Hence loosening the eikonal approximation of the stochastic LPM not only affects the projectile energy as in the θ-LPM approach but also may modify the resulting gluon emission spectrum. However, we demonstrate in Appendix B that assuming non-eikonal emitted gluons only affects the soft $\omega < \mathcal{O}(T)$ emissions that thermalize during their formation time and therefore reach energies $\omega \sim \mathcal{O}(T)$. In contrast, the differential emission rate $\mathrm{d}\Gamma/\mathrm{d}\omega$ at $\omega > \mathcal{O}(T)$ and the resulting radiative energy loss $\mathrm{d}E/\mathrm{d}x$ are independent from the choice of non-eikonal emitted gluons.

- Different to the θ-LPM approach, where a gluon emission occurs instantaneously, the gluon emissions in the stochastic LPM approach are extended over a finite formation time. During this formation time the projectile and the proposed gluon are formally speaking indistinguishable. However, when allowing evolving projectile energies one has to decide *when* to subtract the radiated gluon energy and/or momentum from the parent parton. We present in Appendix B a comparison of different possibilities for subtracting the gluon energies in a non-eikonal simulation. For the moment we define the stochastic LPM approach by subtracting the energy of the proposed gluon from the projectile parton after it is successfully formed and discard the gluon emission if it suppressed by P_{coh}. This specific choice emphasizes the finite formation time before the parent parton loses the radiative energy.

- In the AMY formalism not only processes describing gluon Bremsstrahlung but also flavor changing processes as $\mathrm{g} \to q\bar{q}$ or $q\bar{q} \to \mathrm{g}$ are considered (cf. Section 5.4). We present in Section 6.2.3 that these processes significantly change the identity of the initial quark or gluon projectile. For the moment we ignore this flavor conversion and show the results for the evolution of the projectile indifferently whether the projectile changed its flavor at some point during the evolution.

In the following, we study the case of a parton projectile with initial energy E_0 traversing a static and thermal medium with temperature T. The projectile interacts for the moment only via the radiative processes from the different LPM approaches, which we presented in Chapter 5 and extended by the considerations above. Different to the eikonal limit, the energy and momentum of the projectile are not reset after each scattering. The previous eikonal limit can then be found in the dynamical evolution as the actual energy loss of the projectile with energy $E(t)$ at a given time t in the evolution. Figure 6.5 compares the energy distribution $P(E)$ at different evolution times $t = \left\{5\,\mathrm{T}^{-1}; 10\,\mathrm{T}^{-1}; 15\,\mathrm{T}^{-1}; 20\,\mathrm{T}^{-1}\right\}$ of the different LPM approaches for a quark projectile with initial high energy $E_0 = 250\,\mathrm{T}$. For a medium with, e.g., temperature $T = 0.4\,\mathrm{GeV}$ this corresponds to a projectile energy $E = 100\,\mathrm{GeV}$ and times $t = \{2.5\,\mathrm{fm}; 5\,\mathrm{fm}; 7.5\,\mathrm{fm}; 10\,\mathrm{fm}\}$.

At evolution time $t = 5\,\mathrm{T}^{-1}$ all LPM approaches show a maximum of the energy distribution at $E \approx E_0$: While the stochastic LPM approach and the AMY formalism show a significant amount of projectiles that have not lost energy yet, in the θ-LPM approach less projectiles were unaffected by the radiative processes leading to a mild shift of the whole distribution to smaller $E < E_0$. One reason for the different behavior between the θ-LPM and the stochastic LPM at early times is the finite formation time of gluon emissions in the stochastic LPM approach. Due to the specific choice of energy subtraction the actual radiative energy loss is delayed to the end of the formation time. Hence, especially large ω emissions are forbidden at early times due to their, on average, longer formation time.

Moreover, due to the divergence at $\omega = E$ in the AMY formalism (cf. Section 5.4), the energy distribution of AMY shows a strong peak at $E = 0$ already at the early evolution time. This represents situations in which the projectile loses all its energy by emitting a single hard gluon. Such a situation is however not possible in the stochastic LPM approach since such a gluon emission would have a large formation time and is forbidden at early

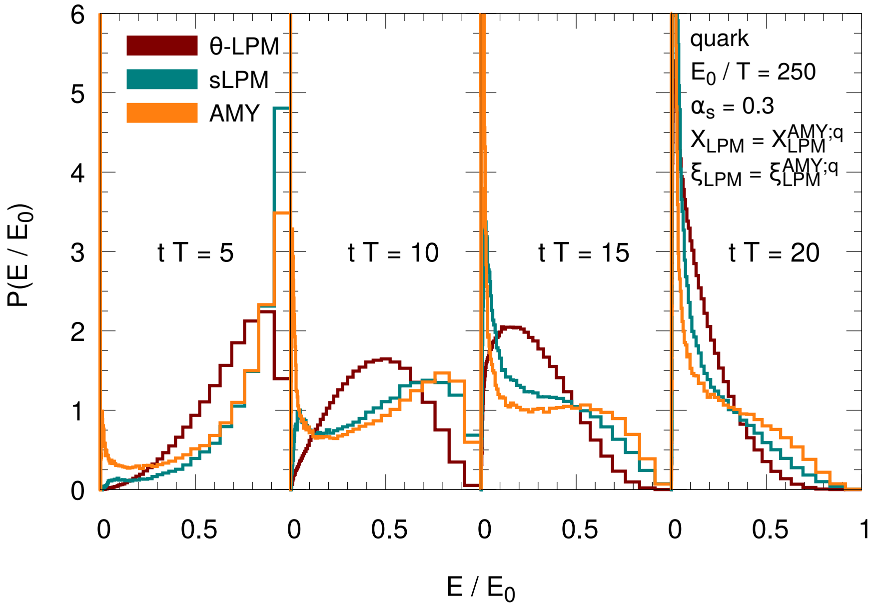

Figure 6.5: Distribution $P(E) = 1/NdN/dE$ of the projectile energy E at different times t for a quark projectile with initial energy $E_0 = 250\,\mathrm{T}$ traversing a static medium with temperature T via the radiative processes from either the θ-LPM (red), the stochastic LPM (green) or the AMY (yellow) approach. The screening parameters of the effective LPM approaches are chosen by $X_{\mathrm{LPM}}^{\mathrm{AMY}} = 0.05$ and $\xi_{\mathrm{LPM}}^{\mathrm{AMY;\,q}} = 0.01$ for reproducing $\mathrm{d}E/\mathrm{d}x$ of AMY and the QCD coupling is fixed to $\alpha_s = 0.3$. The projectile energy E at time t is normalized by the initial projectile energy E_0.

times. Therefore the distribution of the stochastic LPM approach shows no maximum for small projectile energies at early times.

With progressing evolution time the energetic projectile loses energy in all LPM approaches and thereby the distributions shift to smaller values of E. Due to the missing path-length dependence, a projectile in the θ-LPM approach loses energy rather uniformly. This leads to a uniform shift of the projectile energy distribution as a whole with increasing evolution time. In contrast, the finite formation time of the stochastic LPM approach leads to a more stochastic energy loss since the distribution at time t obtains contributions also from emissions started at earlier times. For example, a projectile may start a hard gluon emission at an early time that is formed later in the evolution. At this later time the projectile, which in the mean time could have radiated other (softer) gluons, loses almost all of its energy due to the earlier hard emission. This leads to the second maximum of the stochastic LPM approach at softer projectile energies. On the contrary, the non-uniform distribution of the AMY formalism is again caused by the divergences $\omega \to 0$ and $\omega = E$ in the differential emission rate. This is similar to an all-or-nothing situation, where the projectile loses either almost no energy or almost all of its energy in a single gluon emission.

At later time $t = 20\,\mathrm{T}^{-1}$, corresponding to, e.g., $t = 10\,\mathrm{fm}$ in a medium with temperature $T = 0.4\,\mathrm{GeV}$, all three LPM approaches show distributions with maxima at energies $E \sim \mathcal{O}(T)$. These maxima hint to situations in which the energetic projectiles lost so much energy that they start to thermalize within the medium. This thermalization process is even more pronounced for a “softer” quark projectile with initial energy $E_0 = 25\,\mathrm{T}$ as shown in Fig. 6.6. Already after $t \approx 10\,\mathrm{T}^{-1}$ all three LPM approaches show distributions

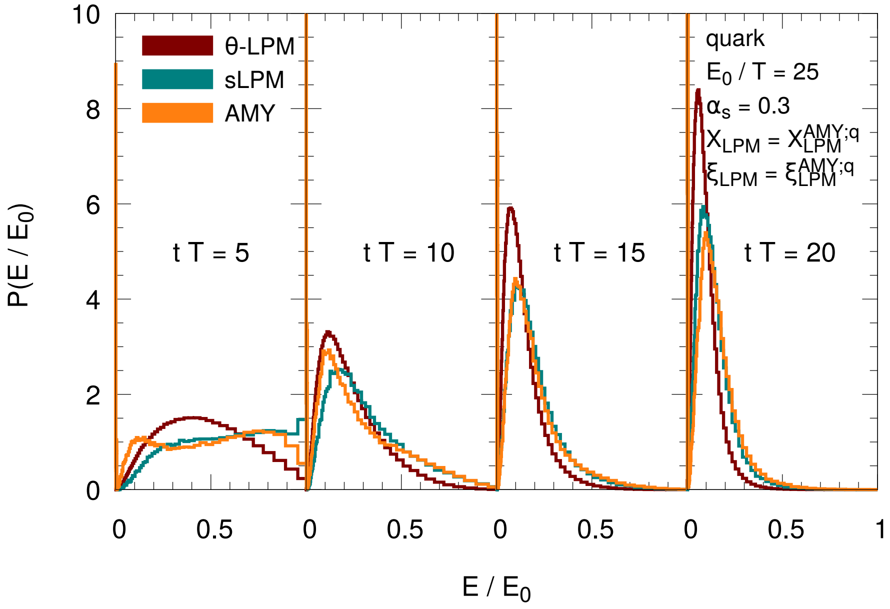

Figure 6.6: Same figure as Fig. 6.5 but with initial projectile energy $E_0 = 25\,\mathrm{T}$.

in which most of the projectiles have already thermal energies. At later times also the remaining more energetic projectiles are shifted to these thermal energies forming a thermal distribution.

The presented energy evolution of the three LPM approaches can be further studied by considering the mean of the presented distributions. Figure 6.7 shows the mean projectile energy $E(t)$ depending on time t for a quark or gluon projectile with initial energy $E_0 = 25\,\mathrm{T}$ (left) or $E_0 = 250\,\mathrm{T}$ (right). Due to the vanishing formation time in the θ-LPM and AMY method, both evolutions are similar at early times for quark and gluon projectiles with smaller and larger projectile energies. At later times the mean radiated energy in the θ-LPM approach is larger than in the other two approaches. On the other hand, the stochastic LPM approach matches the evolution of the AMY formalism at these later times. Due to the larger QCD color factors the initial gluon projectiles show a stronger energy degradation with time for all LPM approaches.

In the previous section we discussed the non-eikonal evolution of a projectile that only scatters elastically via $2 \to 2$ processes within the medium. We found that the differential energy loss is significantly smaller for elastic interactions than for the presented radiative processes. This result is confirmed by Fig. 6.8 that shows the mean projectile energy $E(t)$ vs. time t for a quark projectile with initial energy $E_0 = 25\,\mathrm{T}$ (left) or $E_0 = 250\,\mathrm{T}$ (right) interacting via either only radiative processes or via both elastic and radiative processes. In all three different LPM approaches the inclusion of elastic interactions in the projectile evolution leads to a mild increase of the energy loss.

Finally, we investigate the interplay between the running QCD coupling and the different LPM approaches. As described in Chapter 3 the running of the QCD coupling is considered in a $2 \to 3$ Bremsstrahlung process within BAMPS by setting the relevant scale to both the transverse momentum transfer $q_\perp^2$ of the elastic part and to the transverse momentum $k_{\perp;\,\mathrm{GB}}^2$ of the emitted gluon. However, as it was pointed out in Ref. [KXB18b], due to the elastic scatterings of the gluon during its formation time in the stochastic LPM approach, this transverse momentum may not be the correct scale at the time the gluon is finally

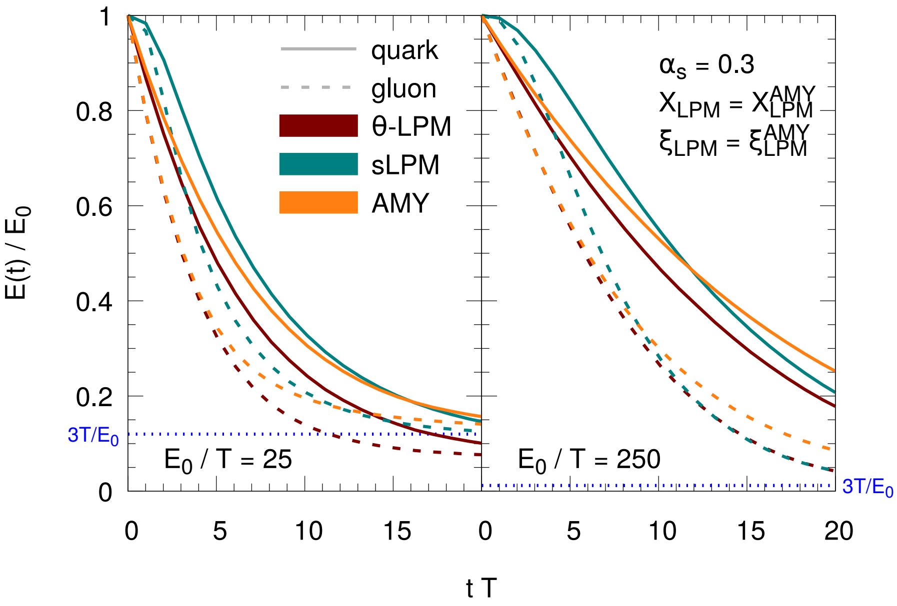

Figure 6.7: Mean projectile energy $E(t)$ depending on time t for a quark (solid lines) or gluon (dashed lines) projectile with initial energy $E_0 = 25\,\mathrm{T}$ (left) or $E_0 = 250\,\mathrm{T}$ (right) traversing a static medium with temperature T via the radiative processes from either the θ-LPM (red), the stochastic LPM (green) or the AMY (yellow) approach. The screening parameters of the effective LPM approaches are chosen by $X_{\mathrm{LPM}}^{\mathrm{AMY}} = 0.05$ and $\xi_{\mathrm{LPM}}^{\mathrm{AMY;\,q}} = 0.01$ or $\xi_{\mathrm{LPM}}^{\mathrm{AMY;\,g}} = 0.015$ for reproducing $\mathrm{d}E/\mathrm{d}x$ of AMY and the QCD coupling is fixed to $\alpha_s = 0.3$. The projectile energy $E(t)$ is normalized by the initial projectile energy E_0. The blue dashed lines denote the mean thermal energy in a medium with temperature T.

formed. Rather the transverse momentum after the formation time, $k_\perp^2$, should have been chosen in the initial Bremsstrahlung process. In order to consider this potentially different scales, the gluon emissions of the stochastic LPM approach with running coupling are *a posteriori* suppressed by an additional suppression factor

$$P_{\text{running } \alpha_s} = \frac{\alpha_s\left(k_\perp^2\right)}{\alpha_s\left(k_{\perp;\,\mathrm{GB}}^2\right)} . \tag{6.1}$$

On the other hand, the original AMY formalism did not consider the running of the QCD coupling. Recently, Park et al. [Par+16] extended the MARTINI framework, that is closely related to AMY, with a running coupling. To this end, they estimated the scale at which the coupling should be evaluated by the mean transverse momentum a gluon can obtain during its formation time. Since such a calculation is out of the scope for the present work, we postpone this study to a future work and depict in the following only the result for AMY employing a constant QCD coupling of $\alpha_s = 0.3$.

We compare in Fig. 6.9 the evolution of the projectile energy with a fixed QCD coupling $\alpha_s = 0.3$ to the case of a running QCD coupling by showing the corresponding energy evolution for a quark projectile with initial energy $E_0 = 25\,\mathrm{T}$ (left) and $E_0 = 250\,\mathrm{T}$ (right) traversing a static medium with temperature T via elastic $2 \to 2$ processes and the radiative processes from the different LPM approaches. Although the modeling of the running coupling is different for the θ-LPM and stochastic LPM approach, the effect of the running QCD coupling is comparable in both approaches. As in the elastic case of Section 6.1 the

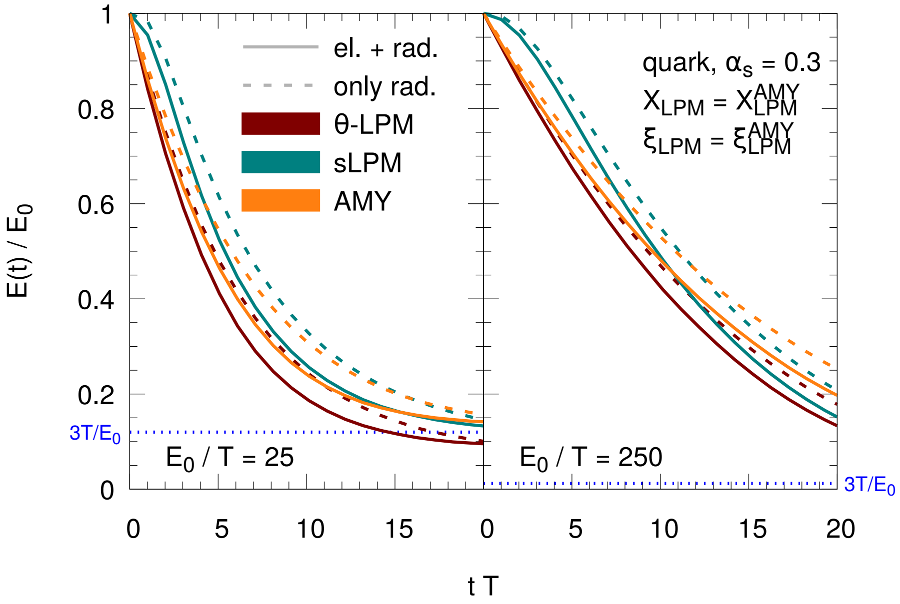

Figure 6.8: Mean projectile energy $E(t)$ depending on time t for a quark projectile with initial energy $E_0 = 25\,\mathrm{T}$ (left) or $E_0 = 250\,\mathrm{T}$ (right) traversing a static medium with temperature T either via only radiative processes (dashed lines) or via both elastic $2 \to 2$ and radiative processes (solid lines). The radiative processes are either described by the θ-LPM (red), the stochastic LPM (green) or the AMY (yellow) approach. The screening parameters of the effective LPM approaches are chosen by $X_{\mathrm{LPM}}^{\mathrm{AMY}} = 0.05$ and $\xi_{\mathrm{LPM}}^{\mathrm{AMY;\,q}} = 0.01$ for reproducing $\mathrm{d}E/\mathrm{d}x$ of AMY and the QCD coupling is fixed to $\alpha_s = 0.3$. The projectile energy $E(t)$ is normalized by the initial projectile energy E_0. The blue dashed lines denote the mean thermal energy in a medium with temperature T.

running coupling affects mostly the softer projectile energies wrt. to the fixed coupling of $\alpha_s = 0.3$ while the more energetic projectiles show a similar evolution as in the fixed coupling case. The stronger coupling at softer initial projectile energy $E_0 = 25\,\mathrm{T}$ leads to a stronger energy degradation for both LPM approaches.

6.2.2 Non-eikonal gluon emission patterns

Although the LPM models were calibrated to each other by comparing the differential radiative energy loss $\mathrm{d}E/\mathrm{d}x$, the underlying gluon emission rates $\mathrm{d}\Gamma/\mathrm{d}\omega$ and $\mathrm{d}\Gamma/\mathrm{d}k_\perp$ showed differences in Section 5.5.2. In this section we investigate how these differences end up in the emission patterns of an energetic projectile dynamically evolving within the medium. These emission patterns can then be understood as a folding of different gluon emission rates from different stages in the evolution of the projectile energy $E(t)$.

We show in Fig. 6.10 the gluon emission spectrum $\omega\,\mathrm{d}N/\mathrm{d}\omega$ of a quark projectile with initial energy $E_0 = 250\,\mathrm{T}$ traversing a medium with temperature T for two different evolution times $t = 1\,\mathrm{T}^{-1}$ (left) and $t = 10\,\mathrm{T}^{-1}$ (right). With progressing evolution time the number of emitted gluons increases. Due to the missing path-length dependence in $\mathrm{d}\Gamma/\mathrm{d}\omega$ the θ-LPM and AMY results shows a linear t dependence in the gluon emission spectra. On the other hand, the finite formation time in the stochastic LPM method suppresses the spectrum at early times and catches up the spectrum at later times when the harder gluons finish their formation time. Besides the suppression of very soft gluon emissions with $\omega \lessapprox 10^{-3}\,\mathrm{E}_0$, due to the chosen screening procedure in the θ-LPM and

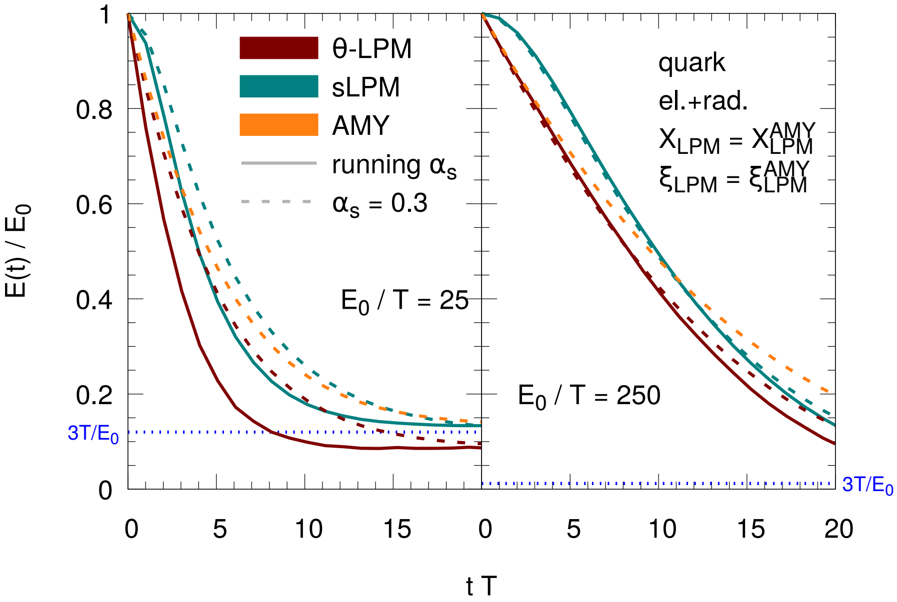

Figure 6.9: Mean projectile energy $E(t)$ depending on time t for a quark projectile with initial energy $E_0 = 25\,\mathrm{T}$ (left) or $E_0 = 250\,\mathrm{T}$ (right) traversing a static medium with temperature T via both elastic $2 \to 2$ and radiative processes from the θ-LPM (red), the stochastic LPM (green) or the AMY (yellow) approach. Solid lines denote the results with a running QCD coupling, whereas the dashed lines show the results with a fixed QCD coupling $\alpha_s = 0.3$ The screening parameters of the effective LPM approaches are chosen by $X_{\mathrm{LPM}}^{\mathrm{AMY}} = 0.05$ and $\xi_{\mathrm{LPM}}^{\mathrm{AMY;\,q}} = 0.01$ for reproducing $\mathrm{d}E/\mathrm{d}x$ of AMY. The projectile energy $E(t)$ is again normalized by the initial projectile energy E_0 and the blue dashed lines denote the mean thermal energy in a medium with temperature T.

stochastic LPM method, the spectra of all three approaches are similar at the later time $t = 10\,\mathrm{T}^{-1}$. Consequently, we expect that the energy loss of partons from the different LPM approaches is similar in larger heavy-ion media, whereas there should be differences in thinner media.

As we discussed in Section 5.4, the transverse momenta of gluon emissions are $k_\perp \sim \mathcal{O}(g_s T)$ and therefore neglected in the presented AMY formalism. On the other hand, we found in Section 5.5.2 that the transverse momentum distribution of an eikonal projectile differs between the two effective LPM approaches, θ-LPM and stochastic LPM. Same still holds in the case of a non-eikonal projectile as shown in Fig. 6.11 where we present the gluon emission spectrum $k_\perp\,\mathrm{d}N/\mathrm{d}k_\perp$ of a quark projectile with initial energy $E_0 = 250\,\mathrm{T}$ at the two evolution times $t = 1\,\mathrm{T}^{-1}$ (left) and $t = 10\,\mathrm{T}^{-1}$ (right). While in the stochastic LPM approach collinear gluons are suppressed at early times due to their longer formation time, the θ-LPM approach shows already at early times a significant contribution of gluons at $k_\perp \approx 10^{-3}\,\mathrm{E}_0$. Overall the spectrum of the stochastic LPM is suppressed wrt. the spectrum from the θ-LPM approach.

In contrast, at later times the gluons from the stochastic LPM approach accumulated enough $k_\perp$ via elastic scatterings to finish their formation time. Consequently, the spectrum of the stochastic LPM increases and passes the spectrum of the θ-LPM method. Due to the thermalization of soft gluons in their formation time, the spectrum of the stochastic LPM at soft $k_\perp$ shows a depletion wrt. the θ-LPM spectrum where such a thermalization cannot occur.

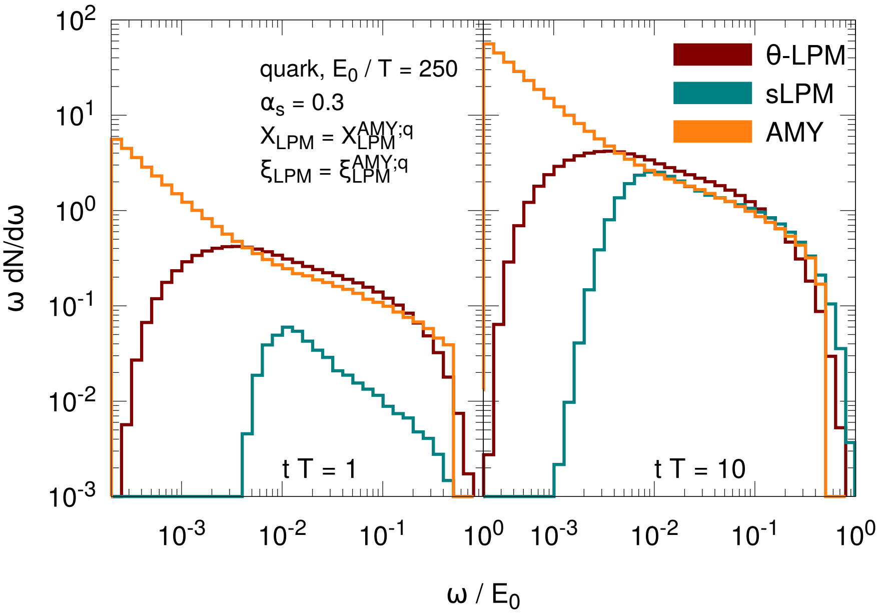

Figure 6.10: Emission spectrum $\omega \mathrm{d}N/\mathrm{d}\omega$ at time $t = 1\,\mathrm{T}^{-1}$ (left) or $t = 10\,\mathrm{T}^{-1}$ (right) of a non-eikonal quark projectile with initial energy $E_0 = 250\,\mathrm{T}$ traversing a static medium with temperature T via radiative processes from the θ-LPM (red), the stochastic LPM (green) or the AMY (yellow) approach. The screening parameters of the effective LPM approaches are chosen by $X_{\mathrm{LPM}}^{\mathrm{AMY}} = 0.05$ and $\xi_{\mathrm{LPM}}^{\mathrm{AMY;\,q}} = 0.01$ for reproducing $\mathrm{d}E/\mathrm{d}x$ of AMY and the QCD coupling is fixed to $\alpha_s = 0.3$.

6.2.3 Flavor conversion of projectiles

The inelastic processes from the θ-LPM or stochastic LPM approach are based on an (initial) $2 \to 3$ Bremsstrahlung process. In the Gunion-Bertsch approximation of this $2 \to 3$ process the matrix element can be separated into an elastic $2 \to 2$ contribution and a probability for emitting an additional gluon. In BAMPS, Bremsstrahlung processes are neglected whose elastic contribution is purely in the s-channel such as $\mathrm{gg} \to q\bar{q}\mathrm{g}$ or $q\bar{q} \to q'\bar{q}'\mathrm{g}$ [Foc11]. These processes change the identity of the incoming partons and are therefore clearly out of the scope of the applied Gunion-Bertsch approximation.

In contrast, the AMY formalism does not rely on this approximation and therefore explicitly considers the quark-antiquark production process from a gluon, $\mathrm{g} \to q\bar{q}$, where a hard gluon “emits” a soft antiquark (or quark) and thereby becomes a quark (or antiquark). Furthermore, also annihilation processes as $q\bar{q} \to \mathrm{g}$ or $q\mathrm{g} \to q$ are calculated in AMY. In these processes a hard parton captures a soft parton from the medium and thereby changes its parton flavor. As we found in Section 5.4, both the “soft (anti-)quark emission” and the annihilation processes can be mainly found at softer projectile energies $E \sim \mathcal{O}(T)$. In the following we study how these flavor conversion processes affect the evolution of parton projectiles in a static medium.

We show in Fig. 6.12 the probability N_i/N_{total} for an initial quark (left) or gluon (right) projectile with initial energies $E_0 = 25\,\mathrm{T}$ or $E_0 = 250\,\mathrm{T}$ to change its initial parton flavor while traversing a static medium with temperature T. While N_{total} gives the total number of projectiles in the simulation, N_i gives the number of projectiles with flavor i at evolution time t. The role of the flavor changing processes for an initial quark seems to be minor for both initial projectile energies: while almost all quark projectiles with $E_0 = 250\,\mathrm{T}$ kept

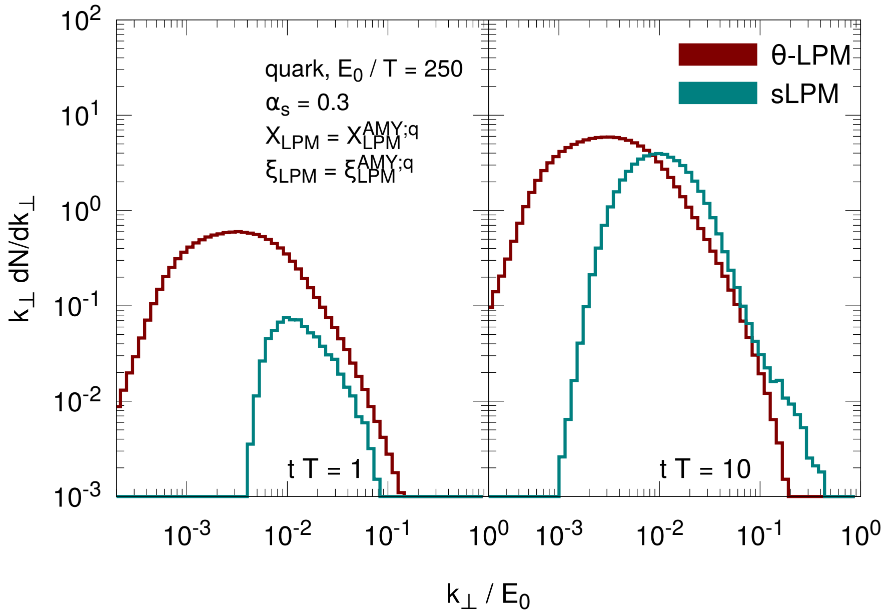

Figure 6.11: Emission spectrum $k_\perp \mathrm{d}N/\mathrm{d}k_\perp$ at time $t = 1\,\mathrm{T}^{-1}$ (left) or $t = 10\,\mathrm{T}^{-1}$ (right) of a non-eikonal quark projectile with the same parameters as in Fig. 6.10.

their initial flavor, only $10\,\%$ of the softer quark projectiles with $E_0 = 25\,\mathrm{T}$ changed its flavor to a gluon projectile after $t = 15\,\mathrm{T}^{-1}$.

On the other hand, the conversion probability for an initial gluon projectile is significantly increased due to the additional pair production process $\mathrm{g} \to q\bar{q}$. Furthermore, the stronger radiative energy loss of a gluon leads faster to an energy degradation with the result that the softer gluon projectiles are faster sensitive to the flavor changing processes. Both leads to the result that after $t \approx 14\,\mathrm{T}^{-1}$ in the case of the higher initial gluon energy $E_0 = 250\,\mathrm{T}$ and already after $t \approx 6\,\mathrm{T}^{-1}$ for the lower initial gluon energy $E_0 = 25\,\mathrm{T}$ more quarks/antiquarks projectiles are in the simulation than gluon projectiles. The annihilation processes of the emerging quark projectiles are not capable to revert the conversion processes but only attenuate a further quark conversion for softer projectiles at later times.

As mentioned above, the $2 \to 3$ processes in BAMPS preserve the projectile flavor and hence an incoming gluon (quark) projectile leaves the interaction as a gluon (quark) projectile. In order to bring the presented results for the flavor conversion in the AMY formalism into a broader context, we show therefore in Fig. 6.13 the conversion probability N_i/N_{total} from only elastic $2 \to 2$ processes. Different to the radiative Gunion-Bertsch processes, the elastic interactions also consider s-channel dominated processes as $\mathrm{gg} \to q\bar{q}$ or $q\bar{q} \to q'\bar{q}'$ that change the incoming parton flavor. The decision which parton is tracked as the projectile after each elastic scattering is determined by evaluating the transferred momentum in this scattering (cf. Section 5.3.3). While the flavor conversion of an initial quark via only elastic scatterings is comparable to the AMY formalism, the probability of a gluon to change its flavor is significantly lower in the case of only elastic scatterings. Again softer projectiles are more sensitive to the flavor conversion processes since then s-channel processes are active. However, even after $t = 20\,\mathrm{T}^{-1}$ only $\approx 30\,\%$ of the gluons became a quark projectile.

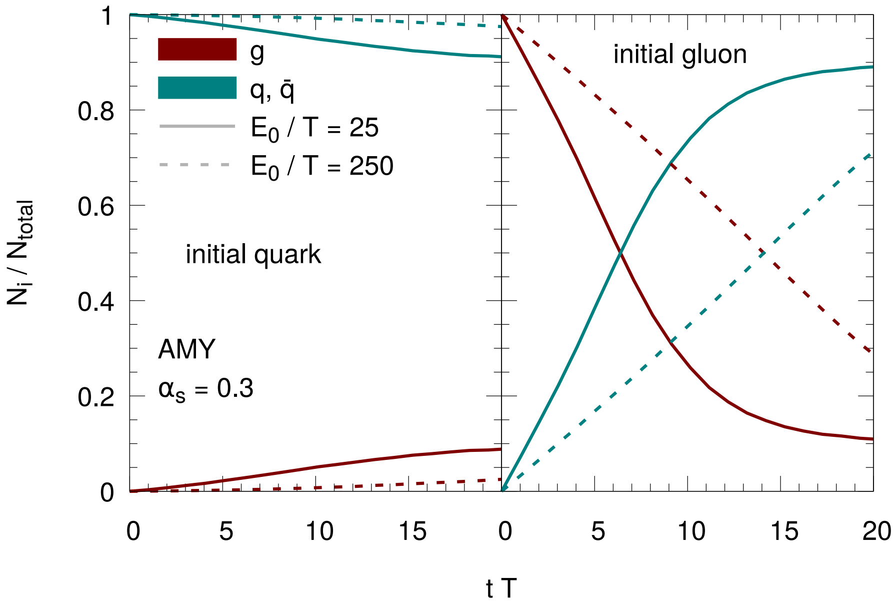

Figure 6.12: Time evolution of the gluon (red) and quark/antiquark (green) fraction N_i/N_{total} of an initial quark (left) or gluon (right) projectile with initial energy $E_0 = 25\,\text{T}$ (solid lines) or $E_0 = 250\,\text{T}$ (dashed lines) traversing a static medium with temperature T via radiative processes from the AMY formalism. The QCD coupling is fixed to $\alpha_s = 0.3$.

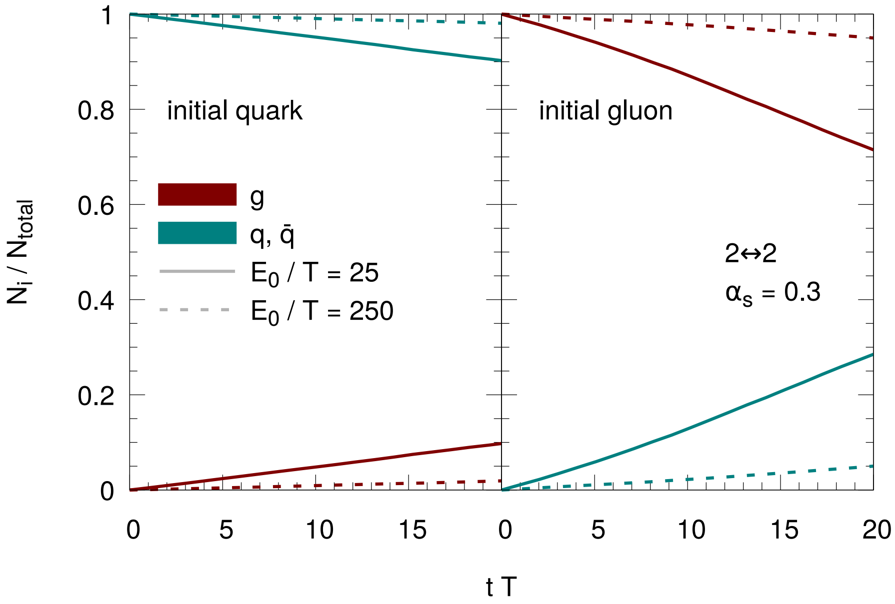

Figure 6.13: Time evolution of the gluon (red) and quark/antiquark (green) fraction N_i/N_{total} of an initial quark (left) or gluon (right) projectile with initial energy $E_0 = 25\,\text{T}$ (solid lines) or $E_0 = 250\,\text{T}$ (dashed lines) traversing a static medium with temperature T via elastic $2 \rightarrow 2$ scatterings. The QCD coupling is fixed to $\alpha_s = 0.3$.

6.3 In-medium modification of parton showers

As we learned in Section 2.3.2 the concept of a single, color charged projectile traversing the QCD medium created in a heavy-ion collision is a rather academic definition of jet quenching. Due to their high virtuality, hard scattered partons from initial nucleon-nucleon scatterings branch via $1 \rightarrow 2$ process in order to reduce their virtuality already in the case without a subsequent in-medium evolution. These splittings then form a spray of partons consisting of a leading parton, which is the most energetic parton corresponding to the remainder of the initial single projectile, and its surrounding parton shower. While this parton system traverses the medium, the previous "vacuum" splittings are supplemented by additional medium-induced gluon radiation as discussed in Chapter 5. Modern jet reconstruction algorithms (cf. Section 2.3.2) define then *a posteriori* macroscopic objects based on these parton showers that are supposed to characterize the energy loss of the initial shower-initiating parton.

In this section, we discuss the in-medium modification of these reconstructed jets in a static and thermal QCD medium and work out how the different assumptions from the presented LPM approaches influence the shower evolution. To this end, we first introduce in Section 6.3.1 how parton showers are generated and subsequently evolved within the BAMPS framework. By investigating the energy loss of reconstructed jets and the distribution of partons around the reconstructed jet axis in terms of shower shapes, as we define in Section 6.3.2, we discuss the underlying mechanisms for the medium modification of parton showers: While Section 6.3.3 studies the modification of jets by only radiative processes from the different LPM approaches, in Section 6.3.4 the shower partons are allowed to also scatter elastically and thereby transport additional energy in and out of the reconstructed jets. Finally, in Section 6.3.5 also recoiled medium partons are reconstructed within the jets that may restore missing energy from the jets by staying close to the jet axis.

6.3.1 Modeling parton showers in BAMPS

In the following we briefly revise how parton showers are generated from initial energetic projectiles and subsequently evolved within BAMPS. For more details about the simulation of parton showers and their subsequent reconstruction into jets within BAMPS we refer to Refs. [Sen12; Sen+15; Sen+17].

In BAMPS we assume that partons are on the mass shell and thereby they are, due to energy and momentum conservation, not able to split via $1 \rightarrow 2$ splittings as described by the vacuum DGLAP equation [AP77; Dok77; GL72][1]. In order to still consider the vacuum splitting processes we employ the final-state shower routines of the Monte-Carlo event generator PYTHIA [SMS06] for generating the initial parton showers. The event generator PYTHIA simulates collisions of particles at high collision energies, as e.g. $\mathrm{p+p}$ collisions at the Large Hadron Collider (LHC). To this end, it incorporates processes based on both QED and QCD as well as non perturbative effects as, e.g., string fragmentation. For more details about PYTHIA and its applications to other fields of high-energy physics we refer to Refs. [SMS06; SMS08].

In PYTHIA, partons from initial hard processes, for example a hard partonic process in the beginning of a $\mathrm{p+p}$ collision, undergo initial- and final-state shower processes. While

---

[1] In contrast, the radiative processes from the AMY formalism are in principle $n \rightarrow n+1$ processes involving multiple elastic scatterings within the medium. These scatterings are resummed in AMY and then modeled by effective "$1 \rightarrow 2$" process.

the initial-state shower increases the virtuality Q^2 from partons before the hard partonic $2 \to 2$ process, the final-state shower decreases the virtuality after the hard scatterings until the partons fragment into hadrons. This shower evolution in Q^2 is described by $1 \to 2$ splitting processes based on the DGLAP splitting kernels $P_{a\to bc}(z)$ (cf. Section 5.4). The differential probability for a parton a to split into two partons b with energy fraction z and c with energy fraction $1-z$ is then given by [SMS06]

$$\mathrm{d}\mathcal{P}_a = \sum_{b,c} \frac{\alpha_s}{2\pi} P_{a\to bc}(z)\, \mathrm{d}t\, \mathrm{d}z \ , \tag{6.2}$$

where we defined $t = \log\left(Q^2/\Lambda_{\mathrm{QCD}}\right)$ and Λ_{QCD} is the QCD scale parameter. The sum in Eq. (6.2) runs over all possible splitting processes as $q \to q\mathrm{g}$ or $\mathrm{g} \to \mathrm{gg}$ [SMS06]. Based on this probability one builds the evolution in the virtuality Q^2 or t by defining Sudakov factors,

$$S_a(t) = \exp\left(- \int\limits_{t_0}^{t} \mathrm{d}t' \sum_{b,c} \mathcal{I}_{a\to bc}(t') \right) , \tag{6.3}$$

where $\mathcal{I}_{a\to bc}(t') = \int \mathrm{d}z\, \alpha_s/(2\pi)\, P_{a\to bc}(z)$ is the probability for a splitting at a given virtuality t'. The Sudakov factors $S_a(t)$ then give the probability for no branching between virtualities t_0 and t and thereby determine at which virtuality the next splitting should occur. Hence the virtuality t or Q^2 can be considered as the evolution variable corresponding to, e.g., the time t in the in-medium evolution in BAMPS. The energy sharing between the daughter partons at each splitting is evaluated based on the splitting kernels. Vacuum coherence effects as *angular ordering* (for a pedagogical review see, e.g., chapter 3 of Ref. [DKT89]) are explicitly considered in this evolution by choosing appropriate kinematical limits at each splitting.

The Q^2 evolution in PYTHIA is stopped at a scale $Q_0^2 = 1\,\mathrm{GeV}$ [SMS06], where the hadronization via string fragmentation begins. Since we are interested in the in-medium modification of parton showers, we do not fragment the partons into hadrons but evolve them within the static BAMPS medium. The remaining virtuality Q_0^2 is then discarded by setting the massless partons on the mass shell $E^2 = \vec{\mathbf{p}}^2 + m^2 = \vec{\mathbf{p}}^2$. While we preserve the energy and momentum direction of each parton, the single momentum components are not conserved.

Inserting fully evolved vacuum parton showers into the BAMPS medium assumes that the vacuum evolution and the subsequent in-medium evolution can be treated separately. However, in nature it seems more realistic that both vacuum and medium interactions occur simultaneously. This potential interference between vacuum and medium processes is still under debate in the community. One possibility to improve the presented method would be to introduce a similar evolution in Q^2 via $1 \to 2$ splittings directly in BAMPS in addition to the medium-induced $2 \to 3$ Bremsstrahlung processes. However, such a study is out of the scope for the present work but should be postponed to a later stage.

In this section the described parton showers are evolved through a static, thermal medium with temperature T within the common BAMPS framework. This serves as a baseline study for the later investigation of reconstructed jets within expanding QCD media from ultra-relativistic heavy-ion collisions in Section 7.4. In each event exactly one parton shower consisting of multiple partons (as described previously) is inserted into the medium.

The initial virtuality of the shower initiating projectile is chosen as $Q_{\text{max}} = 2E_0$, where E_0 is the initial projectile energy[2].

As in the previous section the energy and momentum of each evolving parton is modified by interactions within the medium. We expect different effects that modify the evolution of parton showers:

- While traversing the medium, the leading parton and its surrounding shower partons may emit gluons via the medium-induced radiative processes defined by the different LPM approaches from Chapter 5. On the one hand, the Bremsstrahlung processes from the two effective LPM approaches may emit gluons to larger angles and thereby widen the parton showers. On the other hand, the more collinear emissions from AMY may have the opposite effect and narrow the distribution around the jet axis. We investigate both effects in Section 6.3.3, where we simulate the modification of parton showers by only radiative processes. In order to simplify the present problem and thereby providing a clean comparison of the different LPM approaches, we exclude for the moment radiative processes of the medium-induced gluon radiation itself. Only the initial shower partons are modified by the inelastic processes[3].

- In addition to the previous radiative processes, the parton showers in Section 6.3.4 are allowed to also scatter elastically via $2 \to 2$ processes from Sections 3.1 and 6.1. These elastic processes of both the initial parton showers and the emitted gluons from medium-induced radiation may additionally transport energy away from the initial projectile and thereby broaden the parton showers.

- For the previous considerations, we assumed that the scattered partons from the thermal background medium instantly thermalize again and therefore do not contribute to the modification of parton showers. In Section 6.3.5 we explicitly attribute also the scattered medium particles to the evolving shower and thereby study the effect of these “recoiled” medium partons on the parton showers.

In order to characterize the medium modification of the initial parton and its surrounding shower we reconstruct jets based on the shower partons via the jet reconstruction algorithms provided by the FASTJET package [CSS12; CS05] (cf. Section 2.3.2). The jets are reconstructed with the anti-$k_\perp$ algorithm [CSS08] that clusters partons into jets while preferring clusters around hard partons. Since the anti-$k_\perp$ algorithm is both infrared and collinear safe and thereby should be robust against soft hadronization effects, we reconstruct jets on the parton level. Furthermore, the anti-$k_\perp$ algorithm leads to circular jet shapes in the $y - \phi$-plane, where y is the momentum rapidity and ϕ the azimuthal angle of the partons. The resolution parameter of the clustering algorithm is given by the jet reconstruction radius[4] R. A larger jet radius, corresponding to a small resolution, clusters partons into the same jet that are more distant in y and ϕ. Therefore jets reconstructed with larger jet radii in a medium are more sensitive to a contamination with background momentum. On the other hand, a smaller jet radius resolves also single gluon emissions of

---

[2] In the case of a p + p collision this initial virtuality Q_{max} of the shower-initiating parton is determined by the scale of the hard partonic process. Same arguments do not hold in our case of a partonic projectile initialized in a static medium and therefore the choice for Q_{max} is rather arbitrary and mainly based on an example file of Q-PYTHIA [ACS09].

[3] In Section 7.4, where we compare our calculations to experimental results for the quenching of reconstructed jets we will investigate the case if the medium-induced gluon radiation is allowed to further emit other gluons.

[4] Although the anti-$k_\perp$ algorithm does not rely on the definition of a jet cone (cf. Section 2.3.2), the jet radius R is often denoted as *cone radius*. This terminology is reasonable since the anti-$k_\perp$ algorithm produces approximately circular jet shapes and therefore we use both terms for R interchangeably in the following.

the parton shower. However, with decreasing $R \to 0$ one only measures the energy loss of the leading parton. In the following studies we employ an intermediate value of $R = 0.3$ as it is chosen in most of the experimental studies of jet quenching in heavy-ion collisions. Since we insert one parton shower per event, all results in this section are calculated for the modification of the leading jet—the jet with the highest energy in each event.

6.3.2 Measuring parton distributions around jets

After discussing in the previous section how parton showers are generated and evolved within BAMPS, we discuss in this section how we measure the modification of the shape of these parton showers. First defined by the CMS collaboration [CMS13b], the jet shape observable $\rho(r)$ measures the radial distribution of energy or momentum within a reconstructed jet. To this end, the momentum distribution within the jets is normalized to the reconstructed jet momentum measured in the detectors. Different to experimental studies of jet quenching the initial energy of the shower-initiating parton is available in our numerical simulations. This allows a slightly different definition of jet shapes in contrast to the experimental jet shapes that we will study later in Section 7.4.3. Relating the distribution of energy around each jet to the initial energy E_0 of the shower-initiating parton instead of the reconstructed jet energy E_jet we may define *shower shapes* $\hat{\rho}(r)$ as[5]

$$\hat{\rho}(r) = \frac{1}{\delta r} \sum_{r_i \in [r-\delta/2, r+\delta/2)} \frac{E^i_\text{parton}}{E_0} \tag{6.4}$$

where E^i_parton is the energy of a single parton and $r_i = \sqrt{\left(\phi_i - \phi_\text{jet}\right)^2 + \left(y_i - y_\text{jet}\right)^2}$ is the distance of parton i to the reconstructed jet axis given by azimuthal angle ϕ_jet and rapidity y_jet in the ϕ-y plane. The shower shapes are calculated separately for each jet and then measure the total amount of parton energy in an annulus from $r - \delta r/2$ to $r + \delta r/2$ around each jet axis as sketched in Fig. 6.14. This definition of shower shapes $\hat{\rho}(r)$ allows to study the distribution of the initial projectile energy *around* the jet axis, whereas the common definition of jet shapes $\rho(r)$ [CMS13b], aims to describe the medium modification of distributions *within* the reconstructed jets.

In the following sections we will calculate the medium modification of shower shapes together with the evolution of the reconstructed jet energy from a parton shower traversing a thermal QCD medium. This procedure will allow us to develop a consistent and differential picture for the in-medium modification of parton showers and help us understanding the roles of both elastic and radiative processes from different LPM approaches.

6.3.3 Medium-induced gluon radiation of parton showers

In this section we compare the medium modification of reconstructed jets via only radiative processes defined by the three different LPM approaches presented in Chapter 5. To this end we generate parton showers by PYTHIA based on an initial quark or gluon projectile

---

[5] An additional difference between this definition of shower shapes $\hat{\rho}(r)$ and the common definition of jet shapes $\rho(r)$ in heavy-ion collisions [CMS13b] is that the shower shapes measure the distribution of energy instead of transverse momentum $p_\perp$ of particles wrt. the beam axis around each jet. However, since the distinct direction of a beam axis does not exist in the context of a static medium, the natural choice of kinematic quantity is then the particle energy E. For more details about the common definition of jet shapes and the study of its medium modification in heavy-ion collisions we refer to Section 7.4.3.

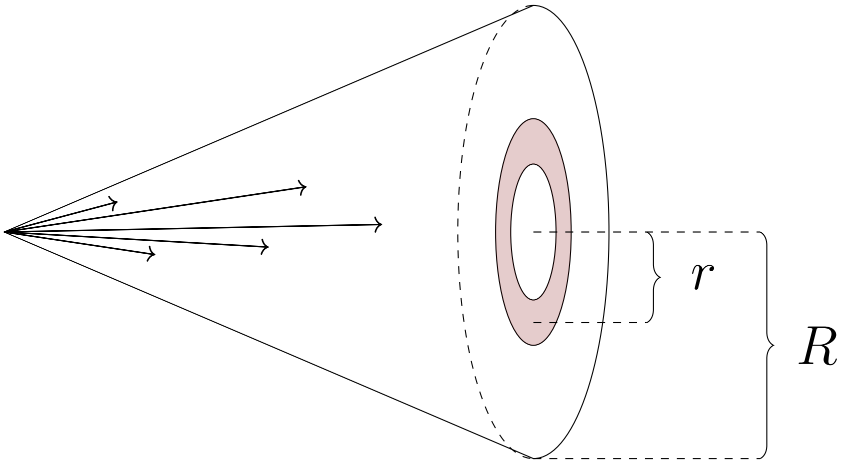

Figure 6.14: Schematic visualization of the shower shape definition.

with energy E_0 and subsequently evolve them within a static, thermal medium with temperature T. In order to provide a clean observation of the underlying mechanisms for the medium-modification of parton showers from the different LPM approaches, only the initial shower partons participate in the radiative processes. The emitted gluons from medium interactions are only allowed to stream freely. For a study of the effect of further elastic scatterings of these gluons we refer to Section 6.3.4. The effective LPM approaches θ-LPM and stochastic LPM are calibrated to the AMY formalism by choosing the screening parameters $X_{\text{LPM}}^{\text{AMY}}$ and $\xi_{\text{LPM}}^{\text{AMY}}$ for reproducing the differential radiative energy loss $\mathrm{d}E/\mathrm{d}x$ of AMY (cf. Section 5.5.1). Due to its diverging rate at soft parton energies, we further limit the radiative evolution of parton showers in the AMY formalism by a minimum parton energy $E_{\text{min}} = 3T$. The jets are subsequently reconstructed by the anti-$k_\perp$ algorithm and a jet radius of $R = 0.3$ based on both the modified shower partons and the medium-induced gluon radiation.

Energy loss of reconstructed jets from medium-induced gluon radiation

Figure 6.15 shows the energy distribution $P\left(E_{\text{jet}}\right) = 1/N \mathrm{d}N/\mathrm{d}E_{\text{jet}}$ of the leading jet at different times t reconstructed from a parton shower that has been initialized by a quark with energy $E_0 = 250\,\mathrm{T}$ and subsequently evolved for time t within a static medium with temperature T. Already the leading jet energy from PYTHIA before the in-medium evolution shows a broad distribution: while most of the projectile energy is recovered in the reconstructed jets, already at $t = 0\,\mathrm{T}^{-1}$ there are reconstructed jets that miss half of their initial projectile energy due to vacuum $1 \to 2$ branchings out of the jet cones. With progressing time this initial distribution is further modified due to medium interactions. While both effective LPM approaches show a strong shift to smaller jet energies, the jet energy distribution from AMY broadens and shifts to values $E_{\text{jet}} > E_0$. The jet energy distribution from the θ-LPM approach shows the strongest shift to small jet energies.

Based on the jet energy distributions, Fig. 6.16 shows the mean jet energy $E_{\text{jet}}(t)$ depending on time t for the leading jet reconstructed from a shower initiated by either a quark or gluon with energy $E_0 = 250\,\mathrm{T}$ for the same interactions as in Fig. 6.15. While for a quark-initiated shower the initial vacuum splittings from PYTHIA lead to a missing energy of $\approx 15\,\%$ in the initial jets reconstructed with $R = 0.3$, the larger QCD color factor of gluons increases this lack of energy to $\approx 25\,\%$ wrt. the initial projectile energy.

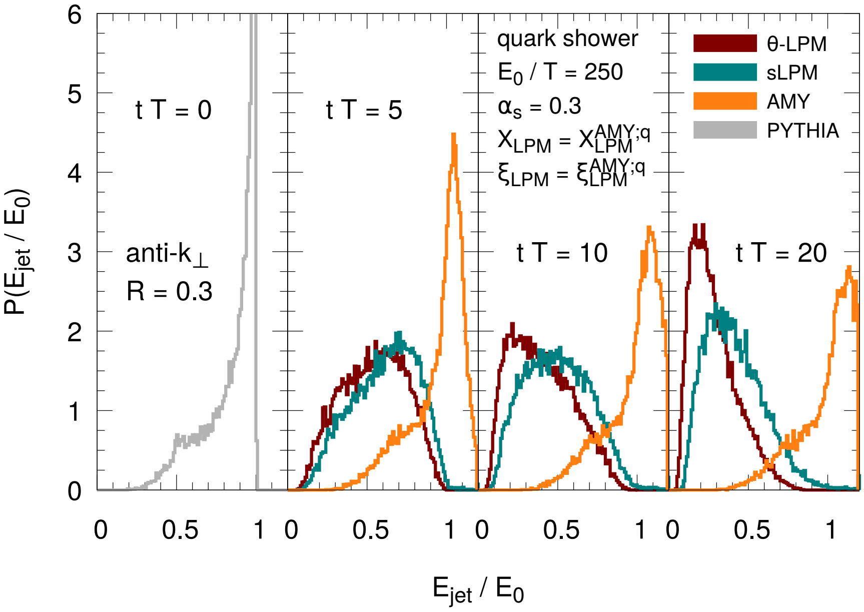

Figure 6.15: Energy distribution $P(E_\text{jet})$ at different times $t = \left\{0\,\mathrm{T}^{-1}; 5\,\mathrm{T}^{-1}; 10\,\mathrm{T}^{-1}; 20\,\mathrm{T}^{-1}\right\}$ of a leading jet reconstructed from parton showers initiated by a quark with initial energy $E_0 = 25\,\mathrm{T}$ that traverses a static medium with temperature T via only radiative processes from either the θ-LPM (red), the stochastic LPM (green) or the AMY (yellow) approach. The left panel shows the corresponding jet energy distribution directly from PYTHIA without any medium-modification. The screening parameters of the effective LPM approaches are chosen by $X_\text{LPM}^\text{AMY} = 0.05$ and $\xi_\text{LPM}^\text{AMY;\,q} = 0.01$ for reproducing $\mathrm{d}E/\mathrm{d}x$ of AMY and the QCD coupling is fixed to $\alpha_s = 0.3$. Jets are reconstructed via the anti-$k_\perp$ algorithm and a jet radius of $R = 0.3$. The leading jet energy E_jet at time t is normalized by the initial projectile energy E_0.

In agreement with the previously discussed distributions of jet energy, both effective LPM approaches show a loss of energy out of the leading reconstructed jets. On the other hand, the reconstructed jets from AMY interactions gain energy with time so that the leading jet reconstructed from a quark shower has more energy after $t \approx 10\,\mathrm{T}^{-1}$ than the initial shower-initiating quark. The jets reconstructed from gluon-initiated showers lose more energy than the corresponding quark showers due to the higher QCD color factor C_A, both in vacuum and in the medium-induced gluon radiation of the different LPM approaches.

In contrast to the energy loss of a single projectile, the energy loss of a reconstructed is a multi-particle effect originating from both the energy loss of single partons and the emission of energy out of the jet cones. Hence, although the single parton radiative energy losses are comparable, the underlying mechanisms of the different LPM approaches lead to the presented different jet energy evolutions:

- In the AMY formalism gluons are emitted collinearly and therefore the emitted gluons stay closely to the reconstructed jet axis. Consequently the leading jet energy shows less medium modification than the effective LPM approaches, θ-LPM and stochastic LPM, that explicitly consider also non collinear gluon emissions. Furthermore, the additional collinear gluon radiation from AMY fills gaps in the y-ϕ plane within the jets and thereby allows partons from the initial parton shower, that were previously emitted out of the jet cones, to be reconstructed in the leading jet. Hence the reconstructed jet after time t may have energy $E_\text{jet} > E_\text{jet}(t = 0)$. In addition to this,

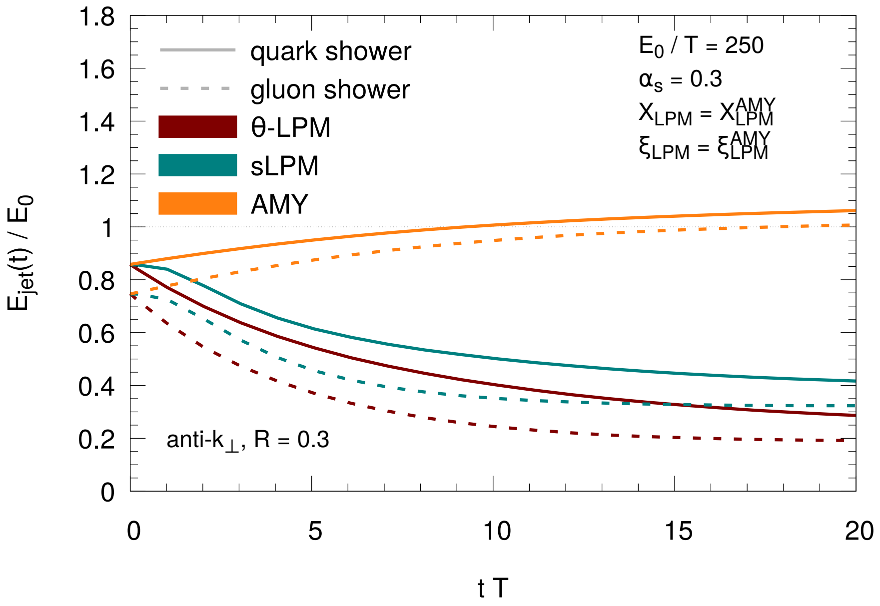

Figure 6.16: Leading jet energy E_{jet} depending on time t reconstructed from parton showers initiated by a quark (solid lines) or gluon (dashed lines) with initial energy $E_0 = 250\,\text{T}$ that traverses a static medium with temperature T via only radiative processes from either the θ-LPM (red), the stochastic LPM (green) or the AMY (yellow) approach. The screening parameters of the effective LPM approaches are chosen by $X_{\text{LPM}}^{\text{AMY}} = 0.05$ and $\xi_{\text{LPM}}^{\text{AMY; q}} = 0.01$ for reproducing $\mathrm{d}E/\mathrm{d}x$ of AMY and the QCD coupling is fixed to $\alpha_s = 0.3$. Jets are reconstructed via the anti-$k_\perp$ algorithm and a jet radius of $R = 0.3$. The leading jet energy E_{jet} at time t is normalized by the initial projectile energy E_0.

the effective $1 \leftrightarrow 2$ processes in AMY implicitly resum elastic interactions with the medium and allow emissions with $\omega > E$ (cf. Section 5.4). This leads to leading jet energies with $E_{\text{jet}} > E_0$.

- In both effective LPM approaches, the single partons lose energy to the medium (comparable to the AMY formalism) and non-collinear gluons are emitted to larger angles and thereby not reconstructed within the leading jet. However, the finite formation time of the stochastic LPM approach delays these emission processes. Consequently the energy loss of reconstructed jets in the stochastic LPM is slower than in the θ-LPM approach, where gluon emissions are instantaneously produced and the leading jet energy distribution is shifted faster to lower energies.
- The jet energy loss due to radiative processes from the θ-LPM approach is stronger than the other LPM approaches since both discussed effects, collinear gluon emissions and finite formation time, play no role for the parametrically suppressed gluon emissions.

Modification of shower shapes from medium-induced gluon radiation

In order to further characterize the jet energy loss from medium-induced radiative processes, we show in Fig. 6.17 the shower shape $\hat{\rho}(r)$ distribution of the leading jet reconstructed from parton showers initiated by a quark with initial energy $E_0 = 250\,\text{T}$ at different times $t = \left\{1\,\text{T}^{-1}; 10\,\text{T}^{-1}; 20\,\text{T}^{-1}\right\}$ in a thermal medium with temperature T. These shower

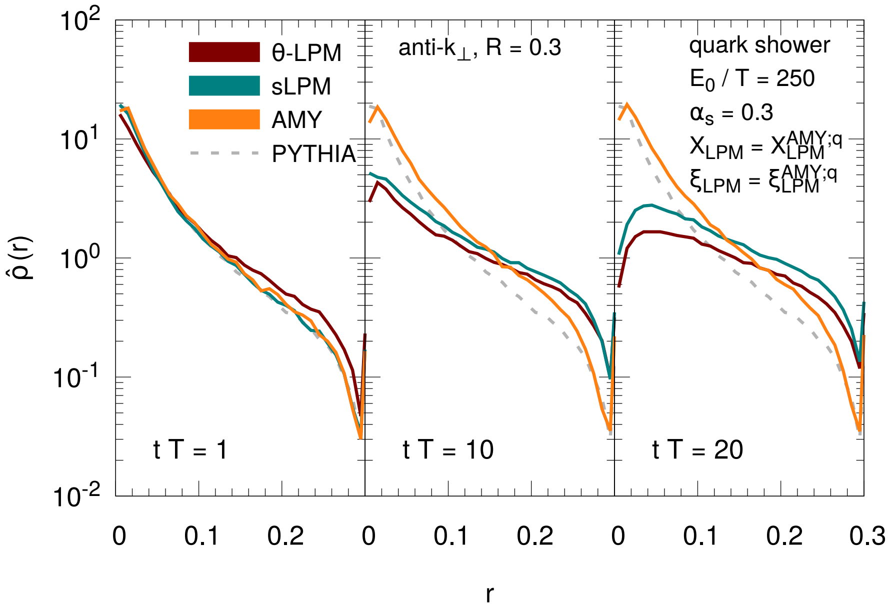

Figure 6.17: Time t evolution of shower shapes $\hat{\rho}(r)$ from parton showers initiated by a quark with initial energy $E_0 = 250\,\mathrm{T}$ that traverses a static medium with temperature T via only radiative processes from either the θ-LPM (red), the stochastic LPM (green) or the AMY (yellow) approach. The initial shower shapes obtained by PYTHIA without medium modification are shown by gray dashed lines. Jets are reconstructed via the anti-$k_\perp$ algorithm and a jet radius of $R = 0.3$. The screening parameters of the effective LPM approaches are chosen by $X_{\mathrm{LPM}}^{\mathrm{AMY}} = 0.05$ and $\xi_{\mathrm{LPM}}^{\mathrm{AMY;\,q}} = 0.01$ for reproducing $\mathrm{d}E/\mathrm{d}x$ of AMY and the QCD coupling is fixed to $\alpha_s = 0.3$.

shapes are compared to the initial distribution obtained from the vacuum splittings by PYTHIA. At early times the distributions from the different LPM approaches are close to each other, although the stochastic LPM and AMY shows slightly less energy at larger radii $r > 0.1$. Reason for this suppression is again the finite formation time in the stochastic LPM approach and the collinear emissions from AMY. With progressing times the distributions of the effective LPM approaches show a depletion of energies at the center of the jets, at $r < 0.1$, while at the same time the distributions at larger angles increases. The energies at large angles stem from partons that are emitted non-collinearly, whereas the radiative energy loss of hard shower partons decreases the distribution at smaller angles. Again, the finite formation time within the stochastic LPM slows down the shift of $\hat{\rho}(r)$. On the contrary, the collinear interactions from AMY only slightly influence the shower shapes: While both the inner core and the outer edge of the reconstructed jets seem to be unmodified, the intermediate r region is enhanced wrt. the vacuum distribution.

The previous findings for the medium modification of leading jet shower shapes are extended in the following by differentially investigating which partons contribute to the shower shapes at given r in the different LPM approaches. To this end, Fig. 6.18 shows the contributions of different parton flavors to the $\hat{\rho}(r)$ distribution at time $t = 20\,\mathrm{T}^{-1}$ of a quark-initiated shower with initial projectile energy $E_0 = 250\,\mathrm{T}$ for the different LPM approaches. In the left panel we show the corresponding initial shower shape distribution from PYTHIA without any medium modification. The inner core of the vacuum distribution is maximum at small angles representing the leading quark of the quark-initiated parton showers. At larger angles the shower shapes mainly consist of energies from gluons emitted

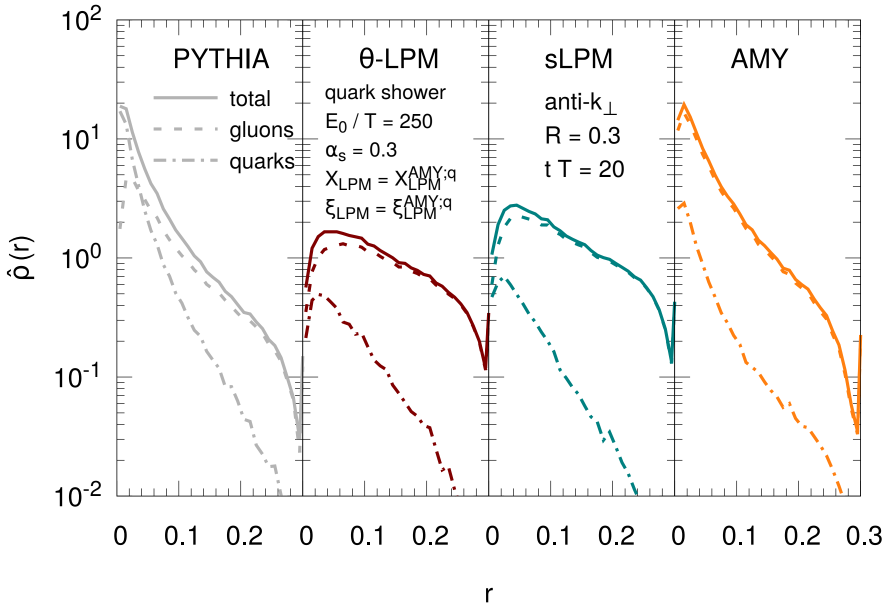

Figure 6.18: Contribution of different parton flavors, quarks (dashed lines) and gluons (dashed-dotted lines), to the total shower shape $\hat{\rho}(r)$ (solid lines) of a parton shower initiated by a quark with initial energy $E_0 = 250\,\mathrm{T}$ that traverses a static medium with temperature T via only radiative processes from either the θ-LPM (red), the stochastic LPM (green) or the AMY (yellow) approach. The initial shower shapes obtained by PYTHIA without medium modification are shown by gray dashed lines in the left panel. Jets are reconstructed via the anti-$k_\perp$ algorithm and a jet radius of $R = 0.3$. The screening parameters of the effective LPM approaches are chosen by $X_{\mathrm{LPM}}^{\mathrm{AMY}} = 0.05$ and $\xi_{\mathrm{LPM}}^{\mathrm{AMY;\,q}} = 0.01$ for reproducing $\mathrm{d}E/\mathrm{d}x$ of AMY and the QCD coupling is fixed to $\alpha_s = 0.3$.

to larger angles in the medium. After traveling for $t = 20\,\mathrm{T}^{-1}$ within the medium with temperature T the contribution of quarks to the shower shapes is suppressed in all different LPM approaches, whereas the shower shape distributions are dominated by gluons over the entire r range.

Furthermore, we show in Fig. 6.19 the same shower shapes of a quark-initiated shower with $E_0 = 250\,\mathrm{T}$ as in Fig. 6.18 but differentially in the energy ω of partons contributing to $\hat{\rho}(r)$ at an given angle r. In the shower shape distribution from PYTHIA a clear hierarchy in the parton energies is identifiable. The leading partons with $\omega > 0.8\,\mathrm{E}_0$ contribute to shower shapes only at very small angles $r \lessapprox 0.02$. Emissions with decreasing energies w contribute to the shower shapes at increasing angle r. Consequently only softer partons with $\omega < 0.05\,\mathrm{E}_0$ are emitted to larger angles and thereby contribute at $r \to R$. There is no contribution of thermal partons with $\omega < 0.01\,\mathrm{E}_0 \sim \mathcal{O}(T)$.

After the parton showers have traversed the medium for $t = 20\,\mathrm{T}^{-1}$ the ω-differential distributions of $\hat{\rho}(r)$ are modified:

- In all three LPM approaches the leading parton has lost significantly energy so that there is almost no contribution of partons with $E_{\mathrm{parton}} > 0.8\,\mathrm{E}_0$ to the shower shapes after $t = 20\,\mathrm{T}^{-1}$.

- Both effective approaches show again a similar behavior: While the inner core is diminished by the energy loss of the leading partons, especially the contribution of gluon emissions with $\omega < 0.05\,\mathrm{T}$ is enhanced wrt. the vacuum distribution. This

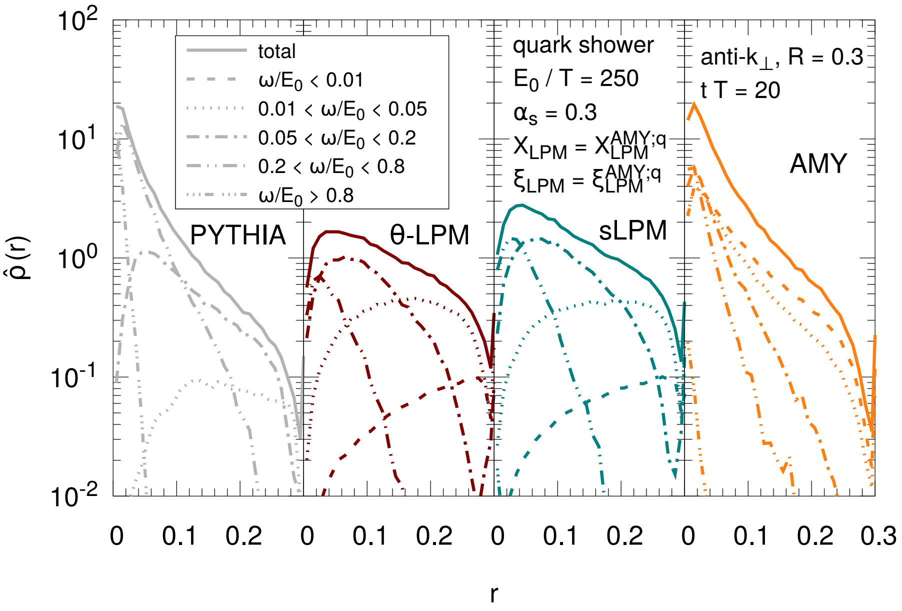

Figure 6.19: Contribution of different parton energies ω to the total shower shape $\hat{\rho}(r)$ (solid lines) of a parton shower initiated by a quark with initial energy $E_0 = 250\,\mathrm{T}$ that traverses a static medium with temperature T via only radiative processes from either the θ-LPM (red), the stochastic LPM (green) or the AMY (yellow) approach. Same parameters as in Fig. 6.18.

enhancement is situated at larger angles $r > 0.1$ representing the emissions of (semi-)soft gluons to large angles. Main difference between the θ-LPM and stochastic LPM approach is the slightly stronger energy loss of leading partons that can be identified by less contribution of $\omega > 0.2\,\mathrm{E}_0$ to the shower shapes.

- On the contrary, the shower shapes from the AMY formalism show a different behavior: While the inner core consisting of the leading parton is suppressed, the emitted energy stays close to the jet axis. Also the other ω regions mainly contribute at smaller angles $r \approx 0.02$ leading to a collimation of energy in the core of the jets. Only emissions with soft energies $\omega < 0.05\,\mathrm{E}_0$ deploy energy at larger angles. Due to the divergence at $\omega \to 0$ in the AMY formalism the relative contribution of thermal partons is significantly larger than in both other LPM approaches.

In conclusion, we found in this section that the effective LPM approaches, θ-LPM and stochastic LPM, show similar in-medium modifications of high-energy parton showers, whereas the radiative processes from the AMY formalism differently modify the parton showers due to the collinearity of gluon emissions. In the next section we discuss how the transport of both the initial parton showers and the medium-induced gluon radiation via elastic processes affect the medium modification of parton showers.

6.3.4 Broadening of parton showers by elastic interactions

In the previous section the in-medium modification of parton showers was caused by medium-induced gluon radiation that both decreased the energy of shower partons and at the same time emitted energy out of the reconstructed jets. However, while this rather academic treatment of jet modification allows a clean investigation of the different LPM approaches, it neglects the further transport of emitted partons in and out of the jet cones.

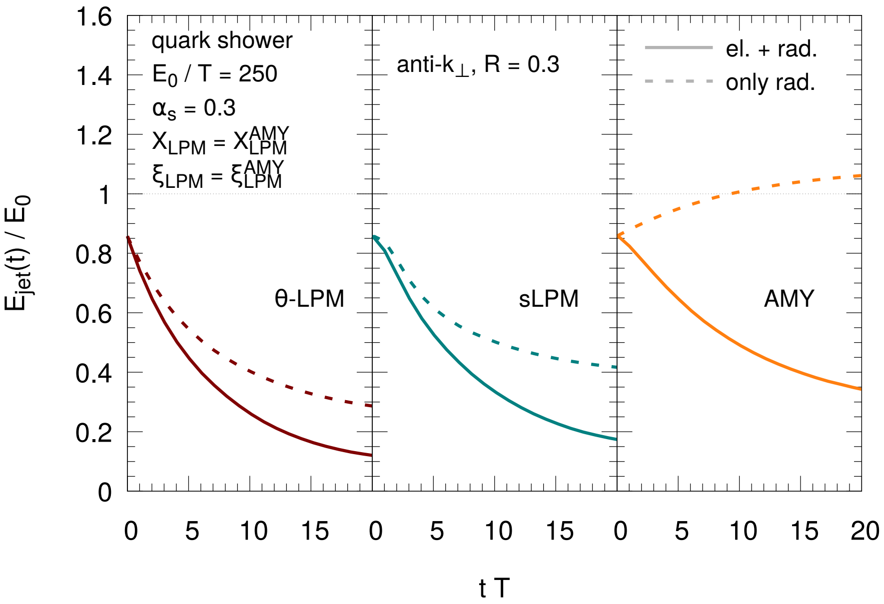

Figure 6.20: Leading jet energy E_{jet} depending on time t reconstructed from parton showers initiated by a quark with initial energy $E_0 = 250\,\text{T}$ that traverses a static medium with temperature T. While the dashed lines denote results from parton showers that are modified by only medium-induced gluon radiation (“only rad.”), the solid lines shows the jet energy evolution based on parton showers that are modified by both elastic scatterings and radiative processes (“el.+rad.”) from the θ-LPM (red), the stochastic LPM (green) or the AMY (yellow) approach. The screening parameters of the effective LPM approaches are chosen by $X_{\text{LPM}}^{\text{AMY}} = 0.05$ and $\xi_{\text{LPM}}^{\text{AMY; q}} = 0.01$ for reproducing $\mathrm{d}E/\mathrm{d}x$ of AMY and the QCD coupling is fixed to $\alpha_s = 0.3$. Jets are reconstructed via the anti-$k_\perp$ algorithm and a jet radius of $R = 0.3$. The leading jet energy E_{jet} at time t is normalized by the initial projectile energy E_0.

Therefore we study in this section how additional elastic $2 \to 2$ processes of both the initial shower partons from PYTHIA and the medium-induced gluons affect the modification of parton showers. To this end, we again generate parton showers by PYTHIA based on an initial quark or gluon projectile with energy E_0 and subsequently evolve them within a static, thermal medium with temperature T via both elastic and radiative processes from the different LPM approaches. The effective LPM approaches θ-LPM and stochastic LPM are again calibrated to the AMY formalism and the radiative evolution of parton showers in the AMY formalism is limited by a minimum parton energy $E_{\text{min}} = 3T$. On the contrary, the same limit does not hold for the elastic scatterings, hence even very soft gluons are allowed to scatter elastically. The jets are again reconstructed by the anti-$k_\perp$ algorithm and a jet radius of $R = 0.3$.

We compare in Fig. 6.20 our previous results for the modification of jets via only medium-induced gluon radiation to the case where the partons are also allowed to scatter elastically via $2 \to 2$ from Section 3.1. We found in Section 6.1 and Section 6.2 (cf. Fig. 6.3) that the contribution of $2 \to 2$ scatterings to the energy loss of single partons is subordinate. However, besides the elastic energy loss of single partons, $2 \to 2$ processes may lead to a transport of emitted gluons (or other shower partons) out of the reconstructed jets. This effect can be identified in Fig. 6.20, where the energy loss of reconstructed jets from all three LPM approaches is significantly increased in comparison to our previous results from only medium-induced gluon radiation. In the AMY formalism, the elastic transport

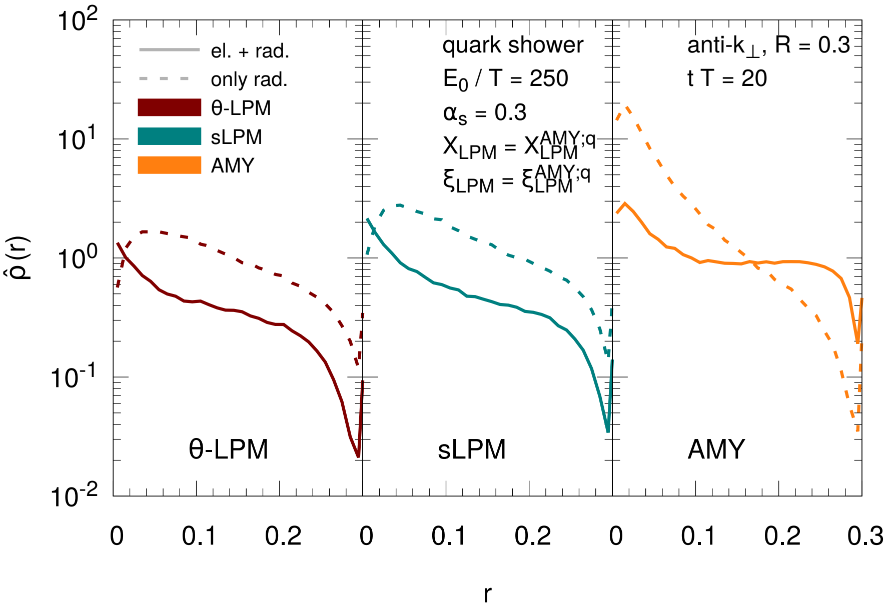

Figure 6.21: Comparison of shower shapes $\hat{\rho}(r)$ from parton showers initiated by a quark with initial energy $E_0 = 250\,\mathrm{T}$ that traverses a static medium with temperature T for time $t = 20\,\mathrm{T}^{-1}$ via either only radiative processes (dashed lines) or via elastic and radiative processes (solid lines) from either the θ-LPM (red), the stochastic LPM (green) or the AMY (yellow) approach. Jets are reconstructed via the anti-$k_\perp$ algorithm and a jet radius of $R = 0.3$. The screening parameters of the effective LPM approaches are chosen by $X_{\mathrm{LPM}}^{\mathrm{AMY}} = 0.05$ and $\xi_{\mathrm{LPM}}^{\mathrm{AMY;\,q}} = 0.01$ for reproducing $\mathrm{d}E/\mathrm{d}x$ of AMY and the QCD coupling is fixed to $\alpha_s = 0.3$.

of partons out of the reconstructed jets significantly displaces the previously found energy gain of the reconstructed jets, which was caused by collinear gluon emissions within AMY that were still reconstructed within the jets. Also the jet energy evolutions of both LPM approaches show an increased energy loss out of the reconstructed jets. Only at early times the result from the stochastic LPM shows again a slower jet energy evolution due to the finite formation time of gluon emissions and thereby path-length dependence of the radiative energy loss. In summary, it can be stated that the additional elastic scatterings of the parton shower levels the jet energy evolution within AMY to the effective LPM approaches.

Figure 6.21 further investigates the role of additional elastic $2 \to 2$ scatterings for the modification of parton showers by comparing the previous result for the shower shapes $\hat{\rho}(r)$ to the case where the shower partons are also allowed to scatter elastically. The jet shapes of both effective LPM approaches, namely the θ-LPM and stochastic LPM approaches, show the same strong depletion of energy at intermediate up to large angles $r \to R$ wrt. the jet axis. This depletion again represents the elastic transport of partons out of the reconstructed jets, which causes the increased jet energy loss presented in Fig. 6.20. At small angles $r \lessapprox 0.02$ the distributions of both θ-LPM and stochastic LPM show an enhancement when considering the elastics scatterings. Reason for this effect is a “wobbling” jet axis due to the elastic scatterings of the leading partons that lead to a “pseudo-collimation” of partons around the jet axis. Although the shower shape distribution from only medium-induced gluon radiation differs between AMY and both effective approaches, the inclusion of elastic scatterings leads to similar shower shape distributions after $t = 20\,\mathrm{T}^{-1}$ in all three

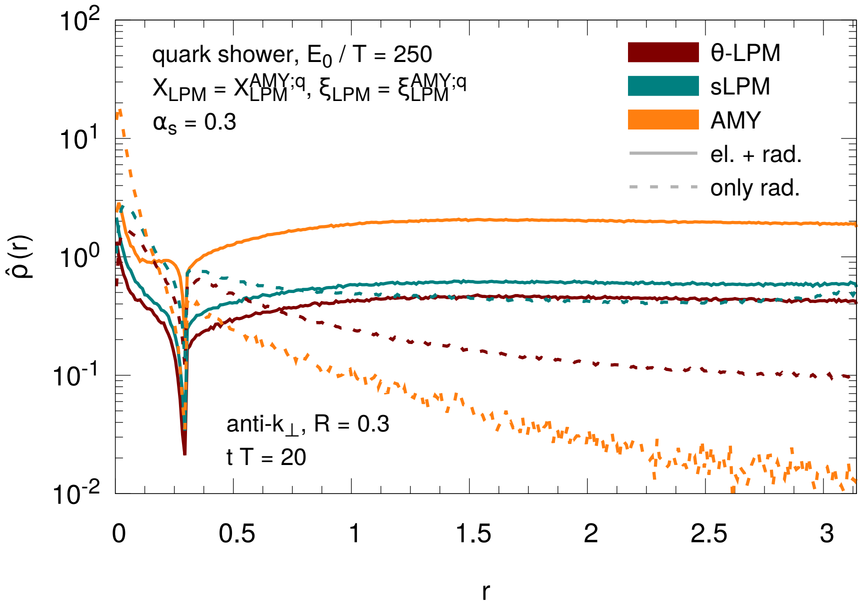

Figure 6.22: Shower shape distribution at larger angles $r \in [0;\pi]$ for the same calculations as in Fig. 6.21.

LPM approaches. Furthermore, the contribution of partons at intermediate angles $r > 0.1$ is significantly larger for the AMY interactions. This is reasoned by the missing initial transverse momentum of partons in the AMY formalism, so that emitted partons from AMY can only be transported to intermediate angles.

Consequently, the question arises where the missing energy of the reconstructed jets has been transported to. We answer this question in Fig. 6.22, where we compare the same shower shape distributions as presented in Fig. 6.21 within a larger region $r \in [0;\pi]$. Since the jet energy is determined by partons with angle $r < R$ the distribution of partons at larger angle provide insight where the lost energy of the reconstructed jets can be found. All shower shape distributions show a dip at $r = R$. This dip is caused by the clustering of particles to reconstructed jets. During the jet reconstruction only partons are clustered to the same jet that have minimum distances in rapidity y and azimuthal angle ϕ between each other. Consequently the reconstructed jets represent clusters with optimized distances $r < R$ and therefore partons with $r = R$ are suppressed[6]. For angles $r > R$ the $\hat{\rho}(r)$ distributions from only medium-induced gluon radiation split up between the different LPM approaches: While the distribution from the stochastic LPM shows the strongest contribution at large angles due to the more transverse gluon emissions (cf. Section 6.2.2), the distribution of the AMY formalism is strongly suppressed due to the collinearity of gluon emissions. After including the additional elastic scatterings of shower partons, the $\hat{\rho}(r)$ distributions from the different LPM approaches become approximately flat for increasing r. While the distributions from θ-LPM and stochastic LPM already without the elastic scatterings show a significant contribution of parton energies at large angles, the elastic scatterings together with the radiative processes from AMY lead to the strongest enhancement of parton energies at large angles. Reason for this enhancement are very soft gluon emissions with energies $\omega \ll T$ emerging from the divergence at $\omega \to 0$ in

---

[6] If one uses a simple cone in y and ϕ around, e.g., the leading parton to define a reconstructed jet, such a dip cannot be found.

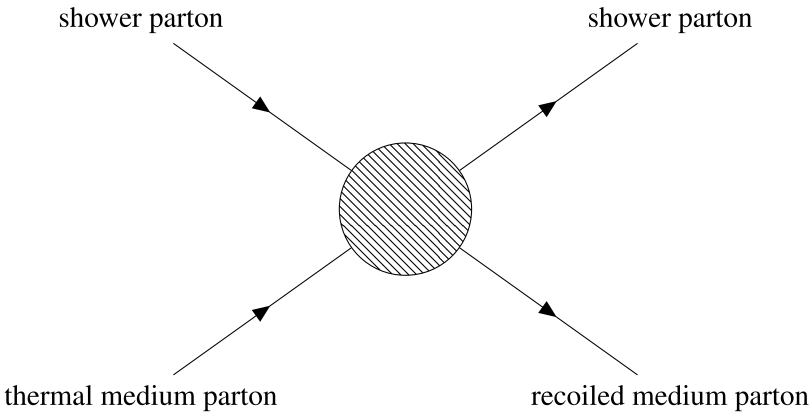

Figure 6.23: Sketch for an elastic scattering of a shower parton with a thermal parton from the background medium. The corresponding sketch for a $2 \to 3$ Bremsstrahlung process has an additional gluon emitted from one of the outgoing legs.

the AMY formalism. Due to the large elastic scattering rate of soft gluons (cf. Fig. 5.21a) these emissions gain energy by elastic scatterings within the medium. For example, if a soft parton with $\omega \ll T$ scatters elastically with a thermal parton (energy $\sim \mathcal{O}(T)$) there are processes with a large momentum transfer ($|\hat{t}| > \hat{s}/2$) so that the initially soft parton leaves the collision with a higher, thermal energy. As a result, the diverging emission rate within AMY together with the increased elastic scattering rate leads to a significant contamination of the reconstructed jets with energy from the background medium. This contamination however disguises the actual energy loss of the reconstructed jets and thereby the modification of the initial parton showers that we are interested in. Therefore we discuss in the following section how to appropriately consider the medium contribution to the reconstructed jets and subsequently subtract the undesired contamination of jets.

6.3.5 Role of recoiling medium partons

In the previous section we found that reconstructed jet momenta get contaminated by scatterings with thermal medium partons. Although this transfer of energy from the medium to parton showers is reasonable, it complicates the study of in-medium modification of the initial parton showers. Therefore we study in this section how to appropriately consider the unintended medium contribution from elastic scatterings and how to subtract this energy appropriately from the reconstructed jets.

The scattering of a shower parton with a thermal parton from the background medium is sketched in Fig. 6.23. For the previous results concerning the medium modification of reconstructed jets we assumed that each outgoing parton can be related to an incoming parton based on the respective momentum transfer of the elastic scattering as described in Section 5.3.3. Hence, we assigned to one of the outgoing partons the role of a shower parton that is allowed to further emit and scatter like the initial shower partons. The other outgoing parton is then regarded as the recoiled medium parton that instantly thermalizes and thereby does not contribute to the parton shower evolution. As we saw previously the discrimination between shower and thermal background partons becomes difficult in the case of soft shower partons interacting with harder thermal partons. Furthermore, the assumption of an instant thermalization of recoiled medium partons seems questionable at least for larger outgoing parton energies. These recoiled partons that incorporate some energy from the parton showers may stay in the vicinity of the parton shower and thereby restore energy in the reconstructed jets that is neglected in the case of an instant thermalization. Therefore we include in the following the recoiled medium partons of both elastic scatterings and the $2 \rightarrow 3$ Bremsstrahlung processes in the θ-LPM and stochastic LPM approaches when reconstructing jets and study how this medium recoil modifies the resulting reconstructed jets.

After discussing the treatment of recoiling medium partons we have to appropriately subtract the energy from the incoming thermal partons contaminating the reconstructed jets with background medium. To this end, we follow an approach previously applied in different approaches [Sen+15; EZ16a] and reconstruct jets by including both the shower partons and the recoiled medium partons together with very soft copies of the scattered thermal partons before the respective scatterings. While preserving their direction, the energy and momentum of these soft copies is scaled down[7] to soft scales so that they do not modify the resulting reconstructed jet energies. For each jet we then find soft copies of medium partons that are reconstructed within the jet and note their energy and momentum. The sum of these energies and momenta represents the amount of thermal energy and momentum that is reconstructed within the jets and has to be therefore subtracted from the jets. Consequently, the background subtracted jet energies are obtained by subtracting the background four-momentum from the previously reconstructed jet four-momentum. If the resulting energy of a background subtracted jet becomes negative, this jet is discarded.

In Fig. 6.24 we compare our previous results for the jet energy evolution without recoil to the evolution of reconstructed jets including the recoiled medium and the discussed subtraction method. And indeed with progressing time the jet energy loss is significantly weakened by recoiled medium partons staying in the reconstructed jets. In the θ-LPM and stochastic LPM approach the recoil effect is considered both in the elastic scatterings of the emitted gluons and the radiative $2 \rightarrow 3$ Bremsstrahlung processes. This leads to a stronger weakening of jet energy loss in both approaches than in the AMY method, where the coherent, elastic interactions are resummed into an effective $1 \rightarrow 2$ process and therefore no recoiling parton exists.

Finally, in Fig. 6.25 we further investigate the role of recoil by showing the shower shape distributions from the different LPM approaches including both the shower partons and the recoiled medium partons. The inclusion of recoiled medium partons that are subtracted in the reconstructed jets further enhances the distributions of $\hat{\rho}(r)$. The contribution of background energies to the shower shapes is calculated based on the energies of the scattered medium partons before the scatterings and increases for larger angles r. After subtracting the background contribution we find that the resulting shower shape distributions from the different LPM approaches are comparable. While the inner core of the jets is suppressed due to the leading parton energy loss, the distribution of $\hat{\rho}(r)$ at intermediate angles is flat representing gluons that are transported to larger angles via elastic scatterings.

In conclusion, we may retain that the different LPM approaches lead to different jet energy losses and shower shape distributions when neglecting the transport of emitted gluons out of the jet cones and that scattered medium partons may remain close to the jet axis. However, when considering both effects, the resulting medium-modifications of parton showers following the different LPM prescription become similar indicating that the role of the specific choice of LPM approach for the modification of reconstructed jets is minor.

---

[7] The energy and momentum of the parton is divided by the scaling factor $1 \cdot 10^8$.

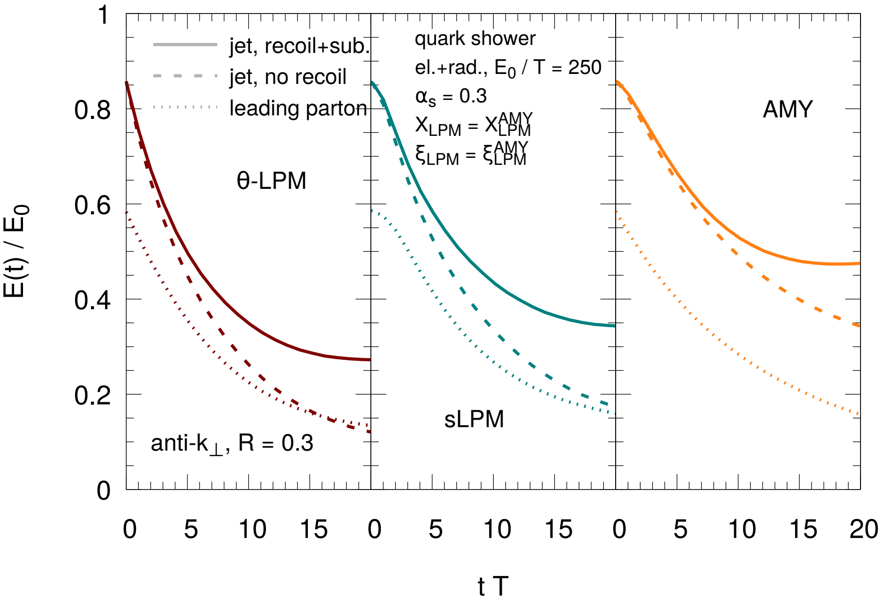

Figure 6.24: Leading reconstructed jet energy E_{jet} depending on time t from parton showers initiated by a quark with initial energy $E_0 = 250\,\text{T}$ that traverses a static medium with temperature T via elastic scatterings and radiative processes from the θ-LPM (red), the stochastic LPM (green) or the AMY (yellow) approach. While the dashed lines denote parton showers without recoil, the solid lines show the results in which also the medium recoil is considered in the reconstructed jets and the medium contribution is subtracted as discussed in the text. The energy evolution of the leading parton via the respective LPM approach is given by the dotted line. The screening parameters of the effective LPM approaches are chosen by $X_{\text{LPM}}^{\text{AMY}} = 0.05$ and $\xi_{\text{LPM}}^{\text{AMY; q}} = 0.01$ for reproducing $\mathrm{d}E/\mathrm{d}x$ of AMY and the QCD coupling is fixed to $\alpha_s = 0.3$. Jets are reconstructed via the anti-$k_\perp$ algorithm and a jet radius of $R = 0.3$. The leading jet energy E_{jet} at time t is normalized by the initial projectile energy E_0.

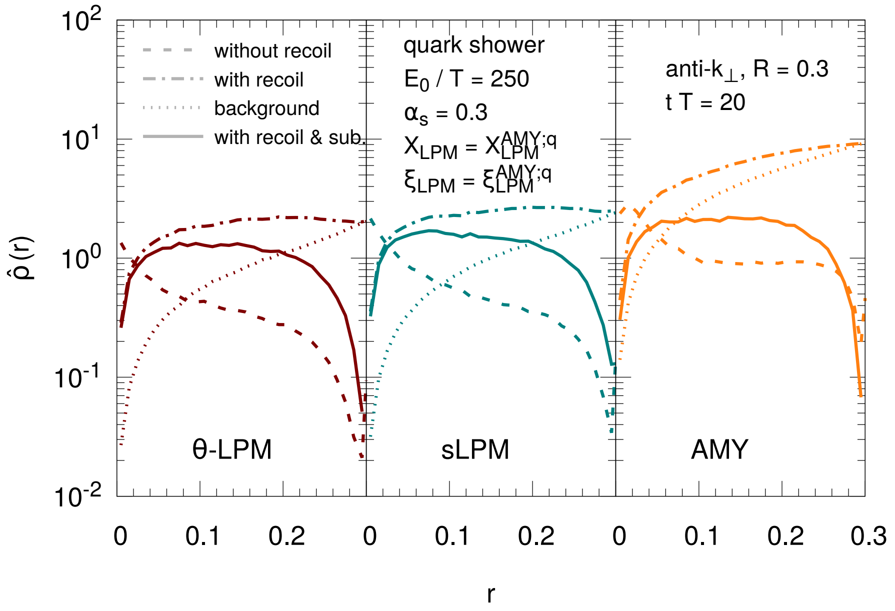

Figure 6.25: Shower shapes $\hat{\rho}(r)$ with recoiling medium from parton showers initiated by a quark with initial energy $E_0 = 250\,\mathrm{T}$ that traverses a static medium with temperature T via elastic scatterings and radiative processes from either the θ-LPM (red), the stochastic LPM (green) or the AMY (yellow) approach. While the dashed lines depict the previously results for $\hat{\rho}(r)$ without recoil, the dashed-dotted lines denote the shower shapes including recoiled medium partons but not subtracting the background contamination. The shower shapes with recoil and after subtracting the background contamination (dotted lines) are given by the solid lines. Jets are reconstructed via the anti-$k_\perp$ algorithm and a jet radius of $R = 0.3$. The screening parameters of the effective LPM approaches are chosen by $X_{\mathrm{LPM}}^{\mathrm{AMY}} = 0.05$ and $\xi_{\mathrm{LPM}}^{\mathrm{AMY;\,q}} = 0.01$ for reproducing $\mathrm{d}E/\mathrm{d}x$ of AMY and the QCD coupling is fixed to $\alpha_s = 0.3$.

7 Jet quenching in ultra-relativistic heavy-ion collisions

In the previous chapters we introduced different ways to consider the non-Abelian LPM effect within the partonic transport approach BAMPS. We found that, although we calibrated the radiative energy loss from the different approaches to each other, the proposed LPM methods show different characteristics for the energy and momentum modification of jets traversing a static and thermal quark-gluon plasma. In order to further clarify these differences we simulate in this chapter the jet modification from the different LPM approaches within expanding, non-thermal bulk media and confront these results with various experimental observables for jet quenching as measured in Pb + Pb collisions with $\sqrt{s_{\mathrm{NN}}} = 2.76\,\mathrm{TeV}$ at the LHC. This will enable us to characterize the different LPM approaches under realistic conditions and thereby allow us to identify key properties for the jet quenching in ultra-relativistic heavy-ion collisions within BAMPS.

After introducing in the next section how the expanding, partonic medium of a heavy-ion collision is simulated within BAMPS, we present in Section 7.1 the properties of the medium created in Pb + Pb collisions at the LHC as calculated from microscopic pQCD interactions. In Section 7.3 we then embed high energy partons into these expanding media and examine how their partonic and, after fragmentation, hadronic spectra are modified in the medium due to the elastic and radiative processes defined by the different LPM approaches. Finally, in Section 7.4 we take advantage of the reconstruction of parton showers and study differentially the in-medium modification of reconstructed jets from the different LPM approaches.

7.1 Evolution of the bulk medium

Before investigating the modification of hard probes traversing the matter created in heavy-ion collisions at LHC, we first discuss in this section the underlying and expanding bulk medium as simulated within BAMPS. Different to other attempts in the heavy-ion community, one major goal of the BAMPS framework is to explore the applicability of perturbative QCD to both the physics of the hard jet regime *and* the soft bulk medium of ultra-relativistic heavy-ion collisions. In the next Section 7.1.1, we introduce how the distributions of soft partons in the bulk medium are initialized and subsequently evolved within BAMPS forming an expanding quark-gluon plasma. Section 7.1.2 presents then properties as, e.g., the temperature or density of this hot and dense matter following from the specific choice of microscopic pQCD interactions within BAMPS. While the study of these properties is interesting for its own, they will also serve later as input parameters for the interactions of jets probing the medium. Finally, we demonstrate in Section 7.1.3 that the chosen setup for the underlying medium leads to a significant built-up of elliptic flow via microscopic pQCD interactions.

7.1.1 Modeling the soft background medium

Hydrodynamical models are successful in describing the expansion of the medium created in ultra-relativistic heavy-ion collisions by a thermal fluid with small or vanishing shear viscosity-over-entropy ratio η/s. However, especially in the beginning of the nucleus-nucleus collision the applicability of an equilibrium theory as hydrodynamics to the anisotropic distribution of parton momenta is questionable. In contrast, by numerically solving the Boltzmann equation the interactions within BAMPS do not rely on an equilibrium but can also be applied to non-equilibrium situations as they presumably can be found in the early stages of a heavy-ion collision. In this section we briefly outline our strategy for simulating heavy-ion collisions within the BAMPS framework. For more details about the different stages and their underlying assumptions we refer to Refs. [XG05; XG07; Uph+15].

Initial distribution of soft partons

The BAMPS framework describes scatterings of partons within a medium via the microscopic processes from Chapter 3. In order to simulate ultra-relativistic heavy-ion collisions at, e.g., RHIC and LHC, an appropriate initial state has to be defined that is then subsequently evolved by the BAMPS interactions. However, a description for the complex initial state of a heavy-ion collision from first-principles is still difficult and topic of ongoing research. One promising approach could be the color-glass-condensate (CGC) that describes the colliding nuclei as Lorentz-contracted discs consisting, due to the high beam energies, predominantly of gluons [McL; IV04; Wei05]. Recently, there were studies [Gre+17a] in our group that combined such a CGC-like initial state based on classical Yang-Mills dynamics (IP-GLASMA [STV12c; SST19]) with the medium evolution from BAMPS in order to study the importance of initial and final state effects in $\mathrm{p}+\mathrm{A}$ collisions.

In this work we choose another model for the initial state of the heavy-ion collisions that was first developed by Uphoff [Uph09; Uph+10]. Within this approach, the single nucleon-nucleon scatterings of the colliding nuclei are simulated by the event generator PYTHIA (cf. Section 6.3) and distributed in configuration space by a *Glauber* calculation [Gla06; Mil+07] (cf. Appendix D). This procedure then models the initial state of the heavy-ion collision as a superposition of independent $\mathrm{p}+\mathrm{p}$ collisions [Uph09].

Within PYTHIA, the nucleon-nucleon scatterings are described as $\mathrm{p}+\mathrm{p}$ collisions that are terminated at the partonic scale before the fragmentation to hadrons. Depending on the momentum transfer of the initial partonic process underlying the $\mathrm{p}+\mathrm{p}$ collision, PYTHIA events can be separated into *hard* and *soft* events. The hard events scale with the number of binary nucleon-nucleon collisions, N_{coll} [Uph09], whereas the soft events from PYTHIA then fill up the remaining energy that is deployed by the two nuclei in the collision region. By employing a Woods-Saxon density profile (cf. Appendix D) for the colliding nuclei, the number of binary nucleon-nucleon collisions, N_{coll}, and the number of participating nucleons, N_{part}, can be calculated within the Glauber model for a given impact parameter b. In Appendix D we outline such a Glauber calculation and give numerical values for N_{part} and N_{coll} obtained for typical impact parameters employed in the following study. Furthermore, we compare in Appendix D these values for N_{part} and N_{coll} to centrality classes defined by the experiments at LHC in order to allow a reliable comparison of our results in this chapter to experimental data. For more details about the presented initial state and its implementation into the BAMPS framework we refer to Refs. [Uph09; Uph+10; Uph13]

Expansion of the background medium

The parton distributions initialized by the previous introduced “PYTHIA+Glauber” model are subsequently evolved via the microscopic processes as introduced in Chapter 3. After finishing their initial formation time $\Delta\tau_f = \cosh y / p_\perp$, where y and $p_\perp$ are the momentum-space rapidity and transverse momentum, respectively, the partons are allowed to scatter elastically via $2 \to 2$ collisions as well as via inelastic scatterings, $2 \to 3$ Bremsstrahlung processes and $3 \to 2$ annihilation processes. While we previously neglected annihilation processes for the energetic jets[1], the inclusion of these processes at soft momenta ensures *detailed balance*, which is crucial at thermal momenta.

Although the LPM effect is more dominant at high parton energies due to the longer formation time of gluon emissions with higher energies, it should also be considered for the inelastic interactions of softer medium partons. Since the AMY formalism is, strictly speaking, only valid within a thermal bath and does not consider the back reaction of the resumed elastic scatterings to the medium, it is not ad-hoc clear how it could be applied to the inelastic processes of partons from the non-thermal background of a heavy-ion collision.

Furthermore, within the stochastic LPM approach gluon emissions are suppressed after finishing their formation time due to the potential coherence of elastic scatterings during the formation time. In the context of medium interactions, the stochastic LPM method could lead to situations in which a gluon emission from a medium parton is suppressed after its formation time. Consequently, the interactions of the gluon with other medium partons during its formation time have to be undone. Obviously, this would change the whole medium history and thereby lead to a significant numerical effort of bookkeeping the different fulfilled and rejected medium evolutions. One potential solution for this issue could be a reweighting procedure for the interactions of gluon emissions during their formation time. Such a study of the stochastic LPM for medium interactions is out of the scope for the present work.

Consequently, we describe in the following the LPM effect for both the $2 \to 3$ Bremsstrahlung and $3 \to 2$ annihilation processes between medium partons by the θ-LPM approach. This allows a microscopic treatment of medium scatterings while the coherence of gluon emissions is effectively considered. As we demonstrated in Refs. [Uph+15] the choice of the θ-LPM approach with a screening parameter $X_{\text{LPM}} = 0.3$ shows both a realistic suppression of charged hadron spectra and at the same time a significant built-up of elliptic flow in the bulk medium. While the choice of $X_{\text{LPM}} = 0.3$ was originally motivated by a comparison to RHIC data, we will show later in this chapter that this choice is also successful in describing experimental data for LHC.

For numerically solving the Boltzmann equation, the BAMPS framework relies on the stochastic method for the scatterings of partons. As we have seen in Chapter 4 whether a parton scatters is determined by calculating its transition rate in a given cell in configuration space. While this cell grid was constant in the case of a static, thermal medium in the previous chapters, the rapidly expanding medium of a heavy-ion collisions requires a grid that dynamically adjusts to the current evolution. Due to the high velocities of the colliding nuclei, the longitudinal expansion of the medium has to be considered relativistically. Therefore the appropriate coordinate choice for describing the longitudinal expansion of the collisions is the space-time rapidity, $\eta_s = 1/2 \log{(t+z)/(t-z)}$, where z is the

---

[1] The $3 \to 2$ annihilation processes were neglected previously and will be neglected later for the hard jet regime since the cross section for annihilation strongly depends on the CoM energy of the collision and thereby is suppressed for energetic partons (cf. Section 3.2).

longitudinal space coordinate of a particle and t is the time. In contrast to the transverse cells, the cells in η_s direction are dynamically adjusted so that a similar number of test-particles are in each η_s-bin at each time step. Typical values for the central η_s bin are then $\Delta\eta_s \approx 0.14$ in central and $\Delta\eta_s \approx 0.22$ in more peripheral Pb + Pb collisions at LHC. This adjusting leads to approximately equally sized bins in the longitudinal direction, indicating an almost Bjorken-type expansion [XG09; Foc11]. In the transverse space wrt. the beam axis, the cell configuration is constant with cell widths of $\Delta x = \Delta y = 0.5$ fm for central and $\Delta x = \Delta y = 0.2$ fm collisions.

In the outer regions of the collision, where the number and energy density is significantly reduced, the stochastic method for particle scatterings is not applicable anymore and scatterings are calculated via geometrical scatterings. Instead of deciding stochastically when partons scatter, in the geometrical method two partons scatter when they are geometrically closer to each other than $\sqrt{\sigma/\pi}$ [Xu04], where σ is the cross section of the respective collision. For more details about this method and its drawbacks we refer to Ref. [Xu04].

In order to provide enough statistics in each cell for applying the stochastic method, the number of partons has to be scaled by N_{test} (cf. Chapter 4). This scaling is considered within BAMPS by inserting N_{test} initial events from PYTHIA into the simulation. The numerical values for N_{test} are then chosen so that a sufficient number of test particles is guaranteed in each cell[2]. For LHC simulations, this leads to values ranging from $N_{\text{test}}(b = 0\,\text{fm}) = 8$ in central collisions up to $N_{\text{test}}(b = 13.2\,\text{fm}) = 918$ in very peripheral, more dilute collisions (cf. Appendix D).

Freeze-out and hadronization of partons

The microscopic processes from pQCD are obviously only applicable for interactions of partons, namely quarks and gluons. With progressing evolution time, the medium created by the initial nucleus-nucleus collision expands and thereby cools down reaching temperatures where the underlying degrees of freedom are not longer partons but change to hadrons. Although there are first-principle QCD calculations for the macroscopic transition from partons to hadrons [Phi13], our understanding of the microscopic processes underlying this phase transition are still limited. While energetic partons as, e.g., jets fragment into hadrons, what can be described by fragmentation functions measured in elementary $\mathrm{e}^+ + \mathrm{e}^-$ collisions and is discussed in Section 7.3.1, a similar procedure for the soft components does not exist at the moment. Some models aim to describe the hadronization by recombining soft partons together building compound hadrons [Fri+03], whereas other models circumvent a microscopic hadronization by coarse-graining the single partons, applying an equation of state from lattice QCD (lQCD) and afterwards particularizing the fields again via the Cooper-Frye method [CF74; Pet+08; HP12]. Also in our group there are first attempts to develop an effective hadronization of partons on the microscopic scale by numerically clustering partons while preserving macroscopic properties of the matter[3].

Within this work we stick to the method employed previously for simulating heavy-ion collisions [XG05; XG07; XGS08; XG09; XG10; FXG09; Uph+15] in BAMPS: if a cell reaches a critical energy density of $\epsilon_c = 0.6\,\text{GeVfm}^3$ we terminate the evolution of all partons within this cell[4]. The choice of a critical energy density ϵ_c instead of a critical temperature T_c allows the application of this approach also in non-equilibrium situations.

---

[2] In LHC simulations a total number of $N \approx 1 \cdot 10^6$–$2 \cdot 10^6$ particles has proven to be successful.

[3] Paper to be published.

[4] The choice of $\epsilon_c = 0.6\,\text{GeVfm}^3$ corresponds via $\epsilon_c = 48/\pi^2 T_c^4$ to a critical temperature of $T_c = 175$ MeV for a pure

Below ϵ_c, hadronization effects come into the play that cannot be described within BAMPS and therefore the partons stream freely until the simulation ends. As a result, after a simulation time of $t = 10\,\text{fm}$ the expanded medium of a central collision at LHC is frozen out at mid-rapidity and no further collisions occur in this region.

7.1.2 Properties of the expanding quark-gluon plasma

After introducing our setup for simulating heavy-ion collisions within the BAMPS framework, we present in this section numerical results for the (macroscopic) properties of the expanding partonic matter in central and peripheral heavy-ion collisions with $\sqrt{s_{\text{NN}}} = 2.76\,\text{TeV}$ at the LHC. In contrast to simulations within hydrodynamical models, where such properties as, e.g., temperature T or particle density n follow from macroscopic evolution equations, these quantities are calculated dynamically from the microscopic distributions of partons within BAMPS. As mentioned previously, the parton distributions are evolved within BAMPS via the discussed pQCD interactions: elastic $2 \to 2$ scatterings and inelastic $2 \leftrightarrow 3$ processes. By solving the 3+1D Boltzmann transport equation, these calculations do not rely on thermal phase space distributions in equilibrium but may also be applied in non-equilibrium situations as, e.g., during the initial stages of a heavy-ion collisions. Consequently, these studies allow a quantitative comparison to other models for the heavy-ion background, as e.g. relativistic (ideal/viscous) hydrodynamics, and thereby shed light on the role of non-equilibrium effects in the medium evolution.

Furthermore, the properties of the bulk medium obviously also determine the energy loss of hard probes traversing it. Experimentally speaking, by studying the modification of jets one aims for measuring and characterizing exactly these medium properties of the quark-gluon plasma. But also in theoretical models the medium properties enter the various energy loss calculations. For example in the BAMPS framework, the Debye mass m_D^2 determines the screening of the elastic and inelastic pQCD matrix elements, whereas the temperature T sets the medium scale in the radiative processes from the AMY formalism.

Different to the macroscopic evolution in hydrodynamics, one needs to integrate different moments of the one-particle phase space distribution $f(\vec{\mathbf{x}}, \vec{\mathbf{p}})$ in order to obtain macroscopic quantities from microscopic particle distributions. Following Ref. [Uph13], the phase space integrations can be evaluated numerically within BAMPS by substituting the integration with a summation over massless parton momenta $\vec{\mathbf{p}}_i$ or energies $E_i = |\vec{\mathbf{p}}_i|$. For example, the zeroth moment of $f(\vec{\mathbf{x}}, \vec{\mathbf{p}})$ can be obtained from

$$d_i \int \frac{d^3p}{(2\pi)^3} \frac{1}{E} f_i(\vec{\mathbf{x}}, \vec{\mathbf{p}}) \to \frac{1}{V N_{\text{test}}} \sum_i \frac{1}{E_i}\,, \tag{7.1}$$

where d_i is the degeneracy and f_i the one-particle phase space distribution of parton species i, N_{test} the number of test particles and the sum runs over all partons with species i in a given space volume V.

While the momentum integrations of these calculations are performed within the entire momentum space, one has to choose a proper integration volume in configuration space in order to preserve locality within the fluid. One way for defining a configuration space region could be the already introduced dynamical cell grid underlying the calculation of scattering probabilities via the test-particles method within BAMPS (cf. Section 7.1.1).

---

gluonic Boltzmann gas or $T_c \approx 133\,\text{MeV}$ after including also quark degrees. For larger values of ϵ_c the medium evolution is stopped earlier leading, e.g., to a $\approx 20\,\%$ decrease of flow for $\epsilon_c = 1\,\text{GeVfm}^3$ [XG09].

This possibility is chosen, e.g., for the calculation of the temperature and flow velocity entering the AMY emission rates as we will present later in this section. Another way for choosing the integration region exploits the cylindric geometry of a heavy-ion collision and calculates the macroscopic quantities based on a ring structure as shown in Fig. 7.1. In order to consider relativistic effects in the expansion of the heavy-ion collisions, the longitudinal coordinate of this ring structure is chosen by the space-time rapidity η_s, which is given in bins coinciding with the bins of the previous test-particles grid. This leads to, e.g., a width $\delta\eta_\mathrm{s} \approx 0.15$ for the central η_s bin in central collisions at LHC. In the transverse direction we assume an azimuthal symmetry and hence define rings with radii $x_\perp$ in which the respective quantities are averaged. While this assumptions is obviously justified for central Pb + Pb collisions, its validity in more peripheral collisions becomes limited and could be substituted by a more elliptic geometry in a future study. The ring structure is employed within the BAMPS framework for calculating e.g. the Debye masses and the energy densities entering both the $2 \rightarrow 2$ and $2 \leftrightarrow 3$ interactions.

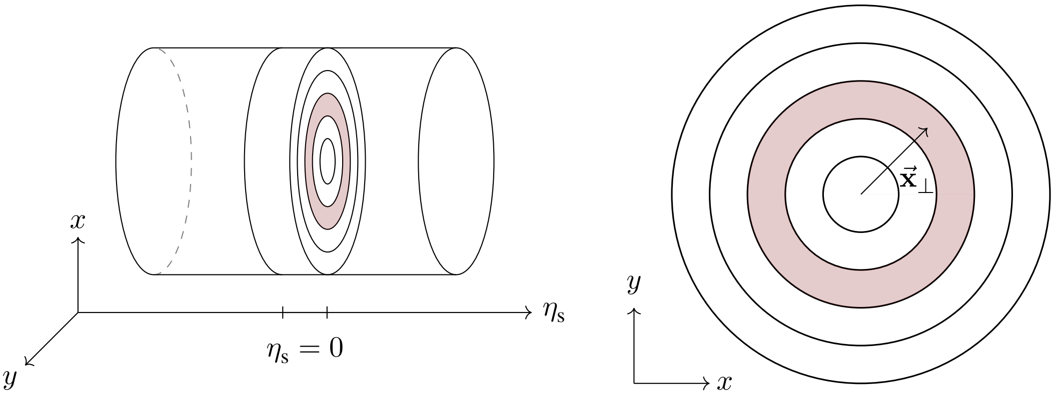

(a) Side view **(b)** Front view

Figure 7.1: Simplified geometry of a central heavy-ion collision. The transverse plane is spanned by the x- and y-axis, whereas the space-time rapidity η_s characterizes the longitudinal direction wrt. the beam axis. This ring structure is employed for calculating macroscopic quantities (cf. text).

In the following, we present numerical results for various macroscopic quantities calculated based on 15–20 independent BAMPS events[5] for Pb + Pb collisions with $\sqrt{s_\mathrm{NN}} = 2.76\,\mathrm{TeV}$ and impact parameters $b = 3.6\,\mathrm{fm}$ representing 0–10 % central collisions or $b = 10.3\,\mathrm{fm}$ representing 40–50 % peripheral collisions, respectively. As mentioned in Section 7.1.1, due to the limitations of the stochastic LPM and AMY method in the context of medium-medium interactions, we describe the LPM effect in the inelastic interactions of medium partons via the θ-LPM approach. For the screening of collinear gluon emissions we choose the previously applied screening parameter $X_\mathrm{LPM} = 0.3$ [Uph+15], which showed a realistic suppression of jets and a significant flow for RHIC collisions and, as we see later, also for collisions at the LHC.

---

[5] As discussed previously, we neglect physical fluctuations of the initial state. Consequently, different heavy-ion events within BAMPS simulate the same unique medium evolution. Potential fluctuations between the events are not physical but emerge from limited statistics. Furthermore, due to the scaling with test particles, each of these events is already a superposition of several realizations of the same heavy-ion medium, which justifies the rather small amount of independent simulations. The scaling with test particles obviously has to be considered when averaging the partons later in this section.

Number density n and energy density ϵ

The number density n of partons, namely quarks and gluons, is given by the first moment of the phase space distribution $f(\vec{\mathbf{x}},\vec{\mathbf{p}})$ and hence can be derived to

$$n = n_{\mathrm{g}} + n_{\mathrm{q}} = \int \frac{\mathrm{d}^3 p}{(2\pi)^3} \left(d_g f_g(\vec{\mathbf{x}},\vec{\mathbf{p}}) + d_q f_q(\vec{\mathbf{x}},\vec{\mathbf{p}}) \right) , \tag{7.2}$$

where $d_g = d_{\text{polarization}} \left(N_c^2 - 1 \right) = 16$ is the degeneracy of a gluon and $d_q = d_{\text{spin}} d_{\text{anti}} N_f N_c = 36$ is the degeneracy of a quark, respectively. For an equilibrated medium with temperature T, the number density $n_{\text{eq}}(T)$ evaluates via the equilibrium phase space distribution $f_{\text{eq}} \sim \exp\left(-E/T\right)$ to

$$n_{\text{eq}}(T) = \frac{\left(d_g + d_q\right)}{\pi^2} T^3 . \tag{7.3}$$

When discussing medium properties of a relativistic fluid, the definition of an appropriate reference frame is mandatory. The natural choice for this reference frame is the *local rest frame* (LRF) of the fluid. Since the number density is not a Lorentz invariant quantity, Eq. (7.2) needs therefore an additional Lorentz factor $\gamma = (1-\beta^2)^{-1/2}$ for boosting the lab quantities to the local rest frame, so that $n_{\text{LRF}} = n/\gamma$ follows. For a quantitative study of the flow velocity $\vec{\beta}$ within BAMPS simulation we refer to the end of this section.

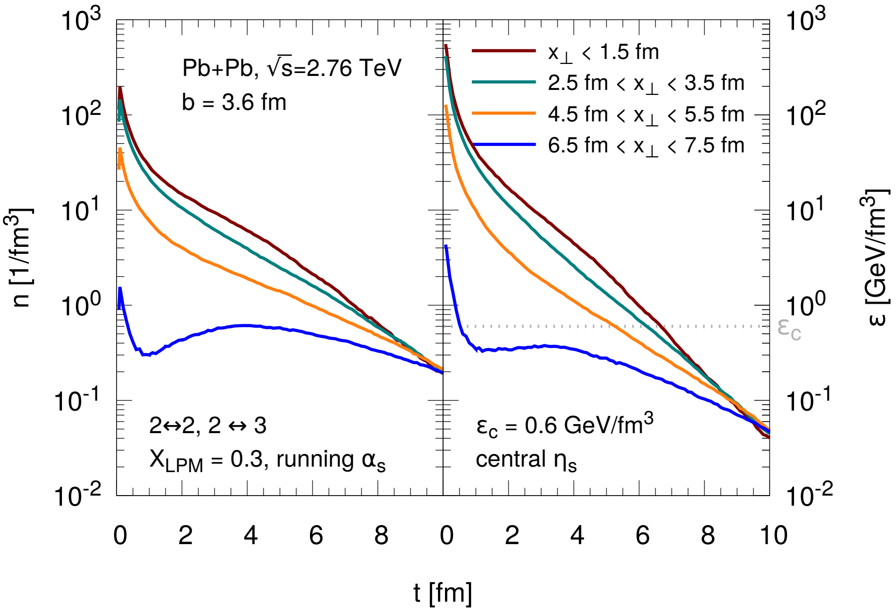

Figure 7.2: Time evolution of the number density n_{LRF} (left) and the energy density ϵ_{LRF} (right) within a ring at mid-rapidity and with radius $x_\perp$ calculated within BAMPS for a central $\sqrt{s_{\text{NN}}} = 2.76$ TeV Pb + Pb collision. The different colors denote different radii of the considered rings. The gray dotted line denotes the chosen value of the critical energy density ϵ_c below which the partons stream freely.

We show in the left plot of Fig. 7.2 the time evolution of n_{LRF} within transversal rings (cf. Fig. 7.1) from the central η_s slice of a central Pb + Pb collision with $\sqrt{s_{\text{NN}}} = 2.76$ TeV and impact parameter $b = 3.6$ fm. Obviously the density is the highest in the center of the collision at early times. In the core of the collision, $x_\perp < 1.5$ fm the density is

$n \approx 200\,\mathrm{fm}^{-3}$ and thereby approximately two magnitudes larger than common nuclear densities $n_{\mathrm{nucl}} \sim \mathcal{O}\left(1\,\mathrm{fm}^{-3}\right)$. With progressing time both the inner and outer regions of the heavy-ion collision rapidly dilute. After $t = 10\,\mathrm{fm}$ the densities of all rings are below $1\,\mathrm{fm}^{-3}$. A high number density obviously leads to an increased number of potential scattering partners and, roughly speaking, to an increased energy loss of jets. Consequently, we expect that the main contribution to the energy loss of jets originates in the center of the collision zone.

The energy density ϵ of a cell determines within BAMPS when the medium cooled down sufficiently so that the application of partonic interactions becomes questionable. Hence, if the energy density of cell is below the critical energy density ϵ_c the partonic interactions terminate and all partons in this cell stream freely. The energy density is given by the second moment of the phase space distribution $f(\vec{\mathbf{x}}, \vec{\mathbf{p}})$,

$$\epsilon = \int \frac{\mathrm{d}^3 p}{(2\pi)^3} E^2 \left(d_g f_g(\vec{\mathbf{x}}, \vec{\mathbf{p}}) + d_q f_q(\vec{\mathbf{x}}, \vec{\mathbf{p}})\right) . \tag{7.4}$$

Inserting as above the equilibrium phase space distribution $f_{\mathrm{eq}} \sim \exp\left(-E/T\right)$ leads to the energy density in equilibrium,

$$\epsilon_{\mathrm{eq}} = \frac{3\left(d_g + d_q\right)}{\pi^2} T^4 . \tag{7.5}$$

Again, the energy density is not a Lorentz invariant quantity and hence the energy density has to be Lorentz transformed in order to obtain the local rest frame observable. The energy density can also be found as the $\hat{T}^{00}$ component of the energy-momentum tensor

$$\hat{T}^{\mu\nu} = \int \frac{\mathrm{d}^3 p}{(2\pi)^3} \frac{1}{E} p^\mu p^\nu f(\vec{\mathbf{x}}, \vec{\mathbf{p}}) . \tag{7.6}$$

Employing the flow velocity $\vec{\beta}$ and the Lorentz transformation rule of a tensor $\hat{T}^{\mu\nu}_{\mathrm{LRF}} = \Lambda^\mu_\alpha \Lambda^\nu_\beta \hat{T}^{\alpha\beta}$, where Λ^μ_α is the Lorentz matrix, one obtains[6]

$$\begin{aligned} \epsilon_{\mathrm{LRF}} = \gamma^2 \hat{T}^{00} &+ \gamma^2 \beta_x^2 \hat{T}^{11} + \gamma^2 \beta_y^2 \hat{T}^{22} + \gamma^2 \beta_z^2 \hat{T}^{33} \\ &- 2\gamma^2 \beta_x \hat{T}^{10} - 2\gamma^2 \beta_y \hat{T}^{20} - 2\gamma^2 \beta_z \hat{T}^{30} \\ &+ 2\gamma^2 \beta_x \beta_y \hat{T}^{21} + 2\gamma^2 \beta_x \beta_z \hat{T}^{31} + 2\gamma^2 \beta_y \beta_z \hat{T}^{32} . \end{aligned} \tag{7.8}$$

The right hand side of Fig. 7.2 shows the time evolution of the local rest frame energy density for the same ring structure at central η_s as for the previous number density study. Similar to the number density the energy density is highest at early times with values $\epsilon \approx 5 \cdot 10^2\,\mathrm{GeV/fm}^3$ in the inner core and still $\epsilon \approx 4\,\mathrm{GeV/fm}^3$ in very peripheral regions. The outer regions of the collision zone are already at early stages frozen out. Since the energy density rapidly decreases, also the inner core of the collision reaches values $\epsilon < \epsilon_c$

---

[6] For the discussed problem again the application of cylindrical coordinates is rewarding. Using the energy-momentum tensor in cylindrical coordinates, one obtains

$$\epsilon_{\mathrm{LRF}} = \gamma^2 \hat{T}^{00} - 2\gamma^2 \beta_r \hat{T}^{0r} - 2\gamma^2 \beta_z \hat{T}^{z0} + \gamma^2 \beta_r \hat{T}^{rr} + \gamma^2 \beta_z^2 \hat{T}^{zz} + 2\gamma^2 \beta_r \beta_z \hat{T}^{zr} , \tag{7.7}$$

where $\vec{\beta} = (\beta_r, \beta_z)$ is the boost velocity in cylindrical coordinates.

after $t \approx 6\,\text{fm}$. This finding justifies the choice of simulation time $t = 10\,\text{fm}$ for the jet quenching studies presented in this work.

Debye mass m_D^2

In principle, the pQCD matrix elements of partonic processes in a hot and dense environment have to be calculated within thermal field theory. Since these formal calculations are highly demanding to implement into a transport approach, we discussed in Chapter 3 that within BAMPS we describe scattering processes of partons within the quark-gluon plasma by Debye-screened, vacuum pQCD matrix elements. The divergences emerging in the internal propagators of these matrix elements are effectively screened by a thermal mass of partons,

$$|\mathcal{M}|^2 \sim \frac{1}{\hat{t}^2} \quad \rightarrow \quad |\mathcal{M}|^2 \sim \frac{1}{\left(\hat{t} - m_D^2\right)^2} \,. \tag{7.9}$$

Consequently, the value of the Debye mass strongly affects both the softness of momentum transfers and, at the same time, the total rate of the different $2 \rightarrow 2$ and $2 \rightarrow 3$ scattering processes. Although the Debye mass is originally derived in thermal field theory, it can conceptually also calculated in non-equilibrium situations by the zeroth moment of the phase space distribution: The Debye mass screening an internal *gluon* propagator is defined as [Won96; XG05; Uph+12]

$$m_D^2 = \pi \alpha_s d_g \int \frac{\mathrm{d}^3 p}{(2\pi)^3} \frac{1}{p} \left(N_c f_g + N_f f_q\right) , \tag{7.10}$$

whereas the Debye mass of an internal *quark* propagator reads

$$m_q^2 = 4\pi \alpha_s \frac{N_c^2 - 1}{2N_c} \int \frac{\mathrm{d}^3 p}{(2\pi)^3} \frac{1}{p} \left(f_g + f_q\right) . \tag{7.11}$$

In a thermal medium that obeys an equilibrated phase space distribution $f_{\text{eq}} \sim \exp\left(-E/T\right)$, the corresponding Debye masses in equilibrium are

$$m_{D;\,\text{eq}}^2(T) = \frac{8\alpha_s}{\pi}\left(N_c + N_f\right) T^2 \tag{7.12}$$

and

$$m_{q;\,\text{eq}}^2(T) = \frac{2\alpha_s}{\pi} \frac{N_c^2 - 1}{N_c} T^2 \,. \tag{7.13}$$

Different to the previously discussed densities, the Debye mass is Lorentz invariant and hence a discussion of the reference frame in which the Debye mass is calculated is not necessary.

Figure 7.3 shows both the gluon and quark Debye mass scaled by the QCD coupling α_s for transversal rings in the central η_s slide of a central Pb + Pb collision with $\sqrt{s_{\text{NN}}} = 2.76\,\text{TeV}$ and an impact parameter $b = 3.6\,\text{fm}$. The largest Debye mass and thereby strongest screening of matrix elements can be found in the center of the collision at early times, when the densities are the highest. With progressing evolution time t the Debye masses drop from these high values $m_D^2/\alpha_s \sim \mathcal{O}(10\,\mathrm{GeV})$ to significantly lower values $m_D^2/\alpha_s \sim \mathcal{O}\left(10^{-1}\,\mathrm{GeV}\right)$ at the end of the collision. Due to the different degeneracy factors entering the Debye mass, the gluon Debye mass is approximately one magnitude larger than the gluon Debye mass over the entire medium evolution. In contrast to the enormous number densities at the beginning of the collision, the larger screening from these high Debye masses decreases the scattering rate of partons.

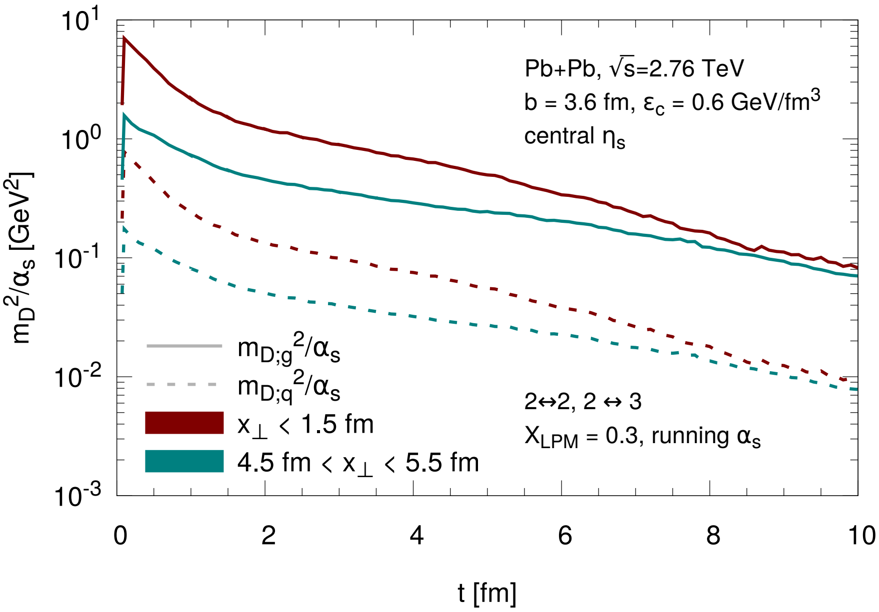

Figure 7.3: Time evolution of the gluon (solid line) and quark (dashed line) Debye mass calculated within BAMPS for a ring at mid-rapidity with radius $x_\perp < 1.5\,\mathrm{fm}$ (red) or $4.5\,\mathrm{fm} < x_\perp < 5.5\,\mathrm{fm}$ (green) within a central $\sqrt{s_{\mathrm{NN}}} = 2.76\,\mathrm{TeV}$ Pb + Pb collision. The Debye masses were scaled by the employed fixed QCD coupling $\alpha_s = 0.3$.

Effective temperature T

In contrast to hydrodynamical models, the microscopic transport of partons via the Boltzmann equation does not explicitly rely on thermal distributions in equilibrium. The microscopic interactions do not differ between a thermalized or a strongly anisotropic system. While this allows a simulation of non-equilibrated systems as the initial stages of heavy-ion collisions, special attention needs to be payed when calculating equilibrium quantities, as e.g. the temperature T, from non-equilibrated phase space distributions. Especially, in situations far from equilibrium the definition of a temperature is not unique.

In the following, we discuss different ways to define an *effective* temperature T and study differences when applied to the medium evolution in a heavy-ion collision. We have seen that various macroscopic quantities can be derived from moments of the phase space distribution $f(\vec{\mathbf{x}}, \vec{\mathbf{p}})$. The respective equilibrium values could be obtained by considering the thermal phase space distribution $f_{\mathrm{eq}} \sim \exp(-E/T)$. Combinations of these equilibrium quantities evaluated in the local rest frame are then proportional to the temperature T. Assuming that the system is close to equilibrium, one may approximate effective temperatures by inserting values for the different quantities obtained from arbitrary phase space distribution. Depending on the employed moments one can then define different effective temperatures:

- From Eq. (7.3) on page 183 and Eq. (7.5) on page 184 we find that the ratio of the number density n_{LRF} (first moment) and the energy density ϵ_{LRF} (second moment) in equilibrium yields the temperature of a thermal system,

  $$T_{\text{ideal}} = \frac{\epsilon_{\text{LRF}}}{3 n_{\text{LRF}}} \,. \tag{7.14}$$

  This is equivalent to the ideal gas law giving the mean energy per particle, $\langle E \rangle \sim N\,T$, in a medium with temperature T. The numerical values for n_{LRF} and ϵ_{LRF} can be obtained from the microscopic phase space distribution within BAMPS via Eq. (7.2) on page 183 and Eq. (7.4) on page 184.

- Another possible definition of temperature is via the equilibrium Debye mass m_D^2, hence only from the zeroth moment of the phase space distribution. With Eq. (7.12) on page 185 follows

  $$T_{m_D^2} = \sqrt{\frac{m_D^2 \pi}{8\left(N_c + N_f\right)}} \,. \tag{7.15}$$

  The numerical values for m_D^2 can be obtained from the microscopic phase space distribution within BAMPS via Eq. (7.10) on page 185.

- Similar to the previous effective temperature via the Debye mass, an effective temperature can also be defined based on the energy density ϵ_{LRF} from Eq. (7.5) on page 184, as

  $$T_{\epsilon} = \sqrt[4]{\frac{\epsilon_{\text{LRF}} \pi^2}{3\left(d_g + d_q\right)}} \,. \tag{7.16}$$

  The numerical values for ϵ_{LRF} can be obtained from the microscopic phase space distribution within BAMPS via Eq. (7.8) on page 184.

- Finally, in the appendix of Ref. [AMY02a] the definition of an effective temperature was discussed in the context of the AMY formalism in non-equilibrium situations. One can show that this definition of temperature coincides with the ratio of the number density n_{LRF} and the Debye mass m_D^2[7],

  $$T_{\text{AMY}} = \frac{\pi}{2} \frac{C_{\text{F}} n_{q;\,\text{LRF}} + C_{\text{A}} n_{g;\,\text{LRF}}}{m_D^2/\alpha_s} \,. \tag{7.17}$$

  The numerical values for n_{LRF} and m_D^2 can be obtained from the microscopic phase space distribution within BAMPS via Eq. (7.2) on page 183 and Eq. (7.10) on page 185.

Please note that the temperature is a Lorentz invariant quantity, as e.g. the Debye mass, and can therefore be evaluated in any reference frame.

---

[7] In the numerical simulations within BAMPS the effective temperature T_{AMY} is calculated via $T_{\text{AMY}} = \frac{\frac{1}{2\gamma}\left(C_{\text{F}} N_q + C_{\text{A}} N_g\right)}{C_{\text{F}} \sum_q \frac{1}{E_q} + C_{\text{A}} \sum_g \frac{1}{E_g}}$, where the factor $1/\gamma$ considers the boost in the local rest frame and the sums run over all partons in a given cell or ring.

As shown in Fig. 7.4 the different temperature definitions lead to different effective temperatures in the beginning of the collision, where the system is supposed to be far from equilibrium. Shown is the temperature profile within two rings $x_\perp < 1.5$ fm and $4.5\,\text{fm} < x_\perp < 5.5$ fm from the central η_s slice of a central Pb + Pb collisions with $\sqrt{s_{\text{NN}}} = 2.76$ TeV and $b = 3.6$ fm. At early times the medium shows a very high effective temperature $T > 1$ GeV in the inner collision region, which is approximately one magnitude larger than common predictions for the critical/crossover temperature $T_c \sim \mathcal{O}(150\,\text{MeV})$ from lattice QCD. However, we would like to note that the concept of a temperature in this early, non-equilibrated stage is highly questionable. This issue can also be seen by the different T evolutions from the different definitions of temperatures at this early time. With progressing time the system then expands and consequently cools down reaching temperatures $T < \mathcal{O}(T_c)$. Since we derived the various definitions for an effective temperature from equations for a thermal system, we expect that the different temperature definitions lead to the same temperature after the heavy-ion medium has equilibrated. An indeed, at these later times the different temperature definitions converge to the same temperatures what can be attributed to the thermalization of the medium. Interestingly, the effective temperatures calculated from the ratio of two moments, T_{ideal} and T_{AMY}, show significantly higher values for the effective temperature at early times than the temperatures from the other two definitions $T_{m_D^2}$ and T_ϵ, each employing only one moment of the phase space distribution. Furthermore, while T_{ideal} and T_{AMY} show similar values for the temperature in the inner and outer ring, $T_{m_D^2}$ and T_ϵ show lower temperatures in the outer than in the inner ring.

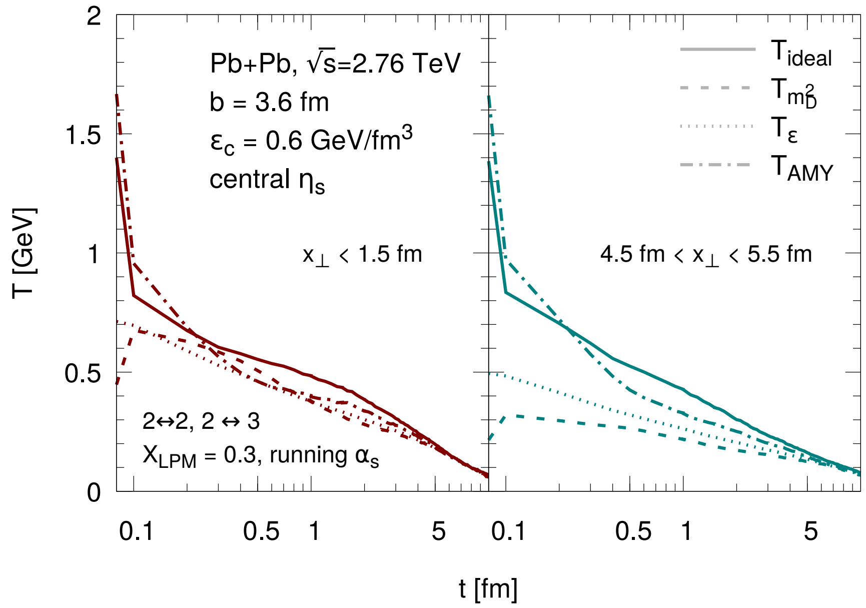

Figure 7.4: Time evolution of the effective temperature T calculated by different temperature definitions (cf. text) within BAMPS for a ring at mid-rapidity with radius $x_\perp < 1.5$ fm (left) or $4.5\,\text{fm} < x_\perp < 5.5$ fm (right) within a central $\sqrt{s_{\text{NN}}} = 2.76$ TeV Pb + Pb collision.

Finally, we would like to note that, while the interactions from leading-order pQCD do not explicitly rely on a temperature, the emission rates from the AMY formalism are calculated based on thermal field theory and therefore directly depend on the medium temperature T. Hence, the temperature presented in this section will be an input parameter for the jet quenching studies via radiative processes from the AMY formalism later in this chapter.

Chemical fugacities n/n_{eq}

After studying the thermalization of the hot and dense matter created in heavy-ion collisions at LHC, we study in the following the chemical equilibration of the partonic medium. Based on the previously discussed effective temperatures one can calculate via Eq. (7.3) on page 183, the number densities of quarks and gluons that should be found in a medium with temperature T. Relating these equilibrium values with the actual densities found in the heavy-ion collisions then defines the chemical fugacities n/n_{eq} of quark and gluons. Figure 7.5 shows these fugacities from the different T definitions for an inner ring with radius $x_\perp < 1.5\,\text{fm}$ of the central η_{s} slice of a $\sqrt{s_{\text{NN}}} = 2.76\,\text{TeV}$ Pb + Pb collision as introduced before. Due to the difficulties when defining the temperature at early times both the quark and gluon fugacities from the different definitions deviate at early times. Again, at later times the equilibrium densities converge to a comparable value. In general, one can state that the quarks are chemically under-saturated over the whole medium evolution independent from the employed temperature definition. On the other hand, gluons are chemically over-saturated in the various temperature scenarios. Due to the enormous collision energy at LHC, the initial partons from the nucleon-nucleon collisions are predominantly produced from the small-x limit in the parton distribution functions of the nucleons. In this region, gluons are produced with a significantly higher probability than quarks. Consequently, the over-saturation of gluons during the medium evolution can be attributed to the enhanced production of gluons already in the initial state of the heavy-ion collision. This chemical over-population of gluons led recently to studies investigating the potential formation of *glueballs* in the heavy-ion collisions at RHIC and LHC [Stö+15; Sto+16]. As one can find in pure Yang-Mills lattice gauge theory such matter consisting of glueballs is supposed to show a first-order phase transition.

Local flow velocity $\vec{\beta}$

As we already mentioned, the appropriate reference frame for evaluating most of the previously introduced macroscopic quantities is the local rest frame of the medium, in which flow effects of the medium vanishes. Furthermore, also the emission rates from the AMY formalism were derived in a medium at rest. Consequently, parton momenta have to be boosted to the local rest frame before applying the AMY emission rates. The local flow velocity β can be calculated within BAMPS by

$$\vec{\beta} = \frac{\sum_i \vec{\mathbf{p}}_i}{\sum_i E_i}\,, \tag{7.18}$$

where the sum runs over all parton momenta in a given volume V.

Different to the previously discussed quantities, the flow velocity $\vec{\beta}$ is obviously a vector with both magnitude and direction. Therefore, for also resolving the flow direction in non central heavy-ion collisions, we substitute the previously employed ring structure by a finer cell grid in (x, y, η_{s}) similar to the cell grid previously employed for calculating the scattering probabilities within BAMPS. Since this cell grid averages over smaller regions in configuration space, it decreases the statistics of the calculation. In order to still ensure a sufficient statistics, we therefore calculate the flow velocity based on clusters consisting

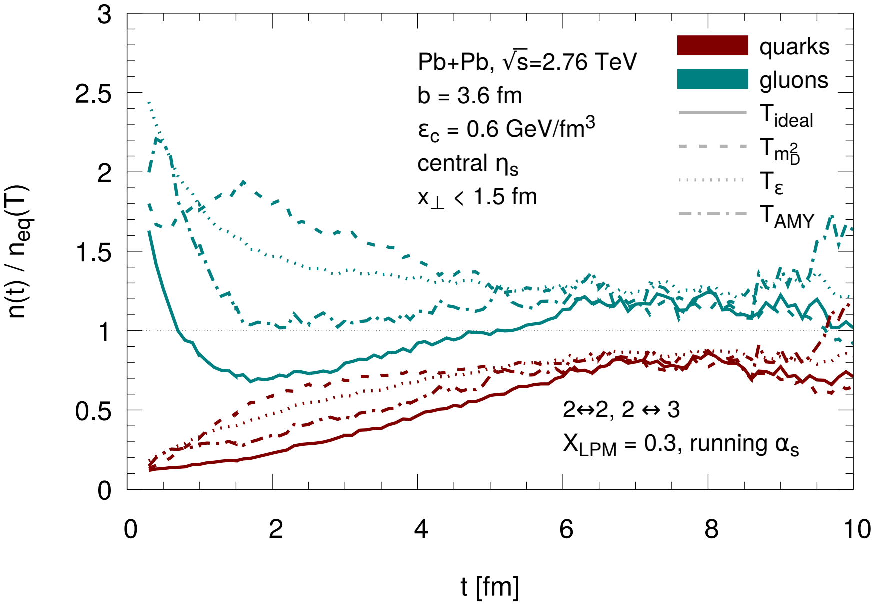

Figure 7.5: Time evolution of the fugacities n/n_{eq} of quarks (red) and gluons (green) calculated based on the different temperature definitions (cf. text) within BAMPS for a ring at mid-rapidity with radius $x_\perp < 1.5\,\mathrm{fm}$ within a central $\sqrt{s_{\mathrm{NN}}} = 2.76\,\mathrm{TeV}$ Pb + Pb collision.

of multiple neighboring cells. In other words, if a cell consists of an insufficient number of partons also the partons from the direct neighboring cells are considered for the calculation of the flow velocity within this cell. Numerical checks have shown that clusters with a minimum number of $N_{\mathrm{cell}}^{\mathrm{min}} \sim \mathcal{O}(30)$ partons show an adequate statistics to define a reliable flow velocity. To be consistent, this cell geometry is also employed later for the temperature entering the energy loss in heavy-ion collisions via radiative processes from the AMY formalism.

We present in Fig. 7.6 the local flow velocity β in the central η_s region of a central ($b = 3.6\,\mathrm{fm}$) Pb + Pb collision at LHC. While the direction of each arrow represents the direction of the flow velocity in a given cell, its color denotes the magnitude of the flow in this cell. In the beginning of the collision, parton momenta are given by the momentum distribution from PYTHIA that are distributed in the circular collision zone of the central collision. Since different nucleon-nucleon collisions are assumed to be independent from each other, also the resulting flow velocities in each cell show a random distribution with rather small flow. With progressing time, the radial pressure gradients in the medium rise, what leads to a strong radial expansion of the medium. This radial expansion is strongest in the outer region, where the medium is more dilute and hence giving the medium more freedom to expand. At late times, the medium becomes so dilute that the clusters do not satisfy the minimum number requirement and hence no reliable flow velocity can be defined anymore.

In contrast to central heavy-ion collisions, more peripheral collisions show an almond shape of the initial transversal collision zone and thereby an initial eccentricity in configuration space. Also the medium simulated within BAMPS shows this eccentricity as demonstrated in Fig. 7.7, where we present the flow velocities as before but for peripheral collisions with impact parameter $b = 10.3\,\mathrm{fm}$. Again the initial flow velocities from PYTHIA are rather small but develop with progressing time due to the increasing density gradients. The initial asymmetric eccentricity leads to a significantly stronger flow in the

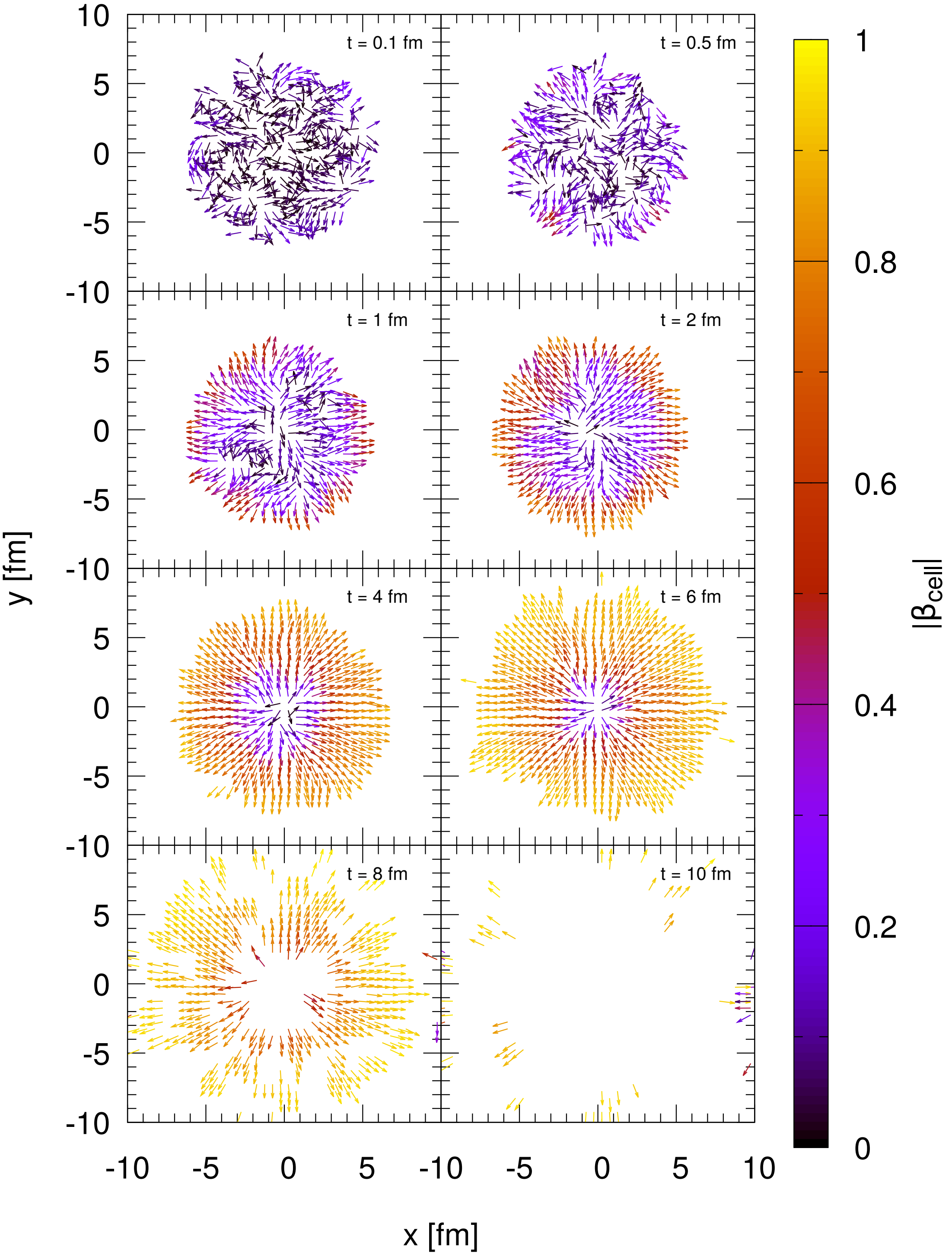

Figure 7.6: Time evolution of the local flow velocity $\vec{\beta}$ at mid-rapidity within a central $\sqrt{s_{\mathrm{NN}}} = 2.76\,\mathrm{TeV}$ Pb + Pb collision. Each arrow points into the direction of the flow velocity in a given cell (cf. text). The color of the arrow corresponds to the magnitude of the flow in this cell.

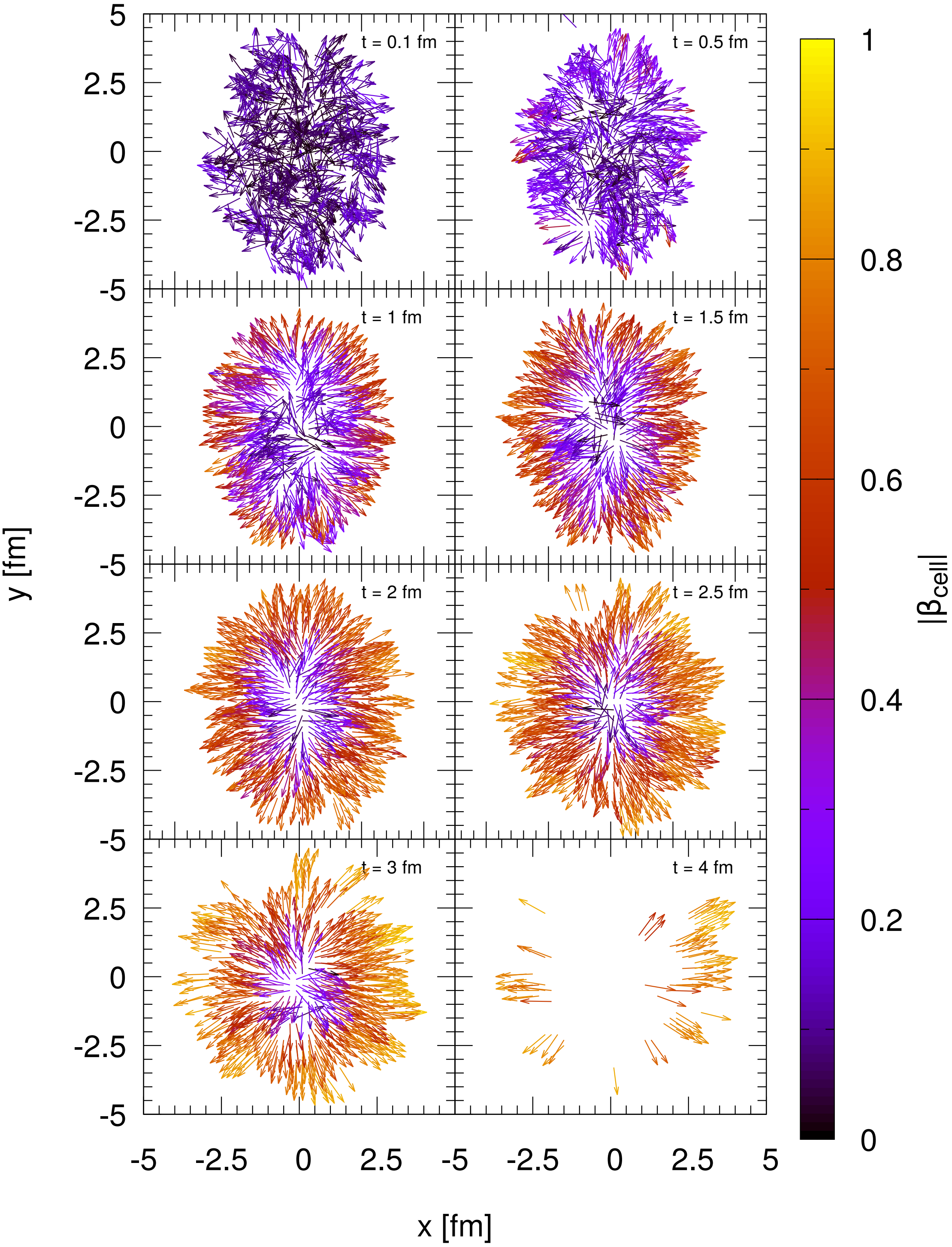

Figure 7.7: Time evolution of the local flow velocity $\vec{\beta}$ at mid-rapidity within a peripheral $\sqrt{s_{\rm NN}} = 2.76\,{\rm TeV}$ Pb + Pb collision. Each arrow points into the direction of the flow velocity in a given cell (cf. text). The color of the arrow corresponds to the magnitude of the flow in this cell.

x-direction than in the perpendicular y-direction. This is reasonable because the medium has more space to expand in this more dilute x-direction. Furthermore, again the flow velocity is higher in the outer, more dilute regions of the collision than in the denser, central region. While we presented in this section a more qualitative discussion of the flow velocity, the next section discusses the built-up of flow more quantitatively in terms of the elliptic flow v_2.

7.1.3 Elliptic flow of the background medium

As introduced in Section 2.3.1 and also demonstrated qualitatively in the previous section, the anisotropy in configuration space of the initial state in peripheral heavy-ion collisions leads to different medium expansions in the x- and y-direction transverse to the beam axis. Consequently, this anisotropic flow of the medium leads also to a transverse momentum asymmetry of the partons flying within this medium. This asymmetry in the transverse momenta p_x and p_y are supposed to be more pronounced, the stronger the interactions between partons are. In the following we present quantitative results for this momentum asymmetry by studying the elliptic flow v_2 of partons in peripheral ($b = 10.3$ fm) Pb + Pb collisions with $\sqrt{s_{\mathrm{NN}}} = 2.76$ TeV. In Section 2.3.1 we have shown that the elliptic flow v_2 is the second harmonic coefficient of a Fourier expansion of the azimuthal particle distribution $\mathrm{d}N/\mathrm{d}\phi$. One can show that this coefficient can be written on the particle level as [VZ96]

$$v_2 = \frac{p_x^2 - p_y^2}{p_\perp^2} \,, \tag{7.19}$$

where p_x and p_y are the momentum components of a parton in x- and y-direction, respectively. The angle ϕ is defined relative to the event plane, which is given by the plane spanned by the beam axis and the impact parameter. While a definition of the event plane is straight-forward in theoretical simulations, a significant part of the experimental effort in studying the elliptic flow is attributed to the precise determination of the event plane in the respective event. In order to circumvent this costly procedure, flow studies in experiments are mainly employing correlations between particles, so called *cumulants*, in order to describe the different flow coefficients v_n. As shown in Ref. [BSV10] the four-particle cumulant $v_2\{4\}$ is the cumulant closest to the theoretical description of v_2 given in Eq. (7.19).

In Ref. [Uph+15] we could demonstrate that the previously chosen parameter set for the microscopic medium interactions within BAMPS, consisting of elastic, Debye-screened $2 \to 2$ and the inelastic $2 \leftrightarrow 3$ processes obeying the θ-LPM effect with $X_{\mathrm{LPM}} = 0.3$, are responsible for a significant built-up of flow in the partonic phase of a heavy-ion collision. However, due to the confinement in QCD, experiments obviously are only able to measure the elliptic flow v_2 of hadrons. On the other hand, since the current version of BAMPS lacks a microscopic hadronization prescription, one can only calculate the flow of the medium on the partonic level within BAMPS. Therefore, one has to be cautious when comparing the partonic v_2 with the hadronic v_2 measured at LHC. One common argument to yet compare both observables is that there is no reason to expect that a phase transition, first-order or crossover, should affect the integrated flow within the medium[8]. Although this assumption clearly needs further evidence from models incorporating a (microscopic) hadronization of partons, we study in the following how the chosen microscopic interactions lead to a

---

[8] In other words: “What flows, that flows.”

finite elliptic flow in peripheral heavy-ion collisions and compare our simulation results to experimental results for $v_2\{4\}$.

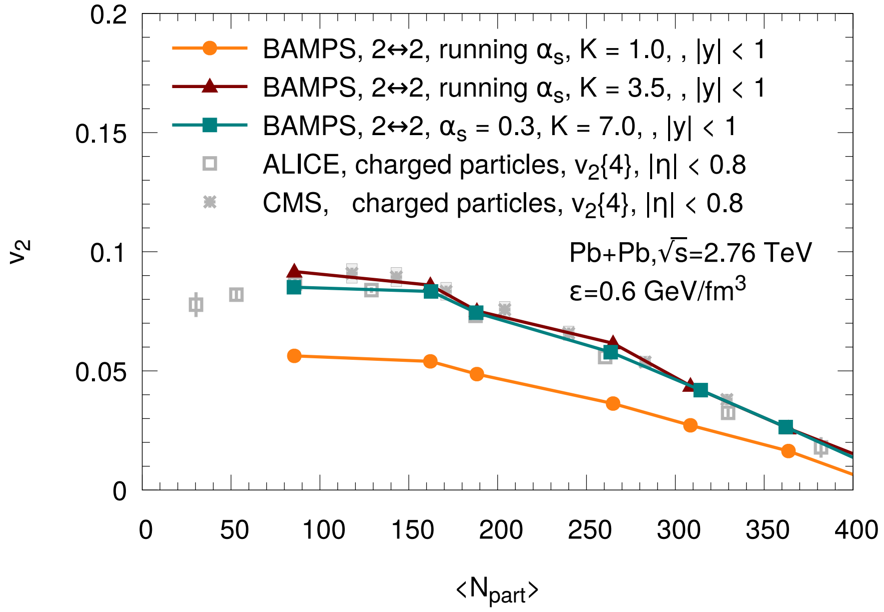

Figure 7.8: Centrality dependence of the integrated elliptic flow v_2 from only elastic $2 \to 2$ interactions within $\sqrt{s_{\mathrm{NN}}} = 2.76\,\mathrm{TeV}$ Pb + Pb collisions. While the lines denote BAMPS simulations varying crucial $2 \to 2$ parameters, the points denote experimental results measured at the LHC [CMS13a; ALI10a].

First we show in Fig. 7.8 the integrated elliptic flow v_2 depending on the collision centrality in terms of the number of participants N_{part} for BAMPS medium evolutions with only elastic $2 \to 2$ processes and neglecting any inelastic $2 \leftrightarrow 3$ processes. While employing a running coupling for the elastic scatterings, the pure elastic $2 \to 2$ interactions show a partonic elliptic flow that is approximately a factor ≈ 2 smaller than the corresponding measured elliptic flow from the experiments at LHC. Hence, medium interactions from only elastic $2 \to 2$ scatterings calculated in pQCD are not able to explain the significant elliptic flow measured at LHC. Only after scaling the $2 \to 2$ cross sections and thereby the elastic scattering rate, $\sigma_{22} \to K\sigma_{22}$, with an effective factor $K = 3.5$ the partonic v_2 from BAMPS is on the order of the experimental results. This still surprisingly high flow from purely elastic interactions is mainly caused by the interplay of the four-gluon vertex (cf. Sections 3.1 and 5.3.3) in the $2 \to 2$ matrix elements and the running of the QCD coupling at small parton energies. At these small parton energies, the $2 \to 2$ cross section of a gluon diverges due to the four-gluon vertex $|\mathcal{M}| \sim 1/\hat{s}$. At the same time, the soft momentum transfers of soft partons additionally enhance the $2 \to 2$ scattering rate via the running QCD coupling. This inclusion of the running coupling can be blamed for approximately half of the elliptic flow from $2 \to 2$ interactions as it can be seen by comparison to the v_2 from only $2 \to 2$ scatterings and a fixed QCD coupling $\alpha_s = 0.3$, which has to be scaled by $K = 7$ in order to reproduce the experimental results.

The strong elliptic flow from gluon interactions is also demonstrated in Fig. 7.9, where we compare the integrated, elliptic flow depending on N_{part} of quarks and gluons, this time from both elastic and inelastic $2 \leftrightarrow 3$ medium interactions obeying the θ-LPM approach. The screening parameter X_{LPM} entering the θ-LPM approach is given by either $X_{\mathrm{LPM}} = 1.0$ or $X_{\mathrm{LPM}} = 0.3$. While the former value effectively corresponds to pure

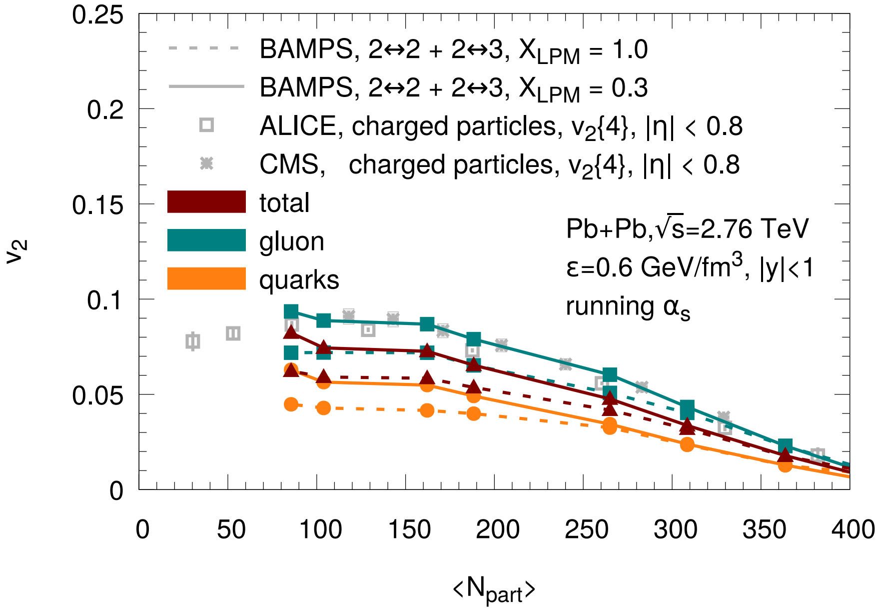

Figure 7.9: Centrality dependence of the integrated elliptic flow v_2 from elastic $2 \to 2$ and inelastic $2 \leftrightarrow 3$ interactions employing a running QCD coupling within $\sqrt{s_{\mathrm{NN}}} = 2.76\,\mathrm{TeV}$ Pb + Pb collisions. While the different colors represent the elliptic flow of different parton species, the line type compares two different choices for the screening entering the θ-LPM approach. Again, the points represent experimental results obtained at the LHC [CMS13a; ALI10a].

incoherent gluon emissions (cf. Section 5.2), the latter value agrees with the fit parameter obtained in previous studies concerning v_2 at RHIC and LHC [Uph+15]. Due to the higher QCD color factor of gluons and the mentioned enhancement from the four-gluon vertex, the integrated flow of gluons is indeed significantly larger than the flow of quarks for both choices of screening parameters. The resulting total, partonic v_2 is obtained by weighting the flavor-differential flows with the distribution of the different parton species. Due to the abundance of gluons wrt. to quarks (see the discussion about fugacities in the previous section) the total elliptic flow of partons is closer to the gluon v_2 than to the quark v_2. The inelastic $2 \leftrightarrow 3$ processes partly compensate the $K = 3.5$ factor needed in the pure elastic scenario.

As mentioned earlier, the built-up of flow strongly depends on the strength of the medium interactions. Hence the smaller screening parameter $X_{\mathrm{LPM}} = 0.3$, which screens less transverse momentum and thereby increases the $2 \leftrightarrow 3$ scattering rate, shows a stronger elliptic flow than the larger parameter $X_{\mathrm{LPM}} = 1.0$. Moreover, the choice of the screening not only affects the scattering rate but also determines how collinear gluon emissions may be. Therefore a smaller value of X_{LPM} additionally enhances the built-up of flow by emitting gluons that fly more collinear with their emitting parent partons and thereby increase the flow in this direction. However, even the significant total flow from $X_{\mathrm{LPM}} = 0.3$ shows approximately $\approx 20\,\%$ less flow than the experiments at LHC. Reasons for this deviation could be the lack of initial state fluctuations within BAMPS[9] and a potential missing after-burner from interactions in the hadronic phase of the heavy-ion

---

[9] Especially higher Fourier coefficients v_n with $n > 2$ are sensitive to these initial state fluctuations. Since these fluctuations are not considered within BAMPS at the moment, these coefficients are supposed to vanish in the current BAMPS simulations and therefore we skip these studies within the present work.

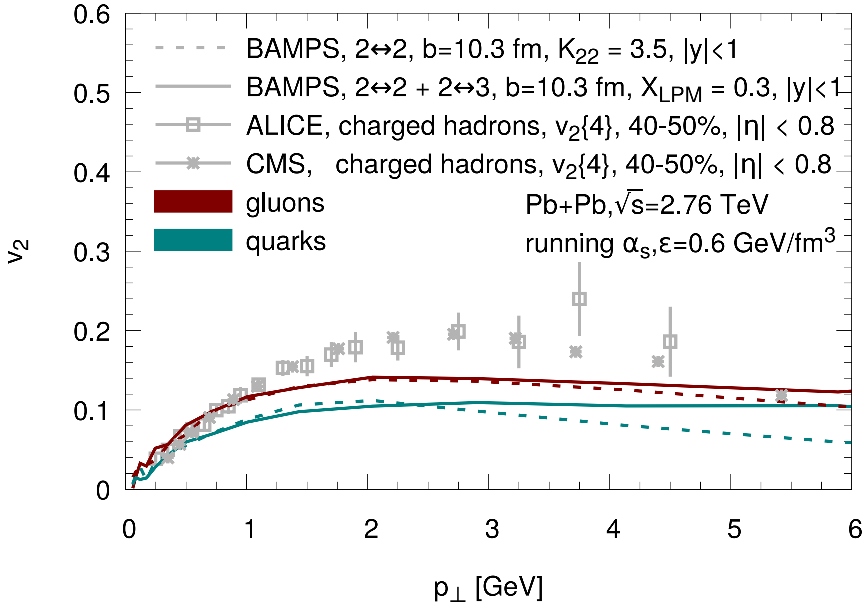

Figure 7.10: Transverse momentum $p_\perp$ dependence of the elliptic flow v_2 of quarks (red) or gluons (green) from either scaled ($K = 3.5$) elastic $2 \to 2$, or elastic $2 \to 2$ and inelastic $2 \leftrightarrow 3$ interactions employing a running QCD coupling within $\sqrt{s_{\mathrm{NN}}} = 2.76\,\mathrm{TeV}$ Pb + Pb collisions. Again, the points represent experimental results obtained at the LHC [CMS13a; ALI10a].

collision. In Ref. [AP13] it could be shown that such hadronic effects may contribute up 10–15 % to the integrated, elliptic flow.

Finally, we present in Fig. 7.10 the $p_\perp$-differential elliptic flow v_2 of quarks and gluons in the same peripheral Pb + Pb collision as above either from the scaled, purely elastic interactions or elastic and inelastic processes from the θ-LPM approach with $X_{\mathrm{LPM}} = 0.3$. The main contribution to the flow stems from partons with $p_\perp \gtrsim 2\,\mathrm{GeV}$. Again the flow of gluons is stronger than the corresponding flow of quarks. Interestingly, the flow from elastic interactions scaled with $K = 3.5$ are remarkably similar to the flow from $2 \to 2$ and $2 \leftrightarrow 3$ interactions with $X_{\mathrm{LPM}} = 0.3$ at small transverse momenta. This indicates that the amount of flow is mainly determined by the scattering rate and not the collinearity of gluon emissions. Only at higher parton $p_\perp$ the two scenarios deviate from each other since the v_2 at high $p_\perp$ is supposed to be more sensitive to the underlying energy loss of partons than bulk medium effects (cf. Section 7.3.3). In the case of the integrated elliptic flow we justified a comparison between partonic and hadronic results by the assumed invariance under a phase transition. A similar argument does not hold for the differential elliptic flow $v_2(p_\perp)$. The transverse momentum of a parton should be rather different from the corresponding hadron momentum. Since fragmentation functions as presented in Section 7.3.1 are only valid for hard parton momenta, other descriptions for the hadronization of soft partons have to be implemented within BAMPS in the future. Until then, more than a qualitative comparison of partonic flow observables within BAMPS to experimental data for the flow of hadrons should not be dared.

7.2 Combining the hard and soft regimes of a heavy-ion collision

Unfortunately the properties of the expanding quark-gluon plasma investigated in the previous section are not directly accessible in experiments: Due to the short lifetime of the medium and the confinement of partons into hadrons, only the final hadronic products of a heavy-ion collision can be measured in the detectors. As we have seen in Chapter 2, one of the most prominent observables for investigating the medium created in $\mathrm{Pb}+\mathrm{Pb}$ collisions at LHC is *jet quenching*. Therefore we extend in the following sections our studies of Chapter 6 and investigate how the previously defined different descriptions for the non-Abelian LPM effect, θ-LPM, stochastic LPM and AMY, influence the resulting energy loss in expanding, partonic matter as it is expected in ultra-relativistic heavy-ion collisions. Before presenting our numerical results for jet quenching, we outline in this section how to appropriately generate hard events consisting of either only leading partons—the partons with highest transverse momentum $p_\perp$— or whole parton showers that subsequently traverse the bulk medium introduced in Section 7.1.

One of the advantages of jet simulations within BAMPS is that the jet energy loss as well as the medium evolution of a heavy-ion collision may be simulated *microscopically* within one common framework. The jet partons scatter with medium partons via the same pQCD interactions as the medium partons scatter between each other[10]. This is different to other jet quenching calculations that determine the energy loss by a Monte-Carlo procedure embedded into a macroscopically evolving hydrodynamical background. In these approaches, the jet modification is mostly described by perturbative quantum chromodynamics, whereas the medium evolution is given by ideal/viscous hydrodynamics.

High-$p_\perp$ partons originate from initial hard partonic interactions between nucleons from the colliding nuclei. Due to momentum conservation they are, in leading order, produced in pairs that leave the initial hard partonic process back-to-back in the transverse direction. Already in $\mathrm{p}+\mathrm{p}$ collisions the production probability for these high-$p_\perp$ partons and hadrons, rapidly decreases with increasing transverse momentum $p_\perp$. Reason for this rare production is the necessary hard momentum transfers in the initial partonic interactions of two colliding nucleons, which can be described by perturbative quantum chromodynamics. Consequently, one finds also in a single heavy-ion collision, if at all, at most one high energy di-jet pair, which subsequently traverses the soft bulk medium as discussed in the previous section before reaching the detector. The measurement and simulation of these few jet events is challenging both for experiments and theory. Simulations within a 3+1D transport approach benefit from the availability of microscopic phase space information of each particle at any given time. This information allows us to record and afterwards “offline reconstruct” the bulk medium evolution of a heavy-ion collision within BAMPS. To this end, every scattering of a parton as well as the macroscopic information presented earlier are saved during the medium evolution. We then take advantage of this setup and embed *a posteriori* high energy jets into the bulk medium at the beginning of the simulation. This procedure significantly enhances the possible statistics since only events are simulated that definitely contain a high-energy parton.

---

[10] Strictly speaking, this statement only holds if the θ-LPM approach is chosen in the radiative processes of jet interactions with the medium. However, due to the higher formation times of energetic partons, coherence effects as introduced by the different LPM prescriptions should affect mostly the high momentum region of the parton distribution and could in principle be neglected in the bulk medium evolution. It remains to be seen in a future study whether this assumption is justified.

Our numerical strategy for simulating these hard events within BAMPS can be formulated as follows:

Generating high $p_\perp$ partons from initial hard processes

The jet quenching observables studied within this work can be separated into two categories: the suppression of individual parton/hadron spectra and the medium modification of whole parton showers, which are afterwards reconstructed into jets. Depending on the specific observable one may choose between two different descriptions for the initial state:

- When studying the suppression of single parton or hadron spectra, one is interested in the energy and momentum loss of only the leading parton emerging from the initial hard partonic process. Therefore it is sufficient to embed individual partons into the recorded expanding medium while neglecting any additional initial- and final-state state radiation of the partons (cf. Section 6.3.1). The momentum distribution of these single partons can be modeled based on the *mini-jet model* [KLL87; EKL89] extended to hard parton momenta. In the mini-jet model the production probability of jets is given by a folding of parton distribution functions (PDFs) with the leading-order cross sections corresponding to the *factorization theorem* in pQCD [CSS89]. The production cross section for a pair of jets can then be written as [WG91]

  $$\frac{\mathrm{d}\sigma_{\text{jet}}}{\mathrm{d}p_\perp^2\,\mathrm{d}y_1\,\mathrm{d}y_2} = \sum_{a,b} x_1 f_a\left(x_1, p_\perp^2\right) x_2 f_b\left(x_2, p_\perp^2\right) \frac{\mathrm{d}\sigma_{a\to b}}{\mathrm{d}\hat{t}}\,, \tag{7.20}$$

  where y_i and x_i denote the momentum-space rapidity and light-cone momentum fraction of parton i and $\mathrm{d}\sigma_{a\to b}/\mathrm{d}\hat{t}$ gives the differential cross section for the underlying partonic process calculated in leading-order pQCD. The sum runs over all possible parton species a and b, namely quarks and gluons. The functions $f_a\left(x_1, p_\perp^2\right)$ and $f_b\left(x_2, p_\perp^2\right)$ represent the PDFs of partons a and b within either a free proton or a nucleon (nPDF). In the following studies, we choose for the PDFs the well-established CTEQ6L parametrization [Pum+02] as provided by the LHAPDF library [Buc+15]. The initial distribution in configuration space of these parton pairs is determined by the same Glauber calculation as for the bulk medium (cf. Section 7.1.1).

  By integrating the momentum distribution one can calculate via $N_{\text{jets}}(|\vec{\mathrm{b}}|) = \sigma_{\text{jet}} T_{AB}\left(\vec{\mathrm{b}}\right)$ [Uph+12] the number of jet pairs expected in a heavy-ion collision with given impact parameter $\vec{\mathrm{b}}$, where T_{AB} is the nuclear overlap function as discussed in Appendix D. Since both the PDFs and the partonic cross section diverges for soft parton momenta, an appropriate cut in the $p_\perp$ distribution, has to be introduced. In previous studies [XG05; XGS08; FXG09] the mini-jet model was not only applied to energetic jets within BAMPS but also to the initial state of the soft bulk medium. To this end, the parton spectrum was cut at an value of $p_{\perp;0} = 2\,\text{GeV}$, while any softer parton production was effectively described by a $K = 2$ factor in Eq. (7.20). In contrast, in the present study we apply the mini-jet model only for the embedded jet events and we are therefore only interested in the hard part of the partonic spectra. Furthermore, since the nuclear modification factor R_{AA} only measures the relative suppression between an initial and a final spectrum, we may neglect the absolute normalization of the parton spectra and sample a fixed number of initial jets per event, $N_{\text{jets}} \sim \mathcal{O}\left(10^5\right)$, based on Eq. (7.20) with an arbitrary momentum cut $p_{\perp;0}$. This cut then only determines the considered $p_\perp$ range for the simulation of jets and the actual suppression is calculated by comparing the initial, arbitrary normalized parton distribution with the final parton spectra after its evolution within the expanding BAMPS medium. While this obviously prevents a quantitative comparison of the resulting spectra to experimental results, it significantly improves the statistics in the simulations up to arbitrary high transverse momenta. In the next section we introduce an appropriate method for obtaining hadronic results from the partonic spectra in order to reliably compare the spectra from BAMPS to experimental data. For more details about the simulation strategy of leading partons within an expanding BAMPS medium we refer to Refs. [FXG09; Foc11; Uph+12; Uph+15].

- Due to their enormous virtuality, the high-$p_\perp$ partons emerging from hard partonic processes of the interacting nucleons initiate vacuum splittings in order to reduce their virtuality and thereby form parton showers. For studying the subsequent medium modification of parton showers traversing expanding heavy-ion media, we insert these parton showers consisting of a leading parton *and* its surrounding parton cloud into the BAMPS bulk medium evolution. As in our previous studies from Section 6.3 regarding the energy loss of reconstructed jets in a static partonic medium, the initial vacuum splitting processes are described by PYTHIA. Therefore we initialize the momentum distribution of shower partons by partonic $\mathrm{p+p}$ events from PYTHIA that consist of *two* parton showers emerging from the two back-to-back partons of the hard partonic process. In order to enhance the statistics of these di-jet events and ensure that indeed a hard process has occurred in a given event, we choose only PYTHIA events with an initial partonic processes from QCD (i.e. forbidding e.g. QED processes[11]) that has a minimum momentum transfer $p_\perp^0$ [12]. Furthermore, this minimum $p_\perp$ allows us to specify the $p_\perp$ region studied by the reconstructed jets. The momenta of the partons initializing the hard partonic process are again distributed based on the CTEQ6L [Pum+02] parton distribution functions. As in Section 6.3 the final-state shower of the outgoing virtual partons is stopped at the typical hadronic mass scale $Q_0 = 1\,\mathrm{GeV}$, which is the default value within PYTHIA. Any subsequent hadronization within PYTHIA is switched off in order to calculate the subsequent in-medium evolution of the parton shower within BAMPS. According to our previous procedure for embedding leading partons into the bulk medium, the spatial insertion point of a parton shower is sampled by a Glauber modeling based on a Woods-Saxon density profile.

Please note, that this distinction between leading partons and parton showers in the initial state is not physical but mainly owed to the limited production probability of partons. Simulating only the leading parton of a hard event significantly improves the numerical efficiency for studies regarding R_{AA}. However, due to the initial vacuum splittings both approaches may lead to slightly different slopes both in the initial partonic spectra and thereby also the partonic R_{AA}. We have checked that the subsequent fragmentation into hadrons (cf. Section 7.3.1) effectively moderates any potential differences in the resulting R_{AA} of charged hadrons.

---

[11] This requirement corresponds to setting MSEL = 1 in PYTHIA 6.4.

[12] This requirement corresponds to setting CKIN(3) = $p_\perp^0$ in PYTHIA 6.4.

Interactions between hard jet and soft medium partons

The high-$p_\perp$ partons generated from the previously presented initial states are subsequently evolved within offline recorded BAMPS events. At each time step, these partons from the hard jet event, either only single partons or whole parton showers, interact with medium partons that are located in the same cell based on the common BAMPS scattering probabilities[13]. This embedding of hard events into a soft background medium is sometimes called *perturbative method*, since one assumes that the modification of the bulk medium due to the jets is perturbatively small. Consequently, within this setup any medium response resulting from jet energy loss is neglected. In other words, the already recorded medium evolution is not affected by the jet-medium interactions. Furthermore, also interactions between jet partons are forbidden. This ignores possible effects of collective behavior between shower particles as, e.g., Mach cone structures [Bou+14].

For studies of the leading parton suppression in terms of R_{AA}, we are only interested in the medium modification of individual hard partons. Consequently, after each interaction of a jet parton with a medium parton we decide, based on the respective momentum transfer of the scattering, which of the outgoing partons should be tagged and considered as the corresponding outgoing hard parton further evolving within the medium. This procedure corresponds to our studies of the non-eikonal parton evolution in a static medium presented in Sections 6.1 and 6.2.

In contrast, reconstructed jets are calculated based on parton showers containing hard leading partons as well as softer shower partons. As we discussed in Section 6.3 the momentum scale of these shower partons may be on the order of the soft scale of the underlying bulk medium. Hence, especially in studies regarding the medium modification of reconstructed jets, an ad-hoc discrimination between soft partons of the showers and soft partons from the underlying bulk medium becomes difficult. While the former is supposed to contribute to the reconstructed momenta of jets, any background contamination of jets by reconstructing thermal medium partons in the parton showers should be prohibited. In experiments this problem of medium momentum contaminating the reconstructed jet momenta is solved by subtracting an event-by-event averaged background medium momentum from the reconstructed jets. Due to the microscopic information provided by the BAMPS framework we are in principle able to discriminate between shower partons from the initial PYTHIA events, scattered medium partons from the underlying bulk medium, and partons from the surrounding medium that have not interacted with any parton shower (yet). Consequently, one scenario for studying jet quenching within heavy-ion collisions with BAMPS is to reconstruct jets based on only the medium-modified initial shower partons and their medium-induced gluon radiation, and neglect both the recoiled medium partons and the surrounding non-interacting bulk medium. We denote this simulation method for reconstructed jets as “no recoil” in the following studies.

However, as we discussed in Section 6.3.5 the recoiling medium partons may have obtained a significant amount of energy and momentum of the initial parton shower by scattering with shower partons. If we neglect these recoiled medium partons we assume that this momentum components instantaneously have thermalized within the bulk medium. Depending on the specific outgoing momentum of the recoiled partons, this assumption is at least questionable. Even recoiled partons scattered to larger angles from the reconstructed jet axis may be transported back to the reconstructed jets by further scatterings within the bulk medium and thereby weaken the resulting reconstructed jet energy loss. In

---

[13] In order to increase the numerical efficiency we limit the microscopic scatterings by $\hat{s} > 1.1\Lambda_{\mathrm{QCD}}$.

Ref. [Sen+15], we studied the influence of these multiple further scatterings of recoiled medium particles on the momentum imbalance A_J of the leading reconstructed jets in heavy-ion collisions. We found that after an appropriate background subtraction, at least the momentum imbalance A_J is insensitive to further scatterings of recoiled medium partons. In order to investigate the effect of recoiling medium partons on the nuclear modification factor $R_\mathrm{AA}^\mathrm{jet}$ and jet shapes observables of reconstructed jets we define a second scenario for studying reconstructed jets within BAMPS, which we call "with recoil+subtraction" method in the following. This scenario is based on similar studies regarding the energy loss of reconstructed jets in the event generator JEWEL [EZ16a] as introduced in Section 6.3.5. Opposite to the "no recoil" method we assume in this scenario that recoiled medium partons do not interact further but stream freely after their interaction with shower partons. At each shower-medium interaction we keep track of both the momentum of the medium parton before the interaction and the momentum of the parton after the interaction. The final jets are then reconstructed based on both the medium-modified shower partons *and* the recoiled medium partons. As described in Section 6.3.5 we additionally insert ultra-soft duplicates of the scattered medium partons before the respective shower-medium interaction into the jet clustering algorithm. If such a ghost particle is reconstructed within a jet, its momentum before the interaction is subtracted[14] from the final reconstructed jet since this momentum represents the contamination of jets by the bulk medium. For more details about this recoil and subsequent subtraction procedure we refer to Section 6.3.5.

Hadronization of parton spectra and reconstruction of jets

As for the bulk medium, at the moment there is no reliable microscopic description for the hadronization of high-$p_\perp$ partons. One effective way to describe the hadronization on the spectra level are fragmentation functions as introduced in Section 7.3.1. Measured in more elementary particle collision, fragmentation functions provide probabilities for hard partons to fragment into hadrons with a given momentum. These fragmentation functions are applied within this work for our results of the suppression of charged hadrons in terms of R_AA presented in Section 7.3.

On the other hand, jet clustering algorithms aim to reconstruct the initial hard parton by combining shower partons. Among the requirements for these clustering algorithm are the collinear and infrared safety (cf. Section 2.3.2). This makes algorithms, as e.g. the anti-$k_\perp$ algorithm employed in this work, robust against hadronization effects that act mostly at soft momentum scales. Consequently, we assume that reconstructed jets on the partonic and the hadronic level are similar and therefore obtain our results for the modification of reconstructed jets purely on the partonic level. Whether this assumption is justified, needs to be proven by hadronic simulations in which partonic information are available.

7.3 Suppression of inclusive hadron spectra

After we have introduced our strategy for simulating hard events within BAMPS in the previous section, we present in this section our numerical results for jet quenching in terms of the nuclear modification factor R_AA (cf. Eq. (2.7) on page 19). To this end, we introduce in Section 7.3.1 how hard parton spectra calculated within BAMPS can be reliably converted to hadronic spectra via experimentally determined fragmentation functions. These fragmented hadron spectra then allow us in Section 7.3.2 to study the

---

[14] Strictly speaking, its four-momentum is subtracted from the four-momentum of the reconstructed jet.

suppression of leading partons/hadrons in central $\sqrt{s_{\mathrm{NN}}} = 2.76\,\mathrm{TeV}$ Pb + Pb collisions and compare it with experimental data measured at the LHC. This comparison with data allows us to further clarify differences and similarities of the different LPM approaches. In order to investigate how the different path length dependences of the radiative energy loss from the different LPM approaches ends up in the final observables, we study in Section 7.3.3 both the R_{AA} in more peripheral Pb + Pb collisions and the elliptic flow v_2 at high transverse momentum $p_\perp$. In these peripheral collisions, the path length of partons flying in-plane (x-direction) and out-of-plane (y-direction) is significantly different, so that the resulting energy loss of partons is supposed to be sensitive to the in-medium path-length.

7.3.1 Fragmentation functions

For a reliable comparison of our partonic results to experimental data from LHC the parton spectra from BAMPS have to be hadronized appropriately. To this end, we employ in the following fragmentation functions previously studied within the BAMPS framework in the context of jet quenching at RHIC based on the original Gunion-Bertsch approximation. For more details about this procedure we refer to these Refs. [FXG09; Foc11].

Different to the considerations regarding the hadronization of soft partons, where effects as *recombination* [Fri+03] are supposed to be dominant, energetic partons fragment into hadrons. Although the microscopic processes of this fragmentation from partons to hadrons are not entirely understood, one can describe the fragmentation processes effectively by *fragmentation functions* (FF). The fragmentation functions $D_i^h\left(z, Q^2\right)$ give the probability for a parton with flavor i and transverse momentum $p_\perp^i$ to fragment into a hadron with species h and momentum $p_\perp^h = z p_\perp^i$. The fragmentation scale at which the fragmentation occurs is given by Q^2 and is fixed to $Q^2 = (p_{\perp;\mathrm{hadron}}/2)^2$ within this work as in previous studies for the fragmentation within BAMPS [FXG09; Foc11]. Assuming the factorization theorem from QCD, these fragmentation functions can be obtained experimentally by global fits to experimental data from more elementary particle collisions as, e.g. $\mathrm{e}^+ + \mathrm{e}^-$ or $\mathrm{p} + \mathrm{p}$ collisions and may be subsequently applied also in the context of heavy-ion collisions. For the results within this work we employ the AKK[15] parametrization [AKK08] of the fragmentation functions. We have checked that the results for R_{AA} do not depend strongly on the specific choice of FF parametrization by calculating the R_{AA} also for an other parameterization (KKP parametrization [KKP00], not shown).

Due to the fragmentation, the hadronic spectra at a given transverse momentum $p_\perp^h$ gets contributions from different partonic transverse momenta $p_\perp^i$ of different parton species i. The resulting hadronic spectrum can be obtained by folding the partonic spectra $\mathrm{d}N_i/\mathrm{d}p_\perp^2\mathrm{d}y$ from BAMPS with the fragmentation function $D_i^h\left(z, Q^2\right)$ via [Foc11]

$$\frac{\mathrm{d}N_h}{\mathrm{d}p_\perp^2\,\mathrm{d}y}(p_\perp^h) = \sum_i \int \mathrm{d}z\, D_i^h\left(z, Q^2\right) \frac{\mathrm{d}^2 N_i}{\mathrm{d}p_\perp^2\,\mathrm{d}y}(p_\perp^i) \tag{7.21}$$

$$= \sum_i \int \mathrm{d}p_\perp^i\, \frac{p_\perp^h}{\left(p_\perp^i\right)^2} D_i^h\left(p_\perp^h/p_\perp^i, Q^2\right) \frac{\mathrm{d}^2 N_i}{\mathrm{d}p_\perp^2\,\mathrm{d}y}(p_\perp^i)\,, \tag{7.22}$$

where the sum runs over the different parton species i.

Before presenting numerical results for this folding we would like to discuss the draw-

---

[15] AKK stands for the authors ALBINO, KNIEHL and KRAMER.

backs of the presented procedure of folding parton spectra with fragmentation functions. Due to the folding any microscopic information from which parton a given hadron originates is lost. A specific hadron rather obtains probabilistic contributions from different partons based on the respective fragmentation function. This leads to another issue, namely that the energy and momentum of a parton is microscopically not conserved when it is fragmented to hadrons. While it contributes with momentum fraction z to a hadron, its remaining momentum $1-z$ is not considered microscopically. To solve both issues, one could substitute the current calculation of spectra at the probabilistic level to a microscopic, effective description of the fragmentation processes. This would allow an explicit conservation of energy and moment at every fragmentation step. Since this is out of scope for the current work, we postpone this for a future study.

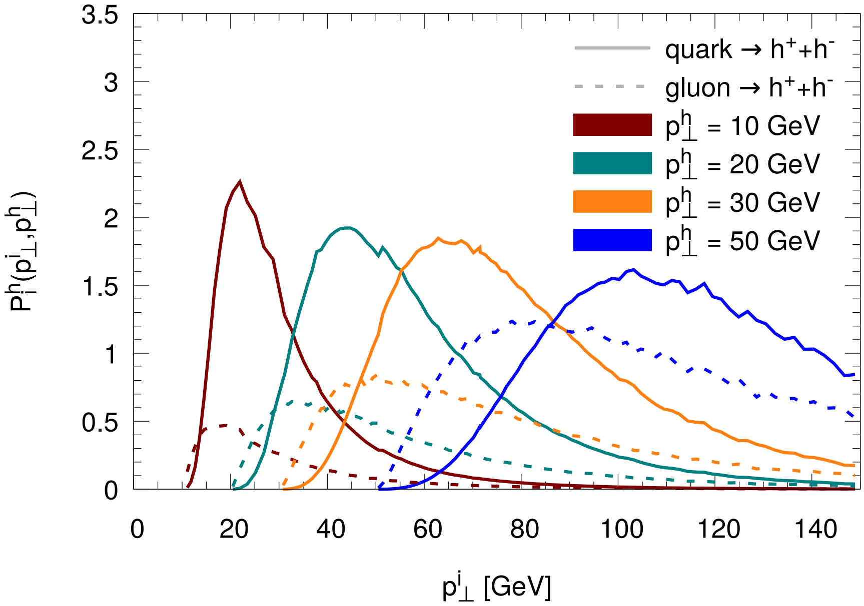

Figure 7.11: Probability for a quark (solid line) or gluon (dashed line) with transverse momentum $p_\perp^i$ to fragment into a charged hadron with transverse momentum $p_\perp^h$.

Nevertheless, in order to quantify probabilistically the origin of a hadron we show in Fig. 7.11 the probability $P_i^h(p_\perp^i; p_\perp^h)$ for a charged hadron h with transverse momentum $p_\perp^h$ to originate from either a quark or gluon with transverse momentum $p_\perp^i$. This probability can be obtained by [Foc11]

$$P_i^h(p_\perp^i; p_\perp^h) = \frac{D_i^h\left(z, Q^2\right) \frac{\mathrm{d}^2 N_i}{\mathrm{d}p_\perp^2 \mathrm{d}y}(p_\perp^i)}{\sum_i \int \mathrm{d}z\, D_i^h\left(z, Q^2\right) \frac{\mathrm{d}^2 N_i}{\mathrm{d}p_\perp^2 \mathrm{d}y}(p_\perp^i)} \,. \tag{7.23}$$

For the partonic spectra $\mathrm{d}N_i/\mathrm{d}p_\perp^2\mathrm{d}y$ in Fig. 7.11 we employ the initial state distribution of hard events from central Pb + Pb collisions with $\sqrt{s_{\mathrm{NN}}} = 2.76\,\mathrm{TeV}$ obtained by the mini-jet model of Section 7.2. The medium modification of these parton spectra is studied in the next section by calculating the nuclear modification factor R_{AA}.

As already mentioned, a final hadron gets contributions from different parton flavors and parton momenta. While a hadron with $p_\perp^h = 10\,\mathrm{GeV}$ originates from a rather narrow distribution of parton momenta peaked at $p_\perp^i \approx 2p_\perp^h$, the distribution for more energetic hadrons with $p_\perp^h = 50\,\mathrm{GeV}$ is significantly broader ranging from $p_\perp^i \approx 1.6\,p_\perp^h$ to $p_\perp^i > 3\,p_\perp^h$. Consequently, the hadronic spectrum at higher hadron momenta will be more sensitive to effects from different parton momentum regions.

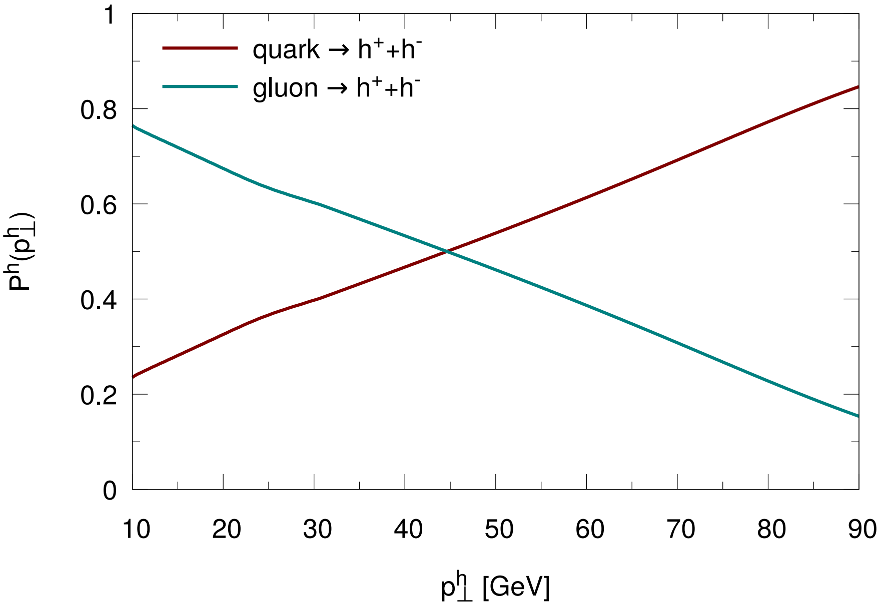

Figure 7.12: Probability for a charged hadron with transverse momentum $p_\perp^h$ to origin from either a quark (red) or a gluon (green).

Depending on the hadron momentum the contributions of quarks and gluons to the hadronic spectrum differ: while at higher hadron momentum $p_\perp^h$ the quark and gluon distribution is on the same order, hadrons with smaller momentum are predominantly originating from a gluon. This can also be seen in Fig. 7.12, where we calculate $P^h(p_\perp^h) = \int \mathrm{d}z\, P_i^h(p_\perp^i; p_\perp^h)$ in order to obtain the probability for a given hadron with momentum $p_\perp^h$ to originate from a specific parton flavor. And indeed, softer charged hadrons with $p_\perp^h \approx 10\,\mathrm{GeV}$ originate $\approx 80\,\%$ from gluons and only $\approx 20\,\%$ from quarks. On the other hand, at larger hadron momenta $p_\perp^h > 45\,\mathrm{GeV}$ the role of quarks and gluons switches and hadrons originate predominantly from quarks.

7.3.2 Suppression of hadrons in central collisions

After setting the stage in the previous sections, we present in this section the suppression of charged hadrons from the different LPM approaches in $\sqrt{s_{\mathrm{NN}}} = 2.76\,\mathrm{GeV}$ Pb + Pb collisions at LHC. This will allow us to check whether the chosen assumptions and parameters for the radiative processes of partons show indeed a realistic energy loss of energetic jets traversing the expanding hot and dense matter. Furthermore, this comparison will help us to discriminate between the different dependences of the studied LPM approaches, namely the different path length dependencies at small medium lengths and the differential distribution of transverse momenta around the jets. As we discussed in Section 7.1 the bulk medium underlying the R_{AA} results presented in this section are simulated by both elastic $2 \rightarrow 2$ and inelastic $2 \leftrightarrow 3$ interactions from the θ-LPM approach with a screening parameter $X_{\mathrm{LPM}} = 0.3$ and a microscopically running QCD coupling.

As introduced in Section 2.3.2, the nuclear modification factor R_{AA} measures the suppression of hadron spectra by comparing the $p_\perp$ spectra measured in heavy-ion collisions with the corresponding spectra in $\mathrm{p}+\mathrm{p}$ collisions scaled by the number of binary nucleon scatterings N_{coll}. Within BAMPS this ratio is obtained by comparing the initial fragmented hadron spectra based on the mini-jet model to the final hadron spectra after the simulation in BAMPS and the subsequent fragmentation.

R_{AA} from purely elastic interactions

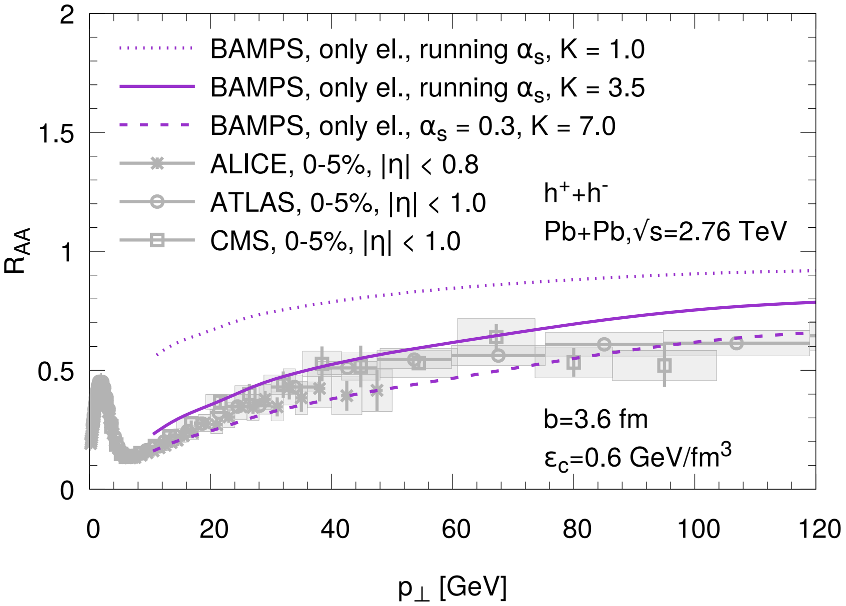

Figure 7.13: Nuclear modification factor R_{AA} of charged hadrons calculated from only elastic $2 \rightarrow 2$ interactions within central $\sqrt{s_{\mathrm{NN}}} = 2.76\,\mathrm{TeV}$ $\mathrm{Pb}+\mathrm{Pb}$ collisions together with experimental data measured by the experiments at LHC [ALI10b; CMS12e; ATL15]. The different lines represent different parameter choices for the elastic interactions.

In Fig. 7.13 we begin our study by presenting the nuclear modification factor R_{AA} calculated from only elastic interactions of partons and thereby neglecting any radiative energy loss in comparison with experimental data measured by the experiments at LHC [ALI10b; CMS12e; ATL15]. As for the elliptic flow v_2, the choice of purely elastic interactions with a running QCD coupling does not show a sufficient suppression of hadrons. Only after enhancing the interactions of partons by increasing the elastic scattering cross section by a $K = 3.5$ factor, the suppression becomes realistic. Moreover, we have seen earlier in this work that the running QCD coupling effectively leads to an increased scattering rate wrt. to a constant coupling $\alpha_s = 0.3$. Consequently, when choosing a fixed $\alpha_s = 0.3$ the K factor has to increase in order to compensate the decreased scattering rate.

R_{AA} from effective LPM approaches

We have seen in the previous discussion that elastic $2 \rightarrow 2$ scatterings (with $K = 1.0$) described by pQCD are insufficient for reproducing the experimental data for R_{AA}. Hence, we present in Fig. 7.14 results for R_{AA} including elastic $2 \rightarrow 2$ as well as the discussed radiative processes following the effective LPM approaches, θ-LPM and stochastic LPM, in comparison with experimental data for central LHC collisions. For the screening parameters of both effective LPM approaches we chose the values $X_{\mathrm{LPM}} = 0.05$ or $\xi_{\mathrm{LPM}}^{\mathrm{AMY;\,q}} = 0.01$ and $\xi_{\mathrm{LPM}}^{\mathrm{AMY;\,g}} = 0.015$ showing the best agreement with the differential energy loss $\mathrm{d}E/\mathrm{d}x$ from AMY (cf. Section 5.5.1). This will allow us later to bring the results into a broader context by comparing to the R_{AA} based on gluon emissions from AMY.

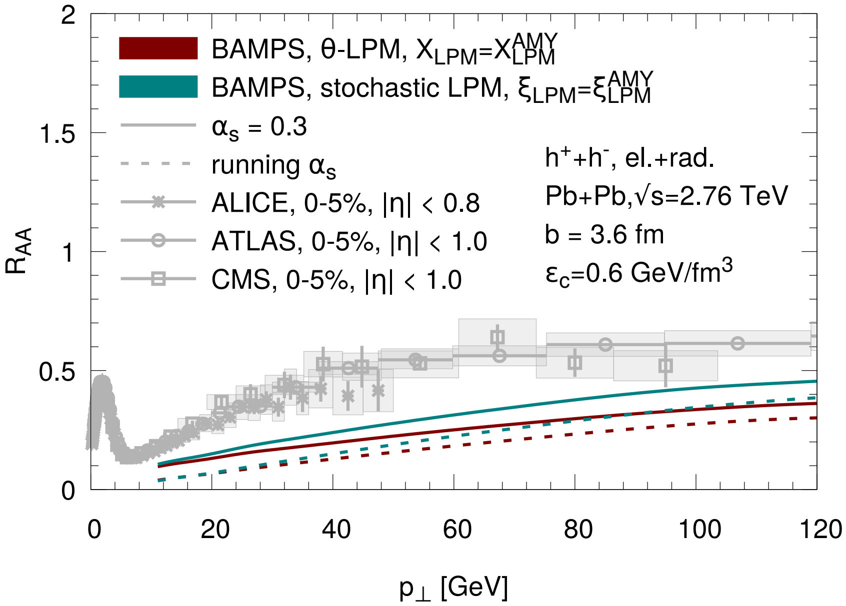

Figure 7.14: Nuclear modification factor R_{AA} of charged hadrons calculated with elastic $2 \to 2$ and radiative $2 \to 3$ interactions employing effective LPM approaches within central $\sqrt{s_{\mathrm{NN}}} = 2.76\,\mathrm{TeV}$ Pb + Pb collisions together with experimental data measured by the experiments at LHC [ALI10b; CMS12e; ATL15]. The screening parameter of both the θ-LPM (red) or stochastic LPM (green) approach is calibrated to the $\mathrm{d}E/\mathrm{d}x$ of the AMY formalism (cf. Chapter 5). The QCD coupling is either chosen by $\alpha_s = 0.3$ (solid line) or by a running α_s (dashed line). Measured data by the experiments at LHC [ALI10b; CMS12e; ATL15] is given by gray points.

The QCD coupling is either fixed to a constant value of $\alpha_s = 0.3$ or described by the running QCD coupling evaluated at the microscopic scale of the respective momentum transfers. In the constant coupling case the different LPM approaches show a similar suppression behavior: While the hadron spectra are suppressed with $R_{\mathrm{AA}} \approx 0.1$ at $p_\perp = 10\,\mathrm{GeV}$, the R_{AA} rises almost linearly with increasing $p_\perp$ up to $R_{\mathrm{AA}} \approx 0.4$ at $p_\perp = 120\,\mathrm{GeV}$. However, both LPM approaches show a significantly too strong suppression in comparison to data. This too strong suppression is even more enhanced if a running QCD coupling is considered. While the suppression at $p_\perp \approx 10\,\mathrm{GeV}$ from the θ-LPM and stochastic LPM approach are similar, at higher hadron energies effects from the finite formation time of more energetic partons enters the radiative energy loss from the stochastic LPM approach.

At least for the θ-LPM approach this result of a too strong suppression is not surprising if one considers our previous results concerning R_{AA} at RHIC and LHC, where a screening parameter $X_{\mathrm{LPM}} = 0.3$ showed the best agreement with experimental data [Uph+15]. This finding is recapitulated in Fig. 7.15, where we depict the R_{AA} of charged hadrons simulated within BAMPS via elastic and radiative processes from the θ-LPM approach for different screening parameters X_{LPM}. As shown before, the value $X_{\mathrm{LPM}} = 0.05$ obtained by fitting $\mathrm{d}E/\mathrm{d}x$ to the AMY radiative energy loss strongly overshoots the suppression measured by experiments. On the other hand, the case $X_{\text{LPM}} = 1.0$ representing gluon emissions that are purely incoherently produced (cf. Section 5.2.1) via the employed θ-function, show a too mild energy loss of partons. Only an intermediate value of $X_{\text{LPM}} = 0.3$, which effectively also incorporates some pseudo-coherent gluon emissions, shows a realistic suppression of charged hadrons. The logarithmic dependence of the radiative energy loss on the screening parameter X_{LPM} found in Section 5.2.2 is also identifiable in the R_{AA}: While increasing X_{LPM} by a factor of $10/3$ from $X_{\text{LPM}} = 0.3$ to $X_{\text{LPM}} = 1.0$ leads to a $\approx 50\,\%$ weaker suppression at $p_\perp \approx 60\,\text{GeV}$, at the same $p_\perp$ decreasing X_{LPM} by a factor of 6 (from $X_{\text{LPM}} = 0.3$ to $X_{\text{LPM}} = 0.05$) leads also to only a $\approx 60\,\%$ stronger suppression of charged hadrons. In other words, the nuclear modification factor is less sensitive to X_{LPM} at smaller values than for larger values of the screening parameter.

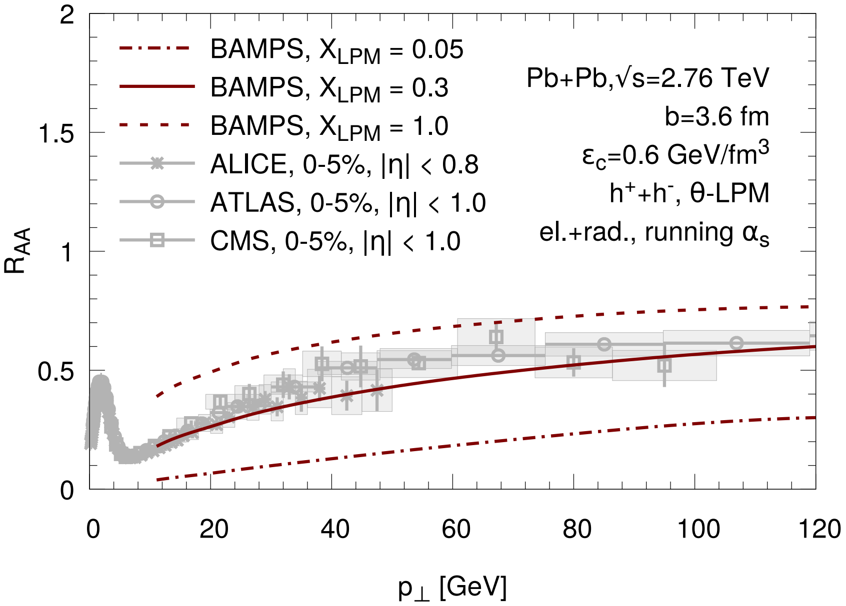

Figure 7.15: Nuclear modification factor R_{AA} of charged hadrons within central $\sqrt{s_{\text{NN}}} = 2.76\,\text{TeV}$ Pb + Pb collisions calculated with elastic $2 \to 2$ and radiative $2 \to 3$ interactions employing the θ-LPM approach with different values of screening parameter X_{LPM}. The QCD coupling is chosen as microscopically running. Measured data by the experiments at LHC [ALI10b; CMS12e; ATL15] is given by gray points.

As for the θ-LPM approach, the screening parameter ξ_{LPM} of the stochastic LPM can be fitted by a comparison to experimental data. Figure 7.16 shows the suppression of charged hadrons calculated within BAMPS while employing the stochastic LPM approach with different values of ξ_{LPM}. Since we are anyhow fitting to experimental data and to simplify things, we choose the same screening parameter for both quark and gluon projectiles. The best agreement with data can be found for $\xi_{\text{LPM}} = 0.05$. Due to the found logarithmic dependence of the radiative energy loss on ξ_{LPM} a stronger screening $\xi_{\text{LPM}} > 0.05$ leads to less suppression, whereas a smaller value $\xi_{\text{LPM}} < 0.05$, as we have seen previously, leads to a too strong suppression of charged hadrons.

Since at the moment there is no physical argument for a specific choice of screening parameter, we fix these values obtained for $X_{\text{LPM}} = 0.3$ and $\xi_{\text{LPM}} = 0.05$ within the remaining work. After introducing the suppression from the AMY formalism in the next section, we then calculate other jet quenching observables based on these set interactions in order to find potential differences between the LPM approaches.

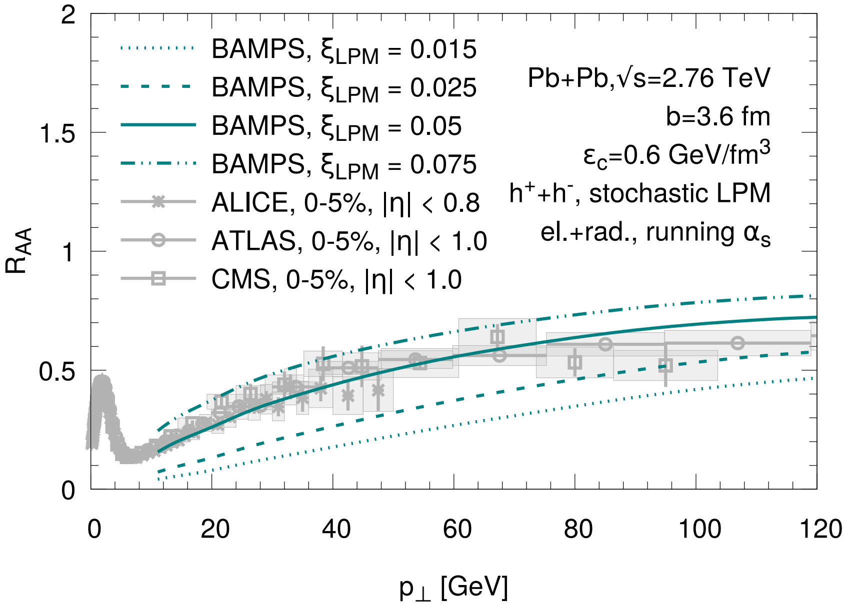

Figure 7.16: Nuclear modification factor R_{AA} of charged hadrons within central $\sqrt{s_{\mathrm{NN}}} = 2.76\,\mathrm{TeV}$ Pb + Pb collisions calculated with elastic $2 \to 2$ and radiative $2 \to 3$ interactions employing the stochastic LPM approach with different values of screening parameter ξ_{LPM}. The QCD coupling is chosen as microscopically running. Measured data by the experiments at LHC [ALI10b; CMS12e; ATL15] is given by gray points.

R_{AA} from the AMY formalism

Both effective LPM approaches are defined completely by microscopic Bremsstrahlung processes that do not rely on thermalized parton distributions. In contrast, the emissions rates from the AMY formalism are calculated in a static, thermal medium. Hence, the temperature T is the quantity defining the radiative processes within the medium and thereby the coupling between jets and the background. Furthermore, while the microscopic interactions via elastic scatterings and both effective approaches are evaluated in the center-of-momentum frame of the scattering partons, such a frame obviously does not exist in a $1 \leftrightarrow 2$ process from AMY. Here it is rather the local rest frame of the cell to which the respective parton belongs. This frame can be obtained by boosting the partons of each cell with the corresponding β as presented in Section 7.1.2. By boosting the partons one explicitly considers the local flow of the bulk medium and ensures a correct application of the AMY rates in the expanding medium.

As we have discussed in Section 7.1.2, especially during the early stages of the heavy-ion collision an unique definition of temperature is out of reach. Therefore we calculate the following results based on two different temperature definitions, namely the effective temperature T_{AMY} from the AMY formalism (cf. Eq. (7.17) on page 187) and the temperature calculated via the energy density T_{ϵ} (cf. Eq. (7.16) on page 187).

In Fig. 7.17 we present our results for the suppression of charged hadrons within BAMPS from elastic and radiative processes given by the AMY emission rates. And indeed the different temperature definitions lead to different suppressions of charged hadrons. While both temperature definitions show almost the same $p_{\perp}$ behavior, the definition via only the second moment of the phase space distribution, namely T_{ϵ}, leads to $\approx 50\,\%$ less suppression at $p_{\perp} = 100\,\mathrm{GeV}$ than the temperature definition by AMY. This result agrees with our previous calculation for the temperature evolution within the medium in Fig. 7.4. We found that during almost the whole medium evolution T_{AMY} shows higher temperature values than the T_ϵ definition. Especially during the strongly non-equilibrated phase at very early times $t < 0.2\,\text{fm}$, the difference between both definitions is almost a factor of ≈ 2. The much higher temperatures in the T_{AMY} scenario then inevitably lead to an increased energy loss and thereby a stronger suppression of charged hadrons.

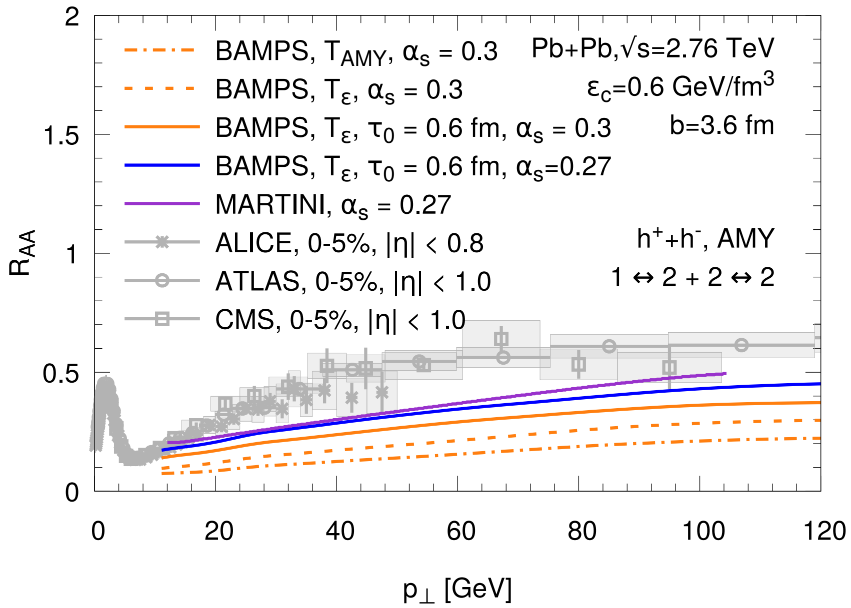

Figure 7.17: Nuclear modification factor R_{AA} of charged hadrons within central $\sqrt{s_{\text{NN}}} = 2.76\,\text{TeV}$ Pb + Pb collisions calculated with elastic $2 \to 2$ and radiative $2 \to 3$ interactions employing the $1 \leftrightarrow 2$ processes from AMY. For the calculation of the thermal AMY emission rate the different temperature definitions from Section 7.1.2 are applied. Furthermore, the R_{AA} calculated within the MARTINI [You+13; Par+16] is shown employing the AMY radiative energy loss within a hydrodynamical background. The QCD coupling is chosen by a fixed α_s. Measured data by the experiments at LHC [ALI10b; CMS12e; ATL15] is given by gray points.

Furthermore, we show in Fig. 7.17 again experimental data from the experiments at the LHC. Both temperature definitions significantly overestimate the suppression of charged hadrons. Also the shape of R_{AA} is flatter in the simulations, whereas the experimental data strongly rises in the intermediate $p_\perp = 10\text{–}50\,\text{GeV}$ region. For a further check, we compare our numerical results to calculations from the Monte-Carlo model MARTINI [SGJ09; You+13; Par+16] (cf. Section 5.1.1). Although MARTINI employs the AMY emissions rates for jets embedded within the 3+1D viscous hydrodynamic framework MUSIC [SJG11; STV12a; GJS13; STV12c], we expect that both approaches are supposed to show similarities. However, without any further modification the results from BAMPS show a $\approx 40\,\%$ stronger suppression than MARTINI. One main reason for this difference is the initial non-equilibrium phase of the heavy-ion collision. Since MARTINI relies on hydrodynamics, it is only applicable after some thermalization time τ_0. Hence, while the AMY energy loss within MARTINI does not start before $\tau_0 = 0.6\,\text{fm}$, partons within BAMPS may radiate already at these early times. These emissions at the early high temperatures significantly contribute to the energy loss within BAMPS. If also partons within BAMPS are only allowed to radiate after $\tau_0 = 0.6\,\text{fm}$, as shown in Fig. 7.17, this increases the R_{AA} by

$\approx$ 15–20 %. Furthermore, the results within MARTINI were obtained for a fixed coupling $\alpha_s = 0.27$. If we also choose this smaller value for the QCD coupling, the results of both BAMPS with AMY interactions and MARTINI are comparable. This again demonstrates the applicability of the chosen approach for incorporating the AMY emission rates in the partonic transport approach BAMPS. However, both results slightly overestimate the suppression measured by the experiments. At the same time the $p_\perp$ dependence seems to be too flat in comparison with data, where a non-linear rise of R_{AA} for increasing $p_\perp$ is found. In Refs. [Par15; Par+16] Park et al. could demonstrate that main reasons for this discrepancy between MARTINI and experiments can be attributed to the running of the QCD coupling and finite size effects, or in other words finite formation times of gluons. Different to our microscopic evaluation of the running coupling for the effective LPM approaches, $\alpha_s\left(Q^2\right)$ is calculated within MARTINI based on the transverse momentum a gluon may accumulate during its formation time. It remains to be seen in a future study, whether the incorporation of both effects into the AMY interactions within BAMPS can also lead to a more realistic suppression of hadrons.

Comparison of R_{AA} from different LPM approaches

After presenting in the previous section the suppression of charged hadrons within the different LPM approaches we compare within this section the approaches and aim to identify possible similarities and differences. To this end, we shows results from the effective LPM approaches, θ-LPM and stochastic LPM, with screening parameters fixed in the previous section and the R_{AA} from AMY calculated based on the more realistic temperature definition T_ϵ via the energy density. The partons may radiate within the AMY scenario only after $\tau_0 = 0.6\,\mathrm{fm}$, whereas in both effective approaches the partons may radiate also at earlier times. Furthermore, while the results for the effective LPM approaches incorporate the running of the QCD coupling, the results for the AMY rates are given by a constant coupling $\alpha_s = 0.3$.

In Fig. 7.18 we recapitulate our results from the previous section by quantitatively comparing the different LPM approaches side by side and to the experimental data. The AMY emission rates lead to the strongest suppression that is approximately 50 % stronger than both effective approaches in the studied $p_\perp$ range. Furthermore, the shape from AMY is significantly flatter than both other approaches, what can be attributed to the missing decreased interaction rates of emissions at higher parton energies due to the running QCD coupling.

Both effective LPM approaches are comparable to the experimental data at intermediate $p_\perp = 20$–$40\,\mathrm{GeV}$. However, at higher $p_\perp$ the stochastic LPM shows $\approx$ 15 % less suppression than the θ-LPM approach. This different behavior originates from the LPM effect dominating the radiative energy loss at high $p_\perp$. While the stochastic LPM explicitly considers a finite formation time of gluon emissions that especially at high $p_\perp$ decreases the emission rate and thereby weakens the suppression, the θ-LPM only suppresses the gluon emissions via the theta function.

The presented results for the suppression of charged hadrons within BAMPS originate from the energy loss at the partonic level. Hence, we compare in Fig. 7.19 the underlying partonic R_{AA} results from the different LPM approaches. We found previously that the radiative energy loss of quarks and gluons is similar in the θ-LPM approach due to the employed different mean free paths of quarks and gluons in the radiative matrix elements. On the other hand, in the stochastic LPM and AMY approaches we demonstrated that the difference between the quark and gluon radiative energy loss is close to the ratio 9/4

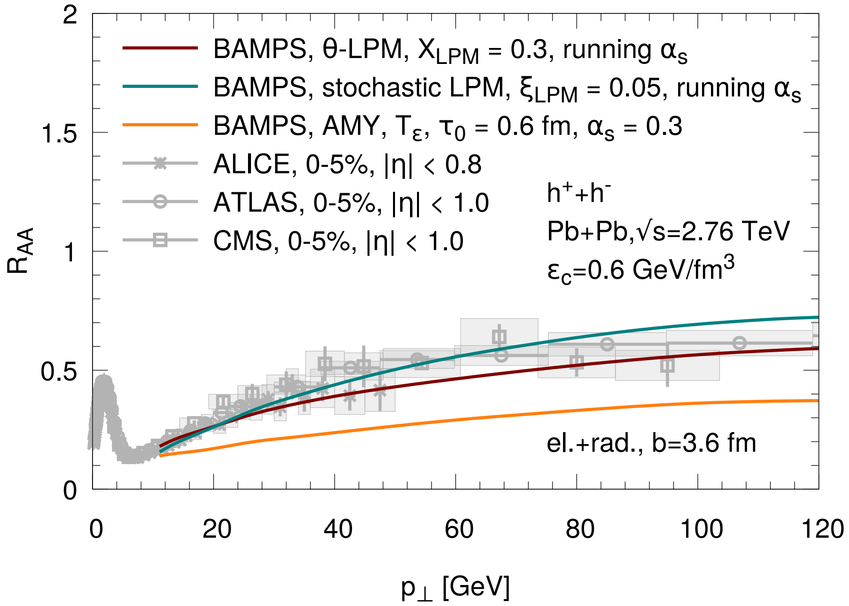

Figure 7.18: Comparison of the nuclear modification factor R_{AA} of charged hadrons within central $\sqrt{s_{\mathrm{NN}}} = 2.76\,\mathrm{TeV}$ Pb + Pb collisions calculated with elastic $2 \to 2$ and radiative $2 \to 3$ interactions employing the different LPM approaches. The values of the screening parameter underlying the effective LPM approaches are fixed to $X_{\mathrm{LPM}} = 0.3$ and $\xi_{\mathrm{LPM}} = 0.05$ representing the best agreement with experimental data [ALI10b; CMS12e; ATL15].

between the QCD color factors of gluons ($C_{\mathrm{A}} = 3$) and quarks ($C_{\mathrm{F}} = 4/3$). This increased energy loss of gluon projectiles wrt. to quark projectiles can also be found in the stronger suppression of gluons than quarks in Fig. 7.19. Interestingly, the interplay between the different initial spectra of quarks and gluons and the elastic and radiative energy loss within the θ-LPM approach also leads to a significantly stronger suppression of gluons wrt. quarks. Furthermore, while the running QCD coupling leads to the already discussed rise of R_{AA} with increasing $p_\perp$, the AMY approach with a constant QCD coupling leads to an almost flat partonic suppression.

After applying fragmentation functions, the three LPM approaches show almost the same suppression behavior: At high transverse momentum $p_\perp \gtrsim 60$–$80\,\mathrm{GeV}$ the hadron R_{AA} resembles the quark R_{AA}, whereas at softer transverse momentum the hadron suppression tends to the suppression of gluons. Reason for this effect is the applied choice of fragmentation function as we shown in Fig. 7.11. Interestingly, although the radiative energy loss from the AMY formalism leads to an almost flat partonic R_{AA}, the different contributions of quarks and gluon via the fragmentation function lead to a slight rise of the hadron R_{AA}. This rise is even more enhanced in the case of the effective LPM approaches, where additionally the running QCD coupling is considered.

Finally, we take advantage of the employed fragmentation function and present in Fig. 7.20 the suppression of different hadron species from the three LPM approaches together with data from the ALICE collaboration [ALI12c]. In all three LPM approaches the suppression of pions, kaons and protons is similar and resembles the suppression of the previously presented results for the inclusive charged hadrons. Since the interactions within BAMPS are not sensitive to the specific parton flavor, any difference between the energy loss of the different hadron species would originate from the interplay of the initial flavor distribution from the mini-jet model and the applied fragmentation functions. Our

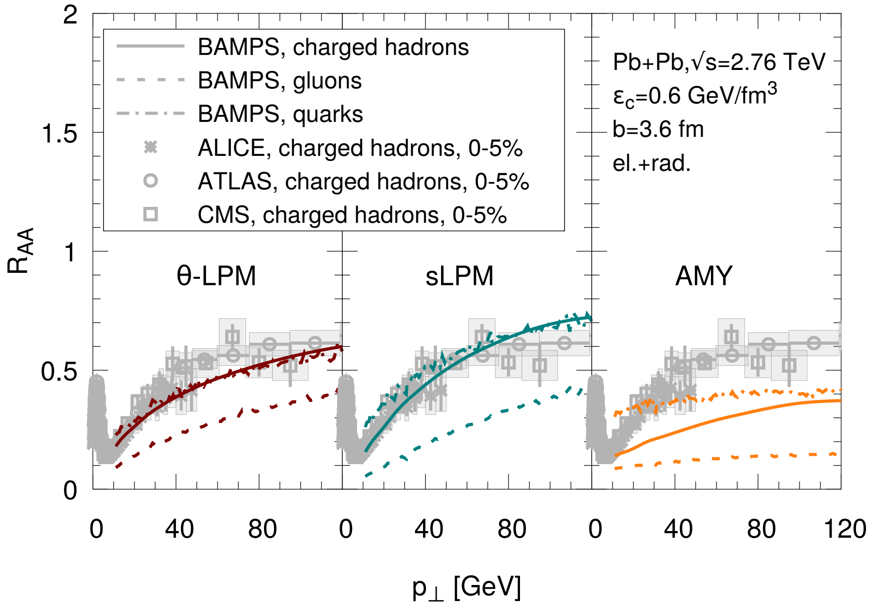

Figure 7.19: Comparison of the nuclear modification factor R_{AA} of different parton species and charged hadrons within central $\sqrt{s_{\mathrm{NN}}} = 2.76\,\mathrm{TeV}$ Pb + Pb collisions calculated with elastic $2 \to 2$ and radiative $2 \to 3$ interactions in the different LPM approaches. Same values of the screening parameter underlying the effective LPM approaches as in Fig. 7.18. Measured data by the experiments at LHC [ALI10b; CMS12e; ATL15] is given by gray points.

result agrees with the experimental data where also no difference in the suppression of the different hadron species at high transverse momentum was found. This demonstrates that the suppression at high transverse momentum is neither caused by a mass ordering of hadrons nor by differences in the fragmentation of mesons and baryons [ALI12c].

7.3.3 Measuring the path-length dependence in peripheral collisions

One characteristic feature of the energy loss, we are interested to study within this work, is the path-length dependence. As we have seen earlier, due to the finite formation of gluon emissions the radiative energy loss from the stochastic LPM approach differs from both other LPM approaches by its $\sim L^2$ path-length dependence in thin media. Since different centralities represent different medium sizes and geometries, different path-length dependences are supposed to be identifiable by comparing the suppression in central with more peripheral collisions. Within this section we aim to investigate the path-length dependence by studying the suppression of charged hadrons in more peripheral collisions and the elliptic flow v_2 at high transverse momentum.

Before presenting the results for the radiative processes from the different LPM approaches within BAMPS, we show in Fig. 7.21 the R_{AA} for $\sqrt{s_{\mathrm{NN}}} = 2.76\,\mathrm{TeV}$ Pb + Pb collisions with different centralities from only elastic $2 \to 2$ scatterings scaled by $K = 3.5$, which we found reproducing the R_{AA} of central LHC collisions. The elastic interactions within BAMPS have no length dependence, hence the resulting differential energy loss ΔE depends linearly, $\Delta E \sim L$, on the medium length L. The R_{AA} data for the different centralities are similar with a trend to less suppression at higher $p_\perp$ in more peripheral collisions. In spite of the linear path-length dependence, the scaled $2 \to 2$ interactions within BAMPS, after they are calibrated to the suppression in central collisions, also reproduce the

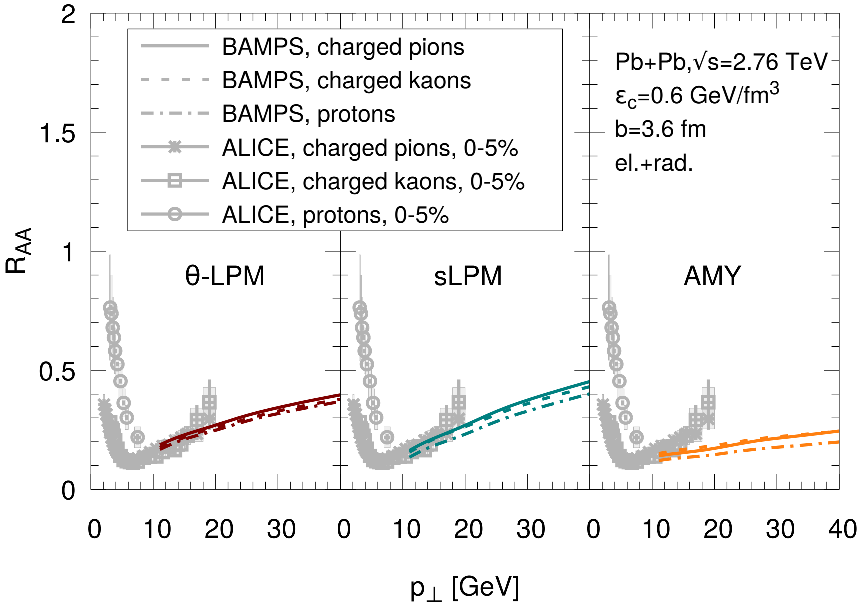

Figure 7.20: Comparison of the nuclear modification factor R_{AA} of different hadron species within central $\sqrt{s_{\mathrm{NN}}} = 2.76\,\mathrm{TeV}$ Pb + Pb collisions calculated with elastic $2 \to 2$ and radiative $2 \to 3$ interactions in the different LPM approaches. Same values of the screening parameter underlying the effective LPM approaches as in Fig. 7.18. Measured data for the different hadron species by the ALICE collaboration [ALI12c] is given by gray points.

suppression in more peripheral collisions. Obviously, the different suppression in collisions with different centralities neither depends on the emitted gluons from radiative processes nor on a $\Delta E \sim L^2$ dependence predicted for the non-Abelian LPM effect but can be described by purely (scaled) elastic scatterings. Consequently, the centrality dependence of charged hadron suppression is completely determined by the choice of Debye-screened $2 \to 2$ scatterings with a microscopically evaluated running QCD coupling.

One reason for the necessary scaling factor $K = 3.5$ in the elastic scenario could again be the lack of radiative processes. In Fig. 7.22 we compare the R_{AA} from elastic scatterings ($K = 1$) and radiative processes described by the different LPM approaches for different centralities. Although the suppression in the AMY formalism decreases for more peripheral collisions, the overall trend of a too strong suppression in the AMY formalism is confirmed also in more peripheral collisions. Again, the inclusion of finite size effects (cf. calculation by Caron-Huot and Gale in Ref.Section 5.5.1) could further decrease the suppression by the AMY rates. On the other hand, both effective LPM approaches showed a better agreement in central collisions. With decreasing centrality, both approaches show less suppression. However, at peripheral collisions also these two approaches show a stronger suppression than the data. Since the stochastic LPM approach showed already less suppression in central collision, the agreement of the stochastic LPM seems to be slightly better than the suppression from the θ-LPM approach.

Another observable that is supposed to be sensitive to the path-length dependence of energy loss is the momentum asymmetry $v_2 = (p_x^2 - p_y^2)/p_\perp^2$ at high transverse momentum $p_\perp$. While, at softer momentum, v_2 represents the asymmetric flow of bulk medium partons originating from the initial eccentricity (cf. Sections 2.3.1 and 7.1.3), the v_2 for hard particles may originate from the different path lengths in the almond shaped collisions zones of peripheral collisions. In these collisions partons flying in the out-of-plane direction

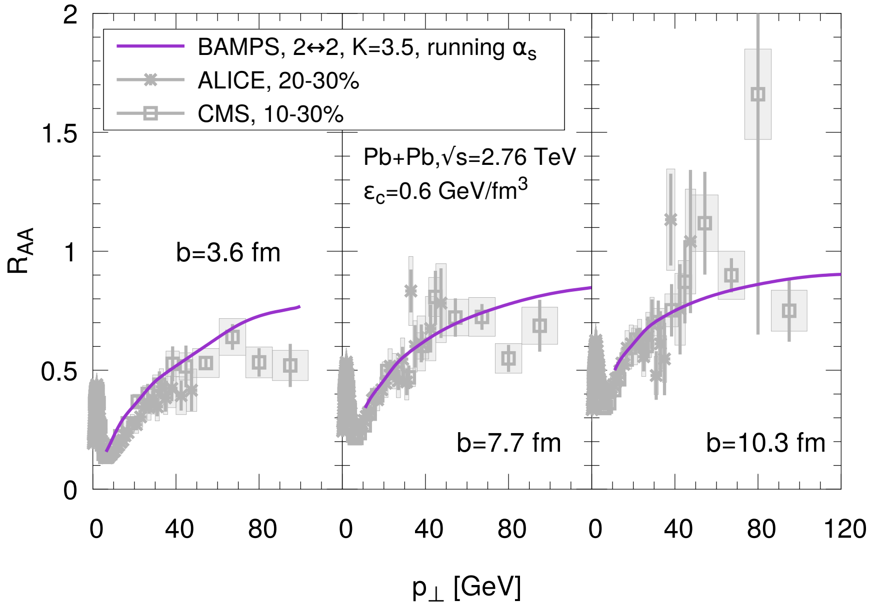

Figure 7.21: Centrality dependence of the nuclear modification factor R_{AA} of charged hadrons within $\sqrt{s_{\mathrm{NN}}} = 2.76\,\mathrm{TeV}$ Pb + Pb collisions calculated with only scaled ($K = 3.5$) elastic $2 \to 2$ interactions. The QCD coupling is described by a running α_s. Measured data by the experiments at LHC [ALI10b; ALI12b; CMS12e] is given by gray points.

(in our notation the y-direction) have on average a longer in-medium path length than partons flying perpendicular in the in-plane direction (in our notation the x-direction). Parametric studies [BGT11; BG14] have shown in a simplified scenario that a quadratical path-length dependence of energy loss can successfully describe the finite v_2 at high $p_\perp$.

Again, the experimental data for v_2 at high transverse momentum can only be measured for colorless hadrons. Consequently, we apply fragmentation functions to our partonic results similar to our considerations for the fragmentation of parton spectra into hadronic spectra from Section 7.3.1. For the hadronic v_2 at a given $p_\perp$ it follows [Foc11]

$$v_2\left(p_\perp^h\right) = \frac{\sum_i \int \mathrm{d}z\, D_i^h\left(z, Q^2\right) \frac{\mathrm{d}^2 N_i}{\mathrm{d}p_\perp^2 \mathrm{d}y}\left(p_\perp^i\right) v_2\left(p_\perp^i\right)}{\sum_i \int \mathrm{d}z\, D_i^h\left(z, Q^2\right) \frac{\mathrm{d}^2 N_i}{\mathrm{d}p_\perp^2 \mathrm{d}y}\left(p_\perp^i\right)}\,, \tag{7.24}$$

where we used the quantities defined in Section 7.3.1.

We present in Fig. 7.23 our result for the momentum asymmetry v_2 at high $p_\perp$ from the different LPM approaches for peripheral ($b = 10.3\,\mathrm{fm}$) Pb + Pb collisions together with data measured by experiments at the LHC. Furthermore, we again depict as a baseline the v_2 from the scaled ($K = 3.5$), purely elastic $2 \to 2$ scatterings. Both the data and our simulations show a finite v_2 for energetic hadrons with momenta $p_\perp > 10\,\mathrm{GeV}$. The interactions from the θ-LPM approach and the scaled purely elastic interactions show the smallest momentum asymmetry with an almost flat $p_\perp$ dependence in the studied $p_\perp$ range. On the other hand, the finite formation time of gluon emissions in the stochastic LPM approach leads to a slight increase of v_2 with decreasing $p_\perp$. The strongest momentum asymmetry can be found in the results based on the AMY emission rates. Due to the collinear gluon emissions within AMY the direction of emitted gluons is the same as the direction of the parent parton. At the same time, the emission rates within AMY explicitly

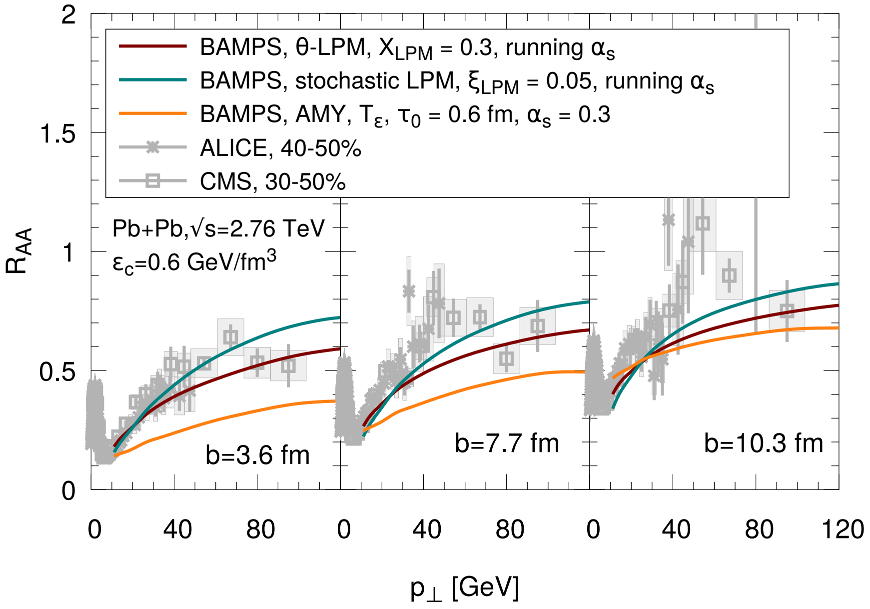

Figure 7.22: Centrality dependence of the nuclear modification factor R_{AA} of charged hadrons within $\sqrt{s_{\mathrm{NN}}} = 2.76\,\mathrm{TeV}$ Pb + Pb collisions calculated with elastic $2 \to 2$ and radiative $2 \to 3$ interactions employing the different LPM approaches. The values of the screening parameter underlying the effective LPM approaches are fixed to $X_{\mathrm{LPM}} = 0.3$ and $\xi_{\mathrm{LPM}} = 0.05$ representing the best agreement with experimental data for R_{AA} in central collisions. The QCD coupling is either described by a running α_s or $\alpha_s = 0.3$. Measured data by the experiments at LHC [ALI10b; ALI12b; CMS12e] is given by gray points.

depend on the local flow of partons, which is different in the x- and y-direction. Both effects together lead to an enhancement of the transverse momentum asymmetry in the AMY formalism. However, all different LPM approaches within BAMPS underestimate the asymmetry in the intermediate $p_\perp = 10$–$30\,\mathrm{GeV}$ region.

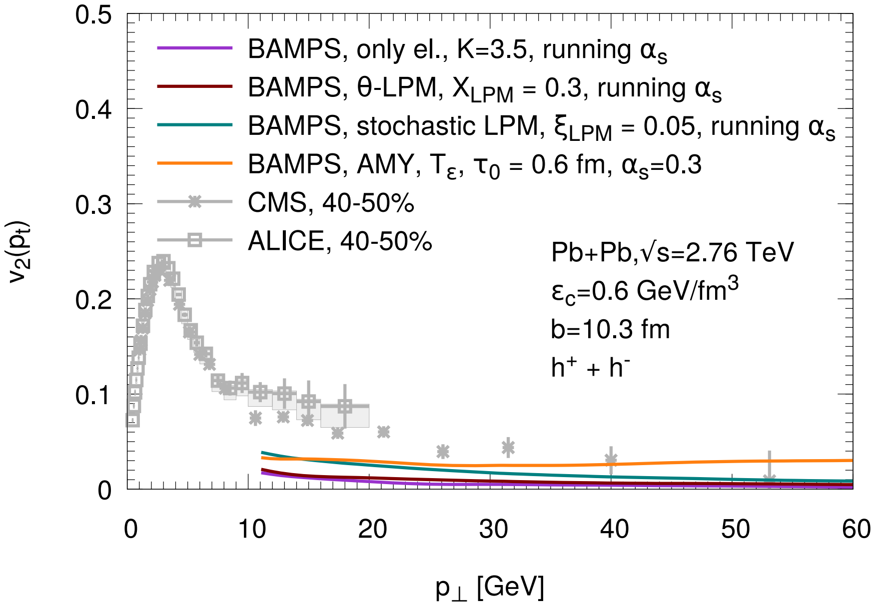

Figure 7.23: Elliptic flow v_2 of charged hadrons at large transverse momentum $p_\perp$ from elastic $2 \rightarrow 2$ and radiative $2 \rightarrow 3$ interactions based on the different LPM approaches in peripheral $\sqrt{s_{\mathrm{NN}}} = 2.76\,\mathrm{TeV}$ Pb + Pb collisions together with experimental data measured at the LHC. The values of the screening parameter underlying the effective LPM approaches are fixed to $X_{\mathrm{LPM}} = 0.3$ and $\xi_{\mathrm{LPM}} = 0.05$ representing the best agreement with experimental data for R_{AA} in central collisions. The QCD coupling is either described by a running α_s or $\alpha_s = 0.3$. Measured data by the experiments at LHC [CMS12a; ALI12a] is given by gray points.

7.4 Medium modification of reconstructed jets

In the previous section we studied the differences of the radiative processes from the different LPM approaches by the modification of leading partons and hadrons. We found that the measured suppression of charged hadron spectra in central Pb + Pb collisions at LHC can be explained by elastic and radiative processes from both effective LPM approaches, whereas the AMY formalism leads to a slightly stronger suppression than the data. In the following we extend this study of jet quenching in central Pb + Pb collisions by evolving parton showers as introduced in Section 6.3.1 within the expanding BAMPS medium and reconstructing jets based on these showers. In contrast to the R_{AA} of charged hadrons, such a study of the in-medium modification of partons showers benefits from information about the medium modification of several partons instead of only the leading parton or hadron. Hence, also differential information about, e.g., the angular structure of the radiative energy loss can be investigated. Furthermore, since different partons with different energies may contribute to the same reconstructed jet, these are intrinsically sensitive to different parton energy regions. Effects visible in the modification of only individual partons are enhanced since they concern multiple partons reconstructed into jets. In order to study the energy loss of reconstructed jets in expanding media we present in Section 7.4.1 the nuclear modification factor $R_{\mathrm{AA}}^{\mathrm{jet}}$ of inclusive reconstructed jet spectra continuing previous studies of reconstructed jets in BAMPS [Sen+17]. Already in p + p collisions, different vacuum evolutions of the parton showers originating from the initial back-to-back partons lead to an imbalance of transverse momenta of the two leading reconstructed jets. In Section 7.4.2 we study how additional medium interactions of these partons enhance this asymmetry and thereby carry on our studies from Ref. [Sen+15]. We conclude this section by investigating in Section 7.4.3 the medium modification of jet shapes in expanding media from the different LPM approaches.

7.4.1 Suppression of reconstructed jet spectra

Correspondingly to our previous studies for characterizing the energy loss of leading partons by the suppression of parton and hadron spectra, we begin the studies of this section by the suppression of reconstructed jet spectra in central $\sqrt{s_{\mathrm{NN}}} = 2.76\,\mathrm{TeV}$ Pb + Pb collisions. By following the simulation strategies introduced in Section 7.2, Fig. 7.24 compares the reconstructed $R_{\mathrm{AA}}^{\mathrm{jet}}$ simulated by the different LPM approaches within BAMPS with experimental data from the ALICE [ALI15] and CMS [CMS17] experiments. Jets are reconstructed by the anti-$k_\perp$ algorithm with a rather small jet resolution parameter $R = 0.2$. As a baseline, we also show the corresponding $R_{\mathrm{AA}}^{\mathrm{jet}}$ from the purely elastic $2 \rightarrow 2$ processes scaled by $K = 3.5$. Please note that the measurements of ALICE and CMS differ in the considered jet rapidity range and we present our results in the wider rapidity range $|y| < 2$. Furthermore, for the results of the ALICE experiment only jets were considered that contain a hadron with at least $p_\perp > 5\,\mathrm{GeV}$. Since parton and hadron momenta are difficult to compare we neglect this experimental prerequisite in our results and assume that every reconstructed jet contains a hard parton.

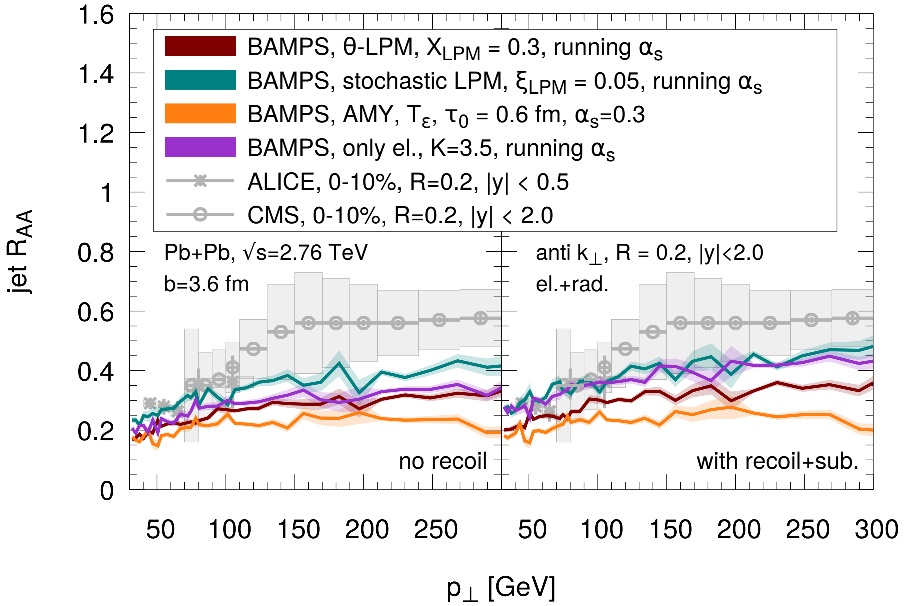

Figure 7.24: Nuclear modification $R_{\mathrm{AA}}^{\mathrm{jet}}$ of reconstructed jets with cone radius $R = 0.2$ from either scaled ($K = 3.5$) elastic $2 \rightarrow 2$ interactions (purple) or elastic $2 \rightarrow 2$ and radiative $2 \rightarrow 3$ interactions based on the different LPM approaches in central $\sqrt{s_{\mathrm{NN}}} = 2.76\,\mathrm{TeV}$ Pb + Pb collisions together with experimental data measured at the LHC. The left panel shows the $R_{\mathrm{AA}}^{\mathrm{jet}}$ without medium recoil effects, whereas the right panel considers recoiling medium partons that are appropriately subtracted subsequently. The values of the screening parameter underlying the effective LPM approaches are fixed to $X_{\mathrm{LPM}} = 0.3$ and $\xi_{\mathrm{LPM}} = 0.05$ representing the best agreement with experimental data for the charged hadron $R_{\mathrm{AA}}^{\mathrm{jet}}$ in central collisions. The QCD coupling is either described by a running α_s or $\alpha_s = 0.3$. Measured data by the experiments at LHC [ALI15; CMS17] is given by gray points.

For both scenarios “no recoil” and “with recoil+subtraction”, the different LPM approaches as well as the scaled elastic interactions lead to a strong suppression of jet spectra within BAMPS wrt. the initial jet spectra from PYTHIA. While this strong suppression can also be found in the data at “softer” jet momenta $p_\perp \approx 50\,\mathrm{GeV}$, the measured suppression at higher jet momenta $p_\perp \approx 60$–$100\,\mathrm{GeV}$ decreases almost linearly before showing for $p_\perp \gtrsim 140\,\mathrm{GeV}$ a flatter suppression around $R_{\mathrm{AA}}^{\mathrm{jet}} \approx 0.6$. In contrast, our results from the different LPM approaches show the strong suppression $R_{\mathrm{AA}}^{\mathrm{jet}} \approx 0.2$–$0.4$ over the whole studied $p_\perp$ range. We find the strongest suppression for the AMY interactions, whereas the stochastic LPM shows the mildest suppression of reconstructed jets. Also the inclusion of recoiling partons only mildly restores the reconstructed jet momenta and thereby counteracts the strong suppression of jets. Reason for this mild effect is the rather small jet radius employed for these results. Interestingly, the best agreement with the data at $p_\perp \gtrsim 140\,\mathrm{GeV}$ can be found for the scaled elastic interactions and the stochastic LPM approach. Obviously, the radiative processes of the θ-LPM and AMY formalism, which both neglect the finite size of gluon emissions, overestimate the energy loss out of the jet cones.

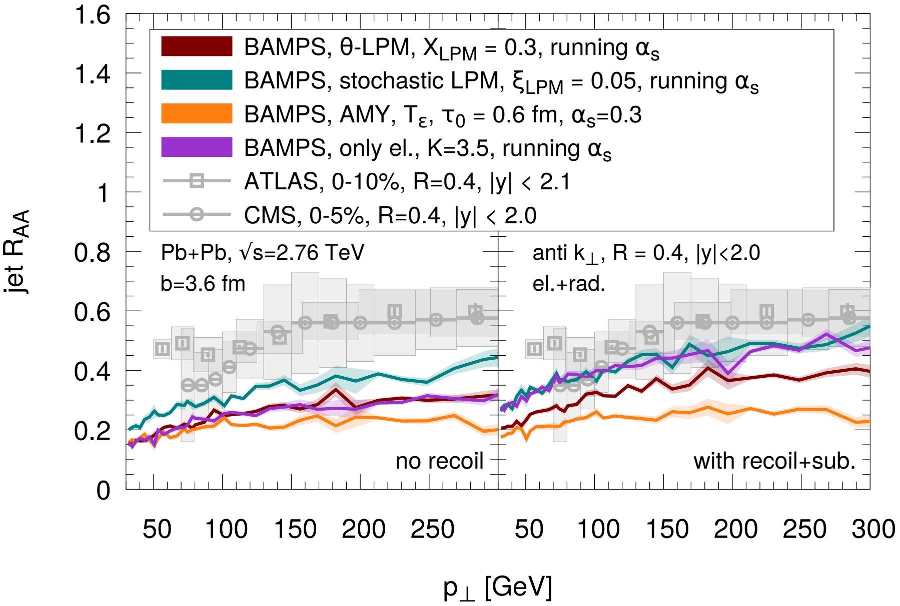

Figure 7.25: Nuclear modification $R_{\mathrm{AA}}^{\mathrm{jet}}$ of reconstructed jets with $R = 0.4$ from either scaled ($K = 3.5$) elastic $2 \to 2$ interactions (purple) or elastic $2 \to 2$ and radiative $2 \to 3$ interactions based on the different LPM approaches in central $\sqrt{s_{\mathrm{NN}}} = 2.76\,\mathrm{TeV}$ Pb + Pb collisions together with experimental data measured at the LHC. Same parameters chosen as in Fig. 7.24. Measured data by the experiments at LHC [CMS17; ATL14] is given by gray points.

After discussing $R_{\mathrm{AA}}^{\mathrm{jet}}$ for a smaller jet radius, we present in Fig. 7.25 the corresponding results for the suppression of jets reconstructed with a larger cone radius $R = 0.4$ together with experimental data obtained by the ATLAS and CMS collaboration at the LHC. At larger radii more shower momentum from larger emission angles can be reconstructed into the jets what leads to an increased $R_{\mathrm{AA}}^{\mathrm{jet}}$ over the $p_\perp$ range measured by the experiments. In contrast, our simulations without recoiled medium partons are almost insensitive to the larger choice of R. The different LPM approaches and the scaled elastic interactions show a too strong suppression of jets with $R = 0.4$ when neglecting the influence of recoiling medium partons. Only the inclusion of recoiling medium partons into the reconstructed jets leads to a visible difference of the $R_{\mathrm{AA}}^{\mathrm{jet}}$ with $R = 0.2$ and $R = 0.4$. Consequently, the $R_{\mathrm{AA}}^{\mathrm{jet}}$ simulated by the scaled elastic interactions and the stochastic LPM effect can again explain the suppression of jets at $R = 0.4$, whereas both other LPM approaches still show a too strong suppression.

In order to explain the found strong suppression of reconstructed jets, we study in Figs. 7.26 and 7.27 the average momentum loss $\langle \Delta p_\perp \rangle$ of reconstructed jets underlying the previous jet $R_{\mathrm{AA}}^{\mathrm{jet}}$ results. To this end, we exploit the information about the initial state of the respective parton shower and define $\langle \Delta p_\perp \rangle = p_\perp^{\mathrm{PYTHIA}} - p_\perp^{\mathrm{BAMPS}}$, where $p_\perp^{\mathrm{BAMPS}}$ is the momentum of a final reconstructed jet after the BAMPS simulation. $p_\perp^{\mathrm{PYTHIA}}$ is then the transverse momentum of the reconstructed jet from the initial state that is reconstructed closest to the respective final jet in the $\phi - y$ plane. Different to experiments, where information about the initial state of a specific reconstructed jet are out of reach, this allows us to calculate the actual momentum loss of reconstructed jets traversing the heavy-ion medium.

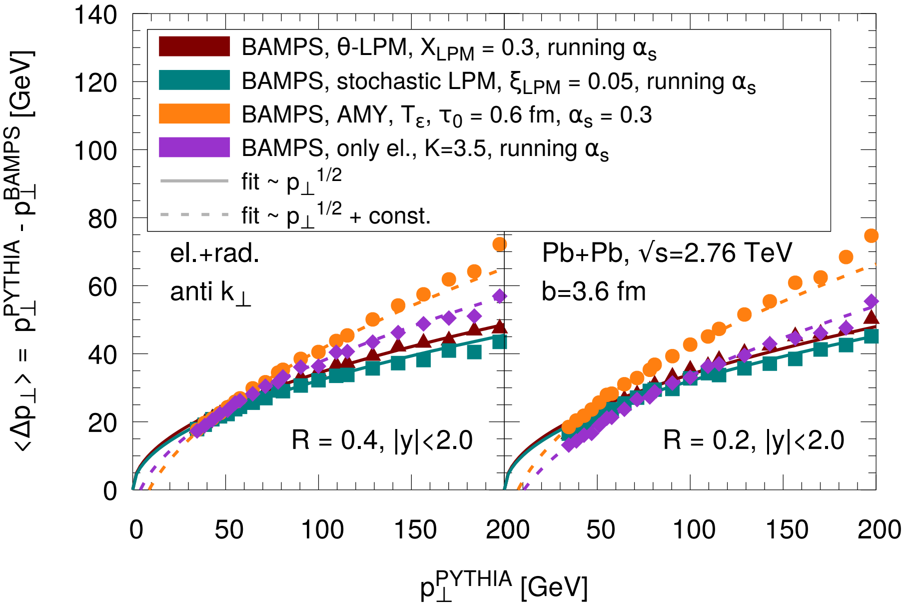

Figure 7.26: Mean transverse momentum loss $\Delta p_\perp$ of jets reconstructed without medium recoil and with cone radius $R = 0.4$ (left) or $R = 0.2$ (right) after traversing a central $\sqrt{s_{\mathrm{NN}}} = 2.76\,\mathrm{TeV}$ Pb + Pb collision wrt. the related unquenched reconstructed jet from PYTHIA with transverse momentum $p_\perp^{\mathrm{PYTHIA}}$. The jets interact with the medium by either only scaled ($K = 3.5$) elastic interactions or elastic and radiative interactions employing the different LPM approaches.

Figure 7.26 shows the average momentum loss of reconstructed jets for both employed cone radii $R = 0.2$ and $R = 0.4$ without recoiling medium partons. In agreement with our results for the suppression of jets, we find that the momentum loss of reconstructed jets is strongest for the radiative processes from the AMY formalism, whereas the stochastic LPM approach shows the mildest jet momentum loss. Furthermore, as the $R_{\mathrm{AA}}^{\mathrm{jet}}$, also the momentum loss of jets calculated within BAMPS is rather insensitive to the difference of both employed cone radii. We found previously that one characteristics of the LPM effect in QCD is the energy dependence $\Delta E \sim \sqrt{E}$ of jet energy loss. This dependence can also be found in the $p_\perp$ dependence of the average jet momentum loss from the different LPM approaches as denoted by fits $\sim \sqrt{p_\perp}$. Interestingly, the interplay of energy loss of the leading parton and transport of partons out of the reconstructed jets also leads to this $\sqrt{E}$ dependence in the pure elastic scenario, where obviously no LPM effect is considered.

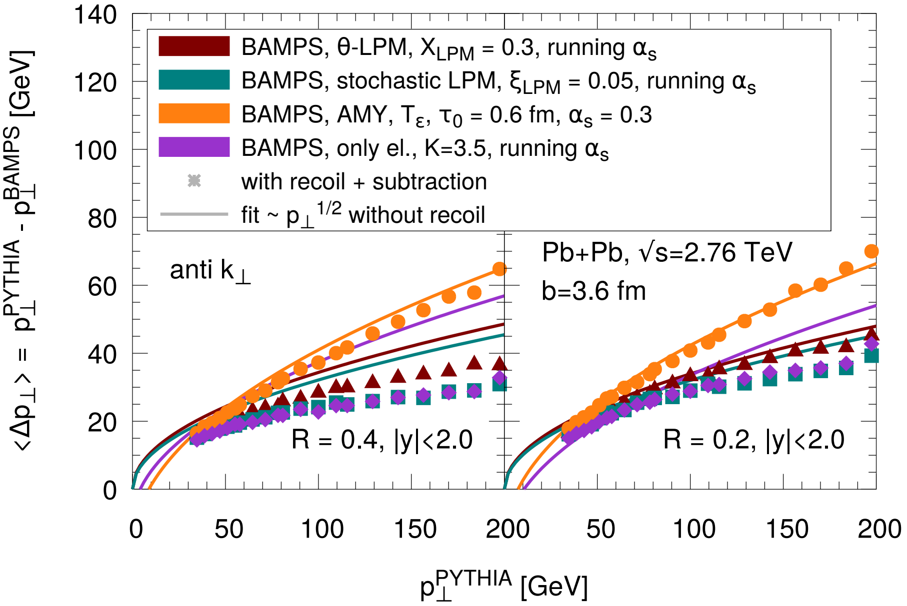

Figure 7.27: Mean transverse momentum loss $\Delta p_\perp$ of jets reconstructed with medium recoil and cone radius $R = 0.4$ (left) or $R = 0.2$ (right) after traversing a central $\sqrt{s_{\mathrm{NN}}} = 2.76\,\mathrm{TeV}$ Pb + Pb collision wrt. the related unquenched reconstructed jet from PYTHIA with transverse momentum $p_\perp^{\mathrm{PYTHIA}}$. The lines correspond to the fit results obtained without medium recoil in Fig. 7.26. Again, the jets interact with the medium by either only scaled ($K = 3.5$) elastic interactions or elastic and radiative interactions employing the different LPM approaches.

Finally, we compare in Fig. 7.27 the fitted $p_\perp$ dependence of $\langle \Delta p_\perp \rangle$ from Fig. 7.26 without recoil to the average momentum loss of the different approaches when considering recoiling medium partons. While the recoil has almost no effect to the momentum loss of AMY interactions, where in the effective $1 \leftrightarrow 2$ processes no recoiling partons are present, the momentum loss is significantly decreased in the other approaches. Especially the scaled elastic interactions benefit due to the increased scattering rate from the effect of recoiling medium partons. Furthermore, with increasing cone radius R more recoiling medium partons at larger angles can be restored within the jets. Consequently, the recoil effect is stronger for jets reconstructed with $R = 0.4$ than for the smaller jet radius $R = 0.2$.

7.4.2 Momentum asymmetry of reconstructed jets within BAMPS

After characterizing the different medium modification of reconstructed jets from the LPM approaches in terms of the suppression of individual jets, we briefly present in this section results for the momentum imbalance A_J of the leading reconstructed jets in central $\sqrt{s_{\mathrm{NN}}} = 2.76\,\mathrm{TeV}$ Pb + Pb events at the LHC. Already in p + p collisions, the two parton showers originating from the virtual partons of hard partonic process differ due to the stochastic nature of QCD splittings. This difference can be characterized by the momentum imbalance A_J defined as

$$A_J = \frac{p_{\perp;\,\text{leading}} - p_{\perp;\,\text{subleading}}}{p_{\perp;\,\text{leading}} + p_{\perp;\,\text{subleading}}}\,, \tag{7.25}$$

where $p_{\perp;\,\text{leading}}$ ($p_{\perp;\,\text{subleading}}$) is the transverse momentum of the reconstructed jet with the highest (second highest) $p_\perp$. After traversing the bulk medium of a heavy-ion collision this initial momentum imbalance could be in principle enhanced by the different in-medium path lengths of both parton showers. We found previously in Ref. [Sen+15] for the radiative processes from the θ-LPM effect that the resulting momentum imbalance is mainly determined by the imbalance already present in the initial A_J distribution from PYTHIA and not by the difference in path length given by the initial spatial production point. In this section we check whether this result still holds for the other LPM approaches studied within this work. For more details about the calculation of A_J and especially the consideration of detector effects we refer to Ref. [Sen+15].

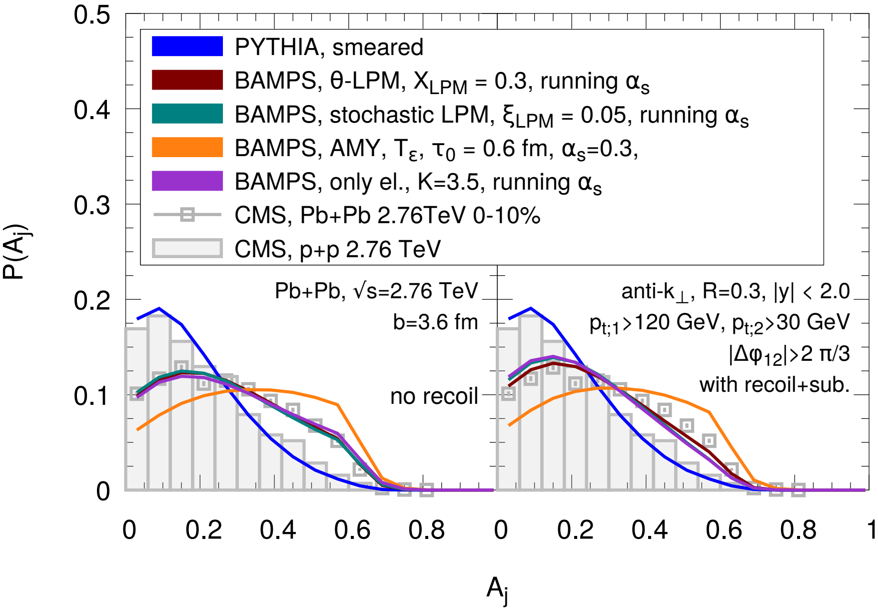

Figure 7.28: Momentum asymmetry A_J of the two leading reconstructed jets from either scaled ($K = 3.5$) elastic $2 \to 2$ interactions (purple) or elastic $2 \to 2$ and radiative $2 \to 3$ interactions based on the different LPM approaches in central $\sqrt{s_\text{NN}} = 2.76\,\text{TeV}$ Pb + Pb collisions together with experimental data measured at the LHC. Same parameters chosen as in Figs. 7.24 and 7.25. The left panel shows the A_J distribution without medium recoil effects, whereas the right panel considers recoiling medium partons that are appropriately subtracted subsequently. Measured data by the CMS experiment at LHC [CMS11b] for the momentum imbalance in p + p collisions is given by gray bars, whereas the results measured in Pb + Pb collisions is denoted by gray points.

Figure 7.28 compares the normalized distribution of A_J from the different LPM approaches and the scaled elastic interactions to experimental data obtained by the CMS collaboration. Jets are reconstructed with a cone radius $R = 0.3$ in the rapidity region $|y| < 2$. We employ the same trigger conditions as defined by the experimental study. While the left panel shows calculations without recoil, the right panel includes also the recoiling medium partons whose medium momenta are appropriately subtracted. The final reconstructed jet momenta were smeared by a Gaussian $\sim \sqrt{p_\perp}$ obtained by a comparison of the initial PYTHIA distribution with results for $\sqrt{s_\text{NN}} = 2.76\,\text{TeV}$ p + p collisions (cf. Ref. [Sen+15]). As already suspected, the distribution of momentum imbalance is rather insensitive to the specific energy loss of the parton showers. Both effective LPM approaches as well as the scaled elastic interactions show a realistic distribution of A_J, both with and without recoiling medium partons. Only the radiative process from the AMY formalism show a slightly too strong enhancement of events at values $A_\mathrm{J} \gtrapprox 0.3$. This is in accordance with A_J results from the MARTINI framework, where the best agreement with data was found for slightly smaller values of the QCD coupling $\alpha_s = 0.25$–0.3 [You+11a].

The similarity of A_J calculated by the broad range of different assumptions about the underlying partonic energy loss confirms our previous results in Ref. [Sen+15]. The resulting momentum imbalance of leading jets is mainly caused by the momentum imbalance already present in the initial state that is further enhanced by the in-medium interactions. The physical relevance of A_J as an observable for studying the characteristics of final-state jet energy loss is therefore at least questionable.

7.4.3 Modification of jet shapes in heavy-ion collisions

After studying the different LPM approaches in terms of $R_\mathrm{AA}^\mathrm{jet}$ and the momentum imbalance A_J we conclude this section by extending our previous studies from Section 6.3 regarding the medium modification of shower shapes $\hat{\rho}(r)$. We found that the shower shapes from the different LPM approaches look similar when considering recoil effects of the scattered medium partons.

In this section we investigate whether this finding still holds in the expanding medium of heavy-ion collisions. To this end, we calculate in this section the jet shapes $\rho(r)$ defined as [CMS13b]

$$\rho(r) = \frac{1}{N_\mathrm{jets}} \sum_\mathrm{jets} \frac{1}{\delta r} \sum_{r_i \in [r-\delta/2, r+\delta/2)} \frac{p^{\,i}_{\perp\mathrm{parton}}}{p_\perp^\mathrm{jet}} \,. \tag{7.26}$$

After normalizing the jet shape distribution to the cone radius R, it represents the distribution of momentum around the jet axis *within* the reconstructed jets. Different to the shower shapes defined in Eq. (6.4) on page 163, jet shapes relate the distribution of momenta around the jet axis to the respective reconstructed *final* jet momenta and not to the *initial* shower-initiating parton. This allows to apply the concept of jet shapes also in experimental studies concerning jet quenching in ultra-relativistic heavy-ion collisions. By comparing jet shape distributions $\rho(r)$ from $\mathrm{p+p}$ collisions with distributions measured in Pb + Pb collisions, one aims to identify characteristics of the underlying processes leading to the observed medium modification of jets.

In Fig. 7.29 we present results for the ratio of jet shapes simulated by the different LPM approaches within central ($b = 3.6\,\mathrm{fm}$) BAMPS events and the corresponding initial jet shapes from the PYTHIA initial state before the BAMPS evolution. While the left panel shows the jet shape ratio without recoiling medium partons, the right panel includes recoiling medium partons, whose medium contamination is subtracted from the jet shape distribution. These ratios are compared to experimental data obtained by the CMS collaboration in 0–10 % Pb + Pb collisions with $\sqrt{s_\mathrm{NN}} = 2.76\,\mathrm{TeV}$. As in the static medium, the different LPM approaches show similar medium modifications of $\rho(r)$. While the inner core $r < 0.05$ of jets is almost unmodified wrt. PYTHIA, the medium interactions of the parton showers lead to a significant enhancement of momenta at larger angles from the jet axis. This enhancement is even stronger when also considering recoiling medium partons that mostly contribute at these larger angles to the reconstructed jets. When considering the medium recoil, the stochastic LPM approach shows the strongest enhancement of momenta at large angles $r \sim \mathcal{O}(R)$. Reason for this enhancement in the stochastic LPM approach is the more transverse emission rate $\mathrm{d}\Gamma/\mathrm{d}k_\perp$ found in Section 5.5. In contrast,

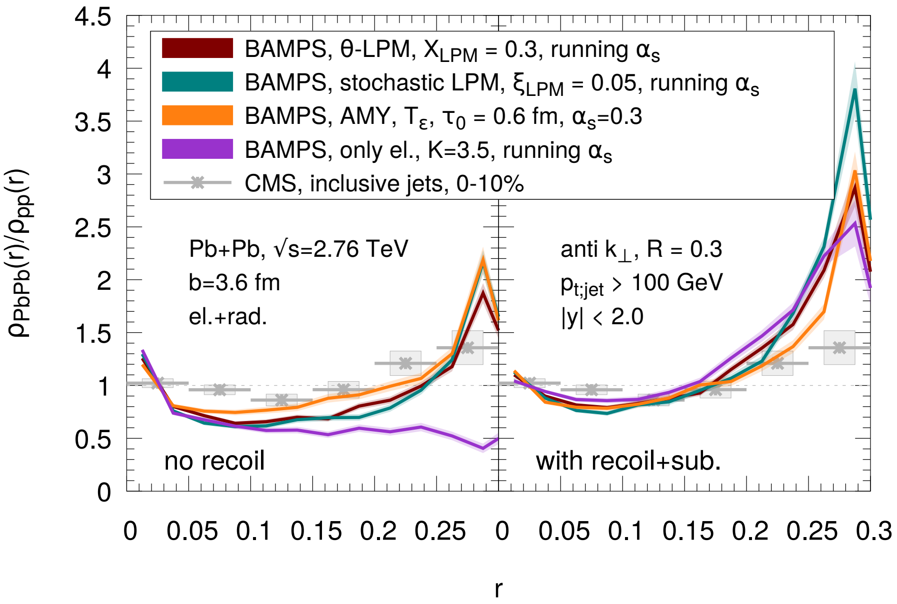

Figure 7.29: Medium modification of the jet shapes $\rho(r)$ of reconstructed jets with cone radius $R = 0.3$ from either scaled ($K = 3.5$) elastic $2 \rightarrow 2$ interactions (purple) or elastic $2 \rightarrow 2$ and radiative $2 \rightarrow 3$ interactions based on the different LPM approaches in central $\sqrt{s_{\mathrm{NN}}} = 2.76\,\mathrm{TeV}$ Pb + Pb collisions together with experimental data measured at the LHC. Same parameters chosen as in Figs. 7.24, 7.25 and 7.28. The left panel shows the jet shapes without medium recoil effects, whereas the right panel considers recoiling medium partons that are appropriately subtracted subsequently. Measured data by the CMS experiment at LHC [CMS13b] is given by gray points.

the pure elastic interactions scaled by $K = 3.5$ differ from the radiative processes of the different LPM approaches by showing a depletion of momentum at larger angles $r > 0.15$ when neglecting the medium recoil. This depletion is caused by the strong $2 \rightarrow 2$ transport of initial shower partons to large angles out of the jet cones, which are not replenished by radiative processes of the hard partons. Only after including the recoiling medium partons this depletion is recovered by recoiled medium partons at this angles that are reconstructed within the jets leading to similar jet shape ratios as in the radiative scenarios from the different LPM approaches. In general, both the scaled elastic interactions and the radiative interactions from the different LPM approaches explain the jet shape modification at small to intermediate angles but overestimate the modification at larger angles $r \rightarrow R$.

In order to further elaborate on the underlying mechanisms leading to the medium modification of jet shapes we show in Fig. 7.30 the jet shapes from the different LPM approaches underlying Fig. 7.29 in the broader range $r \in [0; 1]$ and compare them with the initial jet shapes from PYTHIA. For the different LPM effects, already the jet shapes without recoil show an enhancement of momenta at angles $r > R$ wrt. the distribution from PYTHIA. This enhancement is caused by the radiative processes either emitting partons directly to larger angles (effective LPM approaches) or emitting collinear partons that are subsequently transported to this larger angles (AMY). In contrast, the pure elastic interactions show a depletion of partons at large angle $r > R$ wrt. PYTHIA, again demonstrating the strong transport of initial partons to larger angles relative to the jet axis.

Furthermore, we show in Fig. 7.30 both jet shape distributions from straight-forwardly considering the recoiling medium partons without subtracting the medium contamination

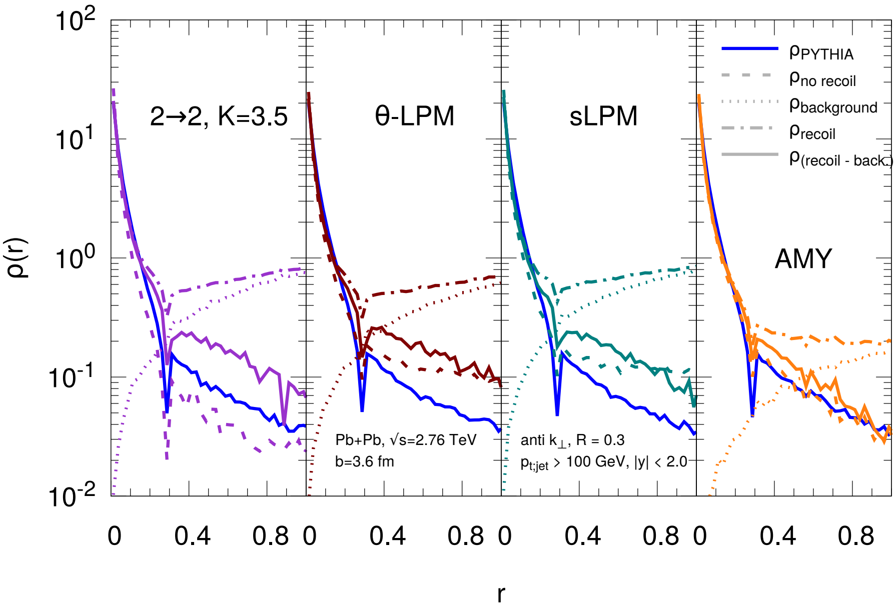

Figure 7.30: Comparison of the different contributions to the medium-modified jet shapes $\rho(r)$ of jets reconstructed with cone radius $R = 0.3$ from either scaled ($K = 3.5$) elastic $2 \to 2$ interactions (purple, left panel) or elastic $2 \to 2$ and radiative $2 \to 3$ interactions based on the different LPM approaches in central $\sqrt{s_{\mathrm{NN}}} = 2.76\,\mathrm{TeV}$ Pb + Pb collisions. Same parameters chosen as in Fig. 7.29. In addition, the unmodified jet shape distribution directly from PYTHIA simulations are given by blue lines.

and after subtracting the medium contamination. This medium contamination is strongest at larger angles from the jet axis. On the other hand, the core of the jet consists of almost only shower partons. The recoiled medium partons contribute mostly in the intermediate region $R < r < 0.6$. Only the jet shapes from the scaled elastic interactions get significant contributions from recoiling medium partons also at larger angles $r > 0.6$.

8 Conclusion

In this chapter we summarize the studies undertaken in this thesis and highlight the main findings about the implementation of the non-Abelian LPM effect into a partonic transport approach. Finally, we conclude this work by giving suggestions for future studies regarding jet quenching in BAMPS.

8.1 Summary

Ultra-relativistic heavy-ion collisions are *the* tool for investigating hot and dense QCD matter as it is supposed to have existed in the early phases of the universe. Among the most promising observables for studying this quark-gluon plasma is jet quenching—the energy and momentum loss of high energetic partons that traverse the expanding heavy-ion collision. Measuring the strength of jet quenching then reveals information about the characteristics and properties of the produced matter. In this work jet quenching has been studied in the partonic transport approach BAMPS. BAMPS numerically solves the 3+1-dimensional Boltzmann equation for partons on the mass shell by considering both binary $2 \rightarrow 2$ interactions described by leading-order perturbative QCD and radiative $2 \rightarrow 3$ processes calculated in an improved Gunion-Bertsch approximation. In order to cure divergences emerging from the internal gluon and quark propagators, Debye masses are introduced that effectively screen the interactions within the hot partonic environment. One of the advantages of BAMPS is the possibility to describe both jet quenching and the evolution of the underlying bulk medium based on the same microscopic interactions.

When considering radiative processes of high energy partons in a medium, coherence effects as the Landau-Pomeranchuk-Migdal (LPM) effect are crucial for the resulting jet energy loss. Due to the finite formation time of emissions, subsequent scattering processes may act coherently and thereby suppress further emissions. While this effect can be found for both photon and gluon emissions, the emitted gluons from radiative QCD processes are allowed to scatter themselves with the surrounding medium so that the formation time of the emissions may be further modified after the emission. Consequently, analytical calculations for the non-Abelian LPM effect show characteristic dependencies of, e.g., the gluon emission spectrum $\mathrm{d}\Gamma/\mathrm{d}\omega \sim \omega^{-3/2}$ at high gluon energies or the radiative energy loss $\mathrm{d}E/\mathrm{d}x \sim L$ in thin and $\mathrm{d}E/\mathrm{d}x \sim \mathrm{const.}$ in thick media.

Furthermore, an emission process obeying the LPM effect cannot be regarded as localized but only as extended over a finite region of space. This finite formation time then complicates a formal treatment of the LPM effect within transport approaches, where interactions are assumed to be local. Therefore a main goal of this work was the systematic study of different approaches for implementing the LPM effect in the partonic transport approach BAMPS. To this end, we compared three different descriptions for the non-Abelian LPM effect in three different energy loss scenarios: first we examined the energy loss of an eikonal projectile traversing a static and thermal brick of quark-gluon plasma, then the corresponding case of a non-eikonal projectile, and finally the energy loss of jets within the expanding medium of an ultra-relativistic heavy-ion collision.

Energy loss in the eikonal limit

Our assumptions and results for the radiative energy loss of an eikonal projectile obeying the different LPM approaches can be summarized as follows:

- In previous studies, the θ-LPM approach was the only implementation for effectively considering the LPM effect within BAMPS. By introducing a theta function in the radiative matrix elements underlying the $2 \leftrightarrow 3$ processes, the θ-LPM approach ensures that only emissions are allowed whose formation time is shorter than the mean free path to the next scattering processes. This treatment then corresponds to the incoherent (Bethe-Heitler) case of gluon emissions. After iterating the mean free path of an emission, we find that indeed already these "incoherent" processes show a $\mathrm{d}\Gamma/\mathrm{d}\omega \sim \omega^{-3/2}$ and a $\mathrm{d}E/\mathrm{d}x \sim \sqrt{E}$ dependence, which are both characteristic for the non-Abelian LPM effect. However, although the formation time of gluon emissions is considered via the theta function, gluons are produced instantaneously at the position of the initial $2 \to 3$ process. Therefore the θ-LPM effects lacks any finite formation time effects and thereby shows a $\mathrm{d}E/\mathrm{d}x \sim \mathrm{const.}$ behavior independent from the medium length L.

  In order to effectively consider also the coherence of gluon emissions, we introduce the screening parameter X_{LPM} controlling the soft-$k_\perp$ divergence of the $2 \to 3$ process in the improved Gunion-Bertsch approximation. Although the individual gluons are still produced incoherently in the $2 \to 3$ process, a smaller X_{LPM} effectively increases the emission rate by opening the phase space for gluon emissions. The interplay between this screening and the employed theta function leads to a logarithmic dependence of the resulting radiative energy loss in the θ-LPM approach on the parameter X_{LPM}.

- In contrast to the previous θ-LPM effect, the stochastic LPM effect (sLPM) explicitly considers the finite formation time of gluon emissions by replacing the mean free path between scatterings by microscopic $2 \to 2$ scatterings of the gluons during their formation time. Following previous studies [ZSW09; ZSW11; ZW12; KXB18b], the stochastic LPM approach then interpolates between the coherent and incoherent case by stochastically suppressing *a posteriori* radiation processes depending on the number of elastic scatterings necessary for forming the emitted gluons.

  Before calculating the actual radiative jet energy loss, we validated our description of the Monte-Carlo algorithm by using a simplified setup of constant elastic and radiative interactions (constant mean free paths λ, constant momentum transfers $q_\perp^2, \ldots$). By varying these simplified interactions we demonstrated that the sLPM approach indeed shows the expected analytical dependencies of the non-Abelian LPM effect for different medium lengths L and projectile energies E.

  On the contrary, the $2 \to 2$ interactions as calculated in leading-order pQCD and considered in the usual BAMPS framework are not constant but follow distributions depending on, e.g., the CoM energy $\sqrt{\hat{s}}$ of the respective microscopic scattering. Therefore we further clarified these dependencies by investigating the capability of elastic scatterings within BAMPS to broaden the transverse momentum of gluons during their formation time. To this end, we compared our Debye-screened $2 \to 2$ processes to the differential elastic scattering rate calculated within the HTL approximation and find that the Debye-screening within BAMPS leads to a significant reduction of soft momentum transfers $q_\perp^2 \lessapprox T^2$, whereas the large-angle scatterings

($q_\perp^2 > T^2$) are comparable to the HTL calculation. Moreover, we studied the energy dependence of the elastic scattering rate Γ_{22} and the mean momentum transfer $\langle q_\perp^2 \rangle$ for Debye-screened $2 \rightarrow 2$ scatterings. We find that the four-gluon vertex of the process $\mathrm{gg} \rightarrow \mathrm{gg}$, which is implicitly considered in our choice of pQCD matrix elements and neglected in the t-channel dominated HTL calculations, leads to a diverging scattering rate and thereby a diverging momentum broadening coefficient $\hat{q}$ at small gluon energies. On the other hand, at larger gluon energies ($\omega \gg m_D$) we are able to reproduce the common $\hat{q} \sim \log(\omega/T)$ behavior. We further confirmed these findings by calculating $\hat{q}$ with a semi-analytical formalism employing the same choice of pQCD interactions. This allowed us to further discriminate between the contributions of different partonic processes to the total momentum broadening $\hat{q}$.

Furthermore, also the $2 \rightarrow 3$ Bremsstrahlung processes calculated in an improved Gunion-Bertsch approximation are not constant but show characteristic distributions for, e.g., the transverse gluon momenta $k_\perp$. While the $k_\perp$-divergence of the Gunion-Bertsch matrix element is effectively screened via the theta function in the θ-LPM approach, same arguments do not hold anymore for the stochastic LPM approach. Hence, we introduced by the screening parameter ξ_{LPM}, which is defined via $k_{\perp;\,\text{min}} = \xi_{\text{LPM}} \sqrt{\hat{s}}$, a similar effective screening of infrared transverse momenta to the stochastic LPM approach and studied its dependencies while neglecting any LPM suppression from the sLPM algorithm. This allowed us to demonstrate that the differential emission rate from purely the Gunion-Bertsch matrix element together with the ξ_{LPM} screening shows the expected $\mathrm{d}\Gamma/\mathrm{d}\omega \sim 1/\omega$ (Bethe-Heitler) limit for gluon emissions.

In order to further clarify the interplay between the stochastic LPM algorithm and the $2 \rightarrow 2$ and $2 \rightarrow 3$ processes from BAMPS, we calculated the differential emission rates $\mathrm{d}\Gamma/\mathrm{d}\omega$ and $\mathrm{d}\Gamma/\mathrm{d}k_\perp$, and the differential radiative energy loss $\mathrm{d}E/\mathrm{d}x$ of an eikonal projectile with energy E traversing a static medium with length L. While at intermediate gluon energies the stochastic suppression of gluon emissions reproduces the expected $\mathrm{d}\Gamma/\mathrm{d}\omega \sim \omega^{-3/2}$ behavior of the non-Abelian LPM effect, the resulting $\mathrm{d}\Gamma/\mathrm{d}\omega$ shows differences to the analytical expectations at both small and large gluon energies due to the initial $2 \rightarrow 3$ process: at small gluon energies the rate is suppressed due to the introduced effective $k_\perp$ screening , whereas at high gluon energies the available phase space of a $2 \rightarrow 3$ process forbids emissions with $\omega \rightarrow E$. Moreover, the finite formation time of gluon emissions leads to the expected $\mathrm{d}E/\mathrm{d}x \sim L$ behavior in thin media and the $\mathrm{d}E/\mathrm{d}x \sim \text{const.}$ dependence in thick media. As in the θ-LPM approach, the radiative energy loss in the stochastic LPM approaches depends logarithmically ($\mathrm{d}E/\mathrm{d}x \sim \log(1/\xi_{\text{LPM}})$) on the introduced screening parameter ξ_{LPM}.

- While both effective LPM approaches, the θ-LPM and stochastic LPM methods, rely on screening parameters for curing the $k_\perp$ divergence originating in the Gunion-Bertsch matrix element, other pQCD calculations for gluon radiation prevent this divergence by resumming an infinite number of emission diagrams. One of these approaches is the AMY formalism, which is a thermal field theory calculation for gluon emission. Assuming a clear separation of scales, one can show within AMY that the transverse momentum of gluon emissions is of order $k_\perp \sim \mathcal{O}(g_s T)$, which can be neglected in the small coupling limit. In the course of this work, we recalculated the collinear gluon emission rate from AMY and implemented it into the

> BAMPS framework. In contrast to both other LPM approaches, the $1 \leftrightarrow 2$ processes from AMY are defined by an emission rate, which is in general only valid in a thermal system with infinite medium length. Consequently, the resulting emission rate from AMY shows the expected $\mathrm{d}\Gamma/\mathrm{d}\omega \sim \omega^{-3/2}$ behavior of the non-Abelian LPM effect but lacks the correct limit of radiative energy loss in thin media. We confirmed our implementation of AMY into the BAMPS framework by comparing it to MARTINI, which is an other model implementing the AMY emission rate into dynamical simulations of the quark-gluon plasma.

After introducing the different descriptions for the LPM effect in a partonic transport approach, we further studied the non-Abelian LPM effect within BAMPS by comparing the LPM methods. Since there is no physical argument for a specific choice of the screening parameters underlying the effective LPM approaches, we first determined their values by a comparison between their differential energy losses $\mathrm{d}E/\mathrm{d}x(E)$ in thick media with the corresponding energy loss within AMY. While we found the best agreement in the θ-LPM approach for $X_{\mathrm{LPM}}^{\mathrm{AMY}} = 0.05$, the screening parameters in the stochastic LPM approach are determined to $\xi_{\mathrm{LPM}}^{\mathrm{AMY;\,g}} = 0.015$ for eikonal gluon and $\xi_{\mathrm{LPM}}^{\mathrm{AMY;\,q}} = 0.01$ for eikonal quark projectiles. However, although the radiative energy losses are calibrated to each other, the underlying emission rates $\mathrm{d}\Gamma/\mathrm{d}\omega$ and $\mathrm{d}\Gamma/\mathrm{d}k_\perp$ show significant differences: While the AMY formalism shows a diverging emission rate at both $\omega \to 0$ and $\omega \to E$, both effective approaches have vanishing rates at small and high gluon energies. Reasons for these differences are different assumptions about the underlying elastic interactions of gluons during their formation time (Debye-screened $2 \to 2$ processes vs. HTL elastic scatterings), the screening of collinear gluon emissions (screening with minimum $k_\perp$ vs. resummation of ladder diagrams) and the initial gluon emission process ($2 \to 3$ Bremsstrahlung process vs. $1 \to 2$ DGLAP emission). The stochastic LPM approach differs from both other approaches by explicitly considering the finite formation time of gluon emissions and therefore showing a different behavior at small medium lengths wrt. to the AMY formalism and the θ-LPM approach. Due to the microscopic interactions of gluons during their formation time, the rate $\mathrm{d}\Gamma/\mathrm{d}k_\perp$ shows a thermal distribution in the stochastic LPM approach, whereas the θ-LPM allows significantly smaller transverse momenta. Furthermore, the stochastic suppression of gluons leads to less, harder gluon emissions in the stochastic LPM approach, whereas the θ-LPM approach has a softer and higher gluon emission rate.

Energy loss of non-eikonal projectiles and medium modification of parton showers

While the previous results were obtained for eikonal projectiles traversing a static quark-gluon plasma, we further compared the different LPM approaches in the case of non-eikonal projectiles. Such projectiles degrade their energy while traversing the medium and therefore the time dependence of their projectile energy can be understood as a convolution of the energy loss at different projectile energies. As expected, the contribution of elastic $2 \to 2$ scatterings to the total energy loss of high energy partons is found to be minor wrt. the radiative energy loss. When comparing the LPM descriptions in the non-eikonal scenario, projectiles suffering from radiative energy loss via the θ-LPM approach lose energy most rapidly. On the contrary, the radiative energy loss from the AMY formalism and the stochastic LPM approach are surprisingly similar: While in the AMY formalism the divergences at small and large ω lead to an “all-or-nothing” kind of energy loss, the finite formation time in the stochastic LPM method delays the radiative energy loss via collinear and high energy gluons to later times. In all three methods, gluon projectiles lose significantly faster energy than corresponding quark projectiles due to their increased QCD color factors.

In order to further characterize the distribution of gluon radiation around the projectiles, we extended our study of the different LPM descriptions by investigating the medium modification of parton showers consisting of a leading parton projectile together with its surrounding parton cloud. To this end, we reconstructed jets with the anti-$k_\perp$ algorithm and a resolution $R = 0.3$ based on parton showers originating from vacuum splittings modeled by the event generator PYTHIA that are subsequently evolved within a static and thermal brick of quark-gluon plasma. The in-medium modification of parton showers was then quantified by either the reconstructed jet energy or the modification of shower shapes $\hat{\rho}(r)$ measuring the distribution of energy around the reconstructed jet axis. In contrast to the case of an individual high energy projectile, the medium modification of parton showers is a multi-particle effect based on different mechanisms:

- The individual shower partons lose energy via elastic $2 \to 2$ scatterings and medium-induced gluon radiation. Depending on their transverse momenta, these radiated gluons are either emitted out of the reconstructed jets and thereby contribute to the jet energy loss (θ-LPM and stochastic LPM) or stay close to the jet axis leaving the reconstructed jet energy unmodified (AMY).
- Both the initial vacuum and the medium-induced gluon radiation are transported to larger angles via further elastic scatterings and thereby increase the energy loss of the reconstructed jets.
- On the other hand, the recoiled medium partons from elastic $2 \to 2$ scatterings of shower partons may stay close to the reconstructed jet axis and therefore weaken the final jet energy loss.

We find that already the pure medium-induced gluon radiation from the different LPM approaches leads to different evolutions of the reconstructed jet energy. Due to the finite transverse momentum of gluon emissions both effective LPM approaches show a degradation of jet energy with increasing time. Again, the θ-LPM loses energy more rapidly than the stochastic LPM approach with finite formation time. In contrast, the AMY formalism shows almost no jet energy loss for the specific choice of resolution parameter $R = 0.3$. Reason for this reduced jet energy loss is the collinearity of medium-induced gluon radiation in the AMY formalism. Only after allowing the emitted gluons to scatter elastically, also the $1 \leftrightarrow 2$ processes from AMY lead to a transport of energy out of the jet cones. In all three LPM descriptions, shower partons and medium-induced gluon radiation are transported via elastic scatterings to large angles out of the jet cone. The similarity of reconstructed jet energy loss between the different LPM approaches is even further enhanced when additionally considering recoiling medium partons. Consequently, both the jet energy and the underlying shower shape distributions of the different LPM approaches are rather similar in the case of a parton shower traversing a static and thermal medium.

Jet quenching in expanding heavy-ion media

As mentioned previously, due to the finite lifetime of a heavy-ion collision, experiments rely on theoretical simulations for determining the properties of the produced hot and

	scaled $2 \to 2$	θ-LPM	stochastic LPM	AMY
parameter	$K = 3.5$	$X_{\mathrm{LPM}}^{\mathrm{exp}} = 0.3$	$\xi_{\mathrm{LPM}}^{\mathrm{exp}} = 0.05$	-
QCD coupling	running α_s	running α_s	running α_s	$\alpha_s = 0.3$
R_{AA} in central collisions	✓	✓	✓	✗
R_{AA} for different hadron species	✓	✓	✓	✓
Centrality dependence of R_{AA}	✓	(✓)	✓	✗
v_2 at high $p_\perp$	✗	✗	✗	✗
Jet R_{AA} with $R = 0.2$				
··· without recoil	✗	✗	✗	✗
··· with recoil+subtraction	✓	✗	✓	✗
Jet $R_{\mathrm{AA}}^{\mathrm{jet}}$ with $R = 0.4$				
··· without recoil	✗	✗	✗	✗
··· with recoil+subtraction	✓	✗	✓	✗
Momentum asymmetry A_j				
··· without recoil	✓	✓	✓	✗
··· with recoil + subtraction	✓	✓	✓	✗
Jet shapes $\rho(r)$				
··· without recoil	✗	✗	✗	✗
··· with recoil + subtraction	✗	✗	✗	✗

Table 8.1: Comparison of our results for jet quenching observables in heavy-ion collisions from either scaled elastic processes or the different LPM approaches.

dense matter. Therefore we calculated macroscopic quantities of the expanding heavy-ion medium, as e.g. densities or temperatures, based on microscopic distributions that are initialized by a superposition of multiple nucleon-nucleon interactions from PYTHIA and subsequently evolved within BAMPS by both $2 \to 2$ and $2 \leftrightarrow 3$ (from the θ-LPM approach) processes. We find that the initially high number ($n \sim \mathcal{O}\left(10^2\,\mathrm{fm}^{-3}\right)$) and energy densities ($\epsilon \sim \mathcal{O}\left(10^2\,\mathrm{GeV\,fm}^{-3}\right)$) within the bulk medium rapidly decrease due to the strong expansion of the medium. Since temperatures are only valid in equilibrated situations and especially the early stage of the heavy-ion collision is expected to be far from equilibrium, we apply different definitions for calculating effective temperatures, which are later crucial for simulating jet quenching via the AMY formalism, and find values of $T \sim \mathcal{O}(1\,\mathrm{GeV})$ in the center of the collision. Furthermore, the microscopic interactions within the medium lead to strong flows in the partonic phase of the heavy-ion collision, which transfer the spatial eccentricity of peripheral collisions to a momentum anisotropy of the partons and finally hadrons. We find that both scaled $2 \to 2$ interactions, and elastic $2 \to 2$ and inelastic $2 \leftrightarrow 3$ interactions obeying the θ-LPM approach with $X_{\mathrm{LPM}} = 0.3$ lead to a significant partonic flow within BAMPS, which is comparable to the measurements for the hadronic elliptic flow v_2 at LHC.

After investigating the non-Abelian LPM effect in the rather academic scenario of projectiles traversing a static brick of quark-gluon plasma, we continued our study of the different LPM methods in the expanding bulk medium of ultra-relativistic heavy-ion collisions. By comparing our simulation results for various jet quenching observables to experimental data measured in central and peripheral Pb + Pb collisions with $\sqrt{s_{\mathrm{NN}}} = 2.76\,\mathrm{TeV}$ at LHC, we aimed to further differentiate between the LPM methods under realistic circumstance. Our simulation results from the different LPM approaches for various jet quenching observables in heavy-ion collisions are summarized in Table 8.1.

In contrast to soft observables as the elliptic flow v_2, hadronic spectra at high transverse momentum $p_\perp$ can be obtained by a folding of the partonic spectra with fragmentation functions measured in more elementary particle collisions. This allows us to calculate the nuclear modification factor R_{AA} of charged hadrons in central and peripheral Pb + Pb collisions based on both scaled elastic interactions ($K = 3.5$) and the three different LPM approaches. Interestingly, we find that the scaled elastic interactions show a realistic suppression of hadron spectra both in central and peripheral collisions, whereas the radiative interactions from the different LPM approaches, calibrated to the AMY energy loss in the static medium case, lead to a too strong energy loss and thereby an unrealistic suppression of the hadronic spectra. This finding of a too strong radiative energy loss from AMY is supported by other models calculating the R_{AA} from AMY emission rates in hydrodynamical simulations. Only after increasing the values of the screening parameters ($X_{\mathrm{LPM}} = 0.3$ and $\xi_{\mathrm{LPM}} = 0.05$) together with the consideration of a running QCD coupling, both effective LPM approaches, θ-LPM and stochastic LPM, are able to explain the measured hadronic suppression at LHC. Furthermore, the finite formation time and thereby the different path-length dependence of radiative energy loss in the stochastic LPM approach leads to a slightly better agreement for the R_{AA} in peripheral collisions in contrast to the path-length independent approaches θ-LPM and AMY. However, neither of the different employed methods for jet energy loss can reproduce the elliptic flow at high transverse momentum.

Furthermore, we compared the different LPM approaches by simulating the medium modification of reconstructed jets in $\sqrt{s_{\mathrm{NN}}} = 2.76\,\mathrm{TeV}$ Pb + Pb collisions at LHC. To this end, parton showers generated by the PYTHIA are evolved within the expanding BAMPS medium while employing the same screening parameters as in the previous single hadron R_{AA} study. We could demonstrate that an inclusion of recoiling partons is essential for describing the suppression reconstructed jets in each of the different approaches. Instead of an instantaneous thermalization of the scattered medium particles, the deposited energy of the parton shower remains close to the jet axis and thereby counteracts the jet energy loss. This is in agreement with other studies considering medium recoil for the reconstructed jets [EZ16a]. Furthermore, although both effective LPM approaches, θ-LPM and stochastic LPM, were capable for explaining the suppression of single hadron spectra, the stochastic LPM slightly better describes the suppression of reconstructed jets at the employed cone radii $R = 0.2$ and $R = 0.4$. Interestingly, also the scaled elastic interactions explain the measured jet suppression. This indicates that rather the scattering rate instead of the kinematic processes determines the jet energy loss. Again, due to the strong radiative energy loss the AMY result overestimates the suppression of reconstructed jets.

As we found in previous studies, the momentum imbalance between the leading reconstructed jets is rather insensitive to the underlying jet energy loss mechanism but is mainly determined by the asymmetry given in the initial state of the collision.

By calculating the jet shapes $\rho(r)$, which measure the momentum distribution around the jet axis, we find that the modification of jets mainly concerns the outer region of the jets. At these large angle, a strong enhancement of momentum can be found in the various choices of microscopic interactions, whereas the inner core of the jets is almost unmodified. While this unmodified inner core is in agreement with experimental data, our calculations overestimate the enhancement at large angles.

Finally, we conclude this summary by Fig. 8.1, where we show a sketch of the words most frequently used within this work.

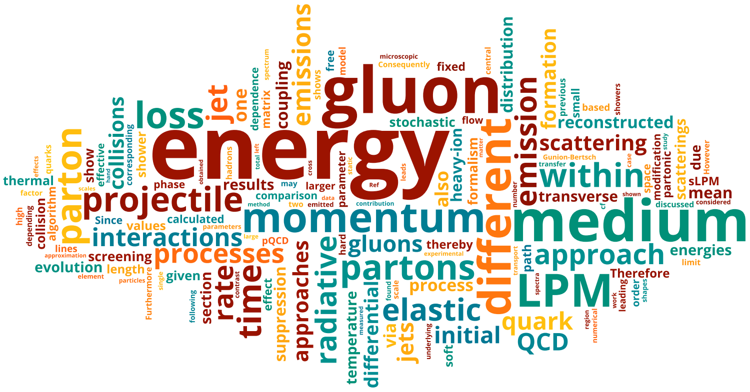

Figure 8.1: Sketch of the words most frequently used in this work. The size of the each word depicts the number of occurrences. The illustration was created by "Wordle" (`http://www.wordle.net`).

8.2 Outlook

In this section we would like to give suggestions for further studies regarding the partonic transport approach BAMPS with an emphasize on jet quenching observables. Some of this projects are already planned or undergoing and we expect their results in the near future.

In the course of this work, we found that many of the investigated observables can be explained by scaled $2 \to 2$ interactions. Furthermore, when comparing the elastic $2 \to 2$ interactions of gluons during their formation time in the stochastic LPM approach, we found that the scatterings from Debye-screened leading-order pQCD are different to the corresponding interactions calculated by thermal field theory in the hard-thermal-loop approximation. These different elastic interactions then lead to a different LPM suppression (and emission rates) between the stochastic LPM and the AMY formalism. A similar discrepancy was obtained in other studies within BAMPS [Uph+11; Uph13; Uph+14] comparing the elastic scatterings of heavy quarks from leading-order pQCD with full HTL calculations. In these studies the energy loss of heavy quarks from Debye-screened pQCD was then calibrated to the HTL results by introducing a fudge factor $\kappa \approx 0.2$ in front of the Debye masses. In principle, such a study would be also conceivable for the light parton flavor sector. An other way for improving the elastic $2 \to 2$ interactions within BAMPS could be an approach similar to Ref. [KXB18b], where the elastic scatterings are separated based on their underlying momentum transfer $\hat{t}$. While hard momentum transfers ($\hat{t} \gtrapprox m_D^2$) are treated via leading-order pQCD matrix elements without Debye-screening, the soft part of the distribution is considered by diffusion processes in a Langevin approach. In order to estimate the potential consequences of such a study for the BAMPS framework, a first step could be a replacement of the microscopic scatterings within BAMPS by the thermal scattering rate given in Eq. (5.67) on page 85. This would be similar to the replacement of the microscopic $2 \leftrightarrow 3$ processes by the $1 \leftrightarrow 2$ processes from AMY. However, as in the AMY case, such an implementation is in principle only valid in thermal systems and its application in non-equilibrium situations is at least questionable.

When discussing the current modeling of parton showers within BAMPS, we mentioned that vacuum $1 \to 2$ processes and in-medium Bremsstrahlung processes should, in principle, occur simultaneously in nature. However, at the moment a simulation of vacuum $1 \to 2$ processes is not possible within BAMPS since we assume that the partons are massless. Therefore one would need to introduce the concept of virtuality into BAMPS and simulate a Monte-Carlo evolution of this virtuality via $1 \to 2$ splittings as in PYTHIA. Based on Sudakov factors one could calculate the probability when and where the next vacuum splitting of the shower partons should occur. Furthermore, also coherence effects between the vacuum and medium-induced gluon radiation need further considerations. Such a treatment could benefit from other approaches studying the interplay between vacuum splitting, elastic scatterings and medium-induced gluon radiation [Zap08; Zap14]. However, it is questionable whether the application of on-shell transport for partons with virtuality is still valid or one needs to consider off-shell transport given by the Kadanoff-Baym equation, for which solutions are still hard to find.

One major drawback of the Boltzmann description of parton interactions within BAMPS, is the lack of a microscopic description for the QCD phase transition between partons and hadrons:

- At high parton energies, fragmentation functions provide a reliable description of hadronization processes, at least for parton spectra. However, when applying fragmentation functions, any microscopic information from which parton the respective hadron emerges is lost. This circumstance prohibits the application of fragmentation functions to studies of reconstructed jets, which are reconstructed on an event-by-event basis. A possible improvement for this situation could be a Monte-Carlo formulation of the fragmentation processes. Based on the probability $D_i^h(z, Q^2)$, partons then microscopically split into hadrons with energies and momenta given by z. One key question in such a study would be how to microscopically conserve energy and momentum at each splitting. For achieving this, a comparison between hadron spectra obtained either via fragmentation functions or via a microscopic fragmentation could be useful.

- A similar description like fragmentation functions does not exist for soft partons as found in the bulk medium of a heavy-ion collision. Recently, there are first efforts in our group for formulating a description for microscopically hadronizing soft partons. By clustering partons based on their distance in configuration and momentum space, first preliminary results were obtained while satisfying common conservation laws as, e.g., entropy maximization. It remains to be seen how such a hadronization prescription affects our results regarding bulk medium observables as the elliptic flow v_2.

Especially flow observables as v_2, v_3, … are supposed to be highly sensitive to fluctuations in the initial state of a heavy-ion collision. At the moment, these fluctuations are not considered within the BAMPS framework but one assumes smooth initial distributions. One recent way to consider fluctuations in the initial state is the combination of an initial state based on Yang-Mills dynamics (IP-Glasma) with a subsequent evolution within BAMPS for the simulation of high energy $\mathrm{p+A}$ collisions [Gre+17a]. Such a study could also be done for the case of heavy-ion collisions, which would provide quantitative answers to the role of fluctuations for flow observables in the BAMPS framework.

Finally, the *run II* of the LHC program was recently finished, in which the center-of-momentum energy is nearly doubled to $\sqrt{s_{\mathrm{NN}}} = 5.02\,\mathrm{TeV}$. Although we expect from a theoretical perspective only minor, quantitative changes in terms of bulk medium properties as, e.g., temperature or density, the higher collision energy allows an increased production probability of jet events with larger transverse momenta $p_\perp$. This increased production probability then allows the experiments to study more differential jet quenching observables at higher accuracies. Among such observables are both inter- and intra-jet observables as, e.g., the modification of fragmentation functions of reconstructed jets or the “golden channel” of jet quenching, namely γ+jet or Z-boson+jet correlations. Furthermore, we expect also for the future further jet quenching studies in heavy-ion experiments at various collision energies. Therefore we suggest to confront the calculations presented in this work with these future studies and further constrain their underlying assumptions.

A Partonic processes at leading-order QCD

As we have seen in Chapters 2 and 3, Feynman diagrams are a comprehensible notation for the perturbative expansion of the QCD Lagrangian in Eq. (2.1). For completeness, we give in this chapter an overview about the Feynman diagrams of the different binary 2 → 2 processes employed in this thesis and their underlying matrix elements at leading-order QCD, either from vacuum QCD or after Debye-screening the internal propagators. From these matrix elements one can calculate both the differential cross section $\mathrm{d}\sigma/\mathrm{d}\hat{t}$ via

$$\frac{\mathrm{d}\sigma}{\mathrm{d}\hat{t}} = \frac{1}{16\pi\hat{s}^2}\left|\overline{\mathcal{M}}\right|^2_{A,B\to 1,2}, \tag{A.1}$$

as given in Eq. (3.4) on page 26, and the total cross section via

$$\sigma = \int\limits_{-\hat{s}}^{0} \mathrm{d}\hat{t}\,\frac{\mathrm{d}\sigma}{\mathrm{d}\hat{t}}\,. \tag{A.2}$$

In the following we cite the matrix elements from Refs. [PS95; CKR77] and the appendices of Ref. [Foc11; Uph13], where such comparisons were already done before.

Processes $\mathrm{gg} \to \mathrm{X}$

Process $\mathrm{gg} \to \mathrm{gg}$ (Fig. A.1)

Vacuum matrix element:

$$\left|\overline{\mathcal{M}}\right|^2_{\mathrm{gg}\to\mathrm{gg}} = 72\pi^2\alpha_s^2\left[3 - \frac{\hat{t}\hat{u}}{\hat{s}^2} - \frac{\hat{s}\hat{u}}{\hat{t}^2} - \frac{\hat{s}\hat{t}}{\hat{u}^2}\right] \tag{A.3a}$$

Debye-screened matrix element:

$$\left|\overline{\mathcal{M}}\right|^2_{\mathrm{gg}\to\mathrm{gg}} = 72\pi^2\alpha_s^2\left[3 - \frac{\hat{t}\hat{u}}{\left(\hat{s}+m_D^2\right)^2} - \frac{\hat{s}\hat{u}}{\left(\hat{t}-m_D^2\right)^2} - \frac{\hat{s}\hat{t}}{\left(\hat{u}-m_D^2\right)^2}\right] \tag{A.3b}$$

Process $\mathrm{gg} \to q\bar{q}$ (Fig. A.2)

Vacuum matrix element:

$$\left|\overline{\mathcal{M}}\right|^2_{\mathrm{gg}\to q\bar{q}} = 6\pi^2\alpha_s^2\left[\frac{4}{9}\left(\frac{\hat{t}\hat{u}}{\hat{t}^2} + \frac{\hat{t}\hat{u}}{\hat{u}^2}\right) + 2\frac{\hat{t}\hat{u}}{\hat{s}^2} + \frac{\hat{t}\hat{u}}{\hat{s}\hat{t}} + \frac{\hat{t}\hat{u}}{\hat{s}\hat{u}}\right] \tag{A.4a}$$

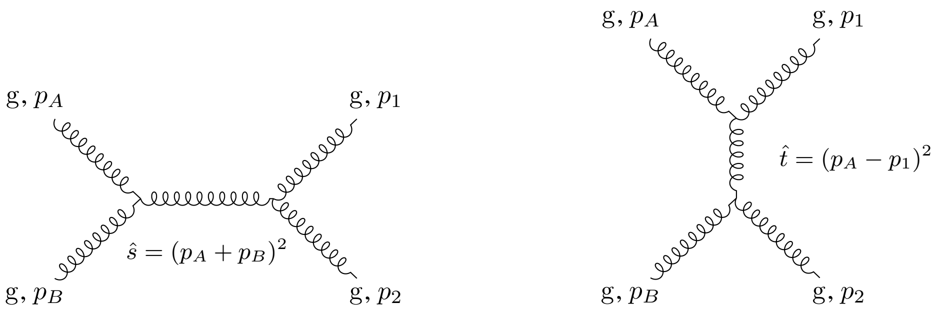

(a) $\hat{s}$-channel **(b)** $\hat{t}$-channel

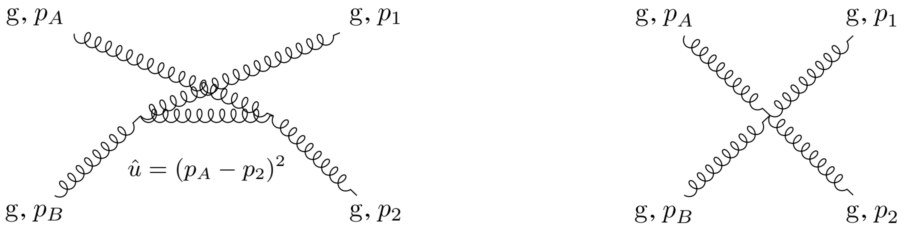

(c) $\hat{u}$-channel **(d)** four gluon-channel

Figure A.1: Scattering channels of the process $gg \to gg$

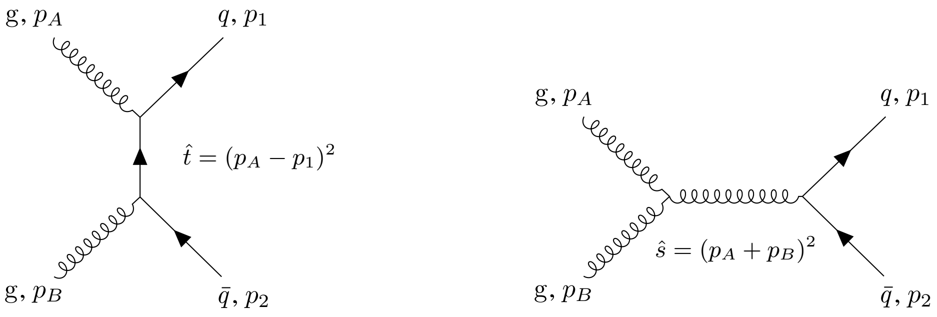

(a) $\hat{s}$-channel **(b)** $\hat{t}$-channel

Figure A.2: Scattering channels of the process $gg \to q\bar{q}$

Debye-screened matrix element:

$$\left|\overline{\mathcal{M}}\right|^2_{gg\to q\bar{q}} = 6\pi^2\alpha_s^2 \left[\frac{4}{9}\left(\frac{\hat{t}\hat{u}}{\left(\hat{t} - m_q^2\right)^2} + \frac{\hat{t}\hat{u}}{\left(\hat{u} - m_q^2\right)^2} \right) + 2\frac{\hat{t}\hat{u}}{\left(\hat{s} + m_D^2\right)^2} + \frac{\hat{t}\hat{u}}{(\hat{s} + m_D^2)(\hat{t} - m_q^2)} + \frac{\hat{t}\hat{u}}{(\hat{s} + m_D^2)(\hat{u} - m_q^2)} \right] \tag{A.4b}$$

Process $gq \to gq$ (Fig. A.3)

Vacuum matrix element:

$$\left|\overline{\mathcal{M}}\right|^2_{gq\to gq} = 16\pi^2\alpha_s^2 \left[-\frac{4}{9}\left(\frac{\hat{s}\hat{u}}{\hat{s}^2} + \frac{\hat{s}\hat{u}}{\hat{u}^2} \right) - 2\frac{\hat{s}\hat{u}}{\hat{t}^2} - \frac{\hat{s}\hat{u}}{\hat{t}\hat{s}} - \frac{\hat{s}\hat{u}}{\hat{t}\hat{u}} \right] \tag{A.5a}$$

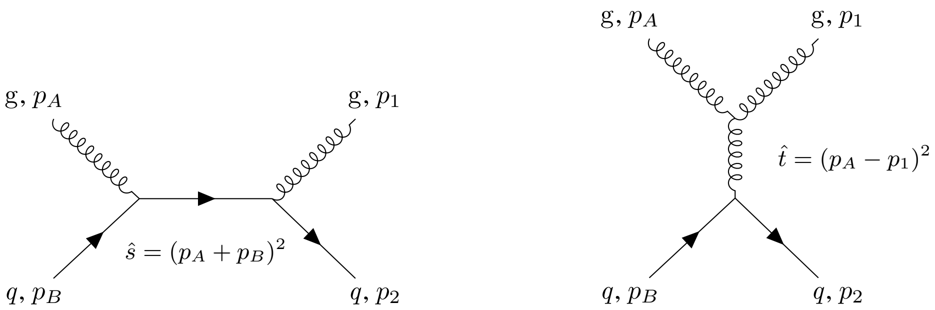

(a) $\hat{s}$-channel **(b)** $\hat{t}$-channel

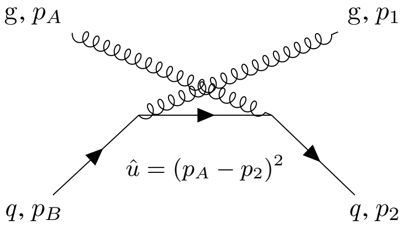

(c) $\hat{u}$-channel

Figure A.3: Scattering channels of the process $g\,q \to g\,q$

Debye-screened matrix element:

$$\overline{|\mathcal{M}|}^2_{gq \to gq} = 16\pi^2\alpha_s^2 \left[-\frac{4}{9}\left(\frac{\hat{s}\hat{u}}{\left(\hat{s} + m_q^2\right)^2} + \frac{\hat{s}\hat{u}}{\left(\hat{u} - m_q^2\right)^2} \right) \right.$$
$$\left. -2\frac{\hat{s}\hat{u}}{\left(\hat{t} - m_D^2\right)^2} - \frac{\hat{s}\hat{u}}{\left(\hat{t} - m_D^2\right)\left(\hat{s} + m_q^2\right)} - \frac{\hat{s}\hat{u}}{\left(\hat{t} - m_D^2\right)\left(\hat{u} - m_q^2\right)} \right] \quad \text{(A.5b)}$$

Process $qq \to qq$ (Fig. A.4)

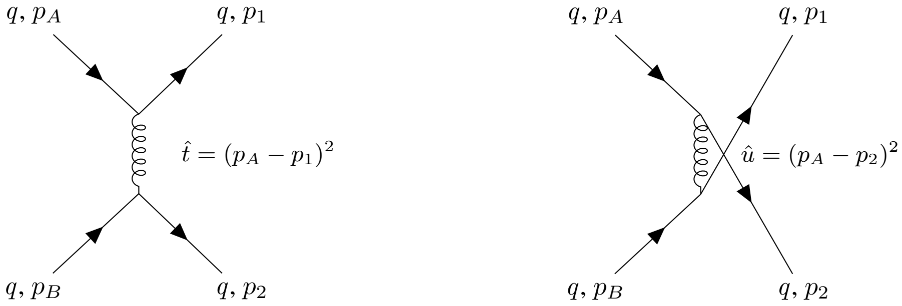

(a) $\hat{t}$-channel **(b)** $\hat{u}$-channel

Figure A.4: Scattering channels of the process $q\,q \to q\,q$

Vacuum matrix element:

$$\overline{|\mathcal{M}|}^2_{qq \to qq} = \frac{64\pi^2\alpha_s^2}{9}\left[\frac{\hat{s}^2 + \hat{u}^2}{\hat{t}^2} + \frac{\hat{s}^2 + \hat{t}^2}{\hat{u}^2} - \frac{2}{3}\frac{\hat{s}^2}{\hat{t}\hat{u}} \right] \quad \text{(A.6a)}$$

Debye-screened matrix element:

$$|\overline{\mathcal{M}}|^2_{qq\to qq} = \frac{64\pi^2\alpha_s^2}{9}\left[\frac{\hat{s}^2+\hat{u}^2}{\left(\hat{t}-m_D^2\right)^2} + \frac{\hat{s}^2+\hat{t}^2}{\left(\hat{u}-m_D^2\right)^2} - \frac{2}{3}\frac{\hat{s}^2}{\left(\hat{t}-m_D^2\right)\left(\hat{u}-m_D^2\right)}\right] \quad \text{(A.6b)}$$

Process $qq' \to qq'$ or $q\bar{q}' \to q\bar{q}'$ (Fig. A.5)

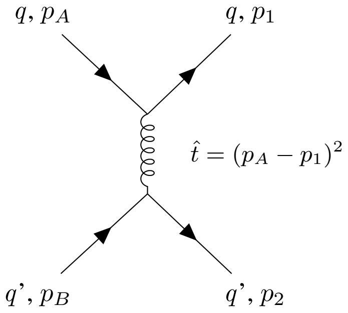

(a) $\hat{t}$-channel

Figure A.5: Scattering channel of the process $qq' \to qq'$

Vacuum matrix element:

$$|\overline{\mathcal{M}}|^2_{qq'\to qq'} = 16\pi^2\alpha_s^2\left[-\frac{4}{9}\left(\frac{\hat{s}\hat{u}}{\hat{s}^2}+\frac{\hat{s}\hat{u}}{\hat{u}^2}\right) - 2\frac{\hat{s}\hat{u}}{\hat{t}^2} - \frac{\hat{s}\hat{u}}{\hat{t}\hat{s}} - \frac{\hat{s}\hat{u}}{\hat{t}\hat{u}}\right] \quad \text{(A.7a)}$$

Debye-screened matrix element:

$$\begin{aligned}|\overline{\mathcal{M}}|^2_{qq'\to qq'} = 16\pi^2\alpha_s^2 & \left[-\frac{4}{9}\left(\frac{\hat{s}\hat{u}}{\left(\hat{s}+m_q^2\right)^2} + \frac{\hat{s}\hat{u}}{\left(\hat{u}-m_q^2\right)^2}\right)\right.\\ & \left. -2\frac{\hat{s}\hat{u}}{\left(\hat{t}-m_D^2\right)^2} - \frac{\hat{s}\hat{u}}{\left(\hat{t}-m_D^2\right)\left(\hat{s}+m_q^2\right)} - \frac{\hat{s}\hat{u}}{\left(\hat{t}-m_D^2\right)\left(\hat{u}-m_q^2\right)}\right] \quad \text{(A.7b)}\end{aligned}$$

Processes $q\bar{q} \to$ X

Process $q\bar{q} \to q\bar{q}$ (Fig. A.6)

Vacuum matrix element:

$$|\overline{\mathcal{M}}|^2_{q\bar{q}\to q\bar{q}} = 16\pi^2\alpha_s^2\left[-\frac{4}{9}\left(\frac{\hat{s}\hat{u}}{\hat{s}^2}+\frac{\hat{s}\hat{u}}{\hat{u}^2}\right) - 2\frac{\hat{s}\hat{u}}{\hat{t}^2} - \frac{\hat{s}\hat{u}}{\hat{t}\hat{s}} - \frac{\hat{s}\hat{u}}{\hat{t}\hat{u}}\right] \quad \text{(A.8a)}$$

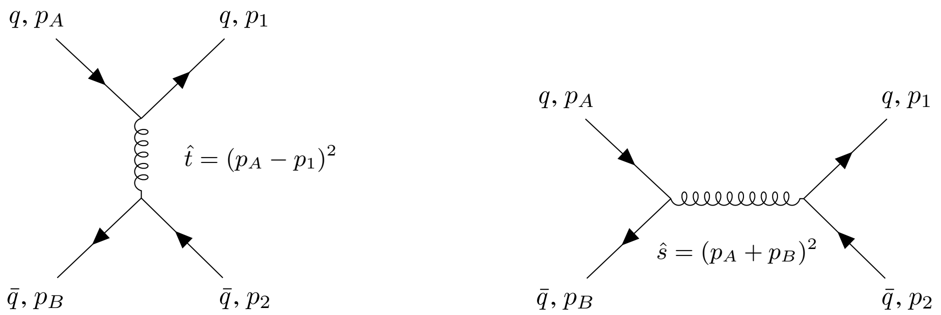

(a) $\hat{t}$-channel **(b)** $\hat{s}$-channel

Figure A.6: Scattering channels of the process $q\bar{q} \to q\bar{q}$

Debye-screened matrix element:

$$|\overline{\mathcal{M}}|^2_{q\bar{q}\to q\bar{q}} = 16\pi^2\alpha_s^2\left[-\frac{4}{9}\left(\frac{\hat{s}\hat{u}}{\left(\hat{s}+m_q^2\right)^2}+\frac{\hat{s}\hat{u}}{\left(\hat{u}-m_q^2\right)^2}\right)\right.$$
$$\left.-2\frac{\hat{s}\hat{u}}{\left(\hat{t}-m_D^2\right)^2}-\frac{\hat{s}\hat{u}}{\left(\hat{t}-m_D^2\right)\left(\hat{s}+m_q^2\right)}-\frac{\hat{s}\hat{u}}{\left(\hat{t}-m_D^2\right)\left(\hat{u}-m_q^2\right)}\right] \tag{A.8b}$$

Process $q\bar{q} \to \mathrm{gg}$ (Fig. A.7)

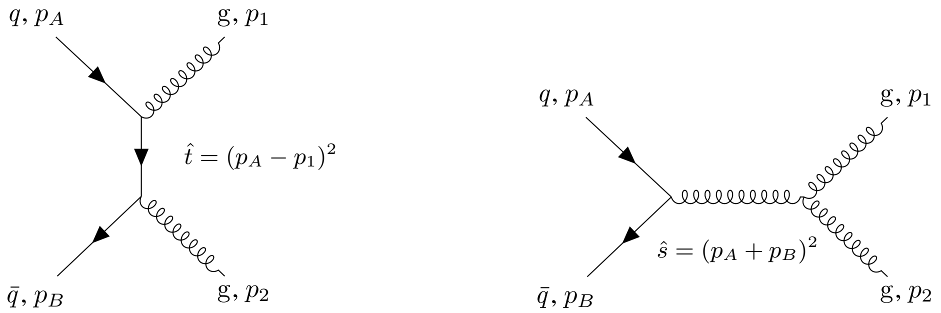

(a) $\hat{t}$-channel **(b)** $\hat{s}$-channel

Figure A.7: Scattering channels of the process $q\bar{q} \to \mathrm{gg}$

Vacuum matrix element:

$$|\overline{\mathcal{M}}|^2_{q\bar{q}\to \mathrm{gg}} = 16\pi^2\alpha_s^2\left[-\frac{4}{9}\left(\frac{\hat{s}\hat{u}}{\hat{s}^2}+\frac{\hat{s}\hat{u}}{\hat{u}^2}\right)-2\frac{\hat{s}\hat{u}}{\hat{t}^2}-\frac{\hat{s}\hat{u}}{\hat{t}\hat{s}}-\frac{\hat{s}\hat{u}}{\hat{t}\hat{u}}\right] \tag{A.9a}$$

Debye-screened matrix element:

$$|\overline{\mathcal{M}}|^2_{q\bar{q}\to \mathrm{gg}} = 16\pi^2\alpha_s^2\left[-\frac{4}{9}\left(\frac{\hat{s}\hat{u}}{\left(\hat{s}+m_q^2\right)^2}+\frac{\hat{s}\hat{u}}{\left(\hat{u}-m_q^2\right)^2}\right)\right.$$
$$\left.-2\frac{\hat{s}\hat{u}}{\left(\hat{t}-m_D^2\right)^2}-\frac{\hat{s}\hat{u}}{\left(\hat{t}-m_D^2\right)\left(\hat{s}+m_q^2\right)}-\frac{\hat{s}\hat{u}}{\left(\hat{t}-m_D^2\right)\left(\hat{u}-m_q^2\right)}\right] \tag{A.9b}$$

Process $q\bar{q} \to q'\bar{q}'$ (Fig. A.8)

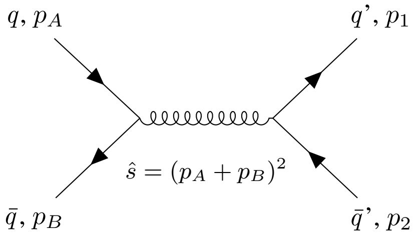

(a) $\hat{s}$-channel

Figure A.8: Scattering channels of the process $q\bar{q} \to q'\bar{q}'$

Vacuum matrix element:

$$\left|\overline{\mathcal{M}}\right|^2_{q\bar{q}\to q'\bar{q}'} = 16\pi^2\alpha_s^2\left[-\frac{4}{9}\left(\frac{\hat{s}\hat{u}}{\hat{s}^2}+\frac{\hat{s}\hat{u}}{\hat{u}^2}\right)-2\frac{\hat{s}\hat{u}}{\hat{t}^2}-\frac{\hat{s}\hat{u}}{\hat{t}\hat{s}}-\frac{\hat{s}\hat{u}}{\hat{t}\hat{u}}\right] \tag{A.10a}$$

Debye-screened matrix element:

$$\begin{aligned}\left|\overline{\mathcal{M}}\right|^2_{q\bar{q}\to q'\bar{q}'} = 16\pi^2\alpha_s^2 &\left[-\frac{4}{9}\left(\frac{\hat{s}\hat{u}}{\left(\hat{s}+m_q^2\right)^2}+\frac{\hat{s}\hat{u}}{\left(\hat{u}-m_q^2\right)^2}\right)\right. \\ &\left.-2\frac{\hat{s}\hat{u}}{\left(\hat{t}-m_D^2\right)^2}-\frac{\hat{s}\hat{u}}{\left(\hat{t}-m_D^2\right)\left(\hat{s}+m_q^2\right)}-\frac{\hat{s}\hat{u}}{\left(\hat{t}-m_D^2\right)\left(\hat{u}-m_q^2\right)}\right]\end{aligned} \tag{A.10b}$$

B Details about parton evolution in the sLPM approach

In this section we discuss possible consequences for the stochastic LPM method when we allow also a non-eikonal evolution in the parton energies. Different to the θ-LPM approach the emitted gluons from the stochastic LPM method scatter themselves elastically during their formation and thereby modify their coherence time. We showed that this procedure not only introduces a non-linear path-length dependence of the radiative energy loss but also coherently suppresses the gluon emission rate (cf. Section 5.3). However, as we have seen in Section 6.1 the elastic interactions of a parton may also lead to an elastic energy loss. Consequently, loosening the eikonal approximation of the stochastic LPM not only affects the projectile energy as in the θ-LPM approach but also may modify the resulting gluon emission spectrum.

Non-eikonal gluon energy during formation time

In Section 5.3 we assumed that for the gluon energy $\omega \gg k_\perp, q_\perp$ holds. Hence the elastic scatterings can be approximated by transverse kicks that keep the gluon energy unchanged and only deflect the gluons during their formation time, which can be characterized by the momentum broadening parameter $\hat{q}$. The energy of the gluon emission ω is then determined already in the initial $2 \to 3$ process. If we loose this approximation, ω is not longer constant but may be modified by elastic gluon interactions during the formation time. As an example, let us assume a constant transverse momentum transfer $q_\perp^2$ per elastic mean free path. From geometrical reasons one can infer that the energy of a gluon after the $i+1$-th elastic scattering is then

$$\omega_{i+1} = \sqrt{1 + \frac{q_\perp^2}{\omega_i^2}}\,\omega_i\,, \tag{B.1}$$

where ω_i is the energy of the gluon before the scattering. Since $q_\perp^2 > 0$ this leads to an energy gain of the gluons by each elastic scattering. Hence an elastic scattering increases both the transverse momentum and the energy of a gluon during the formation time. Both together then determines the formation time of the gluon emission.

We compare in Fig. B.1 the differential emission rate $\mathrm{d}\Gamma/\mathrm{d}\omega$ of an eikonal quark projectile with energy $E = 25\,\mathrm{T}$ or $E = 250\,\mathrm{T}$ for the case of a constant gluon energy (dashed lines) with the corresponding case of a variable gluon energy (solid lines). Gluon emissions with higher ω are almost unaffected from the choice of ω-treatment since the energy gain by an elastic interactions occurs in the softer thermal energy region. In contrast, the softer emission rate differs between the two assumptions: While at the previous constant ω case the emission rate reaches up to very soft $\omega < 1 \cdot 10^{-3}\,\mathrm{E}$, the softer gluons of the variable ω case thermalize and thereby built a maximum at $\omega \sim \mathcal{O}(T)$. Furthermore, the thermalization of softer gluons lead also, on average, to a longer formation time via

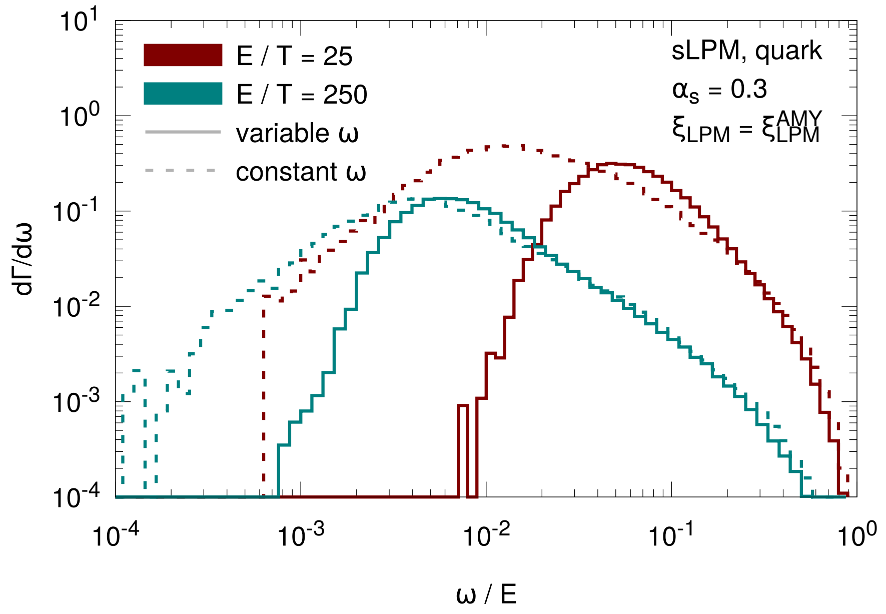

Figure B.1: Differential emission rate $\mathrm{d}\Gamma/\mathrm{d}\omega$ of a quark projectile with energy E within the stochastic LPM approach for either eikonal gluons with constant energy ω (solid lines) or non-eikonal gluons with varying energy resulting from energy loss of the radiated gluon during the formation time (dashed lines).

$\tau_f = \omega/k_\perp^2$ due to the energy gain. The actual shape for the emission rate above $\omega > \mathcal{O}(T)$ is however unaffected by the specific choice of gluon energy treatment and is determined by the presented stochastic LPM suppression. Therefore neglecting the evolution of harder gluon emissions seems to be justified for the differential emission rate.

Since the difference between both choices, constant or variable ω, can only be found at very soft gluon energies, the resulting radiative energy loss is not affected by this choice. This can be seen in Fig. B.2 where we show the E-dependence (left) and L-dependence (right) of the differential energy loss $\mathrm{d}E/\mathrm{d}x$ for a quark projectile traversing a medium with temperature T and length L either with constant ω (point symbols) or variable ω during the formation time (line symbols). Whether the gluon energy is changed after an elastic scattering or not is not recognizable in the resulting differential energy loss since the radiative energy loss is dominated at all medium lengths and projectile energies by the hard region of gluon emissions.

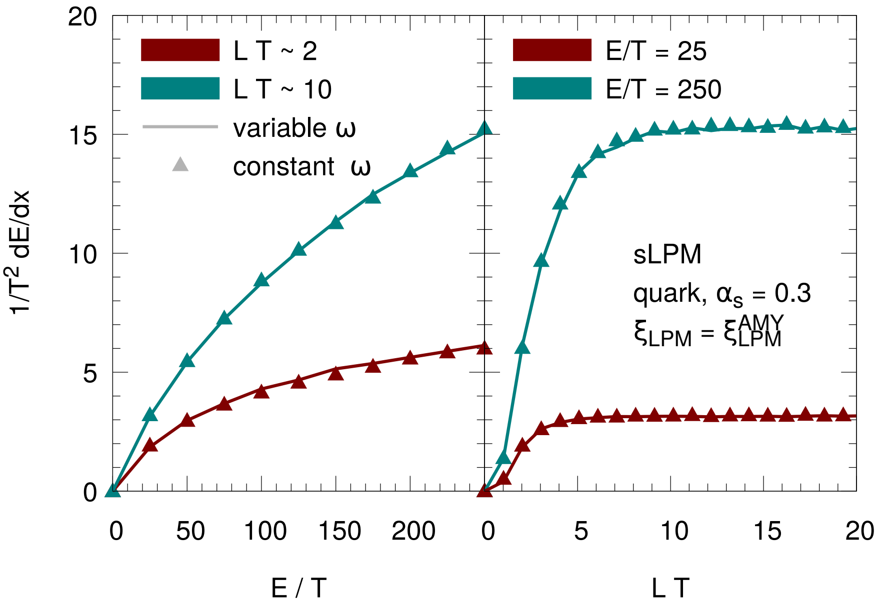

Figure B.2: Differential radiative energy loss $\mathrm{d}E/\mathrm{d}x$ of a quark projectile with energy E within the stochastic LPM approach for either eikonal gluons with constant energy ω (triangles) or non-eikonal gluons with varying energy resulting from energy loss of the radiated gluon during the formation time (lines). The left panel shows the dependence on the projectile energy E, whereas the right panel depicts the length L dependence of the energy loss.

Subtraction of gluon energy/momentum in the non-eikonal sLPM approach

Different to the θ-LPM approach, where a gluon emission occurs instantaneously, the gluon emissions in the stochastic LPM approach are extended over a finite formation time. During this formation time the projectile and the proposed gluon are formally speaking indistinguishable. However, when allowing evolving projectile energies one has to decide when to subtract the radiated gluon energy and/or momentum from the parent parton. In principle, there are two different possibilities: (i) one subtracts the gluon momentum from the initial $2 \to 3$ process after the gluon successfully finishes its formation time or (ii) one subtracts the gluon momentum directly at the initial $2 \to 3$ Bremsstrahlung process. If the gluon is stochastically suppressed by $1/N_{\text{coh}}$ the gluon emission is either discarded in method (i) or the gluon momentum is added back to the parent parton in method (ii). While method (i) violates in principle energy and momentum conservation during the formation time, method (ii) has the drawback that if the gluon emission is finally discarded the projectile has traveled with an underestimated energy during the formation time. Furthermore, method (ii) violates locality since gluons are directly distinguished from the parent parton although they should be indistinguishable.

Furthermore, in the stochastic LPM approach with evolving projectile energy one has the choice *how* to subtract the gluon from its parent parton. One choice would be to subtract the 3-momentum of the emitted gluon from the parent parton as it was sampled at the initial $2 \to 3$ process and calculate the energy of the parent parton as usual for a massless parton on the mass shell ($E^2 = \vec{\mathrm{p}}^2$). Another choice would be to only subtract the gluon energy from the parent parton as given at the initial $2 \to 3$ process and rescale the outgoing parton

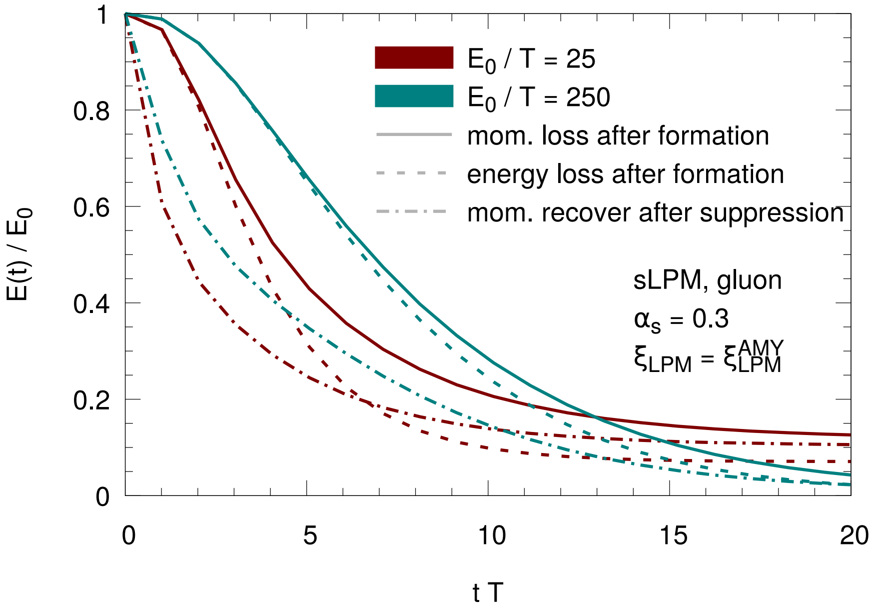

Figure B.3: Different time evolutions of the projectile energy E of a gluon projectile depending on the specific choice of non-eikonal treatment in the stochastic LPM approach.

momenta. While the former prefers the conservation of momentum, the latter ensures the conservation of energy.

In order to quantify the differences between the discussed possibilities for subtracting the gluon energy/momentum from the parent parton, Fig. B.3 shows the time evolution of the mean projectile energy $E(t)$ based on the different discussed subtraction/addition methods for a gluon projectile with initial energies $E_0 = 25\,\mathrm{T}$ or $E_0 = 250\,\mathrm{T}$. While the solid line depicts the evolution in which the gluon *momenta* are subtracted after successfully forming (method (i) above), the dashed line corresponds to the case where the gluon *energy* is subtracted after the formation time. At early times both methods show a similar evolution. With increasing evolution time, the “energy loss” method shows a stronger energy loss than the momentum loss method. Furthermore, we depict by the dash-dotted curve the algorithm where the gluon momentum is subtracted directly in the beginning of the radiative process (method (ii) above). This leads to a much stronger energy loss in the beginning since the gluon momenta are subtracted directly from the parent parton without waiting for the finite formation time. For the results within this work, we choose the method of *momentum* loss *after* successfully formation of the gluon as the default stochastic LPM implementation within BAMPS.

C Numerical calculation of AMY emission kernel

In this section we present a solution of the integral equation Eq. (5.94) on page 116 underlying the AMY formalism for gluon emissions introduced in Chapter 5. For this solution we follow the considerations of Refs. [Aur+02; AGZ02; Abr+14] and adapt them to our notation where it is necessary.

We have seen in Section 5.4 that the emission rate $\mathrm{d}\Gamma/\mathrm{d}k$ consists of prefactors counting the degeneracies of quarks and gluons, respectively, the $1 \to 2$ splitting functions from the DGLAP formalism, and a kernel

$$\mathcal{K}(p,k) := \int \frac{\mathrm{d}^2\vec{\mathbf{h}}}{(2\pi)^2} 2\vec{\mathbf{h}} \cdot \operatorname{Re} \vec{\mathbf{F}}(\vec{\mathbf{h}}, p-k, k)\,, \tag{C.1}$$

resumming ladder diagrams of the interactions of gluons and quarks with the thermal bath during their formation time.

The integral equation Eq. (5.94) on page 116 defining the function $\vec{\mathbf{F}}(\vec{\mathbf{h}}, p-k, k)$ then reads

$$\begin{aligned}2\vec{\mathbf{h}} = i\delta E(\vec{\mathbf{h}}, p-k, k)\vec{\mathbf{F}}(\vec{\mathbf{h}}) + g_s^2 \int \frac{\mathrm{d}^2 q_\perp}{(2\pi)^2} C(\vec{\mathbf{q}}_\perp) \Big\{ &(C_s - C_\mathrm{A}/2)[\vec{\mathbf{F}}(\vec{\mathbf{h}}) - \vec{\mathbf{F}}(\vec{\mathbf{h}} - k\,\vec{\mathbf{q}}_\perp)] \\ &+ (C_\mathrm{A}/2)[\vec{\mathbf{F}}(\vec{\mathbf{h}}) - \vec{\mathbf{F}}(\vec{\mathbf{h}} + p\,\vec{\mathbf{q}}_\perp)] \\ &+ (C_\mathrm{A}/2)[\vec{\mathbf{F}}(\vec{\mathbf{h}}) - \vec{\mathbf{F}}(\vec{\mathbf{h}} - (p-k)\,\vec{\mathbf{q}}_\perp)] \Big\}\,,\end{aligned} \tag{C.2}$$

where $\delta E(\vec{\mathbf{h}}, p-k, k)$ is the inverse formation time of the emitted parton. After rescaling the quantities $\vec{\mathbf{h}} = p\vec{\mathbf{q}}'_\perp$ and $\vec{\mathbf{F}}\big(p\vec{\mathbf{q}}'_\perp\big) = p\vec{\mathbf{f}}(\vec{\mathbf{q}}'_\perp)$ one obtains

$$\begin{aligned}2\vec{\mathbf{q}}'_\perp = i\delta E(p\vec{\mathbf{q}}'_\perp)\vec{\mathbf{f}}(\vec{\mathbf{q}}'_\perp) + g_s^2 \int \frac{\mathrm{d}^2 q_\perp}{(2\pi)^2} C(\vec{\mathbf{q}}_\perp) \Big\{ &(C_s - C_\mathrm{A}/2)[\vec{\mathbf{f}}(\vec{\mathbf{q}}'_\perp) - \vec{\mathbf{f}}(\vec{\mathbf{q}}'_\perp - x\vec{\mathbf{q}}_\perp)] \\ &+ (C_\mathrm{A}/2)[\vec{\mathbf{f}}(\vec{\mathbf{q}}'_\perp) - \vec{\mathbf{f}}(\vec{\mathbf{q}}'_\perp + \vec{\mathbf{q}}_\perp)] \\ &+ (C_\mathrm{A}/2)[\vec{\mathbf{f}}(\vec{\mathbf{q}}'_\perp) - \vec{\mathbf{f}}(\vec{\mathbf{q}}'_\perp - (1-x)\vec{\mathbf{q}}_\perp)] \Big\}\,,\end{aligned} \tag{C.3}$$

where we omitted the $p-k$ and k dependence of the inverse formation time

$$\delta E(p\vec{\mathbf{q}}'_\perp) = \frac{p q'^2_\perp}{2k(p-k)} + \frac{m_k^2}{2k} + \frac{m_{p-k}^2}{2(p-k)} - \frac{m_p^2}{2p} \tag{C.4}$$

and defined $x = k/p$.

Equation (C.3) can be solved by a Fourier transformation into impact parameter space [Aur+02],

$$\vec{\mathbf{f}}(\vec{\mathbf{b}}) = \int \frac{\mathrm{d}^2 q'_\perp}{(2\pi)^2} e^{i\vec{\mathbf{q}}'_\perp\cdot\vec{\mathbf{b}}}\,\vec{\mathbf{f}}(\vec{\mathbf{q}}'_\perp) \qquad \leftrightarrow \qquad \vec{\mathbf{f}}(\vec{\mathbf{q}}'_\perp) = \int \mathrm{d}^2 b\, e^{-i\vec{\mathbf{q}}'_\perp\cdot\vec{\mathbf{b}}}\,\vec{\mathbf{f}}(\vec{\mathbf{b}})\,. \tag{C.5}$$

For this transformation it will be useful to derive the following relations

$$\begin{aligned}\int \mathrm{d}^2 b\, e^{-i\vec{\mathbf{q}}'_\perp\cdot\vec{\mathbf{b}}}\,\vec{\nabla}\delta^{(2)}(\vec{\mathbf{b}}) &= \underbrace{\int \mathrm{d}^2 b\,\vec{\nabla}\Big(e^{-i\vec{\mathbf{q}}'_\perp\cdot\vec{\mathbf{b}}}\delta^{(2)}(\vec{\mathbf{b}})\Big)}_{\to 0} - \int \mathrm{d}^2 b\,\delta^{(2)}(\vec{\mathbf{b}})(-i\vec{\mathbf{q}}'_\perp)e^{-i\vec{\mathbf{q}}'_\perp\cdot\vec{\mathbf{b}}} \\ &= i\vec{\mathbf{q}}'_\perp\,,\end{aligned} \tag{C.6}$$

and

$$\begin{aligned}\int \mathrm{d}^2 b\, e^{-i\vec{\mathbf{q}}'_\perp\cdot\vec{\mathbf{b}}}\,\Delta\vec{\mathbf{f}}(\vec{\mathbf{b}}) &= \underbrace{\int \mathrm{d}^2 b\,\vec{\nabla}\Big(e^{-i\vec{\mathbf{q}}'_\perp\cdot\vec{\mathbf{b}}}\,\vec{\nabla}\vec{\mathbf{f}}(\vec{\mathbf{b}})\Big)}_{\to 0} - \int \mathrm{d}^2 b\,\big(-i\vec{\mathbf{q}}'_\perp\big)e^{-i\vec{\mathbf{q}}'_\perp\cdot\vec{\mathbf{b}}}\vec{\nabla}\vec{\mathbf{f}}(\vec{\mathbf{b}}) \\ &= i\vec{\mathbf{q}}'_\perp\int \mathrm{d}^2 b\, e^{-i\vec{\mathbf{q}}'_\perp\cdot\vec{\mathbf{b}}}\vec{\nabla}\vec{\mathbf{f}}(\vec{\mathbf{b}}) \\ &= -q'^2_\perp\,\vec{\mathbf{f}}\big(\vec{\mathbf{q}}'_\perp\big)\,.\end{aligned} \tag{C.7}$$

With Eq. (C.7) the Fourier transformation of the inverse formation time then reads

$$\delta E(p\vec{\mathbf{q}}'_\perp)\vec{\mathbf{f}}(\vec{\mathbf{q}}'_\perp) \to \left(-\frac{p}{2k(p-k)}\Delta + \frac{m_k^2}{2k} + \frac{m_{p-k}^2}{2(p-k)} - \frac{m_p^2}{2p}\right)\vec{\mathbf{f}}(\vec{\mathbf{b}})\,. \tag{C.8}$$

Furthermore, for the first term in the $q_\perp$-integration of Eq. (C.3) one can derive

$$\begin{align}&\int \frac{\mathrm{d}^2 q_\perp}{(2\pi)^2}\mathcal{C}(q_\perp)\Big(\vec{\mathbf{f}}(\vec{\mathbf{q}}'_\perp) - \vec{\mathbf{f}}(\vec{\mathbf{q}}'_\perp + \vec{\mathbf{q}}_\perp)\Big) \tag{C.9}\\ &\quad = \int \frac{\mathrm{d}^2 q_\perp}{(2\pi)^2}\mathcal{C}(q_\perp)\Big(\int \mathrm{d}^2 b\, e^{-i\vec{\mathbf{q}}'_\perp\cdot\vec{\mathbf{b}}}\,\vec{\mathbf{f}}(\vec{\mathbf{b}}) - \int \mathrm{d}^2 b\, e^{-i(\vec{\mathbf{q}}'_\perp+\vec{\mathbf{q}}_\perp)\cdot\vec{\mathbf{b}}}\,\vec{\mathbf{f}}(\vec{\mathbf{b}})\Big) \tag{C.10}\\ &\quad = \int \mathrm{d}^2 b\, e^{-i\vec{\mathbf{q}}'_\perp\cdot\vec{\mathbf{b}}}\vec{\mathbf{f}}(\vec{\mathbf{b}})\underbrace{\int \frac{\mathrm{d}^2 q_\perp}{(2\pi)^2}\mathcal{C}(q_\perp)\Big(1 - e^{-i\vec{\mathbf{q}}_\perp\cdot\vec{\mathbf{b}}}\Big)}_{:=D(-m_D\,b)}\,, \tag{C.11}\end{align}$$

where we defined the function $D(-m_D\,b)$ and $C(\vec{\mathbf{q}}_\perp) = \frac{m_D^2}{\vec{\mathbf{q}}_\perp^2\left(\vec{\mathbf{q}}_\perp^2+m_D^2\right)}$ is the Debye-screened collision kernel given in Eq. (5.96) on page 117. Correspondingly, the other two terms in the $q_\perp$-integration can be written as

$$\int \frac{\mathrm{d}^2 q_\perp}{(2\pi)^2}\mathcal{C}(q_\perp)\Big(\vec{\mathbf{f}}(\vec{\mathbf{q}}'_\perp) - \vec{\mathbf{f}}(\vec{\mathbf{q}}'_\perp - x\vec{\mathbf{q}}_\perp)\Big) = \int \mathrm{d}^2 b\, e^{-i\vec{\mathbf{q}}'_\perp\cdot\vec{\mathbf{b}}}\vec{\mathbf{f}}(\vec{\mathbf{b}})D(-m_D x b) \tag{C.12}$$

and

$$\int \frac{\mathrm{d}^2 q_\perp}{(2\pi)^2}\mathcal{C}(q_\perp)\Big(\vec{\mathbf{f}}(\vec{\mathbf{q}}'_\perp) - \vec{\mathbf{f}}(\vec{\mathbf{q}}'_\perp - (1-x)\vec{\mathbf{q}}_\perp)\Big) = \int \mathrm{d}^2 b\, e^{-i\vec{\mathbf{q}}'_\perp\cdot\vec{\mathbf{b}}}\vec{\mathbf{f}}(\vec{\mathbf{b}})D(-m_D(1-x)b)\,. \tag{C.13}$$

In Refs. [Abr+14; Aur+02] it was shown that the D function evaluates to

$$D(b) = \lim_{\epsilon\to 0}\int \frac{\mathrm{d}^2 b}{(2\pi)^2}\frac{1}{(q_\perp^2+\epsilon^2)(q_\perp^2+1)} - e^{-i\vec{\mathbf{q}}_\perp\cdot\vec{\mathbf{b}}}\frac{1}{(q_\perp^2+\epsilon^2)(q_\perp^2+1)} \tag{C.14}$$

$$= \frac{1}{2\pi}(\gamma_E + \log(b/2) + K_0(b))\,, \tag{C.15}$$

where $\gamma_E = \lim_{n\to\infty}(-\log n + \sum_{k=1}^{n}\frac{1}{k}) \approx 0.577$ is the Euler-Mascheroni constant and K_0 is the modified Bessel function of the second kind[Abr+14; Aur+02]. Putting above considerations together one obtains the Fourier transformed integral equation

$$\begin{aligned}-i\vec{\nabla}\delta^{(2)}(\vec{\mathbf{b}}) = i\left(\frac{m_k^2}{2k} + \frac{m_{p-k}^2}{2(p-k)} - \frac{m_p^2}{2p} - \frac{p}{2k(p-k)}\Delta\right)\vec{\mathbf{f}}(\vec{\mathbf{b}})&\\ +g_s^2 T\Big\{(C_s - C_\mathrm{A}/2)D(-m_D\,x\,b)&\\ +(C_\mathrm{A}/2)D(-m_D\,b)&\\ +(C_\mathrm{A}/2)D(-m_D\,(1-x)\,b)\Big\}\vec{\mathbf{f}}(\vec{\mathbf{b}})\,.&\end{aligned} \tag{C.16}$$

One can further exploit the rotational symmetry of the problem in the transverse plane [Aur+02] and define $\vec{\mathbf{f}}(\vec{\mathbf{b}}) = h(\vec{\mathbf{b}})\vec{\mathbf{b}}$ so that follows

$$\Delta_\perp\vec{\mathbf{f}}(\vec{\mathbf{b}}) = \left(\frac{\mathrm{d}^2 h}{\mathrm{d}^2 b} + \frac{3}{b}\frac{\mathrm{d}h}{\mathrm{d}b}\right)\vec{\mathbf{b}}\,, \tag{C.17}$$

and the final one-dimensional differential equation then reads

$$\begin{aligned}0 = i\left(\frac{m_k^2}{2k} + \frac{m_{p-k}^2}{2(p-k)} - \frac{m_p^2}{2p} - \frac{p}{2k(p-k)}\left(\frac{\mathrm{d}^2}{\mathrm{d}^2 b} + \frac{3}{b}\frac{\mathrm{d}}{\mathrm{d}b}\right)\right)h(b)&\\ +g_s^2 T\Big\{(C_s - C_\mathrm{A}/2)D(-m_D\,x\,b)&\\ +(C_\mathrm{A}/2)D(-m_D\,b)&\\ +(C_\mathrm{A}/2)D(-m_D\,(1-x)\,b)\Big\}h(b)&\end{aligned} \tag{C.18}$$

The general solution of above ODE can be written as $h(b) = c_+ e^{\lambda b} + c_- e^{-\lambda b}$ and obtained numerically[1]. In order to arrive at our final result for the emission kernel $\mathcal{K}(p,k)$ one can

---

[1] In the BAMPS framework the numerical solution for the ODE is obtained via routines from the GSL computing library [Gal+].

show with the help of Ref. [AGZ02] that

$$\mathcal{K}(p,k) = \int \frac{\mathrm{d}^2\vec{\mathbf{h}}}{(2\pi)^2} 2\vec{\mathbf{h}} \cdot \operatorname{Re} \vec{\mathbf{f}}(\vec{\mathbf{h}}) = 4 \lim_{b\to 0^+} \operatorname{Im} h(b) \tag{C.19}$$

holds with the boundary condition

$$h(b) \overset{b\to 0^+}{\approx} \frac{2}{\pi} \frac{px(1-x)}{b^2} + \mathcal{O}(1)\,. \tag{C.20}$$

For more details about the further evaluation of the correct solution of $h(b)$ we refer to section 4 of Ref. [Aur+02]. In order to increase the computing efficiency, the numerically obtained values for the kernel are tabulated offline and read in via interpolation routines during runtime.

D Glauber model for nucleus-nucleus collisions

The standard tool for describing the single nucleon-nucleon scatterings in the initial state of a heavy-ion collision is the *Glauber model* [Gla06; Mil+07]. While the Glauber model has its origin in quantum optics, in which it describes coherent radiation, its application in the heavy-ion context is justified by the assumption that the wave length of the nucleons is much shorter than their sizes. Assuming the *optical limit* [Mil+07] the scattering nucleons are only loosely bound within the nuclei and get not deflected by a scattering with a nucleon from the other nucleus but fly on eikonal lines.

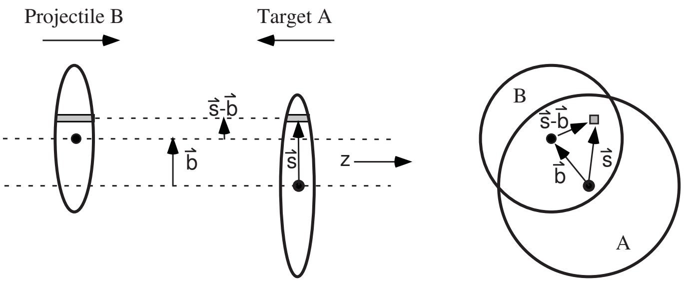

a) Side View b) Beam-line View

Figure D.1: Sketch of a heavy-ion collision as described in the Glauber model. The colliding nuclei are approximated by circular discs. While the left figure shows the collision in the longitudinal plane, the right figure shows the same collision in the transverse plane [Mil+07].

Figure D.1 shows a sketch of a heavy-ion collision, in which a relativistic nucleus scatters with another nucleus under an impact parameter $\vec{b}$. The probability for finding a nucleon in the shaded region of nucleus A with distance $\vec{s}$ from the center of nucleus A reads

$$T_A(\vec{s}) = \int \rho_A(\vec{s}, z_A) dz_A \,, \tag{D.1}$$

where ρ_A is the density distribution of a nucleus normalized to its mass number A. We employ for the density distribution within a nucleus the Woods-Saxon density profile

$$\rho_A(\vec{s}, z_A) = \frac{\gamma n_0}{1 + \exp\left(\left(\sqrt{s^2 + (\gamma z_A^2)} - R_A\right)/d\right)} \,. \tag{D.2}$$

$\gamma = \frac{1}{\sqrt{1-v^2}}$ is the Lorentz boost of the nucleus, $d = 0.54\,\mathrm{fm}$ the skin thickness of the nucleus, and $R_A = 1.12 A^{1/3} - 0.86 A^{-1/3}$ the effective nuclear radius.

As for nucleus A, one can define a probability $T_B(\vec{s} - \vec{b})$ for finding a nucleon at position $\vec{s} - \vec{b}$ in nucleus B. After integrating the combined probability $T_A(\vec{s})\, T_B(\vec{s} - \vec{b})\, \mathrm{d}^2 s$ one obtains the *thickness function*

$$T_{AB}(\vec{b}) = \int T_A(\vec{s})\, T_B(\vec{s} - \vec{b})\, \mathrm{d}^2 s\,, \tag{D.3}$$

which corresponds to the effective overlap area of both nuclei [Mil+07].

When neglecting elastic and diffractive processes, which are rare at large collision energies, the probability for a single nucleon-nucleon interaction is then given by $T_{AB}\, \sigma_{inel}^{NN}$, where σ_{inel}^{NN} is the inelastic cross section for a single nucleon-nucleon interaction. The inelastic nucleon-nucleon cross section can be obtained experimentally and is $\sigma_{inel}^{NN} = (64 \pm 5)\,\mathrm{mb}$ in $\sqrt{s} = 2.76\,\mathrm{TeV}$ collisions at LHC [CMS11a]. Based on this probability one can calculate the probability for n nucleon-nucleon interactions within the collision of a nucleus with mass number A and a nucleus with mass number B at an impact parameter $\vec{\mathrm{b}}$ [Mil+07]:

$$P\left(n, \vec{b}\right) = \binom{AB}{n} \left[T_{AB}\left(\vec{b}\right) \sigma_{\mathrm{inel}}^{\mathrm{NN}}\right]^n \left[1 - T_{AB}\left(\vec{b}\right) \sigma_{\mathrm{inel}}^{\mathrm{NN}}\right]^{AB-n}\,. \tag{D.4}$$

The total number of binary nucleon-nucleon interactions is then given by [Mil+07]

$$N_{coll}\left(b\right) = \sum_{n=1}^{AB} n P\left(n, b\right) = AB\, T_{AB}\left(b\right)\, \sigma_{inel}^{NN}\,, \tag{D.5}$$

whereas the number of participating nucleons can be obtained via [Mil+07]

$$\begin{aligned} N_{part}\left(\vec{b}\right) \quad &= \quad A \int T_A\left(\vec{s}\right) \left\{1 - \left[1 - T_B\left(\vec{s} - \vec{b}\right) \sigma_{inel}^{NN}\right]^B\right\} d^2 s + \\ & \quad\quad B \int T_B\left(\vec{s} - \vec{b}\right) \left\{1 - \left[1 - T_A\left(\vec{s}\right) \sigma_{inel}^{NN}\right]^A\right\} d^2 s\,. \end{aligned} \tag{D.6}$$

The previous expressions were derived for unpolarized nuclei, for which the impact parameter is defined by the absolute value $b = \left|\vec{\mathrm{b}}\right|$.

Among the advantages of the presented *optical* Glauber method is its simplicity for estimating the number of binary collisions and participating nucleons. However, in this approach the position of nucleons is approximated by density profiles. More spatial accuracy can be achieved by simulating individual nucleon-nucleon interactions via numerical methods. The most simple version for such a *Monte-Carlo* Glauber method would be a sampling of the position of the nucleons of both nuclei in position space based on the previous density profiles and a subsequent propagation. If two nucleons come closer than $d \leq \sqrt{\sigma_{inel}^{NN}/\pi}$ to each other, a scattering of both nucleons occur. The assumptions underlying both Glauber methods may lead to different estimates of N_{coll} and N_{part}.

Both the impact parameter $\vec{\mathrm{b}}$ and the quantities N_{coll} and N_{part} of individual heavy-ion collisions cannot be measured directly. Consequently, for classifying the strength of a heavy-ion collision, experiments divide the events in different *centrality classes* based on the energy that is measured in forward calorimeters and therefore did not participate in the actual heavy-ion collisions. The smaller the centrality, the more central the collision. By comparing the centrality classes with theoretical predictions from the presented Glauber methods, one obtains theoretical impact parameters, N_{coll} and N_{part}

values [Mil+07]. Tables D.1 and D.2 show different centrality classes used by the ALICE and CMS collaborations at LHC together with calculated values for N_{coll} and N_{part}.

Centrality	$N_{\text{part}}^{\text{ALICE}}$		$N_{\text{coll}}^{\text{ALICE}}$	
	mean	RMS	mean	RMS
0–5 %	382.0	17	1684.0	140
5–10 %	329.7	18	1316.0	110
10–20 %	260.5	27	922.7	140
20–40 %	157.8	35	440.0	150
40–60 %	69.1	22	128.4	59
60–80 %	22.6	12	26.8	18

Table D.1: Experimental values for N_{part} and N_{coll} depending on the centrality class from the ALICE collaboration [ALI13].

Centrality	$N_{\text{part}}^{\text{CMS}}$		$N_{\text{coll}}^{\text{CMS}}$	
	mean	RMS	mean	RMS
0–10 %	355 ± 3	33	1484 ± 120	241
10–20 %	261 ± 4	30	927 ± 82	183
20–30 %	187 ± 5	23	562 ± 53	124
30–50 %	108 ± 5	27	251 ± 28	101
50–100 %	22 ± 2	19	30 ± 5	35

Table D.2: Experimental values for N_{part} and N_{coll} depending on the centrality class from the CMS collaboration [CMS11b].

Furthermore, Table D.3 shows results for the impact parameter dependence of N_{coll} and N_{part} calculated via an optical Glauber calculation as used in the BAMPS framework. In addition, we show the employed number of test particles N_{test} in order to obtain a sufficient statistics.

b_{BAMPS} [fm]	$N_{\text{part}}^{\text{BAMPS}}$	$N_{\text{coll}}^{\text{BAMPS}}$	N_{test}
0.0	431.76	2195.86	7
2.0	410.46	1994.04	8
3.6	363.68	1661.61	15
5.0	308.51	1302.91	18
6.0	264.99	1044.71	16
7.7	188.35	642.52	26
8.3	162.16	520.76	33
10.3	85.59	202.74	85
13.2	15.94	18.64	918

Table D.3: The number of participating nucleons N_{part} and the number of binary nucleon-nucleon interactions N_{coll} depending on the mean impact parameter b calculated in an optical Glauber model and used in the BAMPS framework.

Bibliography

[Abr+14] M. C. Abraao York et al. “UV cascade in classical Yang-Mills theory via kinetic theory”. In: *Phys. Rev. D* 89.7 (Apr. 2014), p. 074036. DOI: `10.1103/PhysRevD.89.074036` (cit. on pp. 245, 247).

[ACS09] N. Armesto, L. Cunqueiro, and C. a. Salgado. “Q-PYTHIA: a medium-modified implementation of final state radiation”. In: *Eur. Phys. J. C* 63.4 (Oct. 2009), pp. 679–690. DOI: `10.1140/epjc/s10052-009-1133-9`. arXiv: `0907.1014` (cit. on pp. 50, 162).

[AGZ02] P. Aurenche, F. Gelis, and H. Zaraket. “A simple sum rule for the thermal gluon spectral function and applications”. In: *J. High Energy Phys.* 2002.05 (May 2002), pp. 043–043. DOI: `10.1088/1126-6708/2002/05/043` (cit. on pp. 117, 245, 248).

[AK02] N. G. Antoniou and A. S. Kapoyannis. “Bootstraping the QCD Critical Point”. In: *Phys. Lett. B* 563.3-4 (Nov. 2002), pp. 165–172. DOI: `10.1016/S0370-2693(03)00654-3`. arXiv: `0211392 [hep-ph]` (cit. on p. 11).

[AKK08] S. Albino, B. Kniehl, and G. Kramer. “AKK update: Improvements from new theoretical input and experimental data”. In: *Nucl. Phys. B* 803.1-2 (Nov. 2008), pp. 42–104. DOI: `10.1016/j.nuclphysb.2008.05.017`. arXiv: `0803.2768` (cit. on p. 202).

[ALI10a] ALICE Collaboration. “Elliptic flow of charged particles in Pb-Pb collisions at 2.76 TeV”. In: *Phys. Rev. Lett.* 105.25 (Dec. 2010), p. 252302. DOI: `10.1103/PhysRevLett.105.252302` (cit. on pp. 194–196).

[ALI10b] ALICE Collaboration. “Suppression of Charged Particle Production at Large Transverse Momentum in Central Pb–Pb Collisions at $\sqrt{s_{NN}} = 2.76$ TeV”. In: *Phys. Lett. B* 696.1-2 (Dec. 2010), pp. 30–39. DOI: `10.1016/j.physletb.2010.12.020`. arXiv: `1012.1004` (cit. on pp. 205–209, 211–212, 214–215).

[ALI11] ALICE Collaboration. “Higher Harmonic Anisotropic Flow Measurements of Charged Particles in Pb-Pb Collisions at $\sqrt{s_{\mathrm{NN}}}$=2.76 TeV”. In: *Phys. Rev. Lett.* 107.3 (July 2011), p. 032301. DOI: `10.1103/PhysRevLett.107.032301`. arXiv: `1105.3865` (cit. on p. 16).

[ALI12a] ALICE Collaboration. “Anisotropic flow of charged hadrons, pions and (anti-)protons measured at high transverse momentum in Pb-Pb collisions at $\sqrt{s_{\mathrm{NN}}} = 2.76$ TeV”. In: *Phys. Lett. B* 719.1-3 (May 2012), pp. 18–28. DOI: `10.1016/j.physletb.2012.12.066`. arXiv: `1205.5761` (cit. on p. 216).

[ALI12b] ALICE Collaboration. “Centrality Dependence of Charged Particle Production at Large Transverse Momentum in Pb–Pb Collisions at $\sqrt{s_{\mathrm{NN}}} = 2.76$ TeV”. In: *Phys. Lett. B* 720.1-3 (Aug. 2012), pp. 52–62. DOI: `10.1016/j.physletb.2013.01.051`. arXiv: `1208.2711` (cit. on pp. 214–215).

[ALI12c] ALICE Collaboration. “Pion, Kaon, and Proton Production in Central Pb-Pb Collisions at $\sqrt{s_{\mathrm{NN}}}$=2.76 TeV”. In: *Phys. Rev. Lett.* 109.25 (Dec. 2012), p. 252301. DOI: `10.1103/PhysRevLett.109.252301`. arXiv: `1208.1974` (cit. on pp. 211–213).

[ALI13] ALICE Collaboration. “Centrality determination of Pb-Pb collisions at $\sqrt{s_{\mathrm{NN}}}$=2.76 TeV with ALICE”. In: *Phys. Rev. C - Nucl. Phys.* 88.4 (Oct. 2013), p. 044909. DOI: `10.1103/PhysRevC.88.044909` (cit. on p. 251).

[ALI15] ALICE Collaboration. “Measurement of jet suppression in central Pb-Pb collisions at $\sqrt{s_{\mathrm{NN}}}$ = 2.76 TeV”. In: *Phys. Lett. B* 746.January (June 2015), pp. 1–14. DOI: `10.1016/j.physletb.2015.04.039`. arXiv: `1502.01689` (cit. on p. 217).

[AMY01a] P. Arnold, G. D. Moore, and L. G. Yaffe. “Photon emission from quark-gluon plasma: complete leading order results”. In: *J. High Energy Phys.* 2001.12 (Dec. 2001), pp. 009–009. DOI: `10.1088/1126-6708/2001/12/009`. arXiv: `0111107 [hep-ph]` (cit. on p. 116).

[AMY01b] P. Arnold, G. D. Moore, and L. G. Yaffe. “Photon Emission from Ultrarelativistic Plasmas”. In: *J. High Energy Phys.* 2001.11 (2001), pp. 057–057. DOI: `10.1088/1126-6708/2001/11/057`. arXiv: `0109064 [hep-ph]` (cit. on pp. 49, 115–116).

[AMY02a] P. Arnold, G. D. Moore, and L. G. Yaffe. “Effective Kinetic Theory for High Temperature Gauge Theories”. In: *J. High Energy Phys.* 2003.01 (Sept. 2002), pp. 030–030. DOI: `10.1088/1126-6708/2003/01/030`. arXiv: `0209353 [hep-ph]` (cit. on pp. 115–116, 187).

[AMY02b] P. Arnold, G. D. Moore, and L. G. Yaffe. “Photon and gluon emission in relativistic plasmas”. In: *J. High Energy Phys.* 2002.06 (June 2002), pp. 030–030. DOI: `10.1088/1126-6708/2002/06/030`. arXiv: `0204343 [hep-ph]` (cit. on pp. xvi, 115–117).

[Ant+95] P. L. Anthony et al. “An Accurate Measurement of the Landau-Pomeranchuk-Migdal Effect”. In: *Phys. Rev. Lett.* 75.10 (Sept. 1995), pp. 1949–1952. DOI: `10.1103/PhysRevLett.75.1949` (cit. on p. 46).

[Aok+06] Y. Aoki et al. “The order of the quantum chromodynamics transition predicted by the standard model of particle physics”. In: *Nature* 443.7112 (Oct. 2006), pp. 675–678. DOI: `10.1038/nature05120` (cit. on p. 10).

[AP13] J. Auvinen and H. Petersen. “Evolution of elliptic and triangular flow as a function of collision energy in a hybrid model”. In: *Phys. Rev. C* 88.6 (Oct. 2013), p. 064908. DOI: `10.1103/PhysRevC.88.064908`. arXiv: `1310.1764` (cit. on p. 196).

[AP77] G. Altarelli and G. Parisi. “Asymptotic freedom in parton language”. In: *Nucl. Phys. B* 126.2 (Aug. 1977), pp. 298–318. DOI: `10.1016/0550-3213(77)90384-4` (cit. on pp. 18, 47, 116, 160).

[Apo+18] L. Apolinário et al. “Novel subjet observables for jet quenching in heavy-ion collisions”. In: *Eur. Phys. J. C* 78.6 (June 2018), p. 529. DOI: `10.1140/epjc/s10052-018-5999-2`. arXiv: `1710.07607` (cit. on p. 51).

[Arm+12] N. N. Armesto et al. “Comparison of jet quenching formalisms for a quark-gluon plasma “brick””. In: *Phys. Rev. C* 86.6 (Dec. 2012), p. 064904. DOI: `10.1103/PhysRevC.86.064904`. arXiv: `1106.1106` (cit. on pp. 45, 47–49, 85–87, 89, 138, 140).

[Arn09a] P. Arnold. "High-energy gluon bremsstrahlung in a finite medium: Harmonic oscillator versus single-scattering approximation". In: *Phys. Rev. D - Part. Fields, Gravit. Cosmol.* 80.2 (2009), pp. 1–24. DOI: `10.1103/PhysRevD.80.025004`. arXiv: `0903.1081` (cit. on pp. 48, 138).

[Arn09b] P. Arnold. "Simple formula for high-energy gluon bremsstrahlung in a finite, expanding medium". In: *Phys. Rev. D - Part. Fields, Gravit. Cosmol.* 79.6 (2009), pp. 1–14. DOI: `10.1103/PhysRevD.79.065025`. arXiv: `0808.2767` (cit. on pp. 47–48, 85–86, 138).

[ASW04] N. Armesto, C. A. Salgado, and U. A. Wiedemann. "Medium-induced gluon radiation off massive quarks fills the dead cone". In: *Phys. Rev. D* 69.11 (June 2004), p. 114003. DOI: `10.1103/PhysRevD.69.114003`. arXiv: `0312106 [hep-ph]` (cit. on pp. 48–49, 140).

[ATL10] ATLAS Collaboration. "Observation of a Centrality-Dependent Dijet Asymmetry in Lead-Lead Collisions at $\sqrt{s_{\mathrm{NN}}} = 2.76$ TeV with the ATLAS Detector at the LHC". In: *Phys. Rev. Lett.* 105.25 (Nov. 2010), pp. 1–19. DOI: `10.1103/PhysRevLett.105.252303`. arXiv: `1011.6182` (cit. on pp. 21, 23).

[ATL14] ATLAS Collaboration. "Measurements of the Nuclear Modification Factor for Jets in Pb+Pb Collisions at $\sqrt{s_{\mathrm{NN}}} = 2.76$ TeV with the ATLAS Detector". In: *Phys. Rev. Lett.* 114.7 (Nov. 2014), pp. 1–19. DOI: `10.1103/PhysRevLett.114.072302`. arXiv: `1411.2357` (cit. on p. 218).

[ATL15] ATLAS Collaboration. "Measurement of charged-particle spectra in Pb+Pb collisions at $\sqrt{s_{\mathrm{NN}}} = 2.76$ TeV with the ATLAS detector at the LHC". In: *J. High Energy Phys.* 2015.9 (2015). DOI: `10.1007/JHEP09(2015)050` (cit. on pp. 205–209, 211–212).

[Aur+02] P. Aurenche et al. "Landau-Pomeranchuk-Migdal resummation for dilepton production". In: *J. High Energy Phys.* 2002.12 (Dec. 2002), pp. 006–006. DOI: `10.1088/1126-6708/2002/12/006` (cit. on pp. 117, 245–248).

[AX08] P. Arnold and W. Xiao. "High-energy jet quenching in weakly coupled quark-gluon plasmas". In: *Phys. Rev. D - Part. Fields, Gravit. Cosmol.* 78.12 (2008), pp. 1–11. DOI: `10.1103/PhysRevD.78.125008`. arXiv: `0810.1026` (cit. on p. 85).

[Bai+01] R. Baier et al. "Quenching of hadron spectra in media". In: *J. High Energy Phys.* 2001.09 (Sept. 2001), pp. 033–033. DOI: `10.1088/1126-6708/2001/09/033`. arXiv: `0106347 [hep-ph]` (cit. on p. 49).

[Bai+95] R. Baier et al. "Induced gluon radiation in a QCD medium". In: *Phys. Lett. B* 345.3 (Feb. 1995), pp. 277–286. DOI: `10.1016/0370-2693(94)01617-L`. arXiv: `9411409 [hep-ph]` (cit. on pp. xiv, 46–48, 55, 137).

[Bai+96] R. Baier et al. "The Landau-Pomeranchuk-Migdal effect in QED". In: *Nucl. Phys. B* 478.3 (Nov. 1996), pp. 577–597. DOI: `10.1016/0550-3213(96)00426-9`. arXiv: `9604327 [hep-ph]` (cit. on p. 46).

[Bai+97a] R. Baier et al. "Radiative energy loss and pt-broadening of high energy partons in nuclei". In: *Nucl. Phys. B* 484.1-2 (Jan. 1997), pp. 265–282. DOI: `10.1016/S0550-3213(96)00581-0`. arXiv: `9608322 [hep-ph]` (cit. on pp. xiv, 46, 137).

[Bai+97b] R. Baier et al. "Radiative energy loss of high energy quarks and gluons in a finite-volume quark-gluon plasma". In: *Nucl. Phys. B* 483.1-2 (Jan. 1997), pp. 291–320. DOI: `10.1016/S0550-3213(96)00553-6`. arXiv: `9607355 [hep-ph]` (cit. on pp. xiv, 46, 48, 52, 110, 137).

[Bai+98a] R. Baier et al. “Medium-induced radiative energy loss; equivalence between the BDMPS and Zakharov formalisms”. In: *Nucl. Phys. B* 531.1-3 (Oct. 1998), pp. 403–425. DOI: `10.1016/S0550-3213(98)00546-X`. arXiv: `9804212 [hep-ph]` (cit. on pp. 47, 137).

[Bai+98b] R. Baier et al. “Radiative energy loss of high energy partons traversing an expanding QCD plasma”. In: *Phys. Rev. C* 58.3 (Sept. 1998), pp. 1706–1713. DOI: `10.1103/PhysRevC.58.1706`. arXiv: `9803473 [hep-ph]` (cit. on pp. xiv, 46).

[Bas+09] S. A. Bass et al. “Systematic comparison of jet energy-loss schemes in a realistic hydrodynamic medium”. In: *Phys. Rev. C* 79.2 (Feb. 2009), p. 024901. DOI: `10.1103/PhysRevC.79.024901` (cit. on p. 45).

[Bas+98] S. A. Bass et al. “Microscopic Models for Ultrarelativistic Heavy Ion Collisions”. In: *Prog. Part. Nucl. Phys.* 41 (Mar. 1998), pp. 255–369. DOI: `10.1016/S0146-6410(98)00058-1`. arXiv: `9803035 [nucl-th]` (cit. on pp. 13, 38).

[Bet07] S. Bethke. “Experimental tests of asymptotic freedom”. In: *Prog. Part. Nucl. Phys.* 58.2 (Apr. 2007), pp. 351–386. DOI: `10.1016/j.ppnp.2006.06.001`. arXiv: `0606035 [arXiv:hep-ex]` (cit. on p. 8).

[BG14] B. Betz and M. Gyulassy. “Constraints on the path-length dependence of jet quenching in nuclear collisions at RHIC and LHC”. In: *J. High Energy Phys.* 2014.8 (Aug. 2014), p. 90. DOI: `10.1007/JHEP08(2014)090`. arXiv: `1404.6378` (cit. on p. 214).

[BGT11] B. Betz, M. Gyulassy, and G. Torrieri. “Sensitivity of azimuthal jet tomography to early-time energy loss at RHIC and LHC”. In: *J. Phys. G Nucl. Part. Phys.* 38.12 (Dec. 2011), p. 124153. DOI: `10.1088/0954-3899/38/12/124153`. arXiv: `1106.4564` (cit. on p. 214).

[BH34] H. Bethe and W. Heitler. “On the Stopping of Fast Particles and on the Creation of Positive Electrons”. In: *Proc. R. Soc. A Math. Phys. Eng. Sci.* 146.856 (Aug. 1934), pp. 83–112. DOI: `10.1098/rspa.1934.0140` (cit. on p. 54).

[Bil+11] A. Bilandzic et al. “Event-plane flow analysis without nonflow effects”. In: *Phys. Rev. C* 83.1 (Jan. 2011), p. 014909. DOI: `10.1103/PhysRevC.83.014909` (cit. on p. 15).

[Bjo82] J. D. Bjorken. “Energy loss of energetic partons in quark-gluon plasma: possible extinction of high pT jets in hadron-hadron collisions”. In: *Fermilab PUB-82/59-THY* (1982) (cit. on p. 18).

[Ble+99] M. Bleicher et al. “Relativistic hadron-hadron collisions in the ultra-relativistic quantum molecular dynamics model”. In: *J. Phys. G Nucl. Part. Phys.* 25.9 (Sept. 1999), pp. 1859–1896. DOI: `10.1088/0954-3899/25/9/308` (cit. on pp. 13, 38).

[BM15] J.-P. Blaizot and Y. Mehtar-Tani. “Jet structure in heavy ion collisions”. en. In: *Int. J. Mod. Phys. E* 24.11 (Nov. 2015), p. 1530012. DOI: `10.1142/S021830131530012X`. arXiv: `1503.05958` (cit. on p. 45).

[Bor+11] S. Borsanyi et al. “Transition temperature and the equation of state from lattice QCD, Wuppertal-Budapest results”. In: *J. Phys. G Nucl. Part. Phys.* 38.12 (2011) (cit. on p. 10).

[Bou+10] I. Bouras et al. “Investigation of shock waves in the relativistic Riemann problem: A comparison of viscous fluid dynamics to kinetic theory”. In: *Phys. Rev. C* 82.2 (2010), p. 024910. DOI: `10.1103/PhysRevC.82.024910`. arXiv: `1006.0387` (cit. on p. 43).

[Bou+12] I. Bouras et al. “Transition from ideal to viscous Mach cones in a kinetic transport approach”. In: *Phys. Lett. B* 710.4-5 (Apr. 2012), pp. 641–646. DOI: `10.1016/j.physletb.2012.03.040` (cit. on p. 43).

[Bou+14] I. Bouras et al. “Mach cones in viscous heavy-ion collisions”. In: *Phys. Rev. C* 90.2 (Aug. 2014), p. 024904. DOI: `10.1103/PhysRevC.90.024904` (cit. on pp. 43, 200).

[Boy+96] G. Boyd et al. “Thermodynamics of SU(3) lattice gauge theory”. In: *Nucl. Phys. B* 469.3 (June 1996), pp. 419–444. DOI: `10.1016/0550-3213(96)00170-8` (cit. on p. 7).

[BP90] E. Braaten and R. D. Pisarski. “Soft amplitudes in hot gauge theories: A general analysis”. In: *Nucl. Phys. B* 337.3 (June 1990), pp. 569–634. DOI: `10.1016/0550-3213(90)90508-B` (cit. on p. 28).

[BSV10] A. Bilandzic, R. Snellings, and S. Voloshin. “Flow analysis with cumulants: direct calculations”. In: *Phys. Rev. C - Nucl. Phys.* 83.4 (Oct. 2010). DOI: `10.1103/PhysRevC.83.044913`. arXiv: `1010.0233` (cit. on p. 193).

[BSZ00] R. Baier, D. Schiff, and B. G. Zakharov. “Energy loss in perturbative QCD”. In: *Annu. Rev. Nucl. Part. Sci.* 50.1 (Feb. 2000), pp. 37–69. DOI: `10.1146/annurev.nucl.50.1.37`. arXiv: `0002198 [hep-ph]` (cit. on pp. 45, 52–54).

[Buc+15] A. Buckley et al. “LHAPDF6: parton density access in the LHC precision era”. In: *Eur. Phys. J. C* 75.3 (Mar. 2015), p. 132. DOI: `10.1140/epjc/s10052-015-3318-8` (cit. on p. 198).

[Car09] S. Caron-Huot. “O(g) plasma effects in jet quenching”. In: *Phys. Rev. D* 79.6 (Mar. 2009), p. 065039. DOI: `10.1103/PhysRevD.79.065039` (cit. on p. 87).

[Cas+11] J. Casalderrey-Solana et al. *Gauge/String Duality, Hot QCD and Heavy Ion Collisions*. Jan. 2011, p. 292. arXiv: `1101.0618` (cit. on pp. 48, 137–138).

[CBS11] C. E. Coleman-Smith, S. A. Bass, and D. Srivastava. “Implementing the LPM effect in a parton cascade model”. In: *Nucl. Phys. A* 862-863 (July 2011), pp. 275–278. DOI: `10.1016/j.nuclphysa.2011.05.071`. arXiv: `1101.4895` (cit. on p. 68).

[CF74] F. Cooper and G. Frye. “Single-particle distribution in the hydrodynamic and statistical thermodynamic models of multiparticle production”. In: *Phys. Rev. D* 10.1 (July 1974), pp. 186–189. DOI: `10.1103/PhysRevD.10.186` (cit. on pp. 13, 180).

[CG10] S. Caron-Huot and C. Gale. “Finite-size effects on the radiative energy loss of a fast parton in hot and dense strongly interacting matter”. In: *Phys. Rev. C* 82.6 (Dec. 2010), p. 064902. DOI: `10.1103/PhysRevC.82.064902` (cit. on pp. 116, 130–132, 213).

[CI11] J. Casalderrey-Solana and E. Iancu. “Interference effects in medium-induced gluon radiation”. In: *J. High Energy Phys.* 2011.8 (Aug. 2011), p. 15. DOI: `10.1007/JHEP08(2011)015`. arXiv: `1105.1760` (cit. on p. 49).

[CKR77] B. Combridge, J. Kripfganz, and J. Ranft. *Hadron production at large transverse momentum and QCD*. 1977. DOI: `10.1016/0370-2693(77)90528-7` (cit. on p. 235).

[CMS11a] CMS Collaboration. “Determination of jet energy calibration and transverse momentum resolution in CMS”. In: *J. Instrum.* 6.11 (Nov. 2011), P11002–P11002. DOI: `10.1088/1748-0221/6/11/P11002`. arXiv: `1107.4277` (cit. on p. 250).

[CMS11b] CMS Collaboration. “Observation and studies of jet quenching in PbPb collisions at nucleon-nucleon center-of-mass energy $\sqrt{s_{\mathrm{NN}}}$ = 2.76 TeV”. In: *Phys. Rev. C* 84.August (Feb. 2011), p. 024906. DOI: `10.1103/PhysRevC.84.024906`. arXiv: `1102.1957` (cit. on pp. 21, 221, 251).

[CMS12a] CMS Collaboration. “Azimuthal anisotropy of charged particles at high transverse momenta in PbPb collisions at $\sqrt{s_{\mathrm{NN}}}$ = 2.76 TeV”. In: *Phys. Rev. Lett.* 109.2 (Apr. 2012), pp. 1–15. DOI: `10.1103/PhysRevLett.109.022301`. arXiv: `1204.1850` (cit. on p. 216).

[CMS12b] CMS Collaboration. “Jet momentum dependence of jet quenching in PbPb collisions at $\sqrt{s_{\mathrm{NN}}}$=2.76 TeV”. In: *Phys. Lett. B* 712.3 (June 2012), pp. 176–197. DOI: `10.1016/j.physletb.2012.04.058`. arXiv: `arXiv:1202.5022v2` (cit. on p. 21).

[CMS12c] CMS Collaboration. “Measurement of jet fragmentation into charged particles in pp and PbPb collisions at $\sqrt{s_{\mathrm{NN}}} = 2.76$ TeV”. In: *J. High Energy Phys.* 2012.10 (Oct. 2012), p. 87. DOI: `10.1007/JHEP10(2012)087`. arXiv: `1205.5872` (cit. on p. 24).

[CMS12d] CMS Collaboration. “Studies of jet quenching using isolated-photon + jet correlations in PbPb and pp collisions at $\sqrt{s_{\mathrm{NN}}}$ = 2.76 TeV”. In: *Phys. Lett. B* 718.3 (May 2012), pp. 773–794. DOI: `10.1016/j.physletb.2012.11.003`. arXiv: `1205.0206` (cit. on p. 23).

[CMS12e] CMS Collaboration. “Study of high-$p_\perp$ charged particle suppression in PbPb compared to pp collisions at $\sqrt{s_{\mathrm{NN}}}$=2.76 TeV”. In: *Eur. Phys. J. C* 72.3 (Mar. 2012), p. 1945. DOI: `10.1140/epjc/s10052-012-1945-x` (cit. on pp. 19, 205–209, 211–212, 214–215).

[CMS13a] CMS Collaboration. “Measurement of the elliptic anisotropy of charged particles produced in PbPb collisions at $\sqrt{s_{\mathrm{NN}}}$=2.76 TeV”. In: *Phys. Rev. C* 87.1 (Jan. 2013), p. 014902. DOI: `10.1103/PhysRevC.87.014902`. arXiv: `1204.1409` (cit. on pp. 15, 194–196).

[CMS13b] CMS Collaboration. “Modification of jet shapes in PbPb collisions at $\sqrt{s_{\mathrm{NN}}}$ = 2.76 TeV”. In: *Phys. Lett. B* 730 (Oct. 2013), pp. 243–263. DOI: `10.1016/j.physletb.2014.01.042`. arXiv: `1310.0878` (cit. on pp. 24, 163, 222–223).

[CMS14a] CMS Collaboration. “Evidence of b-Jet Quenching in PbPb Collisions at $\sqrt{s_{\mathrm{NN}}}$=2.76 TeV”. In: *Phys. Rev. Lett.* 113.13 (Sept. 2014), p. 132301. DOI: `10.1103/PhysRevLett.113.132301` (cit. on p. 23).

[CMS14b] CMS Collaboration. “Measurement of jet fragmentation in PbPb and p p collisions at $\sqrt{s_{\mathrm{NN}}}$ = 2.76 TeV”. In: *Phys. Rev. C* 90.2 (Aug. 2014), p. 024908. DOI: `10.1103/PhysRevC.90.024908`. arXiv: `1406.0932` (cit. on p. 24).

[CMS16] CMS Collaboration. “Measurement of inclusive jet production and nuclear modifications in pPb collisions at $\sqrt{s_{\mathrm{NN}}}$ = 5.02 TeV”. In: *Eur. Phys. J. C* (Jan. 2016). DOI: `10.1140/epjc/s10052-016-4205-7`. arXiv: `1601.02001` (cit. on p. 24).

[CMS17] CMS Collaboration. “Measurement of inclusive jet cross sections in pp and PbPb collisions at $\sqrt{s_{\mathrm{NN}}} = 2.76$ TeV”. In: *Phys. Rev. C* 96.1 (July 2017), p. 015202. DOI: `10.1103/PhysRevC.96.015202` (cit. on pp. 217–218).

[Col+12] C. E. Coleman-Smith et al. “Jet modification in a brick of QGP matter”. In: (Aug. 2012), pp. 892–894. DOI: `10.1063/1.3700711`. arXiv: `1108.5662` (cit. on p. 22).

[Cor+01] G. Corcella et al. “HERWIG 6: an event generator for hadron emission reactions with interfering gluons (including supersymmetric processes)”. In: *J. High Energy Phys.* 2001.01 (Jan. 2001), pp. 010–010. DOI: `10.1088/1126-6708/2001/01/010` (cit. on p. 22).

[CS05] M. Cacciari and G. P. Salam. “Dispelling the N^3 myth for the Kt jet-finder”. In: *Phys. Lett. B* 641.1 (Dec. 2005), pp. 57–61. DOI: `10.1016/j.physletb.2006.08.037`. arXiv: `0512210 [hep-ph]` (cit. on pp. 21, 162).

[CS07] J. Casalderrey-Solana and C. a. Salgado. “Introductory lectures on jet quenching in heavy ion collisions”. In: *AIP Conf. Proc.* 1031.1 (Dec. 2007), pp. 207–220. arXiv: `0712.3443` (cit. on p. 48).

[CSS08] M. Cacciari, G. P. Salam, and G. Soyez. “The anti- kt jet clustering algorithm”. In: *J. High Energy Phys.* 2008 (2008), pp. 063–063. DOI: `10.1088/1126-6708/2008/04/063`. arXiv: `0802.1189` (cit. on pp. 21, 162).

[CSS12] M. Cacciari, G. P. Salam, and G. Soyez. “FastJet user manual”. In: *Eur. Phys. J. C* 72.3 (Mar. 2012), p. 1896. DOI: `10.1140/epjc/s10052-012-1896-2`. arXiv: `1111.6097` (cit. on pp. 21, 162).

[CSS89] J. C. Collins, D. E. Soper, and G. Sterman. “Factorization of Hard Processes in QCD”. In: *Adv. Ser. Direct. High Energy Phys.* 5 (July 1989), pp. 1–91. DOI: `10.1142/9789814503266_0001` (cit. on pp. 17, 198).

[Dav74] H. David Politzer. “Asymptotic freedom: An approach to strong interactions”. In: *Phys. Rep.* 14.4 (Nov. 1974), pp. 129–180. DOI: `10.1016/0370-1573(74)90014-3` (cit. on p. 9).

[De 80] S. De Groot. *Relativistic Kinetic Theory - Principles and Applications*. 1980 (cit. on p. 37).

[DEn04] D. D’Enterria. “Indications of suppressed high p_T hadron production in nucleus-nucleus collisions at CERN-SPS”. In: *Phys. Lett. B* 596.1-2 (Mar. 2004), pp. 32–43. DOI: `10.1016/j.physletb.2004.06.071`. arXiv: `0403055 [nucl-ex]` (cit. on p. 19).

[DEn09] D. D’Enterria. “Jet quenching”. In: *Nucl. Phys. A* 715 (Feb. 2009), pp. 471–520. DOI: `10.1007/978-3-642-01539-7_16`. arXiv: `0902.2011` (cit. on p. 45).

[DKT89] Y. Dokshitzer, V. Khoze, and S. Troyan. “Coherence and physics of QCD jets”. In: *Adv. Ser. Direct. High Energy Phys.* Vol. 5. July 1989, pp. 241–410. DOI: `10.1142/9789814503266_0003` (cit. on p. 161).

[Dok77] Y. L. Dokshitzer. “Calculation of the Structure Functions for Deep Inelastic Scattering and e+ e- Annihilation by Perturbation Theory in Quantum Chromodynamics.” In: *Sov. Phys. JETP* 46 (1977), pp. 641–653 (cit. on pp. 18, 47, 116, 160).

[EKL89] K. Eskola, K. Kajantie, and J. Lindfors. “Quark and gluon production in high energy nucleus-nucleus collisions”. In: *Nucl. Phys. B* 323.1 (Aug. 1989), pp. 37–52. DOI: `10.1016/0550-3213(89)90586-5` (cit. on p. 198).

[Ela17] R. K. Elayavalli. “Jet structure modifications in heavy-ion collisions with JEWEL”. In: *J. Phys. Conf. Ser.* 832.1 (Oct. 2017), p. 012004. DOI: `10.1088/1742-6596/832/1/012004`. arXiv: `1610.09364` (cit. on p. 50).

[ES93] S. D. Ellis and D. E. Soper. “Successive combination jet algorithm for hadron collisions”. In: *Phys. Rev. D* 48.7 (Oct. 1993), pp. 3160–3166. DOI: `10.1103/PhysRevD.48.3160` (cit. on p. 21).

[EZ16a] R. K. Elayavalli and K. C. Zapp. “Medium Recoils and background subtraction in JEWEL”. In: *Nucl. Part. Phys. Proc.* 00 (Dec. 2016), pp. 1–4. arXiv: `1612.05116` (cit. on pp. 50, 174, 201, 231).

[EZ16b] R. K. Elayavalli and K. C. Zapp. “Simulating V+jet processes in heavy ion collisions with JEWEL”. In: *Eur. Phys. J. C* 76.12 (Aug. 2016), p. 695. DOI: `10.1140/epjc/s10052-016-4534-6`. arXiv: `1608.03099` (cit. on p. 50).

[Fey69] R. P. Feynman. “The behavior of hadron collisions at extreme energies”. In: *Conf. Proc.* C690905 (1969), pp. 237–258 (cit. on pp. 7–8).

[FK01] Z. Fodor and S. D. Katz. “Lattice determination of the critical point of QCD at finite T and μ”. In: *J. High Energy Phys.* 6.3 (June 2001), pp. 217–226. DOI: `10.1088/1126-6708/2002/03/014`. arXiv: `0106002 [hep-lat]` (cit. on p. 10).

[FK04] Z. Fodor and S. D. Katz. “Finite T/μ lattice QCD and the critical point”. In: *Prog. Theor. Phys. Suppl.* 153 (Jan. 2004), pp. 86–92. DOI: `10.1143/PTPS.153.86`. arXiv: `0401023 [hep-lat]` (cit. on p. 10).

[Foc+13] O. Fochler et al. “Radiative parton processes in perturbative QCD: An improved version of the Gunion and Bertsch cross section from comparisons to the exact result”. In: *Phys. Rev. D* 88.1 (July 2013), p. 014018. DOI: `10.1103/PhysRevD.88.014018` (cit. on pp. 30–33, 42).

[Foc11] O. Fochler. “Investigation of high-pT phenomena within a partonic transport model”. PhD thesis. 2011 (cit. on pp. 30, 33–34, 40, 56–57, 59, 62, 157, 180, 199, 202–203, 214, 235).

[For10] P. de Forcrand. “Simulating QCD at finite density”. In: *Proc. XXVII Int. Symp. Lattice F. Theory — PoS(LAT2009)*. Trieste, Italy: Sissa Medialab, June 2010, p. 010. DOI: `10.22323/1.091.0010`. arXiv: `1005.0539` (cit. on p. 11).

[FP02] P. de Forcrand and O. Philipsen. “The QCD phase diagram for small densities from imaginary chemical potential”. In: *Nucl. Phys. B* 642.1-2 (Oct. 2002), pp. 290–306. DOI: `10.1016/S0550-3213(02)00626-0` (cit. on p. 11).

[FP03] P. de Forcrand and O. Philipsen. “The QCD phase diagram for three degenerate flavors and small baryon density”. In: *Nucl. Phys. B* 673.1-2 (Nov. 2003), pp. 170–186. DOI: `10.1016/j.nuclphysb.2003.09.005` (cit. on p. 11).

[Fri+03] R. J. Fries et al. “Hadronization in Heavy-Ion Collisions: Recombination and Fragmentation of Partons”. In: *Phys. Rev. Lett.* 90.20 (May 2003), p. 202303. DOI: `10.1103/PhysRevLett.90.202303`. arXiv: `0301087 [nucl-th]` (cit. on pp. 13, 180, 202).

[Fri+11] B. Friman et al., eds. *The CBM Physics Book*. Vol. 814. Lecture Notes in Physics. Berlin, Heidelberg: Springer Berlin Heidelberg, 2011. DOI: `10.1007/978-3-642-13293-3` (cit. on p. 13).

[FXG09] O. Fochler, Z. Xu, and C. Greiner. “Towards a unified understanding of jet quenching and elliptic flow within a perturbative QCD parton transport.” In: *Phys. Rev. Lett.* 102.20 (May 2009), p. 202301. DOI: `10.1103/PhysRevLett.102.202301` (cit. on pp. 30, 41–42, 62, 180, 198–199, 202).

[FXG10] O. Fochler, Z. Xu, and C. Greiner. “Energy loss in a partonic transport model including bremsstrahlung processes”. In: *Phys. Rev. C* 82.2 (Aug. 2010), p. 024907. DOI: `10.1103/PhysRevC.82.024907` (cit. on pp. 56, 58).

[FZ14] S. Floerchinger and K. C. Zapp. “Hydrodynamics and jets in dialogue”. In: *Eur. Phys. J. C* 74.12 (Dec. 2014), p. 3189. DOI: `10.1140/epjc/s10052-014-3189-4`. arXiv: `1407.1782` (cit. on p. 50).

[Gal+] M. Galassi et al. *GNU Scientific Library Reference Manual*. 3rd ed. (cit. on pp. 120, 247).

[Gal+13] C. Gale et al. “Event-by-Event Anisotropic Flow in Heavy-ion Collisions from Combined Yang-Mills and Viscous Fluid Dynamics”. In: *Phys. Rev. Lett.* 110.1 (Jan. 2013), p. 012302. DOI: `10.1103/PhysRevLett.110.012302` (cit. on p. 51).

[GB82] J. F. Gunion and G. Bertsch. “Hadronization by color bremsstrahlung”. In: *Phys. Rev. D* 25.3 (1982), pp. 746–753. DOI: `10.1103/PhysRevD.25.746` (cit. on pp. 30–32, 42, 53, 72).

[Gel64] M. Gell-Mann. “A schematic model of baryons and mesons”. In: *Phys. Lett.* 8.3 (Feb. 1964), pp. 214–215. DOI: `10.1016/S0031-9163(64)92001-3` (cit. on p. 7).

[GGX17] M. Greif, C. Greiner, and Z. Xu. “Magnetic field influence on the early-time dynamics of heavy-ion collisions”. In: *Phys. Rev. C* 96.1 (July 2017), p. 014903. DOI: `10.1103/PhysRevC.96.014903` (cit. on p. 43).

[GJS13] C. Gale, S. Jeon, and B. Schenke. “Hydrodynamic modeling of heavy-ion collisions”. In: *Int. J. Mod. Phys. A* 28.11 (Apr. 2013), p. 1340011. DOI: `10.1142/S0217751X13400113` (cit. on pp. 12, 209).

[GL72] V. N. Gribov and L. N. Lipatov. “Deep inelastic e p scattering in perturbation theory”. In: *Sov. J. Nucl. Phys.* 15 (1972), pp. 438–450 (cit. on pp. 18, 47, 116, 160).

[Gla06] R. J. Glauber. “Quantum Optics and Heavy Ion Physics”. In: *Nucl. Phys. A* 774 (Aug. 2006), pp. 3–13. DOI: `10.1016/j.nuclphysa.2006.06.009`. arXiv: `0604021 [nucl-th]` (cit. on pp. 178, 249).

[Gla59] S. L. Glashow. “The renormalizability of vector meson interactions”. In: *Nucl. Phys.* 10 (Feb. 1959), pp. 107–117. DOI: `10.1016/0029-5582(59)90196-8` (cit. on p. 6).

[GLV00a] M. Gyulassy, P. Levai, and I. Vitev. “Non-Abelian Energy Loss at Finite Opacity”. In: *Phys. Rev. Lett.* 85.26 (Dec. 2000), pp. 5535–5538. DOI: `10.1103/PhysRevLett.85.5535` (cit. on p. 49).

[GLV00b] M. Gyulassy, P. Lévai, and I. Vitev. “Jet quenching in thin quark–gluon plasmas I: formalism”. In: *Nucl. Phys. B* 571.1-2 (Apr. 2000), pp. 197–233. DOI: `10.1016/S0550-3213(99)00713-0`. arXiv: `9907461 [hep-ph]` (cit. on p. 48).

[GLV01] M. Gyulassy, P. Levai, and I. Vitev. “Reaction operator approach to non-abelian energy loss”. In: *Nucl. Phys. B* 594.1-2 (Jan. 2001), pp. 371–419. DOI: `10.1016/S0550-3213(00)00652-0`. arXiv: `0006010 [nucl-th]` (cit. on p. 49).

[Gre+13] M. Greif et al. “Heat conductivity in relativistic systems investigated using a partonic cascade”. In: *Phys. Rev. E* 87.3 (Mar. 2013), p. 033019. DOI: `10.1103/PhysRevE.87.033019` (cit. on p. 41).

[Gre+14] M. Greif et al. “Electric conductivity of the quark-gluon plasma investigated using a perturbative QCD based parton cascade”. In: *Phys. Rev. D* 90.9 (Nov. 2014), p. 094014. DOI: `10.1103/PhysRevD.90.094014` (cit. on p. 41).

[Gre+17a] M. Greif et al. “Importance of initial and final state effects for azimuthal correlations in p+Pb collisions”. In: *Phys. Rev. D* 96.9 (Aug. 2017), p. 091504. DOI: `10.1103/PhysRevD.96.091504`. arXiv: `1708.02076` (cit. on pp. 43, 178, 234).

[Gre+17b] M. Greif et al. “Nonequilibrium photon production in partonic transport simulations”. In: *Phys. Rev. C* 95.5 (May 2017), p. 054903. DOI: `10.1103/PhysRevC.95.054903` (cit. on pp. 42, 117).

[Gre18] M. Greif. “Electromagnetic probes in heavy-ion collisions”. PhD thesis. 2018 (cit. on pp. 42, 57, 117).

[GW00] X. Guo and X.-N. Wang. “Multiple scattering, parton energy loss and modified fragmentation functions in deeply inelastic e A scattering”. In: *Phys. Rev. Lett.* 85.17 (Oct. 2000), pp. 3591–3594. DOI: `10.1103/PhysRevLett.85.3591` (cit. on p. 49).

[GW73a] D. J. Gross and F. Wilczek. “Asymptotically Free Gauge Theories. I”. In: *Phys. Rev. D* 8.10 (Nov. 1973), pp. 3633–3652. DOI: `10.1103/PhysRevD.8.3633` (cit. on p. 9).

[GW73b] D. J. Gross and F. Wilczek. “Ultraviolet Behavior of Non-Abelian Gauge Theories”. In: *Phys. Rev. Lett.* 30.26 (June 1973), pp. 1343–1346. DOI: `10.1103/PhysRevLett.30.1343` (cit. on p. 9).

[GW74] D. J. Gross and F. Wilczek. “Asymptotically free gauge theories. II”. In: *Phys. Rev. D* 9.4 (Feb. 1974), pp. 980–993. DOI: `10.1103/PhysRevD.9.980` (cit. on p. 9).

[GW94] M. Gyulassy and X.-N. Wang. “Multiple collisions and induced gluon bremsstrahlung in QCD”. In: *Nucl. Phys. B* 420.3 (June 1994), pp. 583–614. DOI: `10.1016/0550-3213(94)90079-5`. arXiv: `9306003 [nucl-th]` (cit. on p. 47).

[Gyu+03] M. Gyulassy et al. “Jet Quenching and Radiative Energy Loss in Dense Nuclear Matter”. In: *Quark–Gluon Plasma 3* (Feb. 2003), pp. 123–191. DOI: `10.1142/9789812795533_0003`. arXiv: `0302077 [nucl-th]` (cit. on pp. 45, 49).

[Hal+98] M. A. Halasz et al. “On the Phase Diagram of QCD”. In: *Phys. Rev. D* 58.9 (Apr. 1998). DOI: `10.1103/PhysRevD.58.096007`. arXiv: `9804290 [hep-ph]` (cit. on p. 11).

[Has70] W. K. Hastings. “Monte Carlo Sampling Methods Using Markov Chains and Their Applications”. In: *Biometrika* 57.1 (Apr. 1970), p. 97. DOI: `10.2307/2334940` (cit. on p. 40).

[He+15] Y. He et al. “Linear Boltzmann transport for jet propagation in the quark-gluon plasma: Elastic processes and medium recoil”. In: *Phys. Rev. C* 91.5 (May 2015), p. 054908. DOI: `10.1103/PhysRevC.91.054908` (cit. on p. 51).

[Hei04] U. W. Heinz. “Thermalization at RHIC”. In: *AIP Conf. Proc.* Vol. 739. AIP, July 2004, pp. 163–180. DOI: `10.1063/1.1843595`. arXiv: `0407067 [nucl-th]` (cit. on p. 12).

[HP12] P. Huovinen and H. Petersen. “Particlization in hybrid models”. In: *Eur. Phys. J. A* 48.11 (Nov. 2012), p. 171. DOI: `10.1140/epja/i2012-12171-9` (cit. on pp. 13, 180).

[HS13] U. Heinz and R. Snellings. “Collective Flow and Viscosity in Relativistic Heavy-Ion Collisions”. In: *Annu. Rev. Nucl. Part. Sci.* 63.1 (Oct. 2013), pp. 123–151. DOI: `10.1146/annurev-nucl-102212-170540` (cit. on p. 12).

[Huo+01] P. Huovinen et al. “Radial and elliptic flow at RHIC: further predictions”. In: *Phys. Lett. B* 503.1-2 (Jan. 2001), pp. 58–64. DOI: `10.1016/S0370-2693(01)00219-2`. arXiv: `0101136 [hep-ph]` (cit. on p. 12).

[IV04] E. Iancu and R. Venugopalan. “The color glass condensate and high energy scattering in QCD”. In: *Quark–Gluon Plasma 3*. World Scientific, Jan. 2004, pp. 249–363. DOI: `10.1142/9789812795533_0005` (cit. on p. 178).

[JET+17] JETSCAPE Collaboration et al. “Multistage Monte-Carlo simulation of jet modification in a static medium”. In: *Phys. Rev. C* 96.2 (Apr. 2017), p. 024909. DOI: `10.1103/PhysRevC.96.024909`. arXiv: `1705.00050` (cit. on p. 51).

[JM05] S. Jeon and G. D. Moore. “Energy loss of leading partons in a thermal QCD medium”. In: *Phys. Rev. C* 71.3 (Mar. 2005), p. 034901. DOI: `10.1103/PhysRevC.71.034901` (cit. on pp. 51, 115, 121–122).

[JZ06] J. Jia and C. Zhang. “Quark number scaling of v_2 in transverse kinetic energy and it’s implications for coalescence models”. In: *Phys. Rev. C* 75.3 (Aug. 2006), p. 031901. DOI: `10.1103/PhysRevC.75.031901`. arXiv: `0608187 [hep-ph]` (cit. on p. 17).

[Kar01] F. Karsch. “Lattice Results on QCD Thermodynamics”. In: *Nucl. Phys. A* 698.1-4 (Mar. 2001), pp. 199–208. DOI: `10.1016/S0375-9474(01)01365-3`. arXiv: `0103314 [hep-ph]` (cit. on p. 10).

[KH03] P. F. Kolb and U. Heinz. “Hydrodynamic description of ultrarelativistic heavy-ion collisions”. In: (May 2003). arXiv: `0305084 [nucl-th]` (cit. on p. 12).

[KKP00] B. Kniehl, G. Kramer, and B. Pötter. “Fragmentation functions for pions, kaons, and protons at next-to-leading order”. In: *Nucl. Phys. B* 582.1-3 (Aug. 2000), pp. 514–536. DOI: `10.1016/S0550-3213(00)00303-5` (cit. on p. 202).

[Kle+94] S. R. Klein et al. “A measurement of the LPM effect”. In: *AIP Conf. Proc.* Vol. 302. 6. AIP, 1994, pp. 172–197. DOI: `10.1063/1.45475` (cit. on p. 46).

[KLL87] K. Kajantie, P. V. Landshoff, and J. Lindfors. “Minijet Production in High-Energy Nucleus-Nucleus Collisions”. In: *Phys. Rev. Lett.* 59.22 (Nov. 1987), pp. 2527–2530. DOI: `10.1103/PhysRevLett.59.2527` (cit. on p. 198).

[KLP00] F. Karsch, E. Laermann, and A. Peikert. “Quark Mass and Flavour Dependence of the QCD Phase Transition”. In: *Nucl. Phys. B* 605.1-3 (Dec. 2000), pp. 579–599. DOI: `10.1016/S0550-3213(01)00200-0`. arXiv: `0012023 [hep-lat]` (cit. on p. 10).

[KSS04] P. Kovtun, D. T. Son, and A. O. Starinets. “Viscosity in Strongly Interacting Quantum Field Theories from Black Hole Physics”. In: *Phys. Rev. Lett.* 94.11 (May 2004). DOI: `10.1103/PhysRevLett.94.111601`. arXiv: `0405231 [hep-th]` (cit. on p. 17).

[KXB18a] W. Ke, Y. Xu, and S. A. Bass. “Linearized Boltzmann-Langevin model for heavy quark transport in hot and dense QCD matter”. In: *Phys. Rev. C* 98.6 (Dec. 2018), p. 064901. DOI: `10.1103/PhysRevC.98.064901`. arXiv: `1806.08848` (cit. on p. 51).

[KXB18b] W. Ke, Y. Xu, and S. A. Bass. “Modeling of quantum-coherence effects in parton radiative energy loss”. In: (Oct. 2018). arXiv: `1810.08177` (cit. on pp. 51, 56, 68, 70, 86, 89, 93, 153, 226, 232).

[Lee16] M. van Leeuwen. “Jet Fragmentation and Jet Shapes in JEWEL and q-PYTHIA”. In: *Nucl. Part. Phys. Proc.* 276-278 (July 2016), pp. 293–296. DOI: `10.1016/j.nuclphysbps.2016.05.067`. arXiv: `1511.06108` (cit. on p. 50).

[Li+11] H. Li et al. “Mach Cone Induced by γ-Triggered Jets in High-Energy Heavy-Ion Collisions”. In: *Phys. Rev. Lett.* 106.1 (Jan. 2011), p. 012301. DOI: `10.1103/PhysRevLett.106.012301` (cit. on p. 51).

[Lin+04] Z.-W. Lin et al. “A Multi-Phase Transport Model for Relativistic Heavy Ion Collisions”. In: *Phys. Rev. C* 72.6 (Nov. 2004). DOI: `10.1103/PhysRevC.72.064901`. arXiv: `0411110 [nucl-th]` (cit. on p. 13).

[LP53a] L. D. Landau and I. Pomeranchuk. “Electron-cascade processes at ultra-high energies”. In: *Dokl. Akad. Nauk Ser. Fiz.* 92 (1953). (English version was published in "Collected papers of L.D. Landau", Landau and Ter-Haar, Pergamon (1965), pp.589-593), pp. 735–739 (cit. on p. 46).

[LP53b] L. D. Landau and I. Pomeranchuk. “Limits of applicability of the theory of bremsstrahlung electrons and pair production at high energies”. In: *Dokl. Akad. Nauk Ser. Fiz.* 92 (1953). (English version was published in "Collected papers of L.D. Landau", Landau and Ter-Haar, Pergamon (1965), pp.586-588), pp. 535–536 (cit. on pp. 33, 46, 52).

[Mag05] M. Maggiore. *A Modern Introduction to Quantum Field Theory*. 2005 (cit. on p. 6).

[Maj12] A. Majumder. “Hard collinear gluon radiation and multiple scattering in a medium”. In: *Phys. Rev. D* 85.1 (Jan. 2012), p. 014023. DOI: `10.1103/PhysRevD.85.014023`. arXiv: `0912.2987` (cit. on p. 49).

[Maj13] A. Majumder. “Incorporating space-time within medium-modified jet-event generators”. In: *Phys. Rev. C* 88.1 (July 2013), p. 014909. DOI: `10.1103/PhysRevC.88.014909`. arXiv: `1301.5323` (cit. on p. 51).

[Mar+92] G. Marchesini et al. “HERWIG 5.1 - a Monte Carlo event generator for simulating hadron emission reactions with interfering gluons”. In: *Comput. Phys. Commun.* 67.3 (Jan. 1992), pp. 465–508. DOI: `10.1016/0010-4655(92)90055-4` (cit. on p. 22).

[McL] L. McLerran. “The Color Glass Condensate and Small-x Physics”. In: *Lect. Quark Matter*. Berlin, Heidelberg: Springer Berlin Heidelberg, pp. 291–334. DOI: `10.1007/3-540-45792-5_8` (cit. on p. 178).

[Mig56] A. B. Migdal. “Bremsstrahlung and Pair Production in Condensed Media at High Energies”. In: *Phys. Rev.* 103.6 (Sept. 1956), pp. 1811–1820. DOI: `10.1103/PhysRev.103.1811` (cit. on pp. 33, 46, 52).

[Mil+07] M. L. Miller et al. “Glauber Modeling in High-Energy Nuclear Collisions”. In: *Annu. Rev. Nucl. Part. Sci.* 57.1 (Nov. 2007), pp. 205–243. DOI: `10.1146/annurev.nucl.57.090506.123020`. arXiv: `0701025 [nucl-ex]` (cit. on pp. 178, 249–251).

[MK89] A. Masayuki and Y. Koichi. “Chiral restoration at finite density and temperature”. In: *Nucl. Phys. A* 504.4 (1989), pp. 668–684 (cit. on p. 11).

[MMT13] Y. Mehtar-Tani, J. G. Milhano, and K. Tywoniuk. “Jet physics in heavy-ion collisions”. In: *Int. J. Mod. Phys. A* 28.11 (Feb. 2013), p. 1340013. DOI: `10.1142/S0217751X13400137`. arXiv: `1302.2579` (cit. on pp. 45, 50).

[MS10] F. Mandl and G. Shaw. *Quantum Field Theory*. 2010 (cit. on p. 6).

[MST11] Y. Mehtar-Tani, C. A. Salgado, and K. Tywoniuk. “Antiangular Ordering of Gluon Radiation in QCD Media”. In: *Phys. Rev. Lett.* 106.12 (Mar. 2011), p. 122002. DOI: `10.1103/PhysRevLett.106.122002`. arXiv: `1009.2965` (cit. on p. 49).

[MST12a] Y. Mehtar-Tani, C. A. Salgado, and K. Tywoniuk. “Jets in QCD media: From color coherence to decoherence”. In: *Phys. Lett. B* 707.1 (Jan. 2012), pp. 156–159. DOI: `10.1016/j.physletb.2011.12.042`. arXiv: `1102.4317` (cit. on p. 49).

[MST12b] Y. Mehtar-Tani, C. A. Salgado, and K. Tywoniuk. “The radiation pattern of a QCD antenna in a dense medium”. In: *J. High Energy Phys.* 2012.10 (Oct. 2012), p. 197. DOI: `10.1007/JHEP10(2012)197`. arXiv: `1205.5739` (cit. on p. 49).

[MST12c] Y. Mehtar-Tani, C. A. Salgado, and K. Tywoniuk. “The radiation pattern of a QCD antenna in a dilute medium”. In: *J. High Energy Phys.* 2012.4 (Apr. 2012), p. 64. DOI: `10.1007/JHEP04(2012)064`. arXiv: `1112.5031` (cit. on p. 49).

[MT13] Y. Mehtar-Tani and K. Tywoniuk. “Jet coherence in QCD media: the antenna radiation spectrum”. In: *J. High Energy Phys.* 2013.1 (Jan. 2013), p. 31. DOI: `10.1007/JHEP01(2013)031` (cit. on p. 50).

[Muk16] S. Mukherjee. *Phase diagram of QCD*. 2016. URL: `https://deixismagazine.org/2016/06/early-universe-soup/` (visited on 11/30/2019) (cit. on p. 10).

[MV11] A. Majumder and M. Van Leeuwen. “The theory and phenomenology of perturbative QCD based jet quenching”. In: *Prog. Part. Nucl. Phys.* 66.1 (2011), pp. 41–92. DOI: `10.1016/j.ppnp.2010.09.001`. arXiv: `1002.2206` (cit. on p. 45).

[MZ16] J. G. Milhano and K. C. Zapp. “Origins of the di-jet asymmetry in heavy-ion collisions”. In: *Eur. Phys. J. C* 76.5 (May 2016), p. 288. DOI: `10.1140/epjc/s10052-016-4130-9` (cit. on p. 50).

[NEP16] H. Niemi, K. J. Eskola, and R. Paatelainen. “Event-by-event fluctuations in a perturbative QCD + saturation + hydrodynamics model: Determining QCD matter shear viscosity in ultrarelativistic heavy-ion collisions”. In: *Phys. Rev. C* 93.2 (Feb. 2016), p. 024907. DOI: `10.1103/PhysRevC.93.024907` (cit. on p. 12).

[Nie+11] H. Niemi et al. “Influence of Shear Viscosity of Quark-Gluon Plasma on Elliptic Flow in Ultrarelativistic Heavy-Ion Collisions”. In: *Phys. Rev. Lett.* 106.21 (May 2011), p. 212302. DOI: `10.1103/PhysRevLett.106.212302` (cit. on p. 12).

[Nie+13] H. Niemi et al. “Event-by-event distributions of azimuthal asymmetries in ultrarelativistic heavy-ion collisions”. In: *Phys. Rev. C* 87.5 (May 2013), p. 054901. DOI: `10.1103/PhysRevC.87.054901` (cit. on p. 12).

[Par+16] C. Park et al. “Rapidity-dependent jet energy loss in small systems with finite-size effects and running coupling”. In: *Nucl. Part. Phys. Proc.* 00 (Dec. 2016), pp. 1–5. arXiv: `1612.06754` (cit. on pp. 51, 154, 209–210).

[Par15] C. Park. “Jet energy loss with finite-size effects and running coupling in MARTINI”. MA thesis. 2015 (cit. on pp. 51, 210).

[Pet+08] H. Petersen et al. “Fully integrated transport approach to heavy ion reactions with an intermediate hydrodynamic stage”. In: *Phys. Rev. C* 78.4 (June 2008). DOI: `10.1103/PhysRevC.78.044901`. arXiv: `0806.1695` (cit. on pp. 13, 180).

[Pet12] P. Petreczky. “Lattice QCD at non-zero temperature”. In: *J. Phys. G Nucl. Part. Phys.* 39.9 (Sept. 2012), p. 093002. DOI: `10.1088/0954-3899/39/9/093002` (cit. on p. 7).

[Phi13] O. Philipsen. “The QCD equation of state from the lattice”. In: *Prog. Part. Nucl. Phys.* 70 (May 2013), pp. 55–107. DOI: `10.1016/j.ppnp.2012.09.003` (cit. on pp. 7, 13, 180).

[Pis89] R. D. Pisarski. “Scattering amplitudes in hot gauge theories”. In: *Phys. Rev. Lett.* 63.11 (Sept. 1989), pp. 1129–1132. DOI: `10.1103/PhysRevLett.63.1129` (cit. on p. 28).

[PJG18] C. Park, S. Jeon, and C. Gale. “Jet modification with medium recoil in quark-gluon plasma”. In: *Nucl. Phys. A* 00 (July 2018), pp. 1–4. arXiv: `1807.06550` (cit. on p. 51).

[Pol73] H. D. Politzer. “Reliable Perturbative Results for Strong Interactions?” In: *Phys. Rev. Lett.* 30.26 (June 1973), pp. 1346–1349. DOI: `10.1103/PhysRevLett.30.1346` (cit. on p. 9).

[Pov+06] B. Povh et al. *Teilchen und Kerne – Eine Einführung in die physikalischen Konzepte*. 7th ed. Springer-Verlag GmbH, Sept. 2006 (cit. on p. 8).

[PS95] M. E. Peskin and D. V. Schroeder. *An Introduction to Quantum Field Theory*. Westview Press, 1995 (cit. on pp. 6–7, 25, 27, 84, 235).

[Pum+02] J. Pumplin et al. “New Generation of Parton Distributions with Uncertainties from Global QCD Analysis”. In: *J. High Energy Phys.* 2002.07 (July 2002), pp. 012–012. DOI: `10.1088/1126-6708/2002/07/012` (cit. on pp. 198–199).

[PV98] A. M. Poskanzer and S. A. Voloshin. “Methods for analyzing anisotropic flow in relativistic nuclear collisions”. In: *Phys. Rev. C* 58.3 (Sept. 1998), pp. 1671–1678. DOI: `10.1103/PhysRevC.58.1671` (cit. on p. 14).

[QM10] G.-Y. Qin and B. Müller. “Explanation of Di-jet asymmetry in Pb+Pb collisions at the Large Hadron Collider”. In: *Phys. Rev. Lett.* 106.16 (Dec. 2010). DOI: `10.1103/PhysRevLett.106.162302`. arXiv: `1012.5280` (cit. on p. 22).

[QM15] G.-Y. Qin and A. Majumder. “Jet transport and photon bremsstrahlung via longitudinal and transverse scattering”. In: *Phys. Rev. C* 91.4 (Apr. 2015), p. 044906. DOI: `10.1103/PhysRevC.91.044906` (cit. on p. 49).

[QW15] G.-Y. Qin and X.-N. Wang. “Jet quenching in high-energy heavy-ion collisions”. In: *Int. J. Mod. Phys. E* 24.11 (Nov. 2015), p. 1530014. DOI: `10.1142/S0218301315300143`. arXiv: `1511.00790 [hep-ph]` (cit. on pp. 45, 49, 51).

[Rei09] F. Reif. *Fundamentals of statistical and thermal physics*. Waveland Press, 2009 (cit. on p. 37).

[Ren08] T. Renk. “Difficulty of extracting energy loss probability distributions from R_{AA}”. In: *Phys. Rev. C* 77.1 (Jan. 2008), p. 017901. DOI: `10.1103/PhysRevC.77.017901` (cit. on p. 50).

[Ren09a] T. Renk. “Comparison study of medium-modified QCD shower evolution scenarios”. In: *Phys. Rev. C* 79.5 (May 2009), p. 054906. DOI: `10.1103/PhysRevC.79.054906`. arXiv: `0901.2818` (cit. on p. 50).

[Ren09b] T. Renk. “Medium-modified jet shapes and other jet observables from in-medium parton shower evolution”. In: *Phys. Rev. C* 80.4 (Oct. 2009), p. 044904. DOI: `10.1103/PhysRevC.80.044904`. arXiv: `0906.3397` (cit. on p. 50).

[Ris04] D. Rischke. “The quark–gluon plasma in equilibrium”. In: *Prog. Part. Nucl. Phys.* 52.1 (Mar. 2004), pp. 197–296. DOI: `10.1016/j.ppnp.2003.09.002` (cit. on pp. 10–11).

[RR07] P. Romatschke and U. Romatschke. “Viscosity Information from Relativistic Nuclear Collisions: How Perfect is the Fluid Observed at RHIC?” In: *Phys. Rev. Lett.* 99.17 (June 2007). DOI: `10.1103/PhysRevLett.99.172301`. arXiv: `0706.1522` (cit. on p. 12).

[Rue+05] S. B. Ruester et al. “The phase diagram of neutral quark matter: Self-consistent treatment of quark masses”. In: *Phys. Rev. D* 72.3 (Mar. 2005). DOI: `10.1103/PhysRevD.72.034004`. arXiv: `0503184 [hep-ph]` (cit. on p. 11).

[Sal10] G. P. Salam. “Towards jetography”. In: *Eur. Phys. J. C* 67.3-4 (June 2010), pp. 637–686. DOI: `10.1140/epjc/s10052-010-1314-6`. arXiv: `0906.1833` (cit. on pp. 20–22).

[Sca+00] O. Scavenius et al. “Chiral Phase Transition within Effective Models with Constituent Quarks”. In: *Phys. Rev. C* 64.4 (July 2000). DOI: `10.1103/PhysRevC.64.045202`. arXiv: `0007030 [nucl-th]` (cit. on p. 11).

[Sen+15] F. Senzel et al. “Influence of multiple in-medium scattering processes on the momentum imbalance of reconstructed di-jets”. en. In: *J. Phys. G Nucl. Part. Phys.* 42.11 (Nov. 2015), pp. 1–14. DOI: `10.1088/0954-3899/42/11/115104`. arXiv: `1309.1657` (cit. on pp. 22, 43, 160, 174, 201, 217, 221–222).

[Sen+17] F. Senzel et al. “The different energy loss mechanisms of inclusive and b-tagged reconstructed jets within ultra-relativistic heavy-ion collisions”. In: *Phys. Lett. B* 773 (Oct. 2017), pp. 620–624. DOI: `10.1016/j.physletb.2017.09.022`. arXiv: `1602.05086` (cit. on pp. 26, 43, 160, 216).

[Sen12] F. Senzel. “Rekonstruktion hochenergetischer Teilchenschauer innerhalb eines partonischen Transportmodells”. MA thesis. Goethe University Frankfurt, 2012 (cit. on pp. 43, 160).

[SGJ09] B. Schenke, C. Gale, and S. Jeon. “MARTINI: An event generator for relativistic heavy-ion collisions”. In: *Phys. Rev. C* 80.5 (Nov. 2009), p. 054913. DOI: `10.1103/PhysRevC.80.054913` (cit. on pp. 51, 115–116, 118–119, 121–122, 209).

[SGQ09] B. Schenke, C. Gale, and G.-Y. Qin. “Evolving distribution of hard partons traversing a hot, strongly interacting plasma”. In: *Phys. Rev. C* 79.5 (May 2009), p. 054908. DOI: `10.1103/PhysRevC.79.054908` (cit. on pp. 51, 121, 125).

[Shi10] S. Shi. “Event anisotropy v_2 at STAR”. PhD thesis. 2010, p. 125 (cit. on p. 12).

[SJG10a] B. Schenke, S. Jeon, and C. Gale. “Elliptic and triangular flow in event-by-event (3+1)D viscous hydrodynamics”. In: *Phys. Rev. Lett.* 106.4 (Sept. 2010), p. 042301. DOI: `10.1103/PhysRevLett.106.042301`. arXiv: `1009.3244` (cit. on p. 51).

[SJG10b] B. Schenke, S. Jeon, and C. Gale. “(3+1)D hydrodynamic simulation of relativistic heavy-ion collisions”. In: *Phys. Rev. C* 82.1 (July 2010), p. 014903. DOI: `10.1103/PhysRevC.82.014903` (cit. on p. 51).

[SJG11] B. Schenke, S. Jeon, and C. Gale. “Anisotropic flow in $\sqrt{s_{\mathrm{NN}}}$=2.76 TeV Pb+Pb collisions at the LHC”. In: *Phys. Lett. B* 702.1 (Feb. 2011), pp. 59–63. DOI: `10.1016/j.physletb.2011.06.065`. arXiv: `1102.0575` (cit. on pp. 12, 16–17, 209).

[SJG12] B. Schenke, S. Jeon, and C. Gale. “Higher flow harmonics from 3+1D event-by-event viscous hydrodynamics”. In: *Phys. Rev. C* 85.2 (Feb. 2012), p. 024901. DOI: `10.1103/PhysRevC.85.024901` (cit. on p. 51).

[SMS06] T. Sjöstrand, S. Mrenna, and P. Skands. "PYTHIA 6.4 physics and manual". In: *J. High Energy Phys.* 2006.05 (May 2006), pp. 026–026. DOI: `10.1088/1126-6708/2006/05/026`. arXiv: `0603175 [hep-ph]` (cit. on pp. 50, 160–161).

[SMS08] T. Sjöstrand, S. Mrenna, and P. Skands. "A brief introduction to PYTHIA 8.1". In: *Comput. Phys. Commun.* 178.11 (June 2008), pp. 852–867. DOI: `10.1016/j.cpc.2008.01.036` (cit. on p. 160).

[Sne11] R. Snellings. "Elliptic flow: a brief review". In: *New J. Phys.* 13.5 (May 2011), p. 055008. DOI: `10.1088/1367-2630/13/5/055008`. arXiv: `1102.3010` (cit. on p. 15).

[SS07] G. P. Salam and G. Soyez. "A practical seedless infrared-safe cone jet algorithm". In: *J. High Energy Phys.* 2007.05 (May 2007), pp. 086–086. DOI: `10.1088/1126-6708/2007/05/086` (cit. on p. 21).

[SST19] B. Schenke, C. Shen, and P. Tribedy. "Features of the IP-Glasma". In: *Nucl. Phys. A* 982 (Feb. 2019), pp. 435–438. DOI: `10.1016/j.nuclphysa.2018.08.015` (cit. on p. 178).

[STA03] STAR Collaboration. "Evidence from d+Au measurements for final-state suppression of high p_T hadrons in Au+Au collisions at RHIC". In: *Phys. Rev. Lett.* 91.7 (June 2003), p. 072304. DOI: `10.1103/PhysRevLett.91.072304`. arXiv: `0306024 [nucl-ex]` (cit. on p. 18).

[STA05] STAR Collaboration. "Distributions of Charged Hadrons Associated with High Transverse Momentum Particles in pp and Au+Au Collisions at $\sqrt{s}_{\mathrm{NN}}$ =200 GeV". In: *Phys. Rev. Lett.* 95.15 (Jan. 2005), p. 152301. DOI: `10.1103/PhysRevLett.95.152301`. arXiv: `0501016 [nucl-ex]` (cit. on p. 18).

[Stö+15] H. Stöcker et al. "Under-saturation of quarks at early stages of relativistic nuclear collisions: The hot glue initial scenario and its observable signatures". In: *Astron. Nachrichten* 336.8-9 (Nov. 2015), pp. 744–748. DOI: `10.1002/asna.201512252`. arXiv: `1509.07682` (cit. on p. 189).

[Sto+16] H. Stoecker et al. "Glueballs amass at the RHIC and LHC! The early quarkless first-order phase transition at T = 270 MeV—from pure Yang–Mills glue plasma to Hagedorn glueball states". en. In: *J. Phys. G Nucl. Part. Phys.* 43.1 (Aug. 2016), p. 015105. DOI: `10.1088/0954-3899/43/1/015105` (cit. on p. 189).

[STV12a] B. Schenke, P. Tribedy, and R. Venugopalan. "Event-by-event gluon multiplicity, energy density, and eccentricities in ultrarelativistic heavy-ion collisions". In: *Phys. Rev. C* 86.3 (Sept. 2012), p. 034908. DOI: `10.1103/PhysRevC.86.034908` (cit. on pp. 12, 17, 209).

[STV12b] B. Schenke, P. Tribedy, and R. Venugopalan. "Event-by-event gluon multiplicity, energy density, and eccentricities in ultrarelativistic heavy-ion collisions". In: *Phys. Rev. C* 86.3 (Sept. 2012), p. 034908. DOI: `10.1103/PhysRevC.86.034908` (cit. on p. 51).

[STV12c] B. Schenke, P. Tribedy, and R. Venugopalan. "Fluctuating Glasma Initial Conditions and Flow in Heavy Ion Collisions". In: *Phys. Rev. Lett.* 108.25 (June 2012), p. 252301. DOI: `10.1103/PhysRevLett.108.252301` (cit. on pp. 12, 17, 178, 209).

[Sve88] B. Svetitsky. "Diffusion of charmed quarks in the quark-gluon plasma". In: *Phys. Rev. D* 37.9 (May 1988), pp. 2484–2491. DOI: `10.1103/PhysRevD.37.2484` (cit. on pp. 90–92).

[SW02] C. A. Salgado and U. A. Wiedemann. “Dynamical Scaling Law for Jet Tomography”. In: *Phys. Rev. Lett.* 89.9 (Aug. 2002), p. 092303. DOI: `10.1103/PhysRevLett.89.092303` (cit. on pp. 48–49, 140).

[SW03] C. A. Salgado and U. A. Wiedemann. “Calculating quenching weights”. In: *Phys. Rev. D* 68.1 (July 2003), pp. 1–45. DOI: `10.1103/PhysRevD.68.014008`. arXiv: `0302184 [hep-ph]` (cit. on pp. 48–49, 140).

[SW59] A. Salam and J. C. Ward. “Weak and electromagnetic interactions”. In: *Nuovo Cim.* 11.4 (Feb. 1959), pp. 568–577. DOI: `10.1007/BF02726525` (cit. on p. 6).

[Tan+18] M. Tanabashi et al. “Review of Particle Physics”. In: *Phys. Rev. D* 98.3 (Aug. 2018), p. 030001. DOI: `10.1103/PhysRevD.98.030001` (cit. on pp. 6, 9, 26).

[Tur+05] S. Turbide et al. “Energy loss of leading hadrons and direct photon production in evolving quark-gluon plasma”. In: *Phys. Rev. C* 72.1 (July 2005), p. 014906. DOI: `10.1103/PhysRevC.72.014906` (cit. on pp. 49, 51, 115–116).

[Tur06] S. Turbide. “Electromagnetic radiation from matter under extreme conditions”. PhD thesis. 2006 (cit. on pp. 115–116, 118–119, 121).

[Uph+10] J. Uphoff et al. “Heavy-quark production in ultrarelativistic heavy-ion collisions within a partonic transport model”. In: *Phys. Rev. C* 82.4 (Oct. 2010), p. 044906. DOI: `10.1103/PhysRevC.82.044906` (cit. on pp. 26, 42, 178).

[Uph+11] J. Uphoff et al. “Elliptic flow and energy loss of heavy quarks in ultrarelativistic heavy ion collisions”. In: *Phys. Rev. C* 84.2 (Aug. 2011), p. 024908. DOI: `10.1103/PhysRevC.84.024908` (cit. on pp. 26, 42, 232).

[Uph+12] J. Uphoff et al. “Open heavy flavor in Pb+Pb collisions at $\sqrt{s_{\mathrm{NN}}}$=2.76 TeV within a transport model”. In: *Phys. Lett. B* 717.4-5 (May 2012), pp. 430–435. DOI: `10.1016/j.physletb.2012.09.069`. arXiv: `1205.4945` (cit. on pp. 26, 38, 56, 58, 185, 198–199).

[Uph+13] J. Uphoff et al. “Momentum imbalance of D mesons in ultra-relativistic heavy-ion collisions at LHC”. In: *Phys. Rev. C* 89.6 (Oct. 2013), p. 064906. DOI: `10.1103/PhysRevC.89.064906`. arXiv: `1310.1340` (cit. on p. 43).

[Uph+14] J. Uphoff et al. “Elastic and radiative heavy quark interactions in ultra-relativistic heavy-ion collisions”. In: *J. Phys. G Nucl. Part. Phys.* 42.11 (Aug. 2014), pp. 1–18. DOI: `10.1088/0954-3899/42/11/115106`. arXiv: `1408.2964` (cit. on pp. 26, 30, 42, 86, 232).

[Uph+15] J. Uphoff et al. “Elliptic Flow and Nuclear Modification Factor in Ultrarelativistic Heavy-Ion Collisions within a Partonic Transport Model”. In: *Phys. Rev. Lett.* 114.11 (Mar. 2015), p. 112301. DOI: `10.1103/PhysRevLett.114.112301`. arXiv: `1401.1364` (cit. on pp. 30, 41–42, 62, 178–180, 182, 193, 195, 199, 206).

[Uph09] J. Uphoff. “Produktion von schweren Quarks in ultrarelativistischen Schwerionenkollisionen”. MA thesis. 2009 (cit. on p. 178).

[Uph13] J. Uphoff. “Open heavy flavor and other hard probes in ultra-relativistic heavy-ion collisions”. PhD thesis. 2013 (cit. on pp. 26, 30–34, 42, 57, 59, 62, 178, 181, 232, 235).

[VZ96] S. Voloshin and Y. Zhang. “Flow study in relativistic nuclear collisions by Fourier expansion of azimuthal particle distributions”. In: *Zeitschrift für Phys. C Part. Fields* 70.4 (May 1996), pp. 665–671. DOI: `10.1007/s002880050141`. arXiv: `9407282 [hep-ph]` (cit. on pp. 14–15, 193).

[Wei+16] J. Weil et al. “Particle production and equilibrium properties within a new hadron transport approach for heavy-ion collisions”. In: *Phys. Rev. C* 94.5 (Nov. 2016), p. 054905. DOI: `10.1103/PhysRevC.94.054905` (cit. on p. 13).

[Wei05] H. Weigert. “Evolution at small : The color glass condensate”. In: *Prog. Part. Nucl. Phys.* 55.2 (Oct. 2005), pp. 461–565. DOI: `10.1016/j.ppnp.2005.01.029` (cit. on p. 178).

[Wei67] S. Weinberg. “A Model of Leptons”. In: *Phys. Rev. Lett.* 19.21 (Nov. 1967), pp. 1264–1266. DOI: `10.1103/PhysRevLett.19.1264` (cit. on p. 6).

[Wei95] S. Weinberg. *The Quantum Theory of Fields - Volume 1: Foundations*. Cambridge University Press, June 1995. DOI: `10.1017/CBO9781139644167` (cit. on p. 6).

[Wei96] S. Weinberg. *The Quantum Theory of Fields - Volume 2: Modern applications*. Cambridge University Press, Aug. 1996. DOI: `10.1017/CBO9781139644174` (cit. on p. 6).

[Wes+11] C. Wesp et al. “Calculation of shear viscosity using Green-Kubo relations within a parton cascade”. In: *Phys. Rev. C* 84.5 (Nov. 2011), p. 054911. DOI: `10.1103/PhysRevC.84.054911` (cit. on p. 41).

[WG01] X.-N. Wang and X. Guo. “Multiple parton scattering in nuclei: parton energy loss”. In: *Nucl. Phys. A* 696.3-4 (Dec. 2001), pp. 788–832. DOI: `10.1016/S0375-9474(01)01130-7`. arXiv: `0102230 [hep-ph]` (cit. on p. 49).

[WG91] X.-N. Wang and M. Gyulassy. “HIJING: A Monte Carlo model for multiple jet production in p p, p A and A A collisions”. In: *Phys. Rev. D* 44.11 (Dec. 1991), pp. 3501–3516. DOI: `10.1103/PhysRevD.44.3501` (cit. on p. 198).

[Wie00a] U. A. Wiedemann. “Gluon radiation off hard quarks in a nuclear environment: opacity expansion”. In: *Nucl. Phys. B* 588.1-2 (Nov. 2000), pp. 303–344. DOI: `10.1016/S0550-3213(00)00457-0`. arXiv: `0005129 [hep-ph]` (cit. on pp. 47–49).

[Wie00b] U. A. Wiedemann. “Transverse dynamics of hard partons in nuclear media and the QCD dipole”. In: *Nucl. Phys. B* 582.1-3 (Aug. 2000), pp. 409–450. DOI: `10.1016/S0550-3213(00)00286-8`. arXiv: `0003021 [hep-ph]` (cit. on p. 48).

[Wie01] U. A. Wiedemann. “Jet quenching versus jet enhancement: a quantitative study of the BDMPS-Z gluon radiation spectrum”. In: *Nucl. Phys. A* 690.4 (July 2001), pp. 731–751. DOI: `10.1016/S0375-9474(01)00362-1`. arXiv: `0008241 [hep-ph]` (cit. on p. 48).

[Wie09] U. A. Wiedemann. “Jet Quenching in Heavy Ion Collisions”. In: (2009), p. 41. arXiv: `0908.2306` (cit. on pp. 17, 45, 48–49).

[Wob00] M. Wobisch. “Measurement and QCD analysis of jet cross sections in deep-inelastic positron proton collisions at $\sqrt{s} = 300$ GeV”. PhD thesis. 2000 (cit. on p. 21).

[Won96] S. M. H. Wong. “Thermal and chemical equilibration in relativistic heavy ion collisions”. In: *Phys. Rev. C* 54.5 (Nov. 1996), pp. 2588–2599. DOI: `10.1103/PhysRevC.54.2588` (cit. on pp. 28, 185).

[WW99] M. Wobisch and T. Wengler. “Hadronization Corrections to Jet Cross Sections in Deep-Inelastic Scattering”. In: *Monte Carlo Gener. HERA physics. Proceedings, Work. Hamburg, Ger. 1998-1999*. July 1999, pp. 270–279. arXiv: `9907280 [hep-ph]` (cit. on p. 21).

[WZ13] X.-N. Wang and Y. Zhu. “Medium Modification of γ Jets in High-Energy Heavy-Ion Collisions”. In: *Phys. Rev. Lett.* 111.6 (Aug. 2013), p. 062301. DOI: `10.1103/PhysRevLett.111.062301` (cit. on p. 51).

[XG05] Z. Xu and C. Greiner. “Thermalization of gluons in ultrarelativistic heavy ion collisions by including three-body interactions in a parton cascade”. In: *Phys. Rev. C* 71.6 (June 2005), p. 064901. DOI: `10.1103/PhysRevC.71.064901`. arXiv: `0406278 [hep-ph]` (cit. on pp. 34, 37, 39–41, 178, 180, 185, 198).

[XG07] Z. Xu and C. Greiner. “Transport rates and momentum isotropization of gluon matter in ultrarelativistic heavy-ion collisions”. In: *Phys. Rev. C* 76.2 (Aug. 2007), p. 024911. DOI: `10.1103/PhysRevC.76.024911` (cit. on pp. 34, 37, 41, 178, 180).

[XG08] Z. Xu and C. Greiner. “Shear viscosity in a gluon gas.” In: *Phys. Rev. Lett.* 100.17 (May 2008), p. 172301. DOI: `10.1103/PhysRevLett.100.172301` (cit. on p. 41).

[XG09] Z. Xu and C. Greiner. “Elliptic flow of gluon matter in ultrarelativistic heavy-ion collisions”. In: *Phys. Rev. C* 79.1 (Jan. 2009), p. 014904. DOI: `10.1103/PhysRevC.79.014904` (cit. on pp. 41, 180–181).

[XG10] Z. Xu and C. Greiner. “Dependence of elliptic flow on number of parton degrees of freedom”. In: *Phys. Rev. C* 81.5 (May 2010), p. 054901. DOI: `10.1103/PhysRevC.81.054901` (cit. on pp. 41, 180).

[XGS08] Z. Xu, C. Greiner, and H. Stöcker. “Perturbative QCD Calculations of Elliptic Flow and Shear Viscosity in $\sqrt{s}$=200GeV”. In: *Phys. Rev. Lett.* 101.8 (Aug. 2008), p. 082302. DOI: `10.1103/PhysRevLett.101.082302` (cit. on pp. 41, 180, 198).

[Xu04] Z. Xu. “Thermalization of gluons in ultrarelativistic heavy ion collisions by including three-body interactions in a parton cascade”. PhD thesis. 2004 (cit. on pp. 12, 38–39, 180).

[You+11a] C. Young et al. “Dijet asymmetry at the energies available at the CERN Large Hadron Collider”. In: *Phys. Rev. C* 84.2 (Aug. 2011), p. 024907. DOI: `10.1103/PhysRevC.84.024907`. arXiv: `1103.5769` (cit. on pp. 22, 51, 115, 222).

[You+11b] C. Young et al. “Monte-Carlo simulation of jets in heavy-ion collisions”. In: (Sept. 2011), pp. 1–6. arXiv: `1109.5992` (cit. on p. 51).

[You+12] C. Young et al. “MARTINI event generator for heavy quarks: Initialization, parton evolution, and hadronization”. In: *Phys. Rev. C* 86.3 (Sept. 2012), p. 034905. DOI: `10.1103/PhysRevC.86.034905`. arXiv: `1111.0647` (cit. on p. 51).

[You+13] C. Young et al. “Realistic modelling of jets in heavy-ion collisions”. In: *Nucl. Phys. A* 910-911 (2013), pp. 494–497. DOI: `10.1016/j.nuclphysa.2012.12.112`. arXiv: `arXiv:1209.5679v1` (cit. on pp. 51, 209).

[Zak96a] B. G. Zakharov. “Landau-Pomeranchuk-Migdal effect for finite-size targets”. In: *J. Exp. Theor. Phys. Lett.* 64.11 (Dec. 1996), pp. 781–787. DOI: `10.1134/1.567248` (cit. on pp. 46–47).

[Zak96b] B. G. Zakharov. “Fully quantum treatment of the Landau–Pomeranchuk–Migdal effect in QED and QCD”. In: *J. Exp. Theor. Phys. Lett.* 63.12 (July 1996), pp. 952–957. DOI: `10.1134/1.567126`. arXiv: `9607440 [hep-ph]` (cit. on pp. 46–47).

[Zak97] B. G. Zakharov. “Radiative energy loss of high energy quarks in finite-size nuclear matter and quark-gluon plasma”. In: *J. Exp. Theor. Phys. Lett.* 65.8 (Apr. 1997), pp. 615–620. DOI: `10.1134/1.567389`. arXiv: `9704255 [hep-ph]` (cit. on pp. 46–47, 130).

[Zap08] K. C. Zapp. “A Monte Carlo Model for Jet Evolution With Energy Loss”. PhD thesis. 2008 (cit. on p. 233).

[Zap14] K. C. Zapp. “Geometrical aspects of jet quenching in JEWEL”. In: *Phys. Lett. B* 735 (July 2014), pp. 157–163. DOI: `10.1016/j.physletb.2014.06.020`. arXiv: `1312.5536` (cit. on pp. 50, 233).

[Zee10] A. Zee. *Quantum Field Theory in a Nutshell*. 2010 (cit. on p. 6).

[ZKW13] K. C. Zapp, F. Krauss, and U. A. Wiedemann. “A perturbative framework for jet quenching”. In: *J. High Energy Phys.* 2013.3 (Mar. 2013), p. 80. DOI: `10.1007/JHEP03(2013)080`. arXiv: `1212.1599` (cit. on pp. 47, 50, 56, 76).

[ZSW09] K. Zapp, J. Stachel, and U. A. Wiedemann. “Local Monte Carlo implementation of the non-Abelian Landau-Pomeranschuk-Migdal effect.” In: *Phys. Rev. Lett.* 103.1 (Oct. 2009), p. 152302. DOI: `10.1103/PhysRevLett.103.152302`. arXiv: `0812.3888` (cit. on pp. xv, 50, 68, 226).

[ZSW11] K. C. Zapp, J. Stachel, and U. A. Wiedemann. “A local Monte Carlo framework for coherent QCD parton energy loss”. In: *J. High Energy Phys.* 2011.7 (July 2011), p. 118. DOI: `10.1007/JHEP07(2011)118`. arXiv: `1103.6252` (cit. on pp. xv, 50, 68–71, 73–74, 226).

[ZW12] K. C. Zapp and U. A. Wiedemann. “Coherent radiative parton energy loss beyond the BDMPS-Z limit”. In: *Eur. Phys. J. C* 72.6 (June 2012), p. 2028. DOI: `10.1140/epjc/s10052-012-2028-8`. arXiv: `1202.1192` (cit. on pp. 50, 68, 226).

[Zwe64] G. Zweig. “An SU(3) model for strong interaction symmetry and its breaking”. In: *Cern Rep. 8182/TH-401* (1964), p. 2 (cit. on p. 7).

Danksagung

Moderne Wissenschaft beruht nicht auf den Leistungen Einzelner, sondern kann nur durch das Zusammenspiel vieler, unterschiedlicher Menschen gelingen. Daher möchte ich mich bei folgenden Menschen, die mich auf meinem Weg unterstützt haben, bedanken:

- Zunächst möchte ich mich bei Prof. Dr. Carsten Greiner, der mich seit meiner Masterarbeit wissenschaftlich begleitet hat, für die langjährige Zusammenarbeit und die Betreuung dieser Dissertation bedanken. Er hat mir in den vielen Phasen dieser Zusammenarbeit immer Vertrauen geschenkt und mir den notwendigen Freiraum für meine Forschung gegeben. Diese gemeinsamen, wissenschaftlichen Lehrjahre weiß ich sehr zu schätzen.

- Weiterhin möchte ich mich bei Prof. Dr. Hannah Elfner für die Erstellung des Zweitgutachtens dieser Arbeit bedanken.

- Ein besonderer Dank geht an Dr. Moritz Greif und Jan Fotakis, die Teile dieser doch recht lang gewordenen Dissertation Korrektur gelesen haben und mir wichtiges Feedback dazu gegeben haben.

- Des Weiteren möchte ich mich bei allen aktuellen und ehemaligen Mitgliedern der "AG Greiner" bedanken, mit denen ich im Büro gearbeitet habe, mit denen ich zu verschiedenen Konferenzen in aller Welt gereist bin, mit denen ich in unzähligen Meetings und Palavern fachlich diskutiert habe, mit denen ich bei jeder sich mir bietenden Gelegenheit (politisch) gestritten habe und auch mit denen ich abends bei dem ein oder anderen Bierchen gefeiert habe.

- Dem Team der Graduiertenschule HGS-HIRe und im Besonderen Prof. Dr. Henner Büsching und Dr. Gerhard Burau möchte ich für ihren Einsatz für die strukturierte Ausbildung von Doktoranden danken, durch die mir sowohl wichtiges Wissen über die Physik als auch das gesamte, berufliche Leben vermittelt wurde.

- Danken möchte ich auch allen meinen Freunden, die ich im Studium bzw. während der Promotion kennengelernt habe. Auch wenn sich viele unserer Wege vorerst getrennt haben, so verbinden uns doch die Erinnerungen an schöne, gemeinsame Zeiten. Vielen Dank an Fritz, Timo, Heidi, Claudi, Jan, Olli, Seve, Pascal, Theo, Sarah, Lenny, Achim und viele Andere für all diese unvergessenen Momente.

Ein umfangreiches Projekt wie die vorliegende Dissertation ist häufig so einnehmend, dass mir leider die Trennung zwischen Wissenschaft und Privatem oft schwer gefallen ist. Deshalb möchte ich zu guter Letzt den Menschen danken, die mich auch außerhalb der Universität bei jeder sich bietenden Gelegenheit unterstützt haben und dabei das Zustandekommen dieser Arbeit maßgeblich ermöglicht haben.

Da jede Reise zunächst mit dem ersten Schritt beginnt, möchte ich meinen Eltern sehr dafür danken, dass sie mir gezeigt haben auf was es im Leben ankommt und dass ich mich vorbehaltlos zu jeder Zeit auf sie verlassen kann. Erst diese Orientierung und eure Unterstützung hat mich so weit kommen lassen!

Der größte Dank geht an meine Ehefrau Carina und meine Töchter Sophia und Katharina. Nur ihr wisst, wie wichtig mir diese Arbeit als Prüfung an mich selbst war. Danke dafür, dass ihr mit mir zusammen durch diese für uns anstrengende Zeit gegangen seid und dass ihr mich dabei uneingeschränkt unterstützt und an mich geglaubt habt. Gleichzeitig möchte ich euch aber auch um Entschuldigung dafür bitten, dass ich viel zu häufig am Wochenende "an Papas Buch" geschrieben habe und dass ich es euch leider oft hab spüren lassen, wenn es mal wieder nicht so funktioniert hat. Genau in diesen Momenten habt ihr mir gezeigt, wie unwichtig scheinbar Wichtiges ist und dass am Ende doch alles gut werden wird. Ohne dieses Vertrauen und eure Liebe hätte ich diese Prüfung nicht geschafft. Danke, dass es euch gibt!